Microstructural Characterization and Mechanical Properties of Super 13% Cr Steel

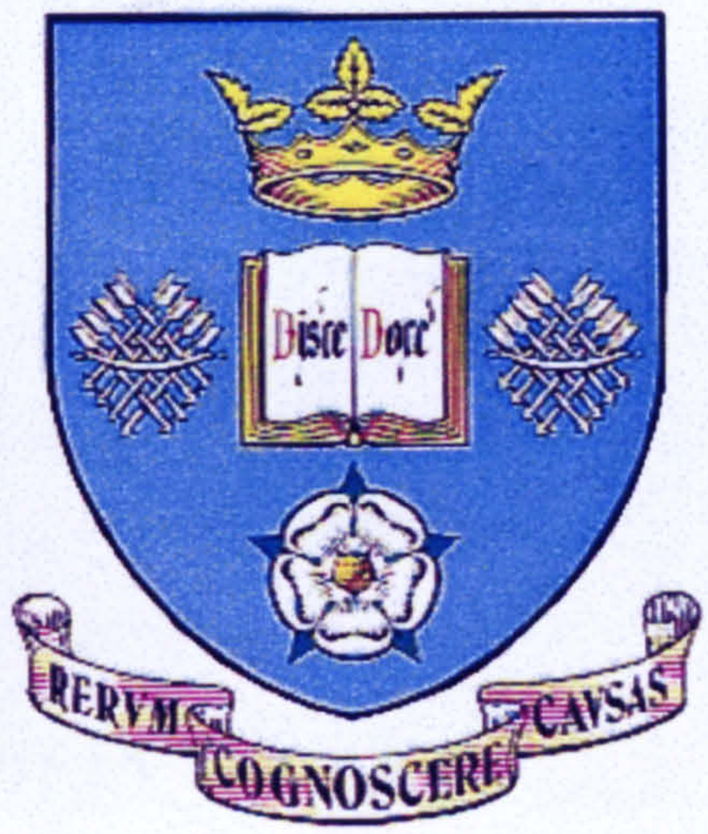

Yun Wei

Thesis submitted for the Degree of Doctor of Philosophy

Department of Engineering Materials
The University of Sheffield

August 2005

Abstract

Super 13% Cr steels are used for offshore applications and have to meet strict tensile strength, yield strength, toughness, elongation, and hardness specifications. The mechanical properties of these steels are strongly dependent on the proportions of retained austenite and martensite, and consequently small changes in heat treatment parameters result in major changes in properties. In this work, a detailed investigation of the effect of heat treatment parameters on microstructural features, hardness and tensile properties of the commercial supermartensitic 13Cr-5Ni-2Mo steels in the as-received and re-heat treated state were undertaken. The re-heat treatment was performed by re-austenitising the samples at 950 °C for 2 h, air-cooling, and then tempering (single and double temper) in the range of 550–700 °C. The effects of tempering temperature, time, and their combination P ($P = (273+T\,(°C) \times (40 + \log_{10} t\,(h)) \times 1000^{-1}$), the Holloman-Jaffe parameter, on retained austenite volume fraction, hardness and tensile properties were investigated. Retained austenite content increased with P to a peak value at P~36.9 and then decreased due to the formation of fresh martensite. However, the second temper increased retained austenite due to the re-transformation of fresh martensite to austenite. This resulted in refined grain size and a high dislocation density. An increase in P gave a decrease in the C and Ni content in austenite on tempering while the austenite grain size increased. The combination of these two effects led to a decrease in the stability of the retained austenite with P, as shown by the increased M_s. For the first temper at P >36.9, the austenite present after the second temper was more stable than after the first temper as a result of re-distribution of C and Ni from the martensite to the austenite. 0.2% proof strength and hardness were inversely related to retained austenite content with P. Both hardness and 0.2% proof strength decreased linearly with increase in retained austenite content, but elongation showed the reverse trend. However, the slope of the relationships depended on whether fresh martensite was present or not. The results have shown that retained austenite with volume fraction between 16-30 vol% and size <208 nm gives the optimum combination of strength, ductility and hardness.

Acknowledgements

First I would like to express my sincere gratitude to my supervisor Professor W. Mark Rainforth for the opportunity to study at The University of Sheffield and his advice and support throughout the course of this work.

I gratefully acknowledge the financial support provided by the Materials Forum and the University of Sheffield. Special thanks go to Dr. Mike Frolish as Materials Forum Fellow for his assistance of the Materials Forum Progress Meetings.

Thanks are due to Corus Engineering Steels for the provision of the research materials. I would also like to thank the industrial members of the Materials Forum Meeting from Corus, in particular Dr. Peter Morris and Dr. Richard Williams of STC, and Doctors Nina Cardinal, Cathy Bell and Martin Worrall of CES for the suggestions and the valuable discussions during the Progress Meetings. Their comments on the work are much appreciated. Thanks must also go to Dr. Dominique Carrouge of Corus UK Ltd. for sending me very useful references and Dr. John Butler of STC for his help in MT DATA calculation.

I would like to express my appreciation to the technical staff of the Department of Engineering Materials for their assistance, in particular Dr Peter Korgul, Mr. Heath Bagshaw and Miss Down Bussey for the training of microscopes. Thanks are also given to my friends in the Department of Engineering Materials and other friends in Sheffield who have made my time so pleasure.

Last, but not least, I would like to thank my parents and my husband Jun Fu for their endless encouragement and support.

Nomenclature and Abbreviations

γ	Austenite
γ_T	Austenite that formed at the tempering temperature
γ'	Retained austenite
α	Ferrite
δ-ferrite	Delta-ferrite
α'	Martensite
α_T'	Tempered martensite
α_F'	Fresh martensite
Ac_1	Austenite formation start temperature on heating
Ac_3	Austenite formation complete on heating
Ms	Martensite-start temperature
M_F	Martensite-finish temperature
σ_y	Yield stress (Yield strength)
d	Average particle/lath width
P	The Hollomon-Jaffe tempering time-temperature parameter
fcc	Face-centred cubic
bcc	Body-centred cubic
XRD	X-ray diffraction
SEM	Scanning electron microscopy
SEI	Secondary electron imaging
BEI	Backscattered electron imaging
TEM	Transmission electron microscopy
SAD	Selected area diffraction
EDX	Energy dispersive X-ray analysis
EDS	Energy dispersive X-ray spectroscopy
MT DATA	Metallurgical and thermochemical databank
h	Hour
T	Temperature
UTS	Ultimate tensile strength

Contents

Chapter 1 Introduction

Offshore oil and gas industries require materials that can withstand the most aggressive environments and are totally reliable. These demands are admirably met by a new family of steels, known as "super 13% Cr steels" or "supermartensitic stainless steels", which have the necessary combined high strength, high toughness and good corrosion resistance. The steels have been applied in increasing quantities to replace traditional 13%Cr martensitic steels and duplex stainless steels in offshore industries.

The properties of super 13% Cr steels are achieved by a quenching and tempering heat treatment carried out after hot working. Figure 1.1 gives schematic of the heat treatment cycles applied to super 13% Cr steels. The microstructure after the two-stage tempering is composed of a mixture of low-carbon martensite and retained austenite, obtained by tempering above the A_{c1} temperature. The volume fraction of retained austenite has a significant effect on the mechanical properties. For a given chemical composition, the volume fraction of retained austenite depends on tempering temperature and time, with temperature the most important parameter. However, these steels have low transformation temperatures (A_{c1}, M_S, M_F), which impose constraints on heat treatment. This, and the multiple heat treatment cycles used, result in complex microstructure which consists of tempered martensite, retained austenite, δ-ferrite, carbides/carbonitrides, and probably fresh martensite. Even small variations in process parameters can have significant variations in phase proportions and consequently major changes in the resultant mechanical properties. In practice, the toughness, tensile strength and elongation specifications can be achieved relatively easily. However, the yield strength and hardness requirements are much more difficult to achieve, with only a narrow range allowed. These impose a serious problem for industrial scale processing to achieve consistent mechanical properties in a repeatable manner.

The stability of the austenite is greatest when formed during tempering at a temperature slightly above the A_{c1}. It does not transform back to martensite on

cooling to room temperature, and forms a key attribute of the microstructure with benefits to weldability and toughness. If this temperature range is exceeded, the austenite formed is not stable, and will partially or completely (depending on tempering temperature) transforms to fresh martensite on cooling to room temperature, resulting in adverse mechanical properties. Thus, the temperature at which the austenite is formed is crucial in determining mechanical properties.

Super 13% Cr steels are relatively new steels and research is required to fully understand and further develop these alloys for the needs of offshore engineering. However, most of investigations have centred on the corrosion and weldability performance (Linne et al. 1997, Miyata et al. 1997, Kimura et al. 1999, Rhodes 2001), and little work has been undertaken to understand the physical basis for the observed mechanical properties. It is clearly important to understand the metallurgy and heat treatment of this class of steel, to correlate microstructural features with mechanical properties and to satisfy the required specifications for offshore application.

The purpose of this work was to characterise the microstructures of the hardened and tempered martensitic stainless steel 13Cr5Ni2Mo, in particular to understand the origin of the stability of retained austenite, to correlate this with mechanical properties (hardness and tensile properties) and thereby optimize microstructure for consistent mechanical properties. The investigations addressed specific aspects and employed techniques, as follows:

- Characterise and quantify microstructural constituents of retained austenite, tempered martensite, fresh martensite, δ-ferrite, and precipitate particles using optical microscopy, SEM, TEM and XRD.

- Assess the variation of microstructural constituents with changes in heat treatment parameters (harden, one-stage temper, and two-stage temper) in controlled laboratory heat treatment furnace. Establish the relationships between tempering temperature/time and retained austenite volume fraction, hardness and tensile properties. The Hollomon-Jaffe tempering time-temperature parameter P

$= (273 + T(°C) \times (C + \log_{10} t\,(h)) \times 1000^{-1}$ was employed to study the combined effect of temperature and time on retained austenite content, hardness and yield strength.

- Correlate microstructural features (retained austenite amount and size, fresh martensite) and mechanical properties. Establish relationships between retained austenite amount and mechanical properties (hardness and tensile properties). The relation $\sigma = \sigma_0 + k\, d^{-n}$ was employed to study the effect of retained austenite particle size on yield strength.

- Relating the industrial properties to the laboratory based trials and implications for commercial practice. Explore the optimum retained austenite amount and size, and try to derive the accurate heat treatment parameters for the combination of mechanical properties required for commercial steel bars.

Chapter 2 Literature Review

2.1 Supermartensitic stainless steels

2.1.1 Introduction

The offshore oil and gas industry requires materials that can withstand the most aggressive environments and are totally reliable, i.e. have to meet strict yield strength, tensile strength, toughness and hardness specifications without losing corrosion resistance. The corrosion environments are characterized by high temperature, partial pressure of CO_2 and a high concentration of chloride irons and in some case the small amount of H_2S (Scnmitt 1983, Amaya et al. 2003). Therefore, improving CO_2 corrosion resistance and sulphide stress cracking (SSC) resistance has become a key target for steels used in these fields. Duplex ferritic-austenitic stainless steels have been used in these conditions for some years due to their high corrosion resistance and high strength. However, they are fairly expensive and raise production costs (Miyata et al. 1998). Conventional mrartensitic 13%Cr stainless steels show appropriate CO_2 corrosion resistance, and are comparatively low in cost. However, they do not have adequate resistance to SSC in a CO_2 environment and less resistant to general and localized corrosion at elevated temperatures, thereby causing their usage to be restricted (Kimura et al. 1998, Amaya et al. 2003). To satisfy the requirements of offshore engineering, a new type of steels were required that could offer (Dufrane 1999):

a. High corrosion resistance in CO_2 and H_2S environments;
b. High toughness to meet offshore design temperatures; high strength;
c. Good weldability using industrial welding techniques;
d. Low cost and availability of industrial components such as seamless and welded pipes.

To achieve this optimum combination of mechanical properties, corrosion resistance, and competitive costs for the need of oil and gas fields, a number of supermartensitic

stainless steels have been developed in the mid 1990's to replace traditional 13%Cr martensitic steels and duplex stainless steels in offshore engineering (Ueda et al. 1994, Farrar 1998, Bhavsar 1998, and Gooch et al. 1999). This type of steels is also called "super 13% Cr steels" or "weldable martensitic stainless steels". The major production is oil country tubular goods (OCTG), such as tubing, used for drilling and production of oil well or gas well; or pipelines, used for transporting oil and gas. They are also used for other purposes such as components of well heads. Potential applications for supermartensitic stainless steels have been opening up in many areas – from oil and gas industry to power generation, chemical process plants, food production and transportation.

2.1.2 Alloy design

2.1.2.1 The Schäffler diagram

The Schäffler diagram is usually used to assess the structure of a stainless steel through its chemical composition. Many researchers have devised correlations of chemical composition with structure to assess the solidification structures from casting or welding, or mechanical working of the materials based on the original Schäffler diagram. However, the basic lines of the Schäffler phase diagram do not move. Figure 2.1 gives a modified Schäffler diagram (Sedriks, 1979), showing the effect of alloying elements on phase constitution of stainless steels after rapid cooling to room temperature from the solution treatment temperature of 1050°C. It is not an equilibrium diagram and was originally established to estimate the δ-ferrite content of welds in austenitic steels. However, it provides a simple, although somewhat approximate, way to relate structure with the composition of stainless steels. The chromium and nickel equivalents in the modified Schäffler diagram are:

$$Cr\ (wt\%) = Cr + 2Si + 1.5Mo + 5V + 5.5\,Al + 1.75Nb + 1.5Ti + 0.75W \quad (2\text{-}1)$$

$$Ni\ (wt\%) = Ni + Co + 0.5Mn + 0.3Cu + 25N + 30C \quad (2\text{-}2)$$

2.1.2.2 Alloy design for supermartensitic steels

As shown in Figure 2.1, the designing of a supermartensitic alloy is a metallurgical balancing act just inside the martensite area of the modified Schäffler diagram, but

almost at the border where ferrite and/or austenite can be formed. The alloy design is driven by the need for good mechanical properties while limiting the alloy cost by using range of ferrite and austenite formers available. At the same time, the desired corrosion properties must be obtained by effectively using a careful mix of the appropriate alloying elements for this purpose. Other fundamental requirements are to reduce C and N for improved weldability and ensure extremely clean steels for getting the good toughness (Winden et al. 2002). As a result, the composition of supermartensitic stainless steels has been developed, which is based around 13%Cr alloys, but containing less than 0.03%C, 11.5~13.5%Cr, 4~6.5%Ni, up to 2.5%Mo, and small amounts (<0.3%) of V, Ti or Nb. The advantages of this alloy design are:

a. The C content is reduced to extra low levels in order to improve CO_2 corrosion resistance and weldability; to obtain good toughness and low hardness.

b. The introduction of Mo, which is the most effective means of improving SSC resistance of 13%Cr.

c. The replacement of C by Ni to promote CO_2 corrosion resistance, toughness and balance Mo to maintain martensitic phase and minimise the formation of δ-ferrite. In addition, the low nickel content makes the steel a cheaper alterative to duplex and superduplex stainless steels.

d. In some grades the addition of small amounts of one or more of the elements of Ti, V and Nb to enhance the SSC resistance, limit secondary hardening, and improve the yield strength and tensile strength levels.

Kondo et al. (1999) have produced a diagram (Figure 2.2) to show the effect of Cr, Ni and Mo on the martensitic single phase when austenitized at 1050 °C. The steel contained 0.01 mass% C, 12-19 mass% Cr, 2-14 mass% Ni, and 0-3 mass% Mo. Figure 2.2 indicates that although Ni is an austenite stabilizer, too greater an addition (>11 mass%) makes the austenite phase too stable such that the retained austenite remains at room temperature because the martensite transformation finishing temperature falls below room temperature. On the other hand, Cr is a ferrite-former, and too much addition of Cr (>18 mass%) results in the formation of δ-ferrite. Mo is also a ferrite-former, and the martensitic single phase region is reduced with

increasing Mo content from 0 to 2 mass% in the steels. As a result, the single phase region for martensite on its own is rather narrow.

Figure 2.3 shows a constitution diagram for supermartensitic weld metals. It was based on the Kaltenhauser Cr and Ni equivalents (Kaltenhauser 1971), and took the different C levels into account. The boundaries between different microstructural regions were defined from microstructure information for a large number of experimental welds. Although this diagram was used to predict weld metal microstructure from chemical composition, it was also found to be very useful in defining the optimum compositions for supermartensitic steels with a varying Mo content (Karlsson et al. 1999).

2.1.2.3 Supermartensitic grades

Three supermartensitic grades: lean, medium, and high, have been gradually developed depending on the environment (CO_2, CO_2 + H_2S) to meet the potential application range of the oil & gas industry (Toussaint and Widen 2001). Table 2.1 lists the composition of some supermartensitic stainless steels produced by manufacturers worldwide to offer their optimal choice for the specific application. It should be noted that the compositions of the various steels may vary in time as developments are still ongoing. The grade designations (lean, medium, high) are only used for guidance as the steels in these groups show in general, a positive correlation with the levels of corrosion resistance, toughness and price.

Table 2.1 Supermartensitic stainless steel grades

Grades	Composition (wt%)									Producer
	C	Mn	Si	Cr	Ni	Mo	Cu	N	Others	
Lean										
X80 11Cr-2Ni	< 0.015	< 2	0.15	11	2	< 0.5	0.4	< 0.012	?	Fabrique De Fer
HP13Cr	< 0.03	0.4	< 0.3	13	4	1	?	0.05	?	Kawasaki
Medium										
D 13.5.2N	0.02	0.7	0.3	13.3	4.8	1.6	0.1	0.08	?	Dalmine
X80 12Cr- 4.5Ni-1.5Mo	< 0.015	< 2	0.15	12	4.5	1.5	0.4	< 0.012	?	Fabrique De Fer
CRS (>95ksi)	0.02	0.5	0.3	12.5	4.5	1.5	1.5	0.05	?	Nippon steel
High										
Super13Cr (12-5-2)	0.02	0.5	0.2	12.2	5.5	2	0.2	0.02	V 0.2	British Steel
Super13Cr (13-5-2)	0.02	0.4	0.2	12.5	5	2	?	< 0.08	?	Sumitomo
Super13Cr13-6-2.5-Ti	< 0.01	0.4	0.3	12	6.2	2.5	?	< 0.01	Ti 0.07	Sumitomo
CRS (>110 ksi)	0.02	0.5	0.3	12.8	5.9	2	1.5	0.02	?	Nippon Steel
X80 12Cr- 6.5Ni-2.5Mo	< 0.015	< 2	0.15	12	6.5	2.5	0.4	< 0.012	?	Fabrique De Fer

(From *http://www.stainless-steel-world.net/supermarten/grades.asp*)

2.1.3 Heat treatment

Supermartensitic grades are commonly used after full heat treatment, but care is required in setting the heat treatment parameters for the combined mechanical and corrosion properties. Like martensitic stainless steels, supermartensitic stainless steels can be austenitic at high temperatures, and at high temperature C is dissolved in the fcc austenite, which in turn is quenched to form a bcc martensitic structure. The heat treatment of supermartensitic stainless steels therefore consists of austenitizing, quenching, and tempering. The austenitizing + quenching process is generally called hardening. A practical aspect for supermartensitic steels is that a full recovery of the mechanical properties can be achieved through a quench and temper cycle (Toussaint and Dufrane 2002). In other words, supermartensitic alloys can tolerate successive heat treatments without losing their original mechanical properties.

2.1.3.1 Hardening

The austenitizing treatment is set to ensure a sufficient combination of time and temperature to produce a fully austenitic structure, and to dissolve carbides. In other words, to dissolve the major secondary phase of carbides, nitrides or carbonitrides, without introducing austenite grain coarsening. Generally the austenitizing temperature for supermartensitic grades is in the range of 900-1050 °C. As shown in Figure 2.4, a complete austenite phase is produced in this temperature range due to the addition of Ni content.

The objective of the quenching process is to completely transform the austenite to martensite for the subsequent tempering treatment. In practice, martensitic stainless steels are usually quenched in oil or water. However, due to the high hardenability of supermartensitic steels, air-cooling may be sufficient to obtain a fully martensitic structure throughout the whole section. Hence sometimes supermartensitic steels are cooled in air. Figure 2.5 shows the continuous cooling transformation (CCT) diagram for the Kawasaki 13Cr6Ni steel, indicating a martensitic structure of matrix is to be expected even after air-cooling (Kvaale and Olsen 1999). Figure 2.6 shows the CCT diagram for supermartensitic three grades. A full martensitic structure is achieved over the whole cooling conditions from water quenching to air cooling (Toussaint

and Dufrane 2002)

.

2.1.3.2 Tempering

When tempering a conventional 13% Cr steel, it is usual to do this below the austenite start formation temperature A_{c1}, in order to prevent localized transformation to austenite, which, on cooling to room temperature may transform into fresh martensite, resulting in a brittle material. On the contrary, supermartensitic 13% Cr steels are tempered at temperature slightly above the A_{c1} temperature to produce a controlled amount of retained austenite in order to improve toughness. However, tight control of temperature is essential. If the tempering temperature is beyond the upper limit, unstable austenite can form, which will partially transform to fresh martensite on cooling to room temperature, resulting in negative effect on mechanical properties.

2.1.3.3 Tempered microstructure

As mentioned above, the purpose of tempering is to produce retained austenite, so that after tempering the phase constitution contains low carbon tempered martensite and retained austenite. However, the microstructure of supermartensitic steels is strongly dependent on tempering conditions (temperatures) and chemical composition. For example, fresh martensite may be present in the structure. Additional phases such as minor δ-ferrite, Cr and Mo rich precipitates may also be present in the tempered microstructure (Rhodes 2001). Figure 2.7 illustrates phase constitution as a function of tempering temperature for a supermartensitic steel 0.023C-13Cr5Ni2Mo (Kimura et al. 2001). After tempering at low temperature (<550 °C), the structure was tempered martensite only, but increasing temperature to above 550 °C, the structure was tempered martensite + retained austenite. A further increase in temperature yielded quenched martensite, i.e. fresh martensite, so that the structure was tempered martensite + retained austenite + fresh martensite, and the amounts of retained austenite and tempered martensite decreased with increasing temperature. When the tempering temperature was much higher (>750 °C), only fresh martensite was present after tempering.

Dual-phase tempered martensite + retained austenite ($\alpha'_T + \gamma'$) is the desirable

structure for tempered supermartensitic steels as it has the advantages of high strength combined with high toughness and good corrosion resistance. δ-ferrite in low carbon CrNiMo martensitic steels forms during casting process or at hot rolling temperatures, so that it is not a product of tempering treatment.

2.1.4 Mechanical properties

2.1.4.1 Strength, toughness and hardness

Supermartensitic grades typical strength values at room temperature are: 550-850 MPa for yield strength (0.2% proof strength), and 780-1000 MPa for tensile strength. For commercial tubular the minimum 0.2% proof strength is 655 MPa (95 ksi) and a preferred upper limit is 800 MPa (116 ksi) (Jackman and Everson 1995). High low-temperature toughness is required to avoid the risk of fracture as the operation often uses cold water. The mechanical properties of three grades of supermartensitic stainless steel: X80 11Cr-2.5Ni (lean alloy); X80 12Cr-4.5Ni-1.5Mo (medium alloy) and X80 12Cr-6.5Ni-2.5Mo (high alloy), produced by CLI-FAFER, are listed in Table 2.2 (Deleu et al. 1999).

Hardness is an important target for martensitic stainless steels used in offshore oil and gas industry. Amaya (2003) pointed out that, on the one hand the maximum hardness of low carbon 13%Cr martensitic stainless steels is restricted since an increase in hardness tends to induce SSC in an environmental containing hydrogen sulphide. On the other hand, however, an increase in the hardness is required to enhance the resistance to corrosive wear. Rhodes (2001) also indicated that SSC risks are yield strength-dependent and generally associated with products having yield strength above the Rockwell C hardness (HRC) limits listed in NACE MR0175 for SSC. The requirements for NACE MR0175 are very dependent on the materials. For example, the hardness limitation for AISI 4000 series are HRC 22 maximum while for 13Cr4Ni steel the limitation is HRC 23. Table 2.3 lists tempering requirements and hardness of some martensitic stainless steels specified in NACE MR0175 (Rhodes 2001). Supermartensitic steels (M13Cr) exhibits a higher maximum hardness than type 410 martensitic stainless steels and F6NM. Table 2.4 gives another example, showing the room temperature strength and hardness balance of

two Ko-HP13Cr steel grades, 655 MPa (95 ksi) grade and 758 MPa (110 ksi) grade, after heat treatment. The steels were produced in Kawasaki Steel, Japan. For the 655 MPa grade, the maximum hardness is 28/29 HRC, and for 758 MPa grade the maximum hardness is 32 HRC. Table 2.4 indicated that, for supermartensitic stainless steel, on the one hand the steel needs to have high strength, and on the other hand it must be soft. Because high strength–low hardness balance is required for the combined mechanical and corrosion properties, it has become a challenge for the steel suppliers on how to treat their materials for the application in hand.

Table 2.2 Mechanical properties of three supermartensitic stainless steel grades (Deleu et al. 1999)

Alloy	0.2% proof stress (MPa)	UTS (MPa)	KCV at -20°C (J)	KCV at -40°C (J)
X80 11Cr-2.5Ni (lean alloy)	598	753	129	120
X80 12Cr-4.5Ni-1.5Mo (medium alloy)	769	918	193	187
X80 12Cr-6.5Ni-2.5Mo (high alloy)	733	931	130	116

Table 2.3 Tempering requirements and hardness of some martensitic stainless steel specified in NACE MR0175 (Rhodes 2001)

Generic name	UNS number	Nominal composition (wt%)					Tempering (MR0175)	HRC Maximum (MR0175)
		C	Cr	Ni	Mo	Other		
Type 410 SS	S41000	0.15	13	-	-	-	Double	22
6FNM	S42400	0.02	12.5	4	0.5	-	Double	22
M13Cr	S41425	0.02	13	5	1.5	-	Single	28
M13Cr	S41426	0.02	12.5	5	2	0.2Ti	Single	27

Table 2.4 Specified strength & hardness of supermartensitic stainless steel Ko-HP13Cr at room temperature after heat treatment

Grade	Yield Strength (MPa)		Tensile Strength (MPa)	Hardness (HRC)
	Minimum	Maximum	Minimum	Maximum
Ko-HP1-13Cr95 Ko-HP2-13Cr95	655	758	724	28 29
Ko-HP1-13Cr110 Ko-HP2-13Cr110	758	896	827	32 32

From: http://www.kawasaki-steel.co.jp

2.1.4.2 Effect of heat treatment on mechanical properties

Generally toughness increases and yield strength decreases with increasing austenite content. Dias and Wilson (1980) studied the effect of heat treatment (normalizing + double tempering) on mechanical properties of low carbon 13Cr4Ni and 13Cr6Ni cast steels. It was found that an increase in nickel content from 4% to 6% led to higher retained austenite content and toughness (low temperature impact strength) but lower yield strength. Kimura et al. (2001) performed different heat treatment conditions on a supermartensitic steel pipe (0.023%C-13%Cr-5.10%Ni-2.01%Mo) and studied the effect of tempering temperature on microstructure, hence strength and hardness. In the paper, the retained austenite content and mechanical property data were given only in table form. This data is plotted in Figure 2.8, and shows interesting trends, not evident from the table. The figure shows tempering temperature had a significant effect on yield strength but only changed the UTS and hardness slightly. After tempering at 550 °C for 180 min (G), the quenched martensite transformed to tempered martensite (TM) and a small amount of retained austenite, resulting in an increase in yield strength but a dramatic decrease in UTS and hardness. Increasing tempering temperature to 630 °C (I), retained austenite content increased, resulting in a decrease in yield strength. A further increase in tempering temperature to 660 °C (J) gave more retained austenite and quenched martensite (QM), i.e. fresh martensite, was also formed, resulting in very low yield strength. No QM was present after the second tempering for the first temper ≥660 °C (E, F), and the yield strength was improved although the steel contained larger amount of retained austenite.

Iwabuchi (1987) indicated carbides precipitation at grain boundaries of low carbon martensitic stainless steel 13Cr4Ni can result in the deterioration of toughness. Brezia (1980) concluded that for low carbon CrNiMo steels, slow cooling from the austenite range gives much lower toughness than faster cooling, but higher yield strengths and lower tensile strengths. This may be due to slight age-hardening at around 450°C or slight temper brittleness.

2.1.5 Corrosion resistance

The corrosion resistance is beyond the scope of this work. In summary, however, many investigations on anti-corrosion properties of supermartenistic stainless steels have been carried out. Corrosion resistance of supermartenistic stainless steels depends mainly on their chemical composition. The addition of Ni and especially Mo improve the corrosion resistance. Investigations carried out by Kimura et al. (2001) show no harmful effect of retained austenite on corrosion resistance of supermartenistic stainless steel; however, increasing the amount of retained austenite can decrease hydrogen content and SSC susceptibility of the steels.

2.2 δ-ferrite in low-carbon martensitic steels

The low-carbon martensitic steels refers to the chromium-nickel martensitic steels with <0.05 % C. The most important alloys are the 13/4 and the 13/6 Cr-Ni steels. The formation of δ-ferrite in low carbon martensitic steels is dependent on chemical composition of the steel and heat treatment conditions. Cr, Mo and Si are ferrite stabilisers and C, N and Ni are austenite stabilisers. If the quantity of the ferrite stabilisers elements is increased, and the equivalent of Cr and Ni (or C) level exceeds the stability, δ-ferrite phase can precipitate in the austenite phase in high-temperature region. As shown in Figure 2.9, the amount of δ-ferrite can be predicted by using C content and Cr equivalent of the steel (Niinaka, 1986). Here the Cr equivalent is:

$$Cr\ (\%) = Cr + 2Si + 1.5Mo - 2Ni - 1Mn - 15N \qquad (2\text{-}3)$$

Ashai et al. (1995) also investigated the relationship between δ-ferrite formation and chemical composition of low carbon CrNiMo steels. It was found that whether δ-ferrite formed or not can be predicted by using the index of phase stability (Ips), where the Ips values are dependent on chemical composition of steels (equation 2-4). Figure 2.10 represents δ-ferrite phase fraction as a function of Ips after heating at 1250°C for 2 hours. To achieve a fully martensitic, the Ips values must be larger than -9.4, otherwise δ-ferrite is produced.

$$Ips = 40\%C + 34\%N + \%Ni + 0.3\%Cu - 1.1\%Cr - 1.8\%Mo \quad (2-4)$$

Hara and Asahi (2000) investigated the effect of heat treatment on the presence of δ-ferrite in a 13Cr4Ni steel and a 13Cr6Ni steel. Some quantity of δ-ferrite was observed distributed parallel to the rolling direction in both steels in the as-rolled state. The Ips values for the two steel were –10.7 and –9.9, respectively, as shown in Table 2.5. After heat treatment, specimen A1 contained 8.6% δ-ferrite, but no δ-ferrite was observed in specimens A2 and B1 due to the homogenzing treatment in the austenite region (1100 °C, and 1150 °C). However, in specimen B2, 10% δ-ferrite was presented after heating at a higher temperature (1350 °C).

δ-ferrite is undesirable in low carbon martensitic steels. Mechanical properties, especially toughness tend to deteriorate with δ-ferrite phase formation. This is due to the compositional differences and lack of cohesion between δ-ferrite and the surrounding matrix, which normally is tempered martensite (Bashuet al. 1990). Jackman and Everson (1995) also indicated that as ferrite was much weaker than austenite at hot rolling temperatures, there was a risk of rupturing along the ferrite during tube billets processing, which can lead imperfections in the tube. On the other hand, the presence of δ-ferrite increased the susceptibility to sulphide stress cracking (SSC) in low carbon 13%Cr martensitic steel (Hara and Asahi 2000). This is because Cr-rich carbides/nitrides precipitated at the ferrite/martensite boundaries and reduced the Cr content in the matrix near the ferrite-matrix boundaries.

Table 2.5 The presence of δ-ferrite after heat treatment (Hara and Asahi 2000)

Steel		Ips	Heat treatment conditions	δ-ferrite fraction (%)
13Cr4Ni	A	A1	-9.9	680°C/30min/WC + 600°C/30min/AC	8.6
		A2		1150°C/3h + 640°C/30min/AC	Nil
13Cr6Ni	B	B1	-	1100°C/3h + 1000°C/3h + 720°C/30min/AC + 660°C/30min/AC	Nil
		B2	10.7	1350°C/1h + 720°C/30min/AC + 660°C/30min/AC	10.0

A: 0.02C-12.9Cr-3.9Ni-1.0Mo-0.5Cu-0.04N
B: 0.02C-12.7Cr-5.8Ni-2.5Mo-1.5Cu-0.02N

2.3 Retained austenite in low-carbon martensitic steels

2.3.1 Retained austenite formation and content

To review "retained austenite" in low-carbon martensitic steels, it is first necessary to define "retained austenite". Generally speaking, "retained austenite" means that during quenching or other heat treatment, austenite transformation to martensite is not complete and therefore a proportion of the austenite remains in the steel after cooling to room temperature, called "retained austenite". However, sometimes "retained austenite" also represents the austenite which forms during tempering period, and remains in steel at room temperature.

As shown in Figure 2.11, the ferrite-austenite ($\alpha+\gamma$) sector extends at ~13% Cr and 4-6% Ni down to about 600 °C, and this is the range for low carbon martensitic Cr-Ni stainless steels. Therefore, during tempering in the temperature range of around 600 °C, new finely dispersed austenite formed from martensite (Folkhard 1988). This kind of austenite that forms on tempering is called "reverted austenite" or "reversed austenite" by some researchers due to the reversion transformation of martensite to austenite (Haynes 1999, Lee et al. 2003). This "reverted austenite" can be stable and does not transform into martensite on cooling to room temperature, so that it is

retained in the steel, and is called "retained austenite". In the current work, unless otherwise noted, the "retained austenite" represents the austenite that remains in the steel at room temperature after tempering treatment. Figure 2.12 schematically illustrated the formation of reversed austenite and retained austenite in a low-carbon Fe-Si-13Cr-7Ni (wt%) steel by Lee et al. (2003) based on the TEM observation. The authors also found that after tempering more austenite was retained at room temperature when cooling in furnace than cooling in air (Figure 2.13).

The amount of austenite formed can be related to a time-temperature parameter of Hollomon-Jaffe type. The details of the Hollomon-Jaffe parameter will be described later in this chapter. Figure 2.14 shows the variations in amount of austenite formed on tempering, stable at room temperature, and stable at -140 °C, respectively, with the Hollomon-Jaffe time-temperature parameter for steels contained 5% Ni. It can be seen that the austenite content retained at room temperature and at -140 °C increased with increasing tempering time-temperature parameter and reached peak values, after which they decreased with increasing temperature. Some researchers also applied the Larson-Miller time-temperature parameter to assess the effect of tempering temperature and time on volume fraction of retained austenite. Details of the Larson-Miller time-temperature parameter will also be reviewed later in this chapter.

2.3.2 The A_{c1}, M_s and M_f temperature

2.3.2.1 The A_{c1} temperature

As described before, in low carbon martensitic steels, to form retained austenite the tempering temperature need to be above the austenite start formation temperature, A_{c1}. The Ac_1 temperature is dependent on chemical composition of steels, and the austenite stabilizers such as C, Ni, and Mn decrease A_{c1} temperature (Pickering et al. 1978). Gooch (1999) developed empirically equation 2-5 to estimate A_{c1} temperature for 13% Cr steels with below about 0.05% C:

$$A_{c1}\,(°C) = 850 - 1500(C+N) - 50Ni - 25Mn + 25Si + 25Mo + 20(Cr-10) \qquad (2-5)$$

where the element designations refer to amounts in wt%. Equation (2-5) indicated that the A_{c1} temperature of low carbon CrNiMo steels decreases greatly due to high Ni content in steel.

Table 2.6 listed the A_{c1} temperatures of some low carbon 13Cr4Ni, 13Cr6Ni and 15%Cr6%Ni steels experimentally determined by different researchers. The values varied in the range of 540-560 °C, depending on chemical composition. Toussaint and Dufrane (2002) indicated the A_{c1} temperature of the supermartensitic grades is in the range of 580 to 650 °C.

Table 2.7 listed the A_{c1} temperature of three typical supermartensitic stainless steels measured by using dilatometer (Dufrane 1999). It can be seen that the A_{c1} is reduced slightly with the small increase in Ni content from 2% to 6%.

Table 2.6 The A_{c1} temperatures of some low carbon-CrNi martensitic Steels

Steels	C content (wt%)	Mo content (wt%)	A_{c1} (°C)	References
13Cr3.5Ni	0.04~0.06	0.20~0.30	~550	Brezia 1980
13Cr4Ni	0.026	0.01	560	Vodarek 1984
13Cr6Ni	0.02~0.07	0.35~1.46	554	Dias and Wilson 1980
15Cr6Ni	0.035	0.02	540	Vodarek 1985

Table 2.7 The A_{c1} temperature of three typical grade supermartensitic stainless steels

	11Cr2Ni	12Cr4.5Ni1.5Mo	12Cr6Ni2.5Mo
A_{c1} (°C)	650	640	630

The A_{c1} temperature depends not only on chemical composition, but also on heating rate. Figure 2.15 plotted the effect of heating rate on A_{c1} temperature of a Fe-13Cr-7Ni-3Si (0.0094 wt%C) steel (Leem et al. 2001). The A_{c1} (A_s) temperature increased

change with heating rate. This result revealed that austenite transformation was a diffusion controlled process when the heating rate was below 10 °C/s, but it became a diffusionless shear process when the heating rate was above 10 °C/s.

2.3.2.2 The M_s and M_f temperature

The austenite to martensite transformation begins at a martensite-start temperature, M_s, and ceases at a martensite finish temperature, M_f. The M_s and M_f temperature are dependent on the alloying elements in the steel. Pickering (1978) indicated that the M_s temperature decreases with increasing C and alloy content, with C and Mn having the major effect. The relationship between composition and M_s have been examined by different investigators and various equations have been developed to calculate M_s temperature as a function of alloying content in steels (Table 2.8). Equation (1) is valid if all the alloying elements are completely dissolved in the austenite; Equation (2) is suitable for high-alloy and medium-alloy steels; Equation (3) is developed by using a very large population of steels, and is suitable for most steels; and equation (4) is specific to soft martensitic stainless steels.

Table 2.9 lists the M_s and M_f temperatures of some 13~16%Cr4~6%Ni steels determined by different researchers. Table 2.10 lists the M_s and M_f of three typical grades of supermartensitic stainless steels measured by Dufrane (1999) using dilatometry. The M_s and M_f decreased dramatically with increasing amounts of alloying elements Cr, Ni and Mo. The M_f is about 120 °C below the M_s for all of the steels, and for 12Cr6Ni2.5Mo steel the M_f dropped to almost room temperature.

Table 2.8 Equations for calculating M_s temperature as a function of chemical composition

Number	Equations	References
1	$M_s = 561 - 474C - 33Mn - 17Ni - 17Cr - 21Mo$	Steven and Hynes 1956
2	$M_s = 550 - 350C - 40Mn - 17Ni - 20Cr - 10Mo - 8W - 35V - 10Cu + 15Co + 30Al$	Jaffe and Hollomon 1946
3	$M_s = 539–432C - 30.4Mn - 17.7Ni - 12.1Cr - 7.5Mo$	Andrews 1965
4	$M_s = 492–125C - 65.5Mn - 29Ni - 17Cr - 10Mo$	Kulmburg et al. 1979

The element designations in the above table refer to amounts in wt%.

Table 2.9 Ac1, M_s and M_f temperatures of some low-carbon martensitic Steels

Steels	C content (wt%)	Mo content (wt%)	M_s (°C)	M_f (°C)	References
13Cr3.5Ni	0.04~0.06	0.20~0.30	260~270	80	Brezia 1980
13Cr4Ni	0.05	0.40	230	100	Niirnaka 1986
13Cr6Ni	0.05	1.5	165	~20	Niirnaka 1986
13Cr6Ni	0.02~0.07	0.35~1.46	210	-	Dias and Wilson 1980
14Cr5NiPH *	0.05	1.5	160	~40	Niirnaka 1986
16Cr5Ni	0.05	1.5	90	40	Niirnaka 1986

*PH: precipitation hardening

Table 2.10 The M_s and M_f temperature of three typical supermartensitic stainless steels

	11Cr2Ni	12Cr4.5Ni1.5Mo	12Cr6Ni2.5Mo
M_s (°C)	360	250	150
M_f (°C)	220	120	30

2.3.3 Retained austenite morphology, distribution and orientation

Vodarek et al. (1984) observed the distribution and morphology of austenite in a 13Cr4Ni steel (with 0.026% C) after single and double tempered at temperatures above the A_{c1} temperature (~560 °C). It was found that after single tempering the majority austenite precipitated in the form of thin discontinuous films, mainly along the original martensitic laths, the packet boundaries, and the prior austenite grain boundaries. Only a small amount of austenite precipitated within the martensite laths in the form of short discontinuous formations. After double tempering, austenite films became more continuous and more precipitated austenite was found within the martensite laths. Crystallographic analysis results indicated that in most cases austenite forms between laths of approximately the same orientation and the Kurdjurmov-Sachs (K-S) relationship is the frequently observed orientation relationship between retained austenite and martensite.

2.3.4 Retained austenite stability

Increasing the stability of the austenite, and thereby decreasing the ease of transformation to martensite is usually referred to as stabilization of austenite (Nishiyama 1978). Stabilization is usually classified as follows:

a. Chemical stabilization due to a change in chemical composition;
b. Thermal stabilization due to thermal treatment;
c. Mechanical stabilization due to plastic deformation.

The chemical stabilization of retained austenite is considered to be related to the concentration of C in the austenite phase, and high C content results in high stability of retained austenite. The austenite lattice parameter differs with amounts of C in austenite. C content in the retained austenite phase can be estimated by using the empirical expression (2-6) (Ruhl and Cohen 1969, and Ridley et al. 1969).

$$a_\gamma = 0.3572 + 0.0033C \text{ (wt\%)} \qquad (2\text{-}6)$$

where a_γ is the lattice parameter (nm) of retained austenite after tempering, and is measured by x- ray diffraction, and C is the carbon content in the austenite phase.

It is found that when tempering low carbon CrNiMo steels at a tempering temperature slightly higher than the A_{c1} temperature, the precipitated austenite is stable and does not transform to martensitic even cooling to -196 °C (Vodarek, 1984). The thermal stability of retained austenite is dependent not only on the chemical composition, but also the morphology of retained austenite and its substructure. Thin film-like retained austenite is found to be more stable than isolated, large austenite particles in TRIP steels (Timokhina et al 2004). A high dislocation density is usually present in austenite phase after tempering. Bilmes (2001) suggesting that the stability of the austenite phase may be associated with these substructures and with the chemical composition of the austenite phase.

The mechanical stability of austenite means the susceptibility of austenite transforms into martensite due to deformation. Saleh and Priestner (2001) defined that mechanical stability of austenite is the amount of strain that is needed to convert the retained austenite completely into martensite. Klotz et al. (1999) indicated that a reduced thermal stability of austenite enhanced its susceptibility to martensite transformation during plastic deformation.

2.4 Precipitation in Cr-, Mo-, and V- containing steels

2.4.1 Precipitation in Cr-, Mo-, and V- containing steels during tempering

Cr, Mo, V are strong carbide forming elements. In Cr-, Mo-, and V- containing steels alloy carbide precipitation occurs when the temperature is in the range of 500-700 °C. The precipitation of carbides can cause secondary hardening (Krauss, 1984). When the temperature is below 500 °C, carbides usually do not form because the alloying elements cannot diffuse sufficient rapidly to allow alloy carbides to nucleate. The mix, composition, size and density of carbides may vary significantly with alloy chemical composition and tempering conditions (temperature and time). As described by Honeycomb and Bhadeshia (1995), in many alloy steels, the first alloy carbide to form is not the final equilibrium carbides, and in some steels, as many as three alloy carbides can form successively. In steels containing V, Cr and Mo, carbides precipitation during tempering is described as following:

a. *Tempering of steels containing V*: V is a very strong carbide former. In steel as little as 0.1wt% V, vanadium carbide VC (face-centred) can be formed. VC forms within ferrite grains on dislocations in the temperature range 550-650 °C, and produces secondary hardening. For steels only containing V, the increase in strength is principally through the formation of vanadium carbonitride precipitates.

b. *Tempering of steels containing Cr*: Cr is a weaker carbide former than V. Cr_7C_3 (trigonal) and $C_{23}C_6$ (face-centred) are the two very common carbides in chromium-steels. The normal carbide sequence during tempering is:

$$\text{Matrix} \rightarrow (FeCr)_3C \rightarrow Cr_7C_3 \rightarrow M_{23}C_6.$$

c. *Tempering of steels containing Mo*: Mo is the predominant alloying element in steel. Initially Mo-rich M_2C (hexagonal) forms during tempering. On prolonged tempering at 700 °C, M_6C (face-centred) forms predominantly at grain

boundaries as massive particles which grow quickly, while the M_2C phase goes back into solution. The carbide sequence is likely to be:

$$Fe_3C \rightarrow M_2C \rightarrow M_6C$$

However, generally steels contain more than one carbides forming element, so that the precipitation process can be complicate during tempering. Honeycomb and Bhadeshia (1995) summarised that, in general terms, the carbide phase which is most stable thermodynamically will predominate if the equilibrium is reached. Irvine (1960) indicated that in tempered steels carbides appeared as M_3C, $M_2(C,N)$, M_7C_3 and $M_{23}C_6$. Pickering (1978) found that $M_2(C,N)$ could be present at the expense of M_7C_3 or $M_{23}C_6$ if the steel contained N and Mo. Here M represents a mixture of alloy elements, and the formula given for each carbide corresponds to general crystallographic structure rather than a specific composition (Peddle and Pickles 2001). Although these precipitates are not pure binary carbides with a precise stoichiometry, and various elements particular Cr, Fe, Mo, Mn and Si are soluble in carbides, the actual solubility depends on the type of carbide.

2.4.2 Precipitation in 9-12Cr steels

In 9-12Cr steels, $M_{23}C_6$ carbides and MX-type carbonitrides are the principal carbides formed. $M_{23}C_6$ carbides mainly precipitate along prior austenite grain boundaries and martensite lath boundaries. These precipitates can retard the sub-grain growth hence increase strength of the steels. MX carbonitrides are based on vanadium nitride (VN), mainly distributed along dislocations in the martensite matrix. Hofer et al. (2000) found that in the 10Cr-0.13C-0.23V-1.03Mo steel, the distribution of $M_{23}C_6$ and VN precipitates overlap.

The distribution and amounts of carbides in 9-12Cr steels are strongly dependent on the C content in steels. Figure 2.16 and Figure 2.17 give examples, showing the equilibrium amount of MX and $M_{23}C_6$ with C content in steels containing 9% Cr and 0.2% V at 1073 K (800 °C) calculated by Thermo-Calc (Taneike et al. 2004). In Figure 2.16, the amount of $M_{23}C_6$ decreased with decreasing C content, while the

MX was almost constant. When C content was less that 0.02%, the amount of $M_{23}C_6$ was smaller than that of MX. In Figure 2.17, MX is almost all nitrides and the change of C content does not affect the amount and composition of MX.

2.4.3 Precipitation in low carbon martensitic steels

Generally speaking, precipitation occurs in tempered low carbon martensitic steels with the main phase formed being $M_{23}C_6$ (Miyata et al. 1998). Sometimes $M_2(C,N)$ carbonitrides may form if the steels contain higher N content (Niinaka et al. 1986, Vodarek 1985, Wabuchi 1984). However, due to the low content of C, precipitation of $Cr_{23}C_6$ is largely suppressed. Figure 2.18 shows phase profiles in 13% Cr steels (Folkhard 1988). It is apparent the $M_{23}C_6$ carbides (C1) is already precipitated from the α phase at temperature below 700 °C at very low C content of around 0.01%. Amaya et al. (2003) investigated 13% Cr steels and found that after quenching, $M_{23}C_6$ carbides precipitated along grain boundaries as the steel passed through the tempering temperature range, thereby reducing corrosion resistance because of localized attack. When the volume fraction carbides (mainly $M_{23}C_6$) located on the prior austenite grain boundaries is more than 0.5 vol%, localized corrosion occurs at a high temperature. Brezia (1980) described that in 13Cr-4Ni steels, $M_{23}C_6$ carbides and M(CN) carbonitrides were present, with the latter being precipitated in the centre of the grains and the former both inside the grain and along the grain boundaries.

In supermartensitic stainless steels, Cr-rich $M_{23}C_6$ carbides are reported to be the common precipitation at prior austenite grain boundaries in the weld heat affected zone (HAZ). If the steel contains Ti, MC titanium carbides can be formed at prior austenite grain boundaries in the weld HAZ during post weld heat treatment (Ladanova and Solberg 2002).

2.4.4 General description of the $M_{23}C_6$, M_6C and MX carbides

a. $M_{23}C_6$

$M_{23}C_6$ is a more general notation of Cr-rich carbides $Cr_{23}C_6$, as often, Mo, Ni, Fe and Si are found to substitute partially for Cr. It has an fcc crystal structure and the lattice parameter varies between 1.057 and 1.068 nm, which is about three times that of austenite. This carbide has been found to dissolve 22 to 40 mass% Cr, 5 to 21 mass% Mo, 29 to 63 mass% Fe, up to 12 mass% Mn and a minor amount of Si (Shaw 1984). $M_{23}C_6$ growth with a cube to cube orientation relationship (Sourmail 2001):

$$\{100\}\ \gamma\ //\ \{100\}\ M_{23}C_6$$
$$<010>\gamma\ //\ <010>M_{23}C_6$$

$M_{23}C_6$ is metastable, and it is always found in the early stage of precipitation because it nucleates very easily. It can partially transform to M_6C when Mo is added (Sourmail 2001). $M_{23}C_6$ precipitates mainly on grain boundaries and intragranular sites. For example, in ferritic steels, $M_{23}C_6$ particles are formed during tempering, and located on grain boundaries and sub-boundaries (Maruyama et al. 2001). On grain boundaries $M_{23}C_6$ is often associated with intergranular corrosion. In 2.25Cr1Mo steels $M_{23}C_6$ has been found to coexist with M_6C steels after extended tempering times (Baker and Nutting 1959). In steels containing higher Cr (>2.25 wt%), $M_{23}C_6$ is the mostly assumed as stable Cr-rich carbides. It is also the main carbide in non-stabilised carbon containing austenitic stainless steels.

b. M_6C

M_6C is Mo-rich carbide in which Fe, Cr, Mn, and Si may dissolve. The Mo content ranges between 30 and 60 mass%, Fe between 28 and 40 mass%, and Cr between 5 and 20 mass% (Peddle and Pickles 2001). It has an fcc crystal structure and lattice parameter varying between 1.095 and 1.128 nm. M_6C has been found to nucleate at the interface between the existing carbides and the ferrite matrix growing at the expense of M_2C, M_7C_3 and $M_{23}C_6$ (Baker and Nutting 1959). M_6C is regarded as the equilibrium carbide for the 2.25Cr-1Mo steels after long ageing times (Sourmail 2001).

c. MX

When strong carbide/nitride formers (Ti, Nb, V, Zr, Ta etc.) are added to steels, MX precipitates can form. It has an fcc crystal structure. In austenite stainless steels MX precipitates usually form on dislocations within the matrix (Sourmail 2001). In V-rich MX particles the MX is presume to be mainly a VN nitride (Taneike et al. 2004). Typical MX precipitates are smaller than $M_{23}C_6$ carbides and reaction with dislocations.

EDX spectra of Mo_2C, M_3C, M_7C_3, $M_{23}C_6$ and M_6C carbides in 2.25Cr-1Mo steels after tempering are given in Figure 2.19. They were identified by different researchers and was summarised by Todd (1986).

2.5 Phase transformation kinetics

To begin the phase transformation kinetics review, it is necessary to define a few of the terms that are frequently used in phase transformation kinetics theory. As described by Porter and Easterling (1992), the *system* means an alloy that can exist as a mixture of one or more phases. A *phase* can be defined as a portion of the system whose properties and composition are homogeneous and which is physically distinct from other parts of the system. *Kinetics* in phase transformation study means how fast a transformation will proceed. For transformations that occur at constant temperature and pressure the relative stability of a system is determined by its Gibbs free energy (G), which is defined by the equation:

$$G = H - TS \qquad (2\text{-}7)$$

where H is the enthalpy, T is the absolute temperature, and S is the entropy of the system.

2.5.1 Arrhenius rate equation

According to kinetic theory, the probability of an atom reaching the activated state is given by exp ($-\Delta G^a/kT$), where k is Boltzmann's constant (R/N_a) and ΔG^a is the

activation free energy barrier. Putting $\Delta G^a = \Delta H^a - T\Delta S^a$ and changing from atomic to molar quantities, the probability of an atom reaching the activated state is changed to $\exp(-\Delta H^a/RT)$, where R is molar gas constant. Because the rate at which a transformation occurs will depend on the frequency with which atoms reach the activated state, the Arrhenius rate equation is derived as:

$$\text{rate} \propto \exp(-\Delta H^a / RT) \qquad (2\text{-}8)$$

This equation is found to apply to a wide range of processes and transformations in metals and alloys. The simplest one is the process of diffusion, which will be described later.

2.5.2 KJMA equation

The volume fraction kinetics of isothermal transformation processes is expressed by the KJMA equation, named after the individual who developed it (Kolmogorov 1937, Johnson & Mel 1939 and Avrami 1939-1941) to describe a three-dimensional nucleation and growth processes:

$$f = 1 - \exp(-k\, t^n) \qquad (2\text{-}9)$$

where f is the volume fraction of the transformation product, t is the reaction time, k is the rate constant and usually empirically evaluated for each temperature, and n is the curve shape constant, is called Avrami exponent. In any case, $f \rightarrow 1$ as $t \rightarrow \infty$.

Using equation (2-9), the constants k and n can be extracted from experimental data and stored as the only values needed for reconstructing the original data set. On the other hand, and more importantly, if k and n are known from knowledge of a steel composition and transformation temperature, the volume fraction of the product phase can be predicted (Fang et al. 1997).

2.5.3 The martensite transformation

2.5.3.1 Thermodynamics of martensite transformation

Unlike ferrite, cemenite or pearlite transformation that occurs by carbon, iron and substitutional atom diffusion, the martensite formation is a diffusionless, displacive transformation process. Honeycombe and Bhadeshia (1995) describe the martensite reaction in steels is the best known of a large group of transformations in alloys in which the transformation occurs by shear without change in chemical composition. This occurs either due to the steel is cooled rapidly form the austenite, or the steel is so alloyed so that there is insufficient time for diffusion. The addition of alloying elements to steel can allow development of martensite at lower cooling rate.

The shear transformation of austenite to martensite is largely independent of time, and dependent only on the degree of undercooling below the M_s temperature. This type of transformation kinetics is referred to as athermal in contrast to the time-dependent, isothermal transformation kinetics of diffusion-controlled transformations. The following equation, after Koistenen and Marburger (1959), describes the athermal transformation kinetics of martensite:

$$f = 1 - \exp(-1.10 \times 10^{-2} \Delta T) \qquad (2\text{-}10)$$

where f is the volume fraction of martensite and ΔT is the extent of undercooling below the M_s temperature, (M_s –T). Since time does not feature in this relation, the fraction of martensite depends only on the ΔT.

2.5.3.2 Martensite morphology

There are two major morphologies of martensite found in steels, termed lath and plate martensite. The two morphologies take their names from the shape of the martensitic crystal which form in a given steel, and differ with their fine structure, habit planes, and the arrangement of the martensite units within a transformed structure. Lath martensite forms in low and medium carbon steels with relatively high M_s temperatures. Plate martensite forms in high carbon steels, with low M_s temperatures.

In low-carbon alloys most of the crystals in a parallel group have the same crystal orientation and the parallel groups are referred to as blocks. The substructure of lath martensite produced by water or oil quenching consists of high densities of tangled dislocations, reflecting lattice invariant deformation and volume accommodation effects during athermal transformation from high temperatures.

2.5.3.3 Crystal structure of martensite and crystallographic orientation relationship

The crystal structure of martensite (α') obtained by quenching the austenite phase in carbon steels has a body-centred tetragonal (bct) lattice. The lattice parameters a and c of α' in steels appear smaller than the lattice parameter a_γ of austenite (γ). In addition, they very with C content in a nearly linear fashion (Figure 2. 20). The axial ratio c/a increases with the C content, and the relation is given by equation

$$c/a = 1.000 + 0.045 \text{ wt\% C} \qquad (2\text{-}11)$$

Equation (2-11) indicates that the martensite can be cubic ($c = a$) as long as the C content is small.

Depending on the alloy composition, the fcc austenite in steels transforms either to a bcc or bct martensite, or to an hcp martensite, which itself may further transforms into bcc martensite. Following the fcc austenite to bcc or bct martensite transformation, certain crystallographic planes and directions in the austenite parent phase (γ) are parallel to specific planes and directions in the martensite (α'). Two well known orientation relationships have been established in steels (Nishiyama 1978). One is called the Kurdjumov–Sachs (K-S) relations:

$$(\bar{1}11)_\gamma // (011)_{\alpha'}$$

$$[\bar{1}01]_\gamma // [\bar{1}\bar{1}1]_{\alpha'}$$

and the other is called Nishiyama (N) relations:

$$(111)_\gamma // (011)_{\alpha'}$$

$$[1\bar{1}\bar{2}]_{\gamma} // [0\bar{1}\bar{1}]_{\alpha'}$$

2.5.3.4 Martensite reverse transformation to austenite on heating

Martensite in Fe-C alloys and steels is a metastable phase. Face-centred cubic austenite can be produced from bcc martensite (α') by reverse transformation during heating. The C atoms are in supersaturation, and high strain energy is associated with the fine structure introduced by the lattice invariant deformation. Further instabilities are contributed by the high interfacial energy associated with the boundaries of large numbers of marteniste laths or plate, by retained austenite (remained after quenching) which according to the Fe-C diagram should not be stable below the A_{c1} temperature, and by residual stress which are introduced by temperature and transformation gradients developed during quenching. The various instabilities in the martensite microstucture provide the thermodynamic driving forces for phase transformation and microstructural changes. Thus, when quenched steels are heated, in a heat treatment operation referred to as tempering, martensitic microstructures are converted to new microstructures (Krauss1992).

The mechanism for the reverse α' to reverted austenite (γ_r) transformation has been studied by many researchers and there are two opinions regarding the character of this transformation: diffusional and diffusionless. Nishiyama (1978) concluded that the reveres transformation depended on the heat treatment conditions. When heating at a rapid heating rate (e.g. 5000 °C/sec), there were two stages of transformation occurred during heating holding time. The first stage is a diffusionless transformation and the second stage is a diffusional transformation process. When α' was heated at a slow heating rate, however, the reverse transformation is only a diffusional process.

2.5.3.5 Stress-induced transformation

It has been known that in some alloys the martensitic transformation is triggered by deformation. The temperature associated with the formation of martensite by deformation, M_d, is at a higher temperature than the M_s temperature (Nishiyama 1978). Figure 2. 21 gives an example, showing the variation of martensite content with strain in a Fe-14.8Cr-12.6Ni alloy (M_s = -78 °C). Increasing strain resulted in

more martensite being formed. The martensite formed by deformation is called strain-induced martensite. When such a transformation occurs, the ductility of alloy increased measureably, an effect used in TRIP steels.

2.5.4 Alloying elements diffusion in ferrite and austenite iron

2.5.4.1 Arrhenius equation for diffusion

The alloying elements diffusion coefficient, D, in metals as a function of temperature can be expressed in the form of the Arrhenius equation:

$$D = A \exp(-Q/RT) \qquad (2\text{-}12)$$

where D is diffusion coefficient (cm^2/sec), A is frequency factor (cm^2/sec), Q is the activation energy (J/mol), T is absolute temperature (K) and R is molar gas constant (8.314J/(mol × K)).

A convenient graphical representation of D can be writing in the form of

$$\log D = \log A - Q/(2.303R) \times (1/T) \qquad (2\text{-}13)$$

Thus log D plotted against (1/T) is a straight line with the slope equal to - Q/(2.303R) and the intercept of log A.

2.5.4.2 Alloying elements diffusion coefficient in ferrite and austenite iron

Diffusion coefficients of some alloying elements in ferrite (α, δ) and austenite (γ) iron at temperatures in the range of 20-1400 °C are listed in Table 2.11. They were investigated by different researchers and summarised by Folkhard (1988). The alloying elements diffusion coefficient increases with increasing temperature in both α (δ) and γ iron, and the diffusivity in α (δ)-iron is faster than in γ-iron for all of the alloying elements. On the other hand, C and N diffuse much faster than other alloying elements in iron. Figure 2.22 displays diffusion coefficient D of some elements in γ and α (δ) iron. D decreases linearly with increasing T^{-1}, where T is temperature in K. Figure 2.23 represents Ni diffusion as a function of T^{-1} in α (δ) iron at the temperature range 600°C-900 °C by different researchers, and the data follows the same trend.

Table 2.11 Summary of diffusion coefficient of some alloying elements in α (δ) and γ iron, including the values for self-diffusion of iron, at different temperatures (Folkhard 1998)

Diffusion coefficient in cm^2/s											
	α (δ)-Iron						γ-Iron				
	Temperature (°C)						Temperature (°C)				
Element	20	400	800	1100	1400	Element	20	400	800	1100	1400
α (γ)-Fe	10^{-46}	10^{-19}	10^{-12}	10^{-9}	10^{-7}	α (γ)-Fe	10^{-53}	10^{-22}	10^{-14}	10^{-11}	10^{-9}
C	10^{-17}	10^{-8}	10^{-5}	10^{-4}	-	C	10^{-27}	10^{-13}	10^{-8}	10^{-6}	-
N	10^{-17}	10^{-8}	10^{-6}	10^{-5}	-	N	10^{-31}	10^{-13}	10^{-8}	10^{-7}	-
Cr	10^{-42}	10^{-18}	10^{-11}	10^{-9}	10^{-7}	Cr	10^{-37}	10^{-18}	10^{-13}	10^{-11}	10^{-9}
Mo	10^{-46}	10^{-18}	10^{-11}	10^{-9}	10^{-7}	Mo	10^{-46}	10^{-21}	10^{-13}	10^{-11}	10^{-9}
V	-	-	10^{-12}	10^{-9}	10^{-7}	V	-	-	10^{-14}	10^{-11}	10^{-9}
Mn	-	-	-	-	-	Mn	10^{-53}	10^{-22}	10^{-14}	10^{-11}	10^{-9}
Ni	10^{-45}	10^{-18}	10^{-11}	10^{-9}	-	Ni	10^{-54}	10^{-23}	10^{-15}	10^{-11}	10^{-9}

2.6 Tempering temperature-time parameter

2.6.1 The Hollomon-Jaffe parameter

The effect of tempering temperature and time on strength and hardness can be combined in a single empirical tempering parameter, named as Hollomon-Jaffe parameter. The Hollomon-Jaffe parameter was first established by Hollomon and Jaffe (1945) to predict hardness in tempered steels. They first established a functional relationship in the form:

$$\text{Hardness} = f(T(C + \log t)) \qquad (2\text{-}14)$$

where T is the absolute temperature, t the time, and C is a constant, characteristic of the steel. T(C + log t) is the Hollomon-Jaffe parameter.

These equations imply that hardness is the function of the parameter T(C + log t). In other words, as long as the parameter T(C + log t) has a constant value, the same hardness is produced with a short tempering time and a high temperature as with a long tempering time and low temperature. The authors also found that the constant C varied somewhat for different steels, and appears to decrease linearly with increasing carbon content. Thus, they introduced the following equation to determine C value for time in hours:

$$C = 21.3 - 5.8 \times (\text{percent carbon}) \qquad (2\text{-}15)$$

The important application of the functional relationship of T(C + log t) is the determination of the various combinations of tempering time and temperature that resulted in a given hardness. However, the Hollomon-Jaffe parameter has been applied successfully to study ultimate tensile strength (UTS) and yield strength after tempering. For example, Saeglitz & Krauss (1997) investigated the changes in hardness as well as UTS as a function of the Hollomon-Jaffe parameter in SAE 43XX steels.

2.6.2 The Larson-Miller parameter

Various modifications of the Hollomon-Jaffe parameter had been carried out by different workers and a typical example is the Larsen-miller parameter (Naylor and Cook, 1992). This parameter original shows the effect of tempering temperature-time on creep-rupture behaviour of steels. For example, Klueh et al. (2000) applied the Larson-Miller parameter with a constant C = 30 to study the creep-rupture of a ferrite/martensitic steel. However, it has also been used for tempering characterization of steels (Haynes 1999). Usually for medium/high alloy steels, with the constant C = 20 and t in h, the Larsen-miller parameter is in the form:

$$P = T\,(20 + \log t) \times 10^{-3} \qquad (2\text{-}16)$$

2.7 Strengthening

2.7.1 Strengthening mechanism

Strength is an important aspect of the mechanical performance. The strengthening of metals can be obtained in several ways such as solid solution strengthening, precipitation strengthening, and grain refinement strengthening. For example, in low carbon 12% Cr martensitic steel, strengthening is due to carbon and nitrogen in solution; solid solution strengthening by the Cr and other substitutional solutes; the fine martensite lath size; and the dislocations present in the lath martensite. Due to the low M_s temperature, there is less likely to be carbide precipitation strengthening in the untempered martensite, but in the tempered condition strengthening by carbides does occur albeit at the expense of solid solution strengthening (Pickering 1979).

The solid-solution hardening of 13% Cr steels is largely dependent on carbon content, but ductility can only be obtained at low carbon levels. Although alloying elements affect hardenability, they have a minor effect on hardness except to reduce it at high carbon levels by causing austenite to be retained. When the steels contain strong carbide forming element such as V, Cr and Mo, and when they precipitate to form

fine carbides such as VC and $Cr_{23}C_6$, there is an increase in hardening, i.e. secondary hardening. This is because carbides are very fine and frequently have coherency strain fields. As shown in Figure 2.24, for a low C 13Cr5Ni2Mo steel, even only 0.1% V content was added in the steel, secondary hardening was observed. After quenching and tempering both yield strength and UTS were improved dramatically and the strongest hardening was observed with the C range around 0.01mass% (Knodo et al 1999). It should be noted that the effect of secondary hardening is attributed to the precipitation of fine alloy carbides. Primary carbides, which are undissolved carbides on hardening, have no effect.

Grain refinement is technologically attractive because it generally does not adversely affect ductility and toughness, contrary to most other strengthening methods (Düber & Künkler, 2004). The term "grain" varies with steel composition and heat treatment. For example, in bainitic steels the main microstructural contribution to the strength of bainte is from the extremely fine grain size of bainitic ferrite. In 9% Ni, grain size strengthening is attributed to the fine lath martensitic. The famous Petch-Hall relation posits a relationship between the yield strength and the grain size of the form $\sigma_y \propto d^{-1/2}$, which will be described below.

2.7.2 Yield strength

To combine the effect of solid solution, precipitates, dislocation density, and grain size etc on yield strength of steels. The yield strength of can be expressed as:

$$\sigma_y = \sigma_i + \sigma_s + \sigma_p + \sigma_d + \sigma_{ss} + \sigma_t + k_y d^{-1/2} \qquad (2\text{-}17)$$

where σ_y is the yield stress, σ_i is the fraction stress opposing dislocation motion, σ_s is the solid solution strengthening, σ_p is precipitation strengthening, σ_d is "forest" dislocation strengthening, σ_{ss} is sub-structure or sub-grain size strengthening, σ_t is a crystallographic texture strengthening parameter, k_y is a constant related to the difficulty of unlocking dislocations, or of actuating dislocation sources, sometimes called the dislocation locking term, and d is the matrix grain diameter (Pickering 1992).

Krauss (1999) described the yield stress of low-carbon martensitic microstructures using the following equation:

$$\sigma_y = \sigma_0 + \sigma_1 + k_y D^{-1/2} + k_S d^{-1/2} + \alpha Gb [\rho_0 + K (\%C)]^{1/2} \quad (2\text{-}18)$$

where σ_0 is the friction stress for pure iron, σ_1 is the solid solution strengthening from Mn and Ni, *d* is the lath width, *D* is the packet size, ρ_0 is the dislocation density of martensitic pure iron, and the other terms have their usual meaning. Equation (2-18) indicates that for a given steel, the yield strength is strongly dependent on the lath size *d*, packet size D and dislocation density ρ_0.

2.7.3 Hall-Petch relation for yield strength and hardness

The Hall-Petch relation was first established by Hall (1951) and Petch (1953) to express the influence of grain size on yield strength of metals and alloys:

$$\sigma_y = \sigma_0 + kd^{-1/2} \quad (2\text{-}19)$$

where σ_y is the yield stress, σ_0 is a fractional stress, d is grain size and k is a constant. This Hall-Petch relationship demonstrates that the yield strength increases as the grain size is decreased. For low carbon martensitic steels the grain size usually apply the prior austenite grain size or the packet size. Equation (2-19) indicates the degree of grain size strengthening is dependent on the *k* value. The grain size strengthening in steels is more significant than in Al alloys (Hall 1970). It was found that k value in steels was in the range 0.5 to 1.6 $MNm^{-3/2}$. In Al alloys, however, the k value was much lower, normally in the range 0.06 to 0.15 $MNm^{-3/2}$ (Lloyd and Court, 2003).

Dubravina et al. (2004) suggested the Hall-Petch type relations can be giving in the form:

$$\sigma = \sigma_0 + K d^{-n} \quad (2\text{-}20)$$

where σ is the flow stress, d the size of the structural element, σ_0 the flow stress of the microstructure without the element boundaries, and K and n are called Hall–

Petch parameters. Both parameters K and n reflect the resistance of the boundary to dislocation glide. Thus, n = 1/2 is valid for high-angle boundaries (mainly in undeformed materials) whereas n = 1 is true for subgrain boundaries (mainly in deformed materials).

Although the Hall-Petch relation developed originally to couple of structure and yield strength, some researchers (Furukawa et al. 1996) followed the equation (2-19), and established the relationship between the grain size and hardness:

$$H = H_0 + k_H d^{-1/2} \tag{2-21}$$

Where H_0 and k_H are appropriate constants associated with the hardness measurements.

Chapter 3 Experimental Procedure

3.1 Aims of experiments

The super 13%Cr stainless steel investigated is used for offshore applications so it has to meet strict tensile strength, yield strength, toughness and hardness specifications. Corus Engineering Steels (CES), which sponsored this project, have had difficulty in achieving the range of properties required in a repeatable manner. It is known that microstructure determines the mechanical properties of steel. Experiments therefore had to be carried out to determine the influence of microstructures on the hardness and yield strength of the as-received materials.

Microstructure of super 13% Cr steels is dependent on heat treatment regimes after hot rolling. Significant amounts of retained austenite formed after tempering strongly affects mechanical properties. Therefore, re-heat treatment had to be carried out to assess the influence of heat treatment parameters on microstructure constituents, hardness and yield strength, to establish relationships between microstructure and mechanical properties.

As retained austenite in super 13%Cr steels has significant effect on mechanical properties, experiments also had to be carried out to investigate the effect of heat treatment parameters on amount, size, stability, and transformation behaviour of retained austenite.

3.2 Materials

A commercial supermartensitic 13%Cr5Ni2Mo type stainless steel was used in this study. The steels were produced by CES, Stocksbridge, and supplied as fully heat treated bars after hot rolling. Eight steel slices cut off from eight as-received bars with different diameters were supplied for this work. Seven of them were used for microstructural examination, retained austenite content determination, and hardness

test in both as-received state and re-heat treated state. They were named as A1, A2, A3, A4 and B1, B2, B3 for this work. The last slice about 70 mm long with 152 mm diameter was used for re-heat treatment and then tensile test. It was named as C1. Bar A1, A2, A3, A4 and C1 were taken from one cast (Cast 1) while B1, B2 and B3 were taken from the other cast (Cast 2). The chemical composition of Cast 1 and Cast 2 are given in Table 3.1. They have very similar composition except Cast 2 contained slightly higher V (0.175 wt%) than Cast 1 (0.13 wt%). In order to calculate equilibrium phase transformation, chemical composition of Cast 3, which contained slightly higher C (0.025 wt%) and V (0.017 wt%), is also listed in the table. The diameter of the eight as-received bars is listed in Table 3.2.

The industrial heat treatment regimes for steels A1- A4, B1 and C1 are shown in Table 3.3. Steel B2 was initially heat treated with the same regime as B1, re-heated, and then re-re-heat treated using the parameter shown in Table 3.4. The industrial heat treatment regimes for steel B3 are shown in Table 3.5.

These as-received steel bars were produced to against two strength levels: 655 MPa (95ksi) and 758 MPa (110 ksi). The related 0.2% proof strength and hardness specifications are listed in Table 3.6.

Table 3.1 Chemical composition of the super 13%Cr steels investigated (wt%, balance *Fe*)

Casts	Steels	Composition												
		C	Si	Mn	P	S	Cr	Mo	Ni	Cu	Ti	V	Al	N
Cast 1	A1, A2, A3, A4, C1	0.016	0.20	0.38	0.018	0.0044	12.21	1.99	5.58	0.13	<0.01	0.13	0.007	0.016
Cast 2	B1, B2, B3	0.016	0.17	0.37	0.011	0.0035	12.36	1.92	5.50	0.09	<0.01	0.175	0.009	0.016
Cast 3*	-	0.025	0.16	0.37	0.016	0.005	12.25	1.92	5.48	0.06	<0.01	0.17	0.005	0.014

* Composition of cast 3 was used for MT DATA calculation

Table 3.2 Diameter of the as-received super 13%Cr steel bars (mm)

Cast 1	A1	216
	A2	203
	A3	165
	A4	121
	C1	89
	B1	133
Cast 2	B2	133
	B3	152

Table 3.3 Heat treatment parameters of the as-received steel bars A1, A2, A3, A4, B1 and C1

Hardening	Tempering	Stress Relieving
950 °C	635 °C	550 °C
2 h	4 h	2 h
Oil quenching	Air cooling	Air cooling

Table 3.4 Final heat treatment parameters of the as-received steel bar B2

Hardening	Tempering	Stress Relieving
950 °C	630 °C	550 °C
2 h	4 h	2 h
Oil quenching	Air cooling	Air cooling

Table 3.5 Heat treatment parameters of the as-received steel bar B3

Hardening	Tempering	Stress Relieving
950 °C	620 °C	550 °C
2 h	3 h	2 h
Oil quenching	Air cooling	Air cooling

Table 3.6 The 0.2% proof strength and hardness targets for the as-received steel bars

Strength level (MPa)	Steel bar	Minimum 0.2% proof strength (MPa)	Maximum 0.2% proof strength (MPa)	Maximum Hardness (HRC)
655	A1, A2, A3, A4, B1, B2, C1	655	758	28
758	B3	758	-	32

3.3 Re-heat treatment

3.3.1 Sample preparation

Samples, approximately 10×12×15 mm were cut from slice A2 (203 mm diameter) across the diameter in the longitudinal direction (see Figure 3.1) for re-heat treatment to study their microstructure especially the retained austenite-martensite transformation behaviour. Blanks, 15×15×68 mm were cut from slice C1 across the diameter in the longitudinal direction for re-heat treatment before being machined for tensile test specimens.

3.3.2 Re-austenitization and tempering

All the 10×12×15 mm samples were initially re-austenitised at 950 °C for 2 h in order to ensure a fully austenitic structure as well as dissolve original carbides completely while avoiding grain coarsening. These samples were subsequently taken out from the furnace, cooled in air to room temperature, and then tempered using the following conditions:

a) Tempered at different temperatures in the range 550 ~ 700 °C, 4 h, furnace cooled (≤1.5 °C/min).

b) Selected specimens from (a) were second tempered at 550 °C, 2 h, furnace cooled (≤1.5 °C/min).

c) Tempered at 635 °C, holding for 0.5, 1, 2, 4, 8, 12 and 24 h, furnace cooled (≤1.5 °C/min).

d) **Tempered at 630 °C, holding for 0.5, 1, 2, 3, 4, 6 and 8 h, furnace cooled (≤1.5 °C/min).*

e) *Tempered at 600/620 °C, 8 h and 24 h, furnace cooled (≤1.5 °C/min).*

f) *1st tempered at 600/620°C, 8 h and 24 h, furnace cooled (≤1.5 °C/min) to room temperature + 2nd tempered at 550 °C, 2 h, furnace cooled (≤1.5 °C/min).*

g) *1st tempered at 625 °C, 4 h, furnace cooled (≤1.5 °C/min) to room temperature + 2nd tempered at 550 °C, 560 °C, 570 °C and 580 °C, 2 h, furnace cooled (≤1.5 °C/min).*

*Specimens were re-austenitised at 940 °C for 2 h before tempering.

The blanks were also re-austenitised at 950 °C for 2 h, air cooled and then tempered using selected conditions from (a) to (g). To determine retained austenite content and hardness of the tensile samples, each blank being heat treated was accompanied by at least one small sample inside the furnace for every re-heat treatment process. The small sample was then be used to calibrate the retained austenite content and hardness of tensile test samples.

All of the re-heat treatments were carried out in a calibrated laboratory furnace. Since the temperature within the furnace chamber varies with position, specimens were always put at the same position in the furnace and a calibrated thermocouple was always used to monitor temperatures during each heat treatment process.

3.3.3 Heating rate and cooling rate

The heating rate for the re-austenitization was set at 5 °C/min from room temperature to 950 °C. The heating rate for tempering was set at 5°C/min initially from room temperature to 350 °C, and then reduced to 2 °C/min in order to simulate the heating process in the practice as well as reduce the risk of temperatures rising beyond the required tempering temperatures. As shown in Figure 3.2, although the cooling rate was set at 1.5 °C/min, only initial cooling took place at this rate, later the cooling rate slowed down so that the average cooling rate was below 1.5 °C/min.

3.4 X-Ray diffraction analysis

3.4.1 Sample preparation

3.4.1.1 Sample preparation for as-received and re-heat treated materials

Both as-received and re-heat treated samples were prepared for X-ray diffraction (XRD) analysis to determine the volume fraction of retained austenite. For the as-received condition, samples were cut from each as-received slice (A1-A4, B1-B3). To examine variations in retained austenite content across the diameter, the samples of approximately 8×10×12 mm were cut from the centre, half radius from the centre and near outside surface using the method shown in Figure 3.1. Samples were also cut across the diameter every 20 mm from the centre to the outside surface of slices A1 and A2 to see continuous variations in retained austenite across the radius. All of the re-heat treated samples shown in section 3.3 were prepared for XRD analysis to determine variations in retained austenite with tempering conditions.

Both as-received and re-heat treated samples were prepared metallographically in a conventional manner, namely, ground on successively finer silicon papers from 120 to 1200 grade under running water. The samples were then polished on cloths with 6μm diamond paste and water based lubricant and finally polished to 1μm finish to give the same surface conditions. Note all of the XRD analysis was carried out on the longitudinal section of these samples.

3.4.1.2 Sample preparation for specimens after tensile testing

To study strain-induced austenite to martensite transformation, the extent of retained austenite before and after straining needs to be determined. To do this, the retained austenite content on both the shoulder and the gauge length near fracture surface of some broken tensile specimens were measured to assess level of retained austenite before and after straining. To measure retained austenite content in the shoulders, the shoulder was cut from the broken tensile specimen and mounted in Bakelite, ground flat and polished to 1μm finish using the method shown in 3.4.1.1. The Bakelite was then broken to take out the samples and fit them in the XRD sample holder. To measure retained austenite in the gauge length near fracture surface, six discs about

1.5 mm thickness each were successively cut along the gauge length near the fracture surface to provide sufficient material for XRD. To avoid deformation induced martensite transformation during cutting, all of the discs were cut by Spark Erosion using a copper wire. The six discs for each sample were stuck securely on a piece of polymethylmethacrylate (PMMA) using a "5 minute glue" to fit in the XRD sample holder. The reason for using PMMA is it does not produce any X-ray peak in the scanning range 30-130° so that it does not affect the retained austenite content measurement. The stuck discs were then carefully ground and polished to 1μm finish using the method in 3.4.1.1.

3.4.2 X-ray diffraction technique (XRD)

A Philips PW1710 diffractometer, operating at 40 kV and 30 mA using monochromatic Co Kα radiation (1.78896 Å) was used for XRD analysis. The polished samples were mounted in a rotating sample holder, and were tilted and rotated during running. A preliminary scan (30-130°) at a rate of 2 °/min was used to determine approximate amounts of austenite and martensite present as well as to identify the existence of any precipitation phase. A set of angles was scanned sequentially by using the "HBX" system to accurately determine austenite content (see Table 3.7). Retained austenite content was determined from the integrated intensities with three austenite peaks $(200)_{fcc}$, $(220)_{fcc}$ and $(311)_{fcc}$ and three martensite peaks $(200)_{bcc}$, $(211)_{bcc}$ and $(220)_{bcc}$ according to references (Durnin 1968 and Cullity 1978). The reason for using these austenite and martensite peaks was to avoid the influence of preferred crystallographic orientation in the specimens (Dickson 1969). The carbon concentration in retained austenite was then estimated by using the lattice parameters of retained austenite shown in equation (2-6).

Table 3.7 XRD scanning parameter for retained austenite content measurement

Scanning from the angle (°)	Scanning to the angle (°)	Scanning rate (°/min)	Scanning step size
58	62	0.1	0.02
75	79	1	0.02
87	92	0.1	0.02
97	102	1	0.02
109	115	0.1	0.02
121	126	1	0.02
30	130	2	0.02

3.5 Hardness test

3.5.1 Hardness tests on the as-received slices

As-received steels A1, A2, A3 and A4 were tested using Vickers test equipment with a load of 30 kg. The tests were taken on the transverse sections of each slice, which had been final ground using 1200 carbide silicon paper. The hardness was measured every 10 mm across the radius of each slice from the centre to within about 2 mm of the outside surface.

3.5.2 Hardness tests on the re-heat treated samples

To study the effect of tempering temperature and time on hardness, the re-heat treated specimens for XRD analysis were tested using Vickers hardness test equipment with a load of 10 kg and Rockwell hardness test equipment with a load of 150 kg.

3.6 Tensile test

3.6.1 Sample preparation

Tensile test specimens were machined in accordance with British Standard EN10002-1:1990, following the diagram in Figure 3.3. The gauge length was marked on the middle section of the specimen with ink and a line scribed from one end to the other. Two short lines were then scribed perpendicular to this line with a distance of 16 mm within the gauge length. The exact gauge length was determined by measuring the separation of the short lines with a travelling microscope.

3.6.2 Tensile testing

Tensile testing was carried out at room temperature on Hounsfield Test Equipment linked with a computer, using a 16 kN load. The extension rate was initially set at 0.24 mm/min and an extensometer was set on the gauge for proof stress and modulus measurements. The extensometer was then removed from the samples and the extension rate automatically increased to 5 mm/min, after 80% of the preset extension range, to stretch the specimen to fracture. The extension after testing was determined by measuring the distance from the short scribed line to the fracture surface on each half of the specimen. Yield strength (0.2% proof strength) and ultimate tensile strength (UTS) data were calculated by the computer software. Percentage elongation (%EI) and reduction in area (%RA) were measured from the broken specimens using a travelling optical microscope.

3.7 Optical microscopy observation

3.7.1 Sample preparation

3.7.1.1 Sample preparation for general morphology

As-received and re-heat treated samples for XRD analysis were selected for optical microscopy. For general morphology observations, samples were re-polished to 1 μm

and etched at room temperature in Vilella's reagent: *1g picric acid + 5ml HCl + 100ml ethanol* (Voort 1984) for 15 seconds. The samples were then taken out from the etching, immediately rinsed in methanol and dried.

3.7.1.2 Sample preparation for δ-ferrite examination

Although Vilella's reagent can outline δ-ferrite, to display δ-ferrite alone without revealing other phase constituents in the as-received steels, samples were re-polished to 1 μm and electrolytically etched in a 20% aqueous solution of NaOH at room temperature for approximately 5 seconds, using an open circuit voltage of 20 V.

3.7.2 Optical microscopy observation

General morphology of the etched samples was observed and imaged using an Olympus CH-2 microscope with digital imaging software. The etched samples for δ-ferrite examination were observed and imaged under a Polyvar microscope with digital imaging software.

3.8 Scanning electron microscopy (SEM)

3.8.1 Sample preparation

As-received and re-heat treated specimens for SEM microscopy imaging and EDX microanalysis used the same samples as optical microscopy. Samples for secondary electron imaging (SEI) and EDX microanalysis were re-polished to 1/4 μm, and then etched using the same etching as for the optical microscopy. To make sure the phases for EDX analysis can be seen, the surface for EDX analysis had to be etched. However, the etching had to be very slight compared to that for optical microscopy to reduce the influence of sample surface conditions caused by etching on EDX quantitative analysis. Samples for backscattered electron imaging (BEI) were re-polished to 1μm and then polished using Silico polishing suspension up to 20 minutes, rinsed immediately with plenty of water and dried.

3.8.2 SEM microscopes

A JEOL JSM 6400 SEM microscope with an operating voltage of 5~20 kV and a FEI Sirion FEG SEM microscope with an operating voltage in the range of 0.5~30 kV were used for this work. Both microscopes were fitted with a link Energy Dispersive X-ray (EDX) system. The JEOL JSM 6400 SEM microscope was used at the beginning of this work to show general microstructural features at lower magnifications (<5,000 ×). The high resolution FEI Sirion FEG SEM microscope was used later to show microstructural features at higher magnifications (up to 100,000×)

3.9 Transmission electron microscopy (TEM)

3.9.1 Sample preparation

3.9.1.1 Carbon extraction replicas

Some as-received and re-heat treated samples selected for SEM were also used to prepare carbon extraction replicas for precipitation analysis. Carbon extraction replicas samples were produced by using the double etching technique (Kay 1965). The polished sample surfaces were initially lightly etched in the Vilella's reagent, cleaned with methanol and dried. To ensure a very clean surface, the surfaces were cleaned with sheets of cellulose acetate before carbon coating. The samples were carbon coated using Edwards Speed device carbon coating equipment at a vacuum of $<5\times10^{-5}$ Torr. The coated carbon layer was scored to form ~2 mm squares using a scalpel and then put back into the Vilella's solution, followed by washing in methanol. The samples were then immersed in distilled water at an angle so that the carbon layers can lift off the sample. As a result, the carbon film detached from the samples, formed fragments and scattered in the water. They were then collected onto copper sample grids with tweezers and dried on filter paper for later TEM observation.

3.9.1.2 Thin foils

To perform matrix microstructural observation and phase composition microanalysis, thin foil specimens were prepared. Specimens were first cut to 1 mm thick from the samples similar to those for XRD analyses and then cut into 3.0 mm discs by using Spark Erosion. The discs were ground and polished on both sides to a thickness of approximately 80 μm and then electrolytically polished in a solution of 5% Perchloric, 35% Butoxyethanol and 60% Analar Methanol, at temperatures between -10 to –30°C and an operating current of 0.08 mA.

3.9.2 TEM microscopes

A Philips 420 TEM microscope with an accelerating voltage of 120 kV and a FEI Tecnai-20 TEM microscope with an accelerating voltage of 200 kV were used in this work. Both microscopes fitted with a link EDS (EDX) system. Carbon extraction replicas were examined on the Philips 420 TEM microscope. Thin foils were examined on the Philips 420 TEM microscope at the beginning of this work. Further microstructural observation and phase composite quantitative microanalyses were carried out with the FEI Tecnai-20 TEM microscope.

3.10 Imaging analysis

3.10.1 Retained austenite/ "retained austenite + fresh martensite" particles size measurement

To determine retained austenite/"retained austenite + fresh martensite" ($\gamma'/\gamma'+\alpha_F'$) grain size, the size of brighter particles in SEM images of the as-received and re-heated samples was measured by using the image analysis software SigmaScan Pro5 with a calibrated scale. The analysis was based on measuring the width of bright particles in a series of SEI SEM micrographs taken from at least 15 random fields of each specimen at 5000× magnification, The mean size distribution of $\gamma'/\gamma'+\alpha_F'$ regions can then be determined by using the data analysis software SigmaPlot.

3.10.2 Area fraction of austenite and retained austenite measurement

To estimate area fraction of austenite content on tempering and retained austenite at room temperature, area fraction of brighter regions in SEM micrographs was also measured using the image analysis software SigmaScan Pro5. Measurements were carried out on the same images used in section 3.10.1 for each specimen and the values were averaged.

3.10.3 Mean size of precipitates measurement

The mean size of precipitate particles in the samples after tempering at 557 °C and 640 °C were measured from negatives of the TEM bright filed images taken from carbon extraction replicas, using the image analysis software SigmaScan Pro5. Each particle was measured in two orthogonal directions and a mean equivalent radius/width was calculated based on equivalent areas. Except those coarse particles, at least 50 precipitates of each particle morphology were measured.

3.11 MT DATA calculation

The equilibrium phase transformation fraction of the super 13% Cr steel, Cast1, was calculated using MT DATA. Another super 13% Cr steel, Cast 3 (see Table 3.1), which had similar composition to Cast 1 but contained slightly higher C (0.025 wt%) and V (0.17 wt%) was also applied to compare the influence of C content on phase transformation. The elements used for the calculation were restricted to C, Si, Mn, Cr, Mo, Ni, Cu, V, N and Fe. The possible present phases used for the calculation were: bcc martensite, fcc austenite, liquid, cementite, M_7C_3, $M_{23}C_6$, M_6C, CMo, CMo_2, $C_{0.88}V$ and NV. The temperature range was 300 to 1500 °C.

Chapter 4

Results on the As-received Materials

This chapter presents microstructure and mechanical properties of the as-received super 13% Cr stainless steel slices.

4.1 Amounts of retained austenite in the as-received slices

Figure 4.1 shows XRD diffraction patterns of the as-received slice A1 across the radius of the original bar. Only fcc austenite and bcc martensite peaks were detected in the as-received materials. Table 4.1 gives the volume fraction of retained austenite in the seven as-received slices (A1-A4, and B1-B3) measured from the centre, half radius, and about 5~10 mm inside the outer rim. Retained austenite content was measured from the integrated intensities of austenite diffraction lines (200)fcc, (220)fcc and (311)fcc and martensite diffraction lines (200)bcc, (211)bcc and (220)bcc. Although (111)fcc and (110)bcc were the strongest peaks for austenite and martensite phase, they were located too close to each other to clearly differentiate (see Figure 4.1) and were therefore not used in the calculation. No obvious change of retained austenite content was found between the centre, half radius and near outside surface of these as-received slices except B1. The highest amount of retained austenite was found in slice A1 and the lowest was in slice B3. The variations of retained austenite content across the radius of slices A1 and A2 are shown in Table 4.2 and Table 4.3. No obvious change of retained austenite content was found from centre to near outside surface in either A1 or A2.

Table 4.1 Retained austenite content in the as-received slices measured by XRD

Slice	Diameter (mm)	Retained austenite content (vol%)		
		Centre	Half radius from centre	5~10 mm from outside surface
A1	216	31.0±1.7	34.0	30.0±2.6
A2	203	25.5±1.5	25.3	23.7±1.3
A3	165	30.4±0.8	29.5	29.5±0.7
A4	121	28.1±0.7	28.0	28.0±0.3
B1	133	28.4	28.1±0.1	17.1±0.6
B2	133	33.5	35.9	32.2
B3	152	18.7	18.8	18.8

Table 4.2 Distribution of retained austenite in the as-received slice A1 across the radius from centre to near outside surface

Distance (mm)	0	16	32	48	64	80	96
Content (vol%)	31.0	32.1	34.8	31.2	34.1	30.3	30.6

Table 4.3 Distribution of retained austenite in the slice A2 across the radius from centre to near outside surface

Distance (mm)	0	20	30	40	55	72	92
Content (vol%)	25.5	24.5	26.6	24.8	25.7	26.0	24.0

4.2 Hardness

Figure 4.2 shows Vickers hardness of the four as-received slices A1, A2, A3 and A4. Slice A4 was the hardest, but the other three slices had similar hardness values. For each slice the centre had lower hardness than other parts across the radius. Hardness tests on longitudinal sections across the radius of slice A2 shows similar values to test results from the transverse section. Table 4.4 lists Rockwell hardness (data supplied by CES) of the as-received slices B1, B2 and B3 tested on the transverse

section across the diameter. The data shows hardness distribution along the radius was not uniform, and B2 had the lowest hardness values.

Table 4.4 Hardness of the as-received slices B1, B2 and B3 (Data supplied by CES)

Slice	HRc on Tensile	Edge	1" Below	Mid-Radial	Centre	Mid-Radial	1" Below
B1	27.5 - -	28.5 30.5, 31, 31	28 28.5, 28.5, 28.5	28 27, 28, 28	28 25.5, 25.5, 23	28.5 26.5, 27, 27.5	29 27.5, 28.5, 28.5
B2	-	20	20.5	22	22	20.5	21
	27.5	-	-	-	-	-	-
B3	30	20	22.5	27	27	24	25.5

4.3 Tensile properties

Table 4.5 and Table 4.6 show tensile properties of the as-received steel bar A1-A4 (Cast 1) and B1-B3 (Cast 2). The data was supplied by CES and the tensile samples were machined from half-radius of the original bars. For Cast 1 (Table 4.5) there was no obvious variation in UTS, elongation (%EI) and reduction in area (%RA) between the four bars. However, bar A1 had slightly lower 0.2% proof strength than the other three bars. Note bar A1 had larger size (diameter) and higher retained austenite content than the others (see Table 4.1). For Cast 2 (Table 4.6), bar B2 had the lowest 0.2% proof strength and bar B3 had the highest. Note these three bars experienced different heat treatment regimes (see Tables 3.3, 3.4 and 3.5), and bar B2 contained the highest retained austenite while bar B3 contained the lowest (Table 4.1).

Table 4.5 Tensile property data of the as-received steel bar A1, A2, A3 and A4 (Data supplied by CES)

Steel bar	Diameter (mm)	0.2% Proof Strength (MPa)	UTS (MPa)	Elongation to Fracture (%)	Reduction in Area at Fracture (%)
A1	216	632	863	24.9	63.3
		610*	853*	25.4*	63.0*
A2	203	708	876	24.8	65.0
A3	165	661	854	26.2	65.5
A4	121	684	867	26.7	66.8

*retest

Table 4.6 Tensile property data of the as-received steel bar B1, B2 and B3 (Data supplied by CES)

Steel bar	Diameter (mm)	0.2% Proof Strength (MPa)	UTS (MPa)	Elongation to Fracture (%)	Reduction in Area at Fracture (%)
B1	133	752	876	28	73.2
B2	133	628	856	27.4	73.0
		641	849	26.4	70.5
B3	152	825	914	24.3	70.8

4.4 Microstructure

4.4.1 Optical microscopy

Optical observations show there was no obvious microstructural difference between the centre and near the outside surface (~10 mm from the outside surface) for a given batch. Moreover, the slices from the seven different batches appeared to have a similar microstructure. Figure 4.3 shows the optical microstructure of the specimen cut from slice A4 in the centre. Tempered martensite structure and a small amount of

δ-ferrite strings/particles can be easily identified. Although XRD analysis indicated that over 18 vol% retained austenite was present in these as-received specimens (Table 4.1), it proved difficult to distinguish the retained austenite by optical microscopy.

Optical observations on the electronic etched specimens found that the distribution of δ-ferrite in the as-received slices was not uniform throughout the bar. Figures 4.4 and 4.5 show the distribution of δ-ferrite in the as-received slices B1 and B3. Images were taken from the area where the highest concentration of δ-ferrite was found. Quantitative image analysis results indicated the volume fraction of δ-ferrite in these as-received slices was less than 1%.

4.4.2 SEM microscopy

4.4.2.1 Morphology

Secondary electron SEM micrographs taken from the centre of the as-received slices on the longitudinal direction after etching are shown in Figures 4.6 through 4.10. The elongated retained austenite laths/particles (brighter region) were found uniformly distributed along the martensite laths and the prior austenite grain boundaries. For Cast 1, the retained austenite in sample A1 appeared to be larger than that in A2 (Figure 4.6(a) and Figure 4.7(a)). For Cast 2, the size of retained austenite appeared in this order: B3 < B1 < B2 (Figures 4.8(a), 4.9(a) and 4.10(a)). Some fine precipitates were also found dispersed in the tempered martensite (darker region) in Cast 2 (Figures 4.8(b), 4.9(b) and 4.10(b)). Figure 4.11 gives the SEM micrographs taken from slice B3 on the transverse surface, showing a different appearance of retained austenite compared to that on the longitudinal surface, indicating that retained austenite grew along different directions.

Figure 4.12 and Figure 4.13 show the BEI SEM microstructures without etching. The images were taken from the centre of the as-received slices B2 and B3 along longitudinal direction. Film-like retained austenite can be seen (appear brighter). Some fine particles (brighter) were found distributed along the prior austenite grain boundaries (Figure 4.12). Figure 4.14 and Figure 4.15 show the morphology of δ-

ferrite in the as-received slices. Fine precipitates were observed distributed within the δ-ferrite particles in as-received slice A2 (Figure 4.14). However, no precipitation was found within δ-ferrite for the as-received slice B3 (Figure 4.15).

SEM EDX microanalysis using the FEI Sirion FEG SEM microscope on the as-received slices A1, A2, B1, B2 and B3 are given in Table 4.7 through Table 4.11. The values listed in the tables are mean composition with one standard deviation. These as-received slices appear to have very similar phase composition. As expected, retained austenite contained higher Ni than the martensite; δ-ferrite was enriched in Cr and Mo but was depleted in Ni (Table 4.9 and Table 4.11). EDX point analysis results show Cr content in δ-ferrite was higher than the surrounding matrix, indicating Cr depleted from the matrix and enriched in δ-ferrite during solidification. EDX point analysis results also show the fine, bright particles distributed along prior austenite grain boundaries (see Figure 4.12) and concentrated in δ-ferrite (Figure 4.14) were Mo-rich particles.

Table 4.7 SEM EDX microanalysis of the as-received slice A1 (wt%)

Area	Phase	Si	Mo	Cr	Fe	Ni
Bright regions	Retained austenite	0.6±0.1	1.9±0.3	12.0±2.4	74.6±1.9	10.4±1.6
Dark matrix	Tempered martensite	0.5±0.1	1.9±0.2	12.1±0.4	79.1±1.4	6.5±1.1

Table 4.8 SEM EDX microanalysis of the as-received slice A2 (wt%)

Area	Phase	Si	Mo	Cr	Fe	Ni
Bright regions	Retained austenite	0.6±2.2	1.9±0.1	12.7±0.2	73.2±0.3	11.6±2.9
Dark matrix	Tempered martensite	0.5±0.2	1.9±0.2	12.4±0.4	79.3±1.5	6.0±1.1

Table 4.9 SEM EDX microanalysis of the as-received slice B1 (wt%)

Area	Phase	Si	Mo	Cr	Fe	Ni
Bright regions	Retained austenite	0.6±0.2	1.9±0.3	12.6±0.5	75.1±2.2	9.9±1.8
Dark matrix	Tempered martensite	0.5±0.1	1.9±0.2	12.2±0.1	79.7±0.8	5.7±0.6
Strings	δ-Ferrite	0.4	3.0	15.8	77.3	3.5

Table 4.10 SEM EDX microanalysis of the as-received slice B2 (wt%)

Area	Phase	Si	Mo	Cr	Fe	Ni
Bright regions	Retained austenite	0.5±0.1	1.9±0.4	12.9±0.7	74.3±1.3	10.4±1.0
Dark matrix	Tempered martensite	0.5±0.1	1.8±0.2	12.6±0.3	80.9±0.4	4.2±0.4

Table 4.11 SEM EDX microanalysis of the as-received slice B3 (wt%)

Area	Phase	Si	Mo	Cr	Fe	Ni
Bright regions	Retained austenite	0.5±0.1	1.8±0.2	12.9±0.4	74.5±1.5	10.4±1.4
Dark matrix	Tempered martensite	0.5±0.1	2.1±0.2	12.5±0.2	79.3±0.8	5.8±0.8
Strings	δ-Ferrite	0.5±0.1	3.2±0.3	15.8±0.7	76.7±1.4	3.9±0.9

4.4.2.2 Retained austenite grain size

Figure 4.16 presents size distribution of retained austenite in the as-received slices. The retained austenite grain size, i.e. the width of elongated retained austenite particles in the as-received slices, was measured using the method described in Chapter 3 Experimental Procedure. The specimens were cut from the centre of the as-received slices. All of the measurements were performed at the surface along the longitudinal direction of the original bar. Size distribution was found to be in the region 50~500 nm for these slices except slice B2, which had some large austenite up to 700 nm. Table 4.12 lists the mean retained austenite particle size with standard deviation. The mean particle size in A1 and B2 was larger than that in A2, B1 and B3. Note the 0.2% proof strength of A1 and B2 was lower than that of A2, B1 and B3 (see Table 4.5 and Table 4.6).

Table 4.12 Mean retained austenite grain size in the as-received slices

Slice	Size (nm)
A1	210±80
A2	175±60
B1	185±70
B2	230±90
B3	150±60

4.4.3 TEM microscopy

As shown in Figure 4.17(a), TEM carbon extraction replicas examination found only a few precipitates presented in the as-received slices. EDS microanalysis on the thin foil specimen (Figure 4.17(b) and (c)) revealed that the block precipitate was enriched in Cr and Mo, suggesting it was $M_{23}C_6$ type carbide. Figure 4.18 through Figure 4.20 show thin foil TEM micrographs and associated selected area diffraction (SAD) patterns of the as-received slice A1, A2 and A3. All of the specimens were

cut from the centre of the as-received slice. SAD patterns indicated that the fine, darker film/particle-like regions in the bright field images were retained austenite, which formed along the martensite laths. The retained austenite contained high dislocation densities. Due to the fine size of retained austenite, SAD pattern taken from the fcc retained austenite was overlapped by the bcc martensite diffraction pattern.

4.5 Summary

The microstructure of the as-received steel consisted of film/particle like retained austenite, tempered martensite and minor δ-ferrite. Retained austenite distributed along martensite lath boundaries. A high dislocation density was observed distributed in retained austenite. SEM EDX analyses indicated the phase composition in the as-received slices was very similar. XRD analysis indicated retained austenite content in the as-received slice was in the range 18~36 vol%. Slices A1 and B2 contained higher levels of retained austenite (~30 vol% and ~36 vol%) than the others, while B3 contained the lowest level of retained austenite (~18 vol%). Image analysis suggested that the mean size of retained austenite was in the range 150~230 nm. Slices with higher levels of retained austenite content (i.e. A1 and B2) also contained larger size of retained austenite but exhibited a lower level of yield strength.

Chapter 5

Results on the Re-heat Treated Materials

This chapter presents the microstructural features and mechanical properties of the super 13% Cr steel after laboratory re-heat treatment, showing the influence of tempering temperature and time on these properties.

5.1 Retained austenite content

5.1.1 Variations in amounts of retained austenite with tempering temperature

XRD analysis was performed on all of the re-heat treated specimens to determine phase constituents and volume fraction of retained austenite. Figure 5.1 shows X-ray diffraction patterns of the specimen in the as-air cooled (after re-austenitisation) state and some specimens after single tempering. For the as-air cooled specimen, only martensite/ferrite peaks were found and no retained austenite peak was detected, indicating that even after re-austenitization all the austenite transformed into martensite on cooling. After tempering in the range 567-700 °C, 4 h, austenite was detected, indicating that austenite did form on tempering. Only fcc austenite and bcc martensite/ferrite peaks were observed and no other phase was detected, which revealed that no large amounts of precipitates were produced during tempering treatment. The X-ray diffraction patterns also show that the highest austenite peaks appeared in the specimen tempered at 635 °C.

Figure 5.2 shows volume fraction of retained austenite as a function of tempering temperature for both single and double tempering. After single tempering (ST), i.e. the first stage of double tempering, the amount of retained austenite increased with tempering temperature up to the peak value of 36 vol% at 635 °C. Thereafter higher temperatures produced less retained austenite, and fresh martensite formed on

cooling after tempering ≥635 °C. When the first stage tempering temperature was below 635 °C, retained austenite content did not change after the second stage tempering (DT), which suggests that no microstructure change occurred during the second stage tempering. However, when the first stage tempering was above 635 °C the retained austenite content increased after the second tempering, indicating that fresh martensite partially re-transformed to austenite during the second stage tempering.

5.1.2 C content in retained austenite after tempering at different temperature

To estimate stability of retained austenite, C content in retained austenite after tempering in the range 580-700 °C was determined by means of XRD. XRD is commonly used to determine C content in austenite by measuring austenite lattice parameter (Cullity 1978 and Onink et al. 1993). Austenite lattice parameter a_γ, was determined using the Nelson-Riley method (Cullity 1978). The Nelson-Riley parameter gives a straight-line extrapolation for a_γ over a range of diffraction angles and then identifies the most accurate a_γ at $\theta = 90°$. C content in retained austenite phase was then calculated by using the empirical equation (5-1) (Ridley 1969 and Ruhl et al. 1969) and the results are plotted in Figure 5.3.

$$a_\gamma = 0.3572 + 0.0032C \text{ (wt\%)} \quad (5\text{-}1)$$

where a_γ is austenite parameter (nm) and C is carbon content in austenite (wt%).

As shown in Figure 5.3 (a) and (b), after single tempering (ST) retained austenite lattice parameter and C content in retained austenite reduced approximately linearly with the increase in tempering temperature, suggesting that the stability of retained austenite declined. However, double tempering (DT) resulted in larger retained austenite lattice parameter and higher C content for the first tempering at 670 °C and 700 °C, and C content in retained austenite remained approximately constant with increasing temperature in the first stage of double tempering, indicating that the stability of retained austenite was improved.

5.1.3 Variations in amounts of retained austenite with tempering time

Figure 5.4 shows volume fraction of retained austenite as a function of tempering time. For tempering temperatures in the range 600-635 °C, initially retained austenite content increased rapidly with increase in tempering time up to 6 h. However, after tempering for longer periods (>6 h) the retained austenite content followed a different trend, depending on tempering temperature. For example, after tempering at 620 °C retained austenite content showed almost no change as tempering time was increased from 8 h to 24 h. However, the steel showed a marked decline in retained austenite content after tempering at 635 °C for 12 h due to the formation of fresh martensite. Figure 5.4 also shows that if the first stage tempering was at a relatively low temperature, i.e. 600 °C to 620 °C, then the second temper did not change amounts of retained austenite even after 24 h, which suggests that no microstructure change occurred after the second tempering. Note specimens tempered at 630 °C were re-austenitized at 940 °C for 2 h, air cooled, before tempering while the other specimens were re-austenitized at 950 °C for 2 h, air cooled, before tempering.

5.1.4 Variations in amounts of retained austenite with combined tempering time-temperature

From the results obtained above, the amount of retained austenite at room temperature is clearly dependent on both tempering temperature and time. This requires further investigation. A time-temperature parameter of the Hollomon-Jaffe type, which was developed originally for correlating the hardness of steels with time and temperature (Hollomon and Jaffe 1945), using an equation constant of 40 (IIW 1983) was applied to determine whether the volume fraction of retained austenite shown in Figure 5.2 and Figure 5.4 could be presented as a single master curve. The Hollomon-Jaffe parameter used in this work is:

$$P = (273+T) \times (40+\log t)\times 1000^{-1} \qquad (5\text{-}2)$$

where T is temperature in degrees Celsius (°C) and t is time in hours (h).

The volume fraction of retained austenite is plotted against the Holloman-Jaffe parameter P in Figure 5.5. It is a very similar appearance to Figure 5.2, and all of the time and temperature-dependent specimens matched to the same curve. Figure 5.5 shows that the maximum amount of retained austenite was ~39vol% at P~36.9, indicating that retained austenite content could not exceed 40vol% after tempering at these tempering temperature/time range.

5.1.5 XRD measurement errors

The accuracy of using XRD equipment to determine austenite content is in the region of ±0.5% for the range of 1.5~38.0% austenite (Durnin and Ridal 1968). To determine measurement errors caused by heat treatment, five specimens were re-austenitized, air-cooled and then tempered at the same temperature for 4 h. The corresponding retained austenite content measured by using XRD is given in Table 5.1, with a standard deviation of ±1.3 vol%.

Table 5.1 Determining retained austenite content measurement error caused by heat treatment. The five specimens had been tempered together in the furnace.

Specimen	1	2	3	4	5
Retained austenite content (vol%)	16.4	15.4	14.2	13.1	15.3
Mean value with standard deviation = 14.7± 1.3 (vol%)					

5.2 The A_{c1} temperature

It is already known that the A_{c1} temperature of martensite to austenite transformation depends not only on chemical composition but also heating rate of the steel (Pickering, 1978). According to Figure 5.2 and considering XRD measurement errors, the A_{c1} point in the current work was around 560 °C. This result is in good agreement with the A_{c1} temperature of low carbon-CrNiMo steels measured by Dias and Wilson (1980).

5.3 Hardness

In industry Rockwell hardness is generally applied to appraise hardness of low-carbon martensitic 13% Cr stainless steels instead of Vickers hardness. In this work both Vickers and Rockwell hardness were measured.

5.3.1 Variations in hardness with tempering temperature

Hardness as a function of tempering temperature is plotted in Figure 5.6. Hardness exhibited the inverse trend to that of retained austenite content (Figure 5.2) as a function of tempering temperature. The lowest hardness was at 635 °C, which is the peak value for volume fraction of retained austenite. The Vickers hardness plot as a function of retained austenite was not symmetrical (Figure 5.6(a)), i.e. for the same austenite content, a greater hardness was found for tempering temperatures above 635 °C than below. However, the hardness did not change after the second tempering even though the first stage tempering temperatures higher than 635 °C increased the austenite content (Figure 5.6(b)). This implies that there is little difference between the hardness of fresh martensite and retained austenite.

Figure 5.7 gives variations in hardness with the second stage tempering temperature after a first stage tempering at 625 °C. After the first stage tempering at 625 °C, 4 h, and the second stage tempering in the range 550-580 °C, 2 h, the hardness decreased slightly as the second tempering temperature increased. This was due to the slightly increase in retained austenite content with higher second tempering temperature.

5.3.2 Variations in hardness with tempering time

Hardness as a function of tempering time for tempering at 600 °C and 620 °C are plotted in Figure 5.8. Hardness decreased linearly after tempering at 4, 8 and 24 h at both temperatures, and the second tempering at 550 °C for 2 h did not change hardness at either temperature. The hardness trend for 600 °C is parallel to that for 620 °C, suggesting that at relatively low tempering temperature (600 °C and 620 °C) hardness is directly proportional to tempering time.

Hardness as a function of tempering time when tempered at 635 °C is plotted in Figure 5.9. This demonstrates that hardness is a function of the retained austenite content. Hardness was inversely related to retained austenite content for tempering times ranging from 0.5 to 24 h. For tempering times of 0.5 to 4 h, hardness decreased gradually with tempering time, due to the increase in retained austenite content. However, after tempering for a longer time of 6 to 24 h hardness increased slightly with tempering time due to the decrease in the amount of austenite, which had transformed to fresh martensite instead.

5.3.3 Variations in hardness with combined tempering time-temperature

The combined influence of tempering time and temperature on hardness is correlated through the Hollomon-Jaffe tempering time-temperature parameter P in equation (5-2), and the result is plotted in Figure 5.10. It appears that hardness for all of the specimens - tempered at different temperatures/times - follow the same smooth curve. For P in the range 33.6-39.6, hardness decreased rapidly as P increased, reaching a minimum while P was in the small range of 36.8-37.1 (i.e. co-incident with the maximum retained austenite- see Figure 5.5). After that, hardness increased gradually with the increase in P, believed to be due to the formation of fresh martensite.

5.4 Tensile properties

5.4.1 Tensile properties after tempering at different temperature

Figure 5.11 gives stress-strain curves of the tensile samples after single and double tempering, showing continuous yielding behaviour. These curves only display the stress-strain behaviour for the extension in the range 0~0.8 mm as the extensometer was removed from the tensile specimens during testing when the extension reached 0.8 mm. When the first tempering temperature was ≤635 °C, the second tempering did not change stress-strain behaviour of the specimens, confirming that no microstructural change occurred after the second tempering (Figure 5.11(a)).

However, when the first tempering temperature was > 635 °C, the second tempering produced different stress-strain behaviour, confirming that microstructural change occurred after the second tempering (Figure 5.11(b)). SEM morphologies of the fracture surfaces are presented in Figure 5.12, showing they were typical ductile fractures with no obvious change in appearance with changes in heat treatment conditions.

The effect of tempering temperature on yield strength (0.2% proof strength), ultimate tensile strength (UTS) and percentage elongation (EI%) are plotted in Figure 5.13. Figure 5.13(a) gives 0.2% proof strength and UTS as a function of tempering temperature. Like hardness, 0.2% proof strength was inversely related to retained austenite content which initially increased with tempering temperature. After tempering at temperatures in the range 600-670 °C, 0.2% proof strength decreased as tempering temperature increased to minimum strength at 635 °C (peak value for retained austenite content), and thereafter increased with further tempering temperature up to 670 °C. When the first tempering temperature was lower than 640 °C, 0.2% proof strength did not change after the second tempering since no phase constituents changed. However, when the first tempering temperature exceeded 640 °C, 0.2% proof strength improved significantly after the second tempering due to the re-transformation of fresh martensite. Conversely, UTS remained almost constant until 640 °C, then increased slightly at higher tempering temperature. The second tempering did not change UTS at any of the tempering temperatures tested. Figure 5.13(b) gives percentage elongation as a function of tempering temperature. Percentage elongation values varied between 25~28% when the first tempering temperature was in the range 600-640 °C, but the second tempering changed percentage elongation only at 640 °C. Percentage elongation values declined rapidly to 21~22% after tempering at >640 °C due to the formation of fresh martensite. However, the values increased to 27~28% after the second tempering at 550 °C due to the increase in retained austenite volume fraction.

Figure 5.14 shows the effect of second tempering temperature on tensile properties after the first tempering at 625 °C, 4 h, associated with retained austenite content. 0.2% proof strength decreased slightly (20 – 30 MPa) with the increase in the second

tempering temperature from 550 °C to 580 °C, accompanied by a slightly increase in amount of retained austenite. However, UTS remained constant. Taking measurement error into account, elongation and reduction in area did not change measurably.

5.4.2 Tensile properties after tempering at different time

Figure 5.15 shows the effect of tempering time on tensile properties associated with the retained austenite content. Increasing holding time from 4 to 24 h at 600 °C and 620 °C respectively resulted in a slight decrease in 0.2% proof strength accompanied by an increase in retained austenite. The second tempering at 550 °C for 2 h did not change 0.2% proof strength since retained austenite content did not change. The specimen tempered at 600 °C exhibited higher 0.2% proof strength than that tempered at 620 °C since the latter contained more retained austenite, which reduced yield strength. When increasing holding time from 8 to 24 h at 620 °C, retained austenite content did not change (~36 vol%), but 0.2% proof strength reduced dramatically from ~600 MPa to ~500 MPa, suggesting that microstructural change occurred with these tempering conditions.

5.4.3 Combined influence of tempering time-temperature on 0.2% proof strength

The combined influence of tempering temperature and time on 0.2% proof strength is also correlated through the Hollomon-Jaffe time-temperature parameter P in equation (5-2), and the results are plotted in Figure 5.16. Like hardness, it appears that the 0.2% proof strength for all of the samples follow the two smooth curves for single and double tempering respectively across the range of tempering temperatures and times tested. After single tempering (ST) for P in the range 35.4-38.3, 0.2% proof strength decreased rapidly as P increased reaching a minimum when the P was in the range 36.8-37.1, corresponding with maximum retained austenite and lowest hardness in Figures 5.5 and 5.10. After that, 0.2% proof increased gradually as P increased. When the first tempering at P<37.1, the second tempering did not change 0.2% proof strength. However, when the first tempering at P >37.1, 0.2% proof strength improved remarkably after the second tempering.

5.4.4 Strain-induced martensite transformation

Strain-induced transformation of retained austenite to martensite occurred during tensile testing. XRD measurement results (Table 5.2) show retained austenite content in the gauge length (deformed during tensile testing) was lower than that in the shoulder (not deformed, therefore represents the original retained austenite content), indicating that retained austenite partially transformed to martensite during deformation. However, the amount of retained austenite that could transform to martensite on straining was dependent on the tempering temperature. For example, after tempering ≥635 °C, more retained austenite transformed to martensite on straining than <635 °C. However, when the first tempering ≥635 °C, after the second tempering more retained austenite remained unchanged after tensile testing than in samples which had received only single tempering.

Table 5.2 Strain-induced retained austenite to martensite transformation during tensile testing, measured by using XRD

Tempering Condition	RA measured from the shoulder	RA measured from the gauge Length	Transformed RA	Transformed RA / Total RA Ratio
620°C/4h	26.5	15.7	10.8	41%
635°C/4h	36.5	9.6	26.9	74%
650°C/4h	15.3	4.8	9.6	67%
650°C/4h+550°C/2h	25.1	16.2	8.9	35%

RA means retained austenite (vol%).

5.4.5 Summary

The amount of austenite remaining at room temperature after tempering, i.e. retained austenite, is dependent on tempering temperature and time. The amount of retained austenite increased with higher tempering temperature or longer holding time until the point at which fresh martensite formed on cooling. Beyond this limit, the amount of retained austenite reduced. The combined influence of tempering temperature and time on the amount of retained austenite can be presented using the Hollomon-Jaffe

time-temperature parameter P with a constant 40:

$$P = (273 + T(°C)) \times (40 + \log_{10}t\ (h)) \times 1000^{-1}$$

where T is tempering temperature (°C) and t is tempering time (h).

Hardness and yield strength (0.2% proof strength) were inversely related to tempering temperature/time in part due to changes in the level of retained austenite. Although retained austenite decreased hardness and yield strength significantly, it was not the only factor to affect hardness and yield strength. The formation of fresh martensite and its transformation behaviour also played a key role. The combined influences of tempering temperature-time on hardness and yield strength can also be presented using the above Hollomon-Jaffe time-temperature parameter P.

P vs. Volume fraction of retained austenite curve shows that after single tempering (ST) the amount of retained austenite increased as P increased up to a value of 36.9, but thereafter the amount of retained austenite decreased with increase in P value due to the formation of fresh martensite. *P vs. hardness* and *P vs. 0.2% proof strength* curves show that hardness and yield strength decreased as P increased reaching minimum hardness and yield strength at P~36.9. Thereafter both increased with increasing P values. After double tempering (DT) with first tempering at P>36.9, amounts of retained austenite increased due to the re-transformation of fresh martensite to austenite. Hardness did not change but yield strength improved significantly after the second tempering. The effect of P on yield strength is therefore more significant than on hardness.

5.5 Matrix (martensite, retained austenite and δ-ferrite) microstructure

5.5.1 Optical and SEM morphology

Figure 5.17 SEM micrographs taken by the secondary electron imaging (SEI) mode

revealed that the as-air cooled (after re-austenization) microstructure was lath martensitic structure with a minor amount of δ-ferrite, consistent with the XRD analysis results. The δ-ferrite phase was not produced during the re-heat treatment, but formed during solidification. However, as shown in Figures 4.4 and 4.5, the volume fraction of δ-ferrite was <1.0%.

The tempering treatment in this work was performed between the austenite formation start temperature A_{c1} and the austenite formation complete temperature A_{c3}. Therefore, during tempering a two-phase microstructure of austenite and martensite formed. Figure 5.18 shows optical micrographs of some tempered specimens. At low temperature, 557 °C, the structure was relatively coarse and the prior austenite grains, packets, and martensite laths can be seen (Figure 5.18(a)). However, with increased tempering temperature, the structures become very fine and optical microscopy is insufficient to see the microstructures in detail (Figure 5.18(b), (c) and (d)).

Secondary electron SEM micrographs taken by the Jeol 6400 SEM microscope at low magnifications (1000 × and 2000 ×) are exhibited in Figures 5.19, 5.20 and 5.21, showing the evolution of microstructure with tempering temperature and time. Figure 5.19 shows the evolution of microstructure with tempering temperature. Bright laths uniformly aligned parallel within the packets in each prior austenite grain. Retained austenite appears brighter than tempered martensite (as a result of standing proud of the surface following etching). The significant changes in microstructure starting to occur at 635 °C can be seen. The micrographs appeared to show more bright laths for samples tempered ≥635 °C than below. However, this qualitative view can be misleading. For example, Figure 5.19(g) and (h) (i.e. 670 °C, 700 °C) appear to contain more austenite than Figure 5.19(c) and (d) (i.e. 620 °C, 630 °C), but XRD indicated that the reverse was true. Figure 5.20 shows after second tempering at 550 °C for 2 h, at a low magnification (1000 ×), the microstructure appeared similar to that after single tempering. Figure 5.21 shows the evolution of microstructure with tempering time. Longer tempering time also resulted in greater amounts of bright laths but again this did not mean larger amounts of retained austenite. For example, tempering at 635 °C for 24 h appeared to have more bright regions than tempering

for 1 h (Figures 5.21(a) and (d)), but XRD results showed the retained austenite content was almost the same (26.1 vol% and 25.3 vol%).

Further microstructure observation was carried out using the high resolution FEI Sirion FEG SEM microscope at relatively higher magnifications (10,000 ~ 100,000 ×). Images at 5,000 × magnification were also taken to show microstructures in a relatively larger area within the specimen. Figures 5.22 through 5.29 represent typical microstructures, taken by secondary electron imaging (SEI) mode at 5,000×, 20,000× and 50,000× magnifications for each specimen, after single/double tempering at different temperatures/times. The increase in amounts and size of bright laths with increasing tempering temperature and time can be seen easily. After single tempering at 600 °C for 4 h, Figure 5.22, retained austenite (γ') appeared as regions of brighter contrast, and exhibited as elongated particles. As mentioned above, this is because they were standing proud of the surface after etching. In other words, the tempered martensite etched more rapidly than the retained austenite. However, for specimens tempered ≥635 °C, the large brighter regions will have consisted of retained austenite (γ') and fresh martensite (α_F'), although they appeared very similar in morphology. As shown in Figure 5.23, after tempering at 700 °C, the specimen contained only 7.8 vol% retained austenite although a large number of brighter laths were observed. After double tempering for the first tempering ≤635 °C (Figure 5.24), the microstructure appeared very similar to that of single tempering. However, as shown in Figure 5.25, for specimens tempered at >635 °C, the second tempering resulted in the original brighter elongated particles decomposing to film/particle-like retained austenite (brighter contrast) and tempered martensite (darker contrast). Increasing holding time from 8 to 24 h at 600 °C and 620 °C also resulted in larger brighter particles, i.e. more retained austenite (Figures 5.26, 5.27, 5.28 and 5.29). Moreover, after the second tempering at 550 °C, 2 h, the microstructures appeared the same as single tempering and no decomposition of bright laths was observed.

Backscattered electron imaging (BEI) mode was also used to characterise the microstructure. The specimens were polished to silco finish but were not etched. Figures 5.30, 5.31 and 5.32 present the SEM BEI micrographs of some tempered specimens. The difference in crystal orientation can be seen from the "channeling

contrast". Fine bright particles were also found precipitated along the prior austenite grain boundaries (Figure 5.31(a)). Details of results for precipitate carbides/carbonitrides will be presented later.

5.5.2 TEM morphology

Thin foil TEM micrographs of the tempered specimens are shown in Figures 5.33 through 5.39. After tempering at 557°C, Figure 5.33, martensite laths aligned within packets of the prior austenite grains. It is not easy to detect retained austenite by electron diffraction in the TEM since the amount of retained austenite was less than 1 vol%. At 630 °C, Figure 5.34, retained austenite formed along the lath martensite boundaries, and some isolated retained austenite particles were also observed. At 635 °C, Figure 5.35, bright field image and selected area diffraction (SAD) pattern (Figure 5.35(a) and (b)) also show the elongated retained austenite particles distributed along the martensite lath boundaries. However, more isolated retained austenite islands were also formed (Figure 5.35(c) and (d)). (Note at 635 °C retained austenite content reached a maximum). After tempering at 700 °C, Figure 5.36, it was very difficult to distinguish retained austenite from martensite although XRD revealed that it should be present. The SAD pattern (Figure 5.36(c)) indicated that the heavily dislocated dark lath in Figure 5.36(b) was martensite. After double tempering, Figure 5.37, however, retained austenite formed as thin films between martensite laths, as shown in the marked area in Figure 5.37(a). This interlath thin film retained austenite is illuminated in dark field image using an $(200)_\gamma$ austenite reflection (Figure 5.37(b)). Note in the dark field image, the bright region appearing in the lath structure resulted from the strong reflection of martensite diffraction, not retained austenite. Due to the fine size (<30 nm), the SAD pattern taken from the retained austenite film (Figure 5.37(c)) comprises two sets of net patterns, the one from the fcc retained austenite which formed from fresh martensite and the other from the bcc martensite. The expected orientation relationship between the retained austenite and the martensite is $[\bar{1}11]_{bcc}$ // $[011]_{fcc}$. Figure 5.38 and Figure 5.39 also shows the bright field images and SAD pattern taken from the double tempered specimen for the first temper at 700 °C for 4 h. The brighter lath structure was tempered martensite. SDA pattern indicated that the darker lath structure with a high

dislocation density was tempered martensite which formed from fresh martensite (Figure 5.39).

5.5.3 Quantitative imaging analysis

5.5.3.1 Quantitative image analysis for amounts of austenite on tempering

Figure 5.40 presents the variation in the amount of austenite at tempering temperatures compared to the retained austenite after cooling to room temperature. As previously, the brighter regions in SEI SEM micrographs for single tempered specimens are either retained austenite (tempered <635°C) or 'retained austenite + fresh martensite' aggregate (tempered >635°C). Since retained austenite and fresh martensite result from austenite formed on tempering, the brighter regions in SEM micrographs for single tempered specimens reflect the austenite formed during the tempering heating period. The area fraction of austenite on tempering can therefore be estimated by measuring the area of brighter regions in SEM micrographs using the quantitative image analysis method described in Chapter 3. Measurements were carried out over eight SEM images and the values were averaged for each specimen. The area fraction of retained austenite at room temperature after double tempering was also measured using the same technique. As shown in Figure 5.40, the area percentage of austenite increased with temperature, which supports that theory that austenite transformation is a diffusion-controlled process. After cooling to room temperature the area percentage of retained austenite decreased with temperature when the first temper >635°C, suggesting that fresh martensite formed on cooling.

5.5.3.2 Retained austenite/'retained austenite + fresh martensite' grain size

Since in the SEM micrographs the difference between retained austenite and fresh martensite could not be reliably determined, the "grain" here can be defined as:

a. Retained austenite (γ') films/particles, which presented in the as-received structure and the laboratory tempered structure for the tempering temperature-time parameter P <36.9.

b. Retained austenite + fresh martensite ($\gamma'+\alpha'_F$) laths/particles, which presented in the laboratory tempered structure for the tempering temperature-time parameter P >36.9.

Therefore, the "grain size" here means the width of the retained austenite or "retained austenite + fresh martensite" ($\gamma'/\gamma'+\alpha_F'$) films/laths/particles, which appeared brighter regions in the SEI SEM micrographs and was the smallest unit in the structure. Figures 5.41, 5.42, 5.43 and 5.44 show the size distribution of the retained austenite or 'retained austenite + fresh martensite' ($\gamma'/\gamma'+\alpha_F'$) after tempering at different temperatures/times. In these figures the width of $\gamma'/\gamma'+\alpha_F'$ films/laths/particles was found to be distributed in the range 50 nm to 800 nm, and although the variations are not dramatic, the size increased with increasing tempering temperature and time. Figures 5.41 shows the variations in grain size with tempering temperature. After tempering at 600 °C for 4 h, there was a narrow range of grain size (Figures 5.41(a)). A small number of coarser grains (>300 nm) were also observed. As the tempering temperature increased up to 700 °C, the distribution of grain size became boarder, with a maximum mean size of 750 nm (Figures 5.41(b) through (f)). The second temper (Figure 5.42) had no obvious change on the grain size for the first temper ≤635 °C. However, grain refinement occurred after the second temper when the first temper ≥650 °C, with a narrower range of grain size seen. Figure 5.43 shows the $\gamma'/\gamma'+\alpha_F'$ became larger with both increasing tempering temperature and time when tempered at 600, 620 and 635 °C. Figure 5.44 shows the retained austenite grain size distribution after double tempering when the first temper at 620 °C for 24 h. The second temper at 550 °C for 2 h had no obvious change the size distribution compared to single tempering (Figure 5.43(f)).

Table 5.3 summarizes the mean grain size of $\gamma'/\gamma'+\alpha_F'$ after tempering at different temperatures/times. Table 5.3a lists the influence of tempering temperature on grain size. The grain size increased from 150±90 nm at 600 °C to 320±120 nm at 700 °C. When the first temper ≤635 °C, the second tempering did not alter the mean size of the films/particles, confirming that no microstructural change occurred and that the grains were retained austentie. However, when the first temper ≥650 °C, the second tempering reduced the size to 210±80 nm, confirming the occurrence of fresh

martensite decomposition. Table 5.3b shows grain size also increased with holding time.

Table 5.3a Summary of mean grain size after tempering at different temperature

Single tempering	Phase	Grain size (nm)	Double tempering	Phase	Grain size (nm)
600°C/4h	γ'	150±90	-	-	-
630°C/4h	γ'	260±80	630°C/4h+550°C/2h	γ'	260±80
635°C/4h	γ' + α'_F	280±100	635°C/4h+550°C/2h	γ'+ α'_F	280±100
650°C/4h	γ' + α'_F	290±110	650°C/4h+550°C/2h	γ'	210±80
700°C/4h	γ' + α'_F	320±120	700°C/4h+550°C/2h	γ'	210±80

Table 5.3b Summary of mean grain size after tempering at 600 °C, 620 °C and 635 °C for different time

Tempering temperature	Tempering time (h)	Phase	Grain size (nm)
600°C	8	γ'	180±65
	24	γ'	225±85
620°C	8	γ'	250±95
	24	γ' + α'_F	280±110
620°C/24h+550°C/2h		γ' + α'_F	310±145
635°C	1	γ'	230±75
	8	γ' + α'_F	265±85
	24	γ' + α'_F	345±125

5.5.4 Chemical microanalysis

5.5.4.1 SEM EDX microanalysis

Phase composition of the tempered specimens was analysed by using EDX with the FEI Sirion FEG SEM microscope and the Jeol 6400 SEM microscope. Figure 5.45 and Table 5.4 show the distribution of alloy element in the specimens tempered at 600°C/4h, 635°C/4h + 550°C/2h and 700°C/4h+550°C/2h using the FEI Sirion FEG

SEM microscope. No obvious variations of Cr and Mo were detected, however, Ni content in the retained austenite (γ') or the 'retained austenite and martensite' aggregate ($\gamma'+\alpha_F'$) (the brighter contrast) appeared higher than in the tempered martensite (α_T') (the darker contrast) for all of these specimens. Moreover, Ni redistribution within the γ' or $\gamma'+\alpha_F'$ laths also occurred when tempering at higher temperature or on subsequent cooling to room temperature. At 600 °C, Figure 5.45 (a) and Table 5.4a, Ni content in the retained austenite was 10~13 wt%, which was twice that in the tempered martensite (~6 wt%). At 635 °C, Ni exhibited a similar distribution to that at 600 °C, and was unchanged by the second temper at 550 °C for 2 h (Figure 5.45(b) and Table 5.4b). However, at 700 °C, Ni content in most austenite and fresh martensite reduced to ~8 wt% although in some laths it remained at ~12 wt% (Figure 5.45(c) and Table 5.4c). The second temper at 550 °C for 2 h (Figure 5.45(d) and Table 5.4d) resulted in Ni being rejected when the newly formed tempered martensite decomposed from the fresh martensite (area 2, 7 and 8), and enriched in the retained austenite (area 1, 3 and 6).

Mean phase composition of some tempered specimens is summarized in Table 5.5. There was no obvious difference in amounts of Cr and Mo between tempered martensite and retained austenite or 'retained austenite + fresh martensite', but higher amounts of Ni was found in the latter. δ-ferrite contained higher Cr (~16 wt%) than martensite and retained austenite.

The SEM EDX quantitative measurements only provide approximate indications of elements distribution after tempering because the size of the films/laths/particles structure was very fine (<500 nm), and therefore the size of the interaction volume was probably larger than the area of interest for EDX analysis. Consequently, the SEM EDX quantitative analysis values were probably overstated as they may have contained a contribution from the region underneath the specimen surface.

Table 5.5a EDX microanalysis of the as-air cooled specimen (wt%)

Microscope	Phase	Fe	Cr	Ni	Mo	V	Si
FEI Sirion FEG	δ-Ferrite	77.2±0.8	15.5±0.1	2.2±0.4	4.0±0.1	0.7*	0.5±0.1
Jeol 6400	δ-Ferrite	77.2±0.3	16.2±0.2	1.9±0.2	4.0±0.3	0.3±0.1	0.3±0.1
FEI Sirion FEG	martensite	78.4±0.5	12.7±0.2	5.6±0.3	2.0±0.2	-	0.4±0.1
Jeol 6400	martensite	79.1±0.3	12.7±0.2	5.3±0.2	2.1±0.1	-	0.3±0.1

Table 5.5b EDX microanalysis of the specimen after tempering at 600°C for 4h using FEI Sirion FEG SEM (wt%)

Phase	Fe	Cr	Ni	Mo	Si
Retained austenite	72.7±1.0	12.9±0.5	11.8±1.1	2.1±0.3	0.5±0.2
Tempered martensite	78.8±0.5	12.8±0.3	6.1±0.6	1.8±0.2	0.5±0.1

Table 5.5c EDX microanalysis of the specimen after tempering at 635°C for 4h using FEI Sirion FEG SEM (wt%)

Phase	Fe	Cr	Ni	Mo	V	Si
Retained austenite + fresh martensite	75.0±1.9	12.7±0.1	8.7±1.1	1.9±0.4	-	0.6±0.2
Tempered martensite *	79.1	12.6	5.3	1.7	-	0.4
δ-Ferrite	76.5±0.1	15.8±0.3	2.5±0.1	4.1±0.4	-	0.6±0.9
Precipitates in δ-ferrite*	72.7	15.8	2.9	7.3	0.5	0.5

* The value was detected from one area, not average value.

Table 5.5d EDX microanalysis of the specimen after tempering at 700°C for 4h using FEI Sirion FEG SEM (wt%)

Phase	Fe	Cr	Ni	Mo	Si
Retained austenite + fresh martensite	76.9±2.1	12.3±0.4	8.4±2.3	2.0±0.3	0.5±0.1
Tempered martensite	79.7±1.0	12.8±0.3	4.9±1.1	2.2±0.3	0.6±0.2

Table 5.5e EDX microanalysis of the specimen after tempering at 635°C/4h + 550°C/2h using Sirion FEG SEM (wt%)

Phase	Fe	Cr	Ni	Mo	Si
Retained austenite	74.7±2.0	12.5±0.5	10.3±2.0	1.9±0.2	0.5±0.1
Tempered martensite	79.2±1.2	12.7±0.3	5.4±0.9	2.1±0.2	0.6±0.1
δ-ferrite with precipitates	77.9±2.6	15.6±0.7	2.3±2.6	3.6±0.5	0.6±0.1

Table 5.5f EDX microanalysis of the specimen after tempering at 670°C/4h + 550°C/2h using FEI Sirion FEG SEM (wt%)

Phase	Fe	Cr	Ni	Mo	Si
Retained austenite	75.2±2.6	12.6±0.4	10.2±2.4	1.9±0.2	0.5±0.1
Tempered martensite	78.8±2.0	12.2±0.5	6.4±2.3	2.1±0.3	0.5±0.1

Table 5.5g EDX microanalysis of the specimen after tempering at 700°C/4h + 550°C/2h using FEI Sirion FEG SEM (wt%)

Phase	Fe	Cr	Ni	Mo	Si
Retained austenite	77.2±2.2	12.3±0.4	8.1±2.1	2.0±0.2	0.5±0.1
Tempered martensite	80.5±1.6	12.5±1.1	4.2±0.7	2.3±0.2	0.7±0.1
Precipitates in δ-ferrite	70.0	14.9	4.0	10.4	0.8

Table 5.5h EDX microanalysis of the specimen after tempering at 600°C for 8h using FEI Sirion FEG SEM (wt%)

Phase	Fe	Cr	Ni	Mo	Si
Retained austenite	73.4±1.5	12.4±0.2	11.6±1.6	2.1±0.3	0.5±0.1
Tempered martensite	81.1±1.6	12.1±0.3	3.6±3.3	1.7±0.2	0.6±0.1
δ-ferrite*	79.4	16.3	-	3.8	0.5
Precipitates in δ-ferrite*	75.4	14.9	3.8	5.3	0.7

* The value was detected from one area, not average value.

Table 5.5i EDX microanalysis of the specimen after tempering at 620°C for 8h using FEI Sirion FEG SEM (wt%)

Phase	Fe	Cr	Ni	Mo	Si
Retained austenite	75.5±1.2	12.5±0.4	9.6±1.3	1.9±0.2	0.6±0.1
Tempered martensite	79.2±0.6	12.6±0.5	5.6±0.2	2.1±0.2	0.6±0.1
δ-ferrite*	75.4	15.6	4.6	3.9	0.5
Precipitates in δ-ferrite	68.2±0.2	16.5±0.3	4.0±1.2	10.5±0.7	0.8±0.1

Table 5.5j EDX microanalysis of the specimen after tempering at 635°C for 8h using FEI Sirion FEG SEM (wt%)

Microscope	Phase	Fe	Cr	Ni	Mo	V	Si
FEI Sirion FEG	Retained austenite + fresh martensite	77.5±1.4	13.2±0.1	6.4±0.4	2.2±0.1	-	-
Jeol 6400	Retained austenite + fresh martensite *	77.8	12.8	6.6	2.2	-	-
FEI Sirion FEG	δ-ferrite with precipitates	77.2±1.3	15.4±0.1	2.7±0.4	4.2±0.3	0.5*	0.5±0.1
FEI Jeol 6400	δ-ferrite with precipitates	76.8±0.2	16.2±0.2	2.2±0.1	4.1±0.8	0.3±0.1	-
FEI Sirion FEG	Precipitates in δ-ferrite*	71.0	16.4	2.2	9.5	-	0.7

*The value was detected from one area, not average value.

Table 5.5k EDX microanalysis of the specimen after tempering at 600 °C for 24h using FEI Sirion FEG SEM (wt%)

Phase	Fe	Cr	Ni	Mo	Si
Retained austenite	75.6±1.3	12.5±0.3	9.7±1.0	1.6±0.3	0.6±0.1
Tempered martensite	79.6±3.7	12.2±1.2	6.0±2.3	1.7±0.3	0.6±0.1

Table 5.5l EDX microanalysis of the specimen after tempering at 620 °C for 24 h using FEI Sirion FEG SEM (wt%)

Phase	Fe	Cr	Ni	Mo	Si
Retained austenite	74.8±2.6	12.4±0.4	10.5±2.3	1.8±0.2	0.5±0.1
Tempered martensite	80.4±1.0	12.4±0.5	4.9±0.5	1.8±0.3	0.5±0.1

Table 5.5m EDX microanalysis of the specimen after tempering at 635 °C for 24 h using Jeol 6400 SEM (wt%)

Phase	Fe	Cr	Ni	Mo	V
Retained austenite + fresh martensite	79.5±1.4	12.7±0.1	5.8±1.2	2.0±0.3	-
Tempered martensite	78.9±1.6	12.9±0.2	4.6±1.3	2.0±0.2	-
δ-Ferrite	77.8±0.6	16.3±0.2	2.1±0.1	3.6±0.6	0.2±0.1

5.5.4.2 TEM EDX microanalysis

Solute elements distribution after tempering was also quantitatively analysed using TEM EDX. The variation in Ni content exhibited a similar trend to that shown by the SEM EDX analysis. At 635 °C, Figure 5.35 and Table 5.6, Ni content in retained austenite was about twice that in tempered martensite. At 700 °C, Figure 5.36 and Table 5.7, the heavily dislocated laths in Figure 5.36(b) (regions 1, 2, 3 and 6) had higher Ni concentration than the regions 4 and 5, suggesting that the former was fresh martensite while the latter was tempered martensite which had rejected Ni (and C) and lost its dislocation density on tempering. After the second tempering at 550 °C for 2h, Figure 5.38 and Table 5.8, Ni content in the darker martensite laths with numerous dislocations (Figure 5.38(a) regions 2, 4 and 6, and Figure 5.38(b) region 2) was about three times that of the brighter tempered martensite with less dislocation (Figure 5.38(a) regions 1, 3 and 5, and Figure 5.38(b) region 3). On the other hand, Ni content in Figure 5.38(a) regions 2, 4 and 6 was slightly higher than that in Figure 5.38(b) region 2, indicating that Ni re-distribution occurred during the second tempering.

5.5.5 M_s calculation

The stability of retained austenite can be estimated from the martensite formation start temperature M_s since solute enrichment in austenite leads to improving austenite stability but decreasing M_s. M_s of the specimens tempered at 600 °C, 635 °C and 700 °C were calculated in terms of retained austenite composition using the following equation (5-3), which has been described in Chapter 2, Literature Review:

$$M_s\ (°C) = 492\text{-}2.5\times(\text{wt\% C})\text{-}65.5\times(\text{wt\% Mn})\text{–}10\times(\text{wt\% Cr})\text{–}29\times(\text{wt\% Ni}) \qquad (5\text{-}3)$$

where C content was determined by XRD, and other elements content were determined by SEM EDX and /or TEM EDX.

M_s thus calculated are given in Table 5.9. Tempering at 600 °C for 4 h, the M_s was below room temperature so austenite formed on tempering remained stable after

cooling to room temperature. Tempering at 635 °C for 4 h the M_s was above room temperature therefore resulted in unstable austenite, which led to unstable retained austenite at room temperature. Tempering at 700 °C for 4 h the M_s was much higher than room temperature, leading to more unstable austenite on tempering which then transformed to fresh martensite on cooling, resulting in less retained austenite at room temperature. These results accord well with the XRD analysis results. Note the actual values should be lower than the data shown in Table 5.9 since these calculations did not consider the Mn element.

Table 5.9 M_s temperatures calculated using equation 5-3

Tempering conditions	600 °C/4 h	635 °C/4 h	700 °C/4 h
M_s (°C)	13	67	171

5.5.6 Summary

The dominate phase in the tempered super 13% Cr steel was composed of tempered martensite and retained austenite, and possibly also fresh martensite. It is easy to identify retained austenite and tempered martensite in SEM micrographs, however, fresh martensite is difficult to distinguish from retained austenite. The decomposition of fresh martensite after the second temper indicated the possible presence of fresh martensite. The fresh martensite in thin foil TEM bright field images appeared as laths with a high dislocation density, distinguishing it from tempered martensite which has less dislocation. The retained austenite/"retained austenite + fresh martensite" size marginally increased with increasing tempering temperature/time. The second tempering at 550 °C for 2 h resulted in finer grain size when the first tempering was >635 °C due to the decomposition of fresh martensite.

SEM EDX and TEM EDX microanalyses show Ni re-distribution occurred in the tempered specimens. The reduced Ni content in retained austenite at higher tempering temperature resulted in increased M_s. After tempering at ≤635 °C, 4 h, Ni in the retained austenite was enriched to approximately twice the level in the as-received state. After tempering at 700 °C, 4 h, more Ni rejected from tempered martensite and enriched the "retained austenite + fresh martensite". However, the

value was slightly lower (~7 wt%) since the laths size was larger. After the second tempering at 550 °C, 2 h, more Ni (~10 wt%) distributed in the laths with numerous dislocations.

5.6 Microstructure - precipitation

5.6.1 Precipitation in the matrix of martensite + retained austenite

5.6.1.1 Precipitation morphology and composition

The number of precipitates in the re-heat treated specimens was rather low since no precipitate peak was detected by means of XRD (see Figure 5.1). As shown in Figures 5.31, 5.46, 5.47 and 5.48, BEI SEM micrographs taken from specimens without etching show some precipitates which appeared brighter distributed along the prior austenite grain boundaries as well as laths interfaces. EDX microanalysis shows these were Mo-rich precipitates.

To study the types, morphology and distribution of precipitates in detail, carbon extraction replicas were taken from specimens in the as-air cooled condition, tempered at 557 °C for 4 h and 640 °C for 4 h. Figure 5.49 shows carbon extraction replica TEM micrographs of the specimen in as-air cooled state. Due to the fine size and small quantity, it was impossible to determine whether the small particles in the as-air cooled specimen after re-austenitization were precipitates from the re-heat treatment or prior existing particles (Figure 5.49(a)). TEM EDS microanalysis showed the large spherical particles in Figures 5.49(b) were MnS inclusions rather than precipitates. As shown in Figure 5.50, after tempering at 557 °C for 4 h, a substantial number of fine precipitates were observed uniformly distributed within the martensite laths as well as along the martensite laths boundaries. Figure 5.50(b) and (c) EDS analysis indicated they were Cr, Mo-rich $M_{23}C_6$ carbides which also contained other elements Si, Fe, and Ni. Although V was detected in the precipitate particles, the V-enriched carbonitrides (V(C,N)) particles were barely detectable in the bright field image using EM 420 TEM. Again, the large spherical particles shown in Figure 5.50(d) were MnS inclusions. Note the high Cu peaks in the X-ray spectra

were from the Cu grid, not the specimens.

After tempering at 640 °C for 4 h, fine precipitates were observed distributed mainly within the retained austenite phase as well as along prior austenite grain boundaries (Figures 5.51, 5.52 and 5.53). A small number of coarse carbides were also found in the tempered specimen (Figure 5.54). Due to their fine size and small quantity, it was not possible to determine crystal structure and composition of these fine particles within retained austenite (Figure 5.51) using the EM 420 TEM. However, the fine crystals which distributed along prior austenite grain boundaries (Figure 5.52 and Figure 5.53) were determined to be consisted of M_6C carbides and V(C,N) carbontrides. EDS analysis showed that these precipitates had higher Mo than Cr, and also dissolved elements V, Si and Fe. Selected area diffraction (SAD) patterns showed they had fcc crystal structure, the interplanar spacing and the lattice parameter matched M_6C carbides (1.106nm) and VN nitrides (0.418 nm). The coarse angular precipitate particles shown in Figure 5.54 were determined to be $M_{23}C_6$ carbides. EDS analysis showed they were enriched in Cr and also dissolved elements Mo, Ni and Fe. SAD patterns showed they had fcc crystal structure, the interplanar spacing (Table 5.10) and the lattice parameter matched $M_{23}C_6$ carbides (1.044nm).

Table 5.10 Measured interplanar spacing of the coarse angular precipitates and the interplanar spacing of $M_{23}C_6$ from the reference

Measured R (mm)	Measured d-spacing (Å)	d-spacing (Å) of $M_{23}C_6$ (Andrews 1971)	hkl
3.9	6.0	6.132	111
6.4	3.7	3.755	220
7.0	3.4	3.203	311
7.8	3.0	3.066	222
-	-	2.655	400
10	2.4	2.375	420
-	-	2.168	422
-	-	2.044	511
12.5	1.9	1.878	440
13	1.8	1.795	531

Precipitation study was also performed on the thin foil specimens used for microstructure investigations. Figure 5.55 shows thin foil TEM bright images of the specimen single tempered at 700 °C for 4 h. In Figure 5.55(a), electron diffraction pattern indicated the coarse angular precipitate was $M_{23}C_6$ carbide. EDX microanalysis showed that it contained higher Cr, Mo and V, agrees with the electron diffraction pattern analysis result. In Figure 5.55(b), EDX analysis showed that the spherical precipitates were enriched in Mo and V. Table 5.11 lists composition of the precipitate particles in the specimens single and double tempered at 700 °C for 4 h determined by TEM EDX. Note the data shown in this Table provides only an indication of element distribution in the precipitates since the figures shown include matrix components.

Table 5.11 TEM EDX precipitates composition analysis for the two tempered specimens

Tempering	Shape	Si	Cr	Fe	Ni	Mo	V
700°C/4h	granular	0.5	60.5	25.1	0.7	12.5	0.7
	spherical	1.5±0.5	10.6±1.7	52.0±12.3	1.7±1.9	34.3±14.5	0.2±0.2
700°C/4h+550°C /2h	granular	0.9	42.4	26.0	1.5	28.2	1.0

5.6.1.2 Mean size of the precipitate particles

The size of carbides/carbontrides distributed in the matrix of the tempered specimens was measured from the TEM negatives and the results are listed in Table 5.12 and Table 5.13. The size of precipitates was fairly uniform after tempering, but larger at 640 °C than at 557 °C. Several coarse angular precipitates in the range of 100-250 nm were also found in the specimen tempered at 640 °C. They were presumed to be the original precipitates which did not dissolved during the re-austenitization process.

Table 5.12 Mean size of the precipitates in the specimen tempered at 557 °C, 4 h

Type	Mean size (nm)	Max size (nm)	Min size (nm)	95% Confident
Spherical /cubic	13±6	32	1	0.82

Table 5.13 Mean size of the precipitates in the specimen tempered at 640 °C, 4 h

Type	Mean size (nm)	Max size (nm)	Min size (nm)	95% Confident
Spherical	23±10	54	3	1.23
Cubic	39±16	94	8	2.16
Coarse angular	Between 100nm to 250nm, 9 numbers			

5.6.2 Precipitation in δ-ferrite

Given the small volume fraction of δ-ferrite, it would prove excessively time consuming to examine precipitates in δ-ferrite phase using TEM, therefore the SEM was used. As shown in Figure 5.17(b), no precipitate particles were observed in δ-ferrite phase in the as-air cooled specimen. However, fine precipitates were found distributed within δ-ferrite phase after tempering (Table 5.5). Figures 5.56, 5.57 and 5.58 show the fine precipitates appeared bright in both secondary electron images (SEI) and backscattered electron images (BEI).

Figure 5.59 SEM EDX qualitative microanalysis showed that the Mo content in particles within the δ-ferrite was higher than in the δ-ferrite itself. EDX quantitative microanalysis found Mo content in the particles was two or three times higher than in the δ-ferrite and four times higher than in the matrix (~2.0 wt%) (Tables 5.5 and Figure 5.60). Some V was found concentrated in δ-ferrite after re-austenitization. However, after tempering, V was detected in the particles rather than in the δ-phase (Table 5.5a, c, j and m). It should be emphasised that SEM EDX analysis of the particles will have included a contribution from the matrix (δ-ferrite) present and thus only provides a rough estimate of precipitate composition.

5.6.3 Summary

Cr-rich $M_{23}C_6$ carbides, Mo-rich M_6C carbides and V-rich V(C,N) carbonitrides precipitated in the tempered samples. After tempering at a relatively lower temperature, 557 °C (4 h), fine $M_{23}C_6$ carbides were found precipitated in the martensitic matrix and the lath boundaries. After tempering at a relatively higher temperature (640 °C, 4 h), fine particles mainly precipitated within the retained austenite phase instead of the martensite phase since the former was rich of carbon. M_6C carbides and V(C,N) carbonitrides were found distributed along the prior austenite grain boundaries. The size of these carbides was rather fine (≤60 nm). Mo rich particles were also found presented in δ-ferrite after tempering.

5.7 Equilibrium phase transformation fraction calculation

MT DATA calculation results show no cementite, M_7C_3, CMo, CMo_2, $C_{0.88}V$ or NV is presented in either steel (Cast 1 and Cast 3, see Table 3.1). In other words, only bcc martensite, fcc austenite, $M_{23}C_6$ and M_6C carbides are presented. The mass% of these phases as functions of temperature is plotted in Figure 5.61. As shown in Figure 5.61(a) and (b), there is no obvious variation in phase mass% for the two steels having different C and V levels, and the γ-phase field is in the range 920-1020 °C. In Figure 5.61(c) MT DATA calculation suggests that small amounts of $M_{23}C_6$ and M_6C carbides are the only precipitation phase present in the steels at temperature range of 500-700 °C. At temperatures above 820 °C, carbides dissolve completely. Steel which contains higher C content results in relatively larger quantities of $M_{23}C_6$ and M_6C carbides. The two curves in Figure 5.61(c) also suggest that M_6C formed at the lower temperature range while $M_{23}C_6$ formed at the higher temperature range.

Chapter 6 Discussion

6.1 Re-heat treatment

6.1.1 Re-austenitization and air-cooling

The laboratory re-austenitization treatment was carried out at 950 °C for 2 h to "restore" the as-received structure to the state before quenching in order to simulate the industrial process. By using the same austenitization temperature-time condition that had been applied to the as-received commercial bars, the original austenitic structure was fully recovered. As has been described in Chapter 5, this thermal cycle was sufficient to dissolve completely the carbides in the as-received samples, while not inducing significant austenite grain growth.

The consequence of air-cooling after re-austenitization was to produce a fully martensitic structure at room temperature (with a minor δ–ferrite content, inherited from the as-cast state). Due to the small size of the samples, and importantly, the characteristic high hardenability of the steel, air-cooling was sufficient to produce a fully martensitic structure, as determined by XRD (Figure 5.1). The purpose of applying air-cooling was to try to make the laboratory cooling rate as close as possible to the industrial oil-quenched cooling rate which was applied to the as-received commercial bars, so that the laboratory re-heat treated microstructures were comparable with the as-received microstructures. The average laboratory air-cooling rate was determined to be about 60 °C/min from 950 °C to room temperature by using a thermocouple. Unfortunately, the industrial oil-quenching cooling rate for the as-received commercial bars was unavailable. However, it can be estimated from the quenching oil cooling curves plotted for round bar stock in the steel heat treatment book (Thelning, 1984). According to those curves, for a 100 mm diameter bar cooling from 850 °C to 200 °C, the average value is about 80 °C/min. For a 200 mm diameter bar cooling from 850 °C to 150 °C, the average value is about 40 °C/min. The diameter of the as-received commercial bars varied between 121~203 mm, therefore, the laboratory air-cooling rate in the current work was reasonably close to

the commercial oil-quenched cooling rate, and the microstructure in this stage was reasonably close to that of the commercial bar after oil-quenching. However, it must be borne in mind that it is very difficult to exactly simulate the industrial process in the laboratory.

6.1.2 Tempering

For most as-quenched martensitic steels the as-quenched/air-cooled structure is highly stressed and brittle due to the high C content in the steel. Tempering is therefore performed to modify the properties of the structure and particularly to improve the toughness. Generally, tempering must be carried out by heating the steel to and holding it at a temperature below the A_{c1} temperature to avoid the accidental formation of austenite. For super 13% Cr steels, however, the as-air cooled/oil quenched martensite is rather soft due to the very low C content in the steel (<0.03 wt%). The most important effect of tempering at a temperature above the A_{c1} temperature is to generate a certain amount of retained austenite in the microstructure for the required strength, hardness and toughness combination. The tempering of super 13% Cr steels should not, therefore, be viewed in the same way as for conventional martensitic steels.

XRD results shown in Figures 5.2, 5.4 and 5.5 indicated that the transformation to austenite during tempering was dependent on both the tempering temperature and time, i.e. the reaction does not reach thermodynamic equilibrium during the commercial process. Moreover, small changes in temperature strongly affect the retained austenite content. Thus, the accuracy of tempering temperature control throughout the thermal cycle is the most important consideration. On the basis of this, the most convenient method for correlating microstructural change with thermal cycle is a Hollomon-Jaffe tempering temperature-time parameter $P = (T(°C) + 273) \times (40 + \log_{10} t(h)) \times 1000^{-1}$ (IIW 1983) that combines temperature and time. This indicates that tempering temperature has the most important effect, while the effect of tempering time t has a relatively small effect, especially when tempering for just a few hours (indicated by the $\log_{10} t$ factor in the tempering parameter of P). Theoretically, according to the Hollomon-Jaffe tempering time-temperature parameter P, using a very short time and fairly high temperature would give the same

strength value as using a very long time and fairly low temperature, although temperature clearly affects the phase constitution. However, in practice it is better to temper at a relative lower temperature for a relatively longer time in order to reduce the risk for overheating, particularly when considering relatively large steel bars with high thermal mass.

6.2 Effect of tempering on hardness and tensile properties

The plots of 0.2% proof strength and hardness as a function of P (Figures 5.10 and 5.16) indicated that, as expect, increasing the tempering temperature-time parameter P resulted in a decrease in 0.2% proof strength and hardness at P<36.9. This was associated with an increase in amounts of retained austenite at the expense of tempered martensite. For P ≥36.9, fresh martensite was formed, so that the second tempering was required to temper the fresh martensite. However, the advantages of double tempering were dependent on the first tempering temperature and time. When first tempering at P slightly above 36.9, the second tempering gave little change on 0.2% proof strength and hardness. However, when first tempering at P further above 37.5, the second tempering induced partial transformation of the fresh martensite to austenite, with the residual fresh martensite being tempered, resulting in a higher retained austenite volume fraction, a refined martensite/retained austenite grain size and higher dislocation density. The combination of these factors led to a higher 0.2% proof strength (and elongation).

6.3 Effect of tempering on microstructure

In this work tempering was carried out at a temperature range above the A_{c1} but below the A_{c3} temperature, resulting in a microstructure after tempering of 'martensite + retained austenite', i.e. a duplex structure. Other constituents included the minor δ-ferrite content (<1%) and fine carbides/carbontrides precipitation, were observed by electron microscopy. As already described in Chapter 4, the δ-ferrite phase was not a product from the heat treatment, but was present in the as-cast state.

Linne et al. (1997) indicated that the presence of very small amount δ-ferrite (<1%) in super 13% Cr steel can be understood as "no trace of δ-ferrite" according to a traditional binocular examination. Although carbides were observed in the tempered specimens, both the size and quantity were small, consistent with the low carbon content. The formation, morphology and distribution of phase constituents produced by tempering are discussed below.

6.3.1 Austenite at tempering temperature

As discussed in Chapter 2 Literature Review, for super 13% Cr steels the austenite that remained at room temperature, i.e. retained austenite (γ'), originated from the stable austenite that formed at the tempering temperature (γ_T). On the other hand, fresh martensite (α'_F) also originated from the unstable γ_T on cooling to room temperature. Therefore, it is necessary to study the formation and properties of the γ_T on tempering in order to understand the properties of γ' and α'_F at room temperature.

6.3.1.1 Formation

As observed by SEM, before tempering the as-air cooled microstructure was martensitic (Figures 5.17). Austenite started to form after heating to temperature above the A_{c1}. To study the transformation kinetics of martensite to austenite at tempering temperature, the KJMA equation (Christian 1975) which has been described in Chapter 2 Literature Review is applied here:

$$y = 1 - \exp(-(k\,t))^n \qquad (6\text{-}1)$$

where y, t, k and n are the volume fraction transformed, the tempering time, constant for a given temperature, and the time exponent, respectively. Taking double logarithm on both sides of the equation (6-1), it is expressed as:

$$\ln(\ln(1/(1-y))) = n \ln t + n \ln k \qquad (6\text{-}2)$$

It is obvious ln (ln (1/(1-y))) and ln t exhibit a linear relationship, and the slope is n and the intercept is n ln k. Thus, the constant n and ln k can be obtained by plotting

the ln (ln (1/(1-y))) against ln t. To apply equation (6-2) in the current work, the volume fraction of retained austenite after tempering at 600 °C (for 4, 8 and 24 h), 625 °C (for 0.5, 2, 3 and 4 h), and 635 °C (for 0.5, 1, 2, 4 and 6 h) respectively, was applied as the austenite (γ_T) volume fraction y, presuming all of the γ_T formed on tempering remained at room temperature. Figure 6.1 plotted the ln (ln (1/(1-y))) against ln t at these three temperatures. The related n and *ln* k values thus were obtained from these plots and listed in Table 6.1. The parameter n was supposed to be independent of temperature if the reaction mechanism did not change over the range of conditions of encountered (Nakagama et al. 2000). However, the n value shown in Table 6.1 was not a constant. This might be a result that only limited data was available for the plots leading to large potential errors. However, the average n value was 0.5, in good agreement with the n value for the growth of "thickening of very large plates" for a three-dimensional nucleation and growth process (Christian, 1975). Similar results were obtained by Nakagama et al. (2000) on a CrNiMo martensitic precipitation hardening stainless steel where n ≈ 0.5, Varga et al. (1998) on a Fe12Cr4Ni steel where n ≈ 0.6, and Takahashi and Bhadeshia (1990) on 0.18 wt% C and 0.097 wt% C steels where n ≈ 0.62.

Table 6.1 The time exponent n and constant ln k in the current steel

Tempering temperature (°C)	n	ln k
600	0.67	-4.38
625	0.48	-3.21
635	0.34	-3.61
Average n = 0.5		

Taking tempering temperature into account, the temperature-dependence of transformation kinetics was estimated by using the Arrhenius equation:

$$k = k_0 \exp(-Q/RT) \qquad (6-3)$$

where k_0 is constant, Q is the apparent activation energy, R is gas constant and T is absolute temperature (K). Taking logarithms on both sides of the equation (6-3), it can be replaced by:

$$\ln k = \ln k_0 - Q/RT \qquad (6\text{-}4)$$

Thus, the plot of ln k against T^{-1} should yield a straight line of slop –Q/T and intercept ln k_0. Figure 6.2 gives the Arrhenius plot for the formation of austenite on tempering by using the ln k values listed in Table 6.1, showing ln k increased linearly with decreasing T^{-1}. From Figure 6.2, the apparent activation energy for the formation of austenite in the current steel was estimated to be 168 kJ/mol, which was close to the activation energy of C diffusion in austenite, 148 kJ/mol, in the temperature range 900-1100 °C (Brandes and Brook 1992).

6.3.1.2 Stability

XRD (Figures 5.2, 5.4 and 5.5) and quantitative imaging analyses (Figures 5.40-5.44) indicated that, as expected, the austenite γ_T formation at the low heating rate (2 °C/min) was a diffusion controlled process, i.e. was dependent on tempering temperature and time. Increasing tempering temperature/time resulted in larger amounts of γ_T. Although the austenite content was not measured directly at the tempering temperature in this work, dilatometer data shown in literature confirmed that higher temperature (beyond stable austenite temperature range) resulted in more unstable austenite on tempering (Haynes, 1999).

In this work, the A_{c1} temperature was about 560 °C at a heating rate of 2 °C/min according to the XRD analysis (Figure 5.2). As described in Chapter 2 Literature Review, the temperature range for forming stable γ_T is determined by the A_{c1} temperature. Using equation (2-5), the A_{c1} temperature was calculated to be about 613 °C, which was higher than the value obtained from Figure 5.2. However, it should be noted that the A_{c1} temperature is dependent not only on the chemical composition of the steel, but also the heating rate, hence equation (2-5) should be regarded as an approximation only. As a result, when tempering in the temperature range 557-635 °C, the austenite γ_T formed on tempering was relatively stable hence

remained relatively stable at room temperature. However, when the temperature was about 75 °C above the A_{c1} temperature, i.e. in the range 635-700 °C, the austenite γ_T formed on tempering became unstable, and then partially transformed into fresh martensite on cooling to room temperature.

6.3.2 Retained austenite

6.3.2.1 Content

The volume fraction of retained austenite (γ') also depended on tempering temperature and time. However, the maximum amount of retained austenite was in the region 35~40 vol% no matter what the tempering temperature/time had been applied (Figures 5.2 and 5.4). Taking the tempering temperature-time parameter P into account (Figure 5.5), in the lower P range, i.e. 33.6~36.9, increasing tempering temperature/time resulted in larger amounts of austenite formed on tempering (γ_T) hence higher volume fraction of retained austenite (γ') after cooling to room temperature. However, in the higher P range, i.e. 36.9~39.8, the amount of retained austenite at room temperature (γ') was smaller than the amount of austenite formed at tempering temperature (γ_T) because part of the γ_T transformed to fresh martensite (α'_F) on cooling to room temperature. In other words, the limited maximum amount of retained austenite was attributed to the transformation of unstable γ_T to α'_F.

The volume fraction of retained austenite at room temperature ($V\gamma'$) as a function of the amount of austenite on tempering had been expressed by Leem et al. (2001) as:

$$V\gamma' = k\, V\gamma_T\, f \qquad (6\text{-}5)$$

where k, $V\gamma_T$ and f are a constant, the volume fraction of the austenite at tempering temperature (γ_T), and the stability of the austenite γ_T. In the current work, the amount of austenite $V\gamma_T$ increased while the stability of the austenite f decreased with increasing tempering temperature. So the variation in amount of retained austenite can be described by equation (6-5) and is schematically illustrated in Figure 6.3.

6.3.2.2 Distribution and morphology

The mean size of the retained austenite films/particles was less than 300 nm, hence below the resolution of optical microscopy. Again due to the fine retained austenite particles, it was difficult to obtain a retained austenite diffraction pattern without a contribution from the martensite by selected area electron diffraction (SAD).

Electron microscopy observations suggested that retained austenite morphology was inherited from the morphology of austenite γ_T. Since the martensite lath boundaries provided nucleate sites, the austenite nucleated and grew along the martensite lath boundaries which therefore existed as continuous films or discontinuous particles between the martensite lath boundaries (Figures 5.22, 5.34, 5.35). This nucleation and growth phenomena was similar to that occurred in TRIP steels (Sugimoto 1993) and dual-phase silicon steels (Saleh and Priestner 2001). Vodarek et al. (1984) considered that the continuous austenite films were better for toughness than the discontinuous films/particles, as the former prevent crack propagation in the martensitic matrix more effectively than the later. Bhadeshia et al. (1983) also found that in bainitic alloys the good fracture toughness obtained was attributed to the presence of thin films of interlath retained austenite (the austenite remained at room temperature after quenching), and the role of the retained austenite is to refine the effective fracture grain size and to blunt a propagating crack.

6.3.2.3 Stability

The stability of retained austenite decreased with increasing tempering temperature. This is believed to be a result of the reduction of C content in the retained austenite, as shown by the change in lattice parameter, Figure 5.3 (a). It is well known that C is the main austenite stabilizer and therefore a reduction in C content will give a decrease in austenite stability. However, the stability of austenite is dependent on not only its chemical composition but also its size; a reduction in size reduces the number of potential nucleation sites and therefore increases stability. Figure 5.41 shows that the retained austenite particle size increased with increasing tempering temperature, may have further decreased its stability. Note that the two effects of C content and particle size would have been additive, such that as the tempering

temperature increased, C content in the retained austenite decreased and at the same time the size increased, both reducing the stability of the retained austenite.

6.3.3 Fresh martensite

6.3.3.1 Formation

The martensite formed after tempering on cooling to room temperature is called "fresh martensite" (α'_F) in order to differentiate it from the tempered martensite. Since the steel had very low C content, the crystal structure of the fresh martensite is body centred cubic, bcc, rather than body centred tetragonal, bct. The formation of the fresh martensite is attributed to the unstable austenite at high temperature. As the stability of austenite decreases with increasing martensite transformation start temperature Ms, the formation of fresh martensite can be interpreted by the M_s (Table 5.9). At 600 °C, the M_s was below room temperature (13 °C), so the austenite γ_T was relatively stable and no fresh martensite could form on cooling to room temperature. At 635 °C, the M_s was slightly above room temperature (67 °C), so a small amount of γ_T became unstable and a small amount of fresh martensite formed on cooling to room temperature. In this case the austenite grain boundaries provided the fresh martensite nucleation site. At 700 °C, however, the M_s was much higher (171 °C) so that almost all of the γ_T became unstable and transformed into fresh martensite on cooling.

6.3.3.2 Identifying fresh martensite from retained austenite

No successful method could be applied to reliably distinguish fresh martensite from retained austenite by optical and SEM microscopy. On the one hand, martensitic transformation takes place by cooperative atomic movement, a great many of martensite crystals can nucleate within a grain of the parent phase (Nishiyama 1978). In this work since the parent austenite (γ_T) grain was small (<500 nm), fresh martensite crystals were of fine grain size for microscopy observation. On the other hand, as a result of the diffusionless transformation, the chemical composition of the fresh martensite was identical to that of the parent austenite (Krauss, 1992), so it is impossible to distinguish fresh martensite from retained austenite using EDX. Colour etching and tint etching techniques have been used successfully to reveal different

phases such as bainite, martensite and ferrite in multiphase TRIP steels (Girault et al. 1998, Ros-yanez et al. 2001). For example, a slight tempering treatment, i.e. 200°C/2h of TRIP steels before tint etching leads to a shallow darkening of the martensite in optical microscopy and allows its distinction from retained austenite. This procedure is also suited to SEM examination because it induces a very fine carbide precipitation in the martensite while leaving the austenite intact (Girault et al. 1998). However, to apply this technique steels must have sufficient carbon, e.g. 0.11wt% C, to produce carbides after tempering at 200°C as well as a large martensite grain size, e.g. >2μm, for SEM observation. The current steel is almost carbon free (0.016wt%) so this technique did not work. However, TEM select area diffraction (SAD) pattern technique combined with EDX microanalysis provide a reliable method for differentiating the fresh martensite from the retained austenite since they had slightly different fcc austenite and bcc martensite lattice parameter although the same chemical composition (Figures 5.36, 5.37, 5.39).

6.3.3.3 Fresh martensite to austenite re-transformation by reheating

The structural state of fresh martensite (α'_F) was unstable, and had the tendency to re-transform into austenite on reheating at 550 °C. This is due to the relatively higher alloy content of C and Ni, in the fresh martensite compared to the regions of tempered martensite. On the other hand, the transformation of $\gamma_T \rightarrow \alpha'_F$ produced a high dislocation density within the fresh martensite laths. Danil'chenko et al. (2003) also indicated that a high density of dislocations in the transformation-hardened alloy intensified the fresh martensite decomposition process. As a result, the second tempering at 550° C would have tempered some of this fresh martensite, but also re-transform some to austenite, leading to the increase in retained austenite volume fraction in microstructure. Figure 6.4 schematically presented the structure evolution of the super 13% Cr steel investigated after two-stage tempering. It is based on the original structure scheme on 13CrNiMo martensitic steels illustrated by Bilmes et al. (2001).

After the re-transformation of $\alpha'_F \rightarrow \gamma'$, a high dislocation density was produced within the newly tempered martensite structure. Investigations on Fe-Ni alloys by Malyshev et al. (1982) also showed that the dislocation density was increased after a

successive γ→α and reverse α→γ transformations. The formation of thin-film retained austenite on the original fresh martensite interlath provided a finer structure than single tempering.

6.3.4 Tempered martensite

The tempered martensite phase contained less C and Ni content and dislocation density compared with the fresh martensite (Figure 5.36). The reason for this is when the specimens were heated to the (γ+α) dual-phase region, with the growth of austenite, C and Ni in particular were rejected from martensite and enriched in the austenite. At the same time the tempering of the martensite resulted in a substantial reduction in dislocation density. Since much of the C present in the alloy segregated into the austenite, and importantly, the very low C content in the steel, this tempered martensite was "soft". This kind of martensite is believed to be important for the steels to retain an adequate combination of toughness and hardness. The dimple mode of fracture noted in tensile testing after heat treatment (Figure 5.12) was indicative of the high ductility of the tempered martensite in this steel. Again, due to the low C content, the crystal structure of the tempered martensite was body-centred cubic, bcc.

6.3.5 Precipitation

6.3.5.1 Precipitation in the matrix

Super 13%Cr stainless steels are superior to conventional 13%Cr steels in terms of corrosion resistance mainly because of their lower C content and the subsequent reduction of carbide precipitation. In the current steel, although precipitation of carbides was observed in the as-received and re-heat treated specimens, their volume fraction was small, consistent with the very low C in the steel (0.016 wt%). $M_{23}C_6$ and M_6C carbides were detected in the TEM carbon extraction replicas of tempered specimens, consistent with the MT DATA calculation (Figure 5.61).

The identification of $M_{23}C_6$ and M_6C type carbides was established by the electron diffraction patterns and EDX microanalysis spectrum. Although it is not possible to

distinguish different carbides purely by their shape and appearance in the TEM bright field images, a type of carbide generally can be identified by an electron diffraction pattern, or by an X-ray spectrum obtained using energy dispersive spectroscopy (EDS/EDX). However, both $M_{23}C_6$ and M_6C have an fcc crystal structure and their lattice parameters are very close (Andrews 1971). Taking measurement error into account, it was not possible from electron diffraction alone to distinguish between the two carbide types. Nevertheless, the two carbides have different chemical composition, so that the appearance of EDX spectrum of each type of carbide is unique. This permits carbides identification using TEM EDX. Therefore, identification of the carbides in the tempered specimens was taken using a combination of electron diffraction patterns and EDX spectra.

a. Tempering at 557 °C

After tempering at 557 °C for 4 h, EDX microanalysis showed that the fine particles dispersed in the martensite matrix and along the martensite lath boundaries were Cr and Mo rich with small amounts of Si, Fe, and V. These particles were believed to be $M_{23}C_6$ carbides and probably V(C,N) carbonitrides (Figure 5.50). The presence of $M_{23}C_6$ carbides was in good agreement with the MT DATA equilibrium precipitation phase evolution with temperature shown in Figure 5.61. Although V(C,N) was not predicted by the MT DATA calculation, small amount of V-rich V(C,N) particles are believed to be formed during tempering since V peak appeared in the TEM EDX traces, although it was rather low (Figure 5.50). The steel (Cast I shown in Table 4.1) contained 0.13% V, so it is most likely to produce V(C,N) precipitation during tempering since V is a very strong carbide/nitride former. Taneike et al. (2004) found that in the tempered martensitic 9Cr steel with 0.018C, 0.2V, 0.05N (mass%), the precipitates along boundaries consisted of fine V-enriched MX particles and $M_{23}C_6$ carbides. The size of V(C,N) would be expected to be very small since this type of particles are resistant to coarsening. Ennis (1997) reported the size of V-rich MX particle was between 2-20 nm. Therefore, the V(C,N) particles if present, would be easily missed. As a result, the fine precipitates in the specimens after tempering at 557 °C for 4 h were more likely to be Cr, Mo-rich $M_{23}C_6$ carbides coexisting with small amount of V(C,N) carbonitrides.

b. Tempering at 640 °C

After tempering at 640 °C for 4 h fine carbides with a mean size <40 nm were more frequently found within the retained austenite rather than the martensite (Figures 5.51), consistent with the higher C content of the austenite. Due to the fine size and small amount, it was not possible to identify the structure and composition of these particles using the two TEM microscopes applied in this work.

Generally, precipitates distribute along prior austenite grain boundaries of stainless steels are expected to be $M_{23}C_6$ (Sourmial 2001). However, in this work after tempering at 640 °C, M_6C carbides were found distributed along prior austenite boundaries (Figure 5.52). TEM EDX spectra of the intergranular precipitates displayed relatively high Mo and Fe peaks and low Cr peak as well as dissolved element Si (Figure 5.52(g)), consistent with M_6C. The precipitation of M_6C along prior austenite grain boundaries resulted from the presence of $M_{23}C_6$ since metastable $M_{23}C_6$ can partially transform to from more stable M_6C in the presence of Mo (Sourmial 2001, Peddle 2001, and Pilling et al. 1982). Generally $M_{23}C_6$ carbides start to form in the early stage of tempering in the temperature range of 500 to 600 °C, or the tempering cooling period when passing through the temperature range of 500 to 600 °C if the cooling rate is sufficient slow, as occurred in 13Cr4Ni cast steel (Iwabuchi 1987). However, M_6C carbides precipitate take place after a long term of tempering/aging on the expense of $M_{23}C_6$ carbides, as occurred in the tempered 2.25Cr1Mo steel (Baker et al. 1959). The current cooling rate was rather slow (≤1.5° C/min), so it provided sufficient time for M_6C carbides to nucleate and growth at the existing $M_{23}C_6$ carbides particles when pass through the temperature range of 500 to 600 °C. The newly formed M_6C carbides were more stable than $M_{23}C_6$ carbides, thus remained along the prior austenite grain boundaries at room temperature. The small V peak shown in the EDS spectrum (Figure 5.52(e)) indicated V(C,N) particles probably also precipitated along the prior austenite grain boundaries. Electron diffraction pattern taken from the prior austenite grain boundary confirmed the presence of V(C,N) particles (Figure 5.53). As a result, fine M_6C and V(,CN) particles coexisted in the prior austenite boundaries. These intergranular carbides had no strengthening effect but deplete the local Cr content in the matrix and may cause intergranular corrosion. Therefore, it is important to avoid forming intergranular

carbides during tempering treatment. The presence of coarse $M_{23}C_6$ carbides after tempering at 640 °C, 4h (Figures 5.54, 5.55(a)) resulted from the growth of the pre-existed $M_{23}C_6$ during re-austenitization. During heating at 950 °C, a small amount of $M_{23}C_6$ carbides may not be dissolved and retained in the steel after air-cooling. They coarsened to 100~250 nm in diameter during subsequent tempering at 640 °C. $M_{23}C_6$ grows with a cube to cube orientation relationship to the austenite (Sourmial, 2001), so that the coarse carbides appeared angular in shape. The amount of these carbides was rather small hence should not have a significant effect on mechanical properties.

6.3.5.2 Precipitation in δ-ferrite

The fine dispersed precipitates concentrated within δ-ferrite (Figures 5.56 through 5.60) were produced during the tempering treatment since no precipitates were observed in δ-ferrite after quenching (Figure 5.17). These precipitates were Mo rich particles instead of Cr rich particles. As shown in Table 5.5, the Cr content in the δ-ferrite was about 3 wt% higher than that in retained austenite and martensite, and the values remained constant whether precipitates were present or not. Moreover, the Cr content in δ-ferrite after tempering exhibited the same value as in as-quenched state. However, the Mo content in the bright particles shown in SEM images was about twice that in δ-ferrite (Figures 5.59, 5.60), suggesting the particles formed within δ-ferrite were Mo-rich not Cr-rich. Hara et al. (2000) also found that in low carbon 13% Cr steel, Cr carbides or nitrides precipitated along the δ-ferrite grain boundary but not within the δ-ferrite phase. These particles were probably Mo-rich M_6C according to the MT DATA calculation (Figure 5.61). Up to 0.7% V was detected in the δ-ferrite and V was not detected in the austenite or martensite phase using SEM EDX. Whether V dissolved in the Mo-rich carbides, precipitated as V-rich particles in δ-ferrite, or dissolved in δ-ferrite only was not known directly by using SEM. However, given that V is a strong carbide/nitride former, the formation of V-rich MX is more probable. Bashu et al. (1990) has reported that vanadium carbonitrides were observed in δ-ferrite in 12% Cr steels. It should be stressed that although Mo was depleted from the surrounding area to concentrate in δ-ferrite, there is no significant change of the Mo content in the matrix since the amount of δ-ferrite is small (<1%).

6.3.5.3 Summary

Cr-rich $M_{23}C_6$ carbides, Mo-rich M_6C carbides and V-rich V(C,N) carbonitrides precipitated in the tempered specimens. After tempering at a relatively lower temperature (557 °C, 4 h), fine $M_{23}C_6$ carbides and V(C,N) carbonitrides coexisted in the martensitic matrix and the grain boundaries. After tempering at a relatively higher temperature (640 °C, 4 h), fine particles mainly precipitated within the retained austenite phase instead of the martensite phase since the former was rich of C. M_6C carbides and V(C,N) carbonitrides were found distributed along the prior austenite grain boundaries. The precipitation of M_6C carbides was attributed to the high Mo content in the steel (1.99 wt%) and the low cooling rate applied after tempering.

6.3.6 Solid solution element re-distribution

6.3.6.1 C and Ni diffusion coefficient and diffusion distance in bcc and fcc iron

To study the effect of alloying element re-distribution on microstructure, only C and Ni were considered while N was ignored owing to its low content (<0.02 wt%) in the steel and low solubility (Table 2.11). The diffusion coefficient and distance of C and Ni in bcc and fcc iron were estimated to investigate the potential for these elements to redistribute during tempering heating, holding and cooling period. Figures 6.5, 6.6, 6.7 and 6.8 represent the diffusion coefficient and diffusion distance of C and Ni in pure bcc and fcc iron as a function of temperature, in the form of $1000K^{-1}$ and °C, respectively. The C and Ni diffusion coefficient data was originated from the references shown in Figures 2.22 and 2.23. The diffusion distance was calculated using equation (6-6):

$$x = (D\,t)^{1/2} \qquad (6\text{-}6)$$

where x is the diffusion distance, D is the diffusion coefficient, and t is time. In this calculation, t = 4 h, which was the tempering holding time applied in this work.

Figures 6.5 through 6.8 indicate that the diffusion of C in bcc and fcc iron is more rapid than that of Ni, which is not surprising given the differences in atomic size. On the other hand, the figures indicate C and Ni diffusing at high temperature are faster

than at low temperature. For example, C diffusivity in fcc iron is 7.5×10^{-9} cm^2/s at 700 °C, which is ~10 times as fast as that at 600 °C (7×10^{-10} cm^2/s). Ni diffusivity in fcc iron is 2.0×10^{-15} cm^2/s at 700 °C, which is ~200 times as fast as that at 600 °C (9.0×10^{-18} cm^2/s). These figures also show that, at the same temperature, C diffusion distance in iron is much larger than Ni. The diffusion distance vs. T^{-1} or T suggested that, at low temperature, the diffusion distance was as expected only over small distances, while at high temperature the diffusion distance was larger. For example, at 600 °C, the diffusion distance of Ni in bcc Fe is almost zero, at 700 °C it was about 300 nm.

The trend for C and Ni diffusion coefficient in pure fcc austenite and bcc ferrite shown in Figures 6.5-6.8 followed the Arrhenius equation (Brandes and Brook 1992):

$$D = A \exp(-Q/RT) \qquad (6\text{-}7)$$

where D is diffusion coefficient of C and Ni (cm^2/sec), A is frequency factor (cm^2/sec), Q is the activation energy (J/mol), T is absolute temperature (K) and R is molar gas constant 8.314J/(mol × K). The A and Q values for C and Ni diffusion in bcc and fcc iron at the temperature range of 500-700 °C can be derived from Figures 6.5 to 6.8, and the results are listed in Table 6.2.

Table 6.2 A and Q values for C and Ni diffusion in bcc and fcc iron at temperature range of 500-700 °C

Element	Iron	A (cm^2/sec)	$1000^{-1}Q/R$ (K)	Q (kJ/mol)
C	bcc	0.5	16	133
	fcc	0.3	17	141
Ni	bcc	2309	37	307
	fcc	37.6	37	307

It must be stressed that C and Ni diffusivity in the current steel were much slower and the diffusion distances were smaller than in pure ferrite and pure austenite phase due to the presence of other alloy elements Ni, Cr, and Mo etc. in retained austenite

and martensite phase. Hence Figures 6.5 through 6.8 only provide a guide of C and Ni diffusivity in the tempered specimens.

6.3.6.2 Formation of austentie (γ_T) by C and Ni re-distribution

The formation of austenite on tempering (γ_T) was a result of C and Ni element re-distribution in specimens at tempering temperatures, i.e. C and Ni were enriched in austenite (γ_T). Krauss (1999) indicated that a more common manifestation of C diffusion in martensite during quenching was segregation to dislocations and lath boundaries. Therefore, in the current investigation after air cooling, C was believed to be enriched in the martensite lath boundaries, which provided nucleation site for austenite formation. During tempering, austenite (γ_T) started to form when heating to the γ-α two-phase region by depleting C (and Ni) from the martensite and enriching in the lath boundaries. C and Ni are austenite stabilizers, so that the enriched C and Ni stabilised the austenite and then enhanced the formation of retained austenite. This phenomenon was confirmed by the relatively higher Ni content in retained austenite than that in the tempered martensite (Table 5.5). Investigations carried out by Nakagawa et al. (1998) on a precipitation hardening stainless steel also showed that the inverse transformation of austenite was mainly controlled by diffusion of Ni.

6.3.6.3 Formation of fresh martensite by C and Ni re-distribution

The formation of fresh martensite was a result of C and Ni re-distribution in the austenite phase at high temperature, i.e. C and Ni content in austenite (γ_T) declined. Despite the fairly low level of C element in the steel, XRD measurements revealed that the C concentration in retained austenite decreased with increase in tempering temperature (Fgure 5.3). The variations of other alloying element (Fe, Cr, Ni and Mo) content in retained austenite with tempering temperature determined by SEM/TEM EDX is shown in Figure 6.9. Despite the much slower Ni diffusion in austenite than C, EDX microanalyses revealed the Ni concentration in retained austenite decreased with increase in tempering temperature. This suggested that when tempering at temperatures further above the Ac_1 temperature, by say >70°C, C and Ni diffusion occurs over a relatively large distance, which in association with the growth of the γ_T, led to relatively lower levels of C and Ni in austenite, leading to a higher Ms temperature and consequently fresh martensite on cooling to room tempering.

6.3.6.4 Fresh martensite re-transformed into austenite by C and Ni re-distribution

The increase in the amount of retained austenite after second tempering for the first tempering temperature higher than 635 °C was also a result of solute re-distribution, i.e. the C and Ni enriched fresh martensite depressed the A_{c1} temperature. Figure 6.10 shows the schematics of heat treatment process when first tempered at different temperature range. It was modified from Figure 1.1 in Chapter 1 Introduction. When the first temper at <635 °C, the tempered martensite was depleted C and Ni compared to the as-air cooled martensite, so that the A_{c1} temperature was believed to be ≥560 °C. As a result, the second temper at 550 °C was below the A_{c1} temperature, as shown in Figure 6.10(a). As a result, the second temper did not change retained austenite content. When the first temper at >635 °C, fresh martensite formed. Fresh martensite was transformed from austenite by a diffusionless process, so the composition of newly formed fresh martensite was identical to that of the parent austenite phase. Thus, the fresh martensite was relatively enriched in C and Ni compared to the as-air cooled martensite, so that the A_{c1} temperature was reduced, to a value believed to be below 550 °C, as shown in Figure 6.10(b). As a result, C and Ni re-distribution in fresh martensite occurred during re-heating at 550 °C. As a result, the second temper would have partly tempered the fresh martensite, but also partly re-transformed some to austenite, leading to the increase in retained austenite content.

6.4 Structure-property relationship

The variation in mechanical properties after tempering was interpreted on the basis of the changes in microstructure. Hardness and tensile test results (Figures 5.10 and 5.16) showed that at P<36.9 hardness and yield strength (0.2% proof strength) decreased with increasing tempering temperature/time. At P>36.9, hardness and yield strength increased with increasing tempering temperature/time, and the second temper at 550 °C improved yield strength while hardness did not change. XRD results showed that retained austenite content exhibited a reverse trend to hardness and yield strength with increasing tempering temperature/time (Figure 5.5). The

microstructural work showed that after tempering the dominant structure was martensite + retained austenite, and no significant amount of carbides were observed. Thus the mechanical properties were regarded as dependent on the size, composition and volume fraction of retained austenite and martensite (tempered and/or fresh martensite) while the effect of precipitation strengthening was negligible.

6.4.1 Relationship between retained austenite content and mechanical properties

Ultimate tensile strength (UTS), hardness, yield strength (0.2% proof strength), and percentage elongation (EI%) as a function of retained austenite content for the laboratory tempered specimens are plotted in Figure 6.11. All of these variables exhibited a near linear function of retained austenite content, although there was some scatter, particularly in the UTS data (Figure 6.11(a)), which decreased slightly from linear with increasing retained austenite for both single and double tempering. Both hardness and yield strength (Figure 6.11(b) and (c)) decreased with increasing retained austenite content and dropped to the minimum values when retained austenite reached the highest value of ~37 vol% at around 635 °C (P~36.9). On the contrary, percentage elongation exhibited a reverse trend (Figure 6.11(d)).

With the exception of UTS, the slopes of the property as a function of retained austenite content (Figure 6.11) depended on whether the first tempering temperature was above 635°C or below (P was above 36.9 or below), i.e. whether fresh martensite was present or not. When the first tempering temperature was <635 °C (P<36.9), there was no fresh martensite produced, thus hardness and tensile properties were controlled by the volume fraction of retained austenite. After the second tempering no significant microstructure change occurred, so that hardness, 0.2% proof strength, and percentage elongation followed the same trend as for single tempering. As a result, high levels of retained austenite led to a reduction in 0.2% proof strength and hardness, but an increase in the percentage elongation values. When the first tempering temperature was >635 °C (P>36.9), fresh martensite was produced, so that retained austenite was not the only controlling factor. In this condition, both 0.2% proof strength and percentage elongation decreased, in contrast to the increase when

tempered <635 °C, even though the retained austenite content was the same. On the other hand, after the second tempering, again with the same retained austenite content, both hardness and 0.2% proof strength improved substantially. This observation shows that other factors contributed to the improved hardness and yield strength. This was attributed to the reverse transformation of fresh martensite to retained austenite, which relieved the internal stresses that was caused by fresh martensite formation; produced a very high dislocation density and fine grain size, led to improved yield strength and ductility.

In Figure 6.11(d), the slope of percentage elongation *vs.* retained austenite content plot for single tempering is rather small; the percentage elongation increased only ~5% although volume fraction of retained austenite increased from ~10% to ~36%. This is in contrast to the expected trend of transformation-induced-plasticity (TRIP). Indeed, this effect is used in TRIP steels, when transformation of the retained austenite is used to enhance tensile deformation. Tensile elongation is believed to be controlled by volume fraction of retained austenite (Sandvik and Nevalainen 1981). An increase in the volume fraction of retained austenite increases the strain-hardening coefficient, leading to an increase in elongation (Timokhina et al. 2004). However, since the C content in retained austenite determines the chemical driving force for the transformation of retained austenite to martensite, a higher amount of retained austenite does not necessarily result in a higher uniform elongation, because the higher amount of retained austenite may have a lower average C content, leading to low stability during deformation (Timokhina et al. 2004). It has been reported that retained austenite with a low C content (<0.5 to 0.6 wt%) transforms to martensite more rapidly during plastic straining and does not contribute to an increase in elongation (Reisner et al. 1997). Therefore, when retained austenite is distributed homogenously as fine particles along martensite boundaries with a higher C content, the m_{def} may be at too low a temperature that strain-induced transformation does not occur, and therefore ductility is not enhanced. However, when tempering at 635 °C, isolated retained austenite (blocky austenite) was present in the structure (Figure 5.35) with a low C content (0.6 wt%), so that some of the retained austenite transformed rapidly during straining, with a small benefit to ductility. This can be confirmed by the changes of retained austenite levels after tensile testing (Table 5.2). As shown in

Table 5.2, after tempering at 620 °C for 4 h, 41 vol% of the original retained austenite transformed to martensite during tensile testing, while at 635 °C, the value increased to 74 %.

6.4.2 Grain size effect

As shown in Chapter 2, Literature Review, the classic Hall-Petch equation (Hall 1951, Petch 1953) relates the yield stress, σ, to the grain size, d, through the expression $\sigma = \sigma_0 + kd^{-1/2}$, where σ_0 is the fraction stress and k is a positive constant (often refereed to as the Hall-Petch slope and is material dependent). This relationship is well established for materials with large grain size (>1μm) (Pande et al. 2002). The Hall-Petch relation is normally explained by the creation of dislocation pileups in grains (Firedman and Chrzan 1998). However, it has not been clear if the explanation of the Hall-Petch effect is valid for sub-micrometer grains. When the grain size is fine (<1μm), the slip dimensions become too small to allow the existence of pile-ups. Yielding is then determined by the stress necessary to expand a dislocation loop across a slip plane. The yield stress in this circumstance varies as the inverse of the grain size, $\sigma \propto d^{-1}$ (Bhadeshia 2001).

Usually grain size strengthening in martensitic steels arises from a reduction in the prior austenite grain size or the "packet" size, D. However, in this investigation grain size strengthening appears to have been related to the retained austenite (γ') particle size (at P<36.9), or the "retained austenite + fresh martensite" ($\gamma'+\alpha_F'$) lath size (at P>36.9)*. The tensile samples had experienced the same re-austenitization and air-cooling thermal cycle before tempering, so that the prior austenite grain size and packet size were the same, since the austenite nucleated and grew along the martensite lath boundaries. The only difference therefore was the $\gamma'/\gamma'+\alpha_F'$ size, d, as shown by the average particle/lath width, after tempering at different tempering

* As has been described in Chapter 5, since the difference between retained austenite and fresh martensite could not be reliably determined in SEM images, the 'lath size' for the tempering time-temperature parameter P>36.9 must be considered to be retained austenite and fresh martensite, which contrasts that for P<36.9 where the measurement would have been from retained austenite alone.

temperature/time. Most of the studies which used lath size (for example, in Bainitic steels) agree that flow stress varies with the reciprocal of some characterisitic lath dimension and not as inverse square root relationship required by a Hall-Petch mechanism (Edmonds and Cochrane, 1990).

Figures 6.12 and 6.13 show retained austenite content and yield strength (0.2% proof strength) as a function of d, in the form of the inverse square root, and the inverse, respectively, for single tempering (ST). The data for the as-received state was added for comparison. As expected, retained austenite content exhibited a reverse trend compared to yield strength. In all cases there appeared to be a linear trend, but the slope was dependent on whether the Holloman-Jaffe tempering time-temperature parameter P was above or below 36.9, i.e. whether fresh martensite was present or not. Figure 6.12 (b) indicated that for P<36.9 the yield strength increased with increasing $d^{-1/2}$ (decreasing d) and correlated with grain size in the form of classic Hall-Petch $[d]^{-1/2}$ relationship. The slope of the trend lines in Figure 6.12 (b) represented the corresponding Hall-Petch constants for yield strength. However, for P≥36.9, the yield strength exhibited an apparent decrease with increasing $d^{-1/2}$ (decreasing d), thereby giving a negative slope in the plot of $\sigma \propto d^{-1/2}$. This confirmed that at P>36.9, retained austenite size was not the strength controlling factor. Figure 6.13 shows a similar correlation for the yield strength as a function of d in the form of $[d]^{-1}$. The as-received data followed the trend for P<36.9, confirmed that in a retained austenite-tempered martensite duplex structure, hardness and yield strength are strongly dependent on the retained austenite (grain size and volume fraction).

6.4.3 Dislocation strengthening

The significant effect of dislocation density on yield strength occurred after double tempering when the first temper at P>36.9. As observed by TEM, numerous dislocations were induced by the austenite → fresh martensite ($\gamma_T \rightarrow \alpha'_F$) transformation after the first tempering on cooling to room temperature, and the fresh martensite → austenite ($\alpha'_F \rightarrow \gamma_T$) re-transformation during the second tempering. As a result, these substructures contributed to the improvement of yield strength.

Although the size of the carbides/carbontrides was rather small, the volume fraction of these precipitate particles was also small. Therefore it is unlikely they had any significant effect on dislocation flow since the combination of size and volume fraction that is important for zener pinning.

6.4.4 Tempering at P close to the retained austenite content peak

It is obvious that after tempering at temperatures giving a P about 36.9 (around 635 ~640 °C, 4 h), 0.2% proof strength and hardness exhibited a pronounced minimum. In this condition even applying the second tempering could not improve the mechanical properties. The low 0.2% proof strength and hardness is believed to have resulted from the complex structure, but most importantly from the size and volume fraction of the austenite that determined its stability. Around P = 36.9 the maximum amount of retained austenite was formed and it had the maximum size for all tempered conditions. Moreover, a small amount of fresh martensite was believed also formed, and intergrannular carbides were also produced. After the second temper at 550 °C for 2 h, the retained austenite content and size was largely unchanged (Figures 5.2, 5.41 and 5.42), and the C content in the retained austenite did not change appreciably (Figure 5.3(b)). As a result, the retained austenite was least stable compared to other temper temperatures/times. This is further shown by the observation that on tempering at slightly higher temperatures/times the austenite formed at temperature increasingly transformed to martensite on cooling. Thus, the highest volume fraction (~37 vol%) and the least stable of retained austenite (low C content) reduced 0.2% proof strength and hardness. From the discussion it is clear that tempering at a value P close to that which gives a maximum retained austenite must be avoided.

6.4.5 Summary

The amount of retained austenite is the key factor in controlling the yield strength, percentage elongation and hardness. The volume fraction of retained austenite was dependent on the tempering time-temperature parameter P. Increasing P up to P~36.9 resulted in increasing in volume fraction of retained austenite hence increased

ductility but decreased hardness and yield strength. After tempering at P>36.9, the second tempering at 550 °C for 2 h resulted in the reverse transformation of fresh martensite to austenite, which led to refined grain size and increased dislocation density thereby improved yield strength and elongation. Tempering at P close to the retained austenite peak (P~36.9) resulted in the highest volume fraction of austenite, the largest austenite particle size and a small amount of fresh martensite, all of which led to the lowest yield strength and hardness.

Clearly the C redistribution was central to the microstructural evolution. The main role of C is its partitioning between martensite and austenite, and particularly changes on heat treatment that affects the stability of the austenite (M_s etc). The secondary role is in forming carbides. However, the size and volume fraction of particles was such small that Zener pinning would have been unlikely.

6.5 Relationship between hardness and strength

UTS and 0.2% proof strength as a function of hardness for the as-received and tempered specimens are shown in Figure 6.14 and Figure 6.15. UTS increased approximately linearly with increasing hardness for both single (ST) and double tempering (DT), and the as-received data followed the same trend for laboratory single and double tempering. Thus, hardness appeared to follow UTS in the often observed manner. According to Figure 6.14, the following linear equations relate UTS to hardness (HRC) for specimens after single and double tempering:

$$\text{UTS (MPa)} = 16.1 \times [\text{HRC}] + 471.5 \qquad (6\text{-}8)$$

Like UTS, the 0.2% proof strength vs. hardness trend also appeared linear. However, after double tempering the 0.2% proof strength exhibited a different trend from single tempering. On the other hand, tempering at P>36.9 the 0.2% proof strength exhibited a different trend form tempering at P<36.9 for both single and double tempering. These result from the different microstructures produced after tempering at different conditions. According to Figure 6.15, the following linear equations

relate 0.2% proof strength to hardness (HRC) for specimens after single and double tempering:

Single tempering:

$$0.2\%\ \text{Proof strength (MPa)} = 37.00 \times [\text{HRC}] - 224 \quad (\text{at } P<36.9) \qquad (6\text{-}9)$$

$$0.2\%\ \text{Proof strength (MPa)} = 21.77 \times [\text{HRC}] + 30 \quad (\text{at } P>36.9) \qquad (6\text{-}10)$$

Double tempering:

$$0.2\%\ \text{Proof strength (MPa)} = 49.26 \times [\text{HRC}] - 509 \quad (\text{at } P<36.9) \qquad (6\text{-}11)$$

$$0.2\%\ \text{Proof strength (MPa)} = 47.38 \times [\text{HRC}] - 575 \quad (\text{at } P>36.9) \qquad (6\text{-}12)$$

Relation (6-9) through (6-12) suggested that if the hardness of the steel is the same, the tensile properties will also be identical, whether a high or a low tempering temperature is used. However, it must be stressed the relations shown above only give a rough relationship between hardness and strength since these relations were derived from limited experimental data. Moreover, the relations between hardness and 0.2% proof strength might be helpful for the process of this specific steel, but there is no physic fundamental.

6.6 Structure-property relationships of the as-received materials

As introduced in Chapter 3, Experimental Procedure, two of the product specifications for the 655 MPa grade are: 655 MPa≤ 0.2% proof strength ≤758 MPa, and the maximum hardness is 28 HRC. For the 758 MPa grade, the minimum 0.2% proof strength is 758 MPa, and the maximum hardness is 32HRC. Bars A1-A4, B1 and B2 were produced to meet the 655 MPa grade while bar 3 was produced to meet the 758 MPa grade.

6.6.1 Effect of retained austenite content on hardness and yield strength of the as-received materials

Figure 6.16 shows UTS, yield strength (0.2% proof strength) and percentage elongation as a function of retained austenite content for the as-received samples A1-A4 and B1-B3. UTS and hardness decreased slightly with increase in retained austenite, accompanied by a slight increase in percentage elongation. However, 0.2% proof strength decreased from 825 MPa to 635 MPa with increasing retained austenite content from 18 vol% to 35.9 vol%. This revealed that the significant effect of retained austenite content was on yield strength, while the effect of retained austenite on UTS, hardness, and percentage elongation of the as-received materials was negligible.

As-received bars A1, A2, A3 and A4 were from the same cast (Cast 1) and had experienced the same heat treatment regimes, so that the different amount of retained austenite might have arisen from the small, but significant, differences in tempering temperatures during tempering. As-received bars B1, B2 and B3 were also from the same cast (Cast 2), so the different amount of retained austenite observed must have resulted from differing heat treatment history (see Tables 3.3, 3.4 and 3.5).

6.6.2 Relationship between retained austenite grain size and yield strength

Figure 6.17 gives the retained austenite content and 0.2% proof strength as a function of the inverse square root of retained austenite grain size d in the as-received specimens. The two relationships appeared linear, i.e. the volume fraction of retained austenite decreased and 0.2% proof strength increased with increasing the $d^{-1/2}$ value (decreasing d). However, the $d^{-1/2}$ vs yield strength does not match the Hall-Petch relation $\sigma = \sigma_0 + kd^{-1/2}$ since the constant k appeared negative. Figure 6.18 gives retained austenite content and 0.2% proof strength as a function of the inverse of retained austenite particle size d in the as-received specimens. The two relationships also appeared linear, i.e. the volume fraction of retained austenite decreased and 0.2% proof strength increased with increasing the d^{-1} value (decreasing d). The d^{-1} vs.

yield strength agrees with the relation $\sigma = \sigma_0 + kd^{-n}$ (Sevillano et al. 1980, Dubravina et al. 2004) for $\sigma_0 \approx 234$ MPa, n = 1, and $k \approx 8.8 \times 10^4$ MPa·nm.

Figure 6.18 shows that the 0.2% proof strength of the as-received samples varied as a function of retained austenite size d, even though the variations were only over a small range. Microstructural examination showed that the dominate structure in the as-received samples was a duplex structure of 'tempered martensite and retained austenite', therefore the variations in retained austenite particle size d reflected the variations in amounts of retained austenite. Figure 6.18 confirmed the 0.2% proof strength of the as-received samples was strongly dependent on the retained austenite content. This result was consistent with the typical tensile behaviour of dual phase steels, i.e. while tensile strength decreased remarkably, retained austenite volume fractions increased in large amount (Kim et al. 2003).

6.7 Relating the industrial properties to the laboratory based trials and implications for commercial practice

6.7.1 The tempering time-temperature parameter P1 for industry tempering

To investigate the effect of the Hollomon-Jaffe tempering time-temperature parameter P on the industrial based tempering, the data for the as-received samples were added to the retained austenite content, hardness, and 0.2% proof strength vs. P plots for the laboratory double tempering (Figures 6.19, 6.20 and 6.21). The parameter P in these figures was calculated using the first tempering, i.e. single tempering (ST), temperature and time. As shown in Figures 6.19(a), 6.20(a) and 6.21(a), the data for the as-received samples does not follow the curve for the laboratory double tempered data. This is due to the different heating and cooling rate for the industry commercial bars and the laboratory specimens. The Hollomon-Jaffe time-temperature parameter P given here did not take into account the influence of heating and cooling cycle of the heat treatment, whereas for large industrial size rods, particularly the heating time would have been considerable. To make a provision for

heating and cooling, the time t in the Hollomon-Jaffe formula should be in the form of:

$$t = t_h + t_e + t_c, \tag{6- 13}$$

where t_h, is correction in holding time for the heating period, which depended on heating rate; t_e is effective holding time, and t_c is correction in holding time for cooling rate, which depended on cooling rate. Unfortunately, both t_h and t_c were unavailable, so that only t_e was used in the time-temperature parameter. As a result, the different t_h and t_c for the industry heat treatment and the laboratory heat treatment induced the as-received data scatter from the laboratory tempered data.

It was found that for the industry heat treatment, after the second tempering at 550 °C for 2 h, both yield strength (0.2% proof strength) and ductility (elongation%) were enhanced compared to single tempering. This suggested that fresh martensite must be present after the first tempering. In other words, the industry tempering was on the right side of the peak in austenite content in Figure 6.19(a). This data suggests that the heating and cooling in the industrial production process equated to approximately a 14.5 °C increase in the isothermal hold temperature in the laboratory based thermal cycle. On the basis of this, to explore the optimum time-temperature parameter range for the industry tempering, the data for the laboratory tempering was shifted to the left by 14.5 °C, the results of which are plotted in Figures 6.19(b), 6.20(b) and 6.21(b), with the Hollomon-Jaffe tempering temperature-time parameter named as P1 to differentiate it from P for the laboratory tempering. However, note that the following assumptions have been made: (i) it has been presumed that only the first stage tempering conditions affect properties, and the effect of the second stage tempering condition was not considered. (ii) The straining rate applied to laboratory tensile testing was the same as applied for the commercial bar, so that the tensile testing conditions for the as-received data and the laboratory data was almost the same. Hence the tensile test results are comparable. To the best of the author's knowledge, this condition was satisfied.

As shown in Figure 6.20(b), to meet commercial specifications of hardness ≤28 HRC, the tempering time-temperature parameter P1 should be ≤36.9. On the other hand, from Figure 6.21(b), to make sure the 0.2% proof strength meets the minimum value of 655 MPa, the P1 value should be ≥36.7. Thus, to satisfy both specifications, the P1 will be in the narrow range of 36.7≤ P1 ≤36.9. Since the P1 range is so critical, tempering conditions, and most importantly, temperature has to be tightly controlled. Note bar B3 was produced to against the 758 MPa strength level, so the heating history was different from other bars (against the 655 MPa strength level). This probably is the reason for the B3 data scatters far from the curves shown in Figures 6.19, 6.20 and 6.21.

6.7.2 Optimum microstructure for combined hardness and yield strength

Figure 6.22 gives the hardness as a function of retained austenite content which shows the data from the commercially processed bar followed the same trend as the laboratory tempered data, although with greater scatter from the trend line. The relationship between the hardness and amount of retained austenite was expressed as:

$$\text{Hardness (HRC)} = 30.8 - 0.18 \times \text{Retained austenite content (vol\%)} \quad (6\text{-}14)$$

Thus, to meet the required hardness ≤28 HRC, the volume fraction of retained austenite has to be no less than 16 vol%, i.e. on the right side of the red line in Figure 6.22.

Figure 6.23 gives the 0.2% proof strength as a function of retained austenite content and shows that, as with the hardness, the data for the commercially processed bar gave greater scatter than the laboratory double tempered data at the first tempering ≥635 °C. The relationship between the 0.2% proof strength and amount of retained austenite was expressed as:

$$\text{0.2\% proof strength (MPa)} = 1330 - 21 \times \text{Retained austenite content (vol\%)} \quad (6\text{-}15)$$

Thus to meet 0.2% proof strength ≥655 MPa, the volume fraction of retained austenite must be less than 32 vol%, ideally <30 vol%, i.e. on the left side of the red

line in Figure 6.23. The red circle indicates values of measured proof strength which were too low because the volume fraction of retained austenite was too high, which is the case for A1 and B2 (see Table 4.1).

From Figure 6.18, the relationship between retained austenite grain size d and the 0.2% proof strength can be expressed as:

$$0.2\%\ \text{proof strength (MPa)} = 233 + 8.8 \times 10^4 \times d^{-1}(nm^{-1}) \quad (6\text{-}16)$$

Thus to meet the 0.2% proof strength ≥655 MPa, the retained austenite grain size must be smaller than around 208 nm. It is obvious the retained austenite particle size of A1 and B2 was in excess of this (see Table 4.12), which further aggravated the excess austenite content.

From the discussions above, to meet the required minimum 0.2% proof strength of 655 MPa and the maximum hardness of 28 HRC, the tempering temperature-time parameter P1 for industry tempering should be controlled in the range of 36.7≤ P1 ≤36.9. Tempering at this temperature/time range will produce a retained austenite-tempered martensite duplex structure in the steel, and the optimum retained austenite is: volume fraction between 16-30 vol% and size <208 nm.

Using the Hollomon-Jaffe tempering time-temperature relation $P1 = (273 + T(°C)) \times (40 + \log(t)(h)) \times 1000^{-1}$, for t = 4 h, the industry tempering temperature was derived to be in the range of 631 °C ≤ T ≤ 636 °C. This specification is extremely tight and perhaps unrealistic on a day to day basis (although it is clearly often achieved commercially). This suggests that perhaps further alloy development is required to change composition to one where the process window is rather larger.

Chapter 7 Conclusions

The work presented in this thesis was concerned the effect of tempering temperature and time on microstructural characterization hence hardness and room temperature tensile properties of the super 13% Cr stainless steel. The results obtained in this work are briefly summarized below:

1. The microstructure of the single tempered super 13% Cr steel consisted of tempered martensite, retained austenite, a minor δ-ferrite (<1%), carbides/carbonritrides, and probably fresh martensite. δ-ferrite was produced on solidification before heat treatment, and therefore the volume fraction remained constant during heat treatment. Retained austenite precipitated as small elongated particles, mainly distributed along the martensite laths when tempered above the A_{c1} (A_{c1}~560 °C). Fresh martensite transformed from unstable austenite (tempered at about 70 °C above the A_{c1}) on cooling to room temperature. Fresh martensite partially re-transformed to austenite during re-heating. Therefore double tempering is required to ensure that any fresh martensite produced in the first temper is subsequently tempered such that no fresh martensite is present in the final structure.

2. $M_{23}C_6$ and M_6C carbides, V(C,N) carbonitrides were found precipitated in the tempered specimens. After tempering at 557 °C for 4 h, fine particles (<20 nm) were observed distributed in the martensite matrix and along the lath boundaries. EDX microanalysis results indicated they coexisted Cr-rich $M_{23}C_6$ and Mo-rich M_6C carbides and probably V(C,N) carbonitrides. After tempering at 640 °C for 4 h, the fine particles (<60 nm) distributed along prior austenite grain boundaries were found to be overlapped by Mo-rich M_6C carbides and V-rich V(C,N) carbonitrides. Mo-rich particles were found concentrated in δ-ferrite phase after tempering.

3. The volume fraction of retained austenite is strongly dependent on tempering temperature and time, but the temperature has the most important effect. The

combination effect of temperature and time can be expressed using the Hollomon-Jaffe tempering time-temperature type parameter P, where P = (273 + T (°C)) × (40 + $\log_{10}$ t (h)) × 1000^{-1}. After the first tempering in the range $33.7 \leq P \leq 39.5$, volume fraction of retained austenite increased with P up to a peak value of ~37 vol% at P~36.9 (T = 635 °C, t = 4 h). After that, retained austenite content decreased due to the formation of unstable austenite on tempering, which consequently transformed to fresh martensite on cooling to room temperature. For a first stage temper at P<36.9, retained austenite content did not change after the second stage temper at 550 °C for 2 h. However, for a first stage temper at P>36.9, retained austenite content increased after the second tempering. This is due to the re-transformation of fresh martensite to austenite during the second tempering. Therefore, a first temper at P>36.9, followed by a second temper at 550 °C, resulted in increase in total retained austenite, even though it was expected to be below the A_{c1} temperature. This was a result of re-distribution of solute elements, in particular C and Ni, which resulted in a change in the A_{c1} temperature.

4. 0.2% proof strength and hardness were inversely related to retained austenite content with increase in P. Both 0.2% proof strength and hardness decreased with P to a minimum at P~36.9 (T = 635 °C, t = 4 h). After that, they increased with increase in P. When the first stage temper at P<36.9, hardness and 0.2% proof strength did not change after the second tempering at 550 °C for 2 h since no microstructure change occurred. When the first stage temper at P>36.9, the hardness did not change after the second tempering since the steel had the very low C content (0.016 wt%), so the fresh martensite was soft. However, 0.2% proof strength was improved after the second stage tempering. The reverse transformation of fresh martensite to retained austenite resulted in the internal stresses relief, a high dislocation density and fine grain size, and the combination of which led to improved yield strength.

5. Both 0.2% proof strength and hardness decreased linearly with increase in retained austenite content while elongation showed a reverse trend. However, these relationships depended on whether fresh martensite was present or not.

When the first temper was at P<36.9, 0.2% proof strength, hardness, and elongation were controlled by retained austenite content. For P>36.9, not only retained austenite, but also the formation of fresh martensite played a vital role on 0.2% proof strength, hardness and elongation.

6. The retained austenite average grain size increased from 150 nm to 280 nm when tempered in the range 600-635 °C for 4 h (P<36.9). Although it is in a very small range, 0.2% proof strength (σ_y) and the retained austenite grain size (d) exhibited $\sigma_y = \sigma_0 + k\ d^{-1}$ relationship, confirmed that in this temperature range, 0.2% proof strength was controlled by retained austenite.

7. C and Ni element re-distribution occurred during tempering cycles. After the first tempering in the range 600-700 °C for 4 h, C and Ni content in retained austenite steadily dropped with increase in tempering temperature. However, after the second tempering at 550° C for 2 h, C content appeared almost constant as a function of the first stage tempering temperature. For the first stage temper at 700 °C, the second tempering increased both C and Ni content in retained austenite. This explains the higher retained austenite volume fraction for double temper compared with single temper specimens, for a first temper > 635 °C (P>36.9).

8. The stability of retained austenite decreased with increasing tempering temperature. This was a result of the reduction of C and Ni content in austenite, γ_T, and the enlarged austenite grain size on tempering with temperature/time. The M_s increased from 13 °C when tempered at 600 °C, to about 171 °C when tempered at 700 °C, indicating the stability of retained austenite declined. Strain-induced transformation of retained austenite to martensite occurred during tensile testing, indicating a wide range in instability of retained austenite.

9. When the first temper at P~36.9, retained austenite content reached maximum (~37 vol%) but was less stable due to the larger size (280 nm) and lower C content in retained austenite (0.6 wt%). As a result, both hardness and 0.2% proof strength reached the minimum values. In this condition, the second tempering at

550 °C for 2 h could not reduce retained austenite size, or improve C content in retained austenite, so yield strength could not be improved.

10. It has been shown that to meet the required minimum 0.2% proof strength of 655 MPa and the maximum hardness of 28 HRC, the optimum microstructure would be a tempered martensite-retained austenite duplex structure, with retained austenite volume fraction between 16-30 vol% and size <208 nm. To achieve this microstructure, accurate control during tempering period is important.

Chapter 8 Further Work

- In this work, retained austenite volume fraction was measured at room temperature after tempering. However, austenite content at the tempering temperature was not measured experimentally. Therefore, it would be helpful to do some high-temperature XRD experiments or dilatometry experiments to determine amounts of austenite at tempering temperatures, in order to further understand austenite to fresh martensite phase transformation mechanisms and retained austenite stability.

- The effect of microstructure on hardness and tensile properties has been shown in this work. However, impact properties have not been studied. It is would be helpful to carry out low-temperature charpy impact test to explore the effect of microstructure on low-temperature toughness for the optimum combination of mechanical properties.

- As discussed in this work, the tempering temperature range for the two steel casts, Cast 1 and Cast 2 (see Table 3.1), is tight. Therefore, further investigations may be based on a broad range of composition to study the effect of composition on microstructure and mechanical properties, so that further optimum super 13% Cr steel composition in order to achieve a rather large process window.

References

Amaya, H., et al., 2003, "Martensitic Stainless Steel", Patent, Inter. Publication No. WO 03/033754 A1

Andrews, K.W., 1971, "Interpretation of Electron Diffraction Patterns", 2nd ed., Adam Hilger Ltd., London, p202

Andrews, K.W., 1965, "Empirical Formulae for the Calculation of Some Transformation Temperatures", J. Iron Steel Inst., 203, 721-727

Asahi, H., et al., 1995, "Development of Sour Resistant Modified 13Cr OCTG", in: Corrosion 95, the NACE International Annual Conference and Corrosion Show, Paper No. 79

Avrami, M., 1939, "Kinetics of Phase Change, I: General Theory", J. Chem. Phys., 7, 1103-1112

Avrami, M., 1940, "Kinetics of Phase Change, II: Transformation Time Relations for Random Distribution of Nuclei", J. Chem. Phys., 8, 212-224

Avrami, M., 1941, "Kinetics of Phase Change, III: Granulation, Phase Change on Microstructure", J. Chem. Phys., 9, 177-184

Baker, R.G. and Nutting, J., 1959, "The Tempering of 2.25Cr-1Mo Steels after Quenching and Normalizing", J. Iron Steel Inst., 193, 257-268

Bashuet, S.A., Singh, K. and Rawat, M.S., 1990, "Effect of Heat Treatment on Mechanical Properties and Fracture Behaviour of a 12CrMoV Steel", Mater. Sci. Eng. A , 127, 7-15

Bhadeshia, H.K.D.H, 2001, "Bainite in Steels", 2nd ed., The Institute of Materials, London, p290

Bhadeshia, H.K.D.H and Edmonds, D.V., 1983, "Bainite in Silicon Steels– New Composition Property Approach 2", Met. Sci., 17, 420-425

Bhavsar R.B. and Montani R., 1998, "Application of Martensitic, Modified Martensitic and Duplex Stainless Steel Bar Stock for Completion Equipment", in: Corrosion 98, NACE International, page No. 96

Bilmes, P.D., Solari, M. and Liorente, C.L., 2001, "Characteristics and Effects of Austenite Resulting from Tempering of 13Cr-NiMo Martensitic Steel Weld Metals", Mater. Char., 46, 285-296

Brandes, E.A. and Brook, G.B., 1992, "Smithells Metals Reference Book", 7th ed., Butterworth-Heinemann Ltd, Oxford, p13-7, 13-33

Brezia, P., 1980, "Martensitic CrNi Steels with Low Carbon Content", Escher Wyss News, 1-2, 218-236

Christian, J.W., 1975, "The Theory of Transformation in Metals and Alloys", Part I, 2nd ed., Pergamon Press Ltd., Oxford, p540, 542

Cullity B.D, 1978, "Elements of X-ray Diffraction", 2nd ed., Addison-Wesley Publishing Company, INC., London, p351

Danil'chenko, V.E., Sagarader, V.V. and I'Heritier, P.H., 2003, "Martensite Crystal Structure of Nickel Steel at Cryogenic Temperatures", Mater. Sci. Eng. A, 358, 26-31

Deleu, E., Dhooge, A. and Dufrane, J.J., 1999, "Weldability and Hot Deformability of Different Supermartensitic Stainless Steel Grades by Weld Simulation Testing", in: Supermartensitic Stainless Steels, Brussels, pp232-240

Dias N.N. and Wilson F.G., 1980, "Metallurgy, Heat treatment, and Mechanical Properties of 13Cr-4Ni and 13Cr-6Ni Steel Castings", in: Proc. of an Inter. Conf. on Solidification Technology in the Foundry and Cast House, Beecroft, K.A.., eds., Metals Soc., London, pp602-606

Dickson, M.J., 1969, "The Significance of Texture Parameters in Phase Analysis by X-ray Diffraction", J. Appl. Cryst., 2, 176-180

Düber, B., et al., 2004, "Short Crack Propagation in Duplex Steel– Experimental Characterization and Modelling", in: 15th European Conference of Fracture – ECF15, Schweden, (auf CD-ROM)

Dubravina, A., Zehetbauer, M.J., et al., 2004, "Correlation between Domain Size Obtained by X-ray Bragg Profile Analysis and Macroscopic Flow Stress in Severely Plastically Deformed Copper", Mat. Sci. Eng. A, 387-389, 817-821

Dufrane, J.J., 1999, "Metallurgical for the Development of Weldable Martensitic Stainless Steels", in: Supermartensitic Stainless Steels 99, Brussels, pp19-24

Durnin J. and Ridal K.A., 1968, "Determination of Retained Austenite in Steel by X-Ray Diffraction", J. Iron Steel Inst., 196, 60-67

Edmonds, D.V. and Cochrane, R.C., 1990, "Structure-Property Relationships in Bainitic Steels", Metall. Trans. A, 21A, 1527-1540

Ennis, P.J., et al., 1997, "Microstructural Stability and Creep Rupture Strength of the Martensitic Steel P92 for Advanced Power Plant", Acta Mater., 45, 4901-4907

Fang, L., Wood, W.E. and Atteridge, D.G., 1997, "Identification and Range Quantification of Steel Transformation Products by Transformation Kinetics", Metall. Mater. Trans. A., 28A, 5-14

Farrar, J. and Marshall, A.W, 1998, "Supermartensitic Stainless Steels-Overview and Weldability", IIW Doc 1998, No IX-H432-98.

Folkhard, H., 1988, "Welding Metallurgy of Stainless Steels", Springer-Verlag Wien, New York, p16

Friedman, LH. and Chrzan, D.C., 1998, "Scaling Theory of the Hall-Petch Relation

for Multilayers", Phys. Rev. Lett., 81, 2175-2178

Furukawa, et al., 1996, "Microhardness Measurements and the Hall-Petch Relationship in an Al-Mg Alloy with Submicrometer Grain Size", Acta Mater., 44, 4619-4629

Girault, E., et al., 1998, "Metallographic Methods for Revealing the Multiphase Microstructure of TRIP-Assisted Steels", Mater. Character., 40, 111-18

Gooch, T.G., Woollin, P. and Haynes, A.G., 1999, "Welding Metallurgy of Low Carbon 13% Chromium Martensitic Steels", in: Supermartensitic Stainless Steels 99, Brussels, pp188-195

Hall, E.O., 1970, "Yield Point Phenomena in Metals and Alloys", New York, NY, Plenum Press, p38

Hall, E.O., 1951, "The Deformation and Ageing of Mild Steel: III Discussion of Results", Proc. R. Soc. B., B64, 747-753

Hara, T. and Asahi, H., 2000, "Effect of δ-ferrite on Sulfide Stress Cracking in a Low Carbon 13 Mass% Chromium Steel", ISIJ Int., 40, 1134-1141

Haynes, A.G., 1999, "Some Factors Governing the Metallurgy and Weldability of 13%Cr and Newer Cr-Ni Martensitic Stainless steels", in: Supermartensitic Stainless Steels 99, Brussels, pp25-32

Hofer, P., Cerjak, H., and Warbichler, P., 2000, "Quantification of Precipitates in a 10%Cr Steel Using TEM and EFTEM", Mater. Sci. Tech., 16, 1221-1225

Hollomon, J.H. and Jaffe, L.D., "Time-Temperature Relations in Tempering Steel", Trans. AIME, 1945, 162, 223-249

Honeycomb, R.W.K. and Bhadeshia, H.K.D.H, 1995, Steels: Microstructure and Properties, 2nd ed., Butterworth-Heinemann, p82, 181

International Institute of Welding (IIW), 1983, "Guide to the Welding and Weldability of Ni-alloyed Cryogenic Steels", Bratislava, Welding Research Institute, p7

Irvine, K.J., 1960, "The 12%Cr Stainless Steels", J. Iron Steel Inst., 193, 398-405

Iwabuchi, Y., 1987, "Temper embrittlement of type 13Cr-4Ni Cast Steel", Trans. ISIJ, 27, 211-217

Jackman, P.S. and Everson, H., 1995, "Development of New Martensitic Stainless Steels for OCTG: the Challenges for the Steelmaker and the Tubemaker", in: Corrosion 95, the NACE International Annual Conference and Corrosion Show, paper No. 89

Jaffe, L.D. and Hollomon, J.H., 1946, "Hardepability and Quench Cracking", Trans. AIME, 167, 617-626

Johnson, W.A. and Mehl, R.F., 1939, "Reaction Kinetics in Progress of Nucleation

and Growth", Trans. AIME, 135, 416-458

Kaltenhauser, R.H., 1971, "Improving the Engineering Properties of Ferritic Stainless Steels", Metals Eng. Quart., 11, 41-47

Karlsson, L., et al., 1999, "Development of Matching Composition Supermartensitic Stainless Steel Welding Consumables", Svetsaren, 54, 3-7

Kay, D.H., 1965, "Techniques for Electron Microscopy", 2nd ed., Blackwell Scientific, Oxford, p115

Kim, S.J., et al., 2003, "Effect of Cu, Cr and Ni on Mechanical Properties of 0.15 wt% C TRIP-Aided Cold Rolled Steels", Scripta Materialia, 48, 539-544

Kimura, M., et al., 2001, "Effect of Retained Austenite on Corrosion Performance for Modified 13%Cr Steel Pipe", Corrosion, 57, 433-439

Kimura, M., et al., 1999, "Corrosion Resistance of High-strength Modified 13% Cr Steel", Corrosion, 55, 756-761

Kimura, M., Miyata, Y. and Kitahaba, Y., 1998, "Development of New OCTG HP-13Cr-with Superior CO_2 Corrosion Resistance and SCC Resistance", Kawasaki Steel Technical Report, No.38, 47-52

Klotz, U.E., et al., 1999, "Alloy Compositions and Mechanical Properties of 9–12% Chromium Steels with Martensitic–Austenitic Microstructure", Mater. Sci. Eng., A 272, 292-299

Klueh, R.L., et al., 2000, "A Potential new Ferrite/Martensitic Steel for Fusion Applications", J. Nuclear Mater., 283-287, 697-701.

Koistinen, D.P. and Marburger, R.E., 1959, "A General Equation Prescribing Extent of Austenite-Martensite Transformation in Pure Iron-Carbon Alloys and Carbon Steels", Acta, Metall., 7, 59-68

Kolmogorov, A. 1937, "A statistical theory for the recrystallization of metals", Akad. nauk SSSR, Izv., Ser. Matem., 1, 355-359

Kondo, K., et al., 1999, "Alloy Design of Super 13Cr Martensitic Stainless Steel (Development of Super 13Cr Martensitic Stainless Steel for Line Pipe-1)", in: Supermartensitic Stainless Steels 99, Brussels, pp11-18

Krauss, G., 1999, "Martensite in Steel: Strength and Structure", Mater. Sci. Eng. A 273-275, 40-57

Krauss, G., 1992, "Microstructure and Transformation in Steel", in: Materials Science and Technology (Vol. 7), Cahn, R.W., Hassen, P. and Kramer, E.J., eds., VCH Publisher Inc, New York, pp1-40

Krauss, G. 1984, "Phase Transformation in Ferrous Alloys", Marder, A.H. and Goldstein, J.L., eds., Metals Society of AIME, Warrendale, PA, pp101-123

Kulmburg, A., et al., 1979, "Ds Umwandlungsvaerhalten komplexlegierter stähle mit 12 bis 18% Chrom", Berg-u.hüttenm. Mh., 124, 400-406

Kunze, E., 1976, "Über einen besonderen Legierungsbereich im Vierstoffsystem Eisen-Kohlenstoff-Chrom-Nickel", Thyssen Edelstahl Techn, Ber, 2, 70-74

Kvaale, P.E. and Olsen, S., 1999, "Experience with Supermartensitic Stainless Steels in Flowline Applications", in: Stainless Steels World 99 Conference, the Netherlands, pp19-26

Ladanova, E and Solberg, J.K., 2002, "Transmission Electron Microscopy of Precipitation Reactions in Coarse-Grained Heat Affected Zone in two 13% Cr Supermartensitic Stainless Steels", in: Supermartensitic Stainless Steels 2002, Brussels, pp205-214

Lee, Y.K., et al., 2003, "Reverse Transformation Mechanism of Martensite to Austenite and Amount of Retained Austenite after Reverse Transformation in Fe-3Si-13Cr-7Ni (wt%) Martensitic Stainless Steels", Mater. Sci. Tech., 19, 393-398

Leem, D.S., et al., 2001, "Amount of Retained Austenite at Room Temperature after Reverse Transformation of Martensite to Austenite in an Fe-13%Cr-7%Ni-3%Si Martensitic Stainless Steel", Scripta Materialia, 45, 767-772

Linne, C.P., et al., 1997, "Corrosion Performances of Modified 13Cr for OCTG in Oil and Gas Environments", in: Corrosion 97, NACE International, Paper No. 28

Lloyd, D.J. and Court, S.A., 2003, "Influence of Grain Size on Tensile Properties of Al-Mg Alloys", Mater. Sci. and Tech., 19, 1349-1354

Malyshev, K.A., et al., 1982, "Phase Hardening in Iron-Nickel Austenitic Alloys", Nauka, Moscow, p9

Maruyama, K., Sawada, K. and Koike, J., 2001, "Strengthening Mechanisms of Creep Resistant Tempered Martensitic Steel", ISIJ Int. 41, 641-653

Miyata, Y., Kimura, M. and Murase, F., 1998, "Development of Martensitic Stainless Seamless Pipe for Linepipe Application", Kawasaki Steel Technology Report, No.38, pp 53-60

Miyata., Y., Kimura., M. and Koseki, T., 1997, "Martensitic Stainless Steel Seamless Linepipe with Superior Weldability and CO_2 Corrosion Resistance", in: Corrosion 97, NACE International, Paper No. 19

Nakagawa, H., Yokota, H. and Miyazaki, T., 1998, "Effects of Aging Temperature on the Microstructures and Mechanical Properties of a Precipitation Hardening Martensitic Stainless Steel Containing Retained Austenite", Tetsu-To-Hagane, 84, 381-386

Nakagawa, H., Miyazaki, T., H. and Yokota, H., 2000, "Effects of Aging Temperature on the Microstructures and Mechanical Properties of 1.8Cu-7.3Ni-15.9Cr-1.2Mo-low C, N Martensitic Precipitation Hardening Stainless Steel", J. Mater. Sci., 35, 2245-

2253

Naylor, D.J. and Cook, W.T., 1992, "Heat Treated Engineering Steels", in: Materials Science and Technology (Vol. 7 Constitution and properties), Cahn, R.W., Hassen, P. and Kramer, E.J., eds., VCH Publisher Inc, New York, pp433-488.

Niinaka, H., et al., 1986, "13Cr-3.5Ni Martensitic Stainless Steel Castings for Hydraulic Turbine Runners", Kawasaki Steel Technical Report, 14, 141-152

Nishiyama, Z., 1978, "Martensitic Transformation", Fine, M.E., Meshii, M. and Wayman, C.M., eds., Academic Press, London, p7, p14

Onink M., et al., 1993, "The Lattice Parameters of Austenite and Ferrite in Fe-C Alloys as Functions of Carbon Concentration and Temperature", Scripta Metall. Mater., 29, 1011-1016

Petch, N.J., 1953, "The Cleavage Strength of Polycrystals", J. Iron Steel Inst., 174, 25-28

Pande, C.S., Masumura, R.A. and Hazzledline, P.M., 2002, "Yield Stress of Nanocrystalline Materials", Mater. Phys. Mech., 5, 16-22

Peddle, B.E. and Pickles, 2001, "Carbide Development in the Heat Affected Zone of Tempered and Post-weld Heat Treated 2.25Cr-1Mo Steel Weldments", Can. Metall. Quart., 40, 105-126.

Pickering, F.B., 1992, "Structure-property Relationships in Steels", in: Materials Science and Technology (Vol. 7 Constitution and properties), Cahn, R.W., Hassen, P. and Kramer, E.J. (eds.), VCH Publisher Inc, New York, pp 41-94

Picking, F.B., 1979, "Introduction: the metallurgical evolution of stainless steels", in: The Metallurgical Evolution of Stainless Steels, Pickering, F.B. ed., ASM, Ohio, pp1-43

Pickering, F.B., 1978, "Physical Metallurgy and Design of Steels", Applied Science Publisher Ltd., London, p185

Pilling, J. and Ridley, N., 1982, "Tempering of 2.25%Cr–1%Mo Low-Carbon Steels", Metallurgical Trans. A, 13, 557-563

Porter, D.A. and Easterling, K.E., 1992, "Phase Transformation in Metals and Alloys, 2nd ed., Chapman & Hall, London, p1

Reisner, G., Werner, E.A., et al., 1997, "Modelling of Retained Austenite in Low-Alloyed TRIP Steels", JOM, 49, 62-65

Rhodes, P.R., 2001, "Environment-Assisted Cracking of Corrosion-Resistance Alloys in Oil and Gas Production Environments: A Review", Corrosion, 57, 923-966

Ridley, N., Stuart, H. and Zwell, L., 1969, "Lattice Parameter of Fe-C austenites at Room Temperature", Trans. Metall. Soc. AIME, 245, 1834-1836

Ros-yanez, T., Houbaert, Y. and Mertens, A., "Characterization of TRIP-Assistant Multiphase Steel Surface Topography by Atomic Force Microscopy", Mater. Character., 2001, 47, 93-104

Ruhl R. and Cohen M., 1969, "Splat Quenching of Iron-Carbon Alloys", Trans. Met. Soc. AIME, 245, 241-251

Saeglitz, M. and Krauss, G., 1997, "Deformation, Fracture, and Mechanical Properties of Low Temperature-Tempered Martensite in SAE 43XX Steels", Metall. Mater. Trans. A, 28A, 377-387

Saleh, M.H. and Priestner, R., 2001, "Retained Austenite in Dual-phase Silicon Steels and its Effect on Mechanical Properties", J. Mater. Proc. Technol., 113, 587-593

Sandvik, B.P. and Nevalainen, H.P., 1981, "Structure-Property Relationships in Commercial Low-Alloy Bainitic-Austenitic Steel with High Strength, Ductility, and Toughness", Met. Tchnol., 15, 213-220.

Scnmitt, G., 1983, "Fundamental Aspects of CO_2 Corrosion", in Corrosion 83, NACE International, Paper No. 43

Sedriks, A.J., 1979, "Corrosion of Stainless Steels", John Wiley & Sons, New York, p2

Sevillano, J.G., Houtte, P.V. and Aernoudt, E., 1980, "Large Strain Work Hardening and Textures", Mater., Sci., 25, 69-412

Shaw, B.J., 1984, "A study of Carbides Formed in Low-Alloy Cr-Mo Steels", in: Research on Chrome-Moly Steels, MPC-21, Swift, R.A. ed., ASME, New York, pp117-128

Sourmail, T., 2001, "Precipitation in Creep Resistant Austenitic Stainless Steels", Mater. Sci. & Tech., 17, 1-14

Steven, W. and Haynes, A.G., 1956, "The Temperature Formation of Martensite and Bainite in Low-alloy Steels-Some Effects of Chemical Composition", J. Iron Steel Inst., 183, 349-359

Sugimoto, K.I., et al., 1993, "Effects of Second Phase Morphology on Retained Austenite Morphology and Tensile Properties in a TRIP-Aided Dual Phase Steel Sheet", ISIJ Int., 33, 775-782

Takahashi, M. and Bhadeshia, H.K.D.H., 1990, "Model for Transition from Upper to Lower Bainite", Mater. Sci. Technol., 6, 592-603

Taneike, M., Sawada, K and Abe, F., 2004, "Effect of Carbon Concentration on Precipitation Behavior of $M_{23}C_6$ Carbides and MX Carbonitrides in Martensitic 9Cr Steel during Heat Treatment", Metall. Mater. Trans. A, 35,1255-1262

Thelning, K.E., 1984, "Steel and its Heat Treatment", 2nd ed., Butterworth, London, p272

Timokhina, I.B., Hodgson, P.D. and Pereloma, E.V., 2004, "Effect of Microstructure on the Stability of Retained Austenite in Transformation-Induced-plasticity Steels", Metall. Mater. Trans. A, 35, 2333-2343

Todd, J.A., 1986, "The Early Stages of Tempering in a 3Cr-1.5Mo Steel", Scripta Metall., 20, 269-274

Toussaint, P. and Dufrane, J., 2002, "Advances in the Making and Base Material Properties of Supermartensitic Stainless Steels (SMSS)", in: Supermartensitic Stainless Steels 2002, Brussels, pp23-27

Toussaint, P. and Winden, H., 2001, "Vices and Virtues of Supermartensitic Stainless Steels", in: Conf. Stainless Steel Word 2001, The Netherlands, pp 9-16

Ueda, M., et al., 1994, "Development of Super 13Cr Martensitic Stainless Steel for OCTG Services", The Sumitomo Search, No. 56, 1-7

Varga, I., Kuzmann, E. and Vértes, A., 1998, "Kinetics of $\alpha \rightarrow \gamma$ Phase Transformation of Fe-12Cr-4Ni Alloy Aged Between 500-650 °C", Hyperfine Interactions, 112, 169-174

Vodarek, V., Hubackova, J. and Mazanec, K., 1984, "Structural and Phase Analysis of 13%Cr4%Ni Steel", Kovove Mater., 22, 641-653.

Vodarek, V., Hubackova, J. and Mazanec, K., 1985, "Stability, Morphology and Distribution of Austenite in Marternsitic-Austenitic Steels", Kovove Mater., 23, 17-28

Voort, G.F.V., 1984, "Metallography: Principles and Practice", McGraw-Hill Book Company, London, p362

Wabuchi, Y., 1984, "Effect of Tempering Condition on Toughness Degradation in 13Cr-3.8Ni Cast Steel", Testu-to-Hagané, 70, 1437-1444

Winden, H., Toussaint, P. and Coudreuse, L., 2002, "Past, Present and Future of Weldable Supermartensitic Alloys", in: Supermartensitic Stainless Steels 2002, Brussels, pp 9-13

"Elements Diffusion Coefficients as a Function of Temperature in γ (fcc) and α (bcc) Fe", www.clarkson.edu/class/es260/CHAPTER5.260-Supplemental Result

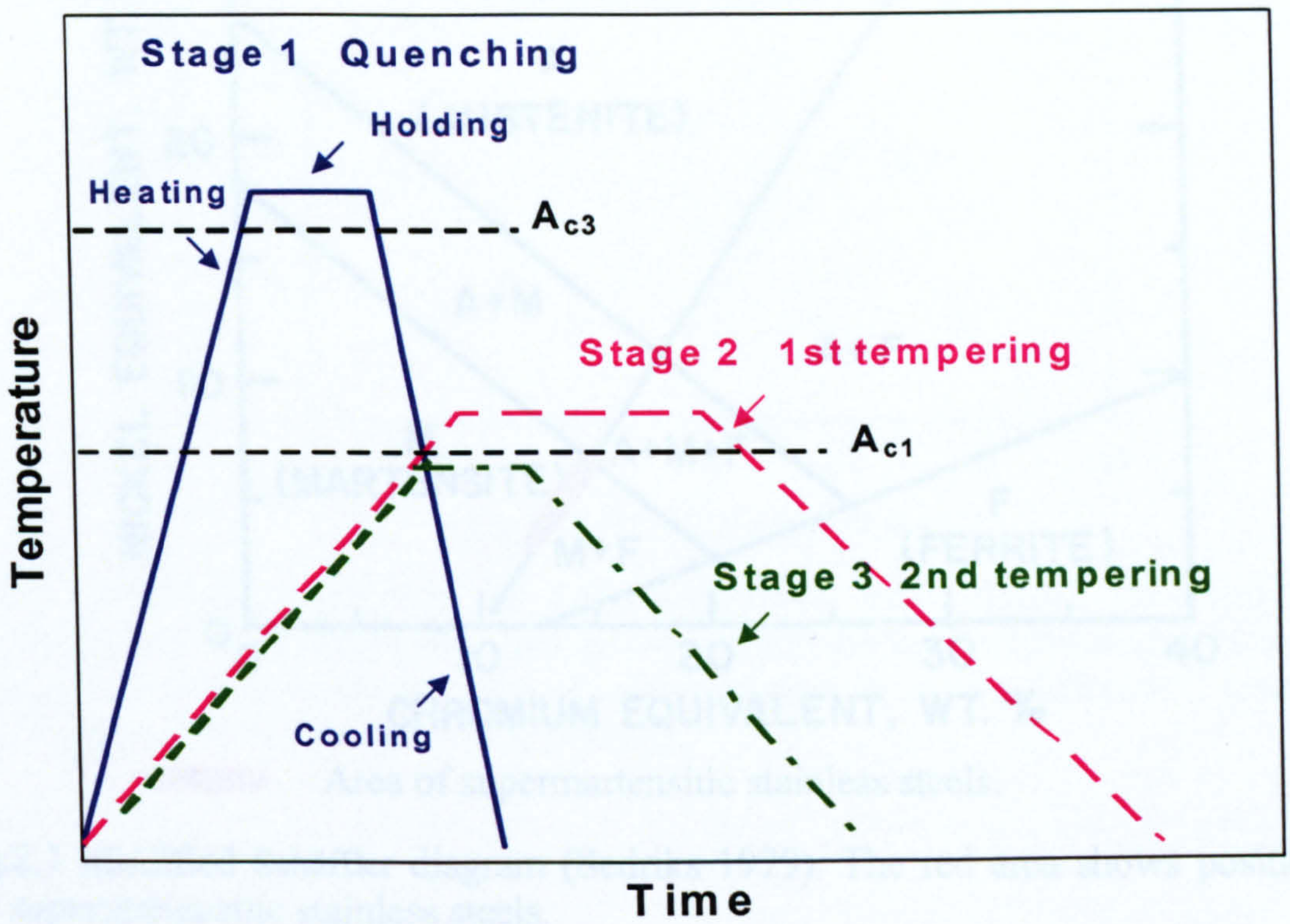

Figure 1.1 Schematic of the heat treatment process for super 13% Cr steel.

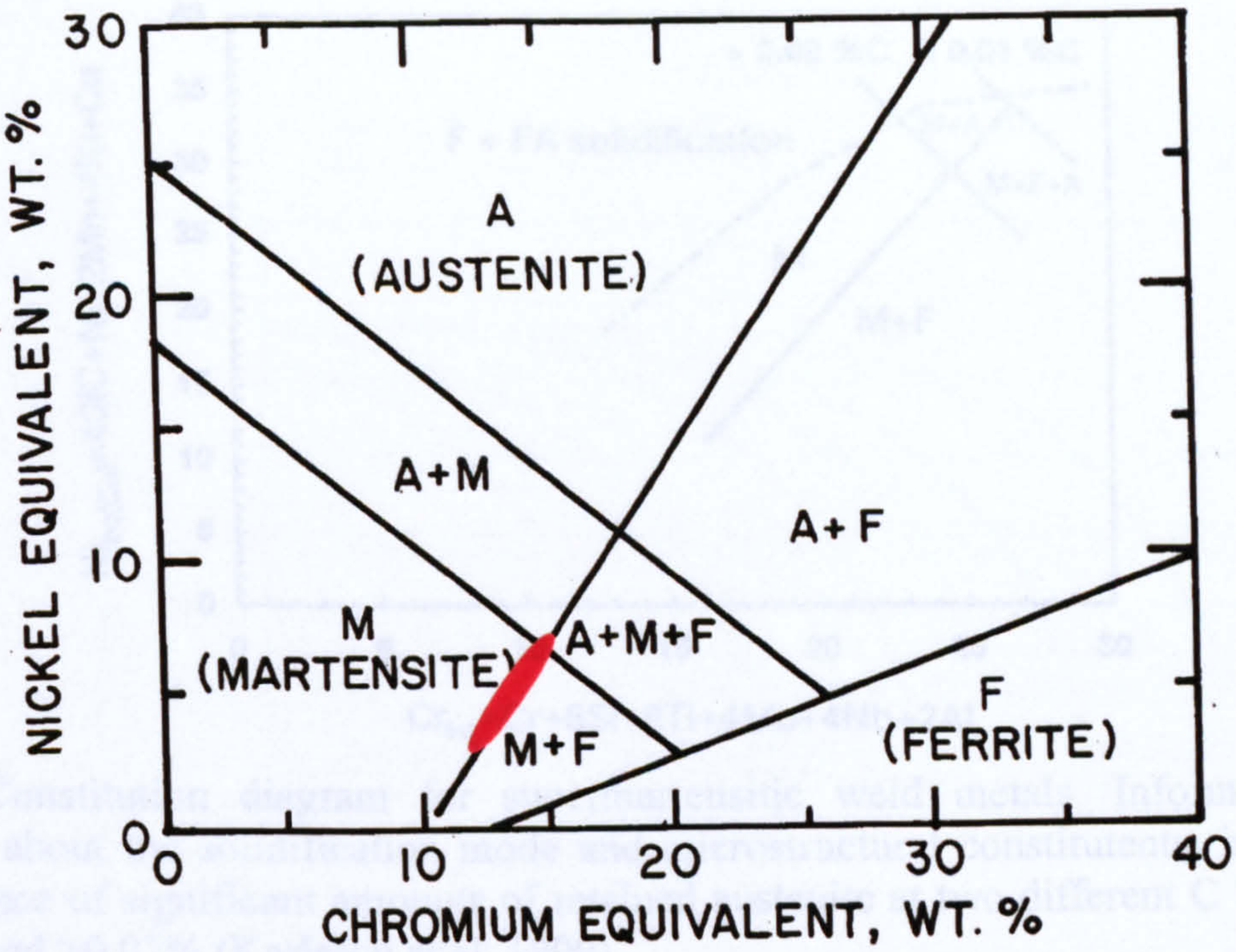

Area of supermartensitic stainless steels.

Fig.2.1 Modified Schäffler diagram (Sedriks 1979). The red area shows position of the supermartensitic stainless steels.

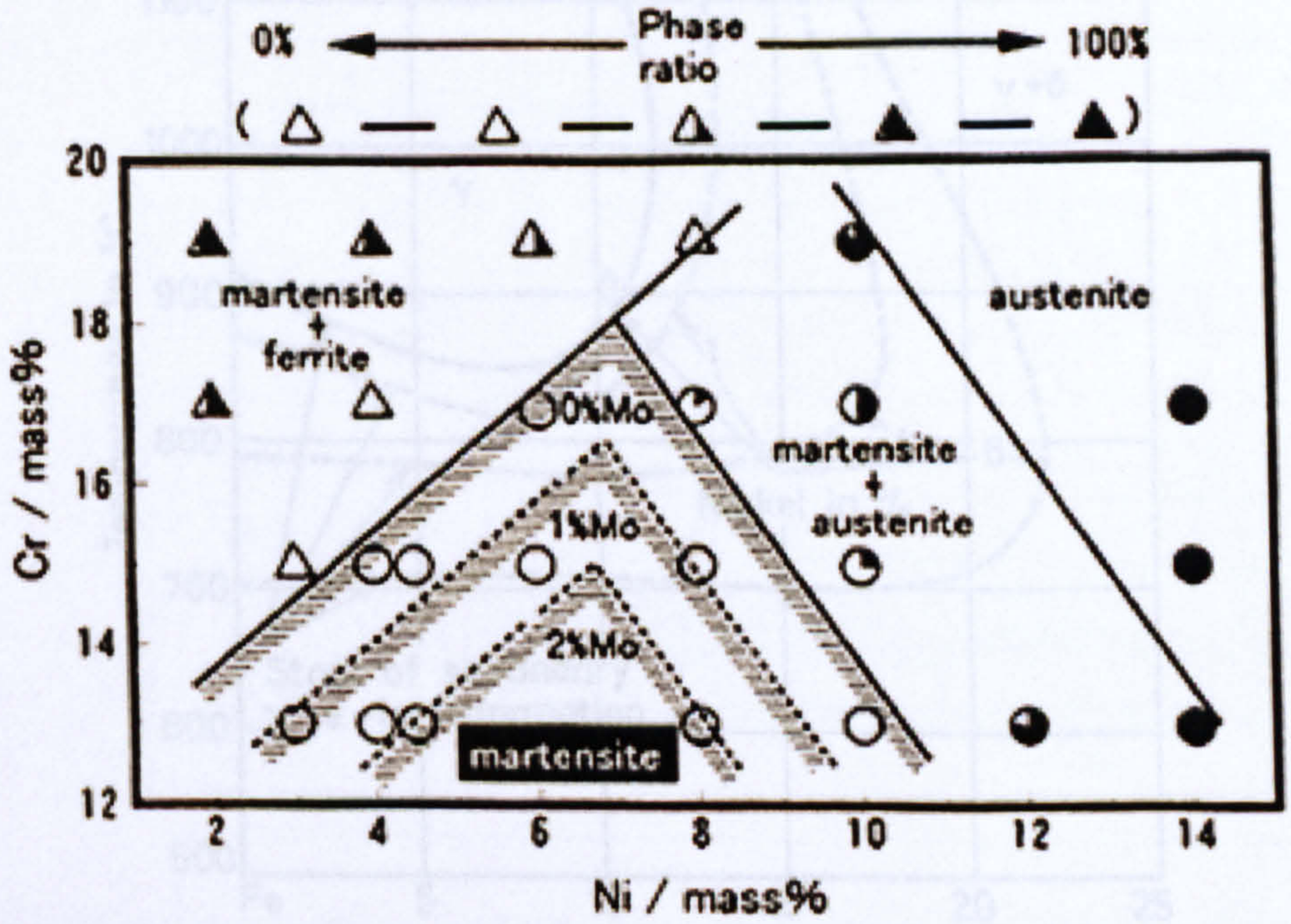

Fig.2.2 Effect of Cr, Ni and Mo content on martensitic single phase range of 0.01 mass% C steels after austenitization at 1050 °C and air cooling (Kondo et al. 1999).

Cr (mass%) = Cr + 2Si + 1.5Mo + 5V + 5.5 Al + 1.75Nb + 1.5Ti + 0.75W
Ni (mass%) = Ni + Co + 0.5Mn + 0.3Cu + 25N + 30C

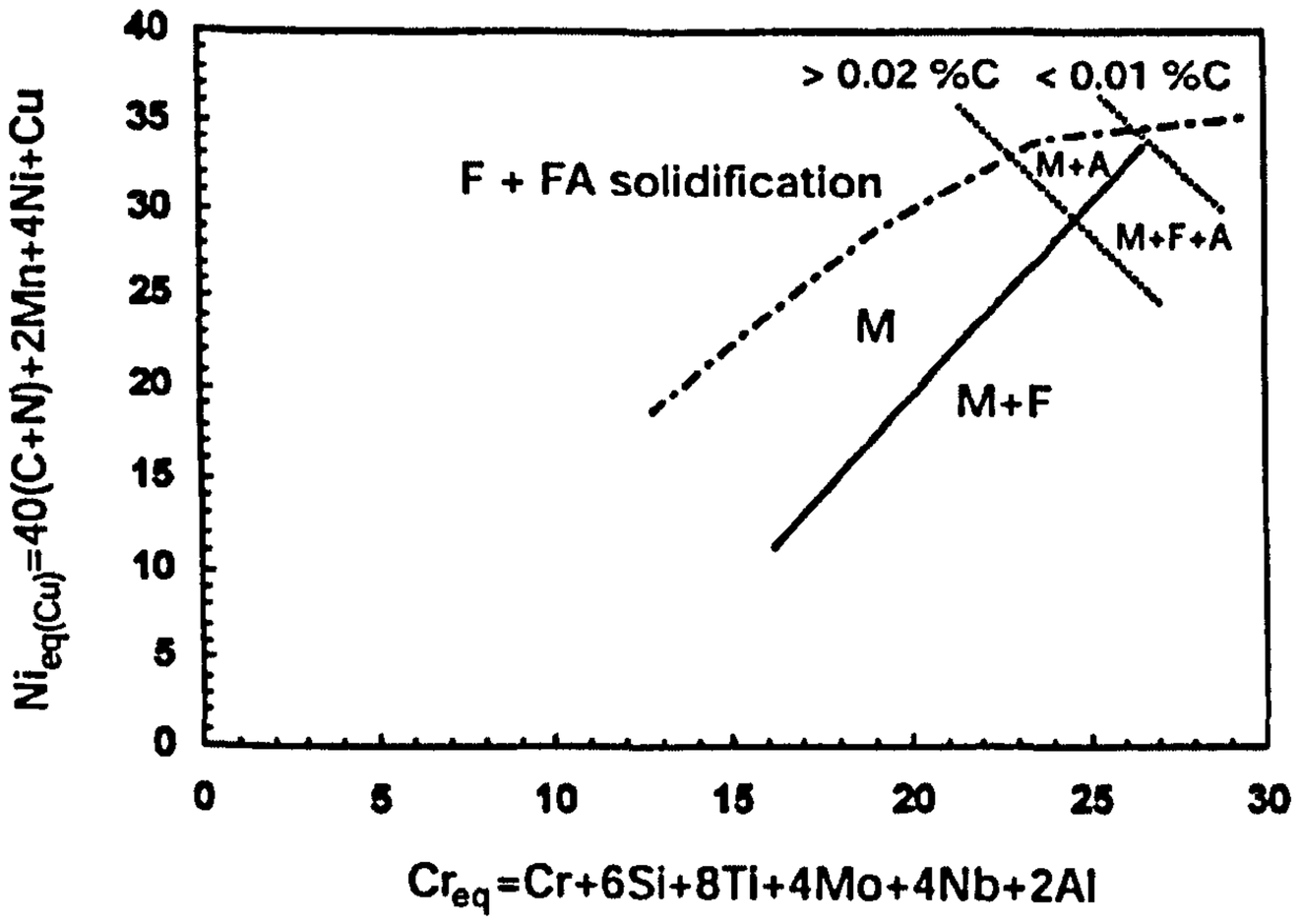

Fig.2.3 Constitution diagram for supermartensitic weld metals. Information is provided about the solidification mode and microstructural constitutents, including the presence of significant amounts of retained austenite at two different C levels of >0.01% and >0.02% (Karlsson et al. 1999).

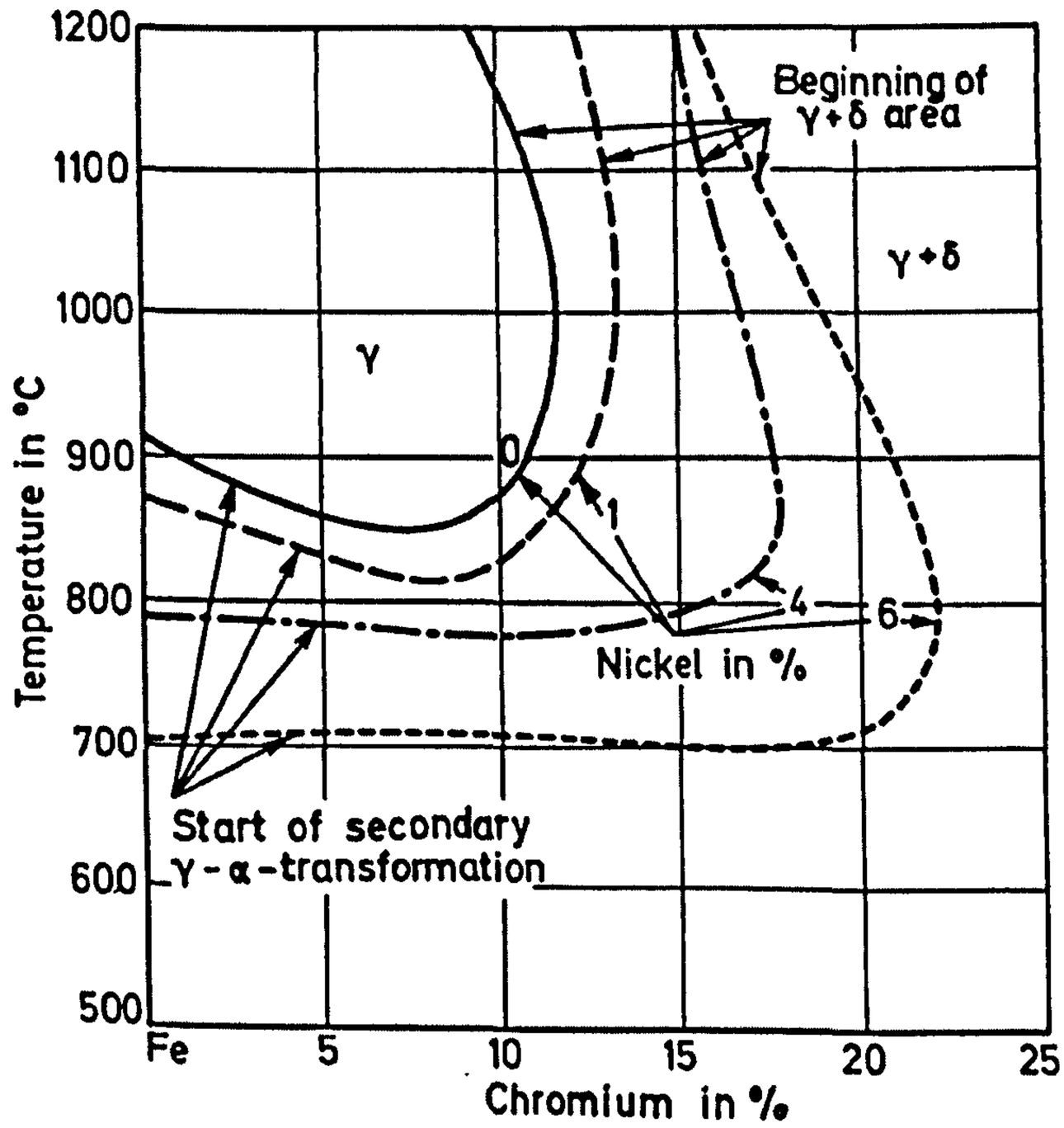

Fig.2.4 Effect of Ni on the extent of the austenite range in the iron-chromium system for 0%, 1%, 4% and 6% Ni and 0.05% C (Kunze 1976).

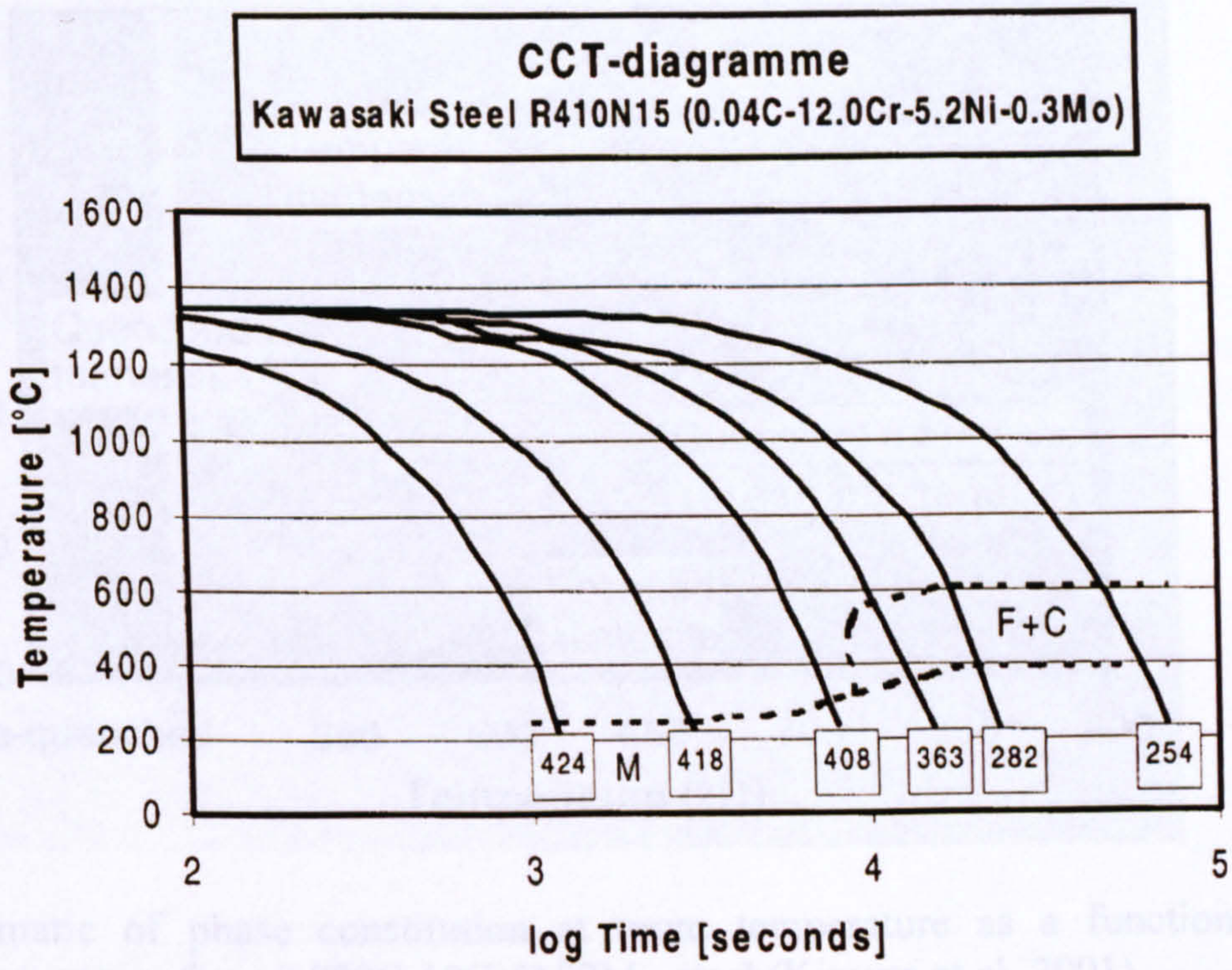

Fig.2.5 The austenite continuous cooling transformation (CCT) diagram for a Kawasaki chromium steel (Kvaale and Olsen 1999).

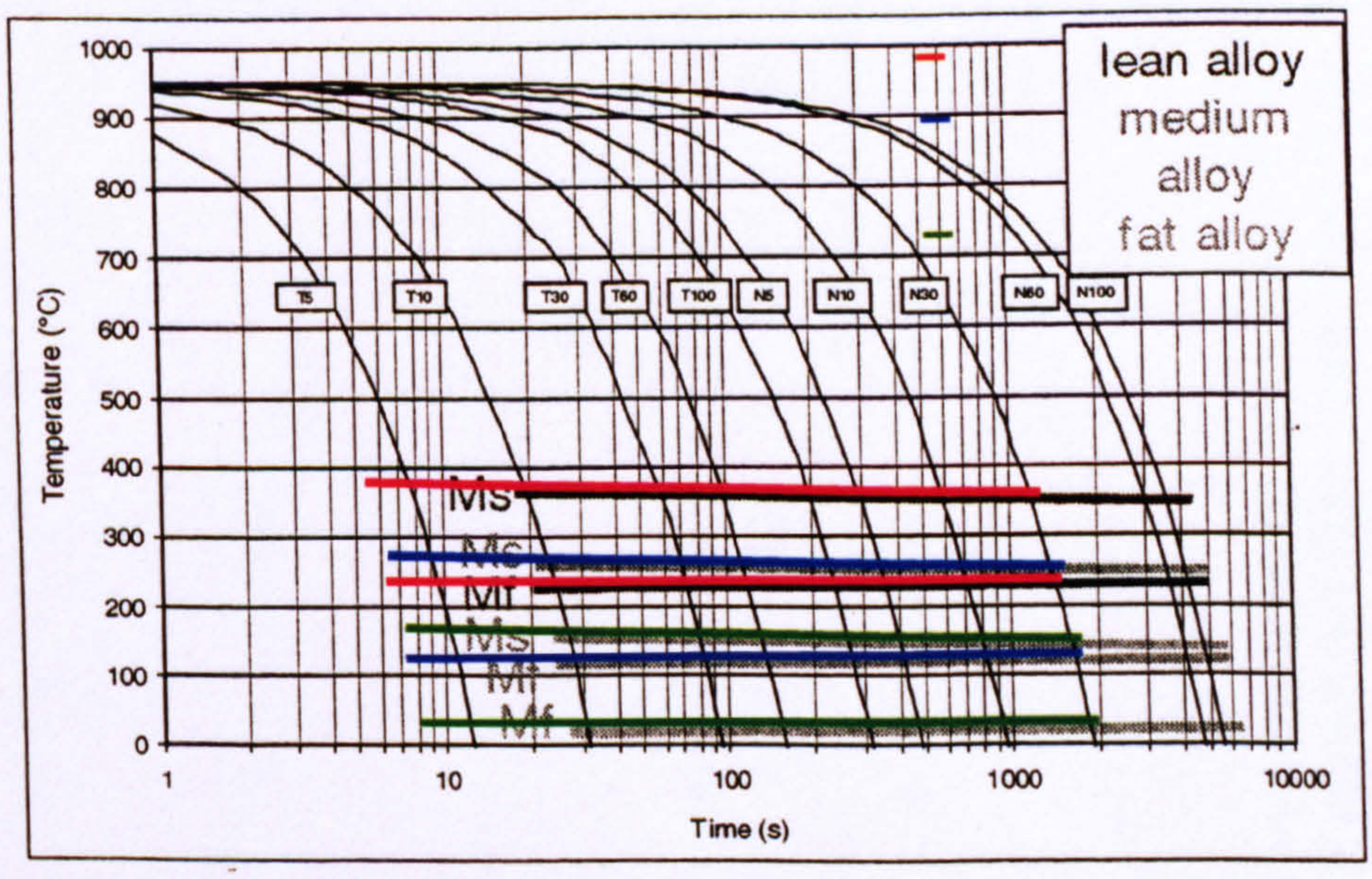

Fig.2.6 Continuous cooling curves of supermartensitic steels, showing the martensitic transformation over the full range of cooling conditions, from water quenching of a 5 mm plate (curve T5) to the still air cooling of a 100 mm plate (curve N100). The three supermartensitic grades are: lean, medium, and fat (high). (Toussaint and Dufrane 2002).

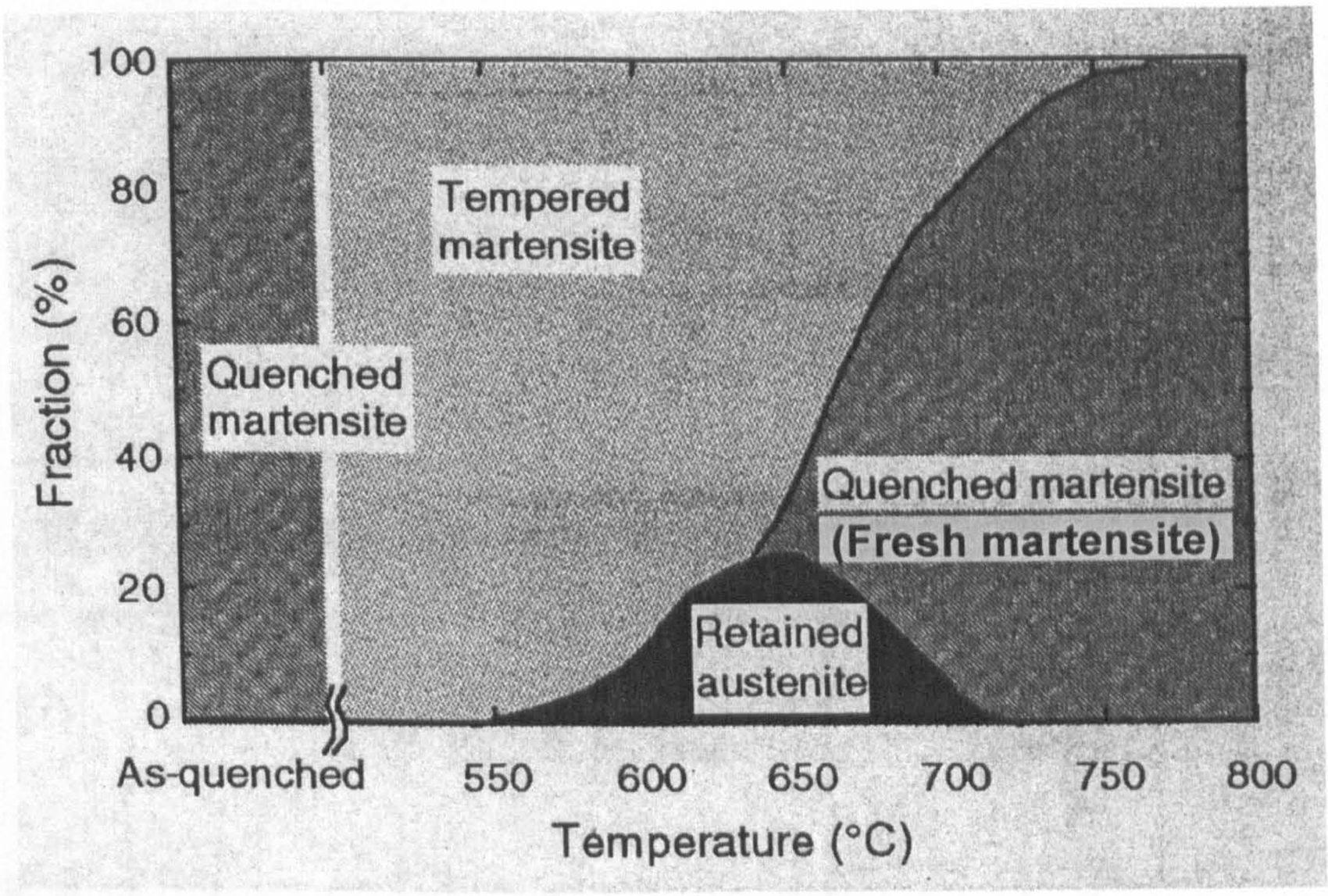

Fig.2.7 Schematic of phase constitution at room temperature as a function of tempering temperature for a 0.023C-13Cr5Ni2Mo steel (Kimura et al. 2001).

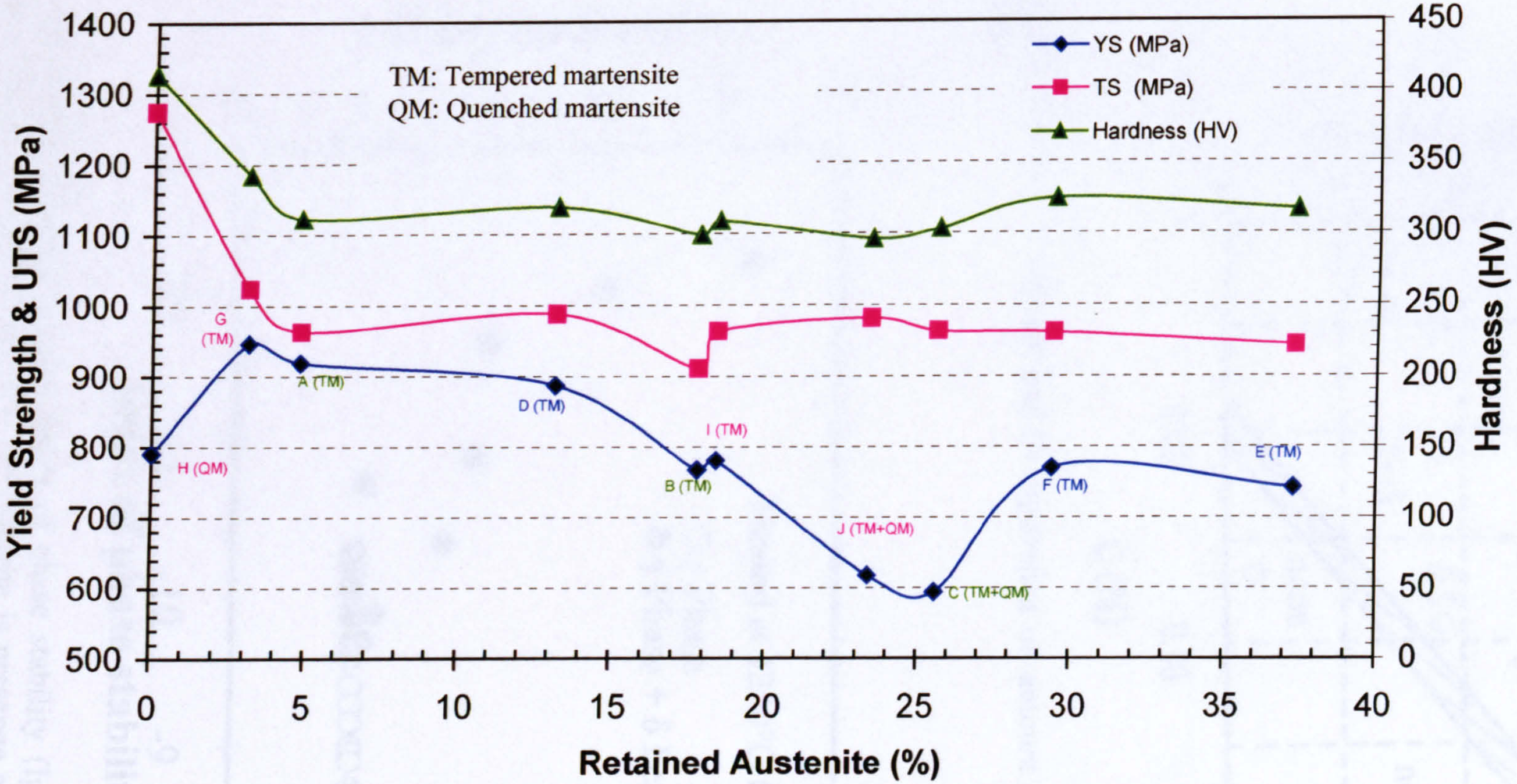

Steel	Q	Q`	T	Steel	Q	Q`	T	Steel	Q	Q`	T
H	910°C×30min	-		B	920°C×30min	630°C×30min	--	D*	-	630°C×30min	590°C×30min
G	910°C×30min	-	550°C×180min	I	910°C×30min	630°C×30min	-	E*	-	660°C×30min	610°C×30min
A	920°C×30min	-	590°C×30min	J	910°C×30min	660°C×30min	--	F*	-	690°C×30min	610°C×30min
				C	920°C×30min	660°C×30min	-	*		As-rolled + Q`+T	

Fig.2.8 Mechanical properties and phase constitution of the supermartensitic steel (0.023%C-13%Cr-5.10%Ni-2.01%Mo) after heat treatment. The figure is plotted from the tabulated data in the paper by Kimura et al. (2001).

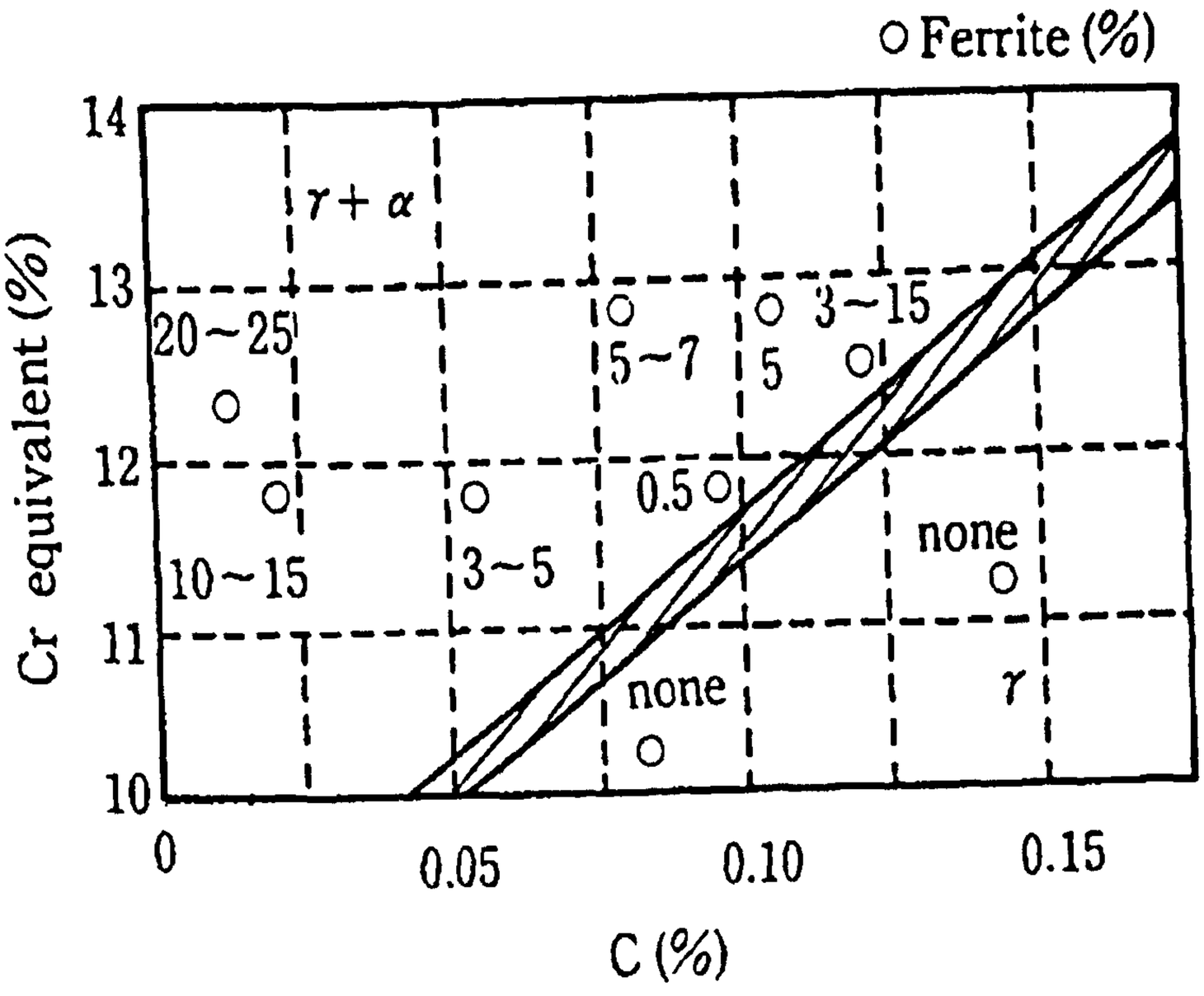

Fig.2.9 Effect of C content and Cr equivalent on amount of ferrite (Niinaka et al. 1986).

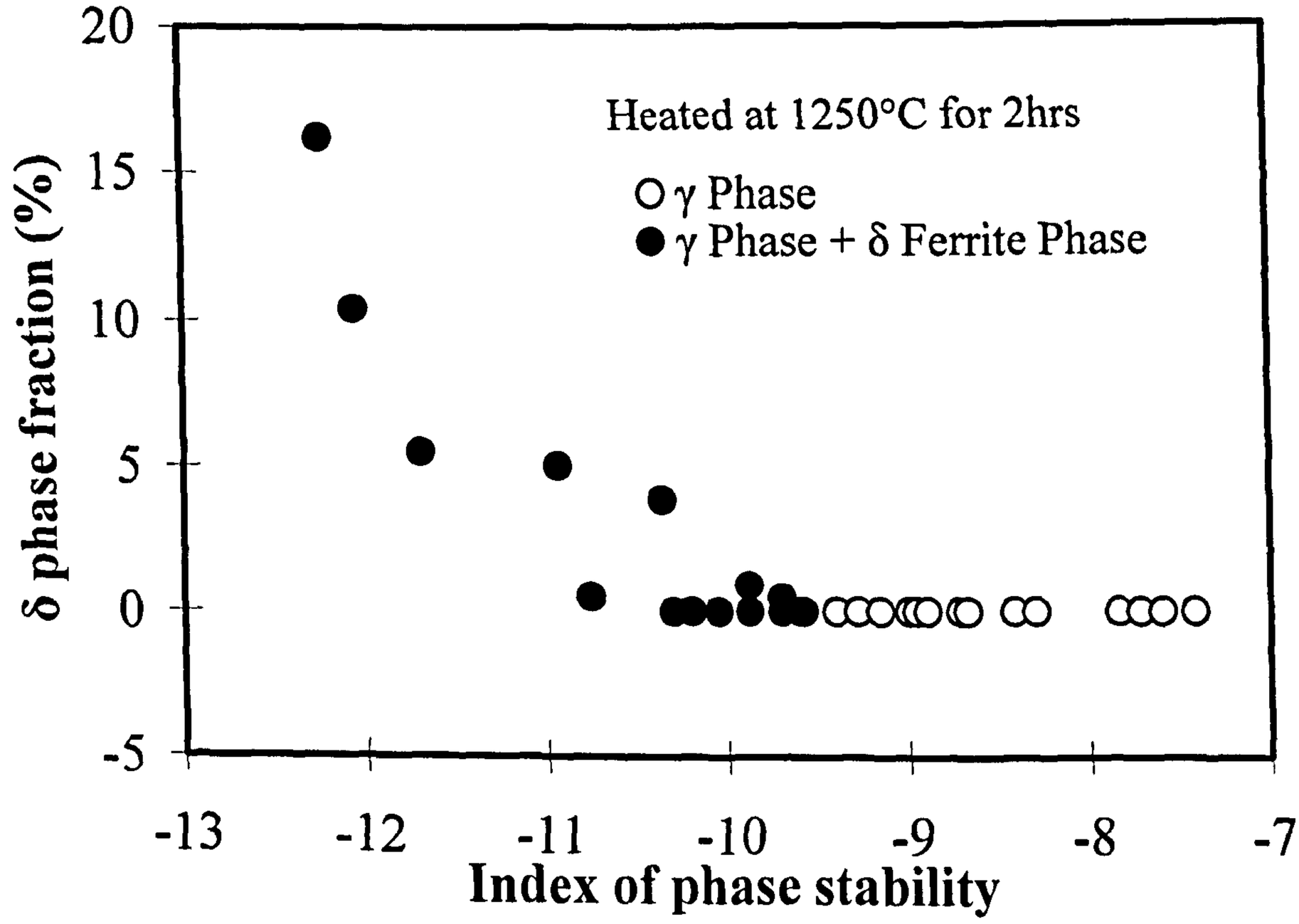

Fig.2.10 Relationship between index of phase stability (Ips) and δ-ferrite fraction after heating at 1250 °C for 2 h. No δ-ferrite is presence at Ips < -9.4 where Ips = 40C+34N+Ni+0.3Cu-1.1Cr-1.8Mo (mass%) (Asahi 1995).

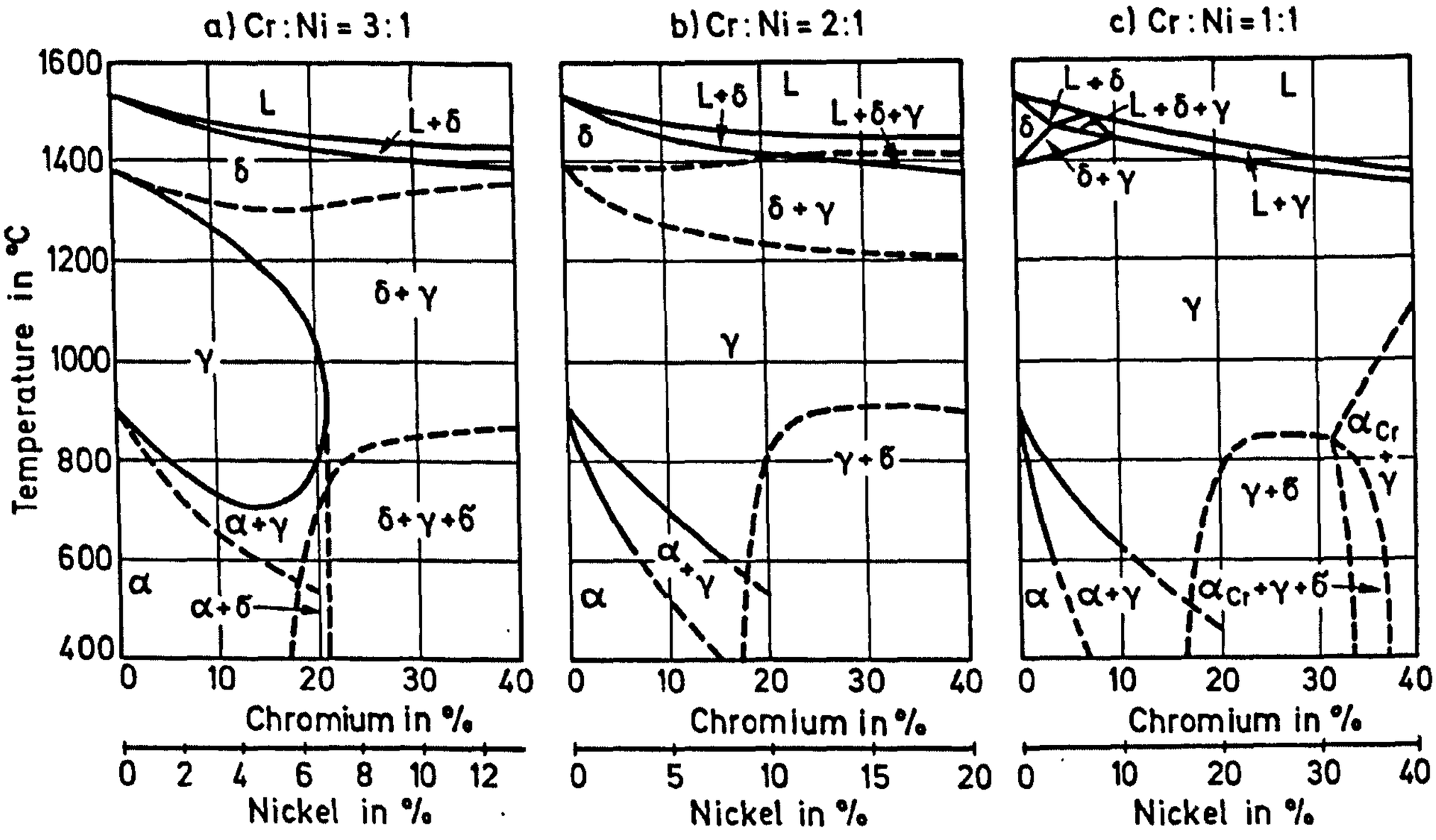

Fig.2.11 Concentration profiles of the ternary iron-chromium-nickel constitution diagram for Cr: Ni ratios of 3:1, 2:1 and 1:1 (Folkhard 1988).

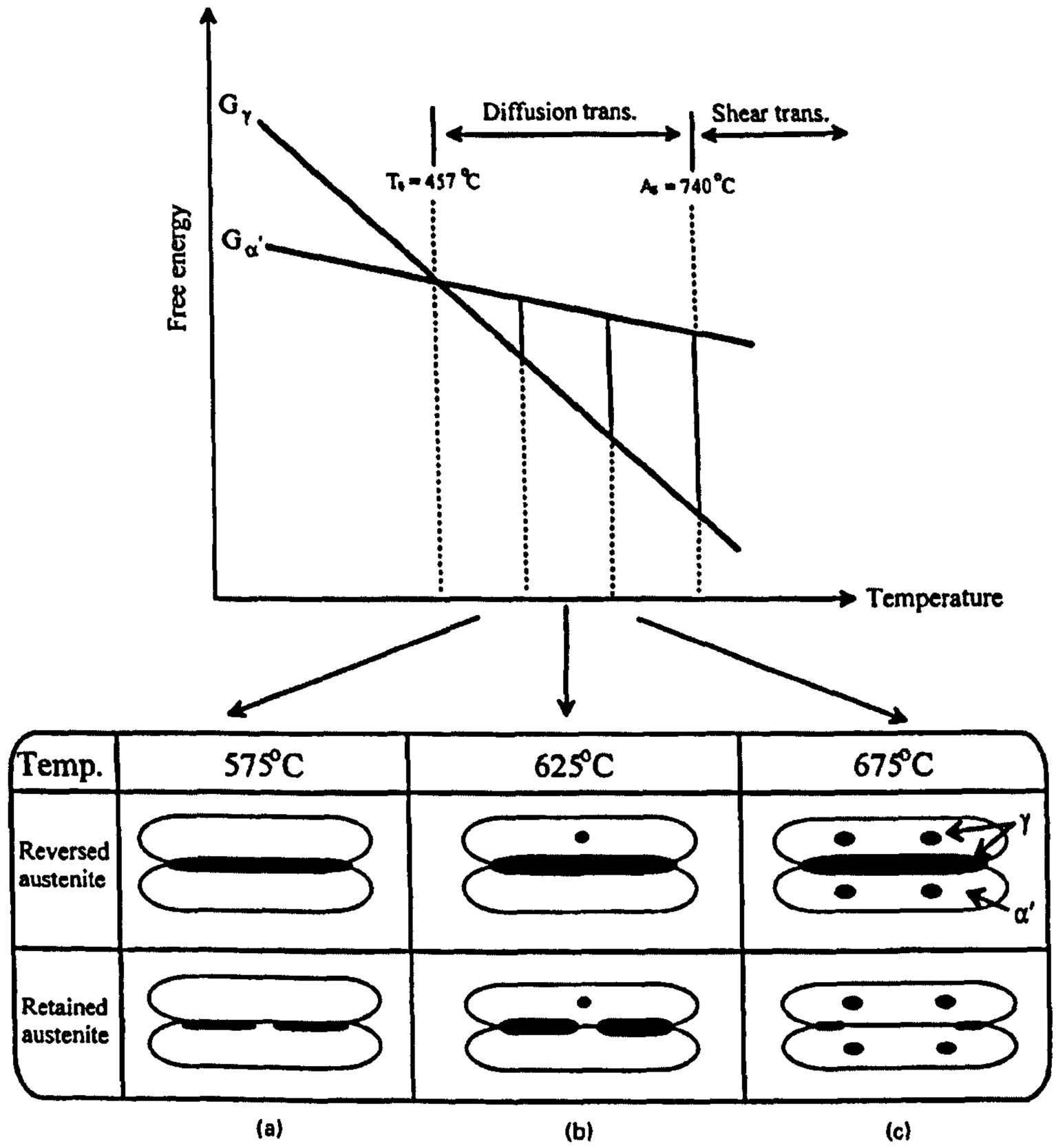

Fig.2.12 Schematic illustration of formation behaviour of reversed and retained austenite based on TEM images (Lee et al. 2003).

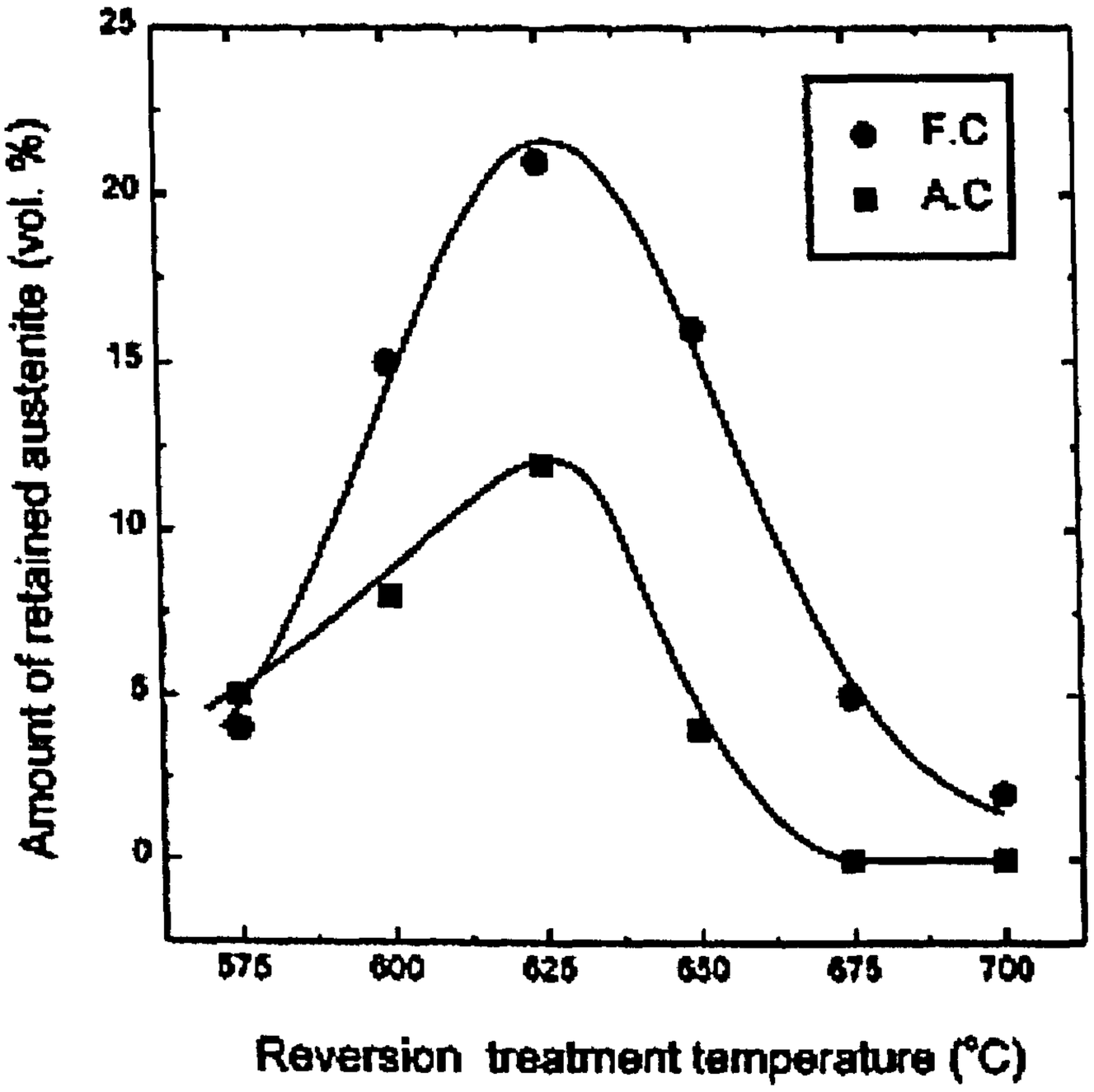

Fig.2.13 Variations in amount of retained austenite with tempering temperature. A higher amount of retained austenite was formed after furnace cooling than air cooling. (Lee et al. 2003). FC: furnace cooling; AC: air cooling.

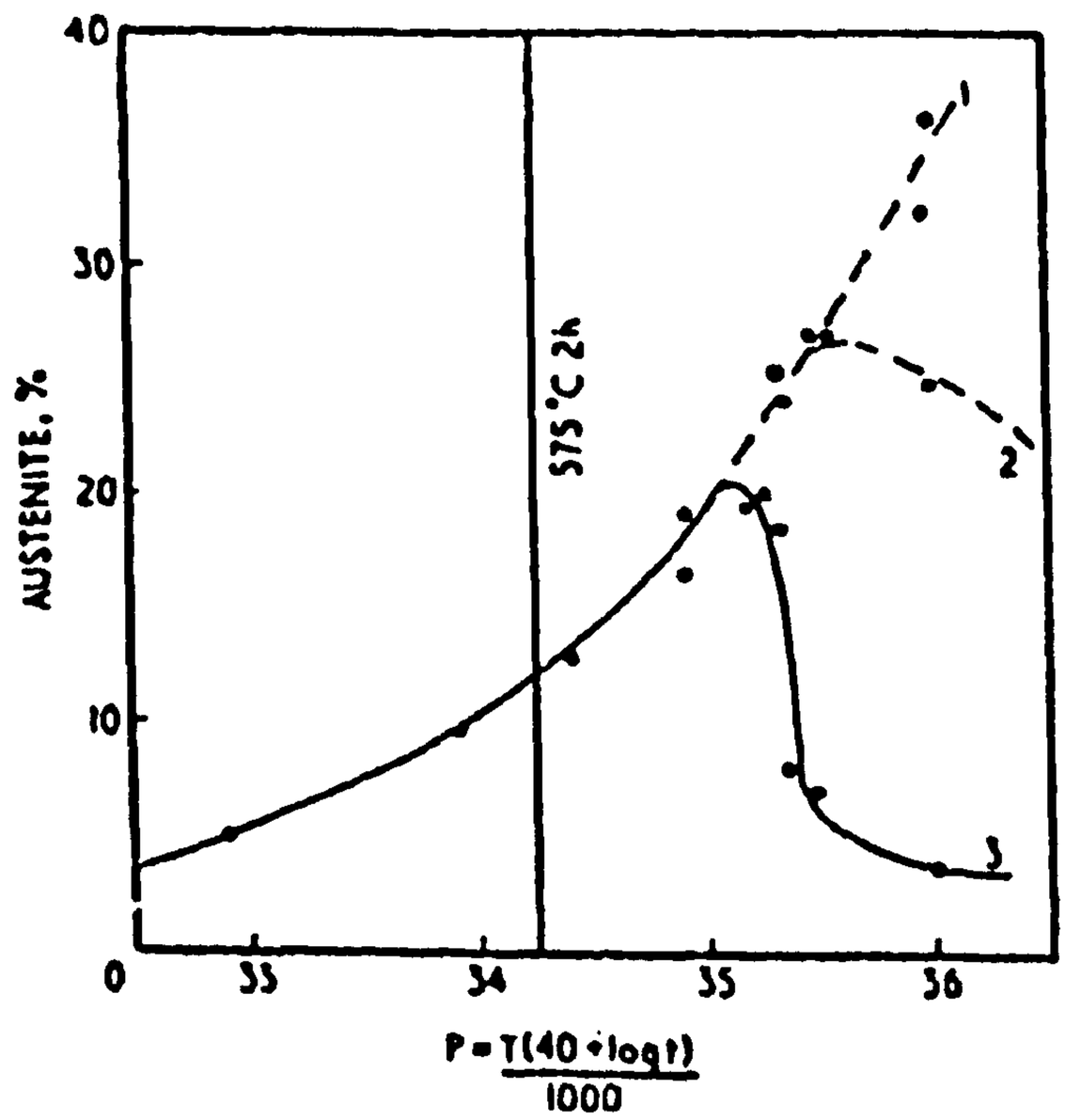

1 austenite formed on tempering

2 austenite stable at room temperature

3 austenite stable at -140°C

Fig.2.14 Relationship between the amount of stable austenite at different temperatures and the Hollomon-Jaffe time-temperature parameter P for 5% Ni steels (International Institute of Welding, 1983).

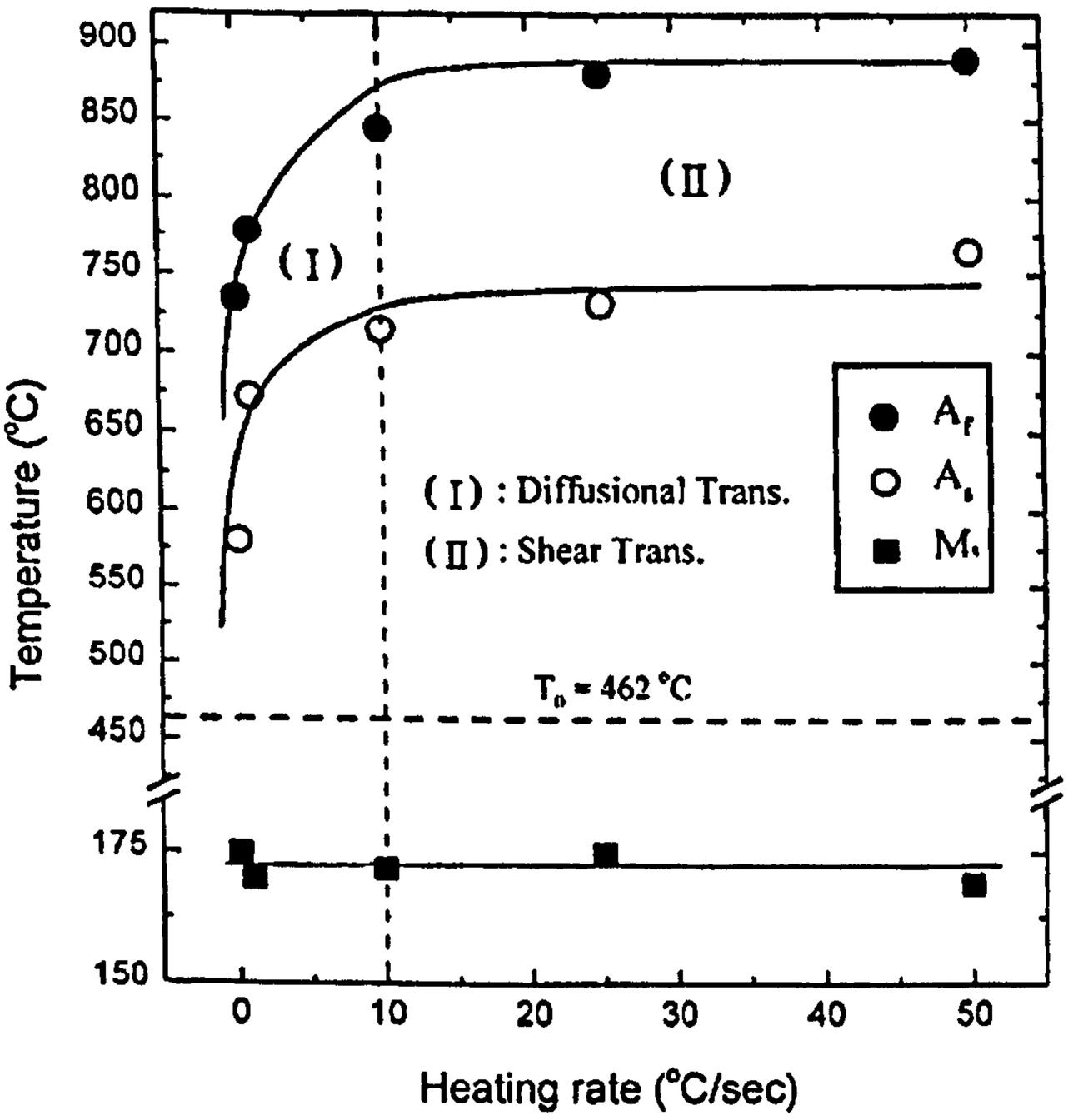

Fig.2.15 Variation in A_s, austenite formation start temperature, i.e. Ac_1; A_f, austenite formation finish temperature temperature; and M_s, martensite start transformation temperature with heating rate. The austenite transformation was a diffusion controlled process when the heating rate was below 10 °C/s, but it became a diffusionless shear process when the heating rate was above 10 °C/s (Leem et al. 2001).

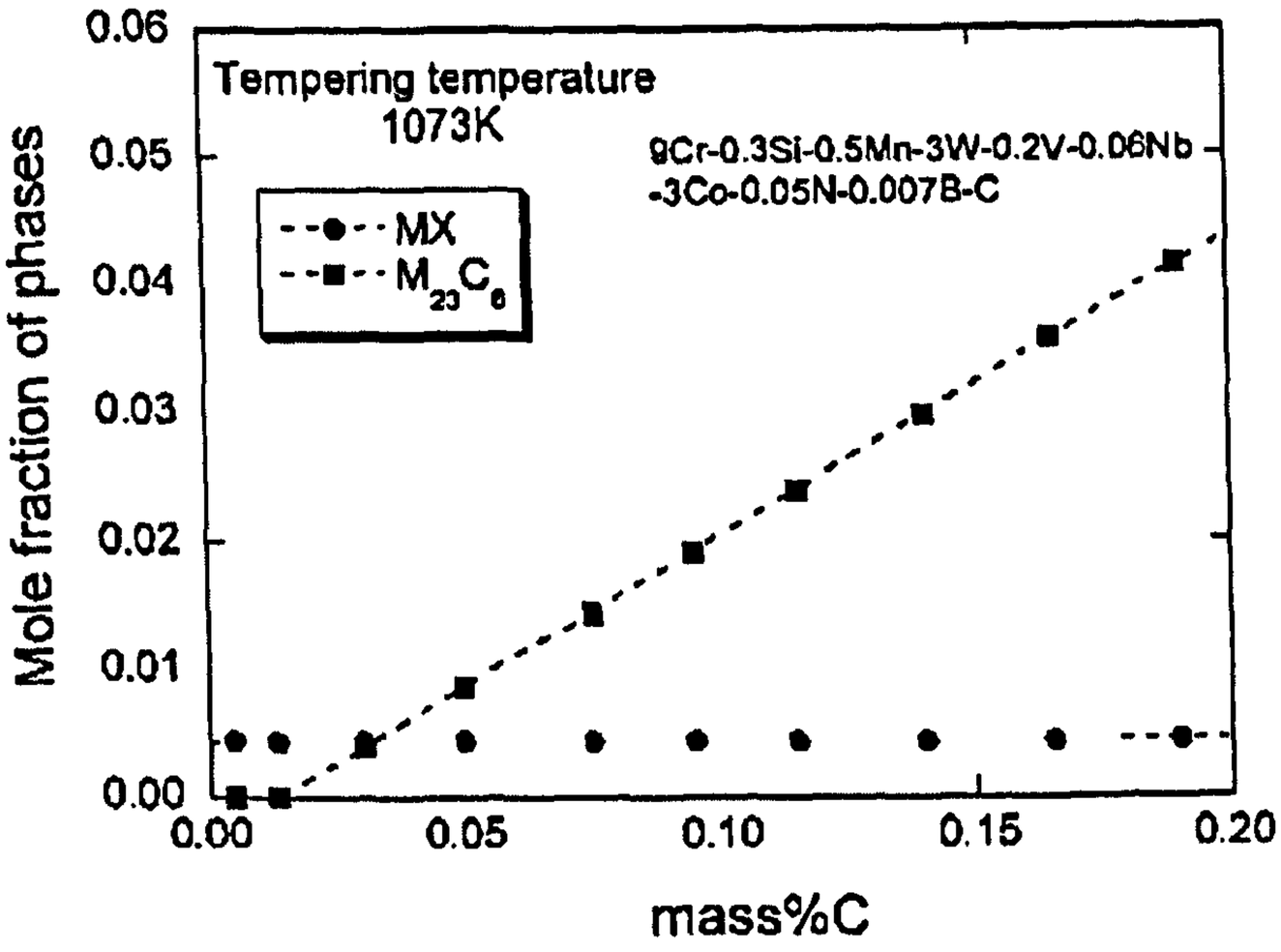

Fig.2.16 Equilibrium mole fraction of phase at 1073 K (800 °C) calculated by Thermo-Calc (Taneike et al. 2004).

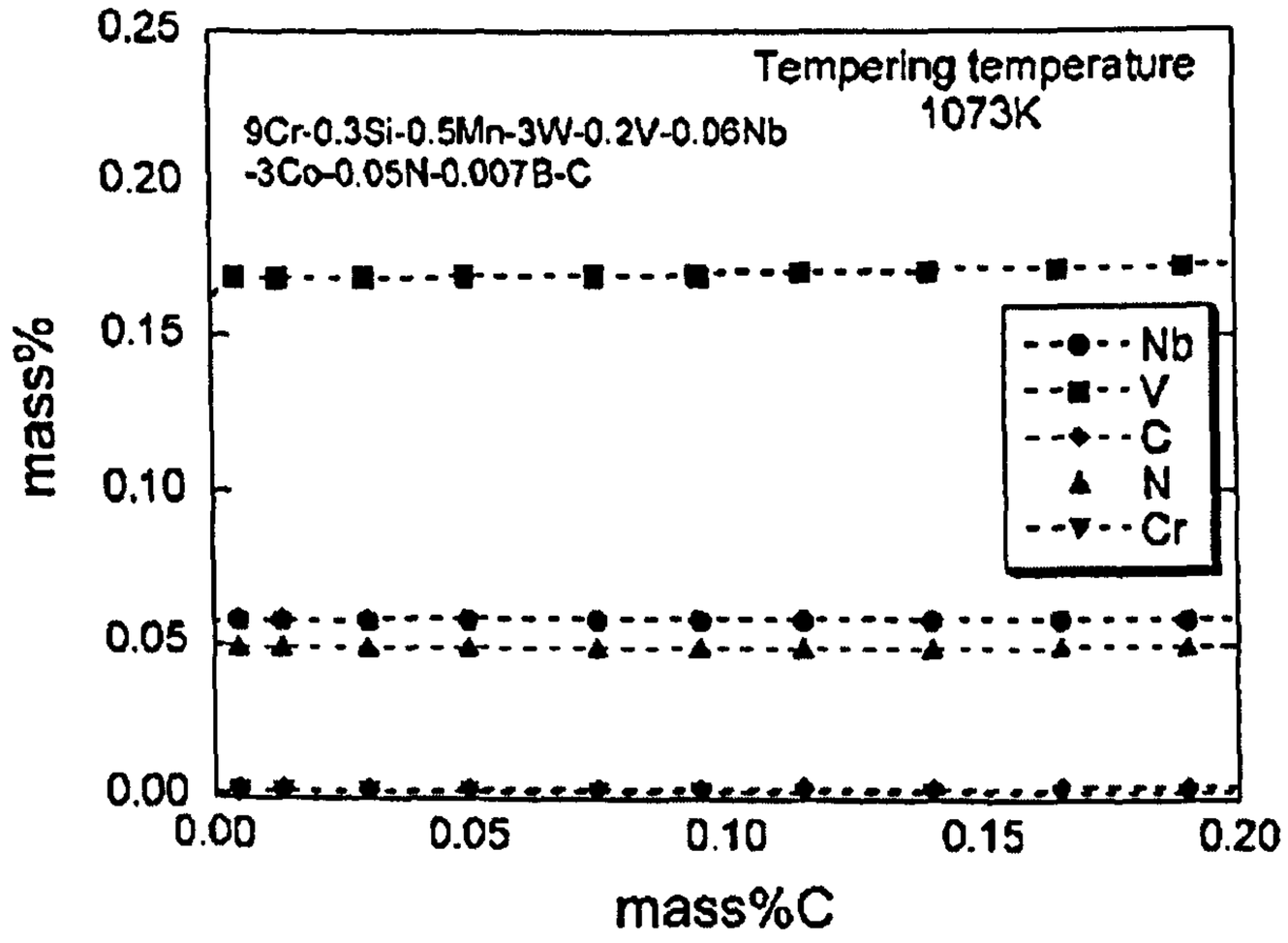

Fig.2.17 Equilibrium precipitated amount of elements contained in MX at 1073 K (800 °C) calculated by Thermo-Calc (Taneike et al. 2004).

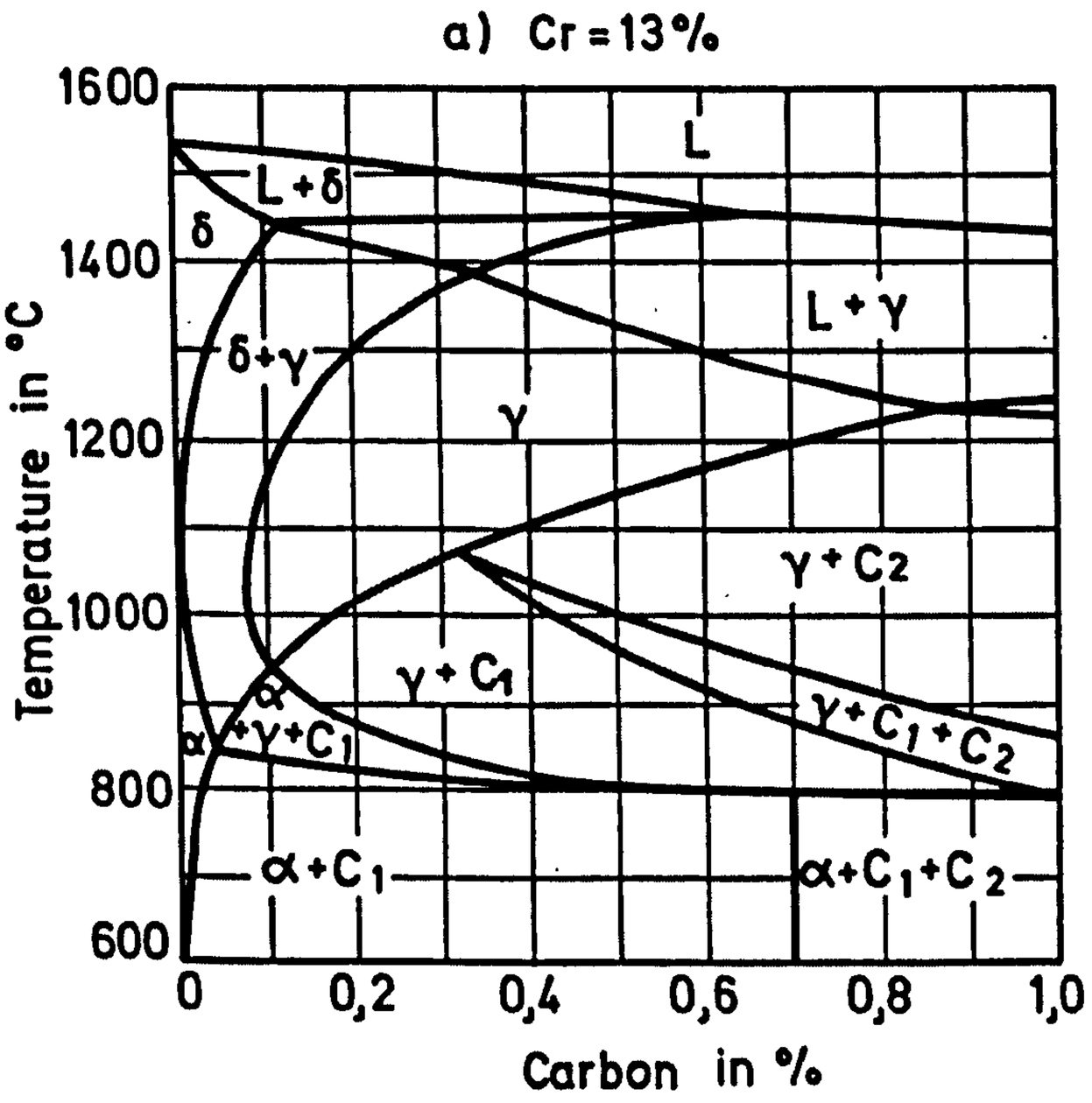

Fig.2.18 Concentration profile in the ternary iron-chromium-carbon constitution diagram at 13% Cr (Folkhard 1988).

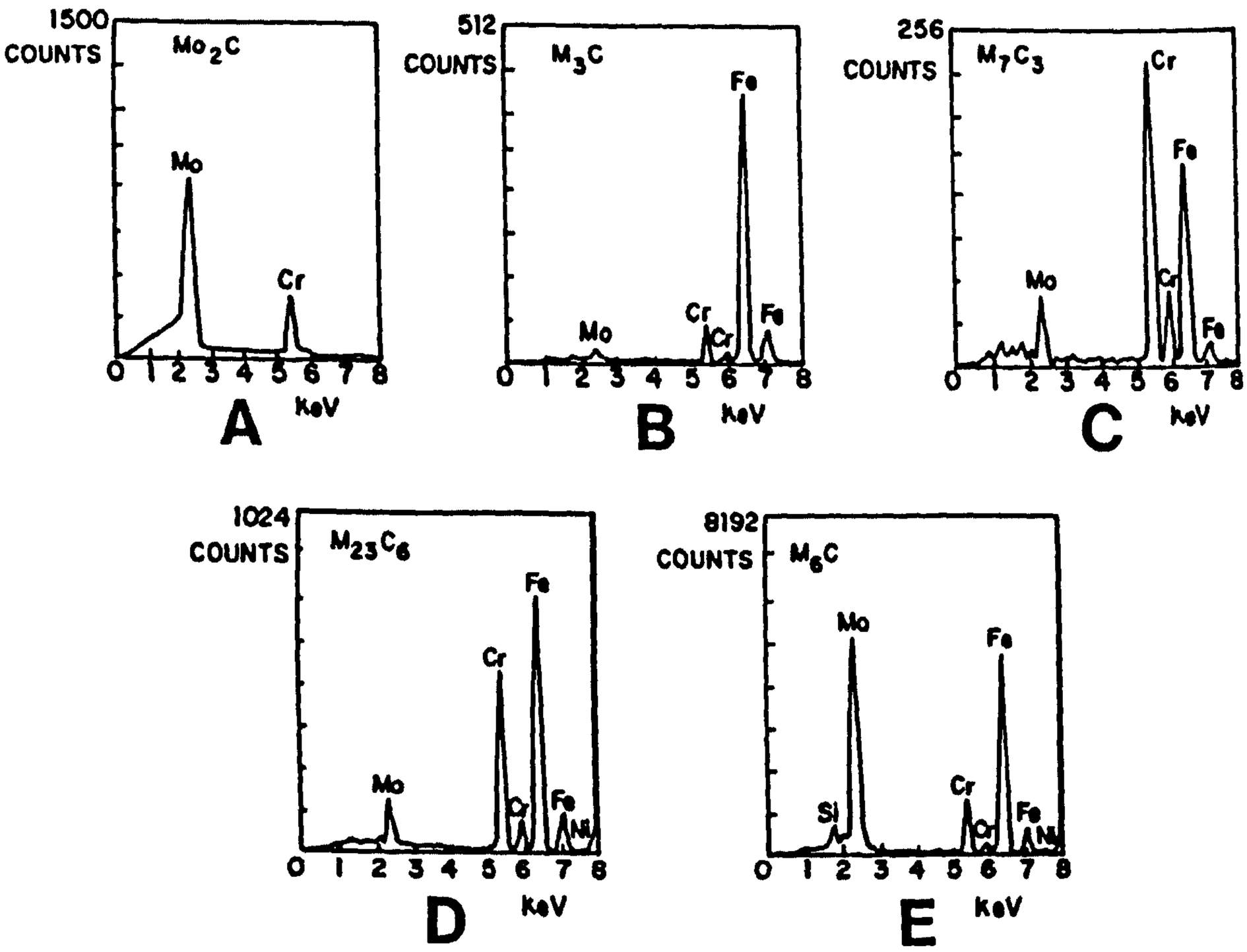

Fig.2.19 Typical EDX spectra for the carbides observed on tempering a normalized 2.25Cr1Mo steel (Todd 1986).

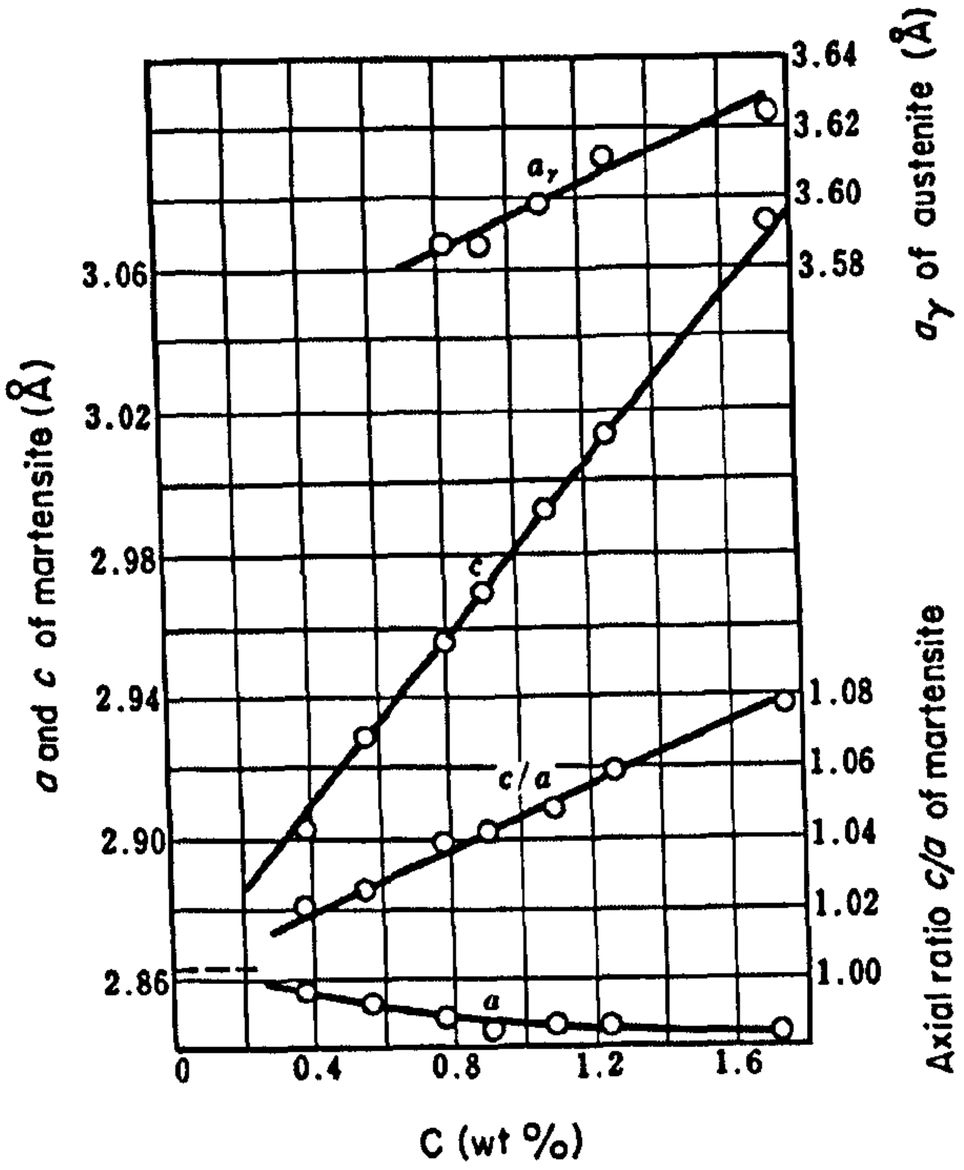

Fig.2.20 Lattice constants of tetragonal martensite and austenite in quenched carbon steels (Nishyama 1978)

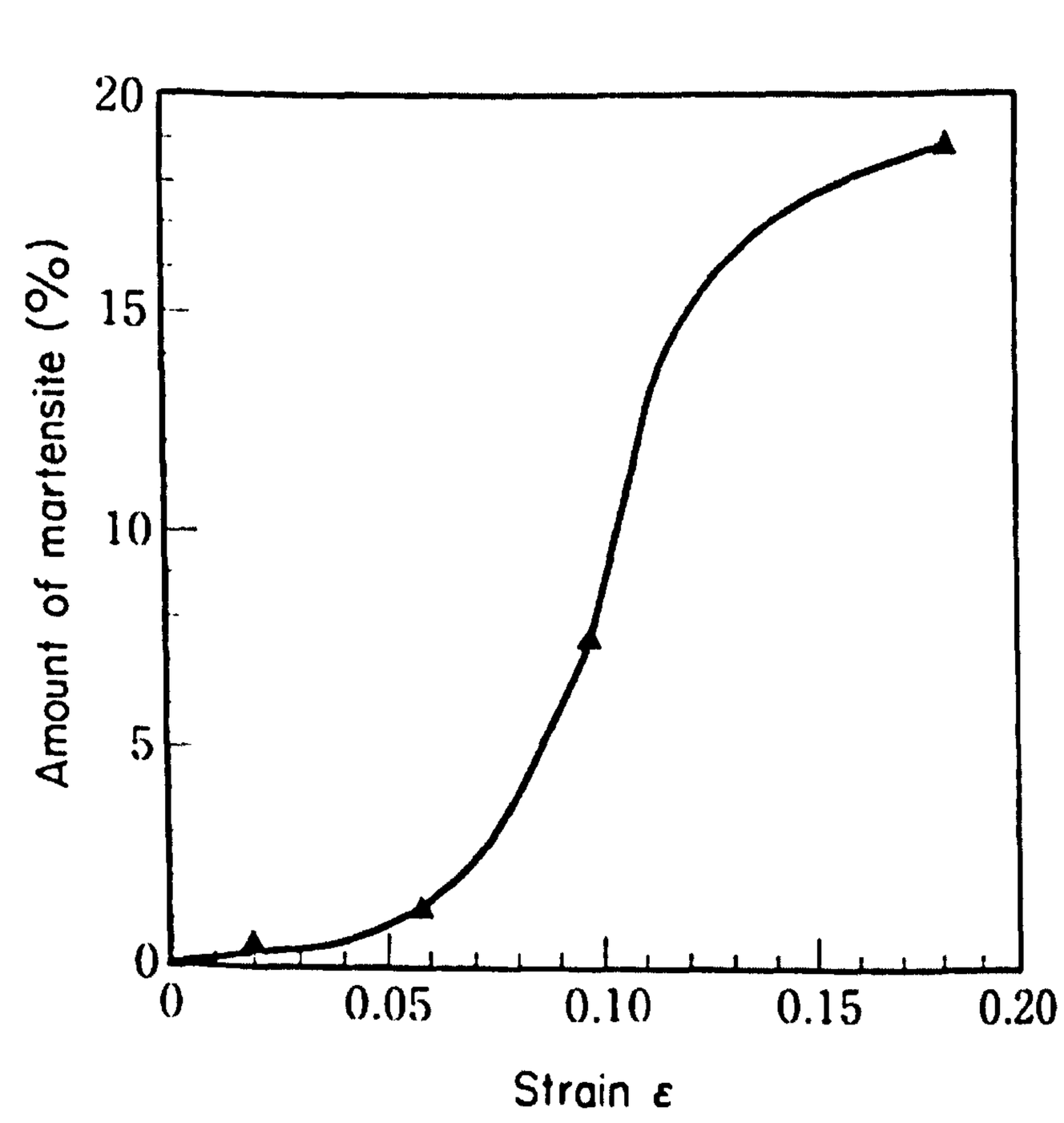

Fig.2.21 Variations in amount of martensite during deformation at -40°C (the original M_s = -78°C) for a Fe-14.8Cr-12.6Ni steel. (Nishiyama 1978).

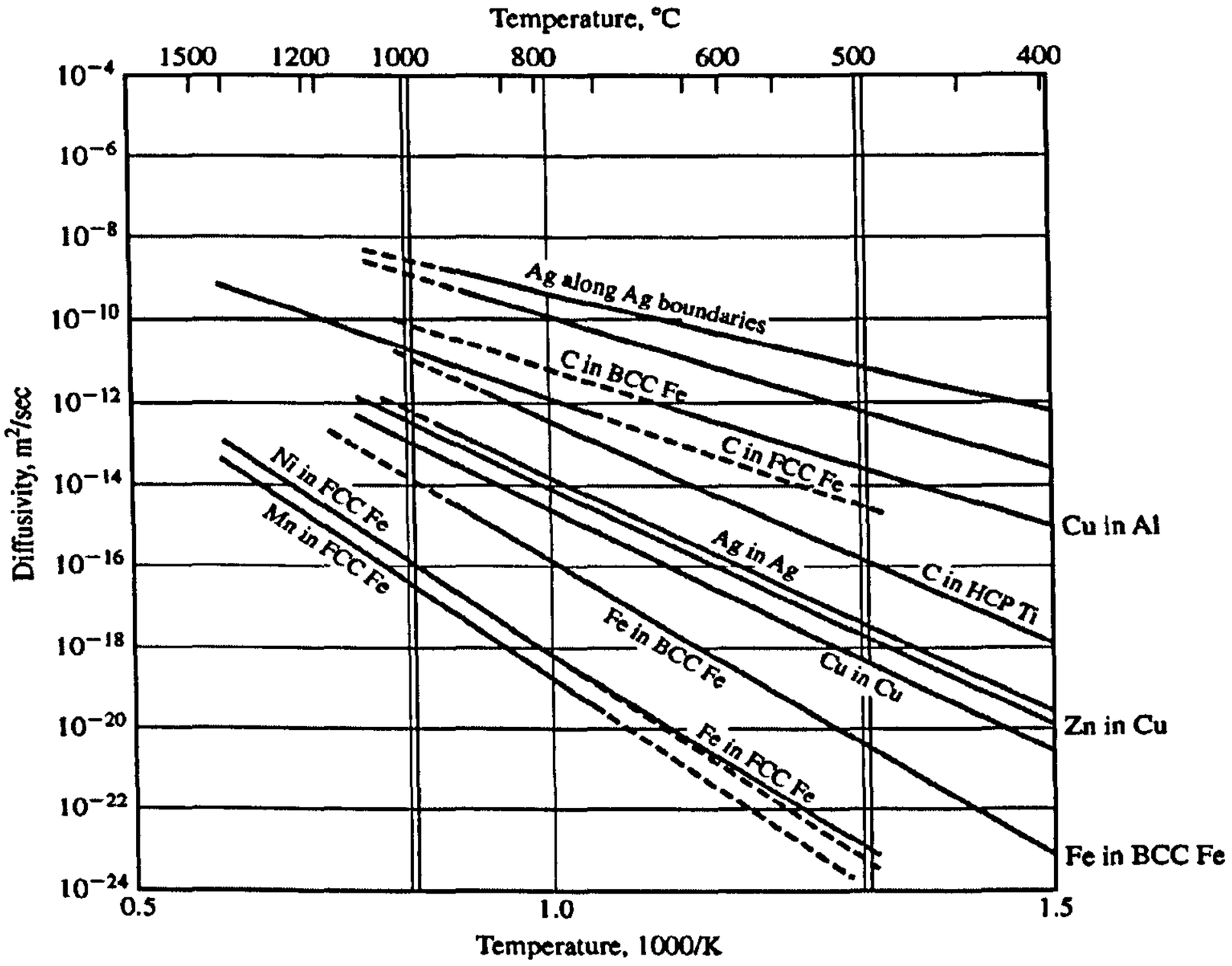

Fig.2.22 Elements diffusion coefficients as a function of temperature in γ (fcc) and α (bcc) Fe. (www.clarkson.edu).

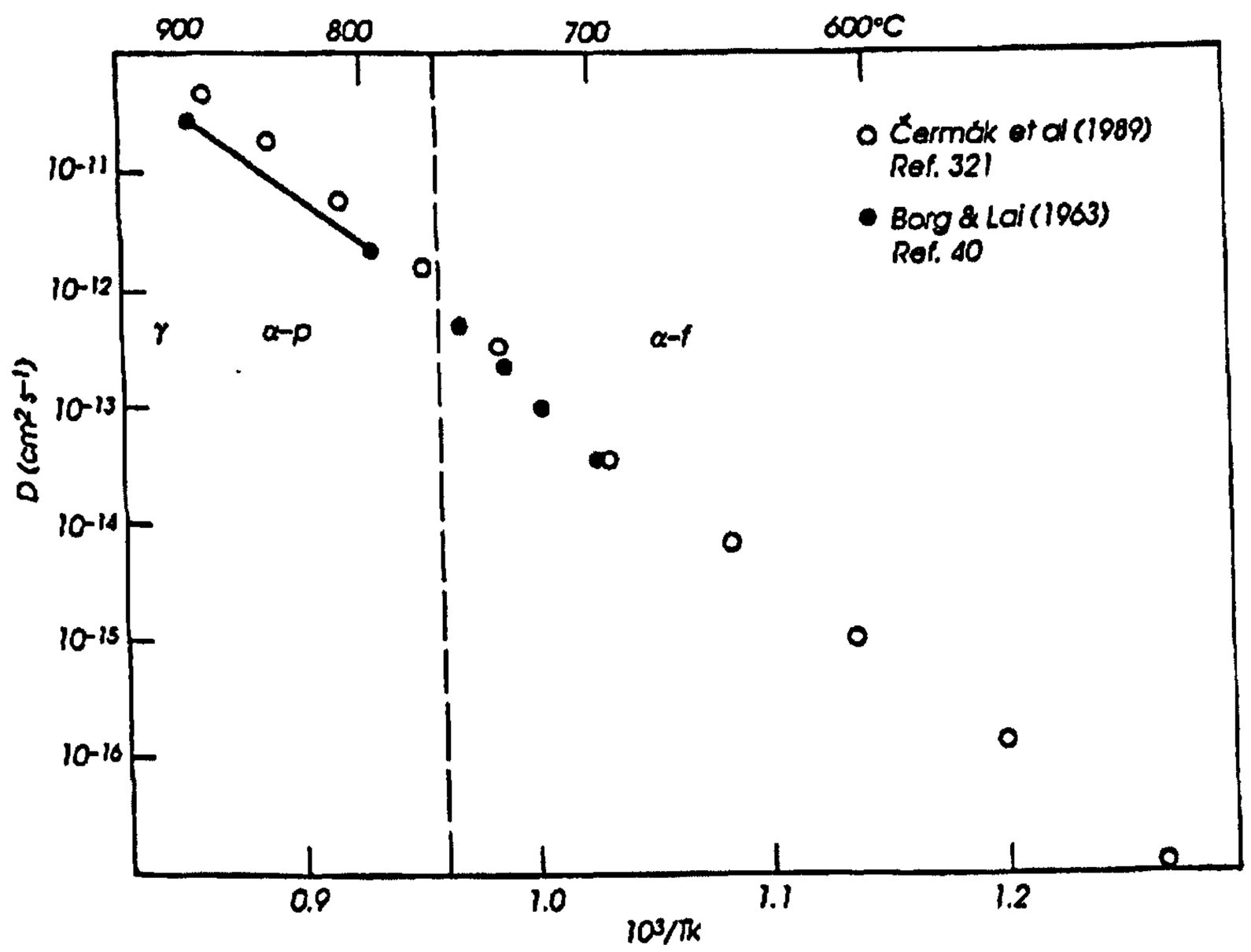

Fig.2.23 Ni diffusion coefficient as a function of temperature (10^3/T) in α Fe (Brandes and Brook 1992).

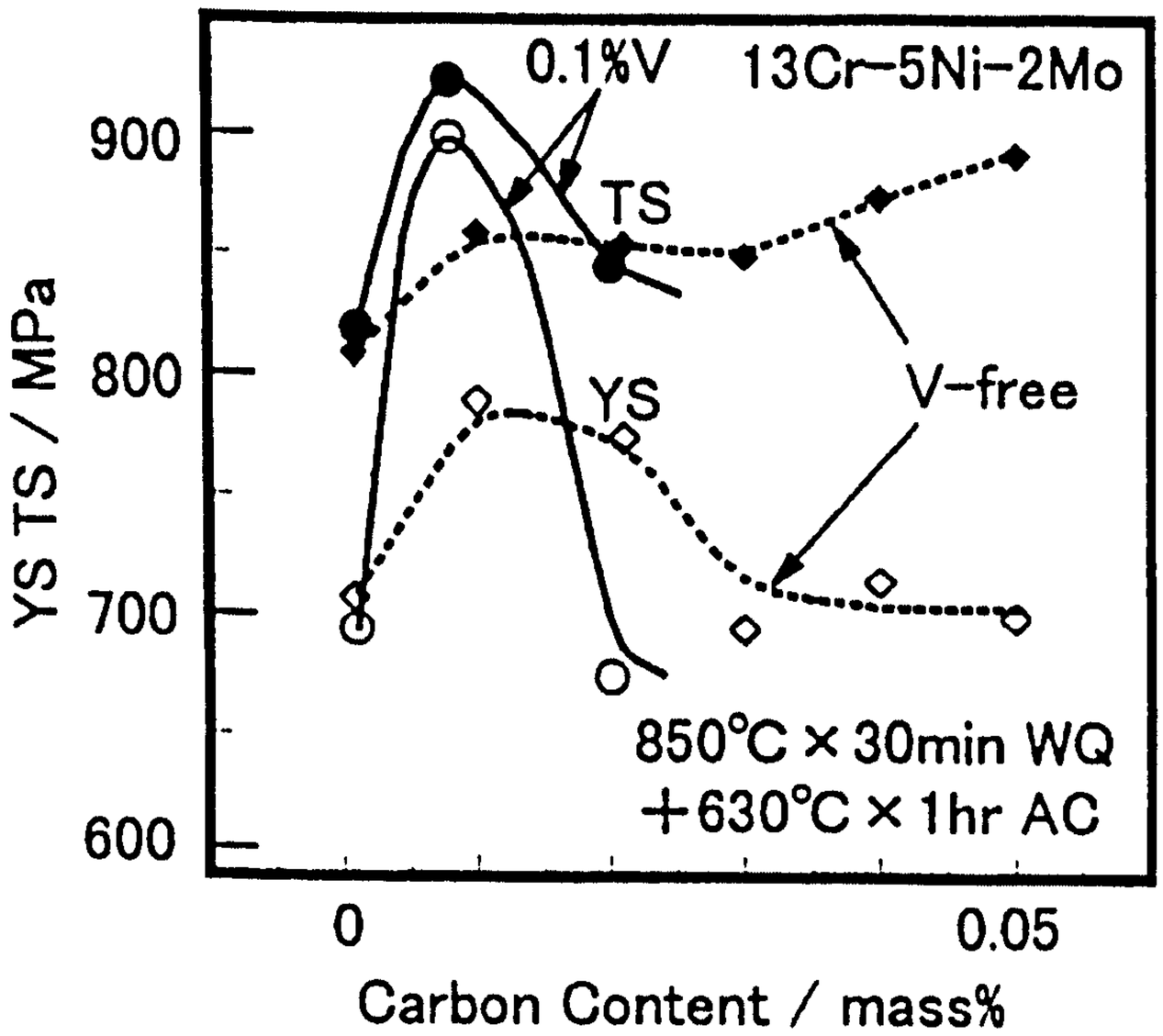

Fig.2.24 Effect of V and C on the tensile strength of 13%Cr steel after tempering (Knodo et al. 1999).

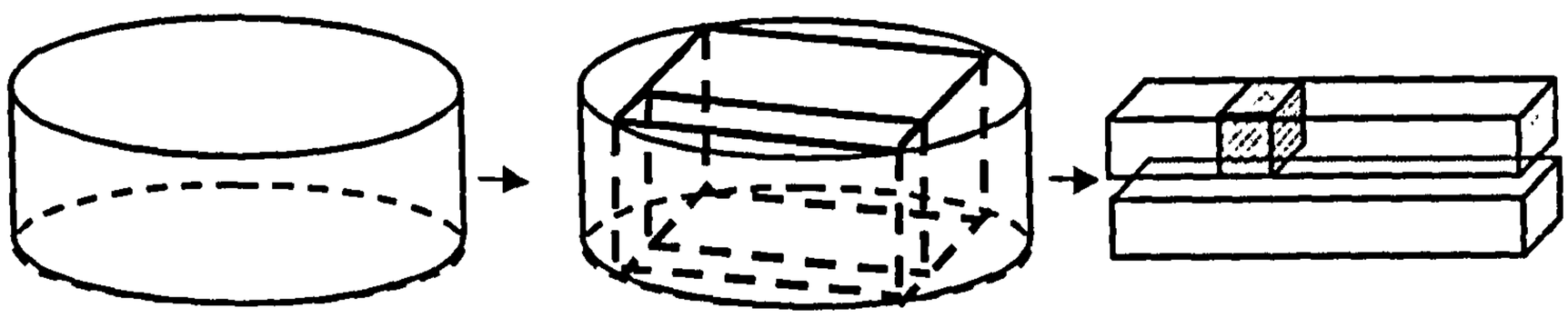

Fig.3.1 Schematic of the samples cutting from the as-received slice A2 for re-heat treatment.

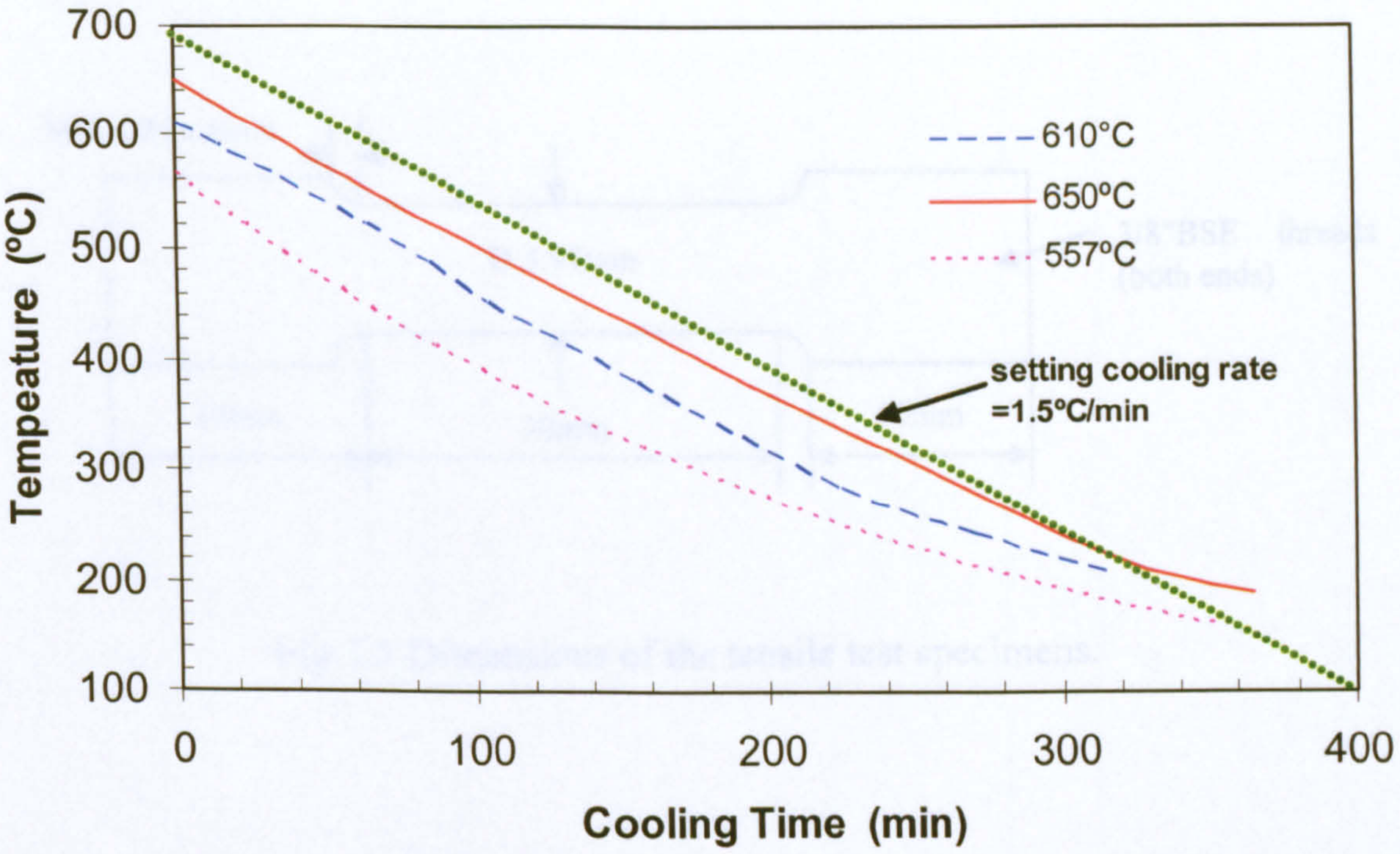

Fig.3.2 Cooling rates of specimens from some tempering temperatures to room temperature. The set cooling rate was 1.5 °C/min.

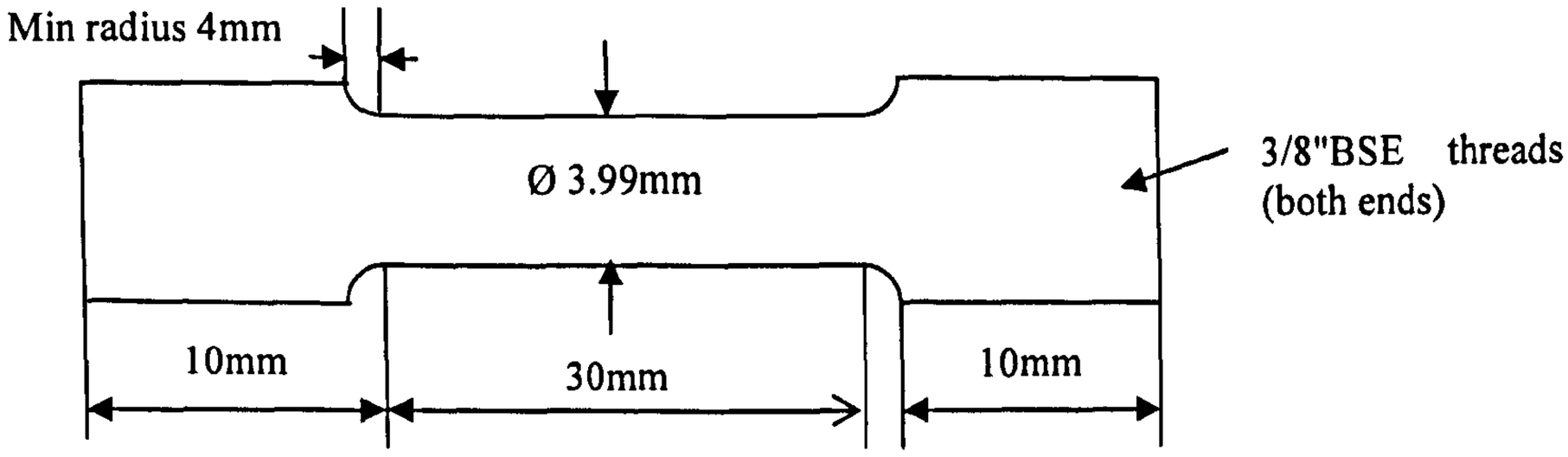

Fig.3.3 Dimensions of the tensile test specimens.

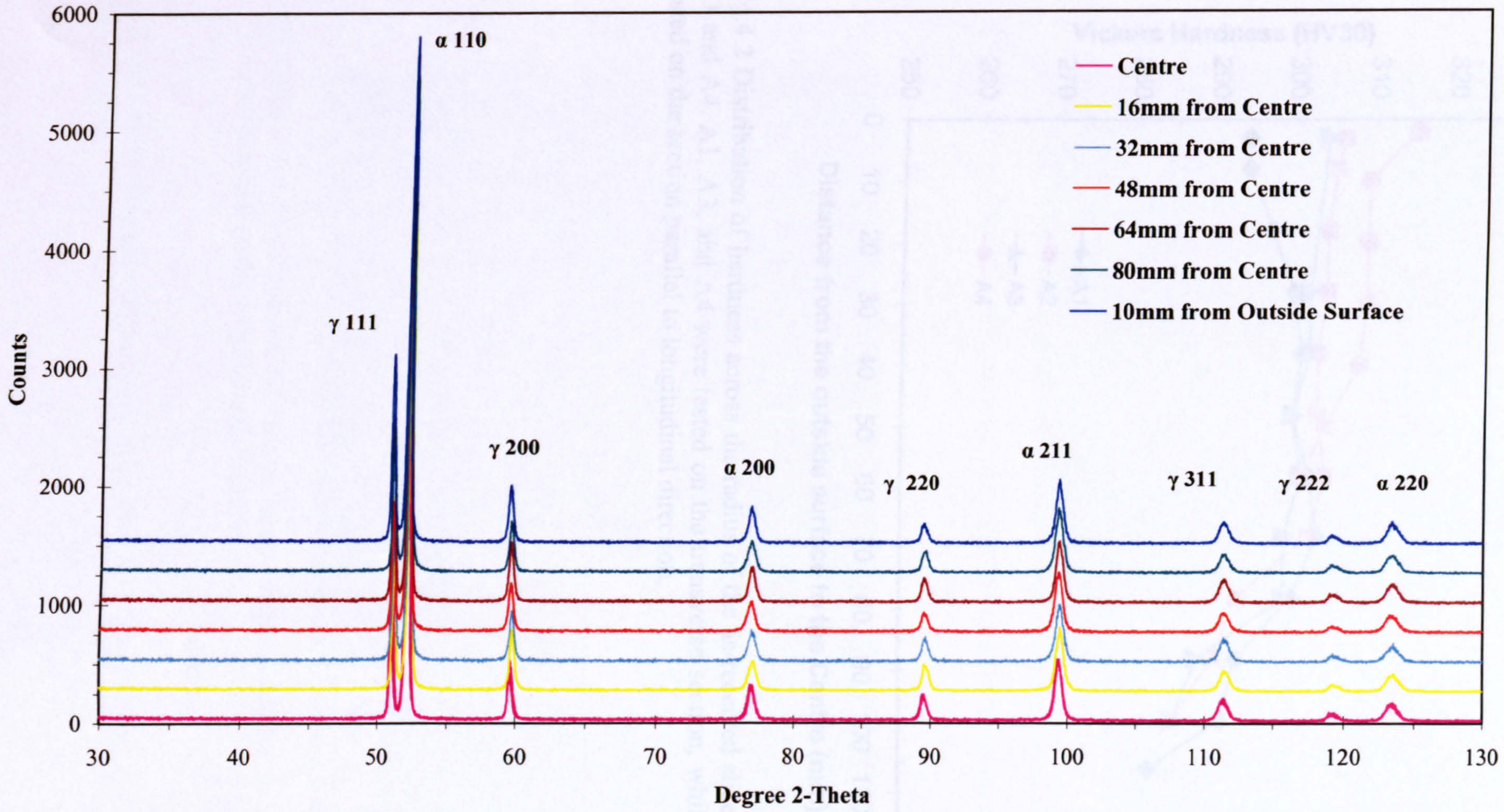

Fig.4.1 X-Ray diffraction patterns of retained austenite and martensite in the as-received slice A1 across the radius from centre to outside surface.

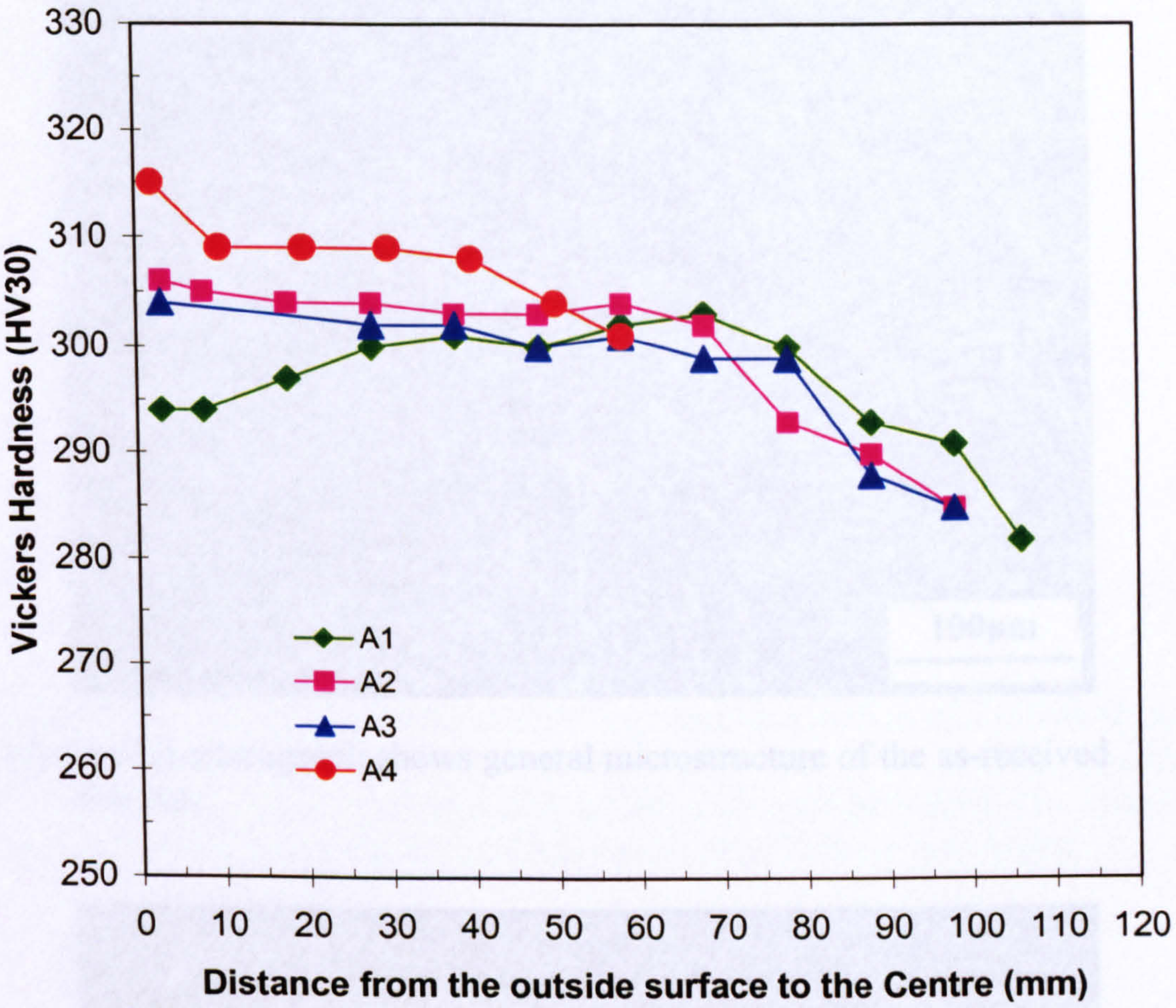

Fig.4.2 Distribution of hardness across the radius of the as-received slices A1, A2, A3 and A4. A1, A3, and A4 were tested on the transverse section, while A2 was tested on the section parallel to longitudinal direction.

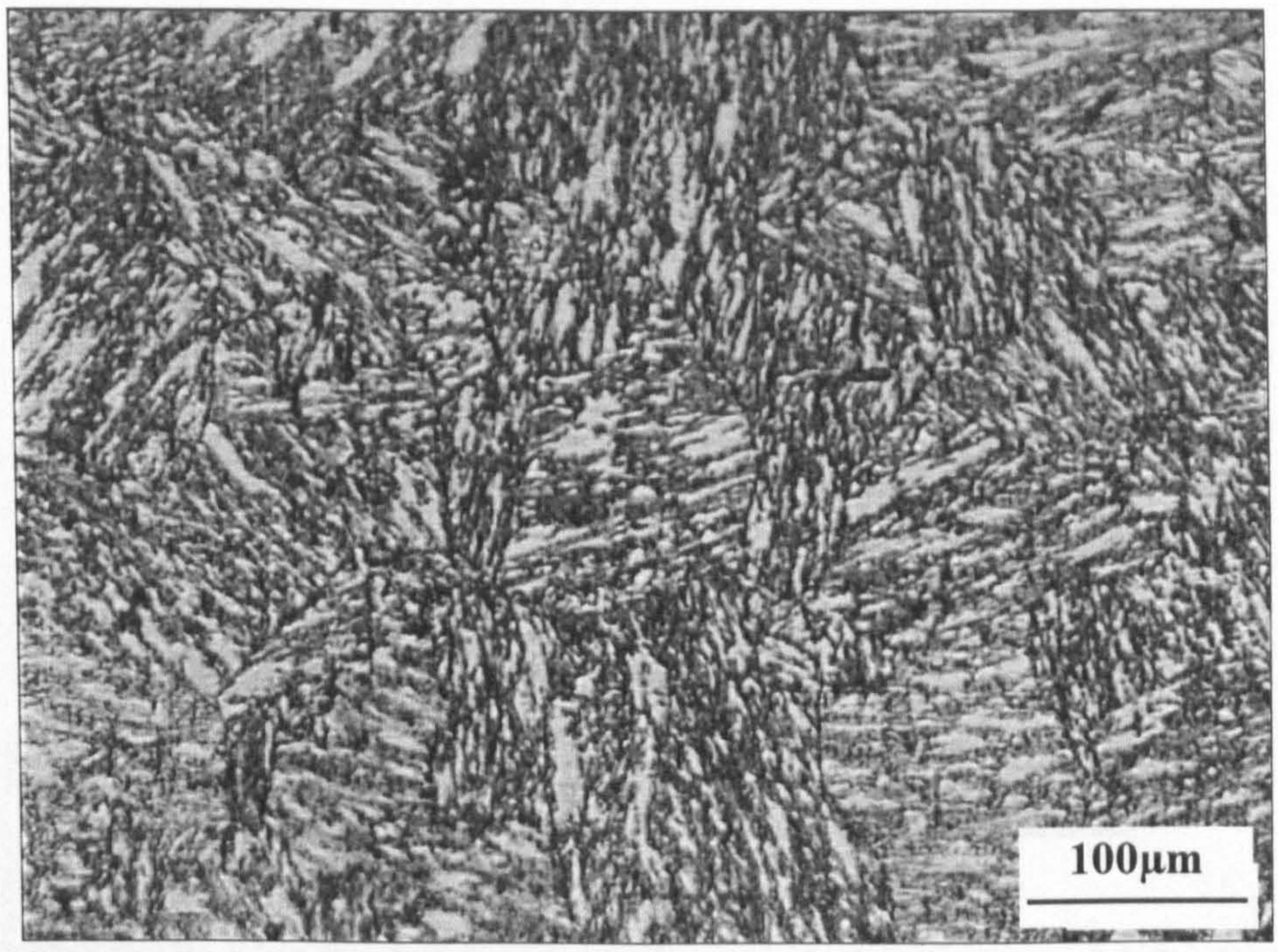

(a) Optical micrograph shows general microstructure of the as-received slice A4.

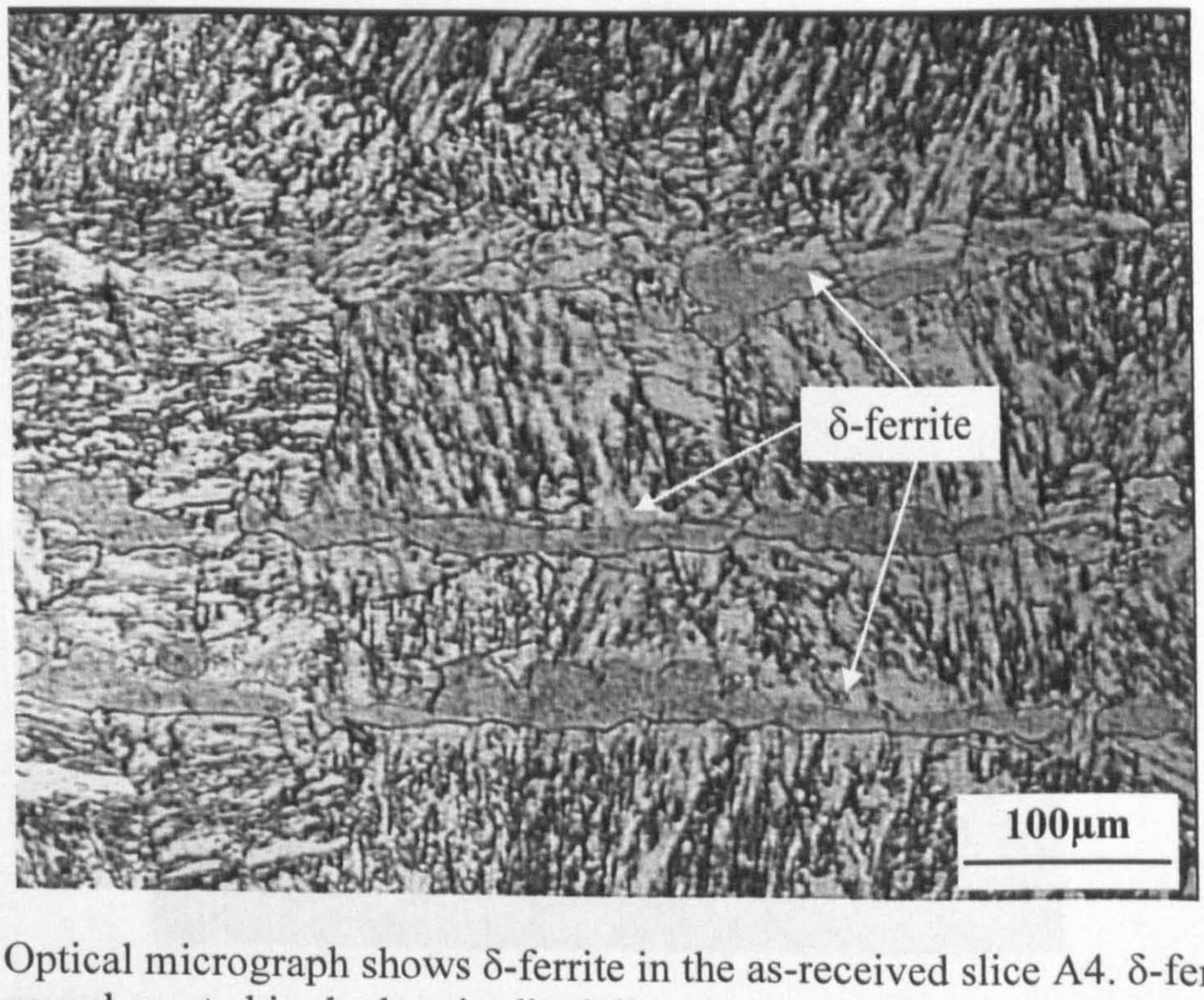

(b) Optical micrograph shows δ-ferrite in the as-received slice A4. δ-ferrite was elongated in the longitudinal direction.

Fig.4.3 Optical micrographs of the as-received slice A4. The specimen was etched by Vilella's regent.

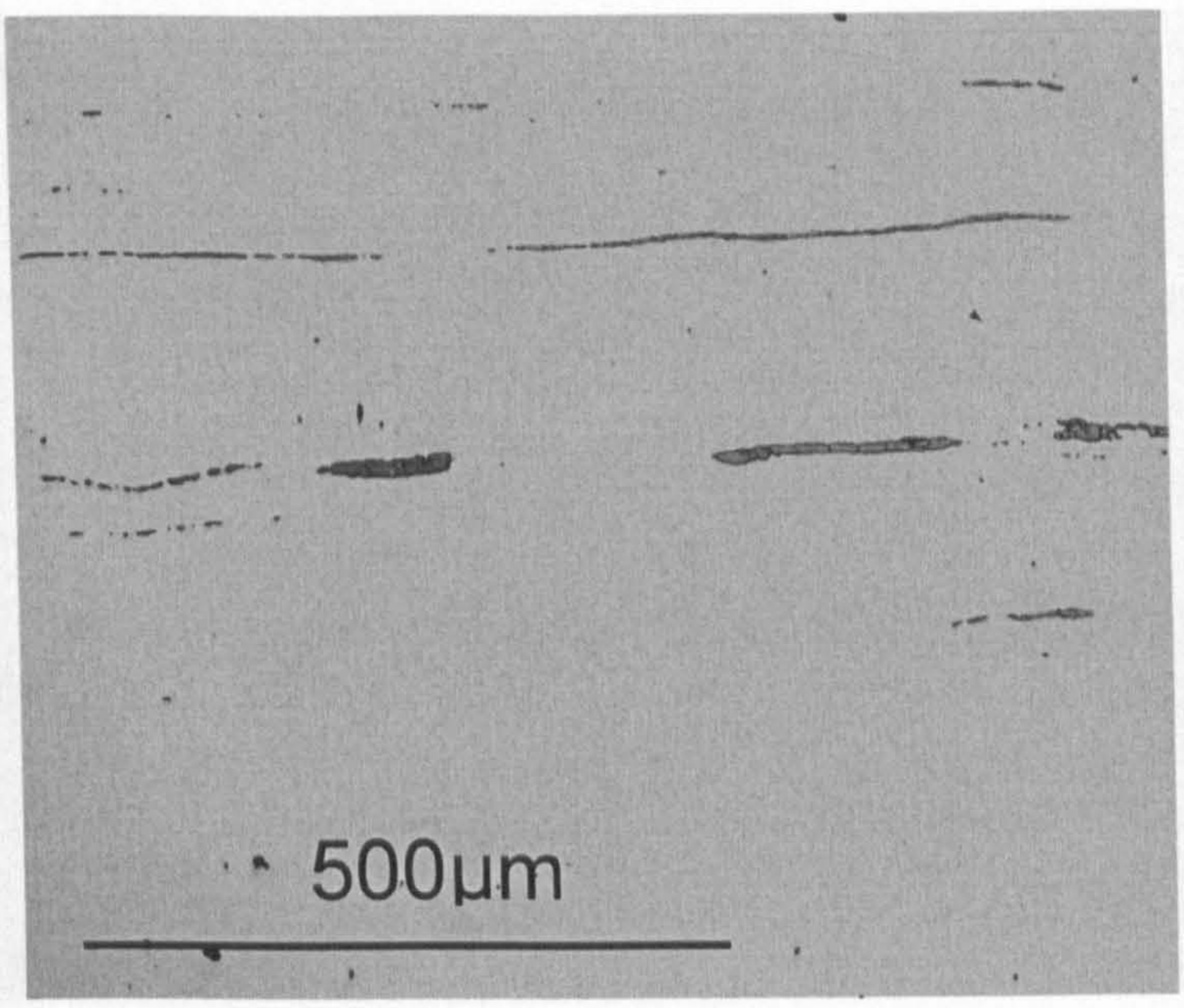

Fig.4.4 Optical micrograph shows morphology and distribution of δ-ferrite in the as-received slice B1. The specimen was cut from half-radius of the as-received slice B1 and was electrolytically etched in a 20% aqueous solution of NaOH. The image was taken from the area where the highest concentration of δ-ferrite was found.

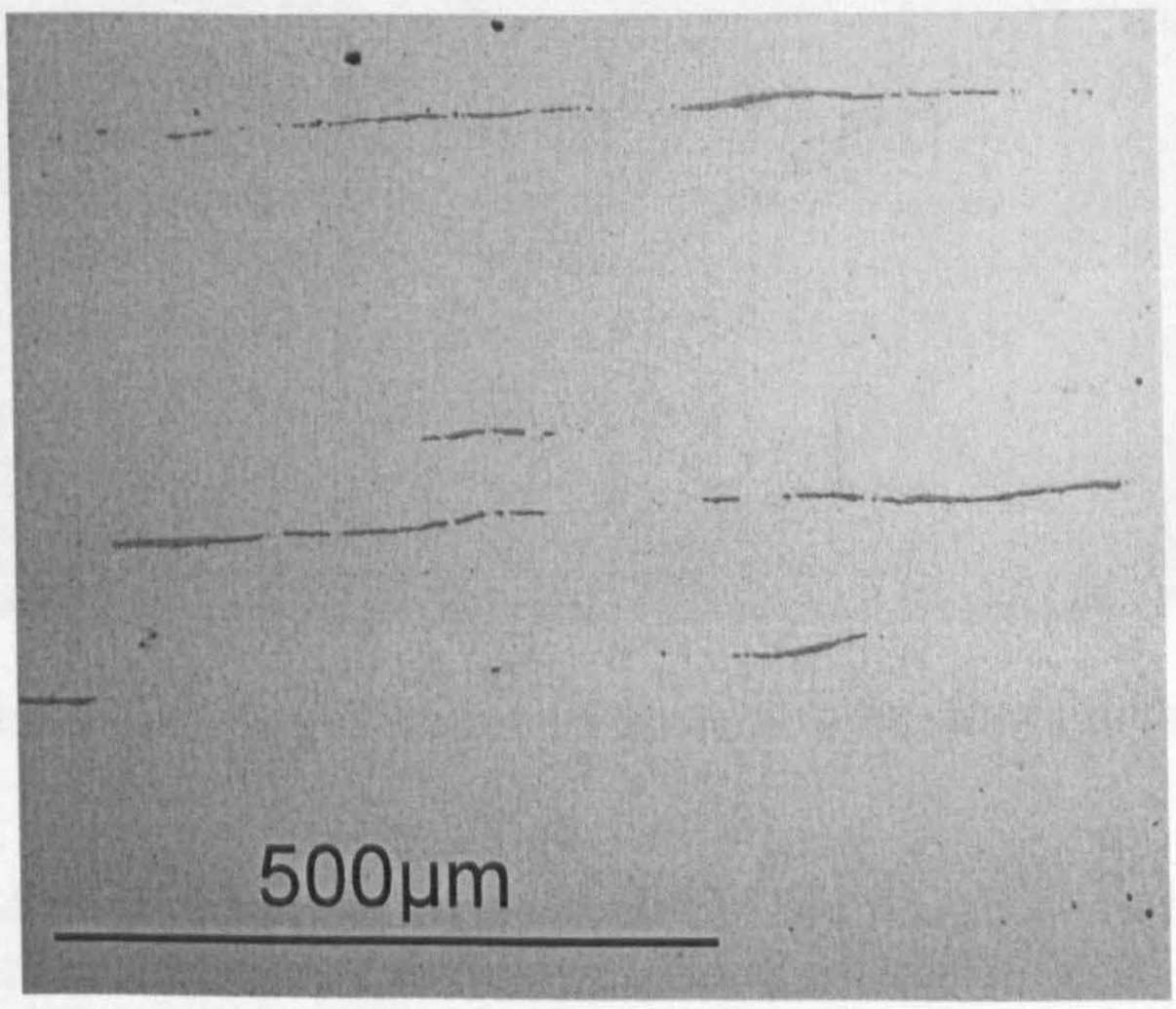

Fig.4.5 Optical micrograph shows morphology and distribution of δ-ferrite in the as-received slice B3. The specimen was cut from half-radius of the as-received slice B3 and was electrolytically etched in a 20% aqueous solution of NaOH. The image was taken from the area where the highest concentration of δ-ferrite was found.

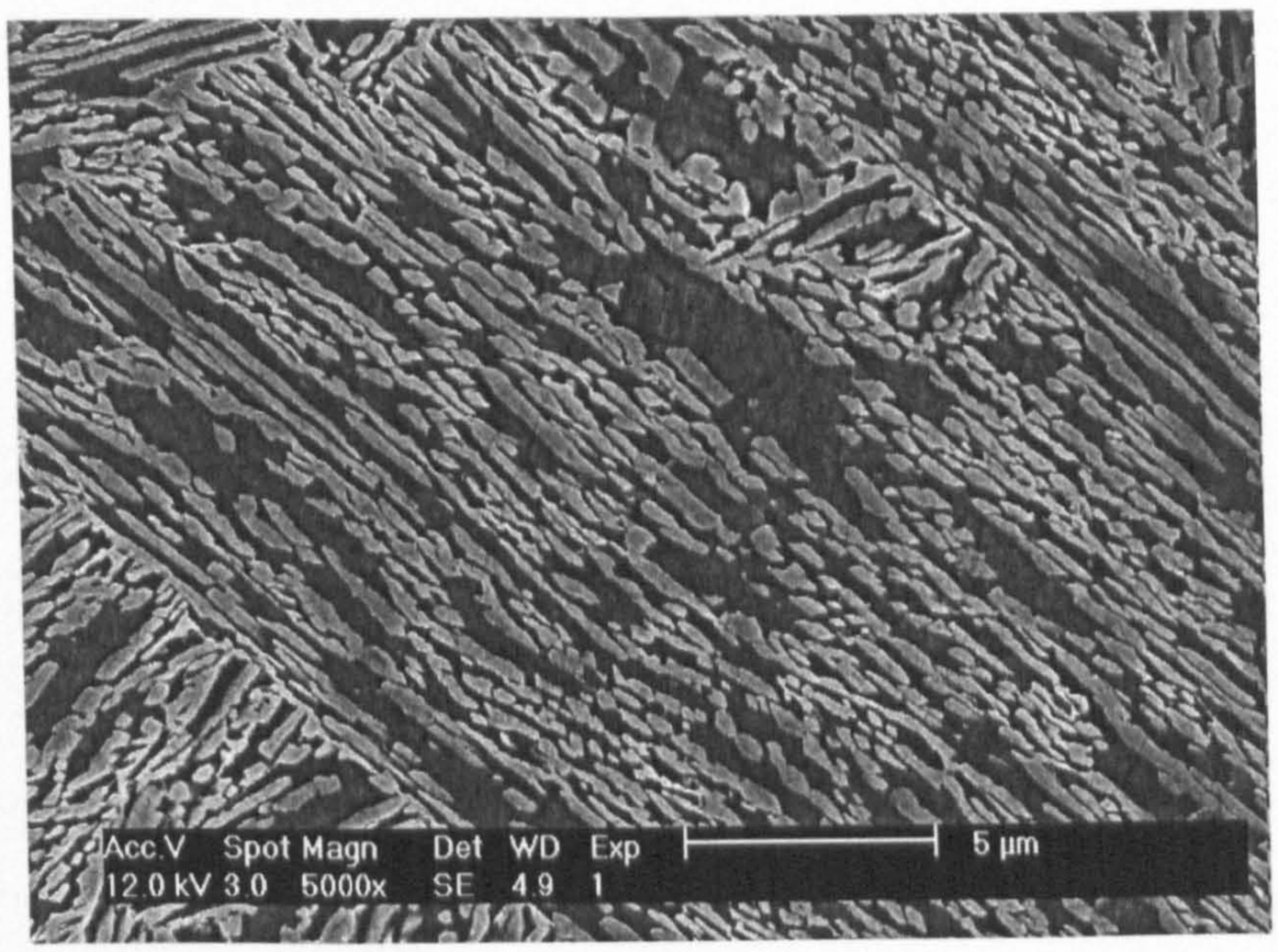

(a)

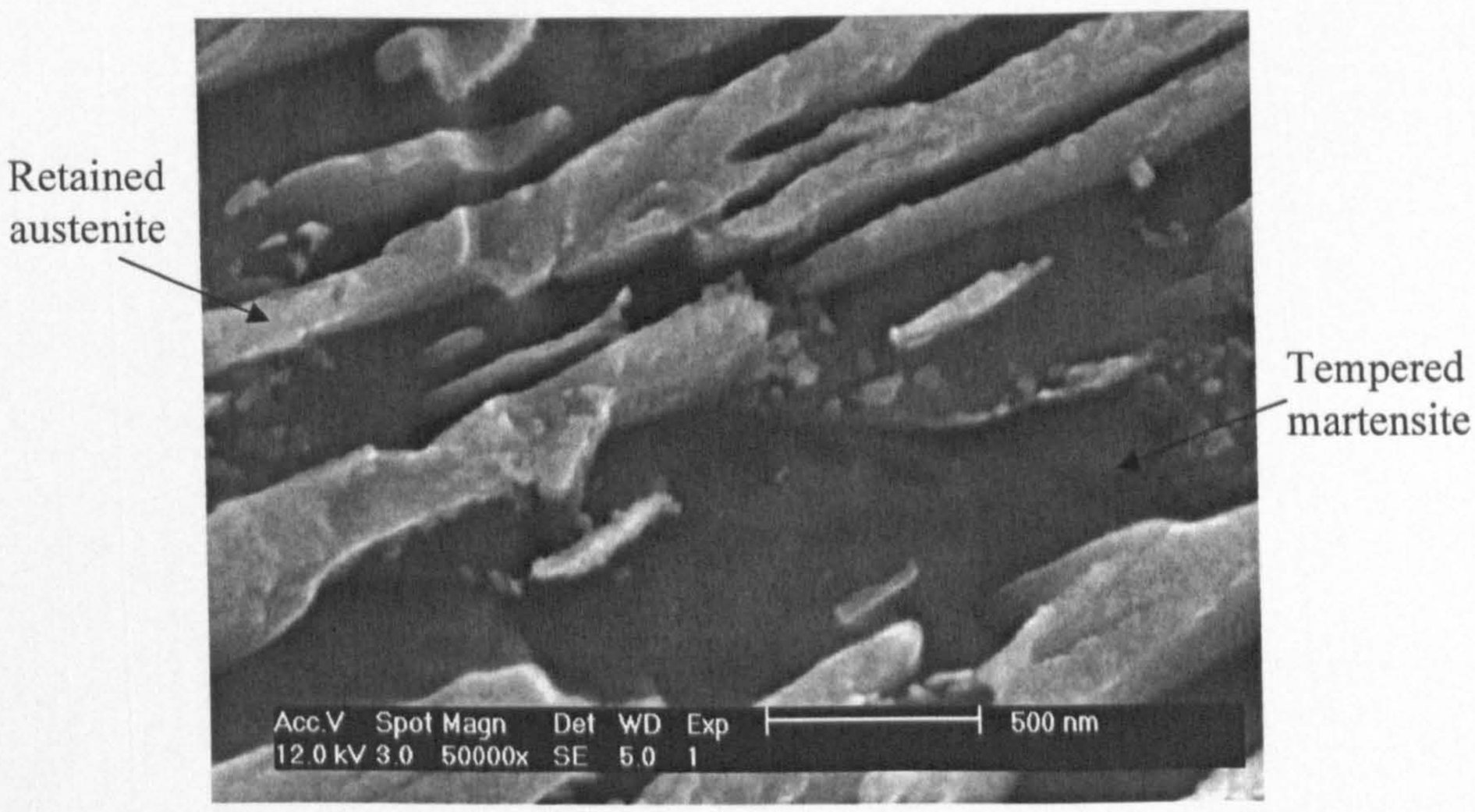

(b) Higher magnification of the same area shown in (a).

Fig.4.6 SEI SEM micrographs of the as-received slice A1, showing retained austenite (brighter contrast) and tempered martensite (darker contrast).

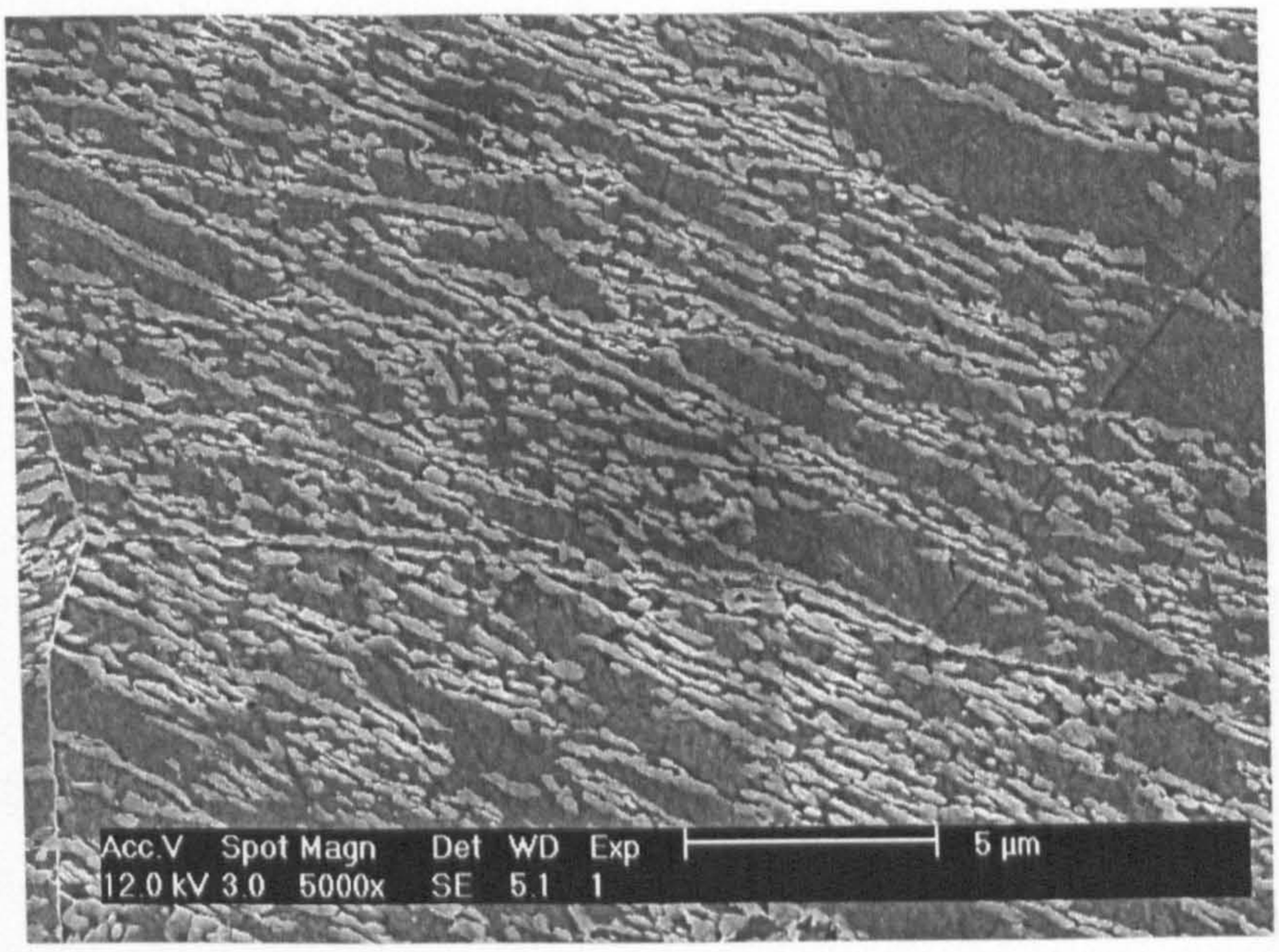

(a)

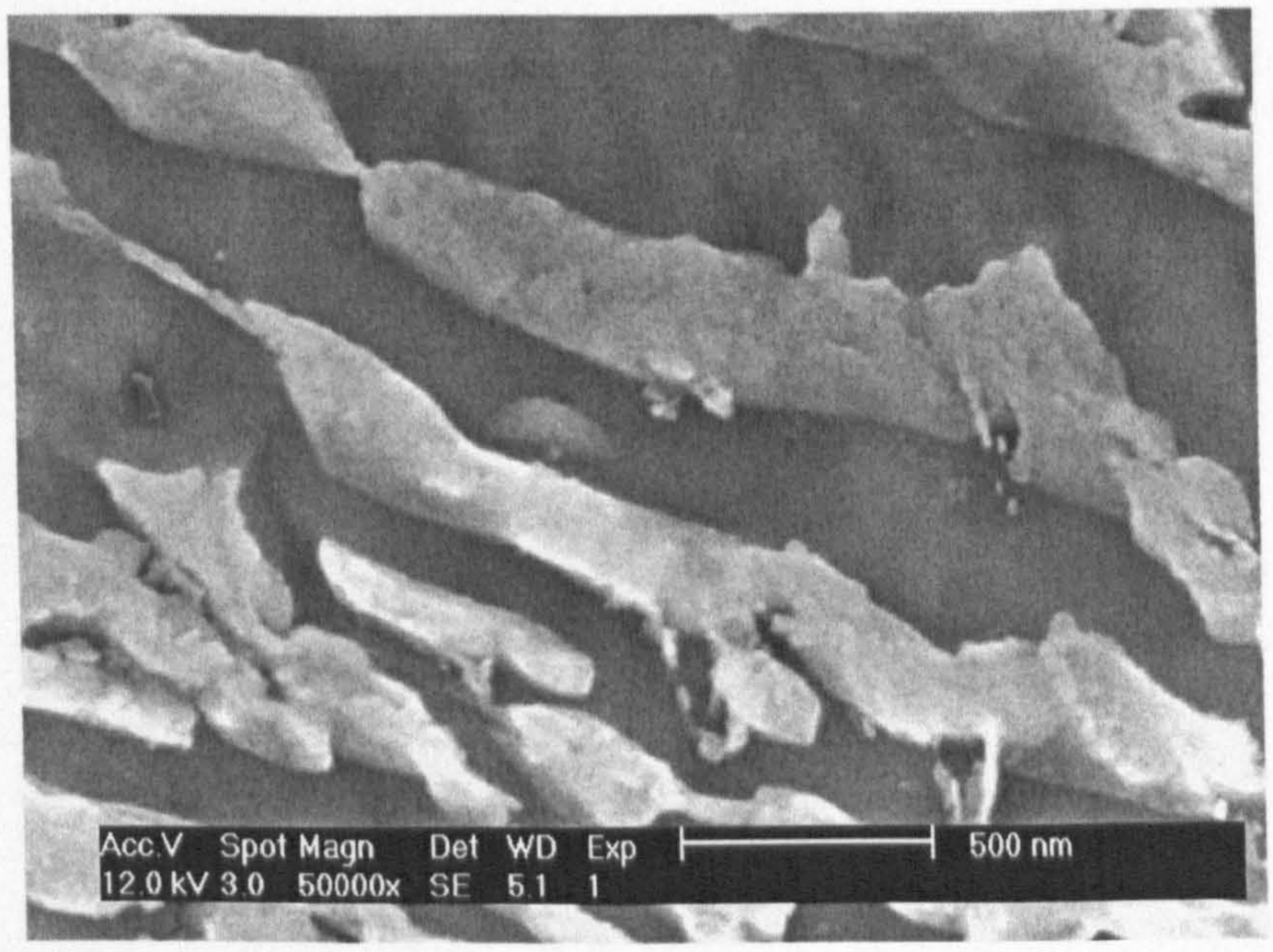

(b) Higher magnification of the same area shown in (a).

Fig.4.7 SEI SEM micrographs of the as-received slice A2, showing retained austenite (brighter contrast) and tempered martensite (darker contrast).

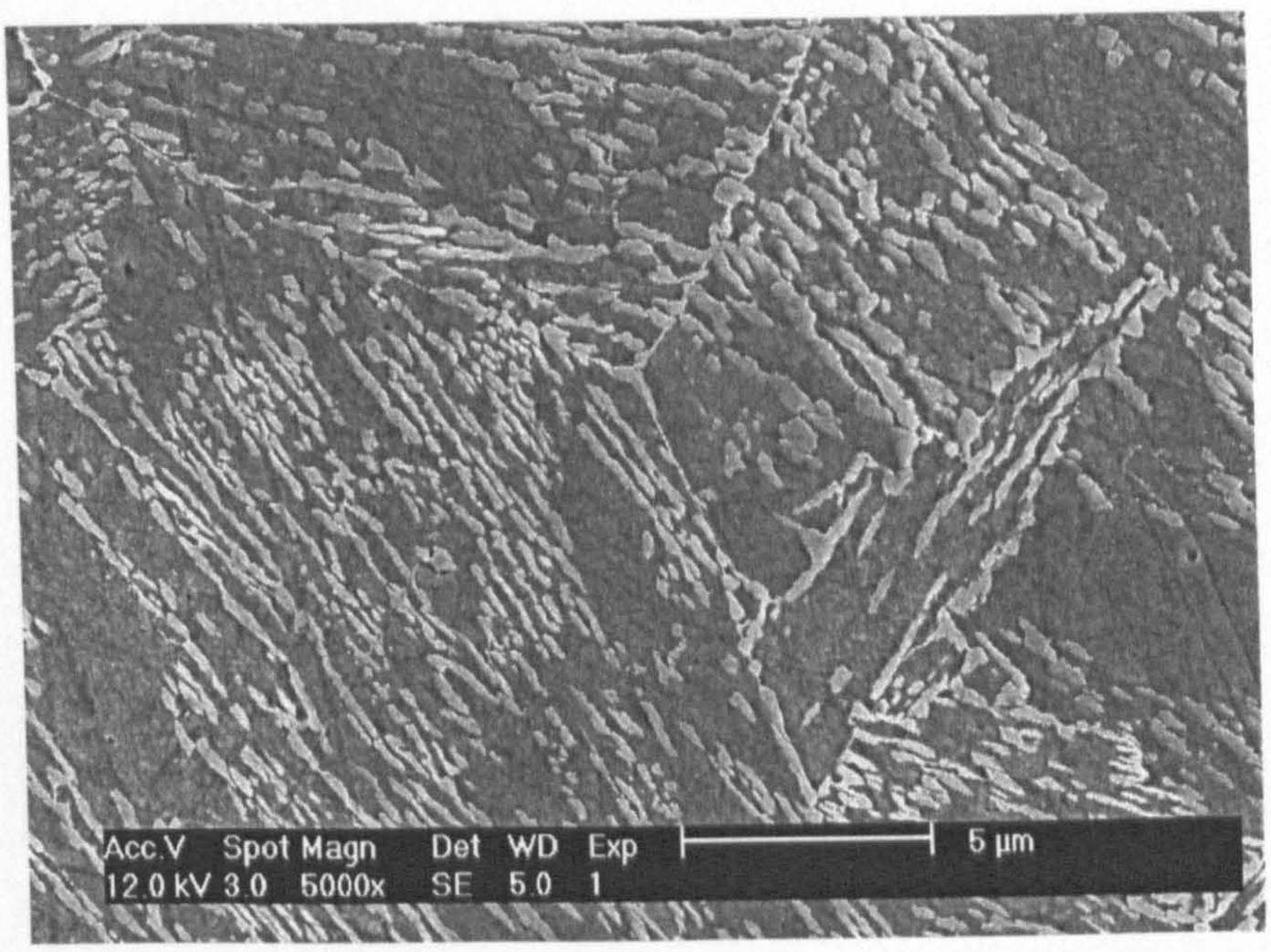

(a)

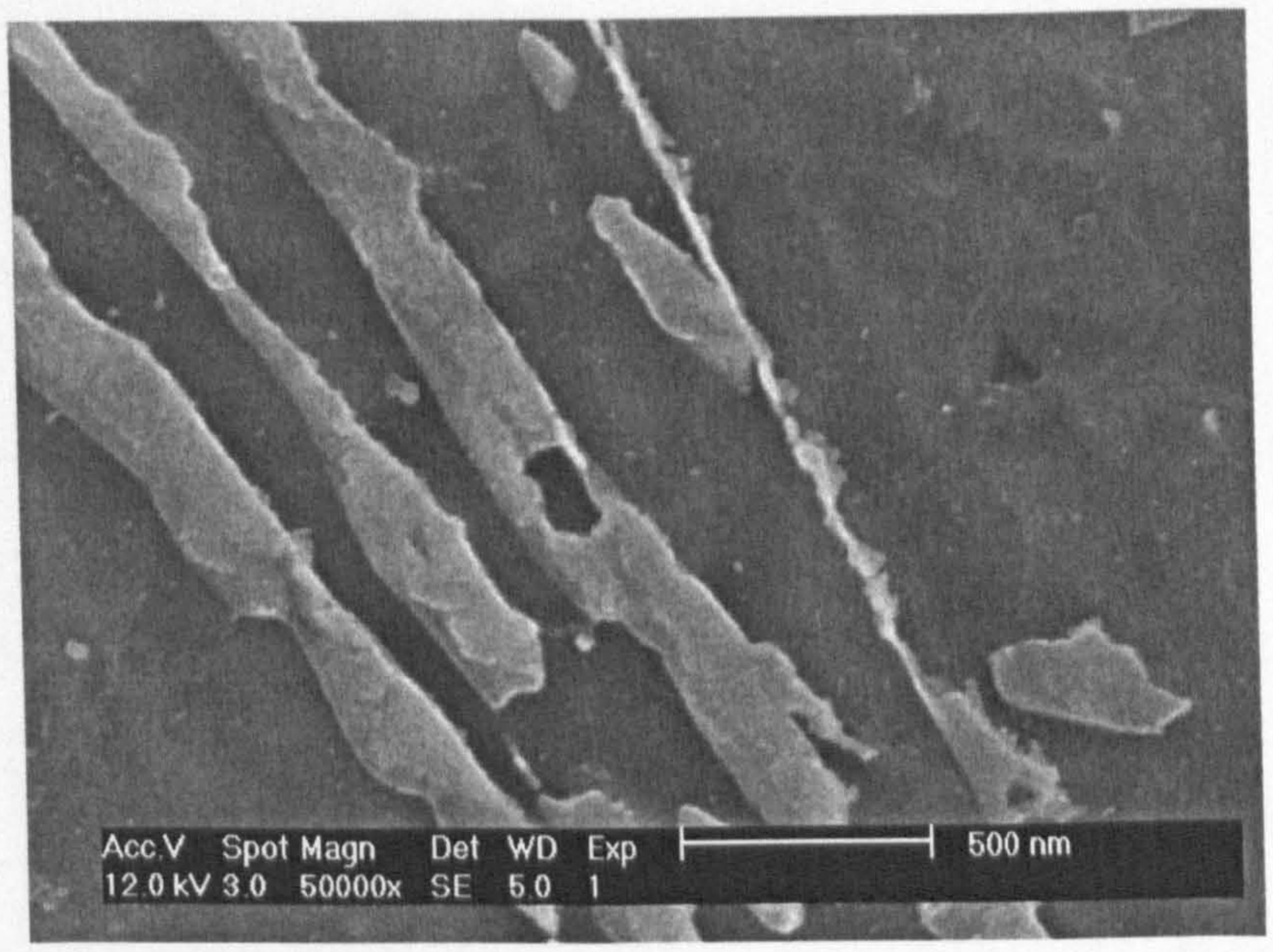

(b) Higher magnification of the same area shown in (a).

Fig.4.8 SEI SEM micrographs of the as-received slice B1, showing retained austenite (brighter contrast) and tempered martensite (darker contrast). Fine precipitates were also found distributed in the tempered martensite.

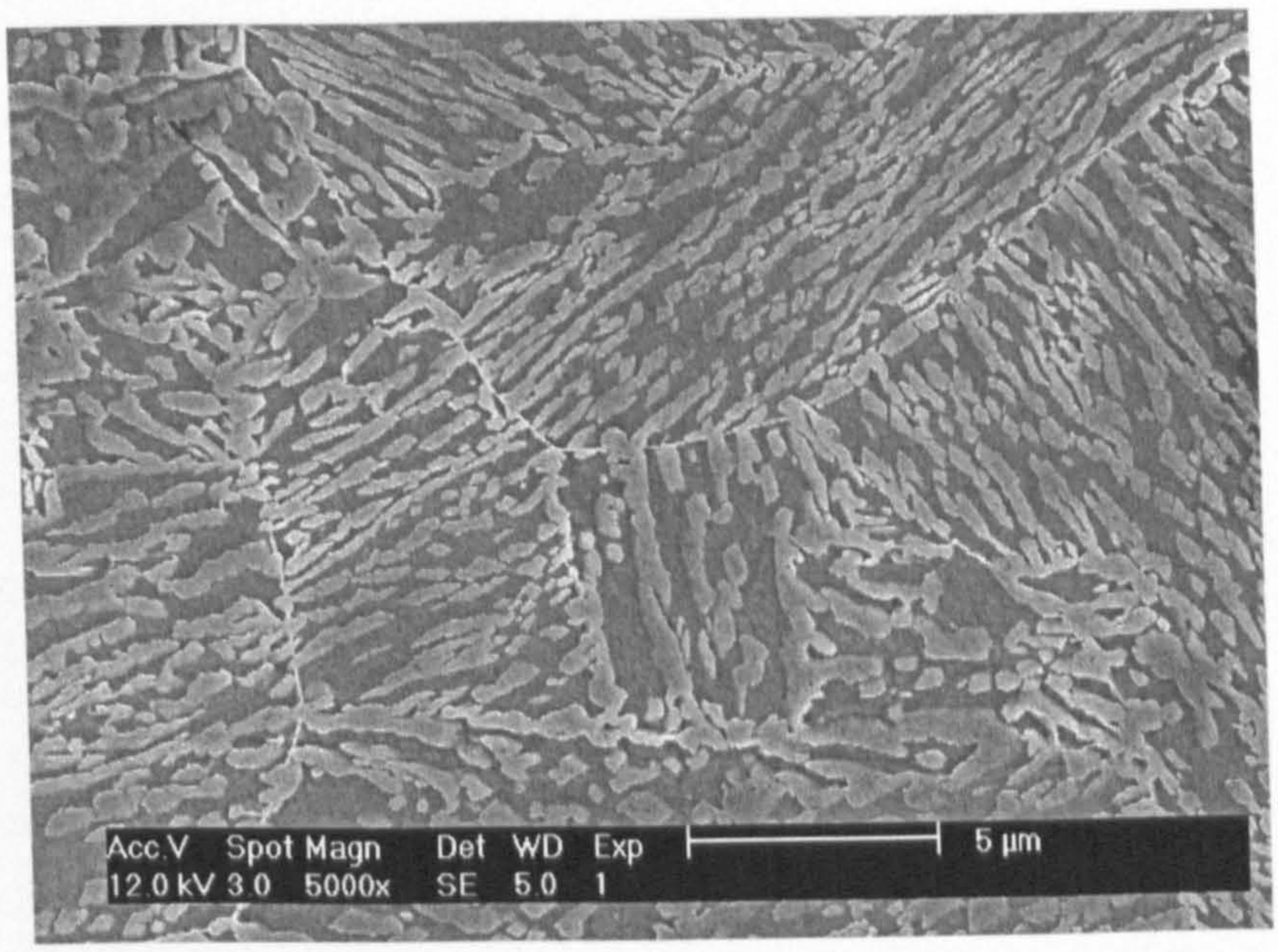

(a)

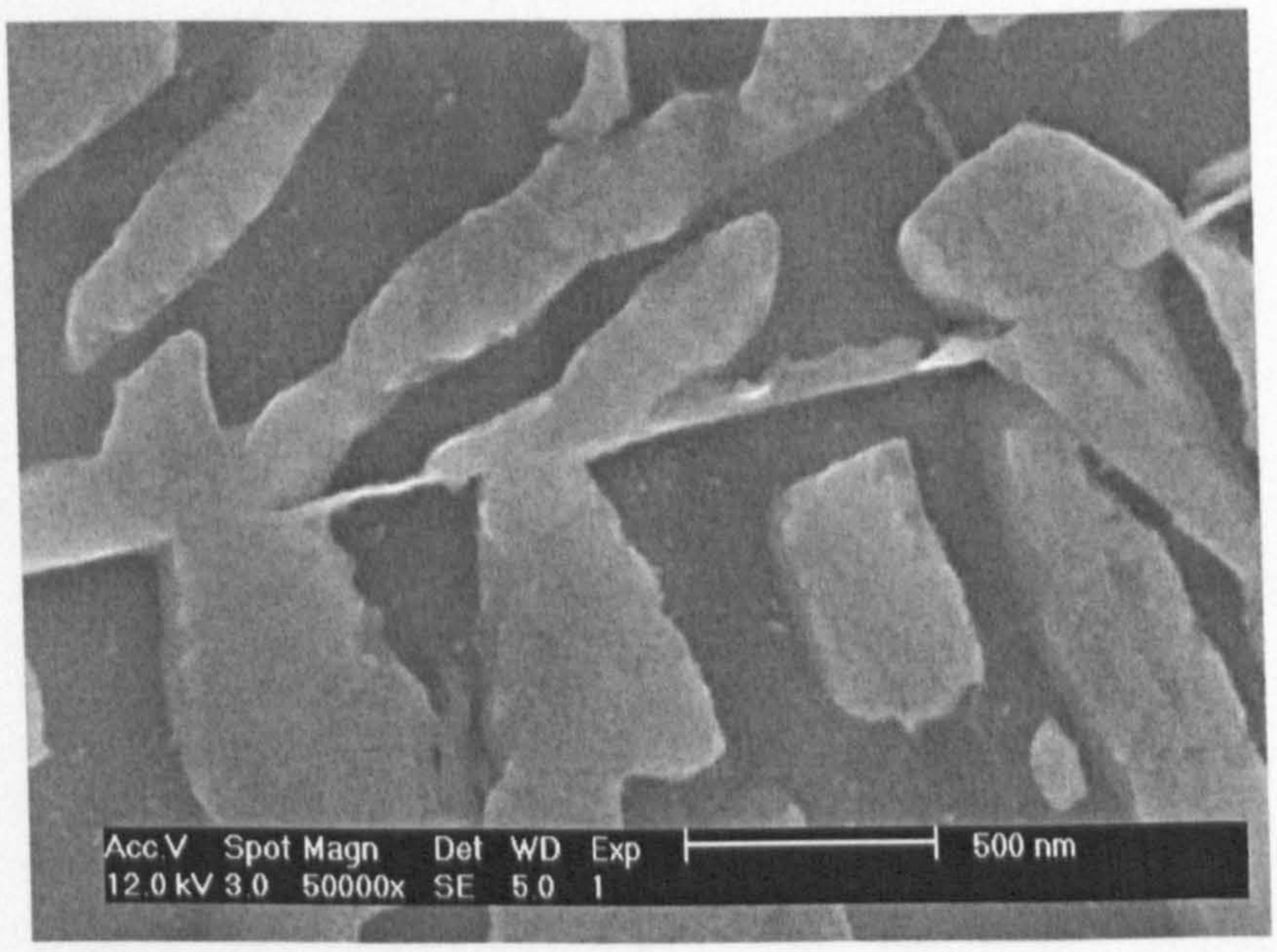

(b) Higher magnification of the same area shown in (a).

Fig.4.9 SEI SEM micrographs of the as-received slice B2, showing retained austenite (brighter contrast) and tempered martensite (darker contrast). Fine precipitates were also found distributed in the tempered martensite.

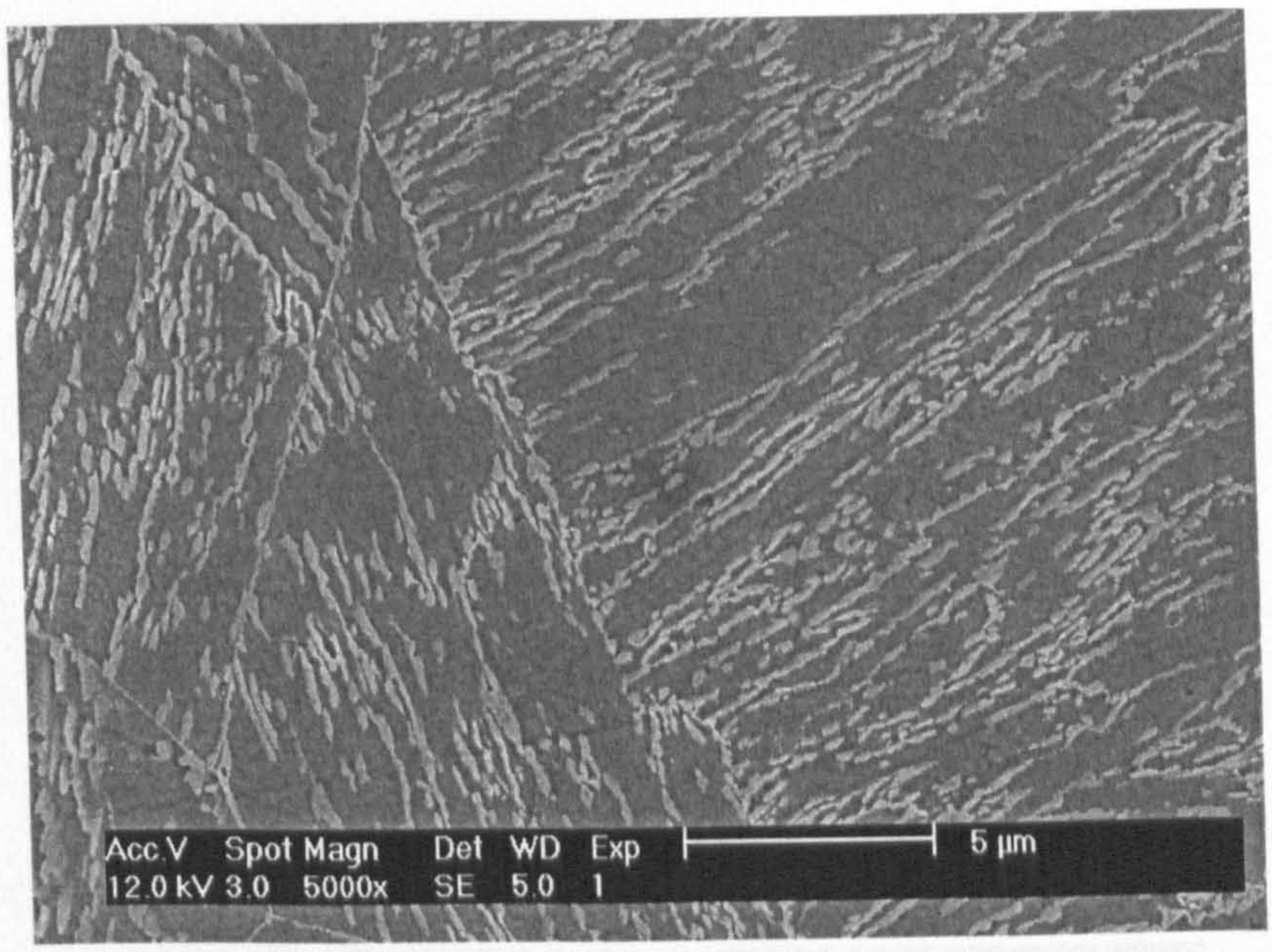

(a)

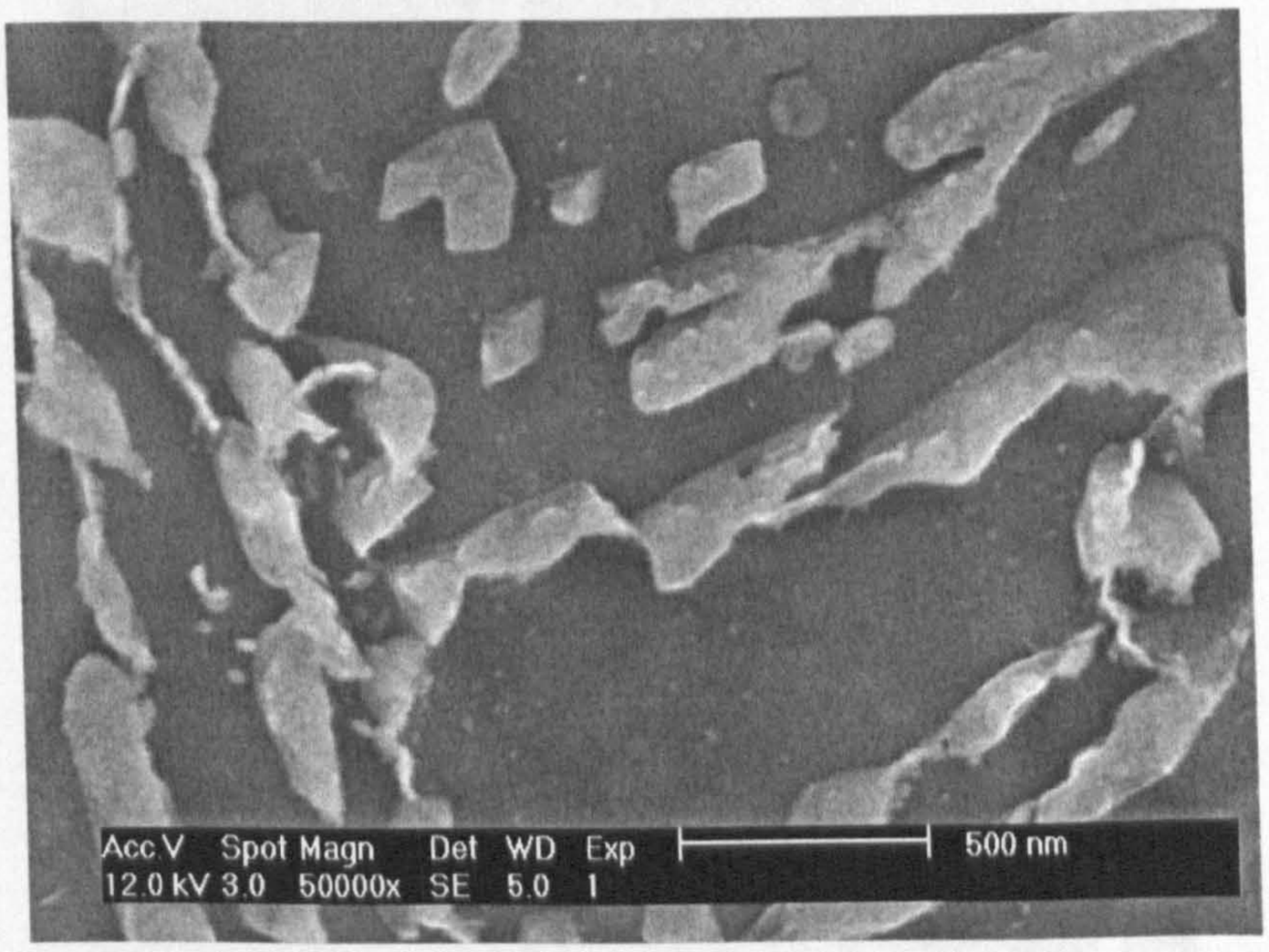

(b) Higher magnification of the same area shown in (a).

Fig.4.10 SEI SEM micrographs of the as-received slice B3, showing retained austenite (brighter contrast) and tempered martensite (darker contrast).

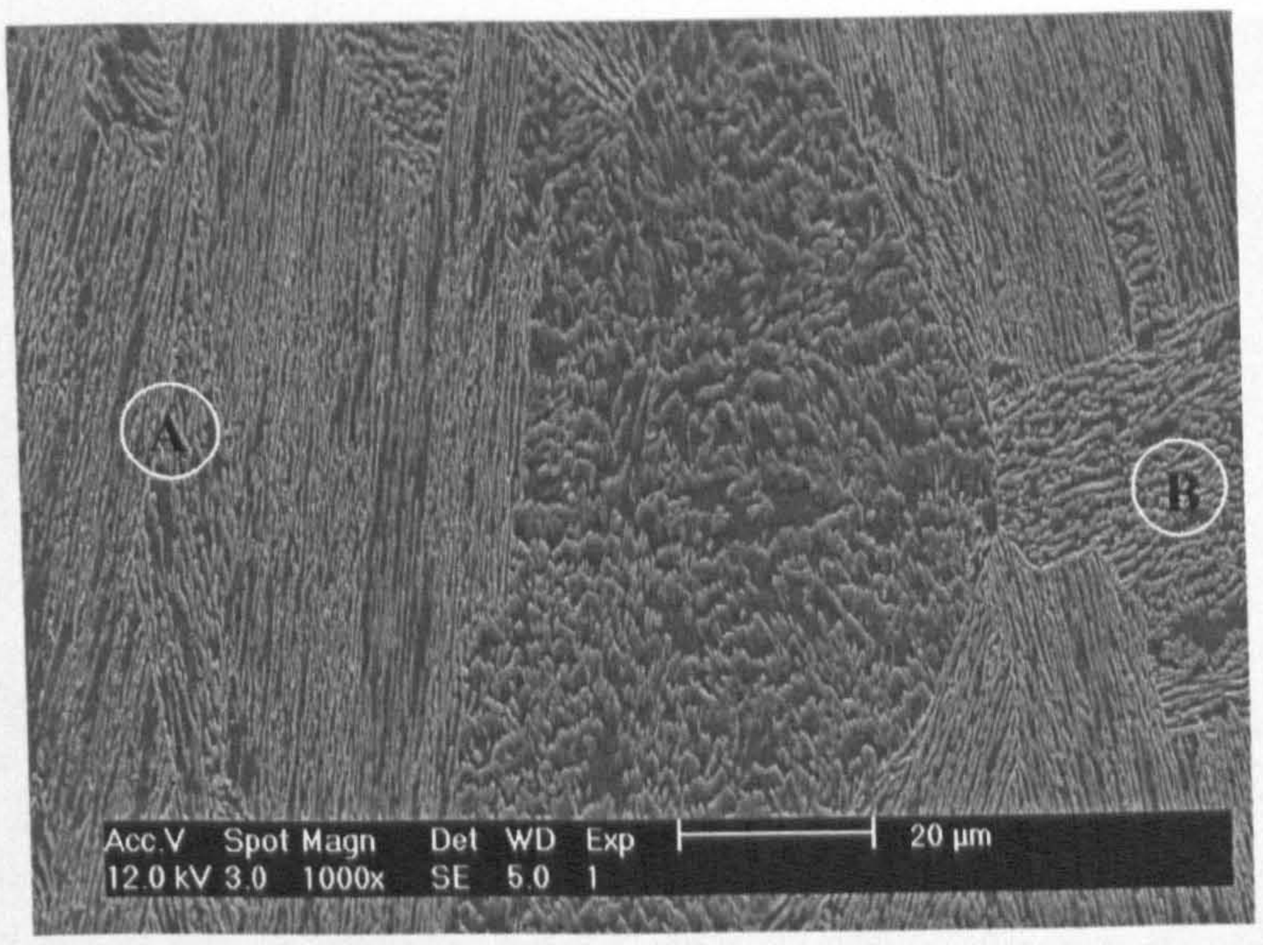

(a)

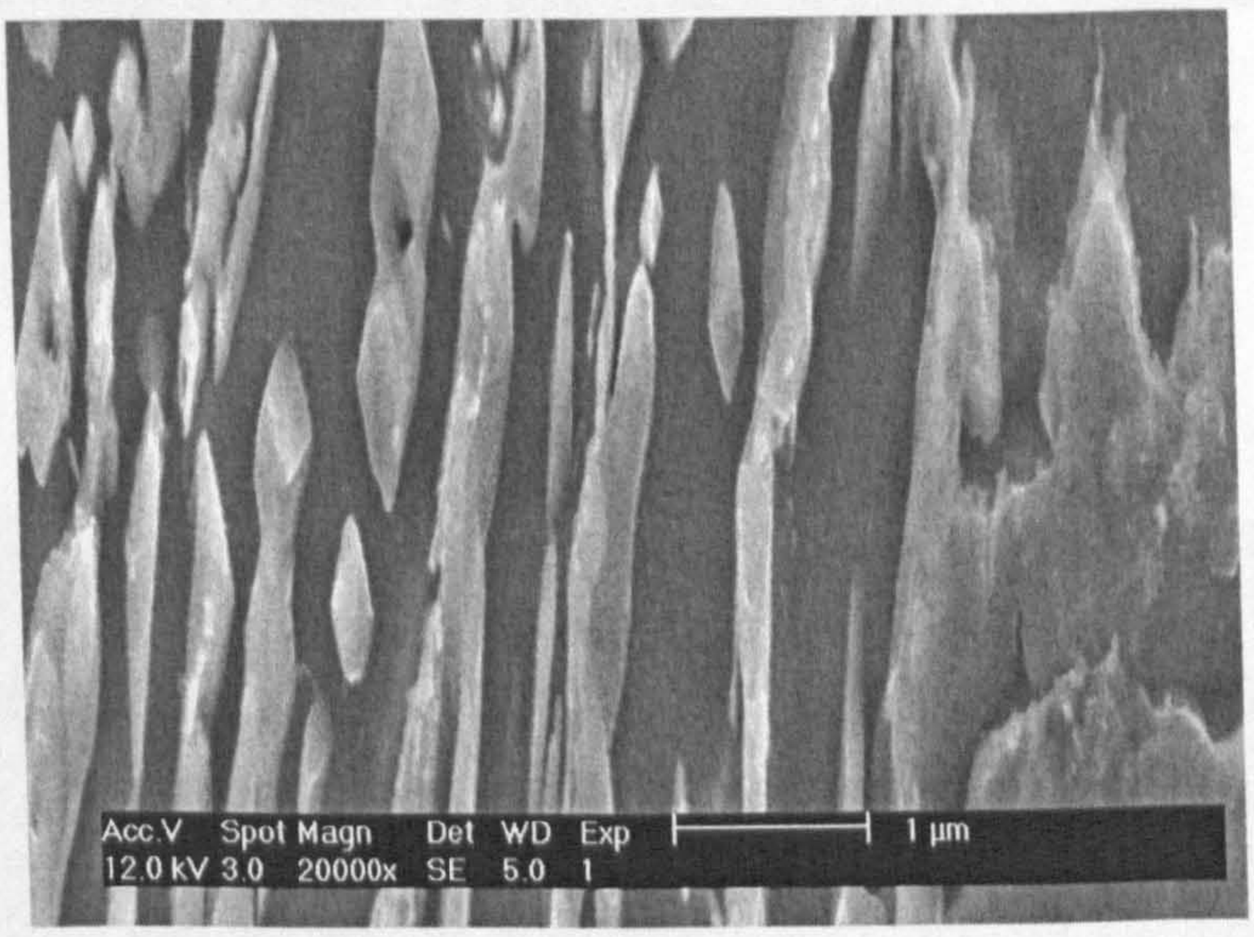

(b) Higher magnification from the marked area A in (a).

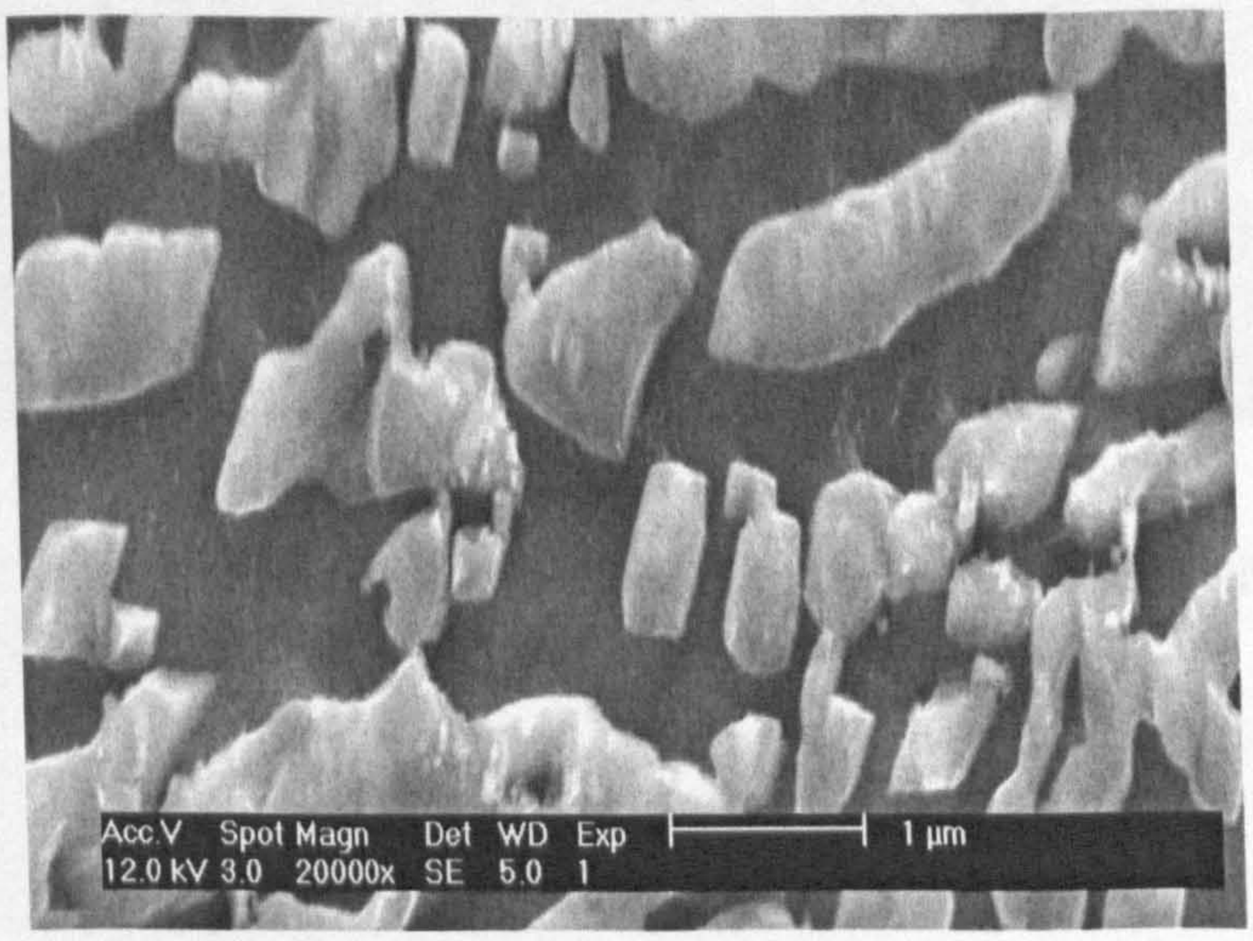

(c) Higher magnification from the marked area B in (a).

Fig.4.11 SEI SEM micrographs of the as-received slice B3 taken from the transverse section, showing retained austenite (brighter contrast) and tempered martensite (darker contrast).

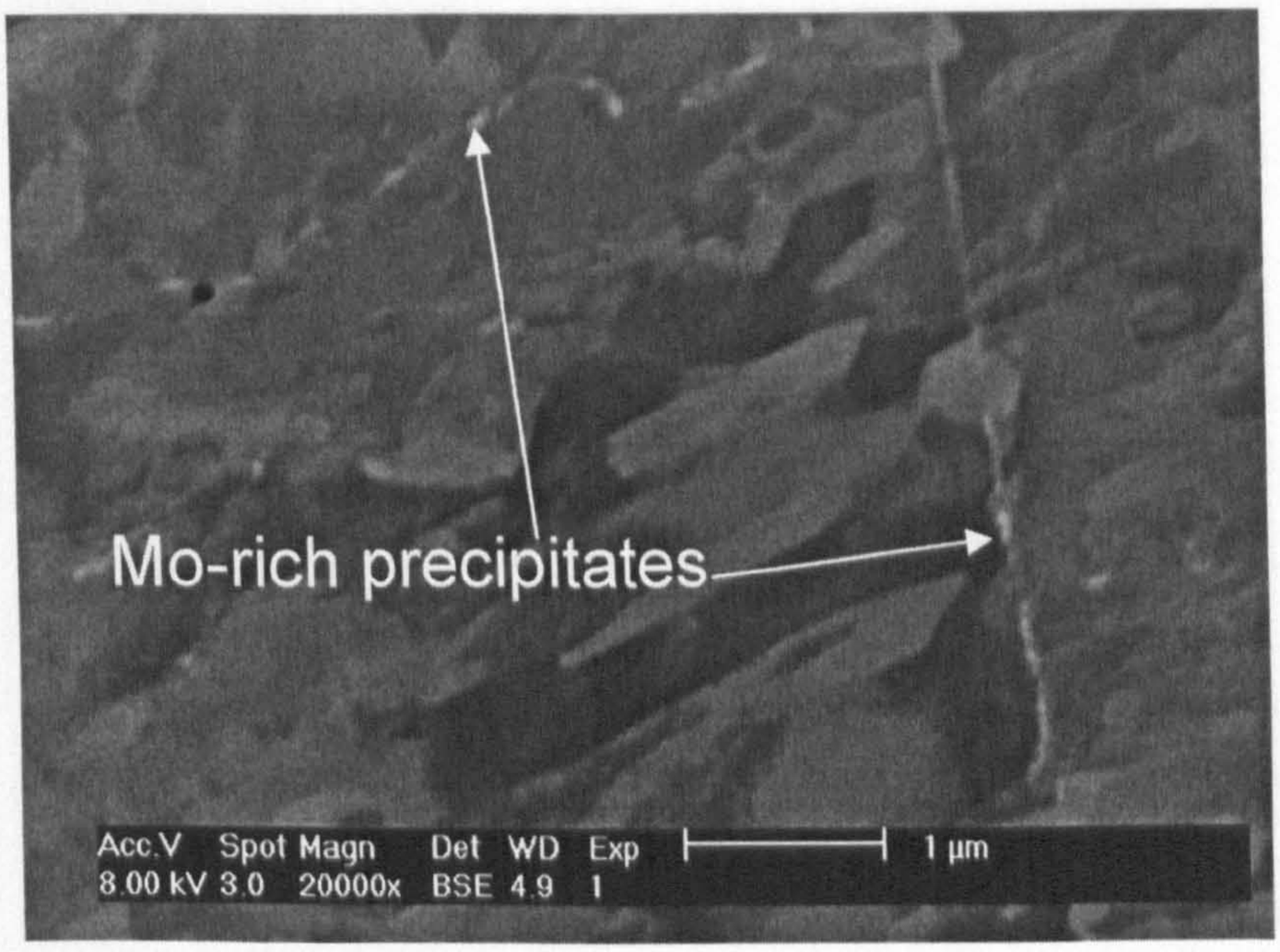

Fig.4.12 BEI SEM micrograph of the as-received slice B2 (without etching). EDX microanalysis indicated the brighter particles distributed along the prior austenite grain boundaries were Mo-rich particles.

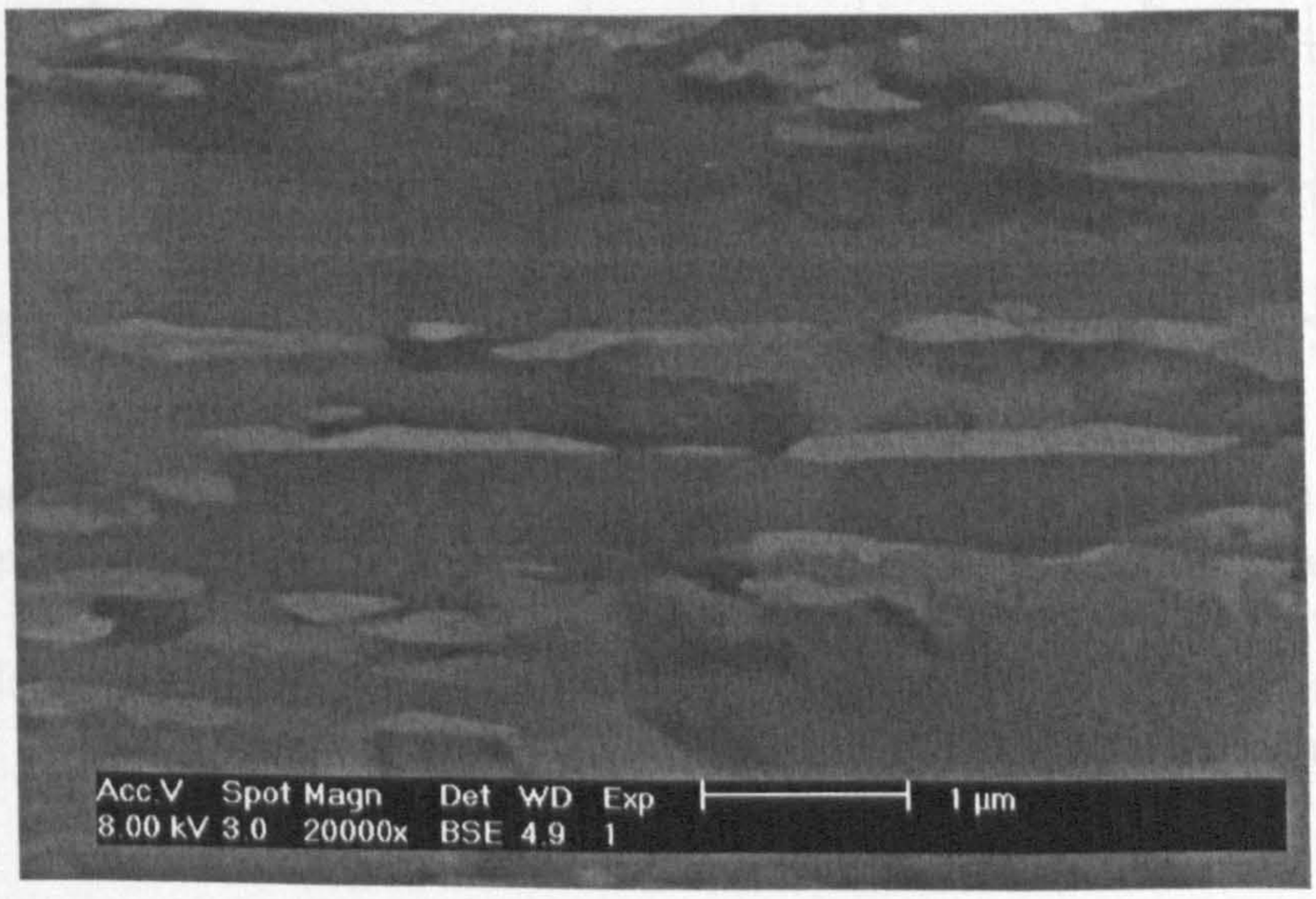

Fig.4.13 BEI SEM micrograph of the as-received slice B3 (without etching), showing particle-like retained austenite (brighter contrast).

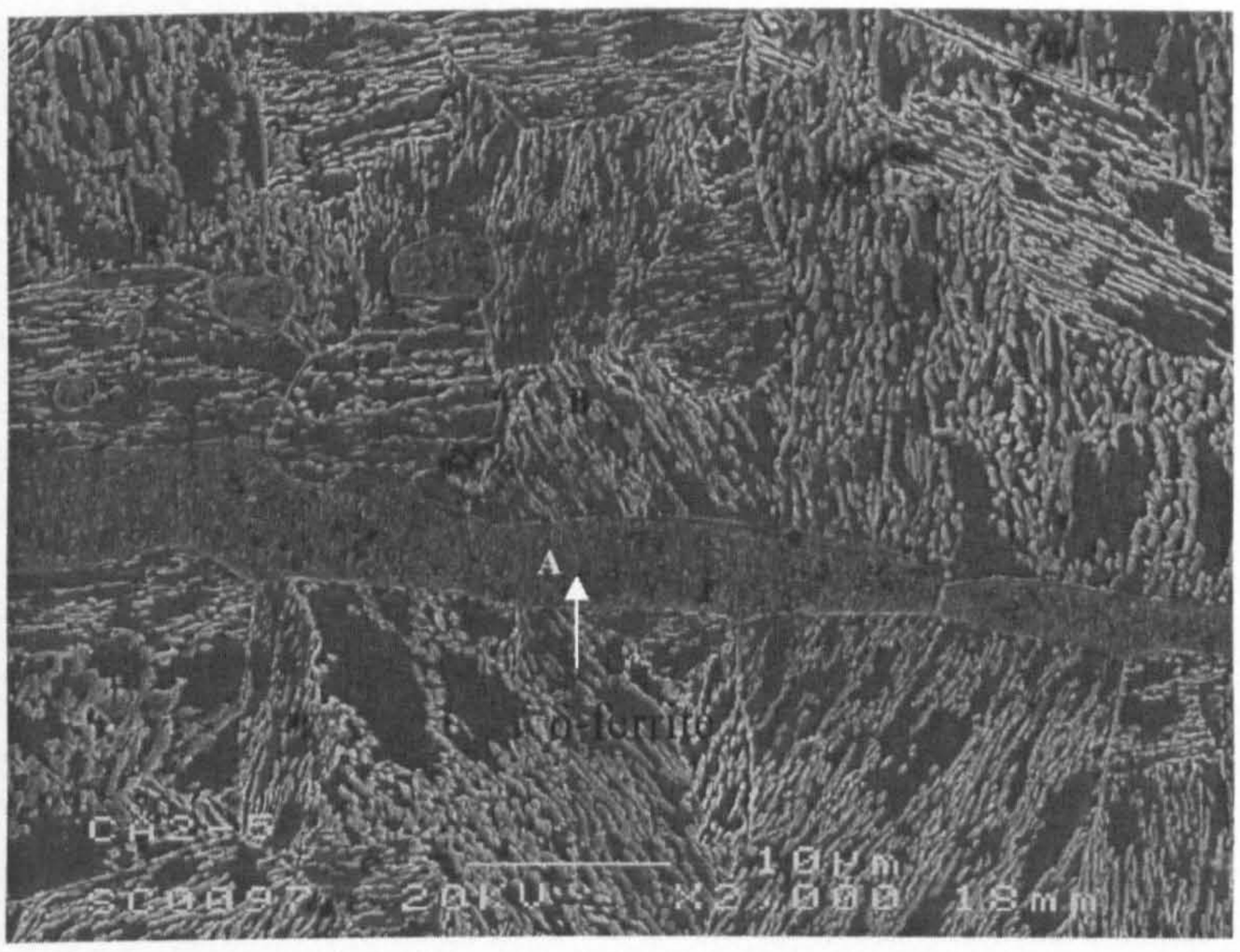

(a) SEI SEM micrograph of the as-received slice A2, showing string-like δ-ferrite.

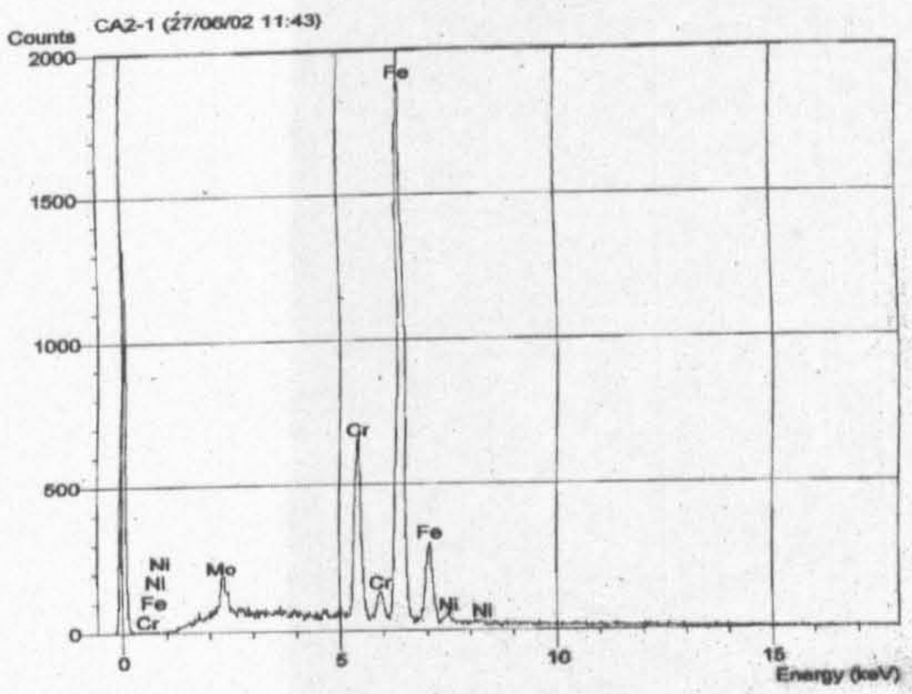

(b) EDX microanalysis on the δ-ferrite string (area A in (a)), indicating it is enriched in Cr and Mo while depleted in Ni.

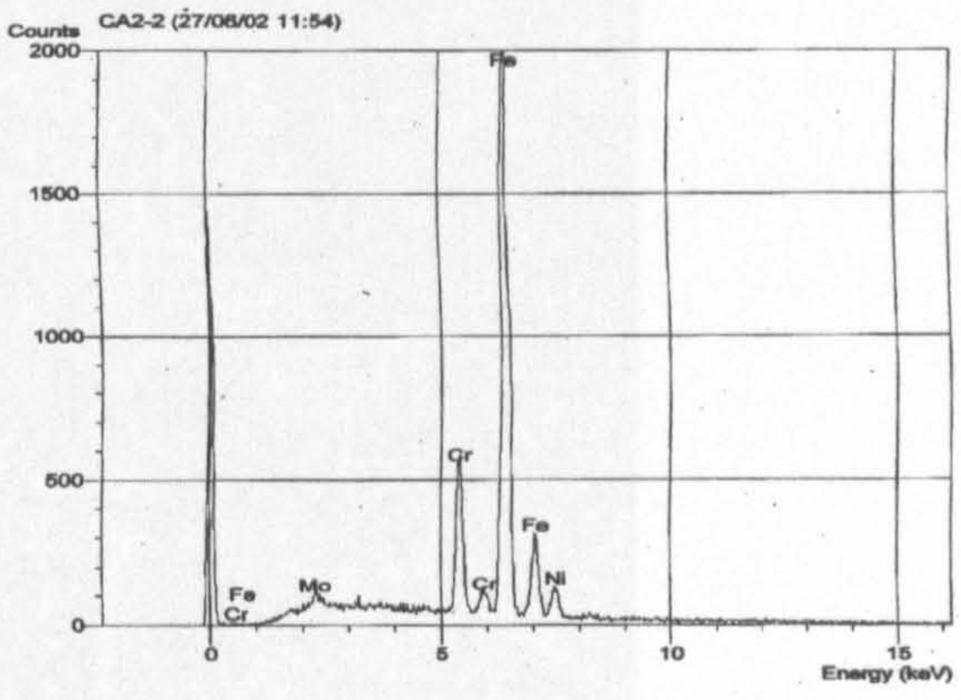

(c) EDX microanalysis on the matrix of the "martensite and retained austenite" (area B in (a)), indicating the matrix contained higher Ni content but lower Cr and Mo compared with (b).

Fig.4.14 SEI SEM micrograph and EDX microanalysis of the as-received slice A2.

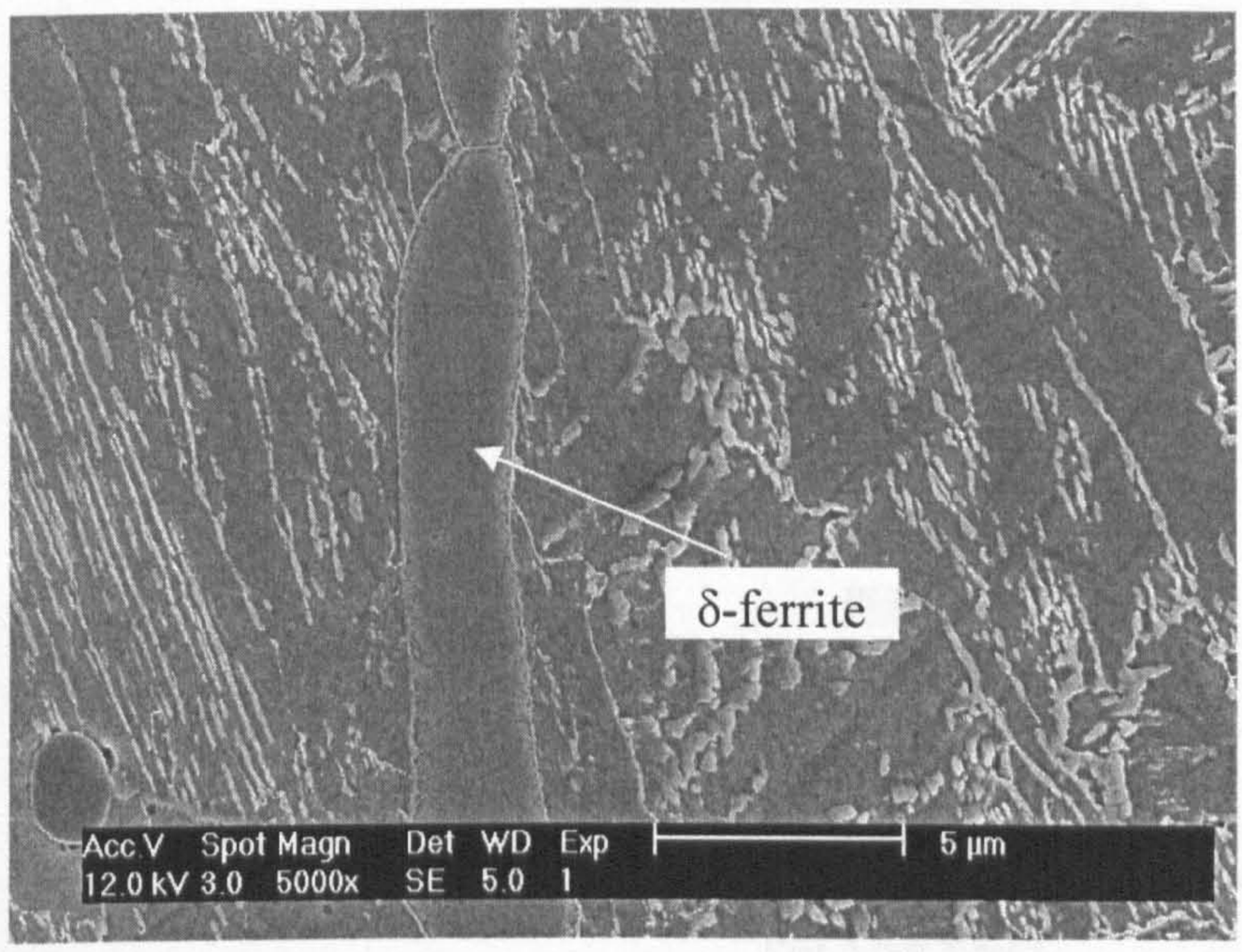

(a) SEI

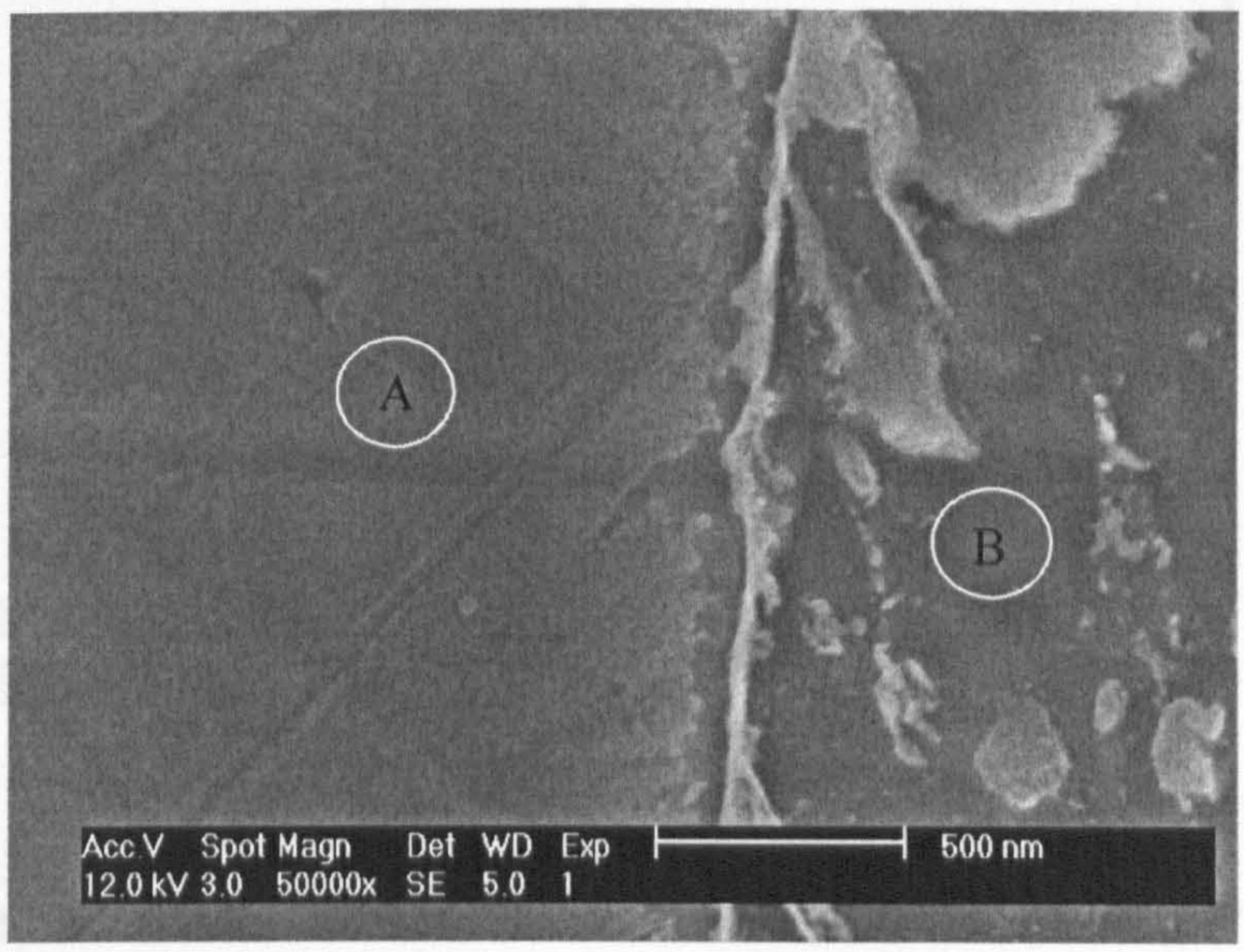

(b) δ-ferrite at higher magnification.

A: 0.5Si-3.5Mo-15.9Cr-75.2Fe-4.9Ni; B: 0.5Si-2.6Mo-13.1Cr-79.1Fe-4.7Ni.

Fig.4.15 SEI SEM micrograph and EDX microanalysis of the as-received slice B3.

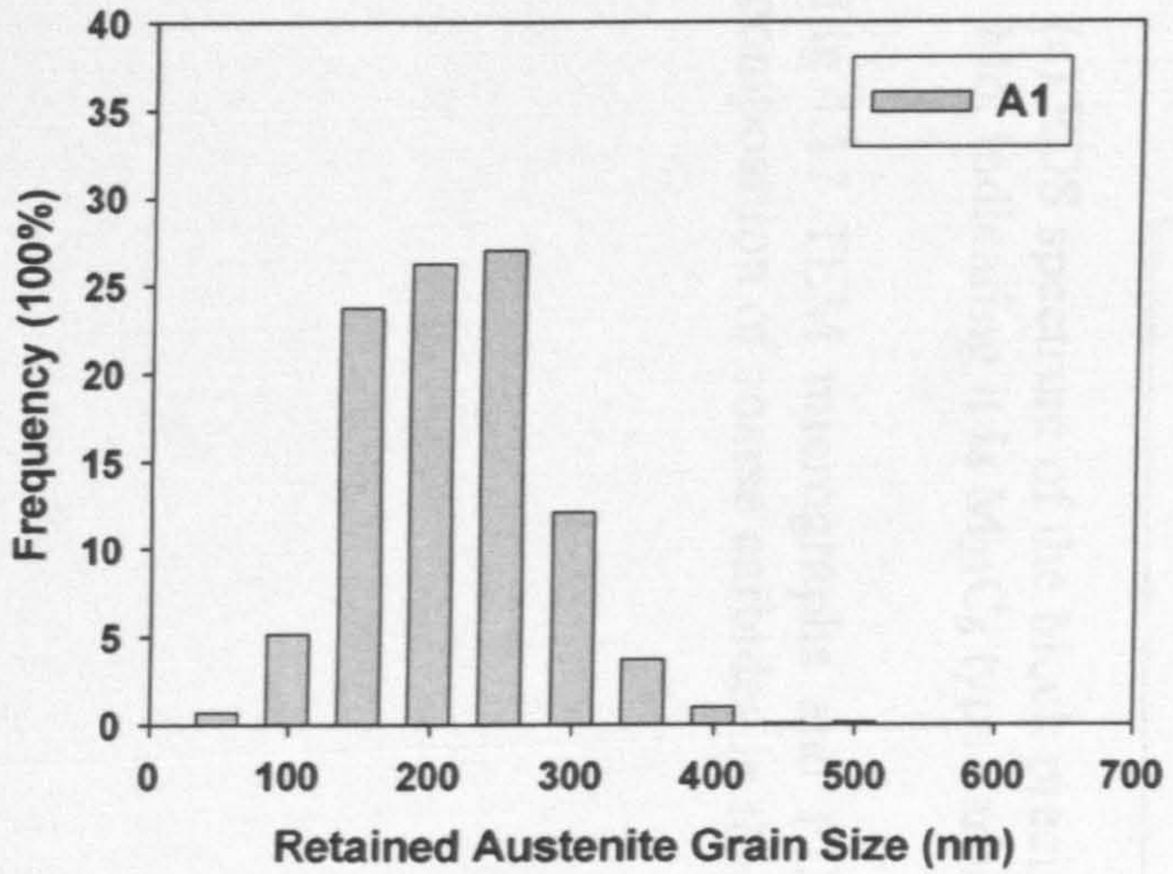

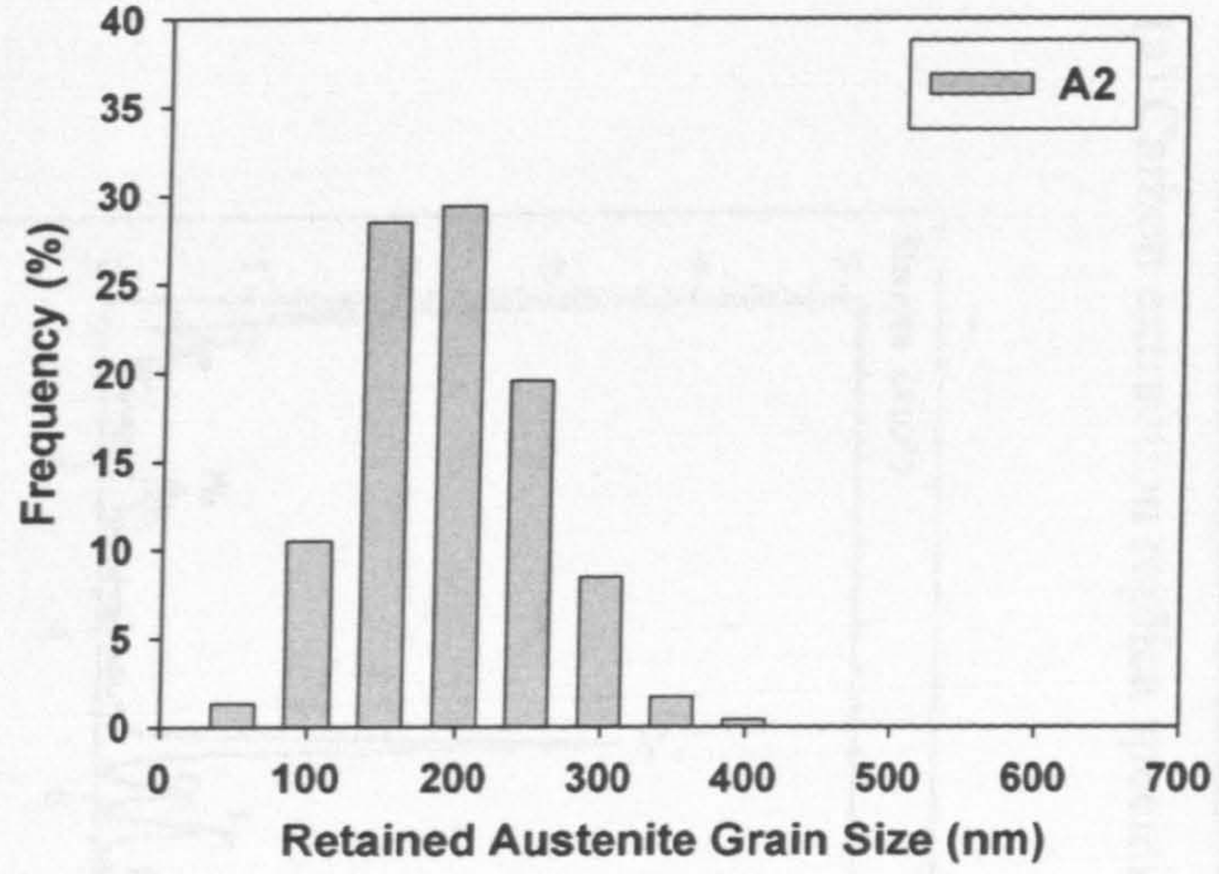

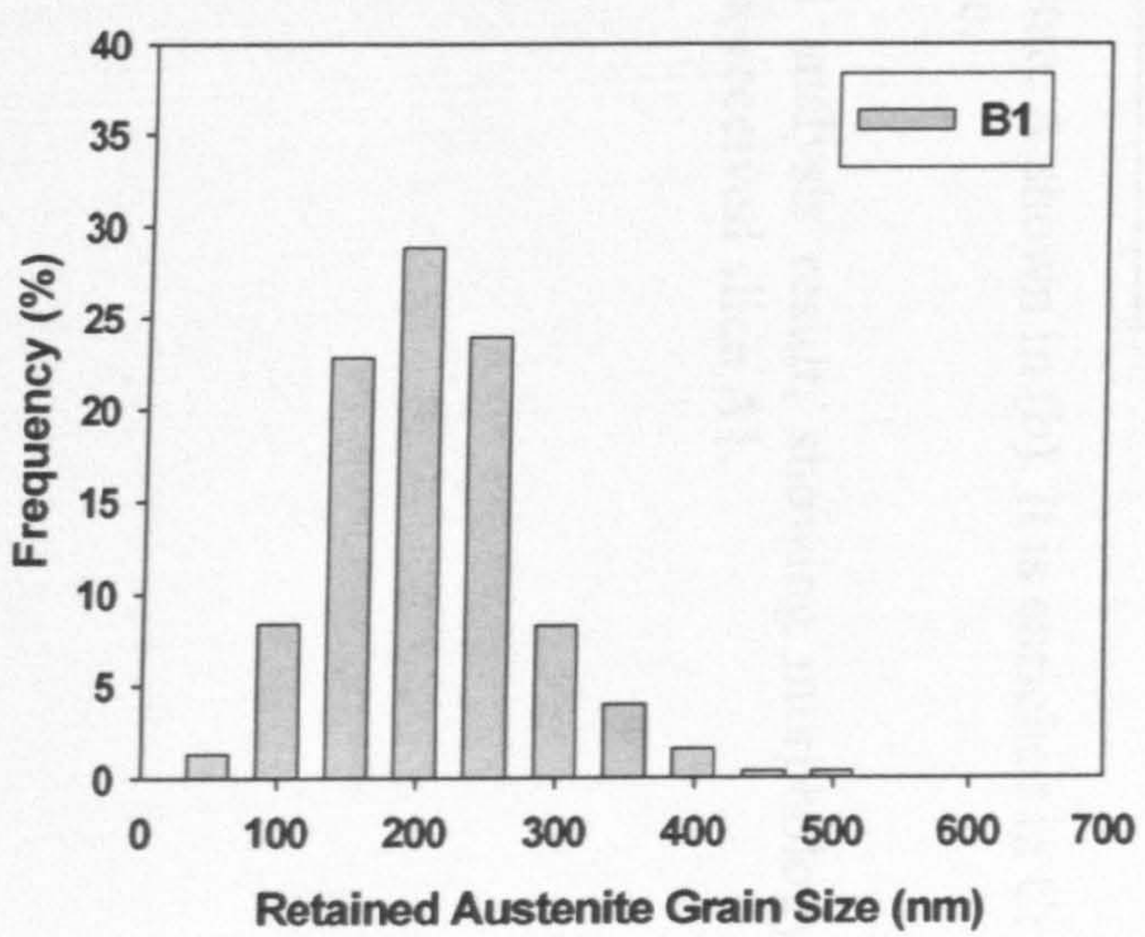

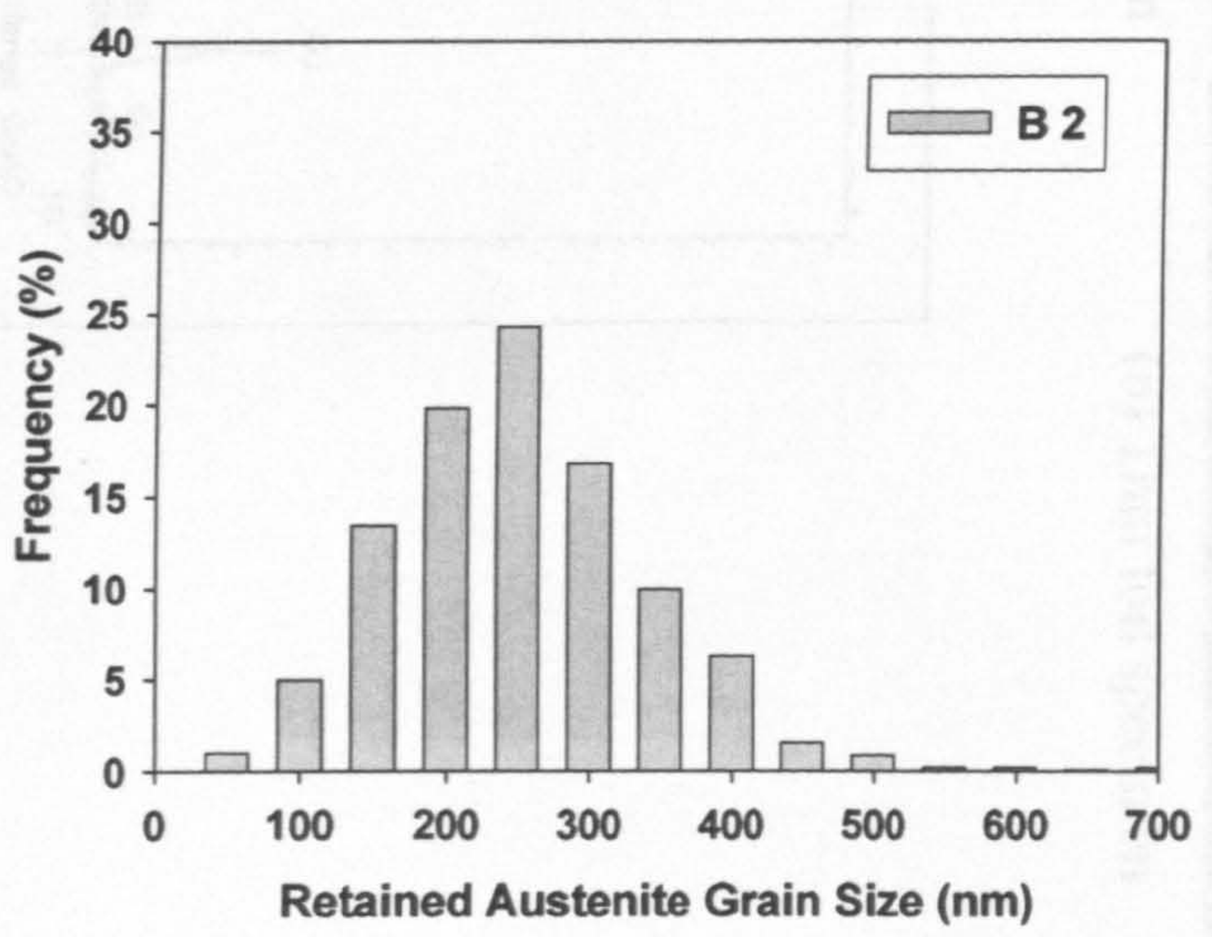

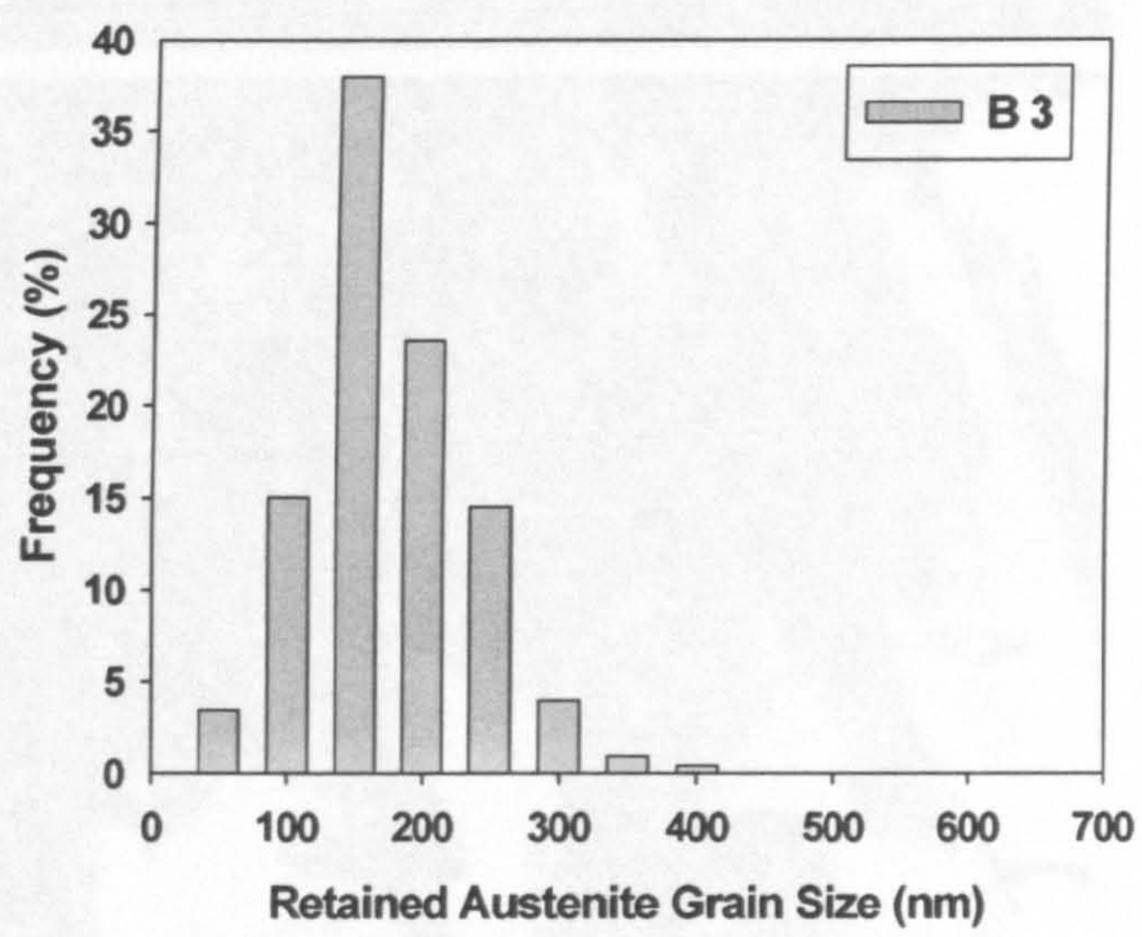

Fig.4.16 Size distribution of retained austenite in the centre of the as- received slices.

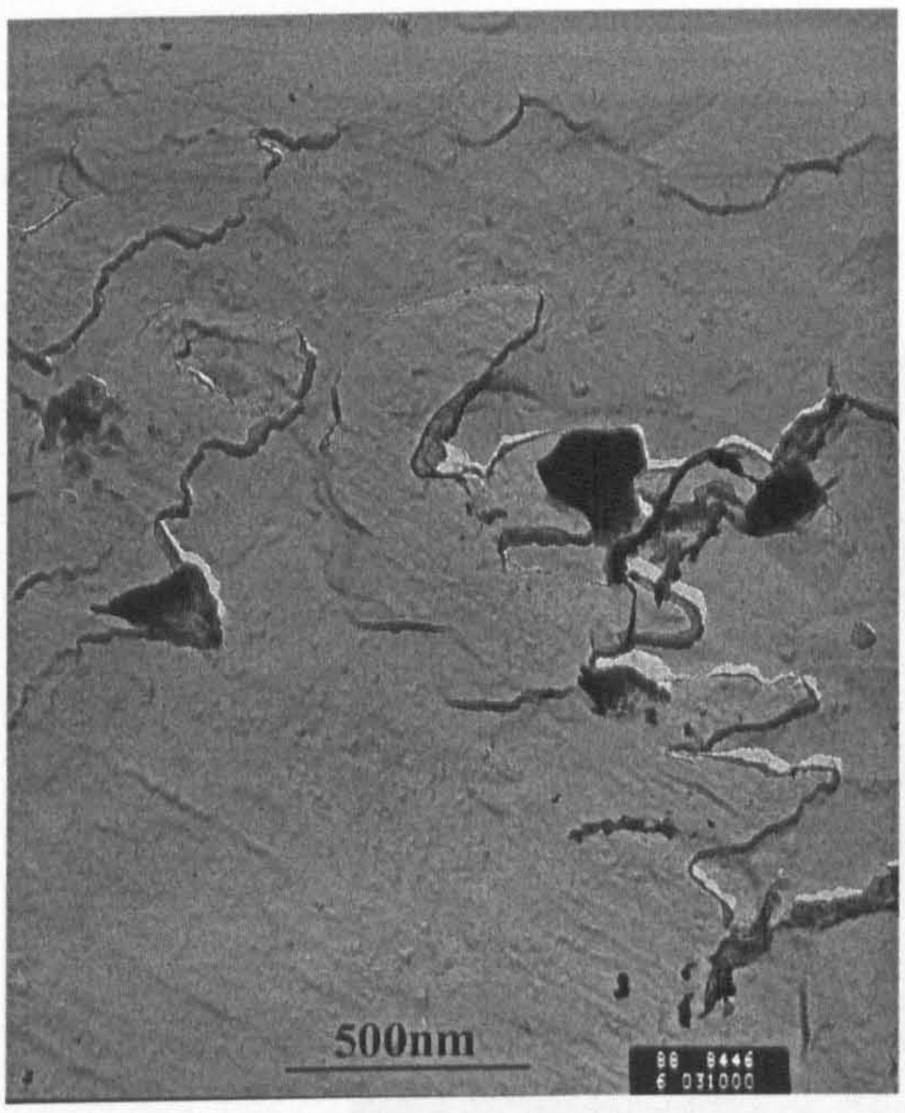

(a) Carbon extraction replica specimen

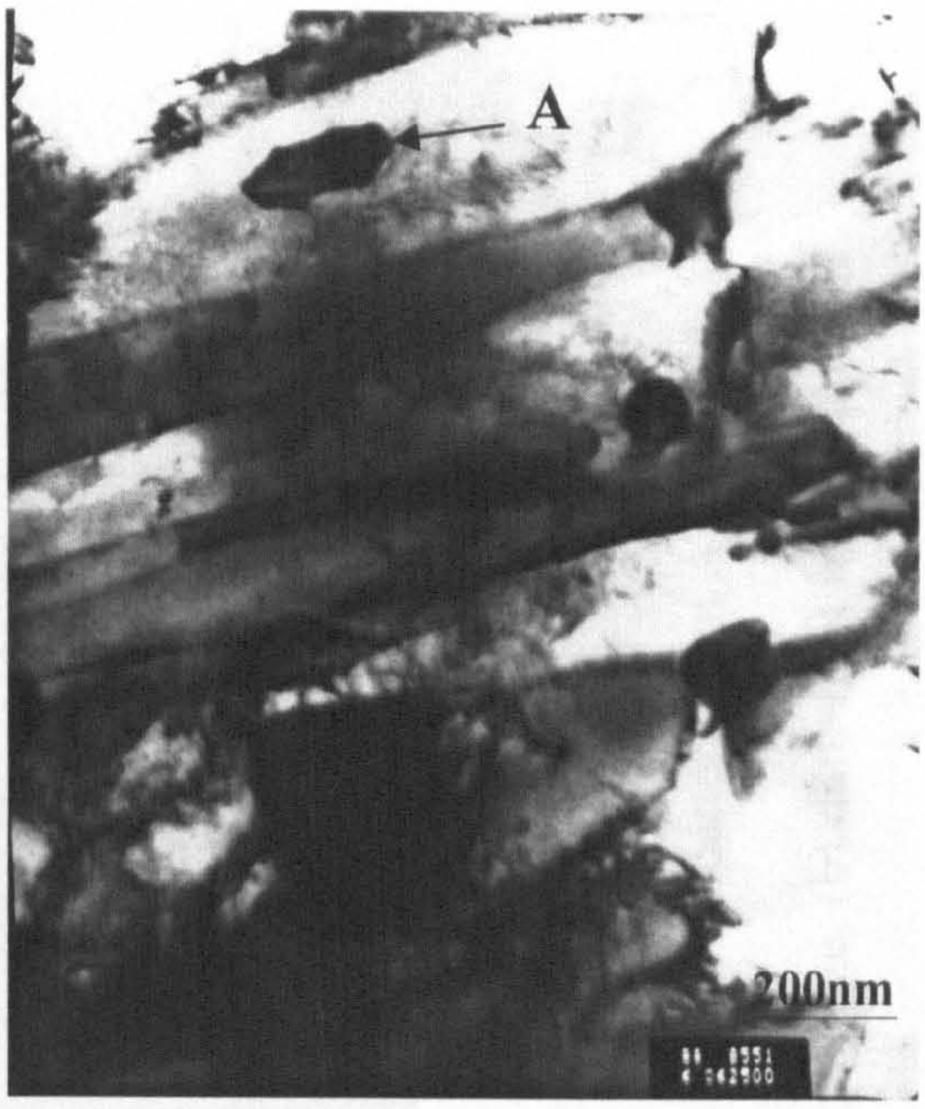

(b) Thin foil specimen

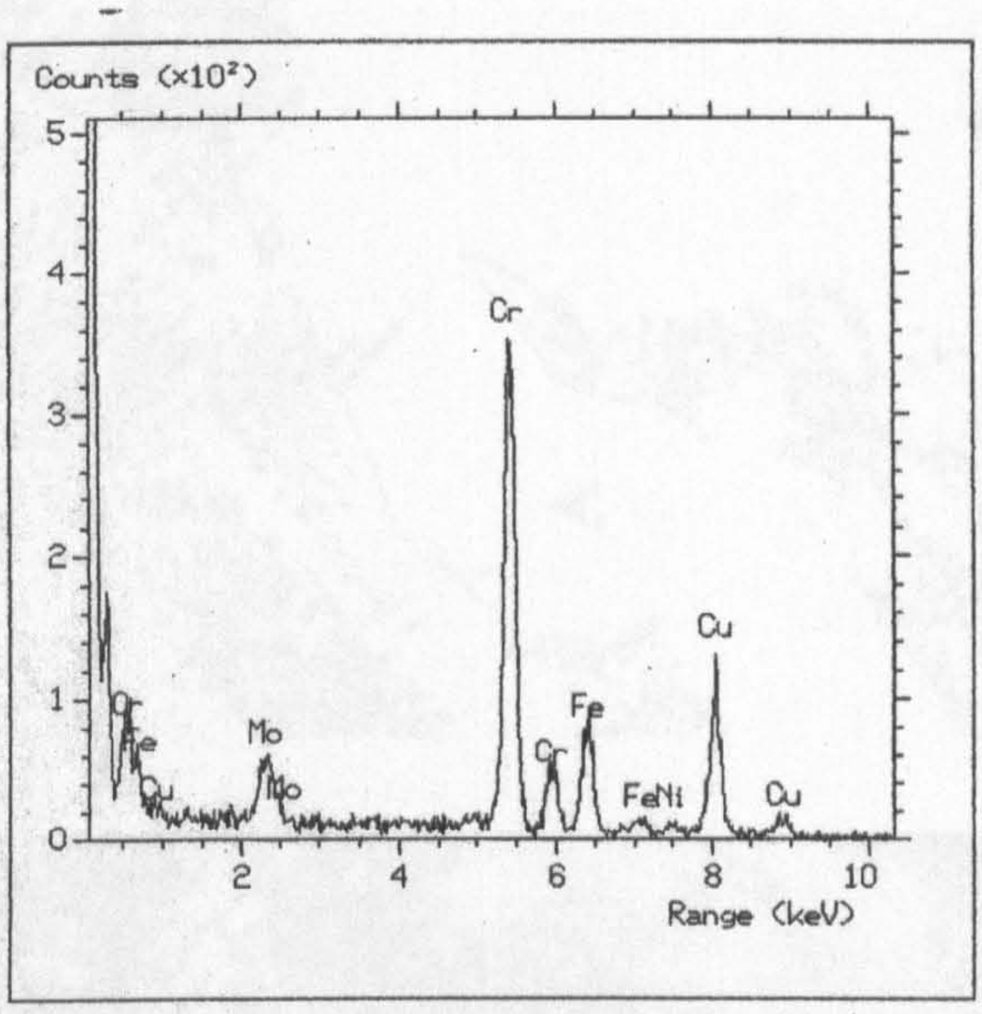

(c) EDS spectrum of the block precipitate A shown in (b). It is enriched in Cr and Mo, indicating it is $M_{23}C_6$ type carbide.

Fig.4.17 TEM micrographs and EDS analysis result, showing morphology and composition of coarse carbides in the as-received slice A1.

(a) Bright field image

(b) Dark field image

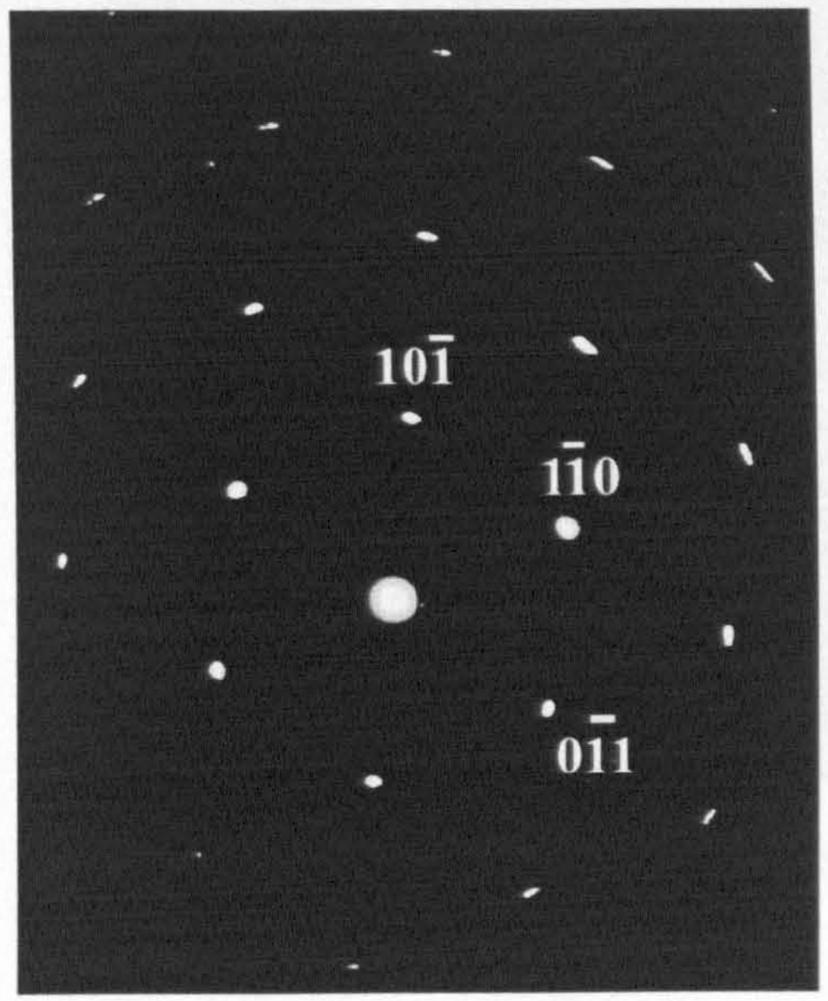

(c) SAD pattern from A, α′ [111]

Fig.4.18 TEM micrographs and SAD pattern of the as-received slice A1. (a) Bright field image, (b) dark field image, and (c) SAD pattern taken from area A in (a), indicating the lath structure is martensite (α′).

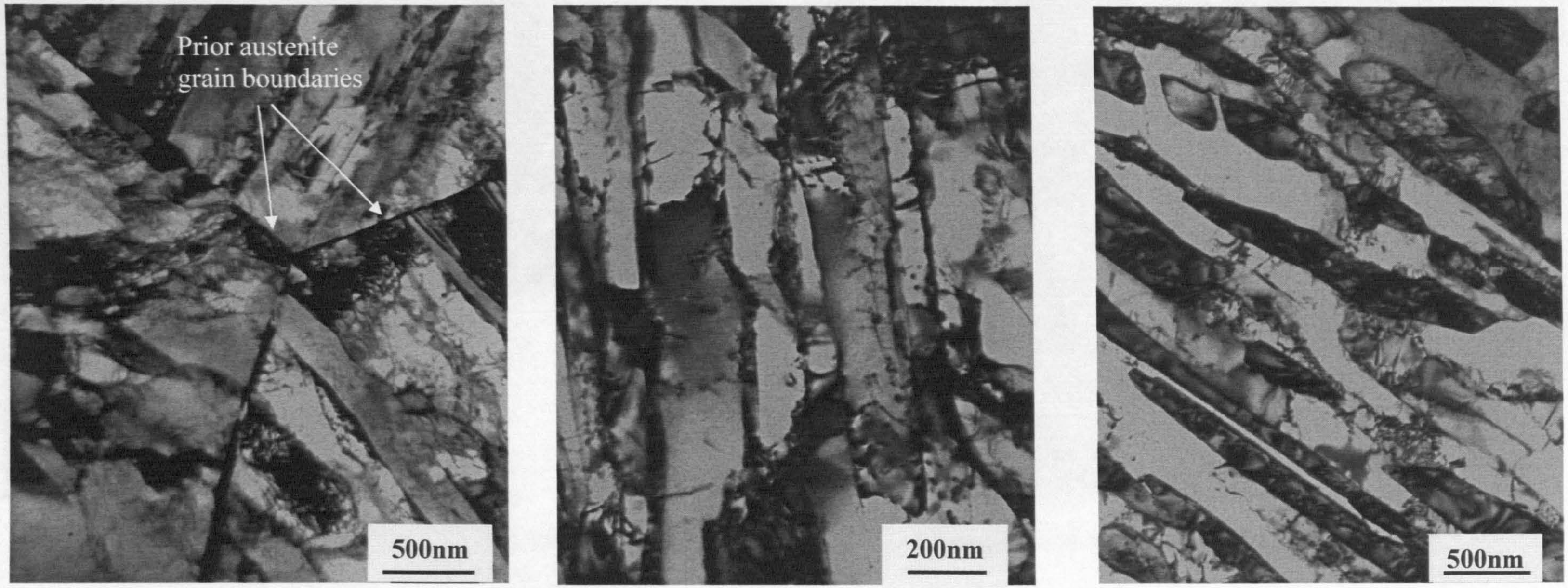

(a) (b) (c)

Fig.4.19 TEM bright field images of the as-received slice A2, showing film/particle-like retained austenite distributed along the martensite lath. A high dislocation density is observed distributed in retained austenite.

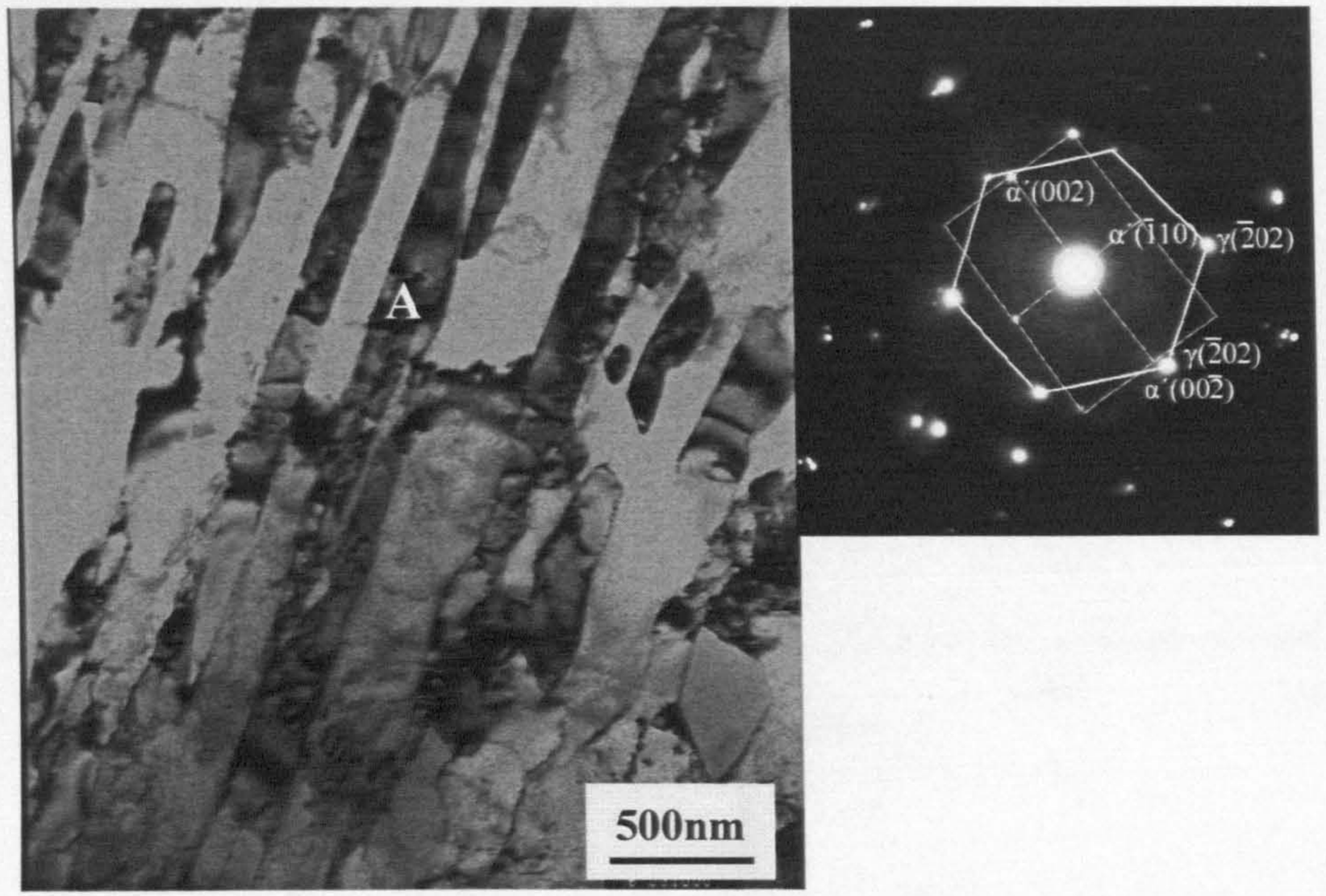

(a) Bright field image

(b) SAD patterns taken from A, showing α′[110] and γ′[111].

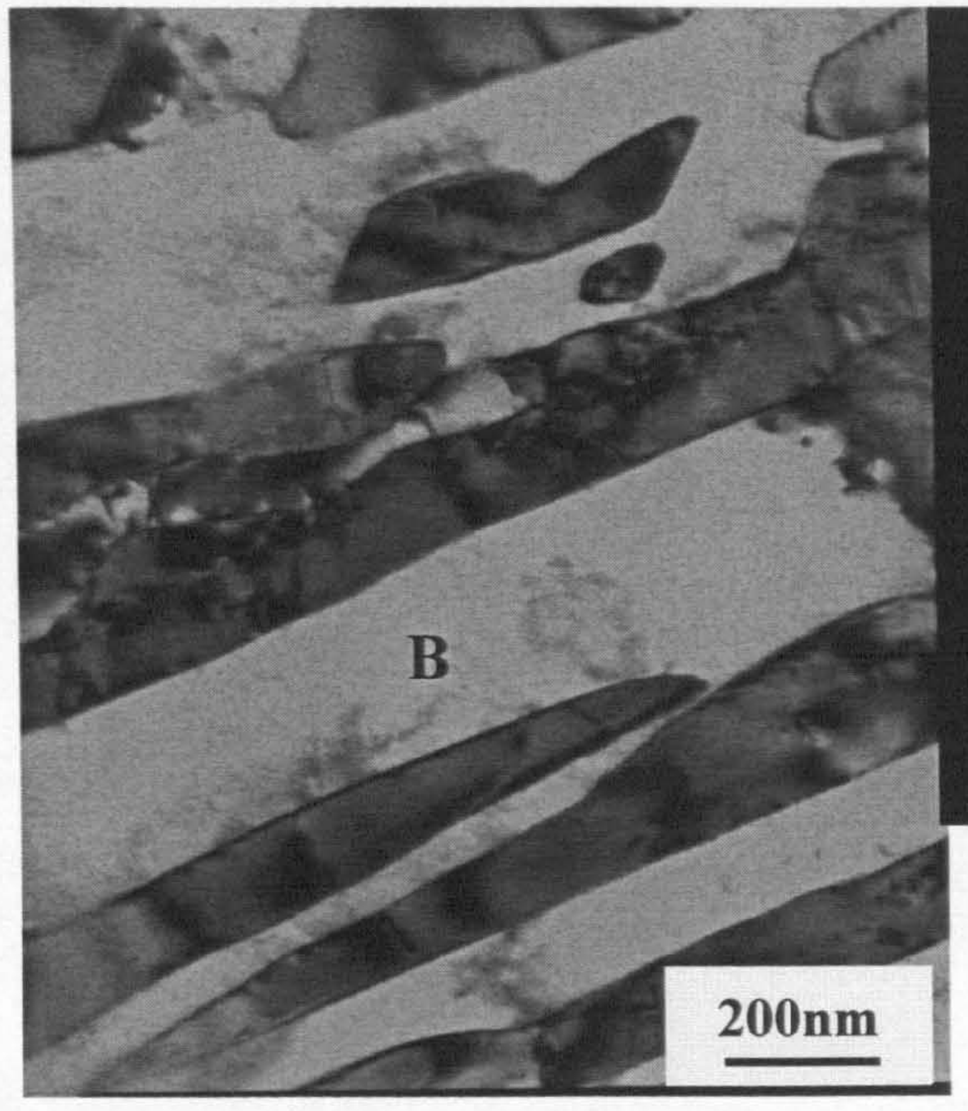

(c) Bright field image

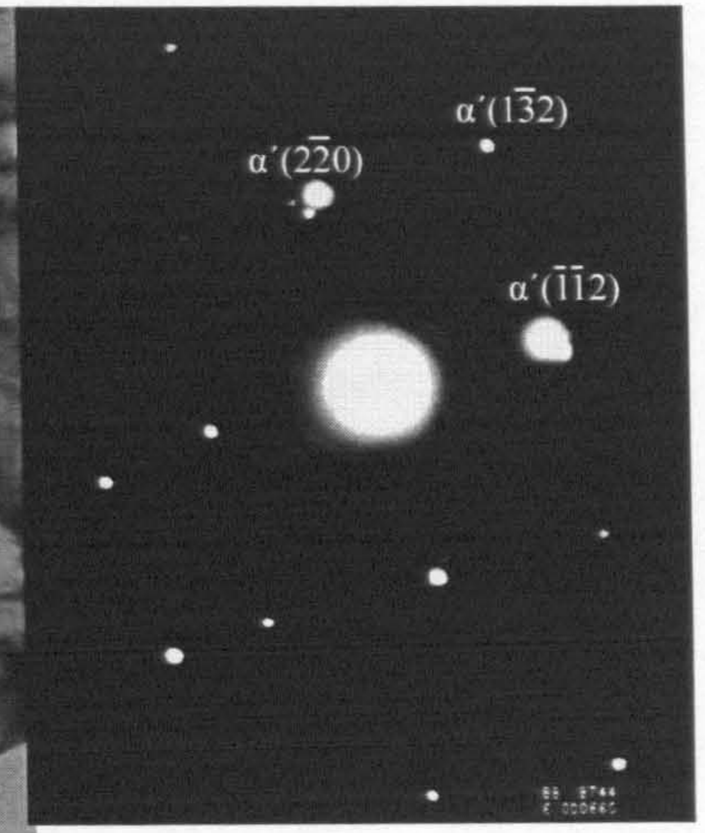

(d) SAD pattern taken from B, showing α′[111].

Fig.4.20 (a) & (c) TEM bright field images of slice A3, showing fine retained austenite distributed along martensite lath boundaries. (b) is SAD patterns taken from A, indicating the presence of retained austenite. (d) is SDA pattern from B, indicating martensite α′.

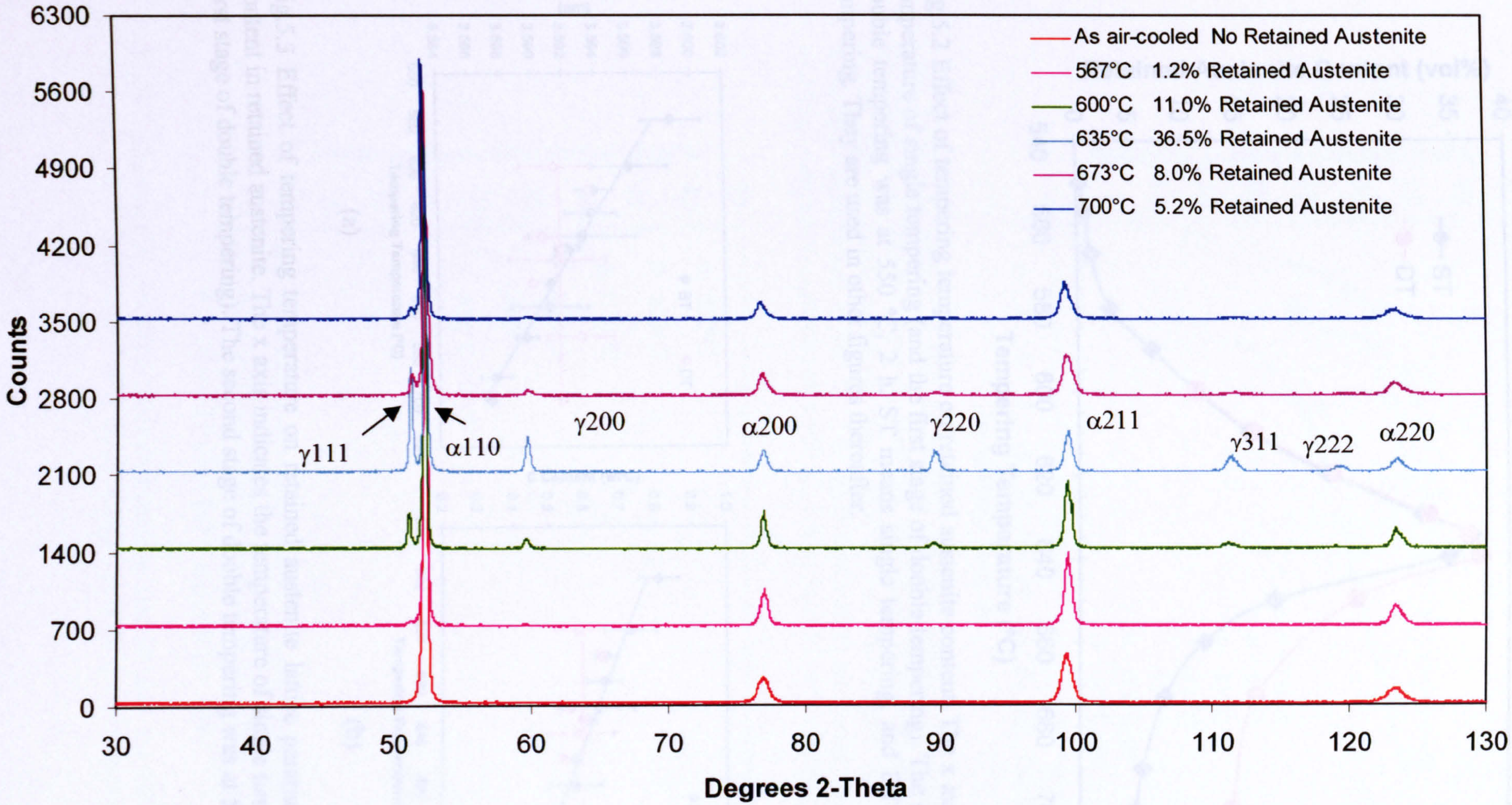

Fig.5.1 X-ray diffraction patterns of retained austenite and martensite in the super 13% steel after air-cooling and tempering. The tempered specimens were heated to 950 °C, held for 2 h and cooled in air before tempering. The tempering time was 4 h.

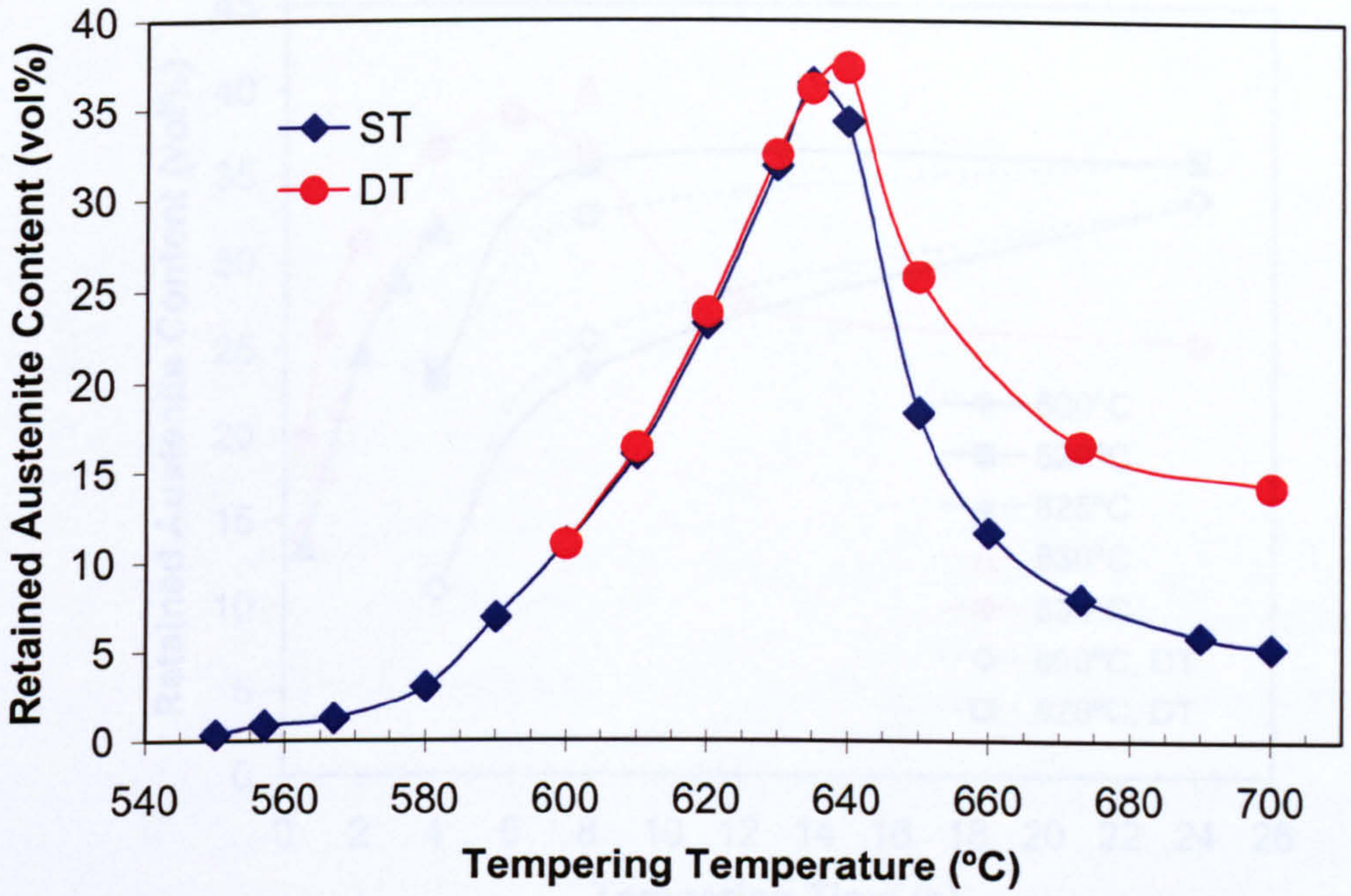

Fig.5.2 Effect of tempering temperature on retained austenite content. The x axis indicates the temperature of single tempering (and the first stage of double tempering). The second stage of double tempering was at 550 °C, 2 h. ST means single tempering, and DT means double tempering. They are used in other figures thereafter.

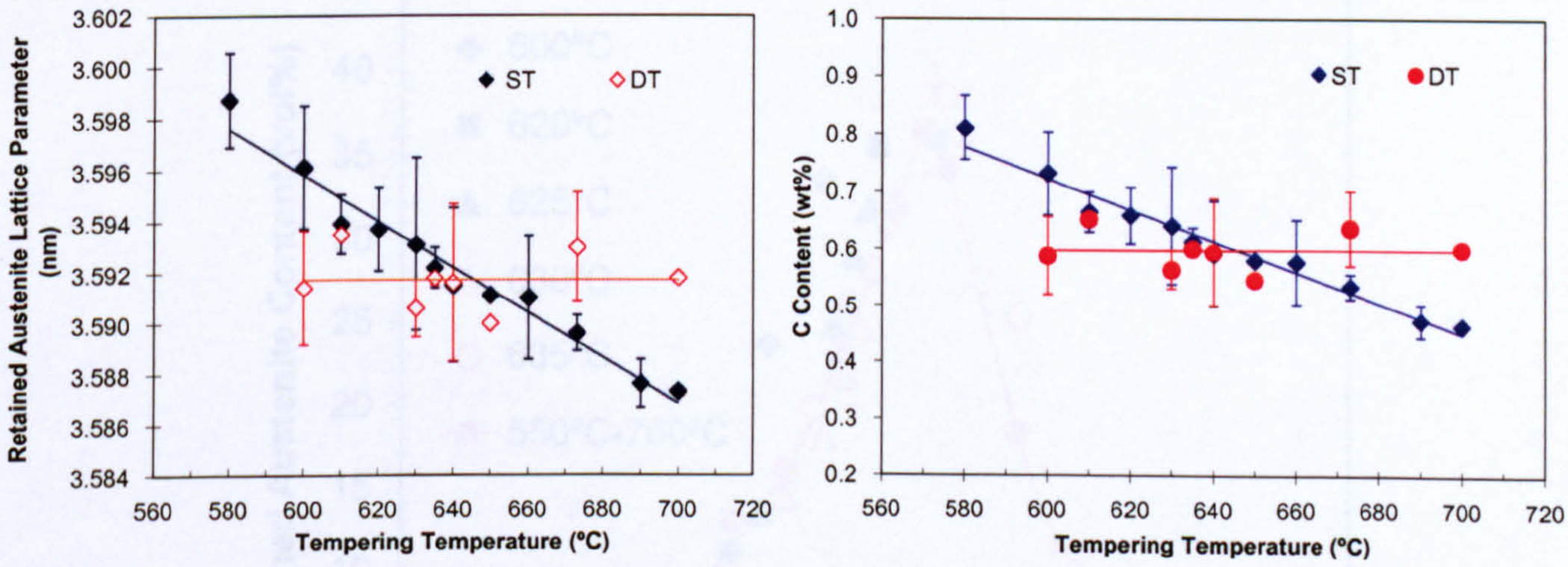

Fig.5.3 Effect of tempering temperature on retained austenite lattice parameter and carbon content in retained austenite. The x axis indicates the temperature of single tempering (and the first stage of double tempering). The second stage of double tempering was at 550 °C, 2 h.

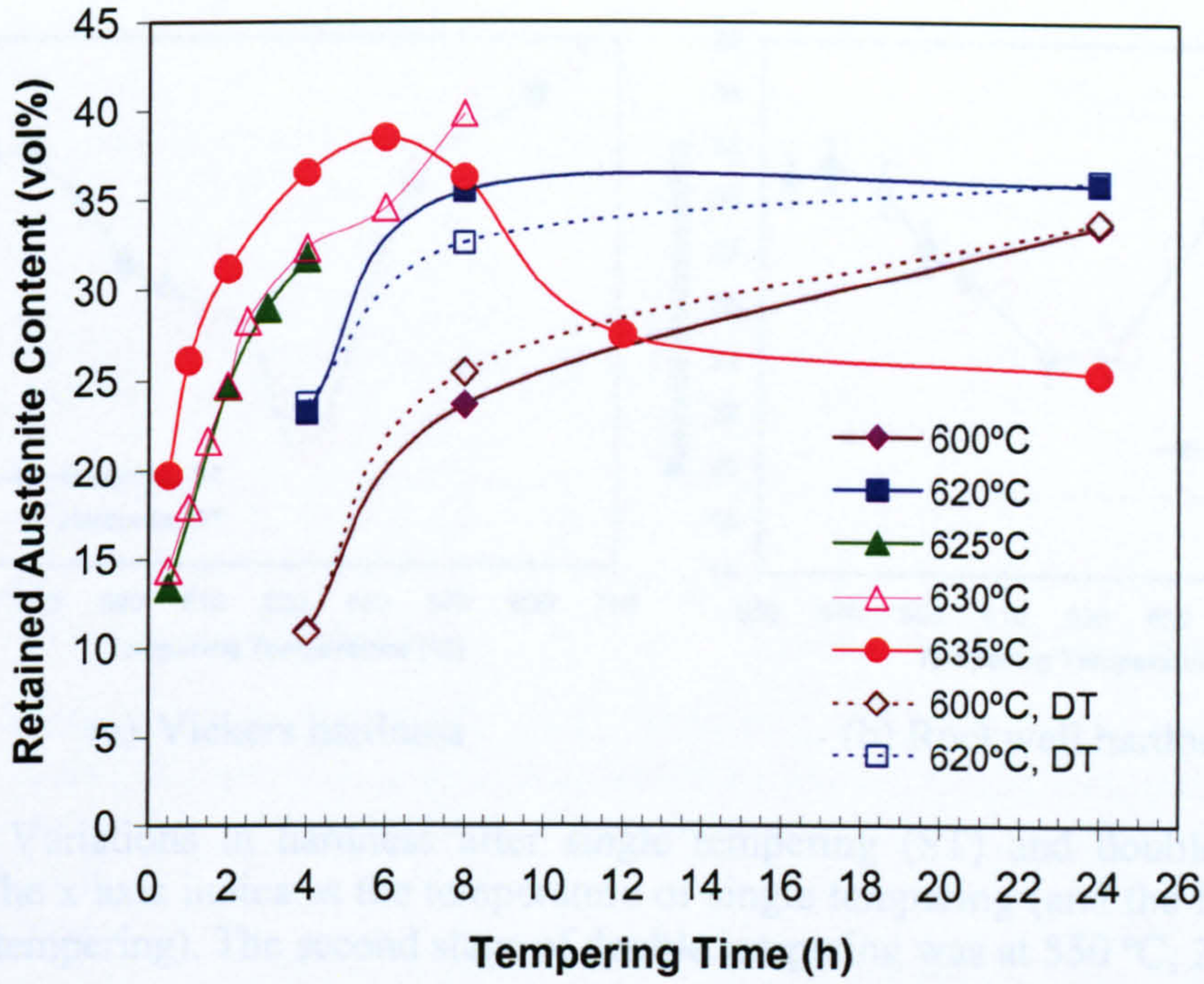

Fig.5.4 Effect of tempering time on retained austenite content. The legend presents temperatures of single tempering (and the first stage of double tempering). The second stage of double tempering was at 550 °C, 2 h. The samples tempered at 630 °C were re-austenitized at 940 °C, 2 h, air-cooled before tempering. All other data was from samples re-austenitized at 950 °C, 2 h, air-cooled before tempering.

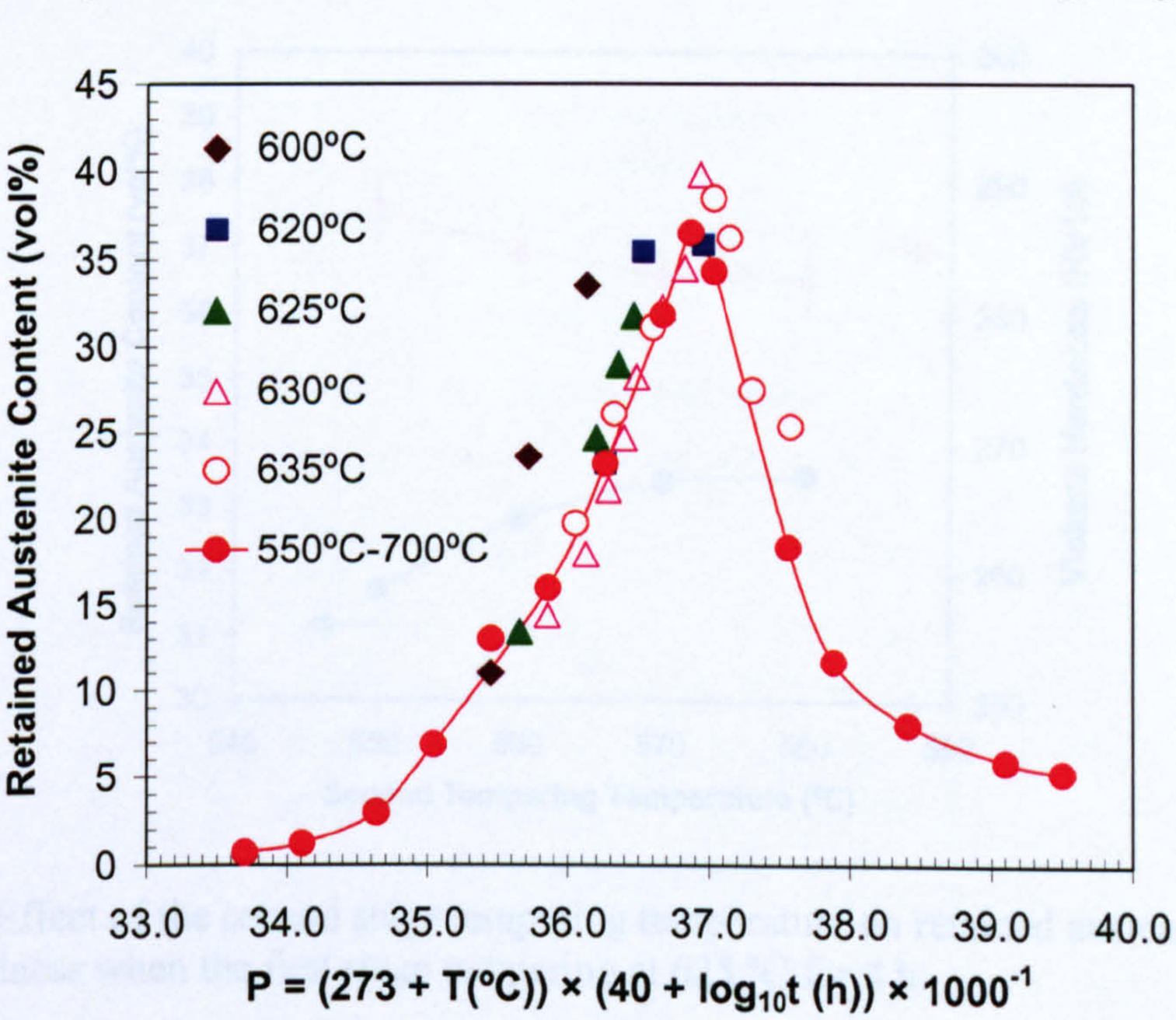

Fig.5.5 Relationship between retained austenite content and the Hollomon-Jaffe time-temperature parameter P after single tempering at different temperature/time.

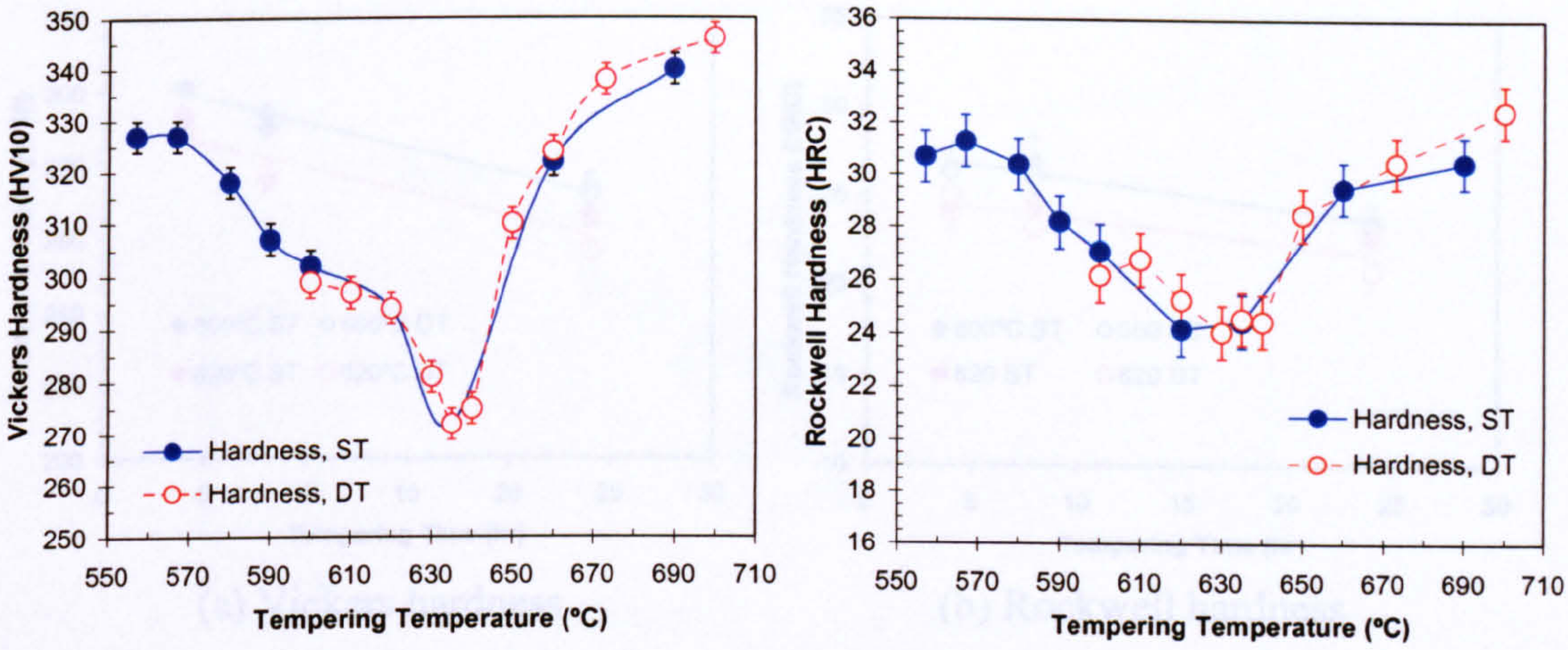

(a) Vickers hardness (b) Rockwell hardness

Fig.5.6 Variations in hardness after single tempering (ST) and double tempering (DT). The x axis indicates the temperature of single tempering (and the first stage of double tempering). The second stage of double tempering was at 550 °C, 2 h.

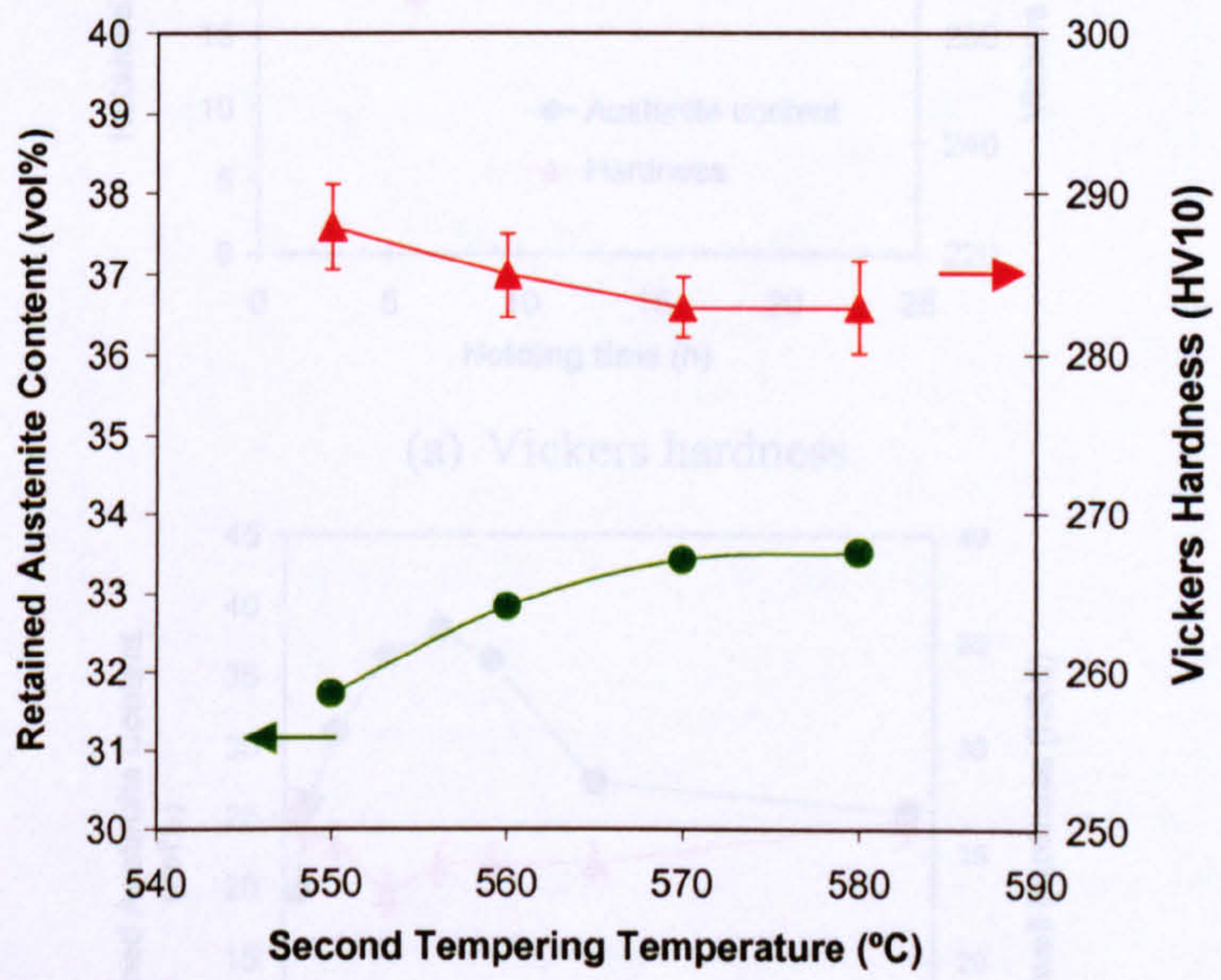

Fig.5.7 Effect of the second stage tempering temperature on retained austenite content and hardness when the first stage tempering at 625 °C for 4 h.

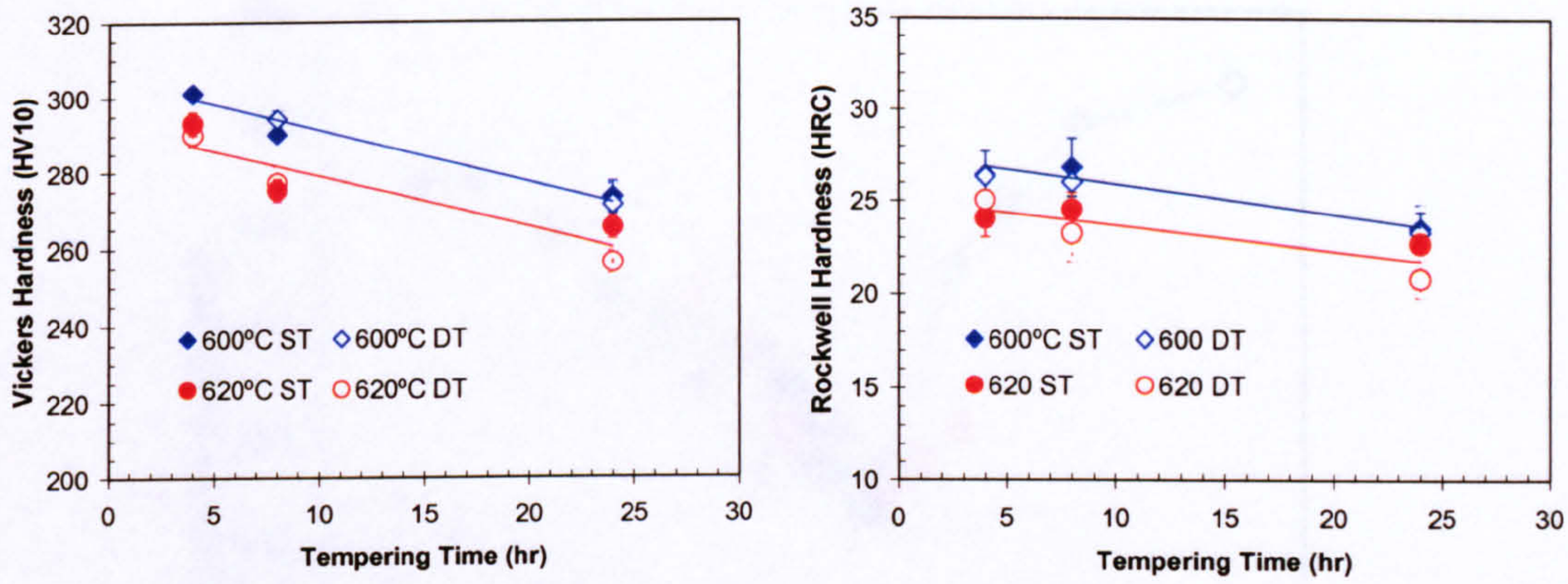

(a) Vickers hardness (b) Rockwell hardness

Fig.5.8 Variations in hardness after single tempering (ST) and double tempering (DT) at different time. The x axis indicates the time for single tempering (and the first stage of double tempering). The second stage of double tempering was at 550 ºC, 2 h.

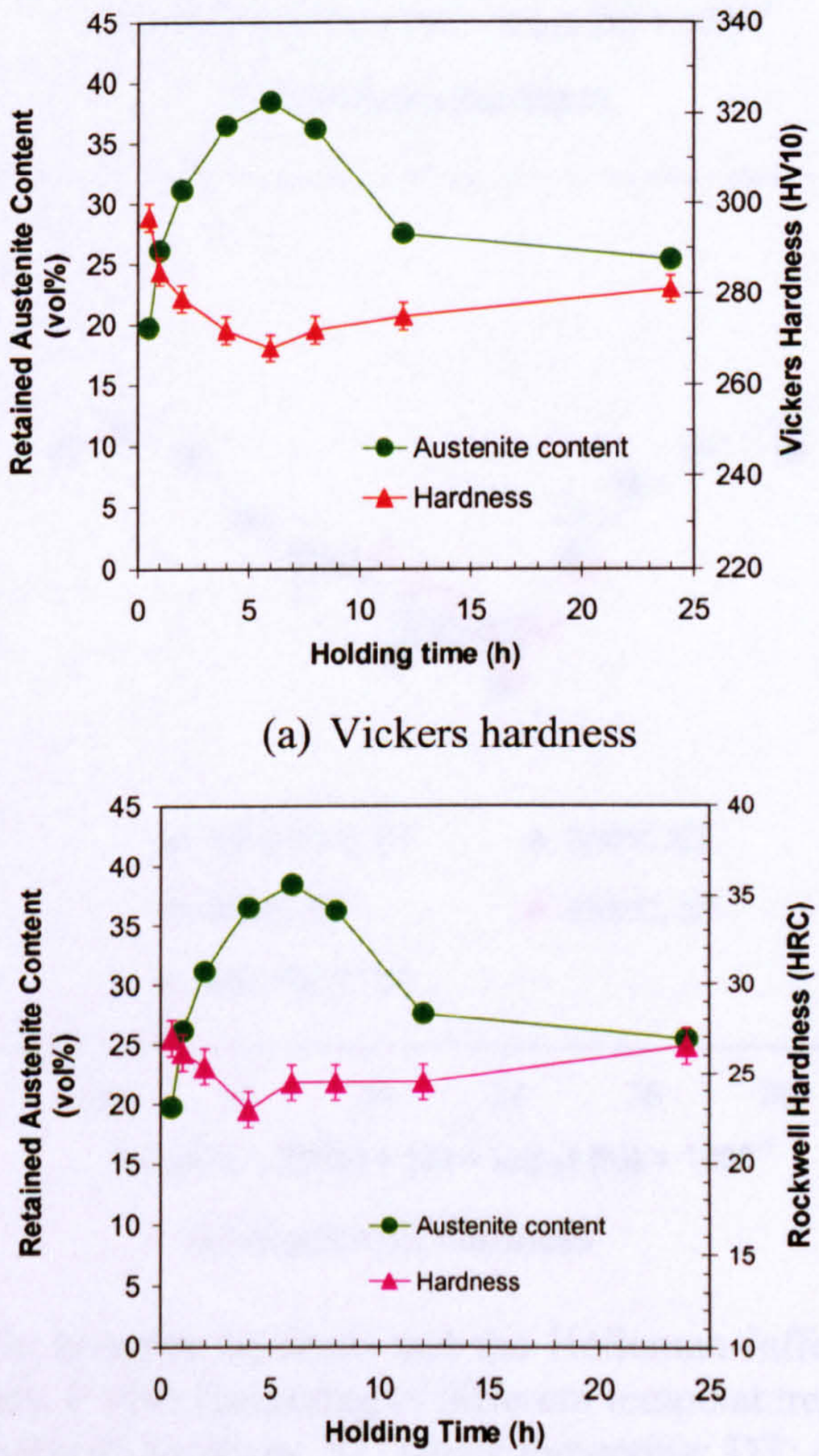

(a) Vickers hardness

(b) Rockwell hardness

Fig. 5.9 Variations in hardness after tempering at 635 ºC for different time.

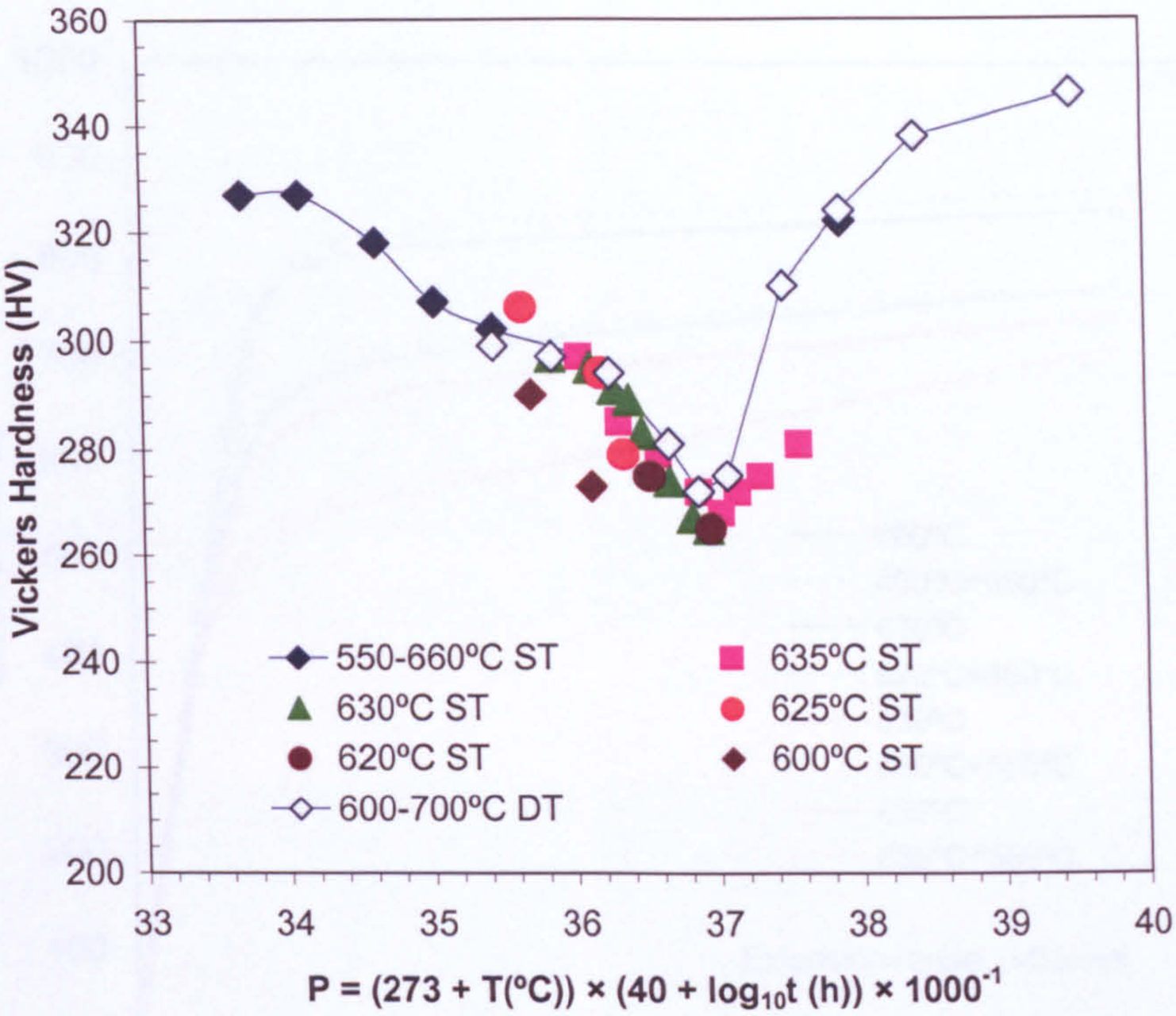

(a) Vickers hardness

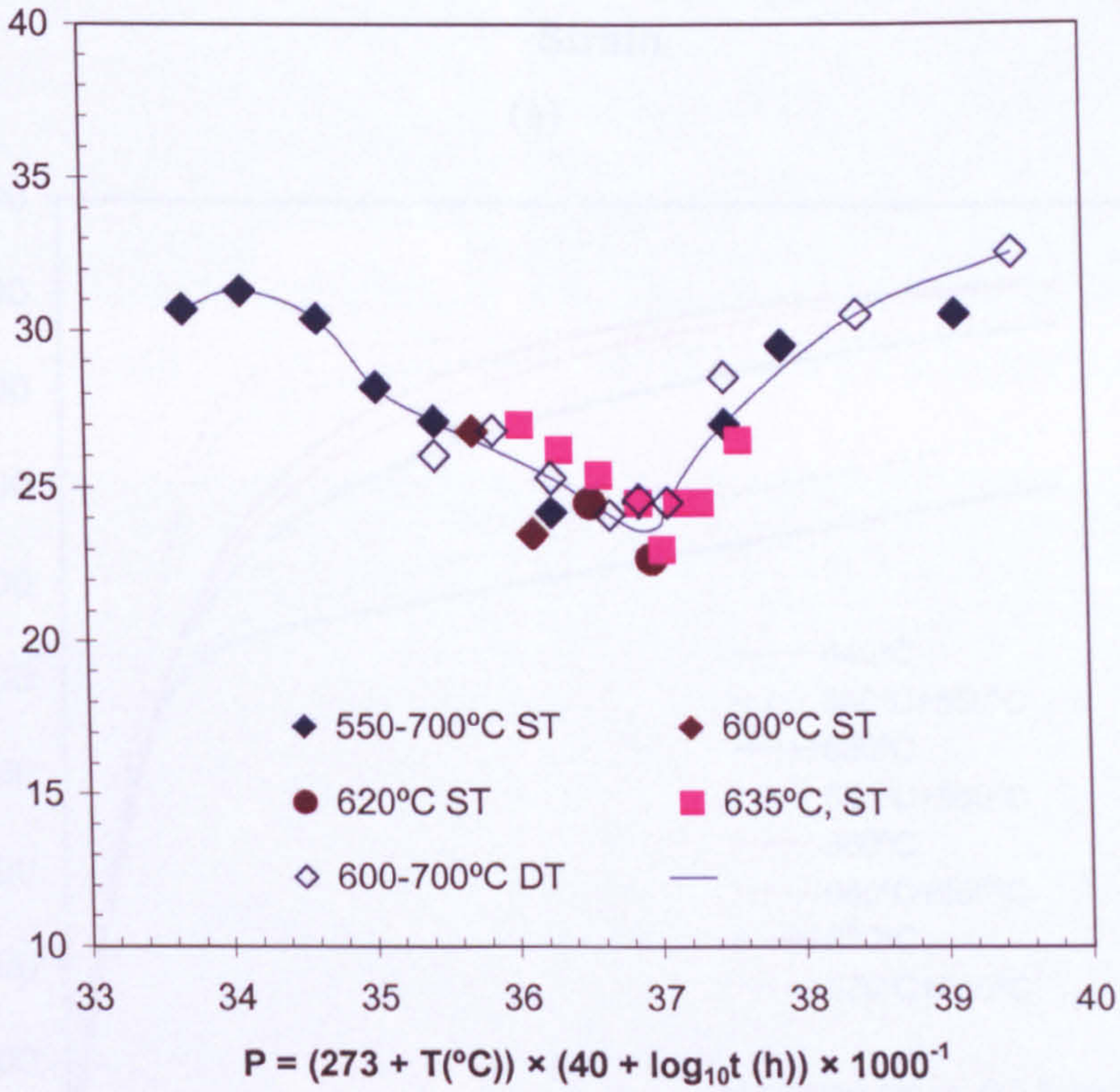

(b) Rockwell hardness

Fig.5.10 Relationship between hardness and the Holloman-Jaffe tempering time-temperature parameter P after tempering at different temperature/time. (a) Vickers hardness and (b) Rockwell hardness. ST: single tempering; DT: double tempering. The ledge represents the temperature for single tempering and the first stage of double tempering. The second stage of double tempering was at 550 °C for 2 h.

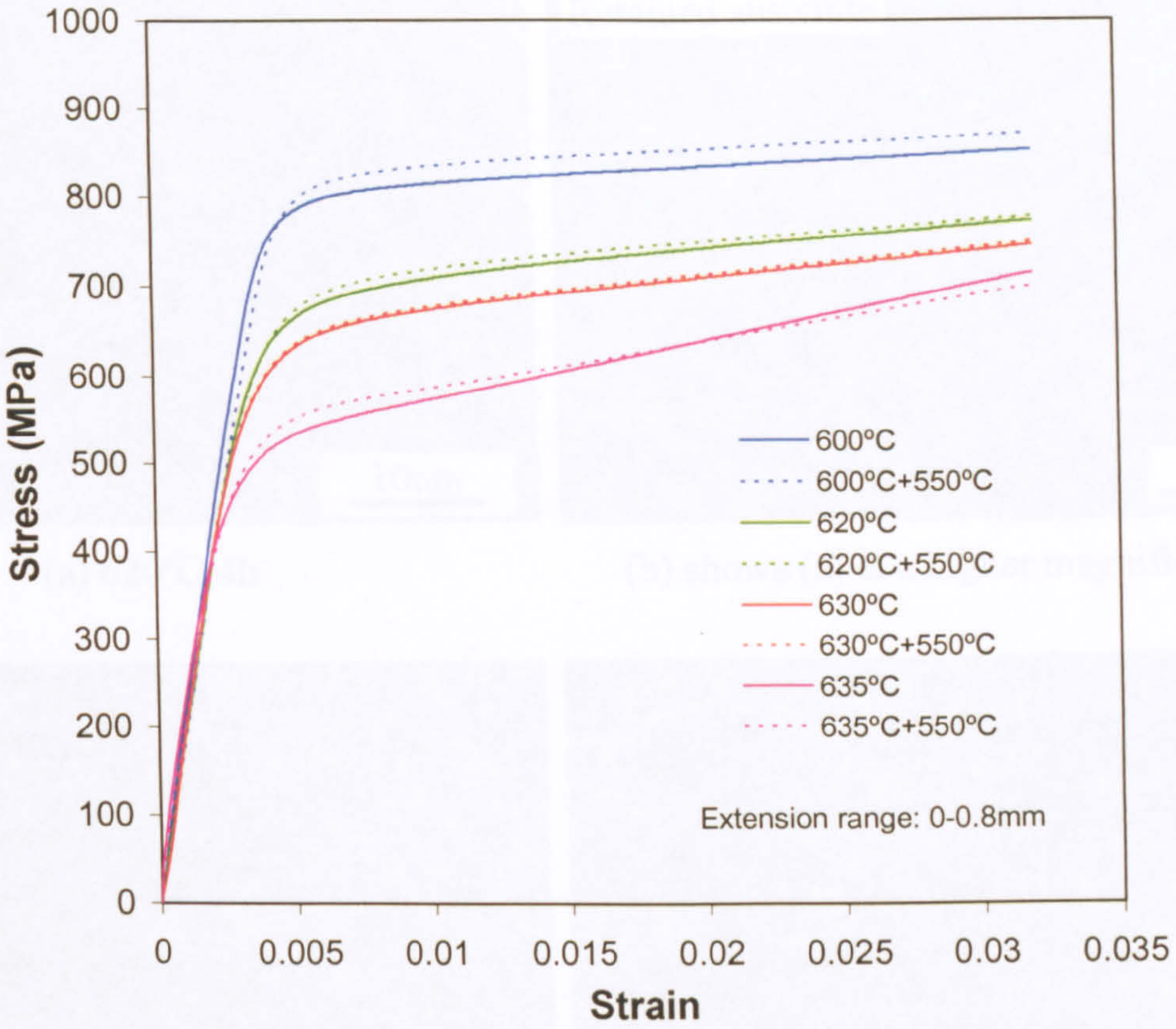

(a)

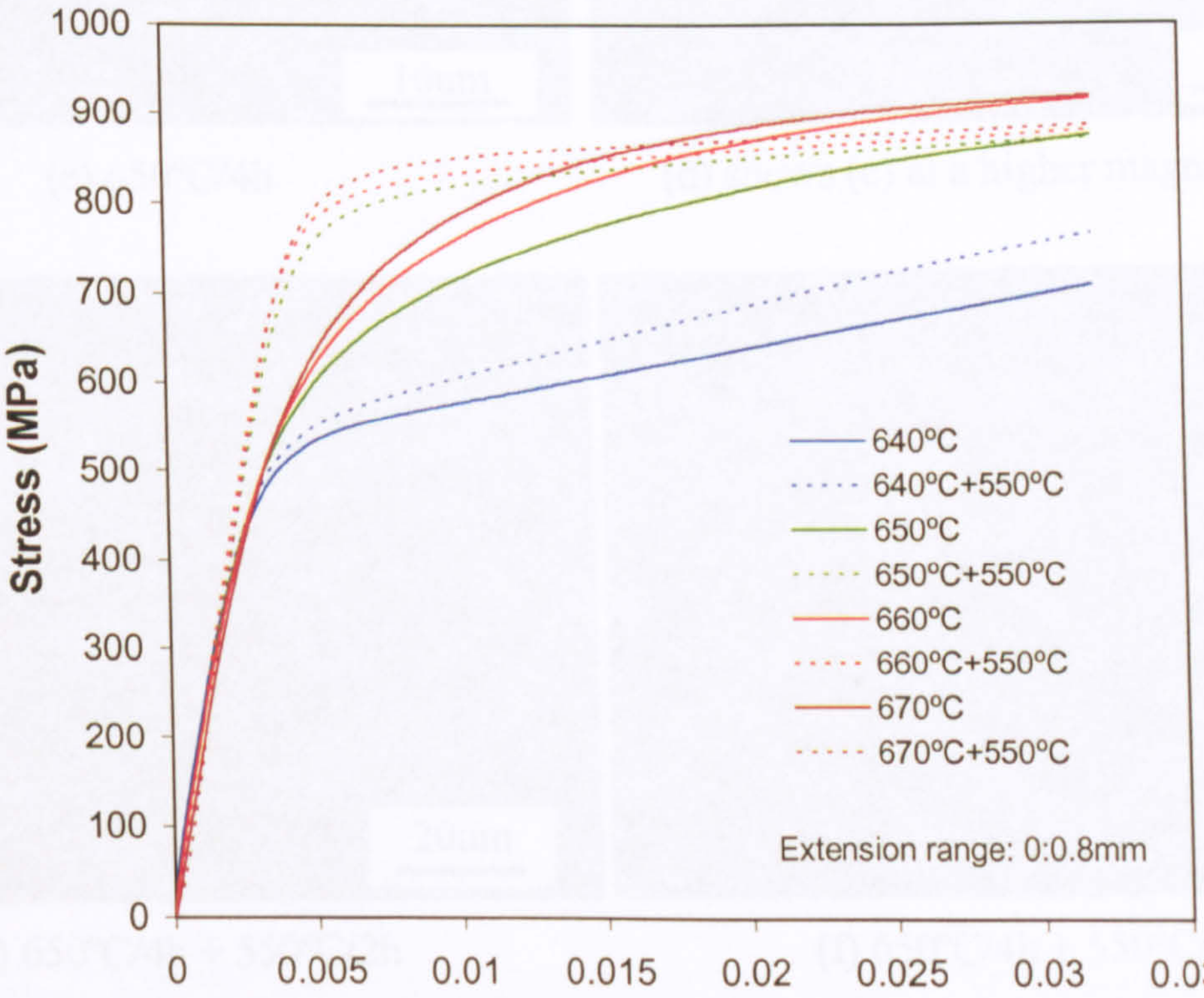

(b)

Fig.5.11 Tensile strain-stress curves of the specimens after single and double tempering.

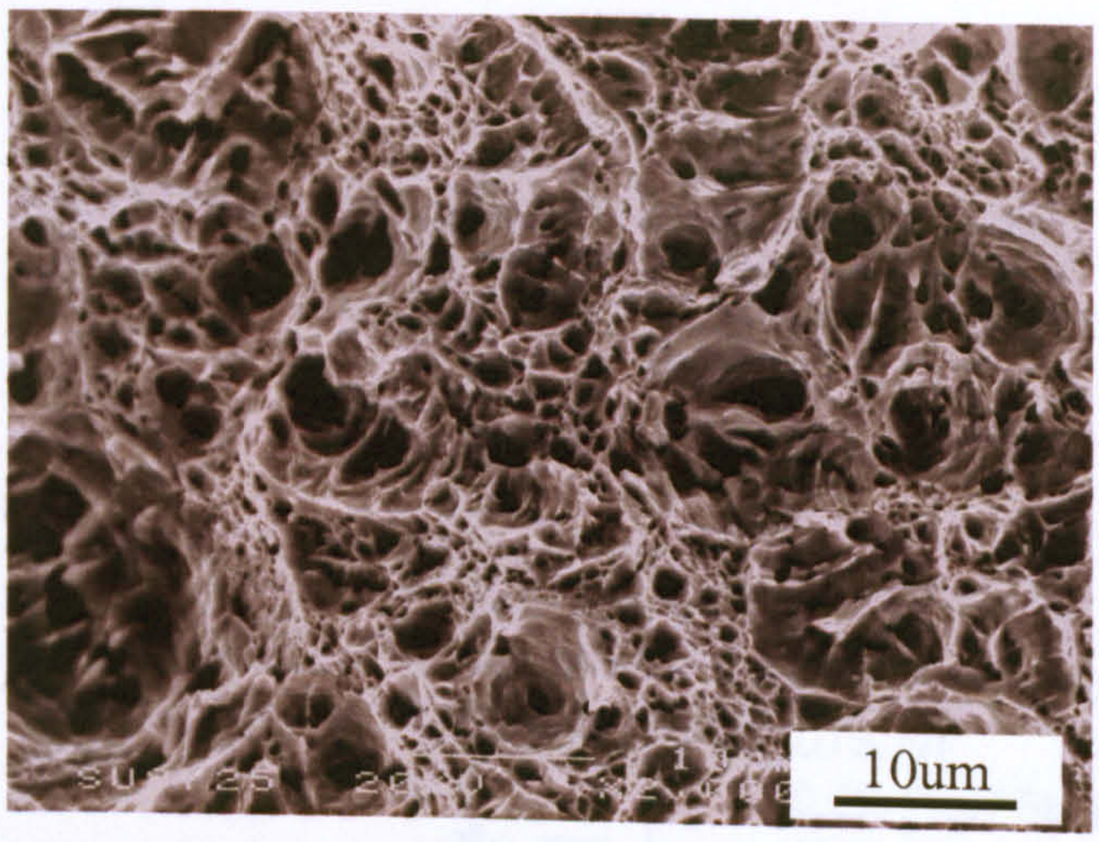

(a) 620°C/4h

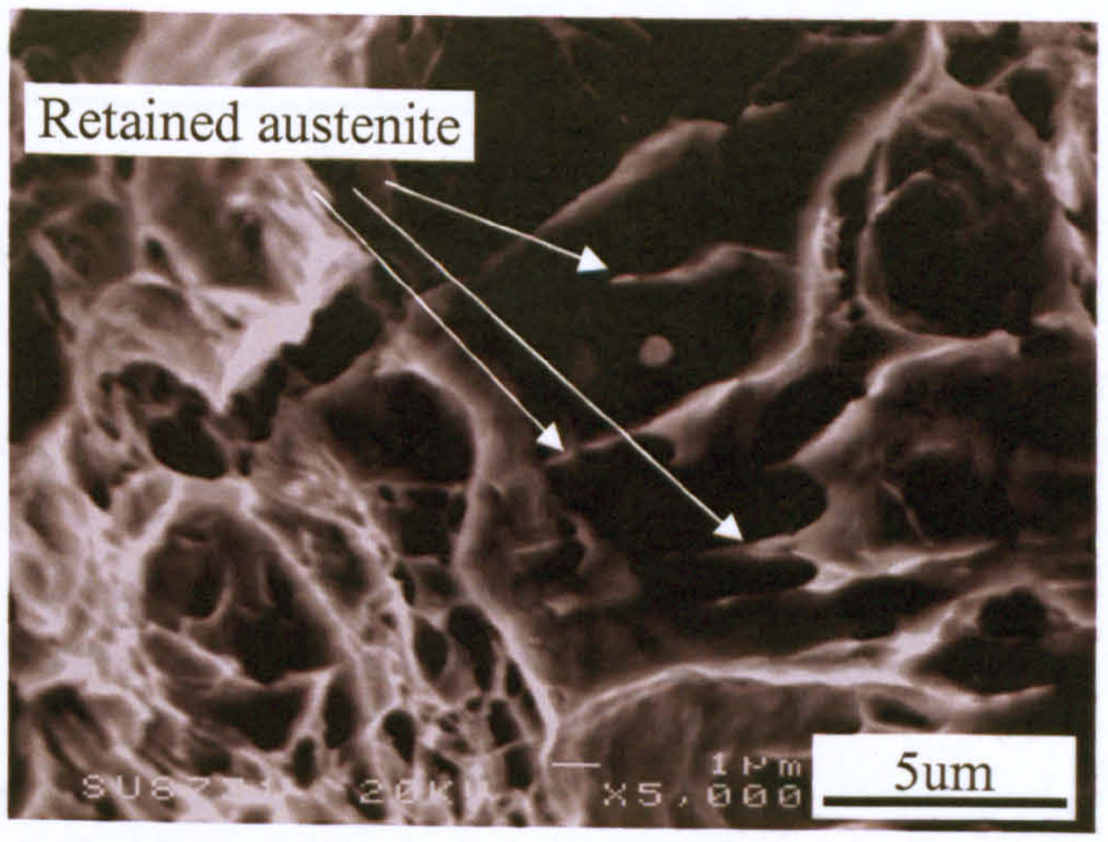

(b) shows (a) at a higher magnification.

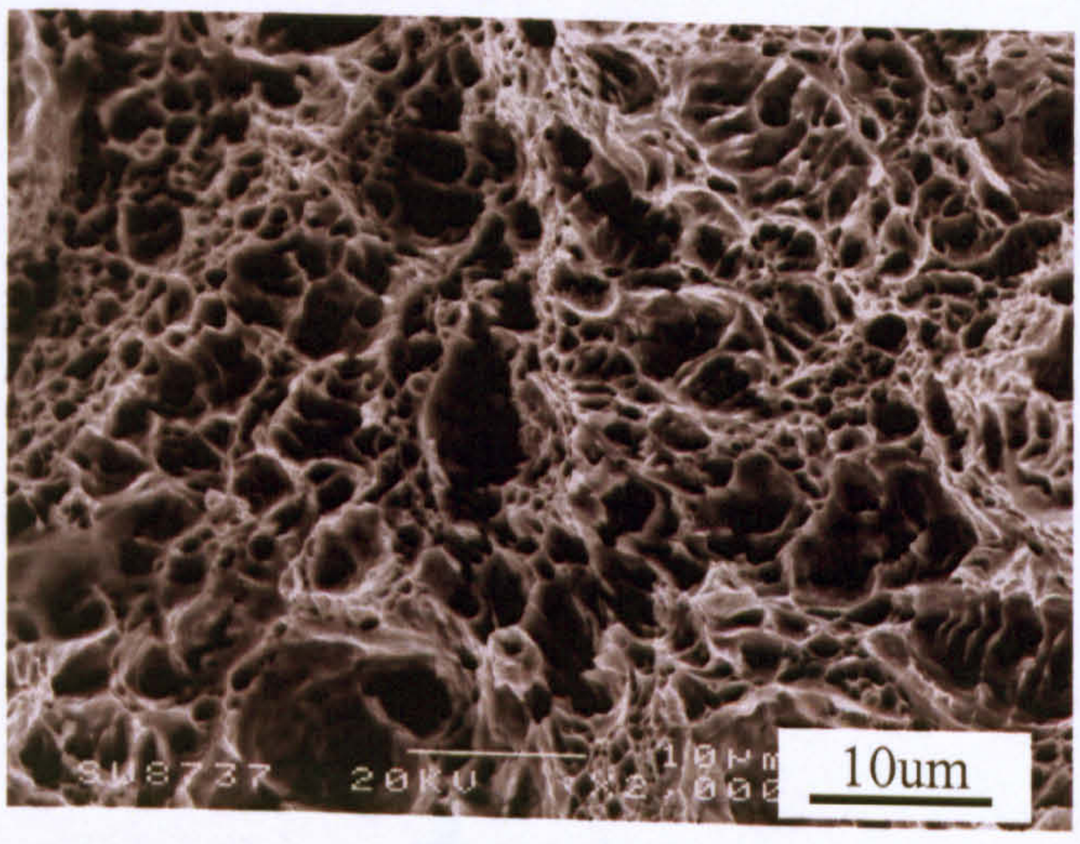

(c) 650°C/4h

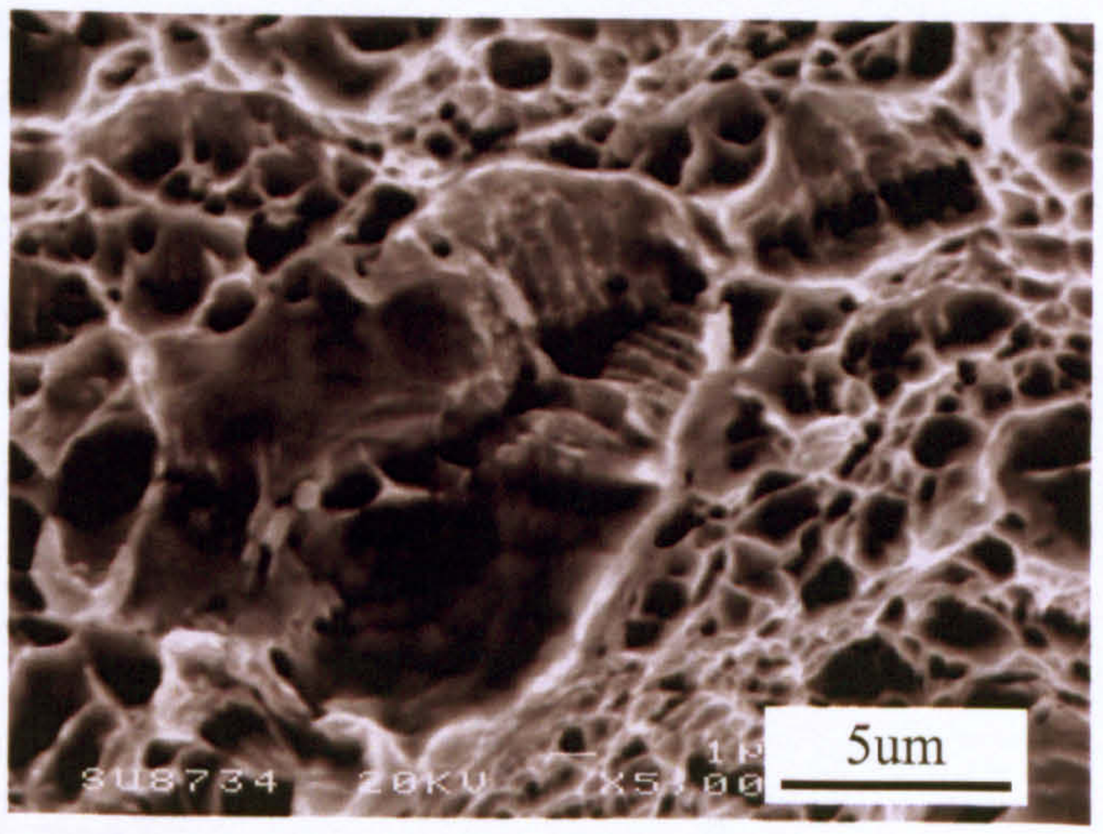

(d) shows (c) at a higher magnification.

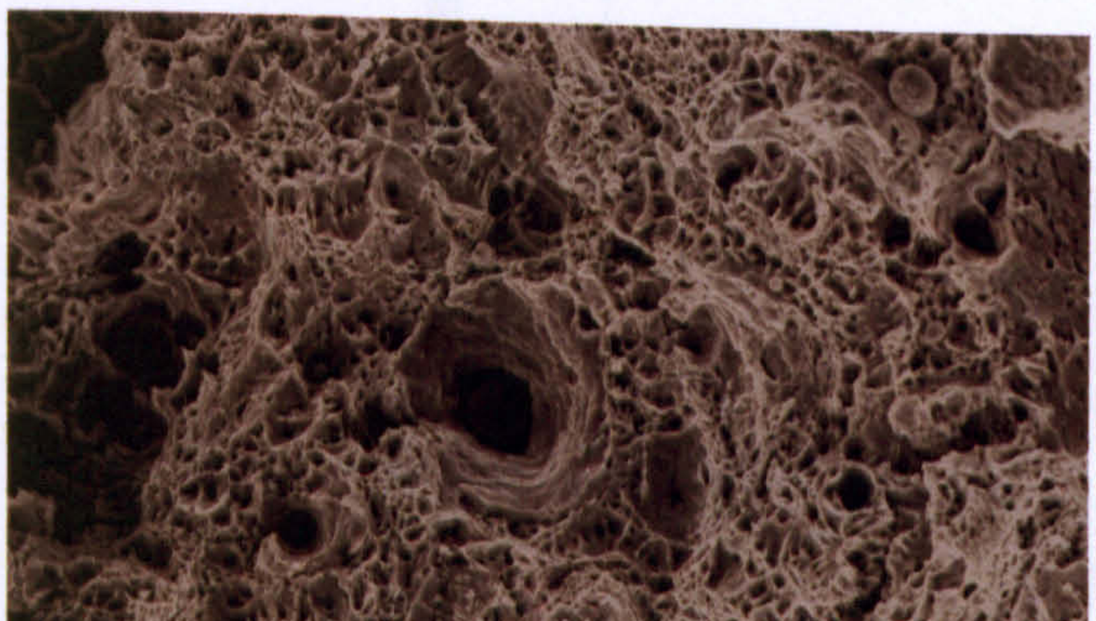

(e) 650°C/4h + 550°C/2h

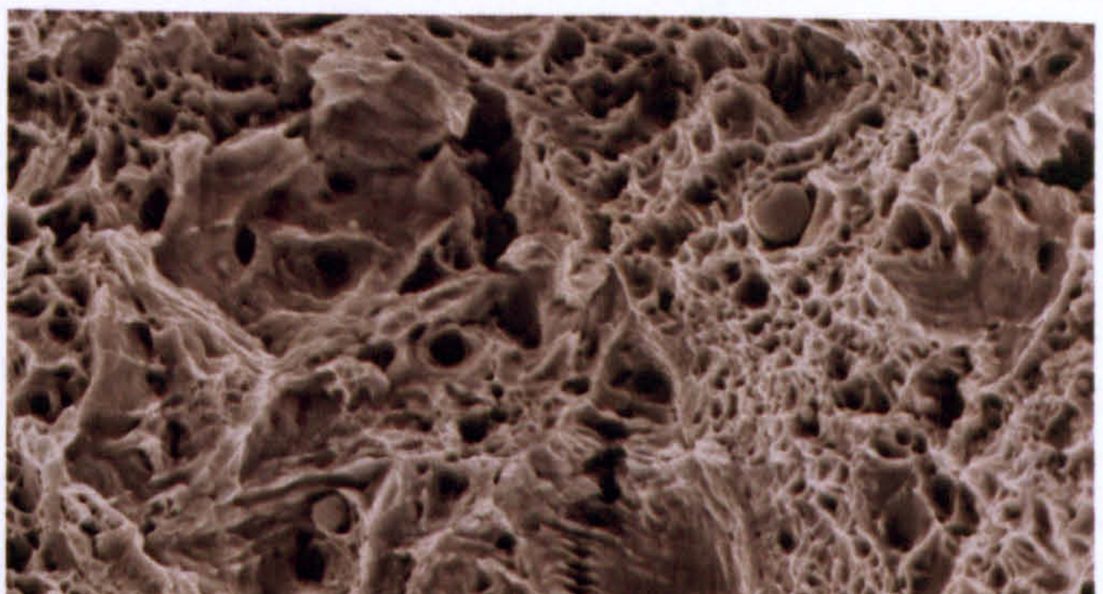

(f) 650°C/4h + 550°C/2h

Fig.5.12 SEM micrographs of fracture surface after tensile testing, showing ductile morphology.

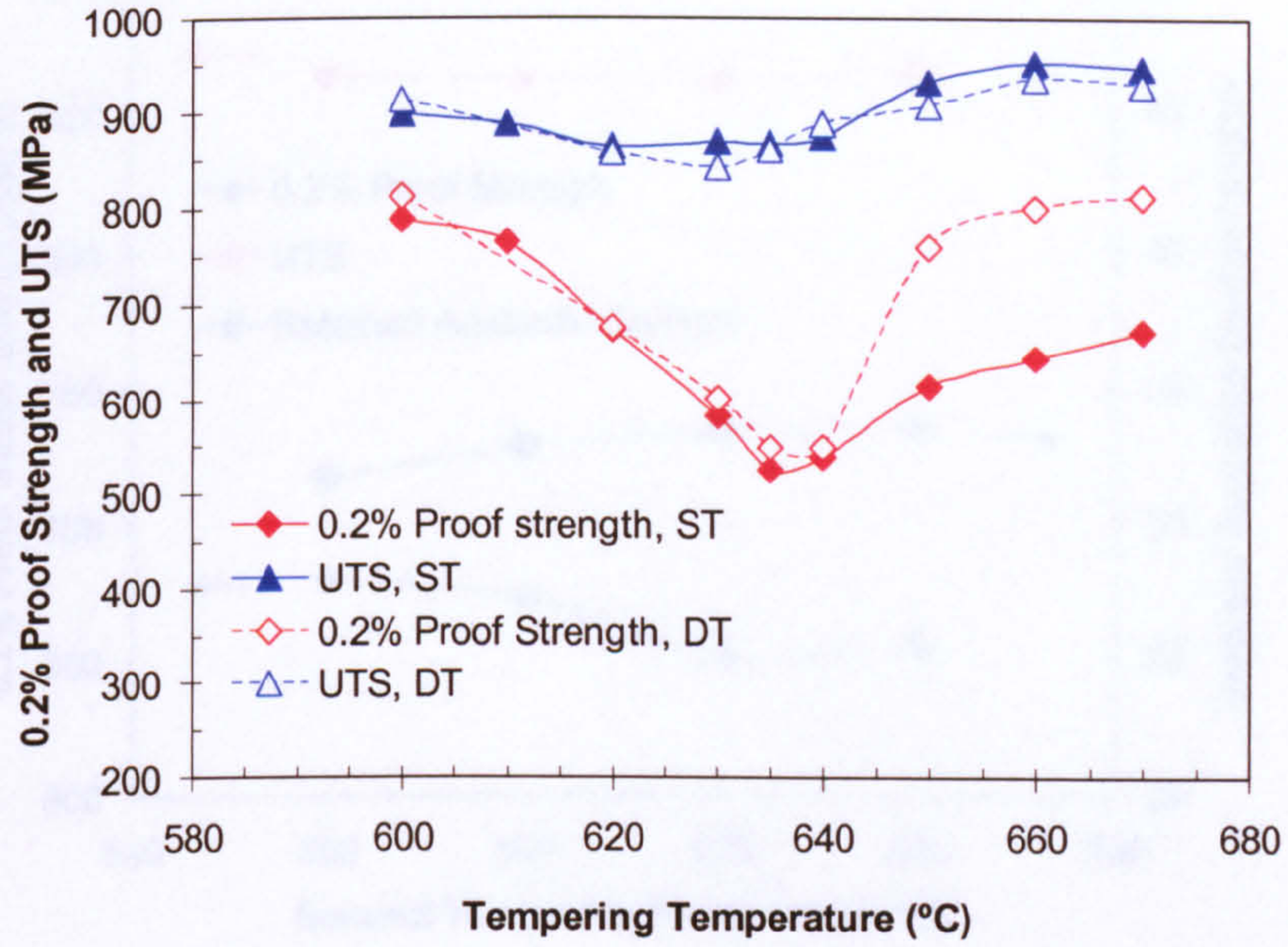

(a) Effect of tempering temperature on 0.2% proof strength and UTS.

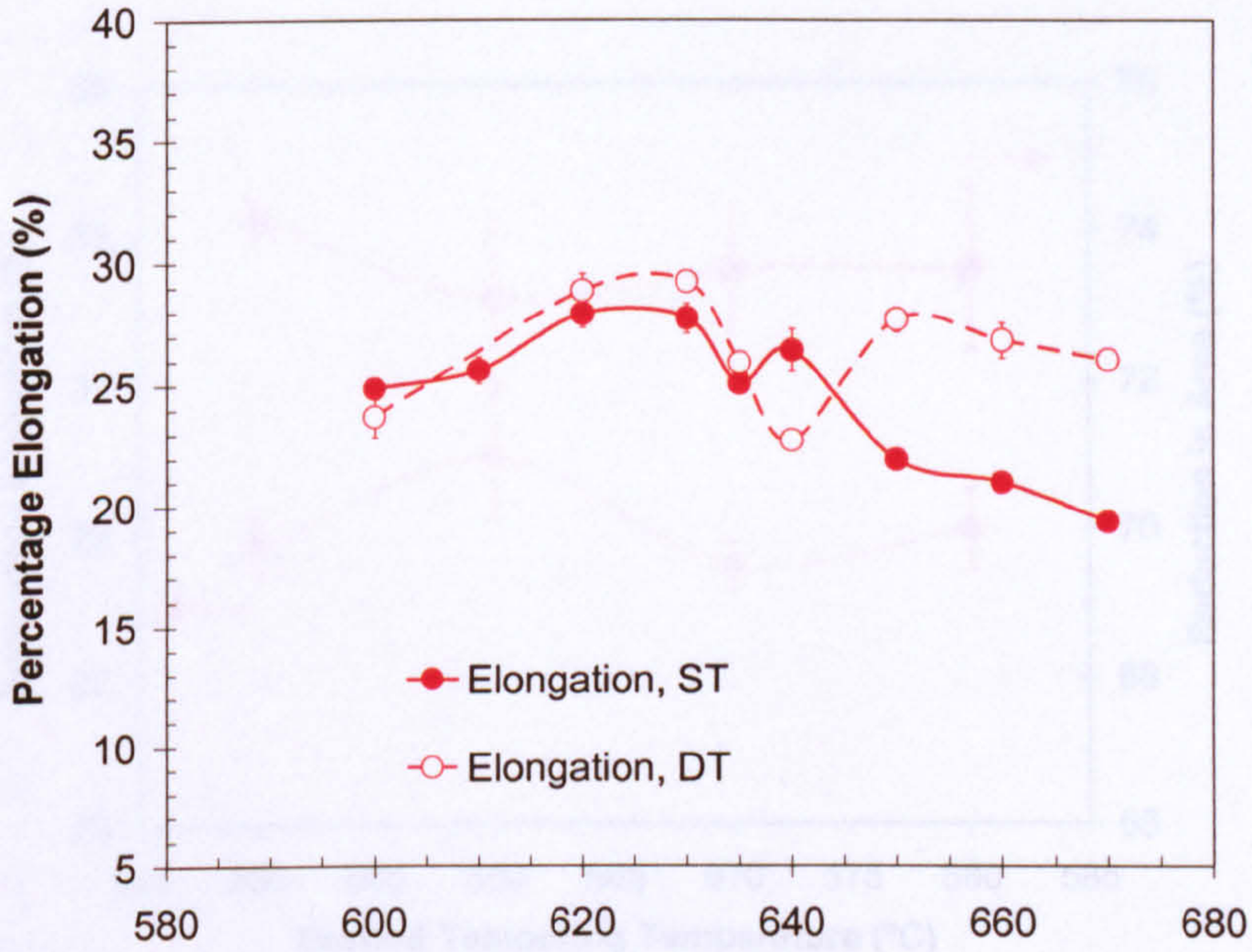

(b) Effect of tempering temperature on elongation.

Fig.5.13 Effect of tempering temperature on tensile properties. ST: single tempering, DT: double tempering. The single tempering (and the first stage of double tempering) was in the range 600-670 °C, 4 h. The second stage of double tempering was at 550 °C, 2 h. All of the specimens were cooled in furnace after tempering.

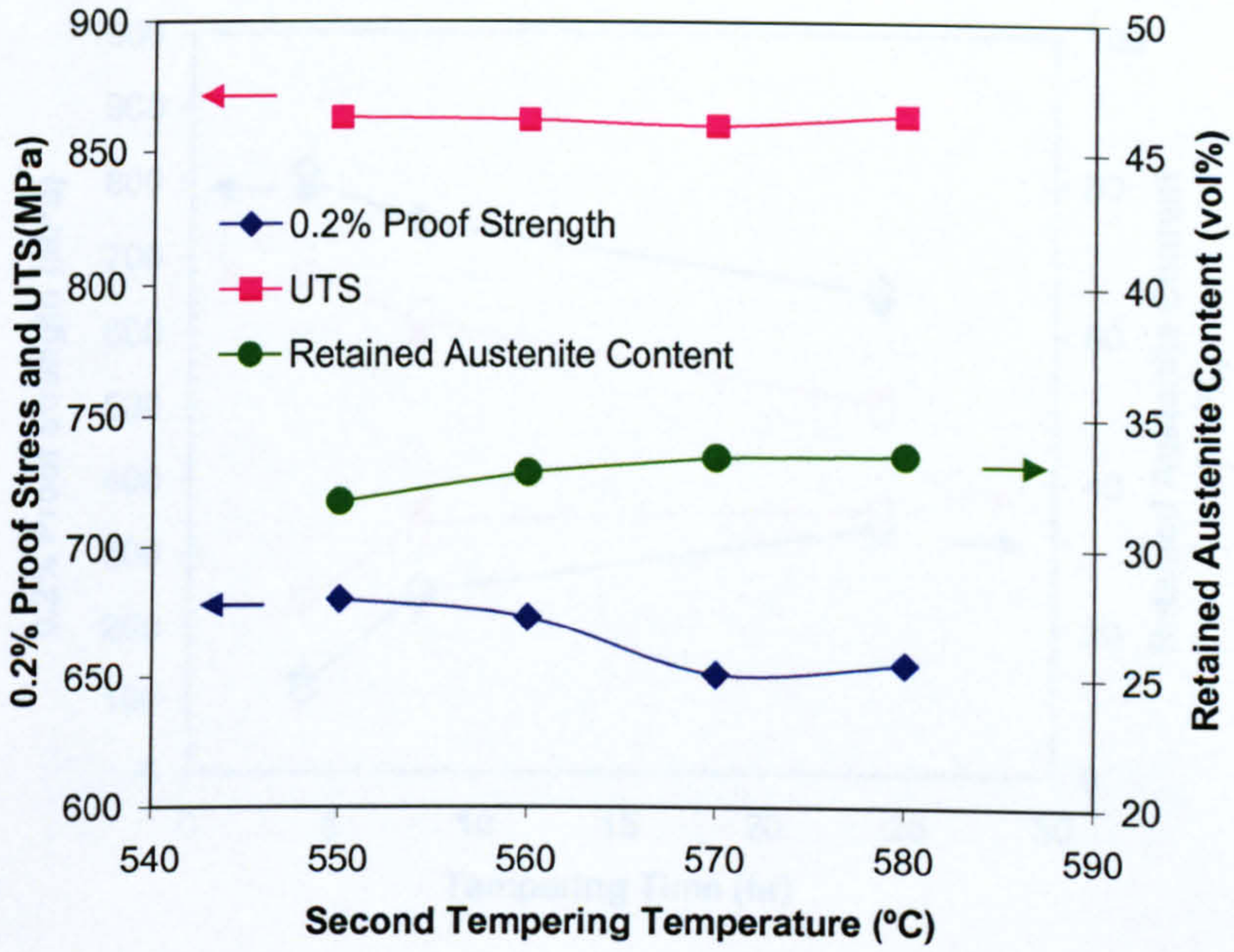

(a) Effect of the second tempering temperature on retained austenite content, 0.2% proof strength and UTS.

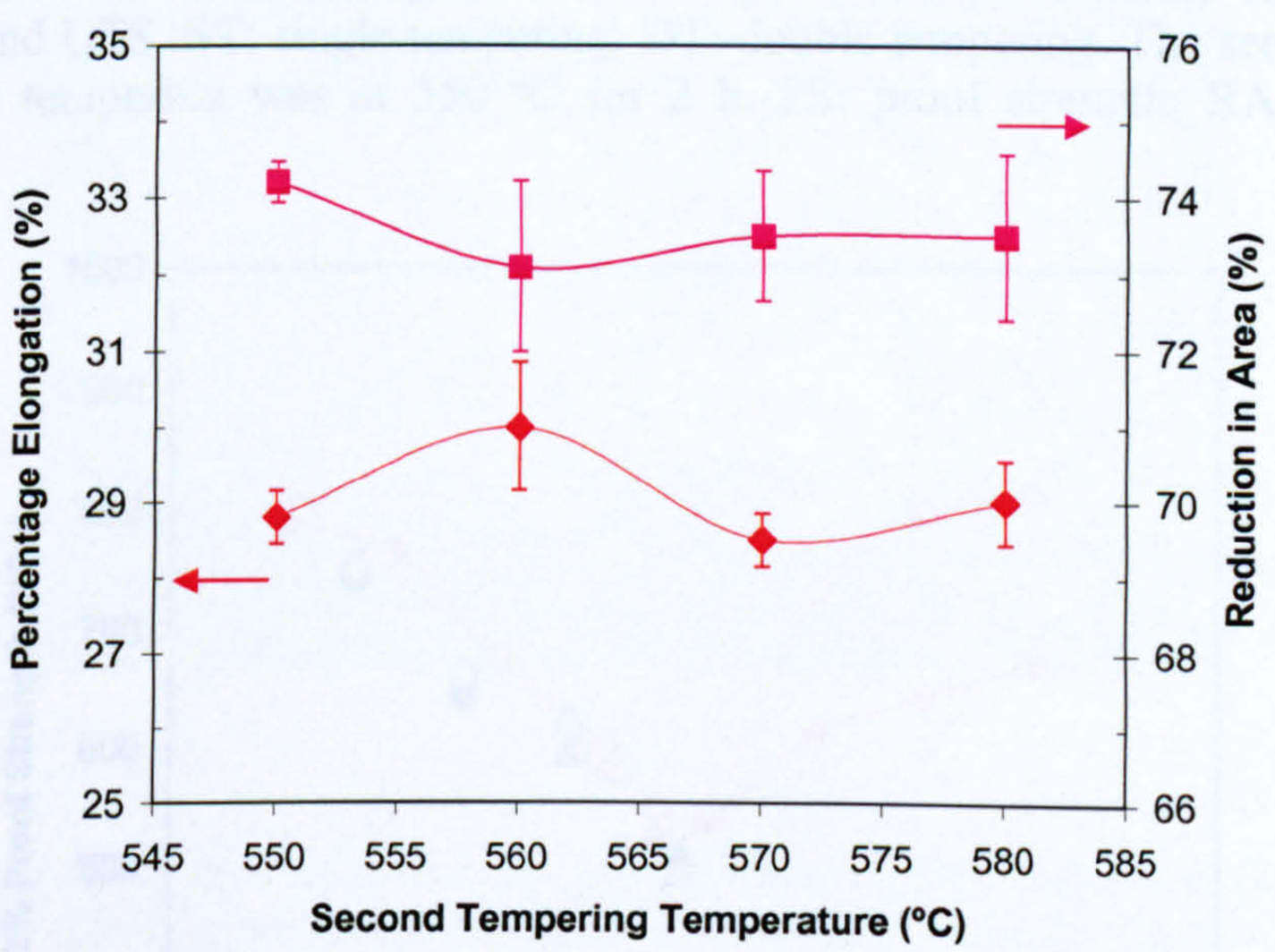

(b) Effects of the second tempering temperature on elongation and reduction in area.

Fig.5.14 Effects of the second tempering temperature on tensile properties. The specimens were first tempered at 625 °C for 4 h and then second tempered in the range 550-580 °C for 2 h.

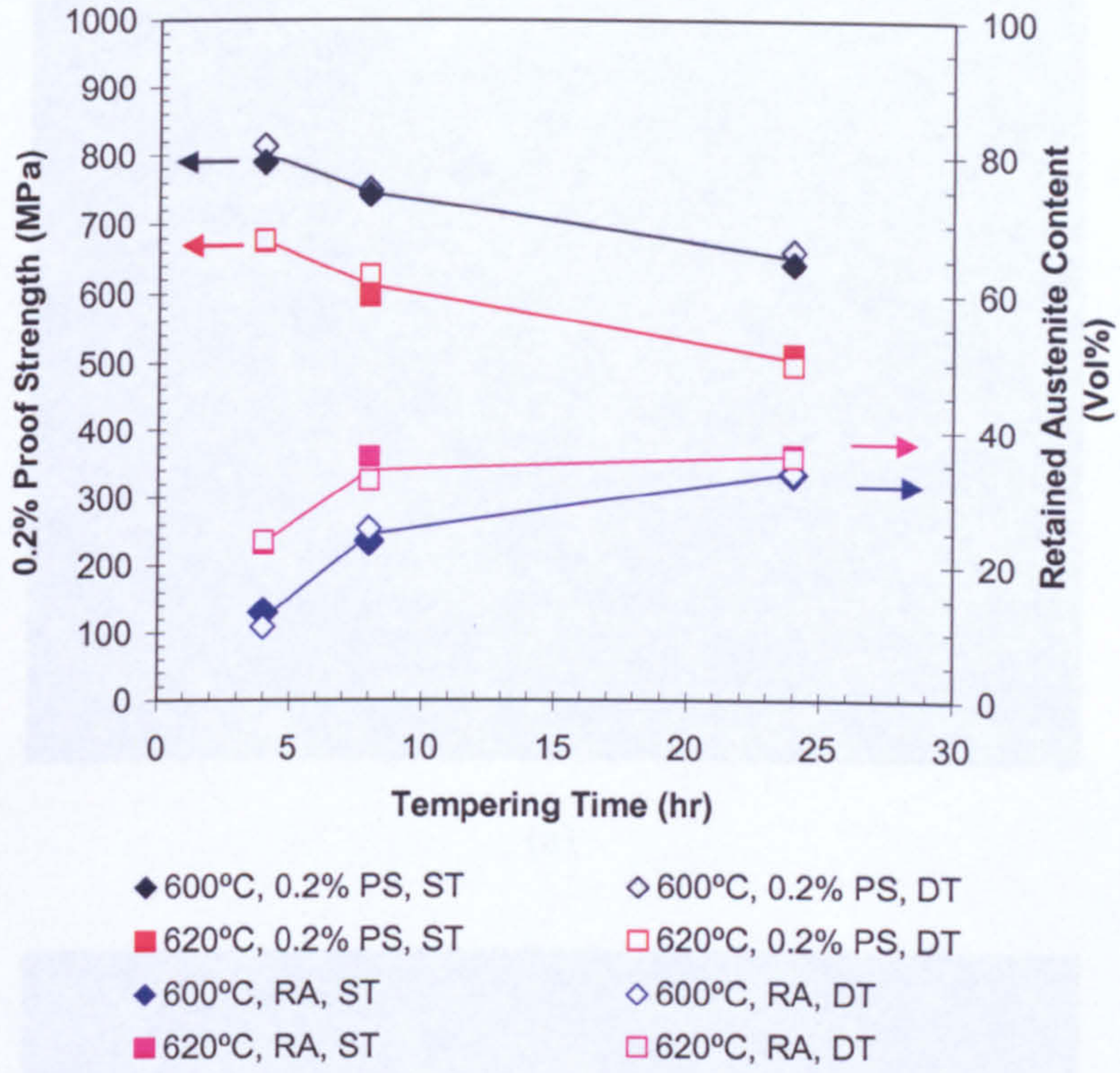

Fig.5.15 Effects of tempering time on retained austenite content, 0.2% proof strength and UTS. ST: single tempering; DT: double tempering. The second stage of double tempering was at 550 °C for 2 h. PS: proof strength; RA: retained austenite.

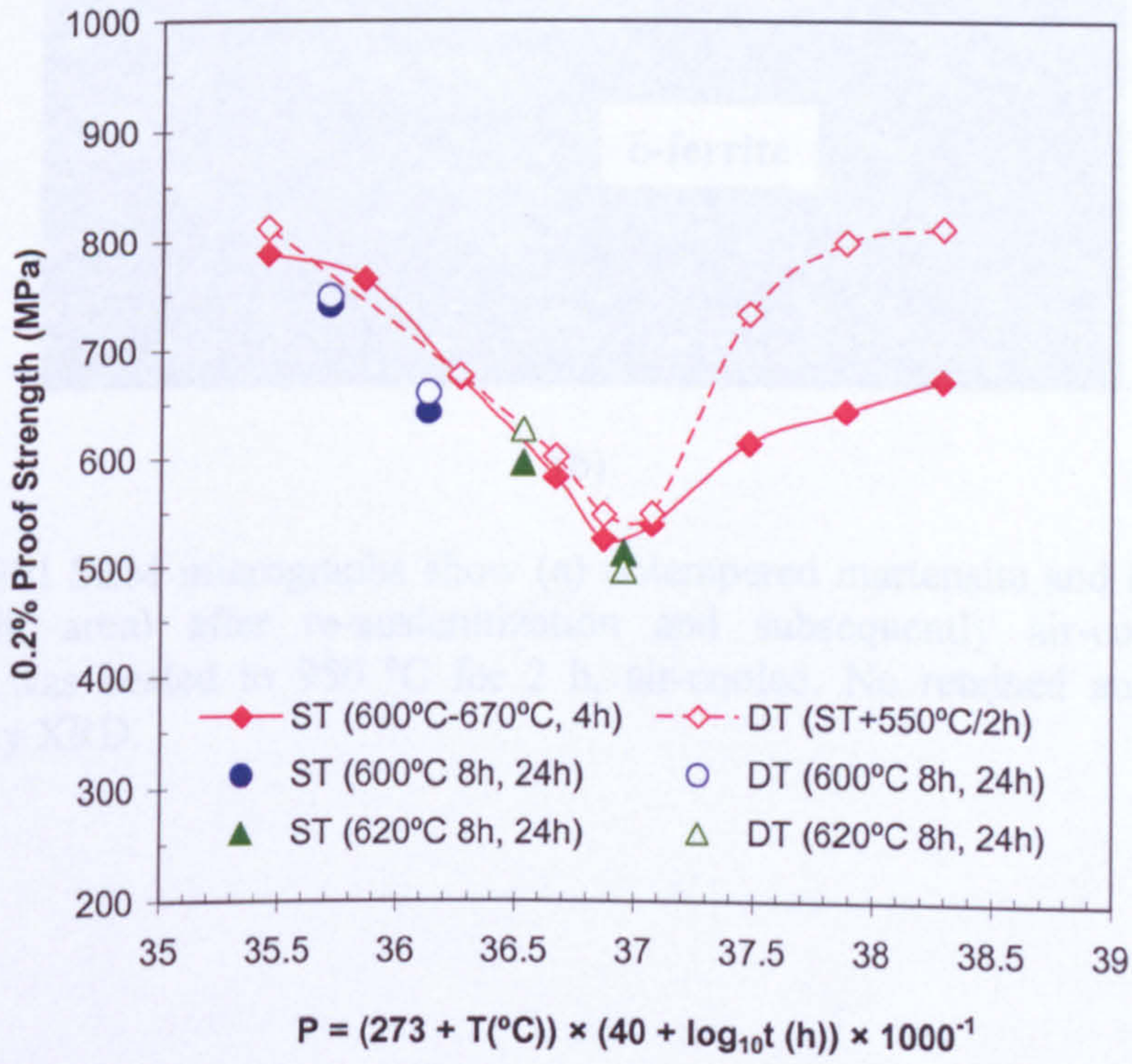

Fig.5.16 Relationship between 0.2% proof strength and the Hollomon-Jaffe tempering time-temperature parameter P.

(a)

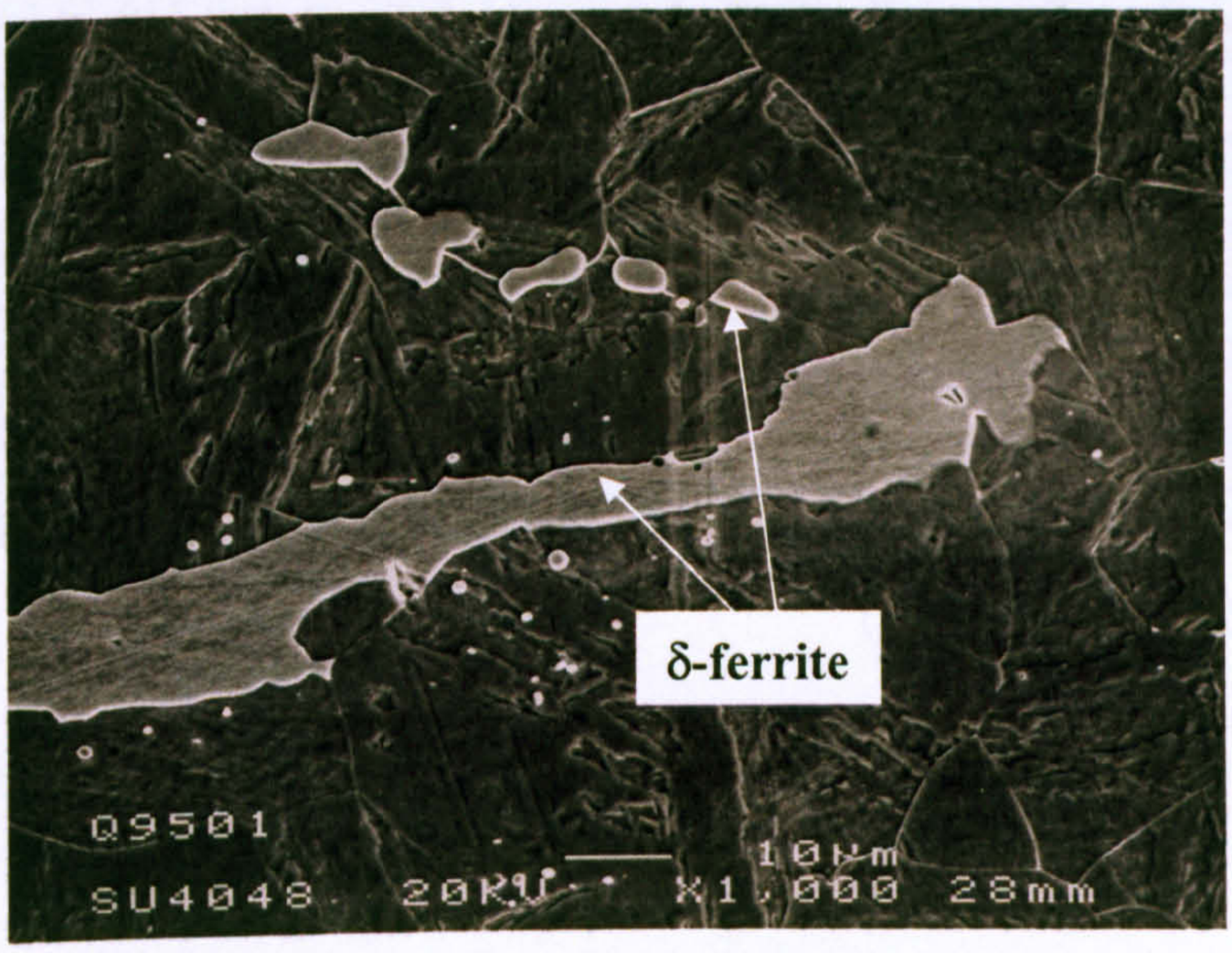

(b)

Fig.5.17 SEI SEM micrographs show (a) untempered martensite and (b) δ-ferrite (the bright area) after re-austenitization and subsequently air-cooling. The specimen was heated to 950 °C for 2 h, air-cooled. No retained austenite was detected by XRD.

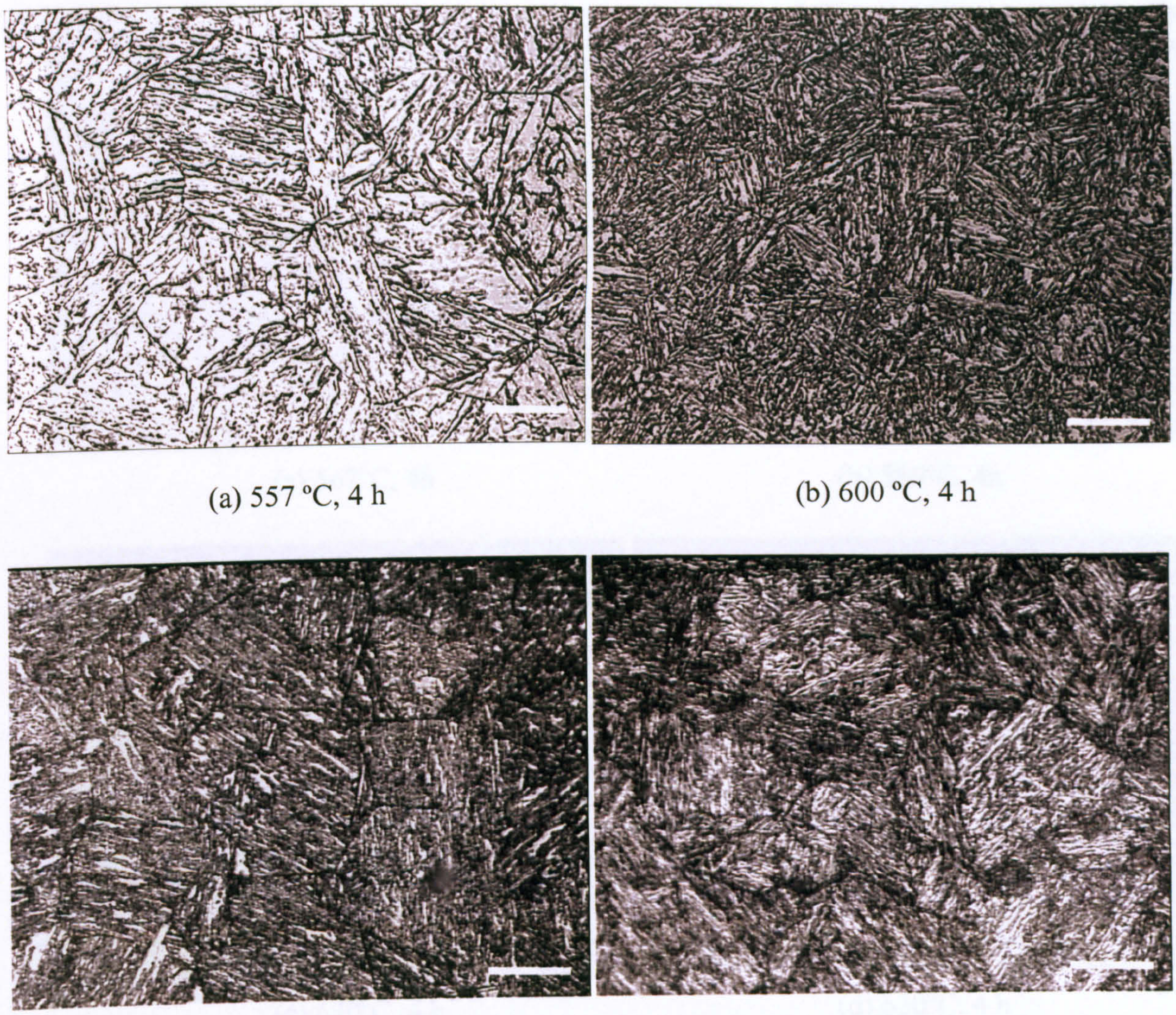

(a) 557 °C, 4 h

(b) 600 °C, 4 h

(c) 630 °C, 4 h

(d) 700°C/4h + 550°C/2h

Fig.5.18 Optical micrographs of the tempered specimens (scale mark indicates 10 μm).

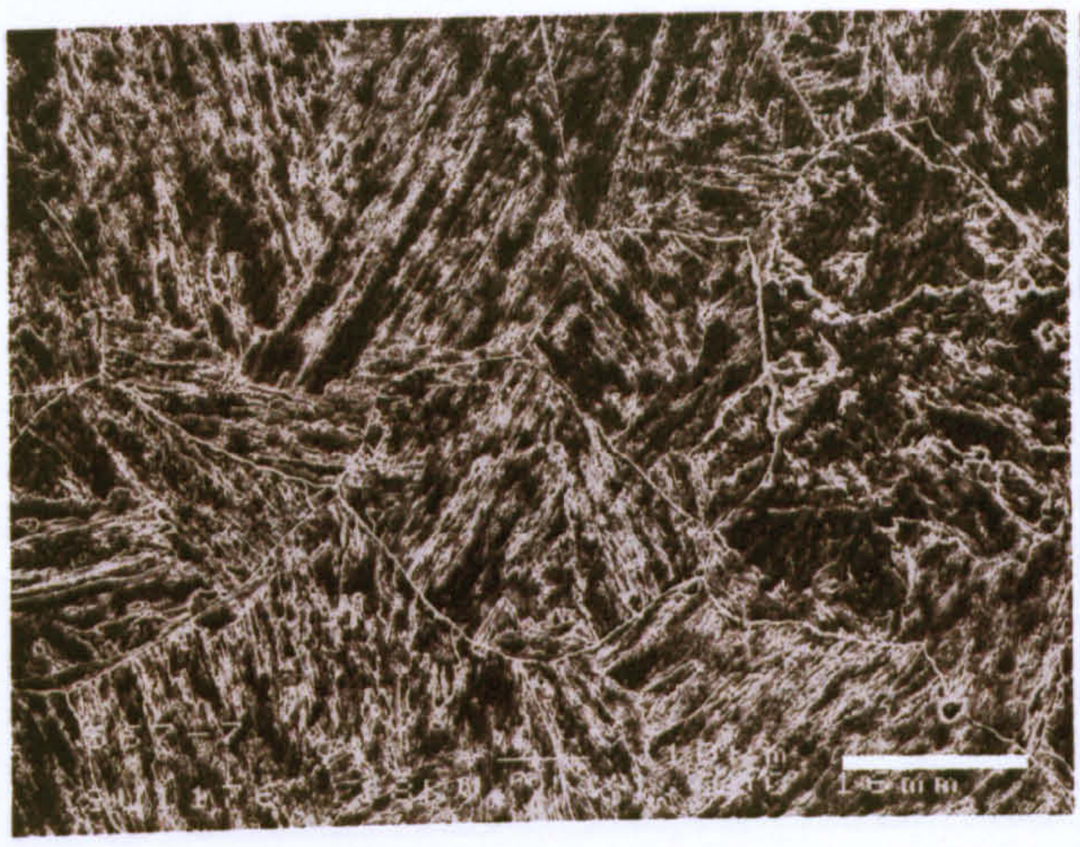

(a) 567°C, 4h

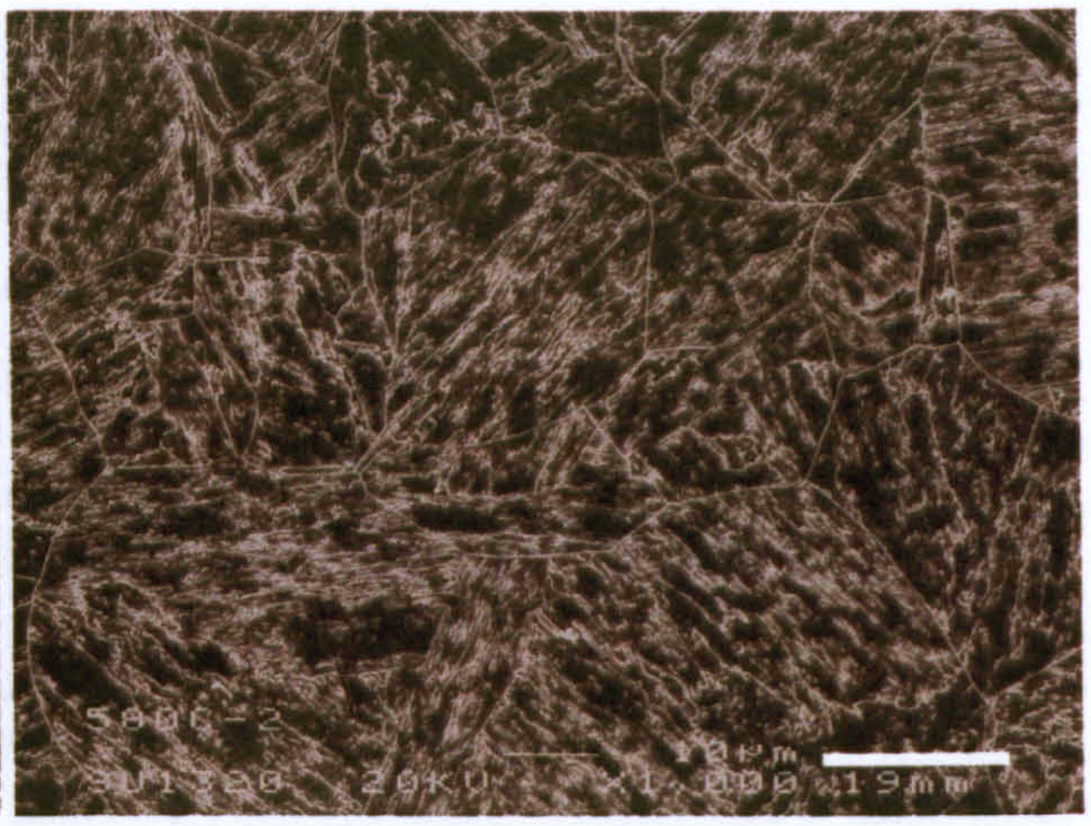

(b) 580°C, 4h

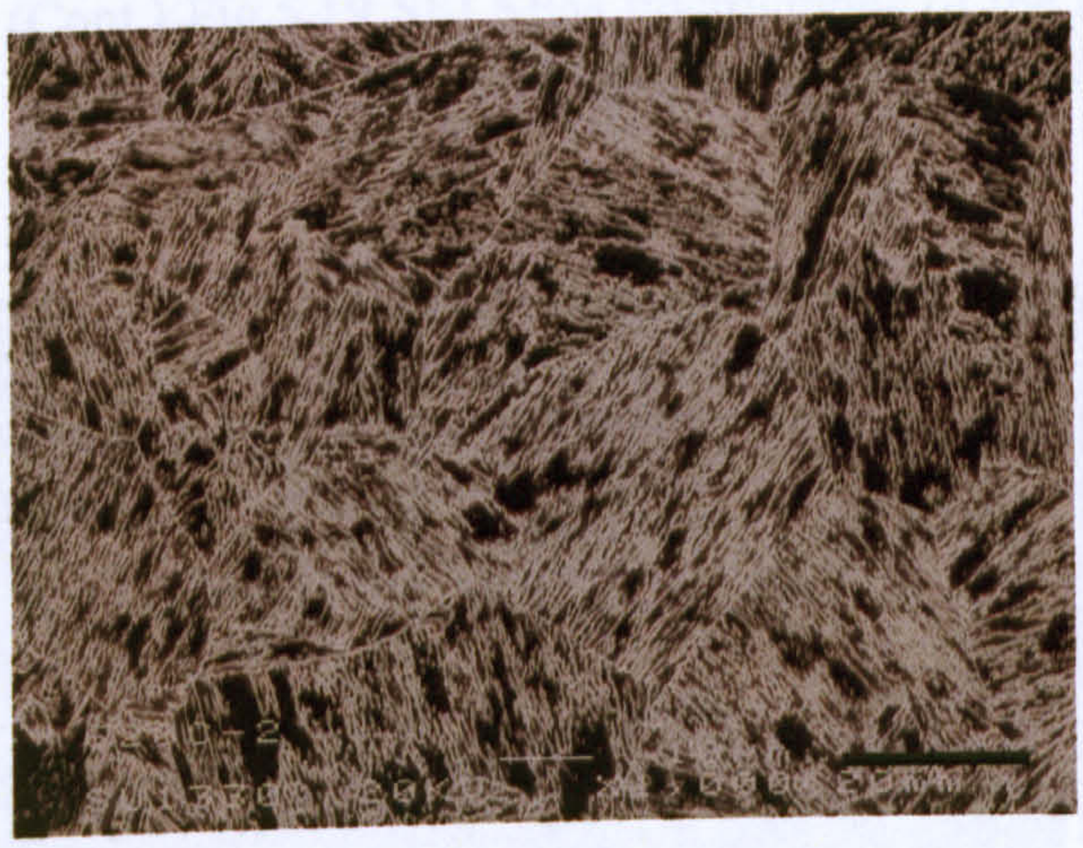

(c) 620°C, 4 h

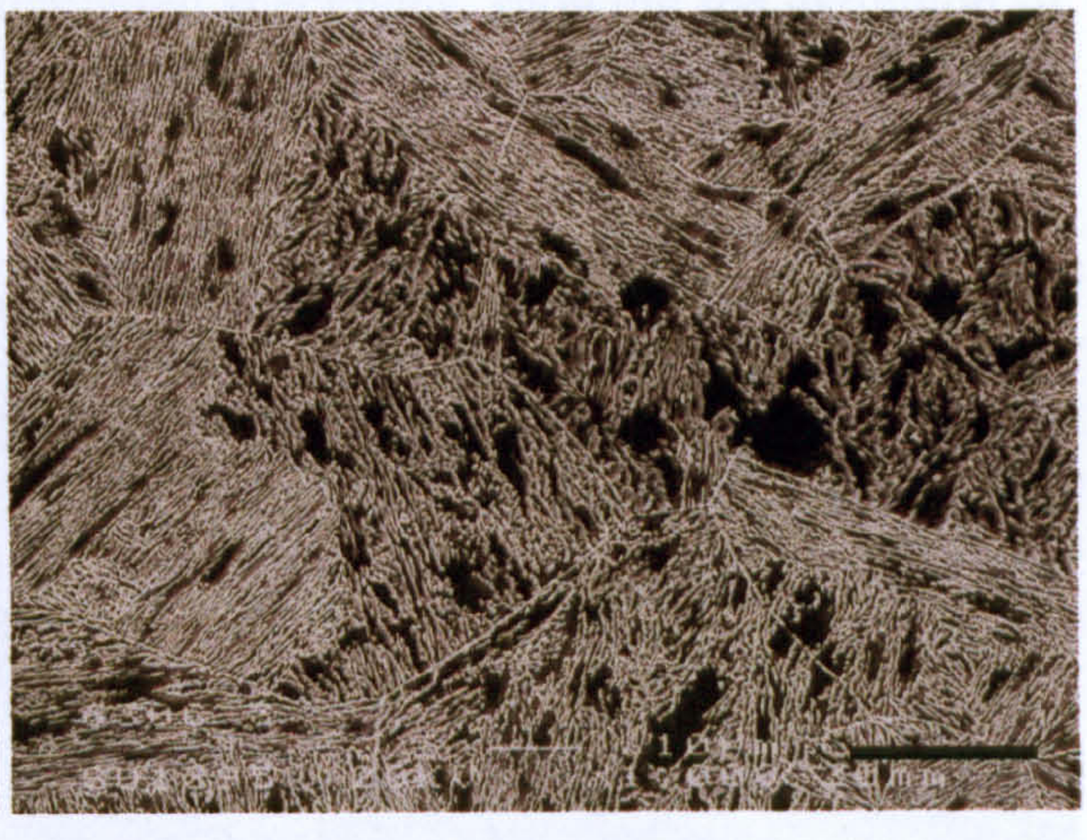

(d) 630°C, 4 h

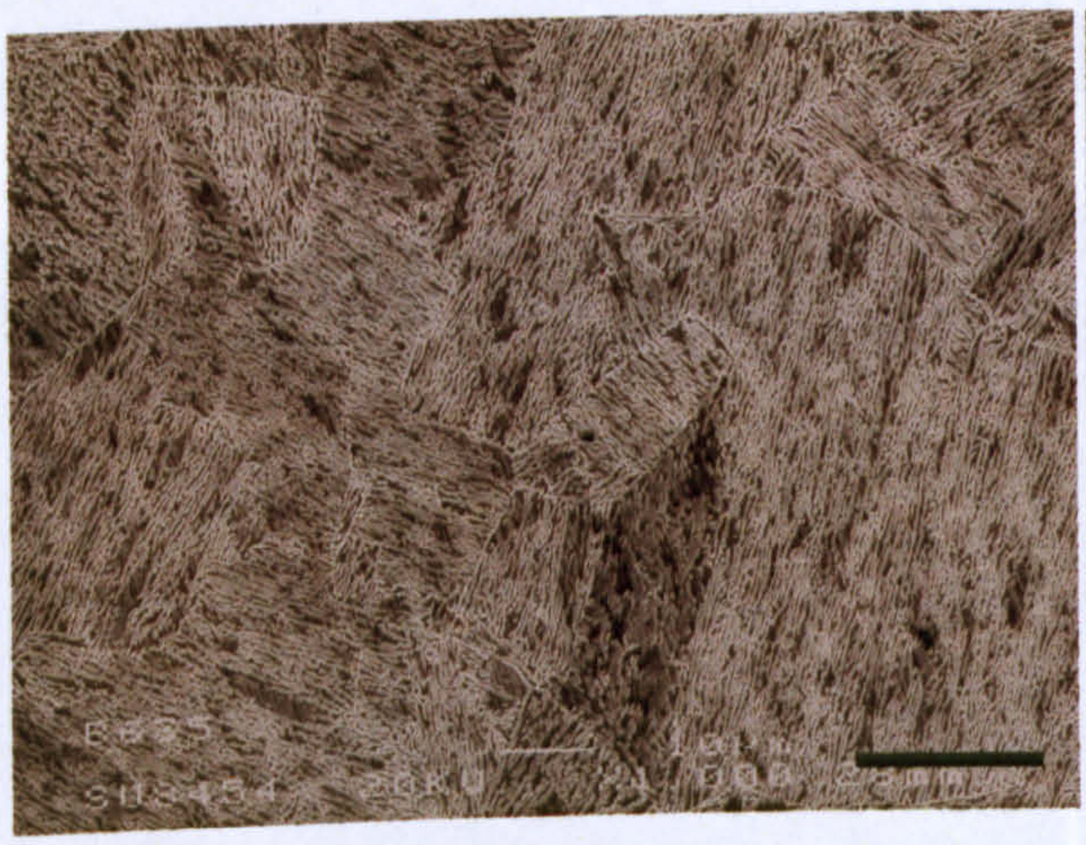

(e) 635°C, 4 h

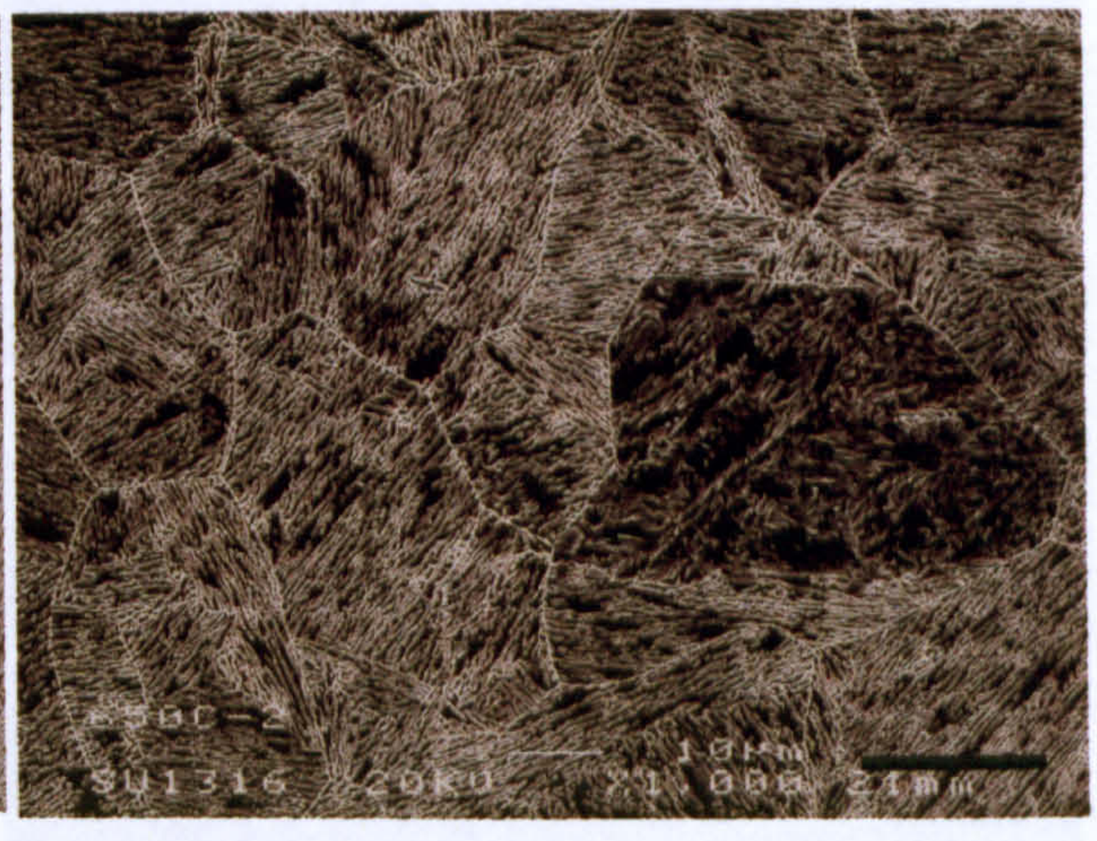

(f) 650°C, 4 h

Fig.5.19 SEI SEM micrographs of the tempered specimens, showing the evolution of microstructure with tempering temperature (scale mark indicates 20 μm).

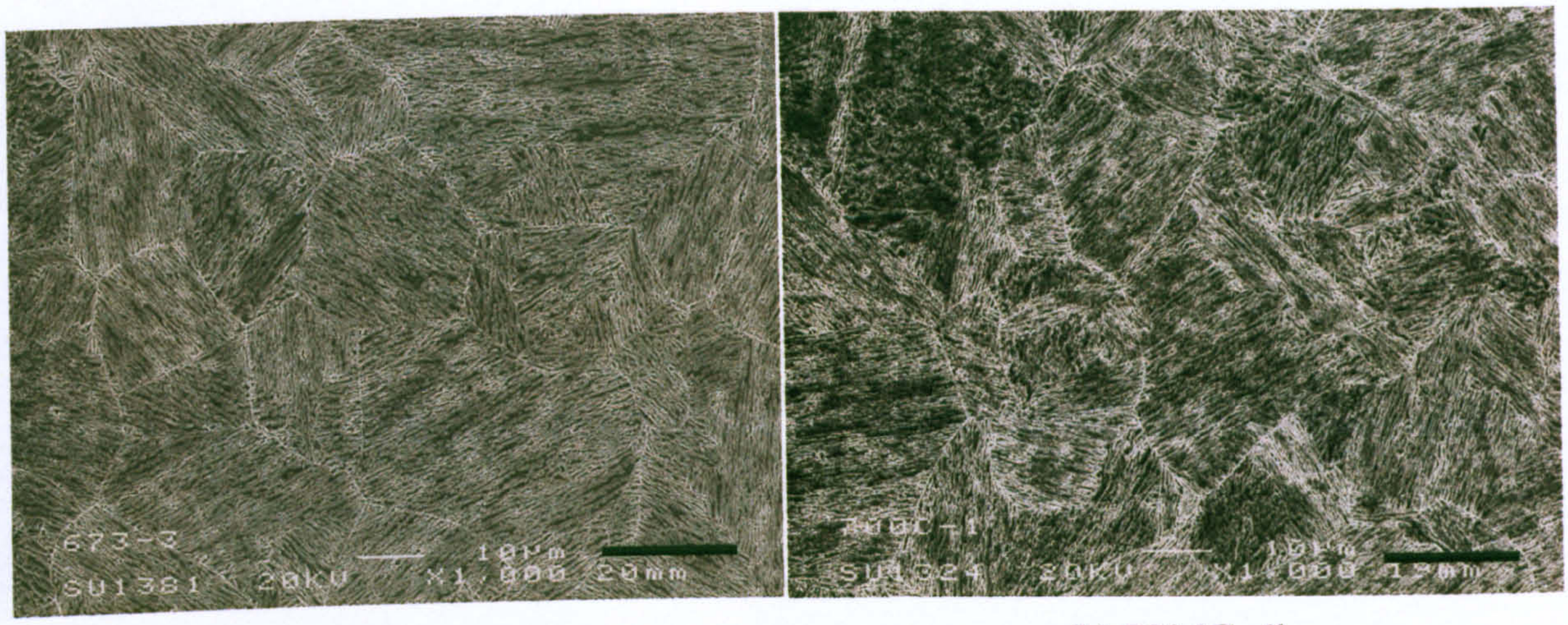

(g) 670 °C, 4h (h) 700 °C, 4h

(Cont.) Fig.5.19 SEI SEM micrographs of the tempered specimens, showing the evolution of microstructure with tempering temperature (scale mark indicates 20 μm).

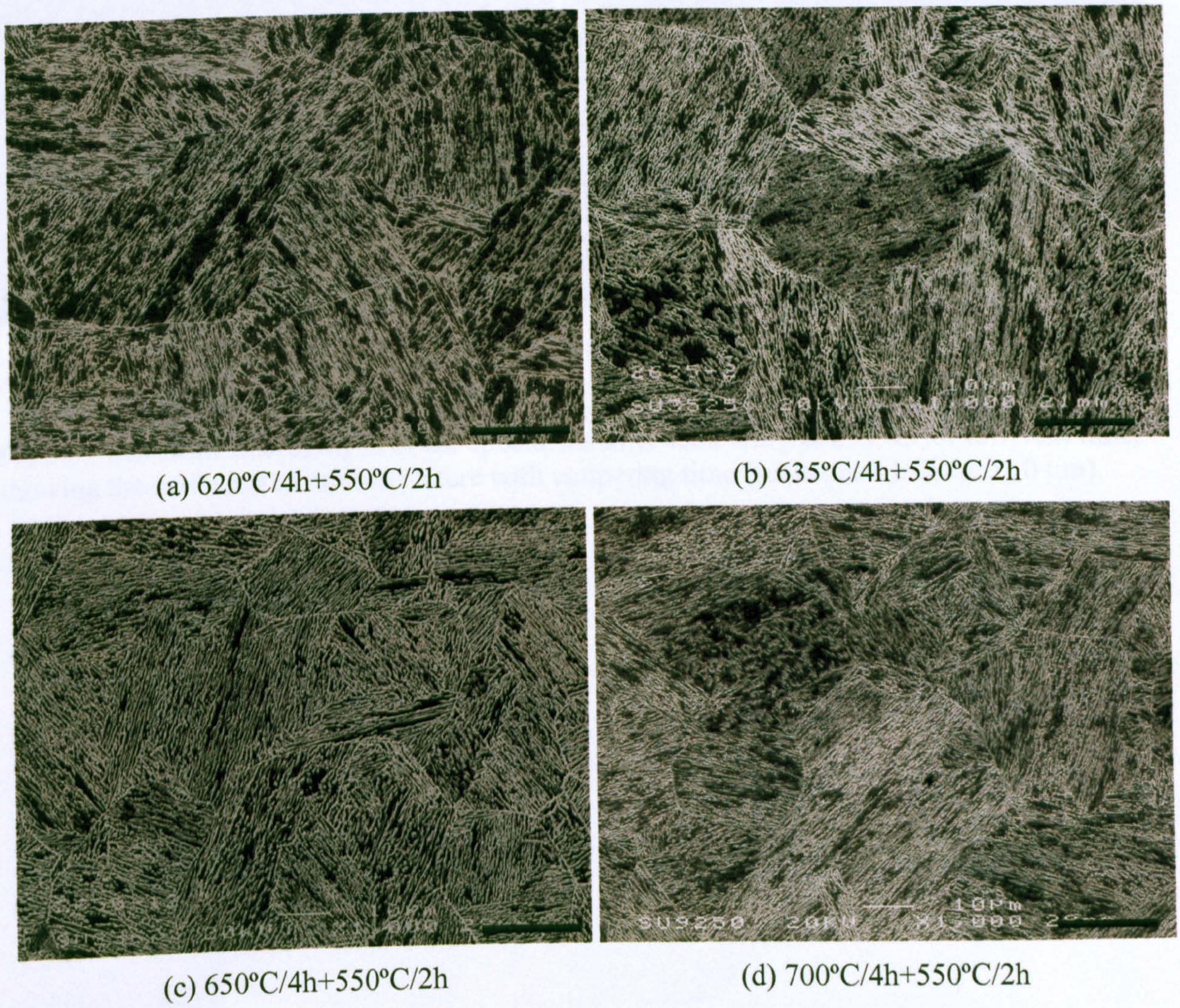

(a) 620°C/4h+550°C/2h (b) 635°C/4h+550°C/2h

(c) 650°C/4h+550°C/2h (d) 700°C/4h+550°C/2h

Fig.5.20 SEI SEM micrographs of the tempered specimens, showing the evolution of microstructure after double tempering (scale mark indicates 20 μm).

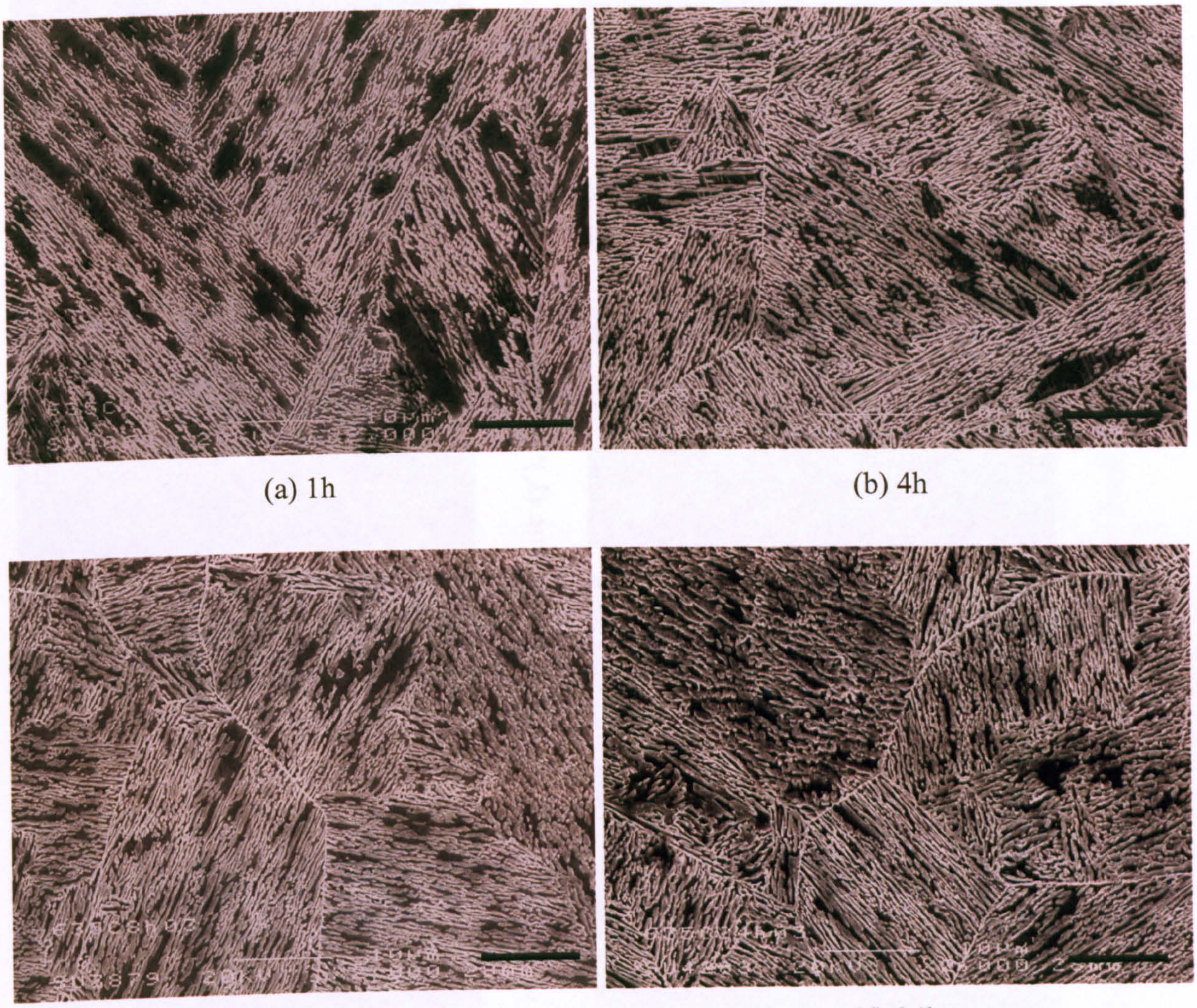

(a) 1h (b) 4h

(c) 8h (d) 24h

Fig.5.21 SEI SEM micrographs of the specimens after tempering at 635 °C for different time, showing the evolution of microstructure with tempering time (scale mark indicates 10 μm).

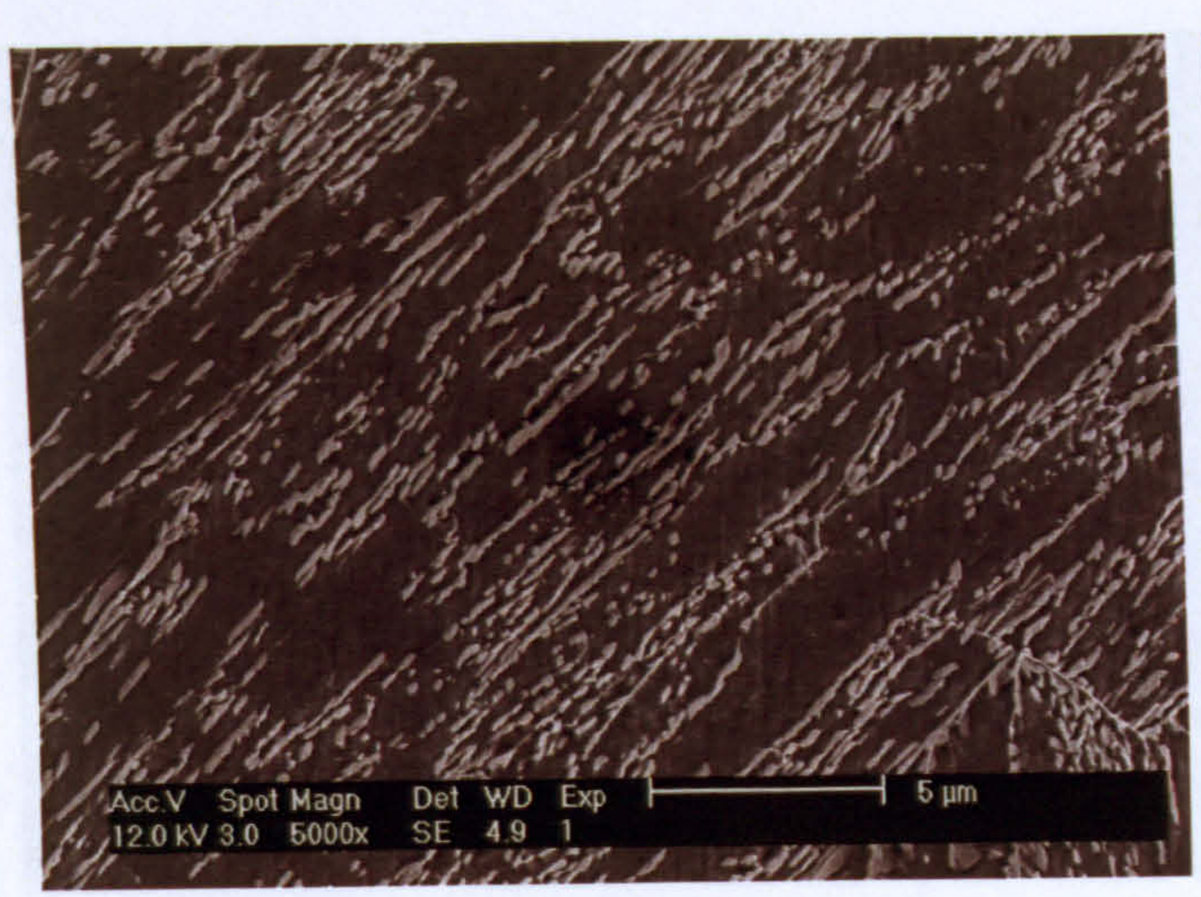

a

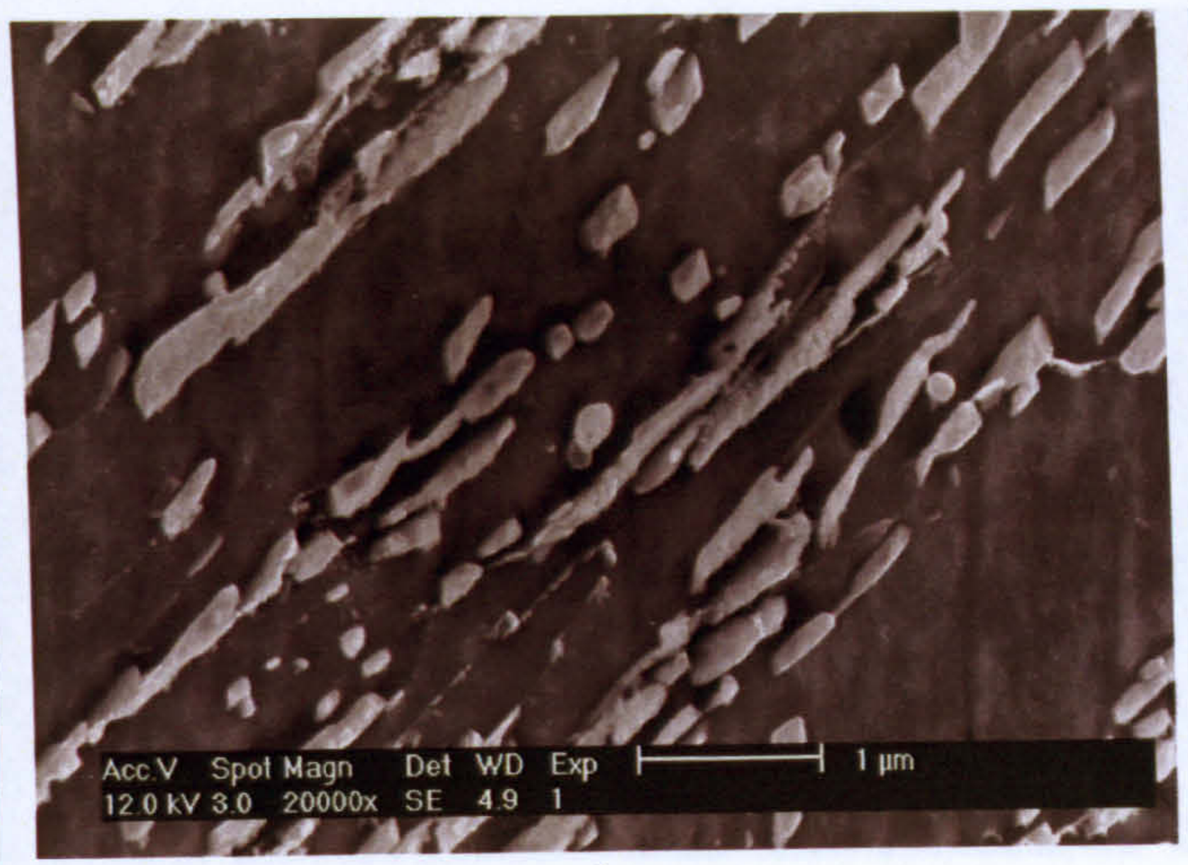

b

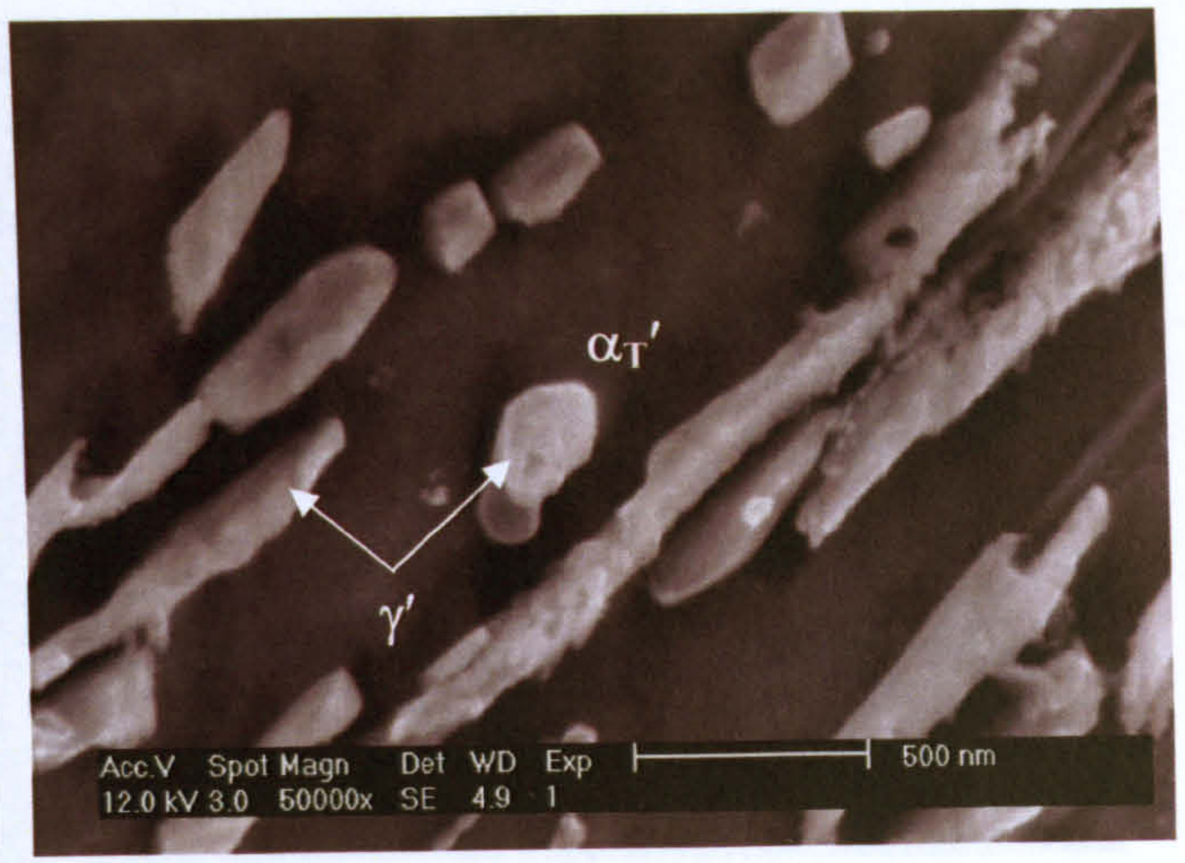

c

Fig.5.22 SEI SEM micrographs of the specimen tempered at 600 ºC for 4 h, showing retained austenite (γ'), brighter contrast and tempered martensite (α_T'), darker contrast.

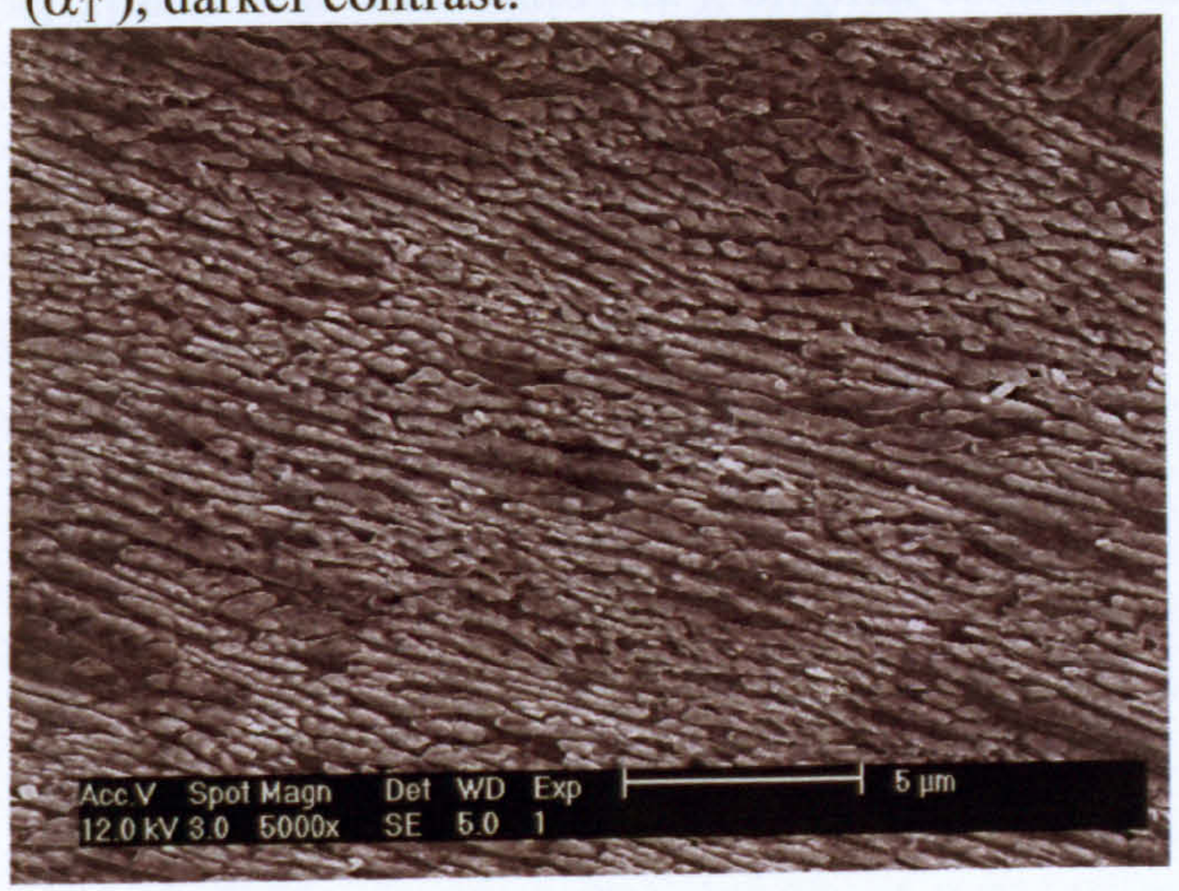

a

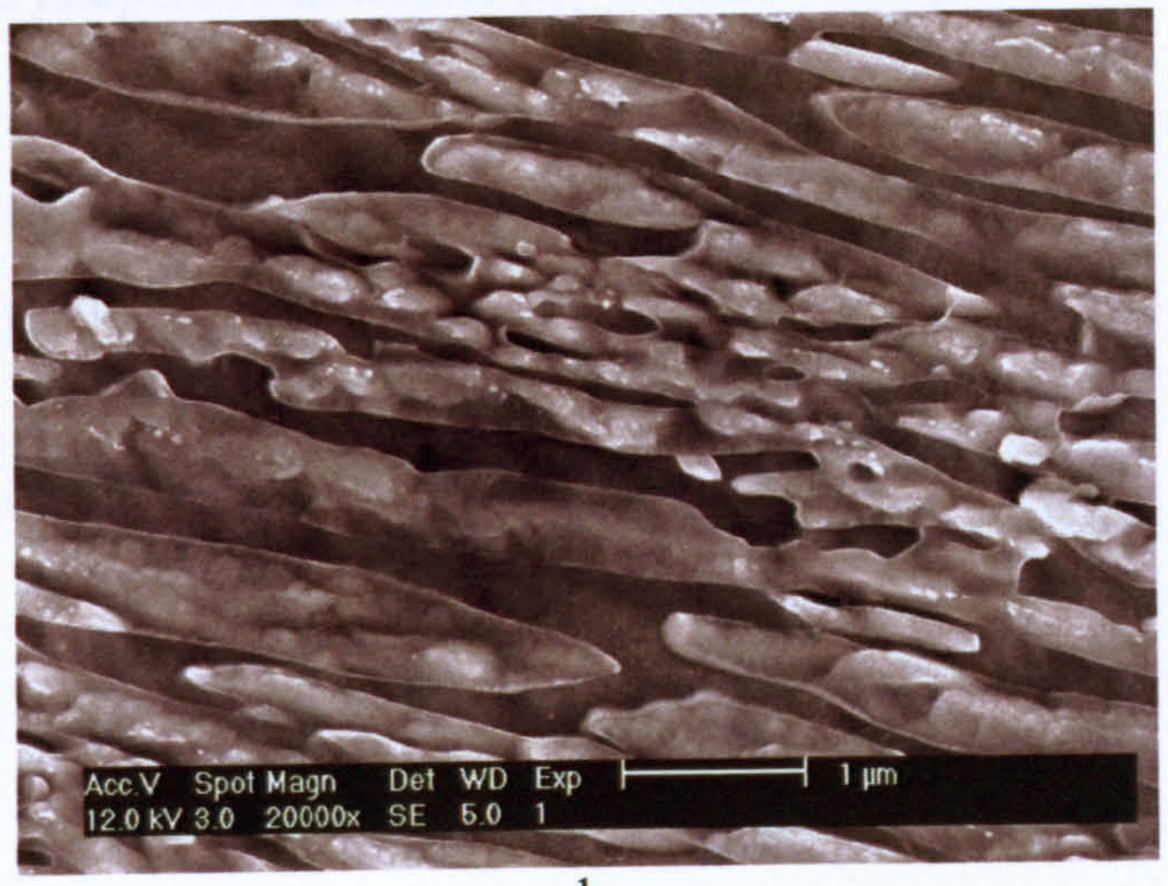

b

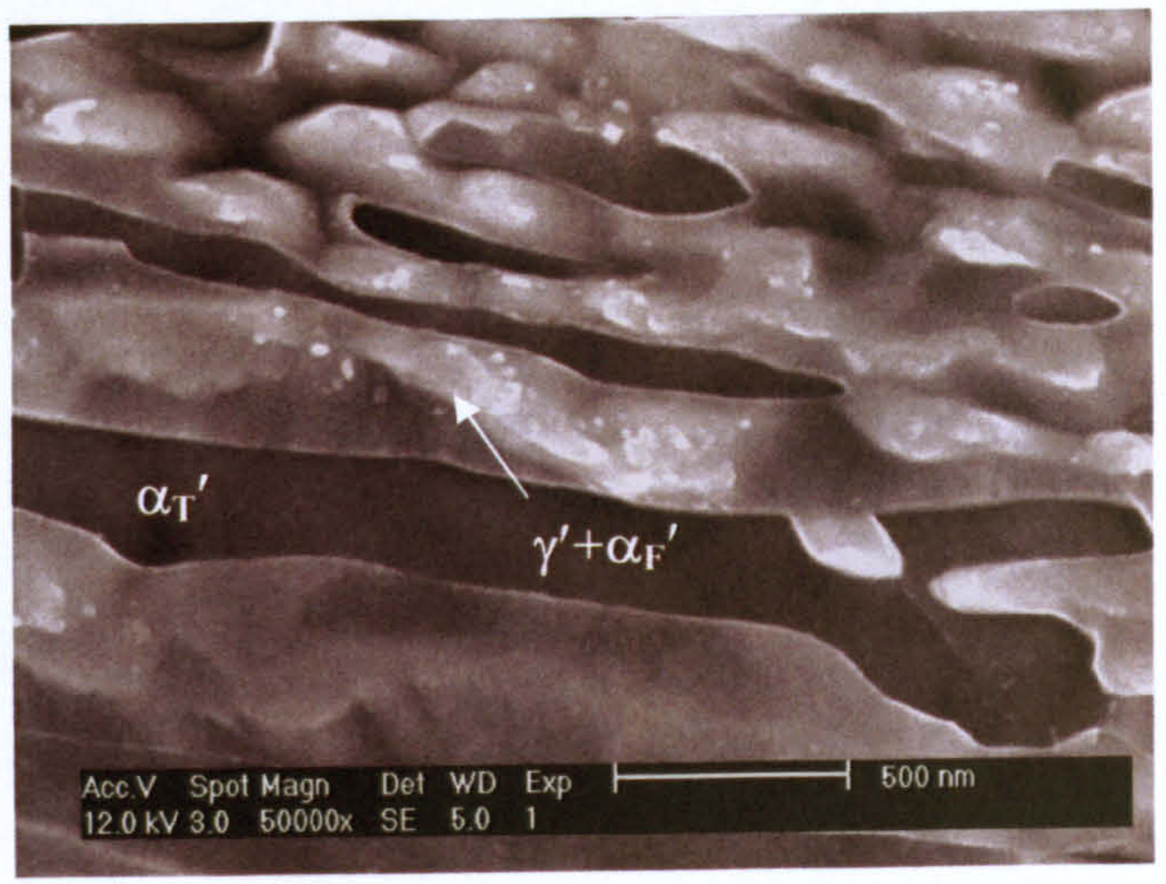

c

Fig.5.23 SEI SEM micrographs of the specimen tempered at 700 ºC for 4 h, showing "retained austenite + fresh martensite" ($\gamma'+\alpha_F'$), brighter contrast, and tempered martensite (α_T'), darker contrast.

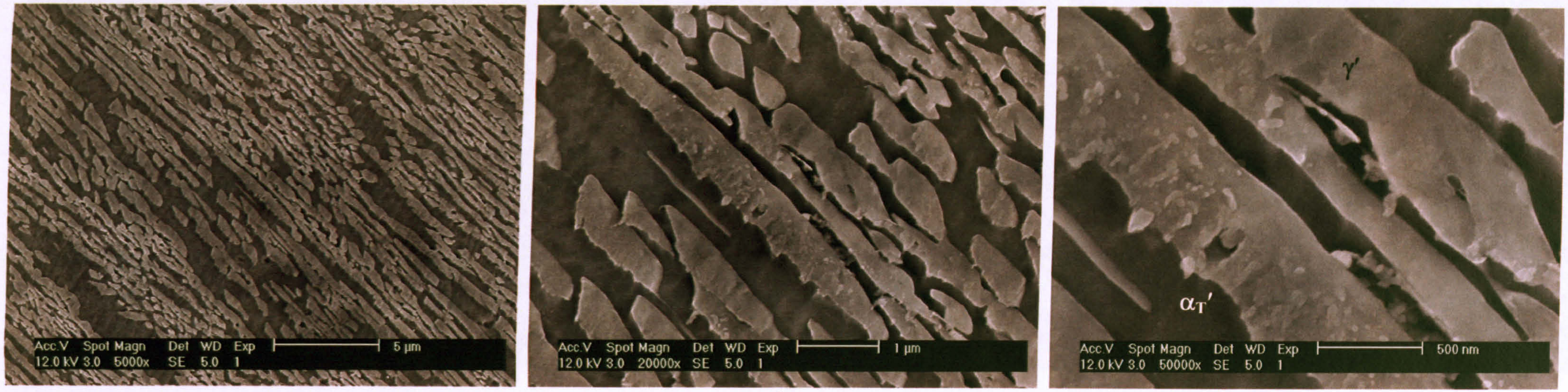

a b c

Fig.5.24 SEI SEM micrographs of the specimen first tempered at 635 ºC for 4 h and then second tempered at 550 ºC for 2 h, showing retained austenite (γ') plus fresh martensite (α_F'), brighter contrast, and tempered martensite (α_T'), darker contrast.

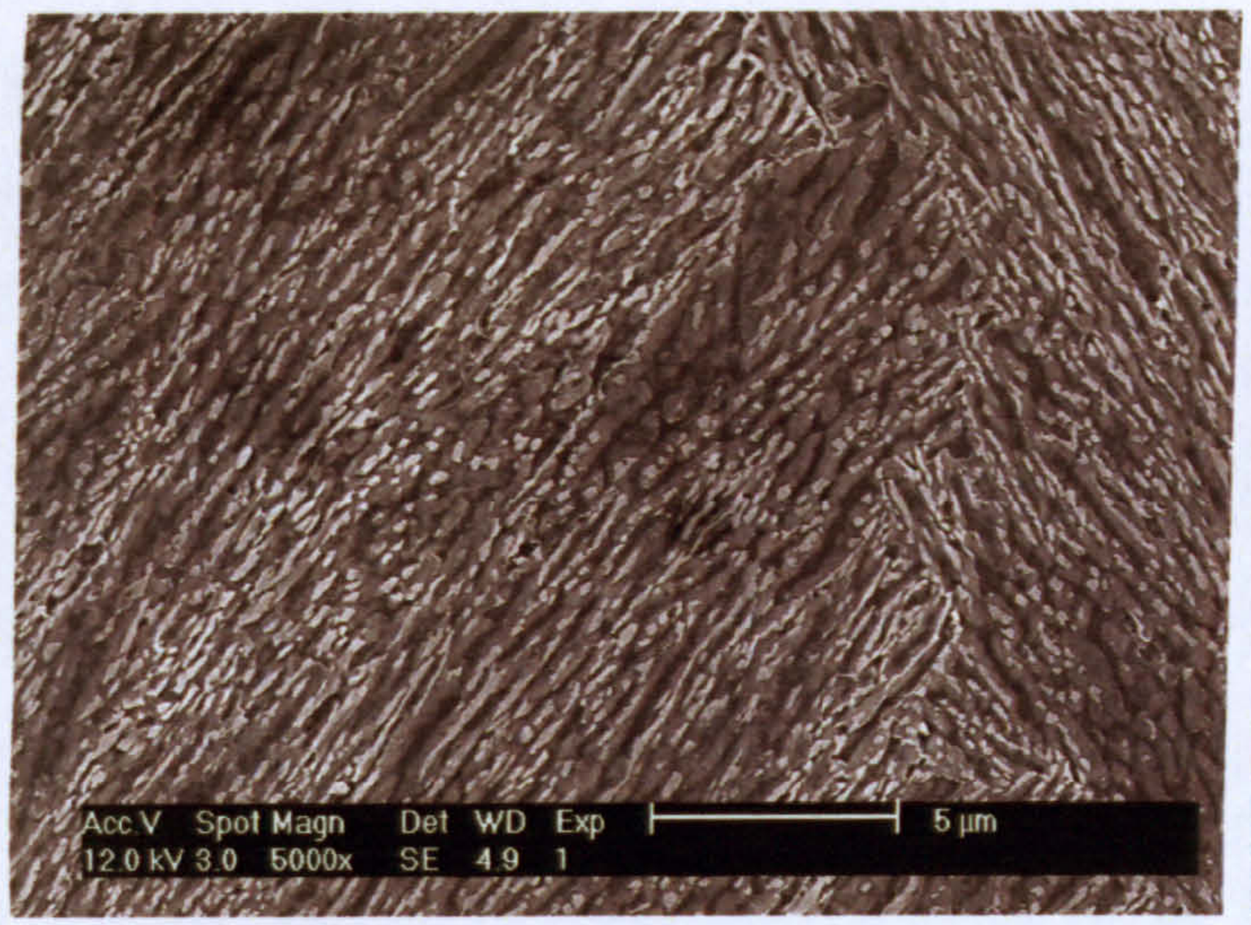

a

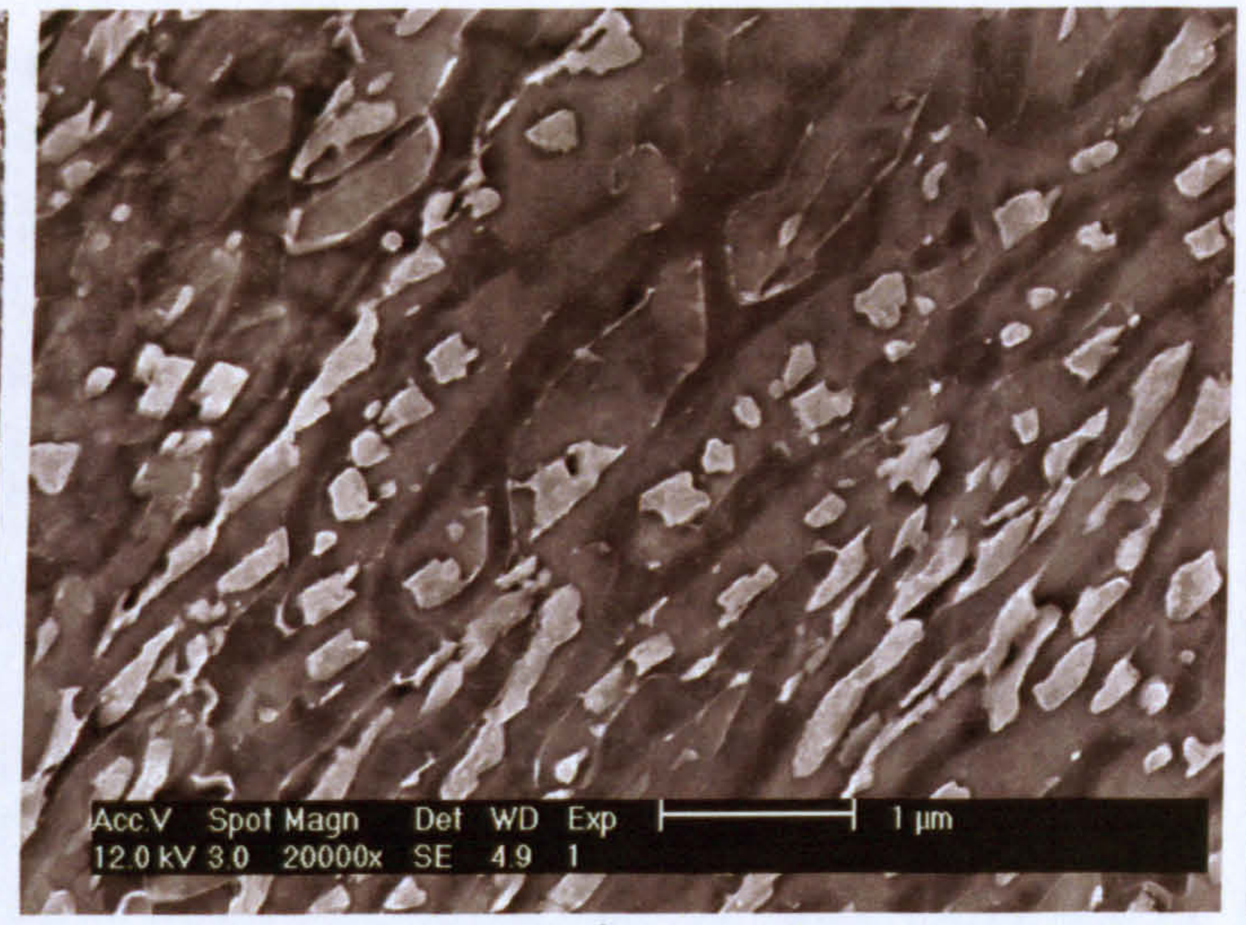

b

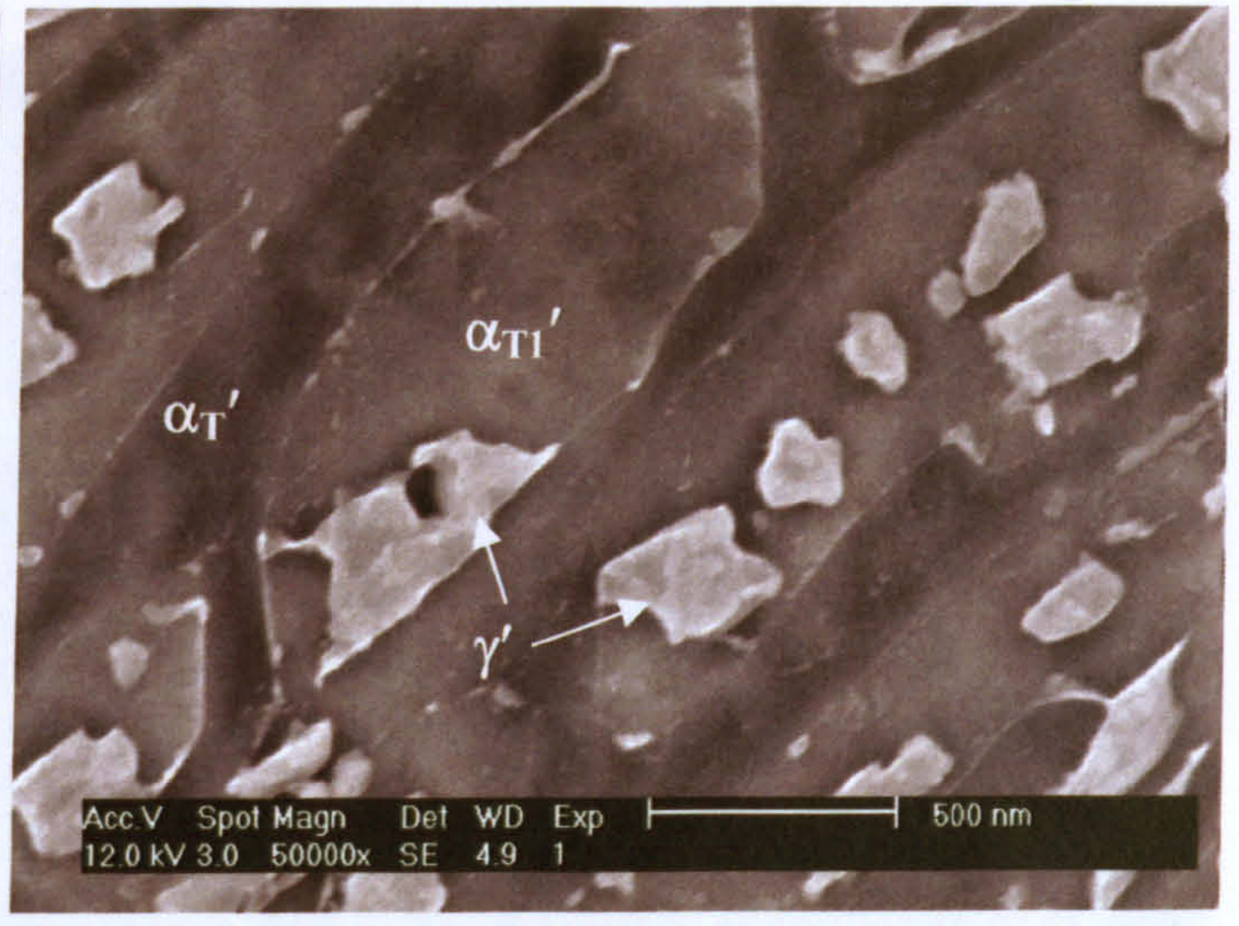

c

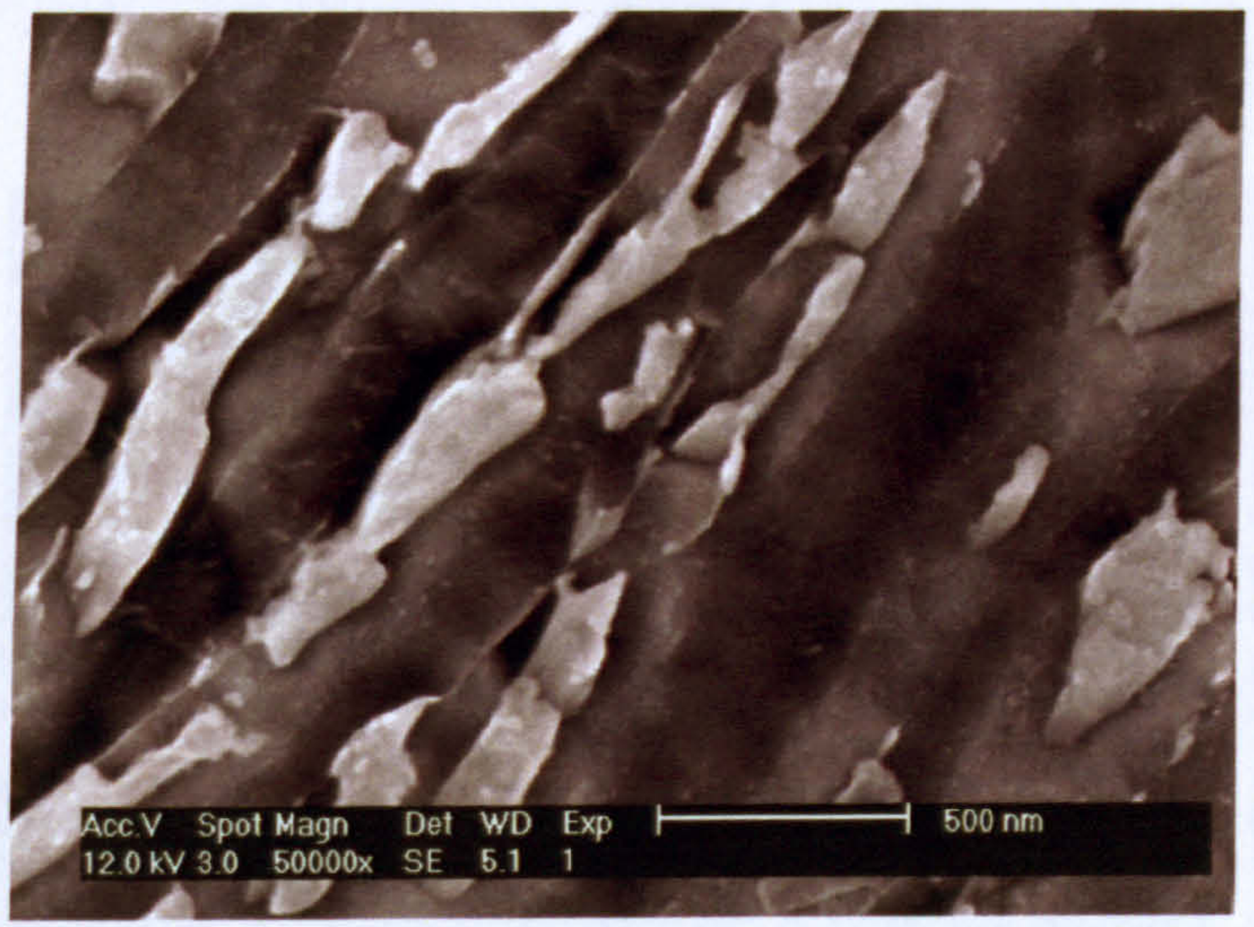

d

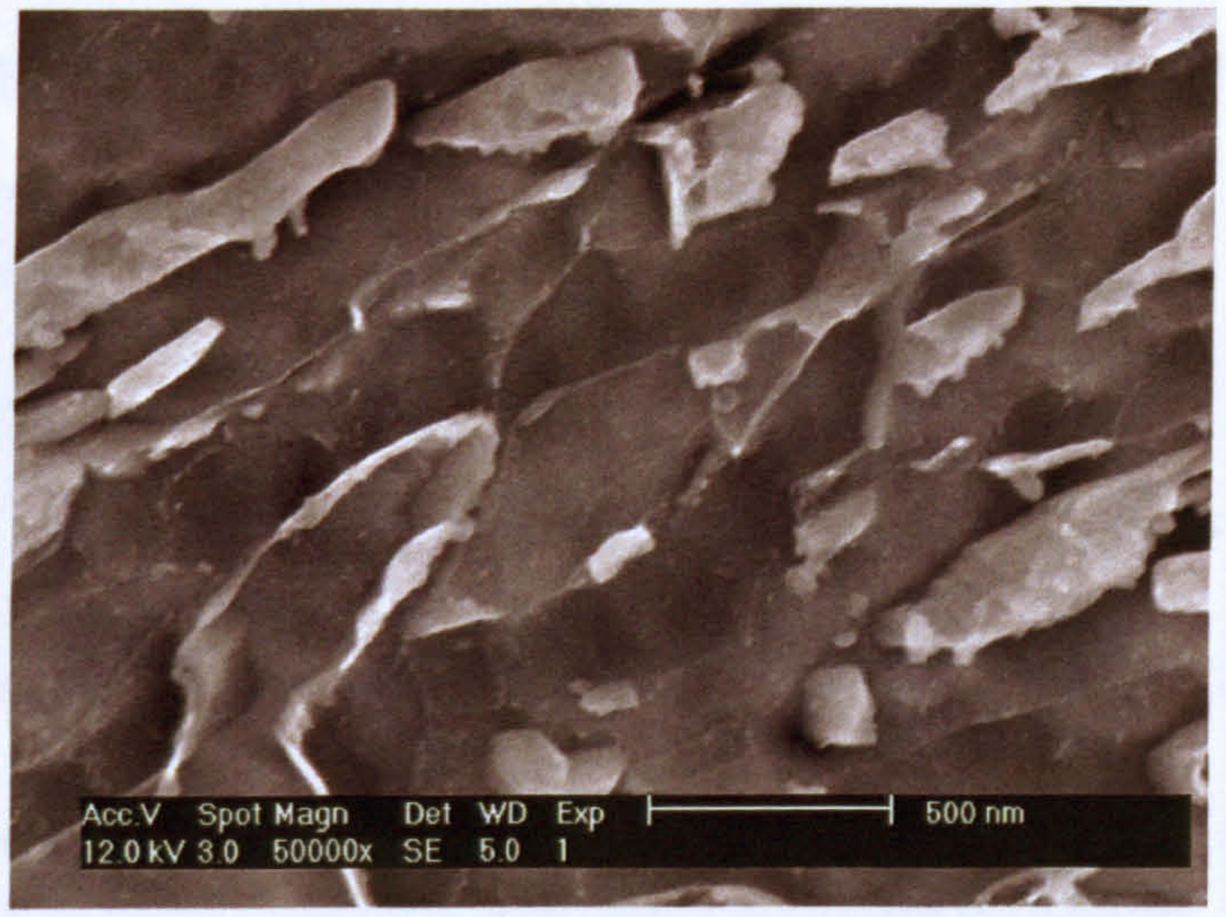

e

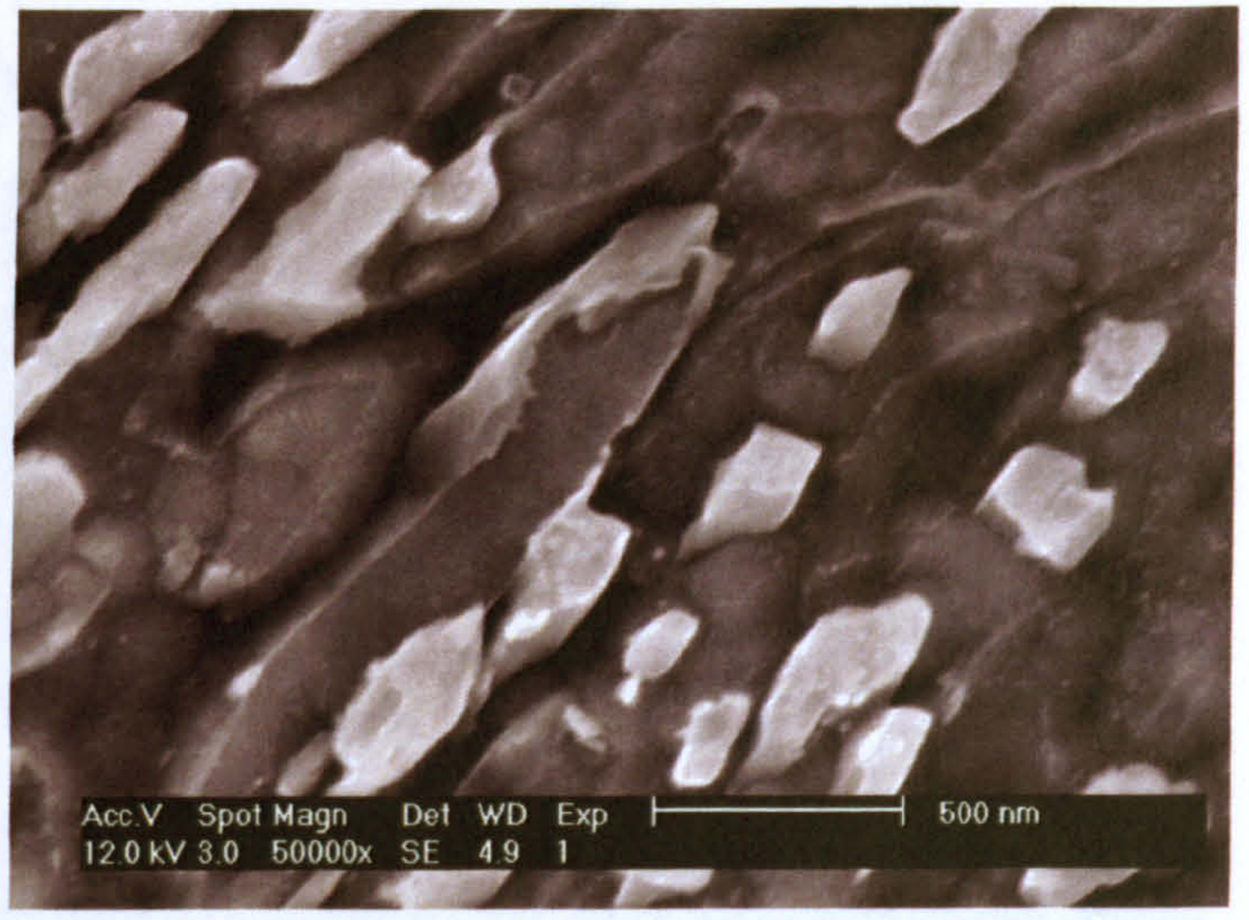

f

Fig.5.25 SEI SEM micrographs of the specimen first tempered at 700 ºC for 4 h and then second tempered at 550 ºC for 2 h, showing tempered martensite (α_T'), retained austenite (γ'), and tempered martensite (α_{T1}') which decompose from fresh martensite (α_F'). (a)-(c) were taken from the same area at different magnifications while (d)-(f) were taken from different areas.

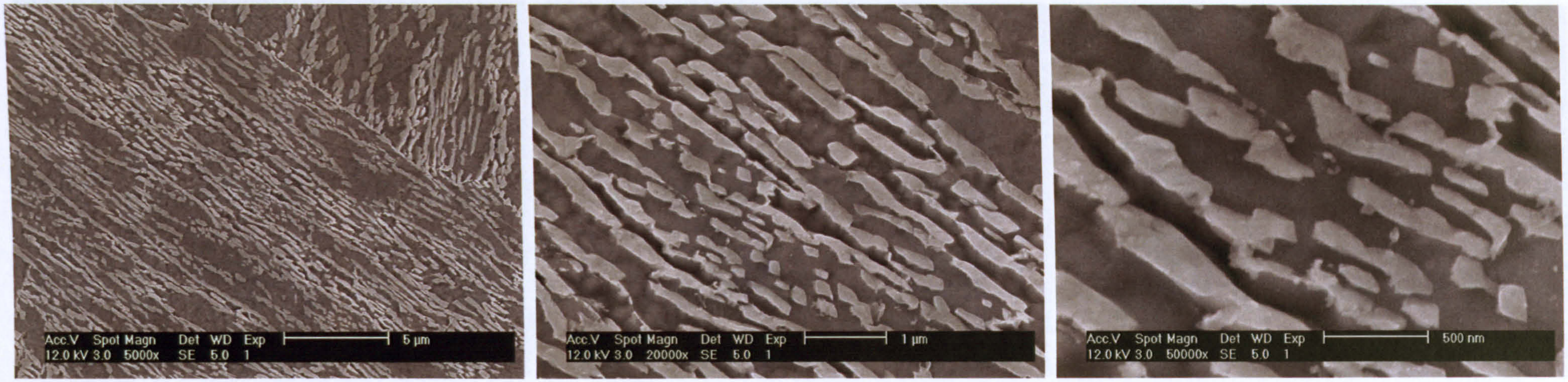

a b c

Fig.5.26 SEI SEM micrographs of the specimen tempered at 600 ºC for 8 h.

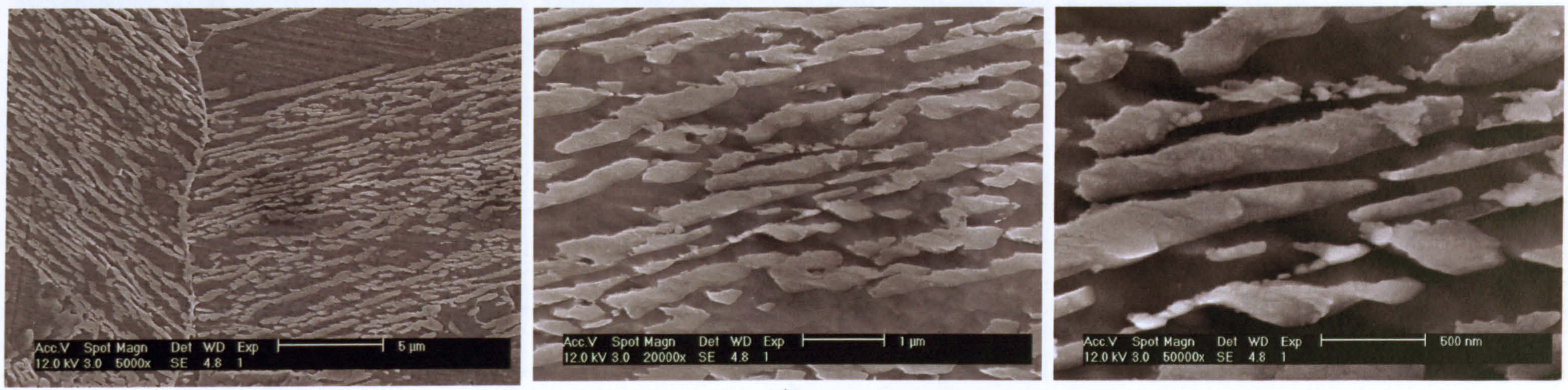

a b c

Fig.5.27 SEI SEM micrographs of the specimen tempered at 600 ºC for 24 h.

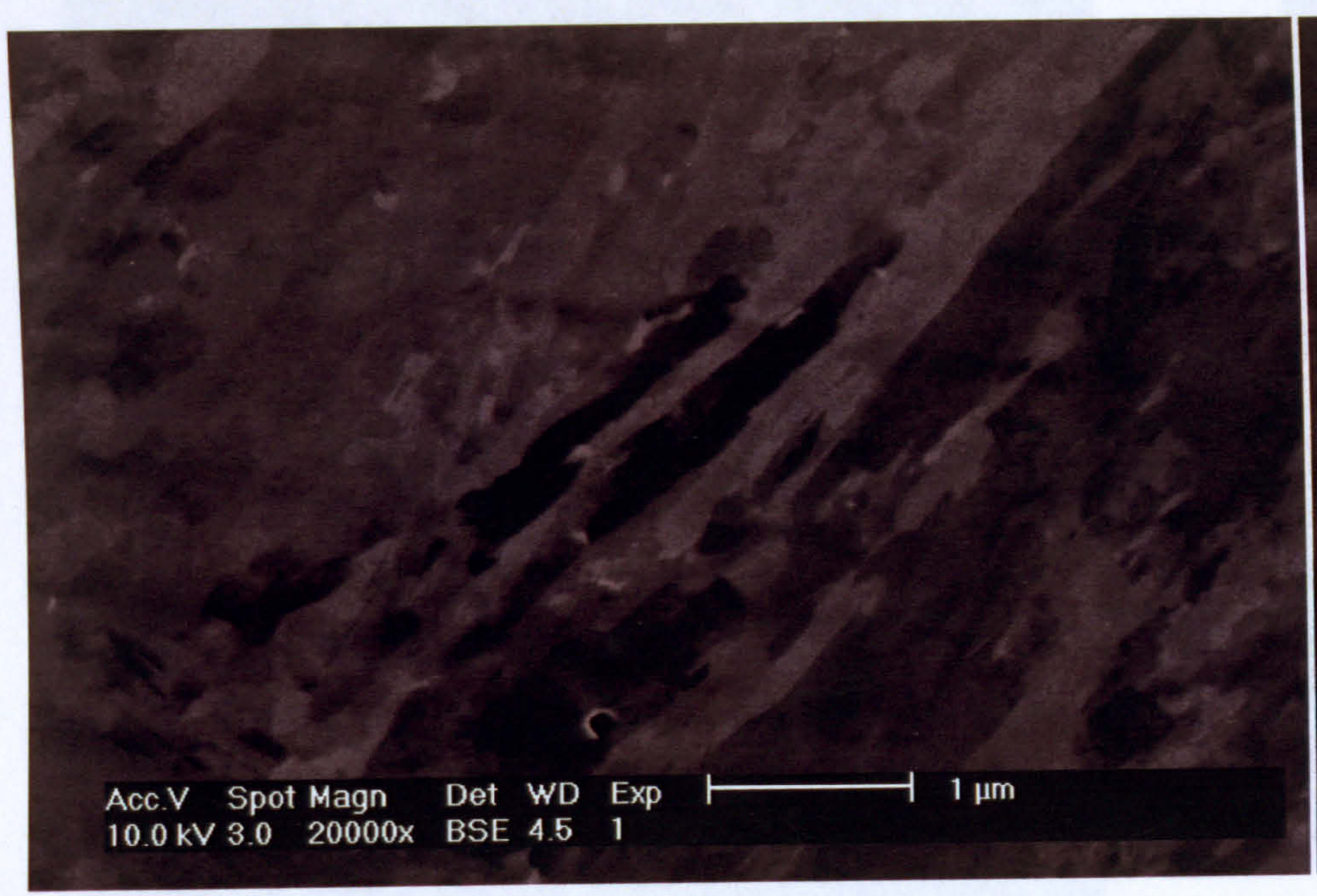

(a)

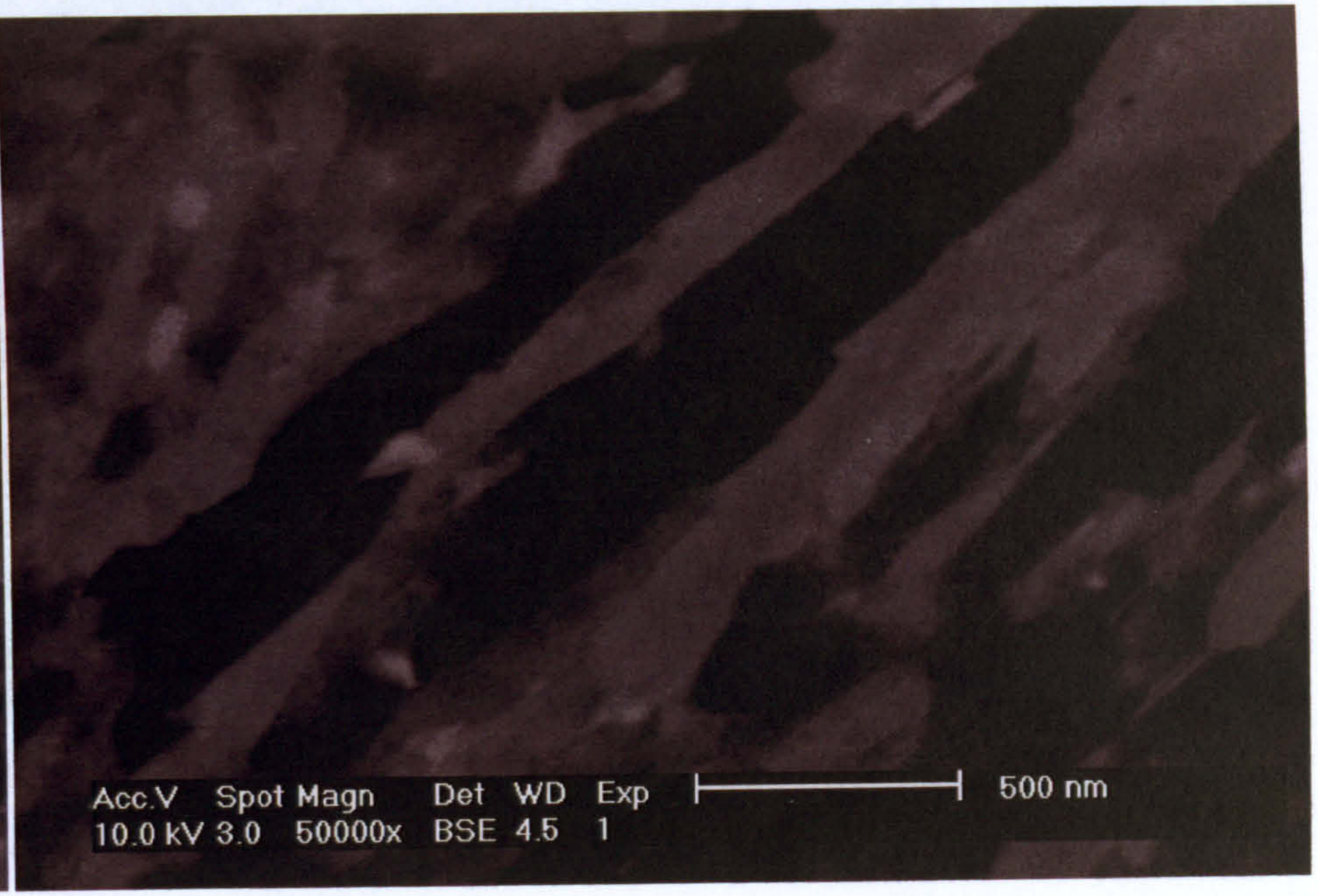

(b)

Fig.5.30 BEI SEM micrographs of the specimen tempered at 660 ºC for 4 h. (a) and (b) were taken from the same area but at different magnifications.

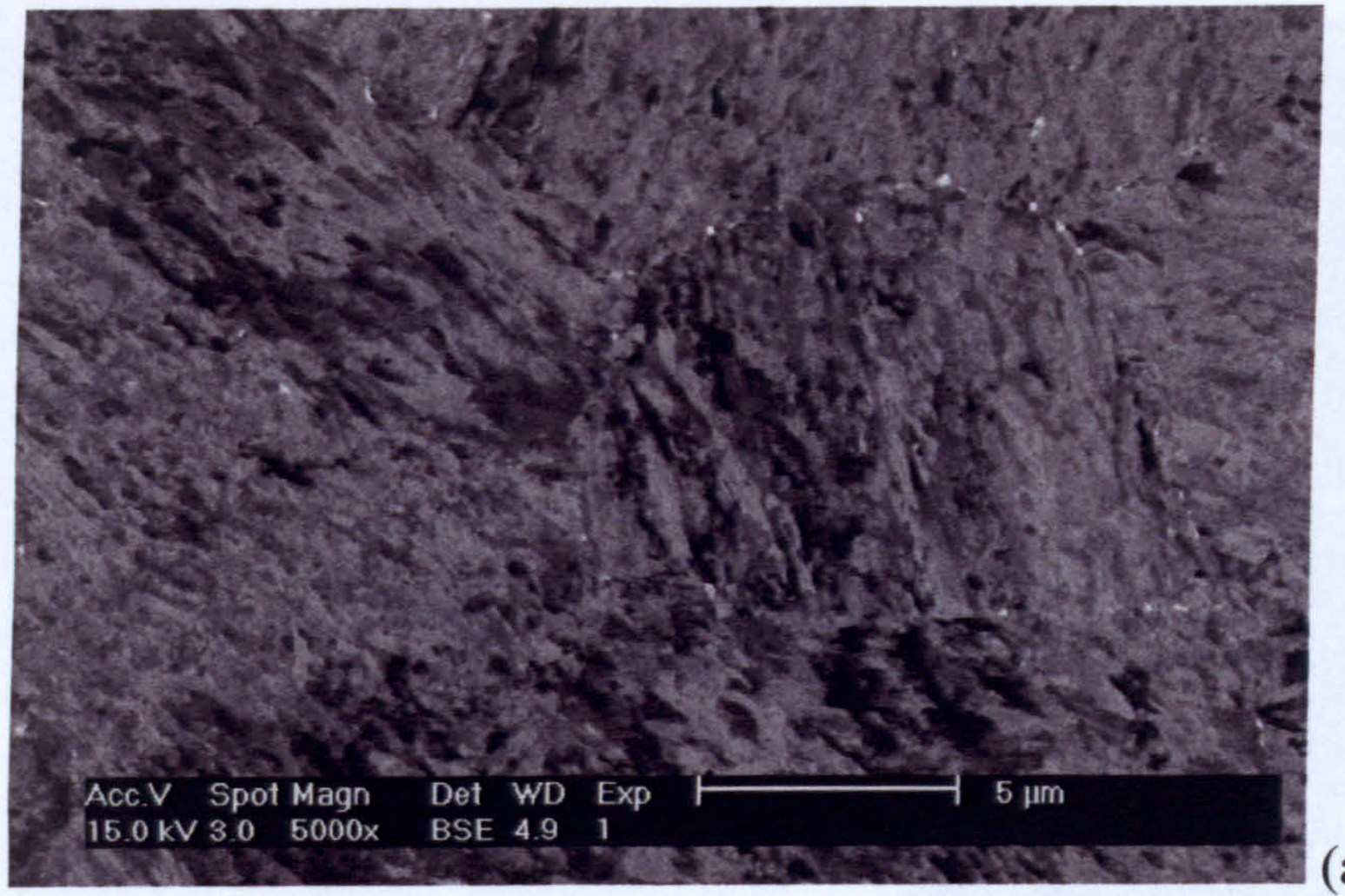

(a)

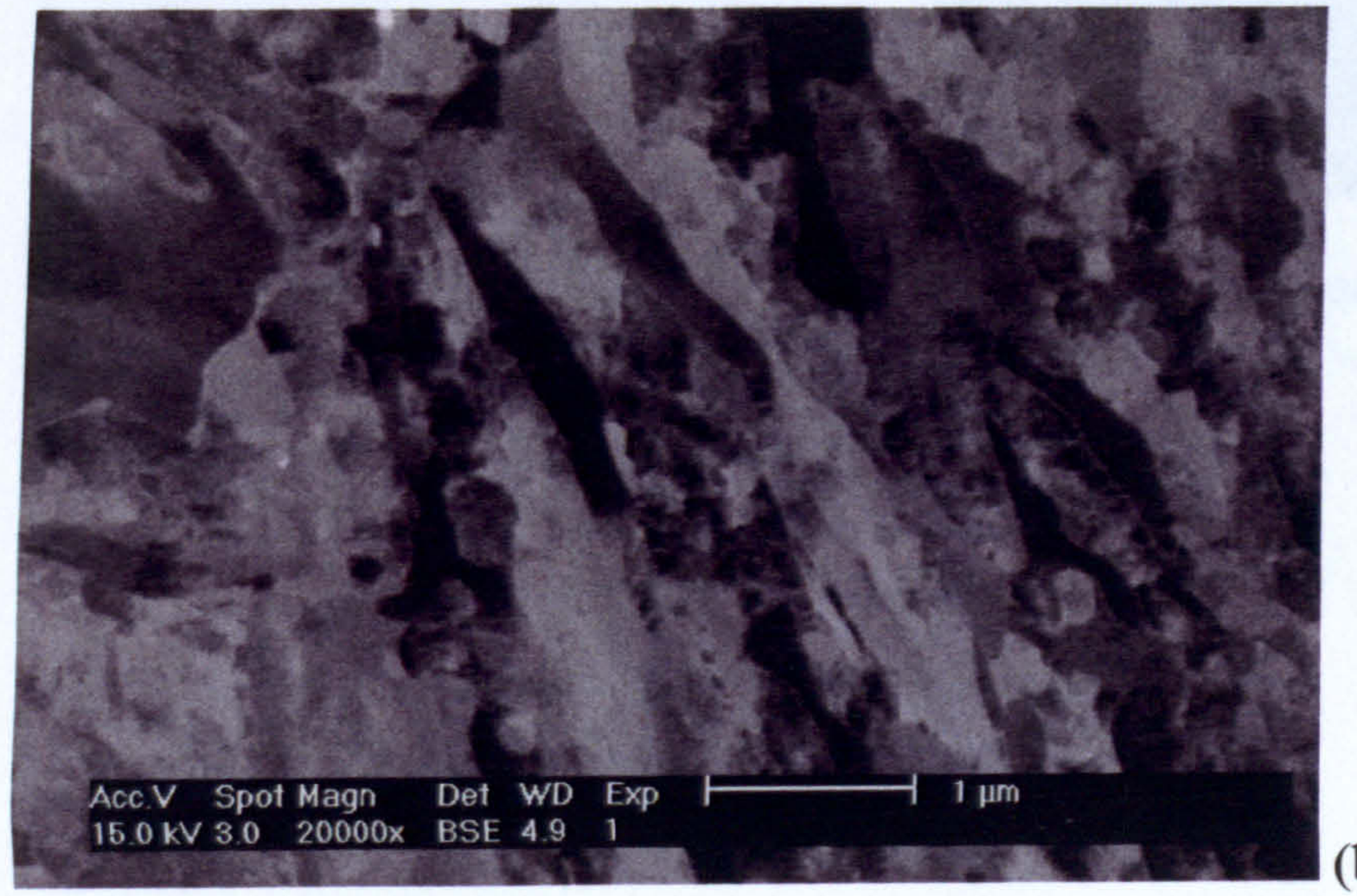

(b)

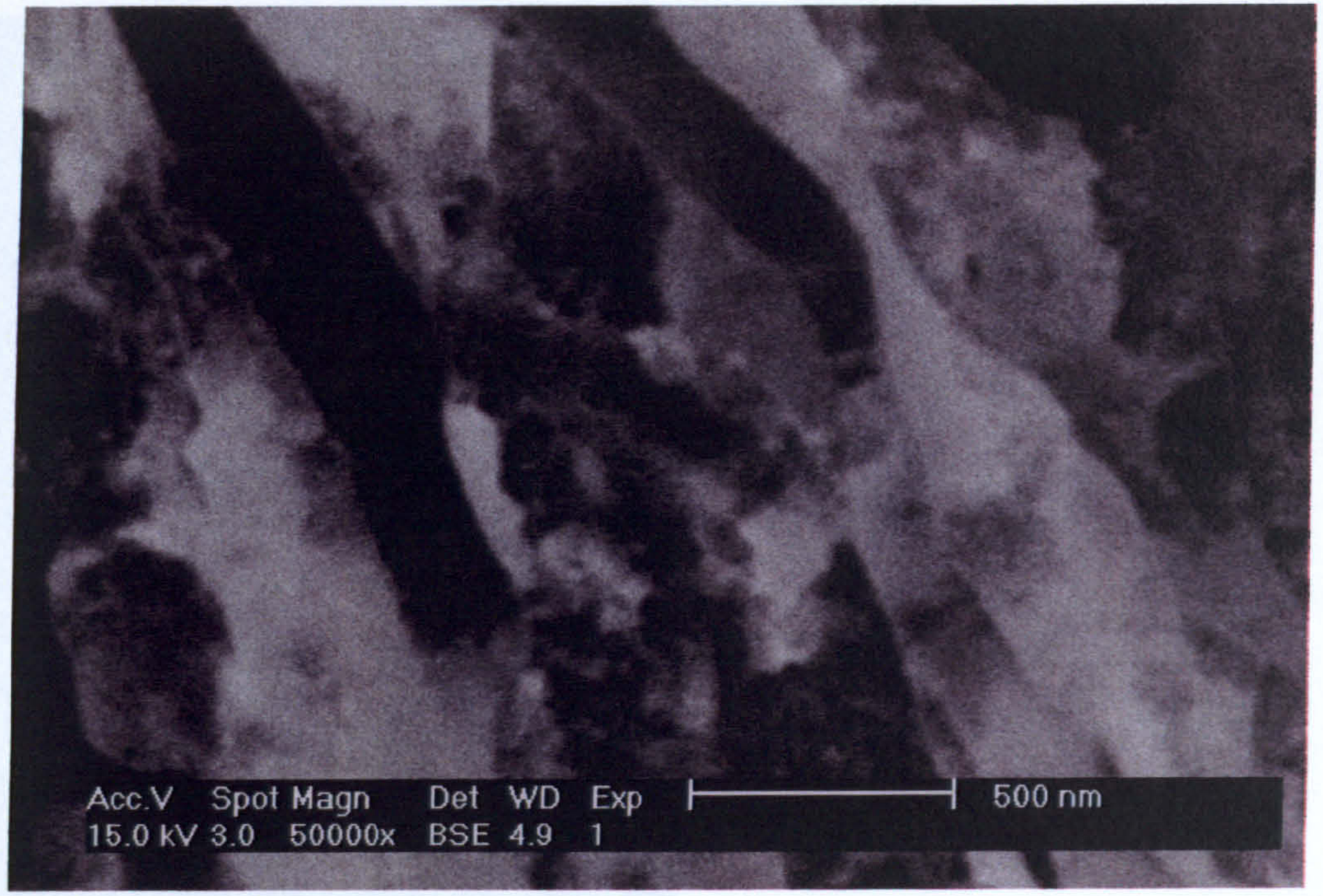

(c)

Fig.5.31 BEI SEM micrographs of the specimen tempered at 700 ºC for 4 h. The images were taken from the same area but at different magnifications. Fine brighter precipitates distributed along prior austenite grain boundaries, as shown in (a).

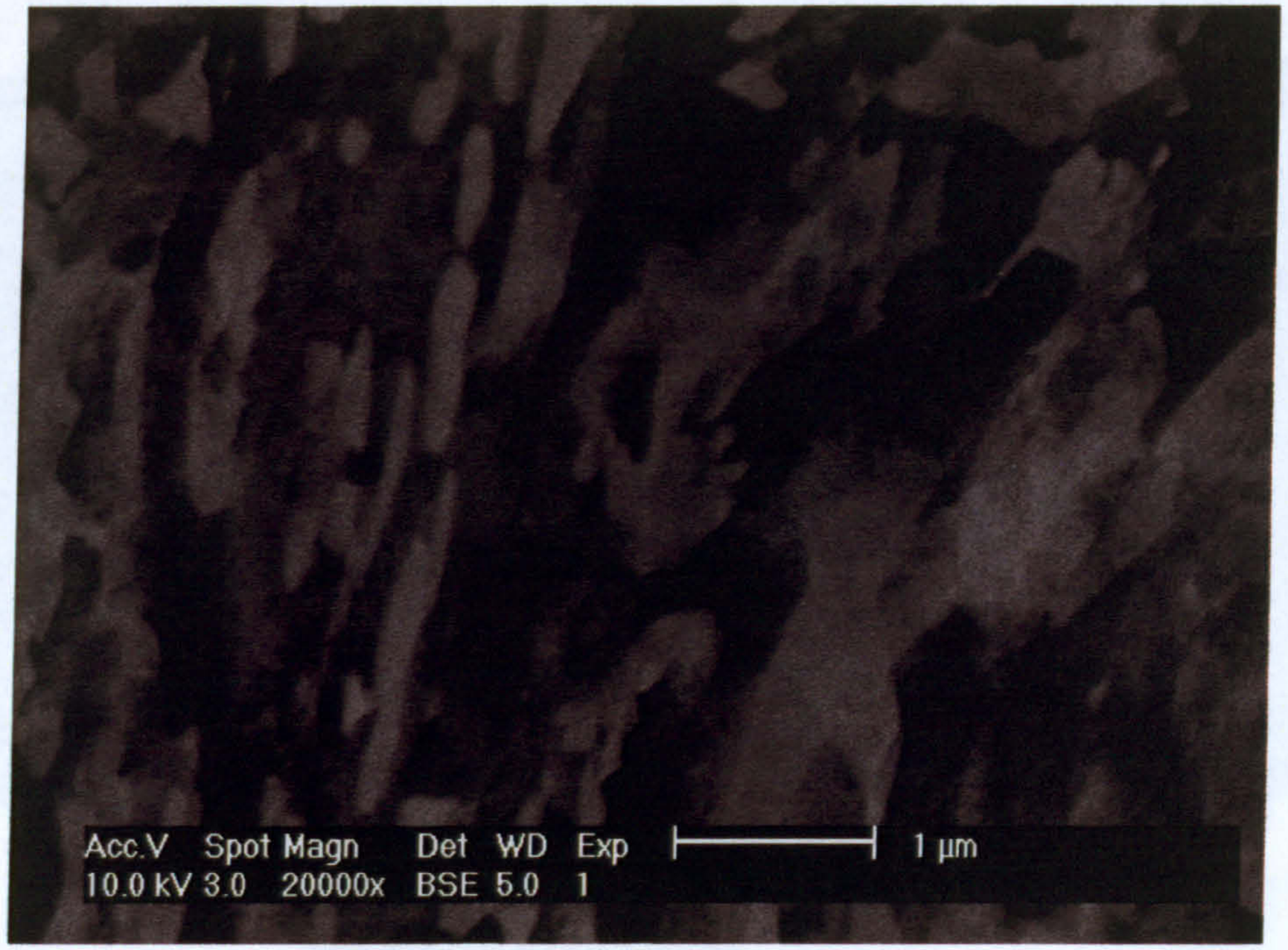

Fig.5.32 BEI SEM micrograph of the specimen first tempered at 700 ºC for 4 h, and then second tempered at 550 ºC for 2 h.

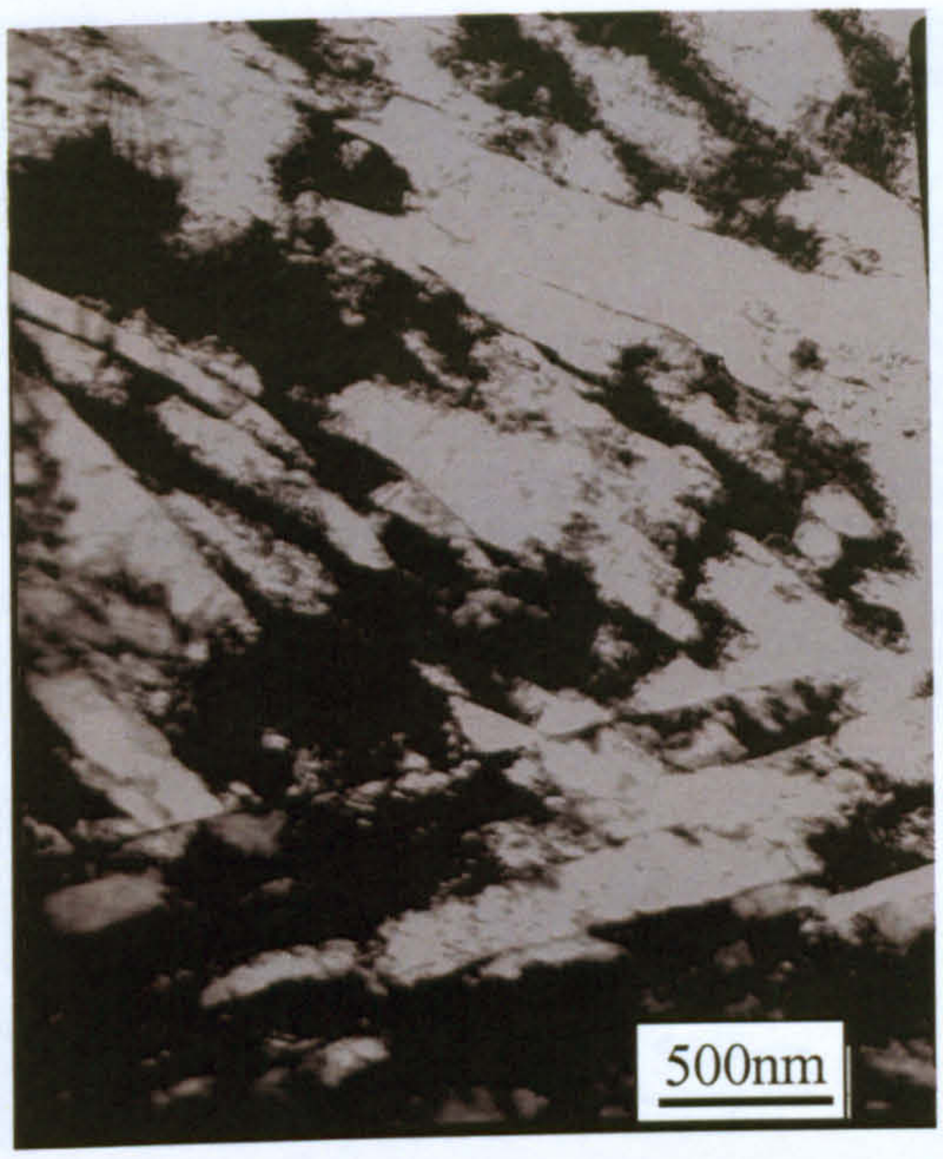

Fig.5.33 Thin foil TEM bright field image of the specimen tempered at 557 °C for 4 h, showing martensitic lath structure.

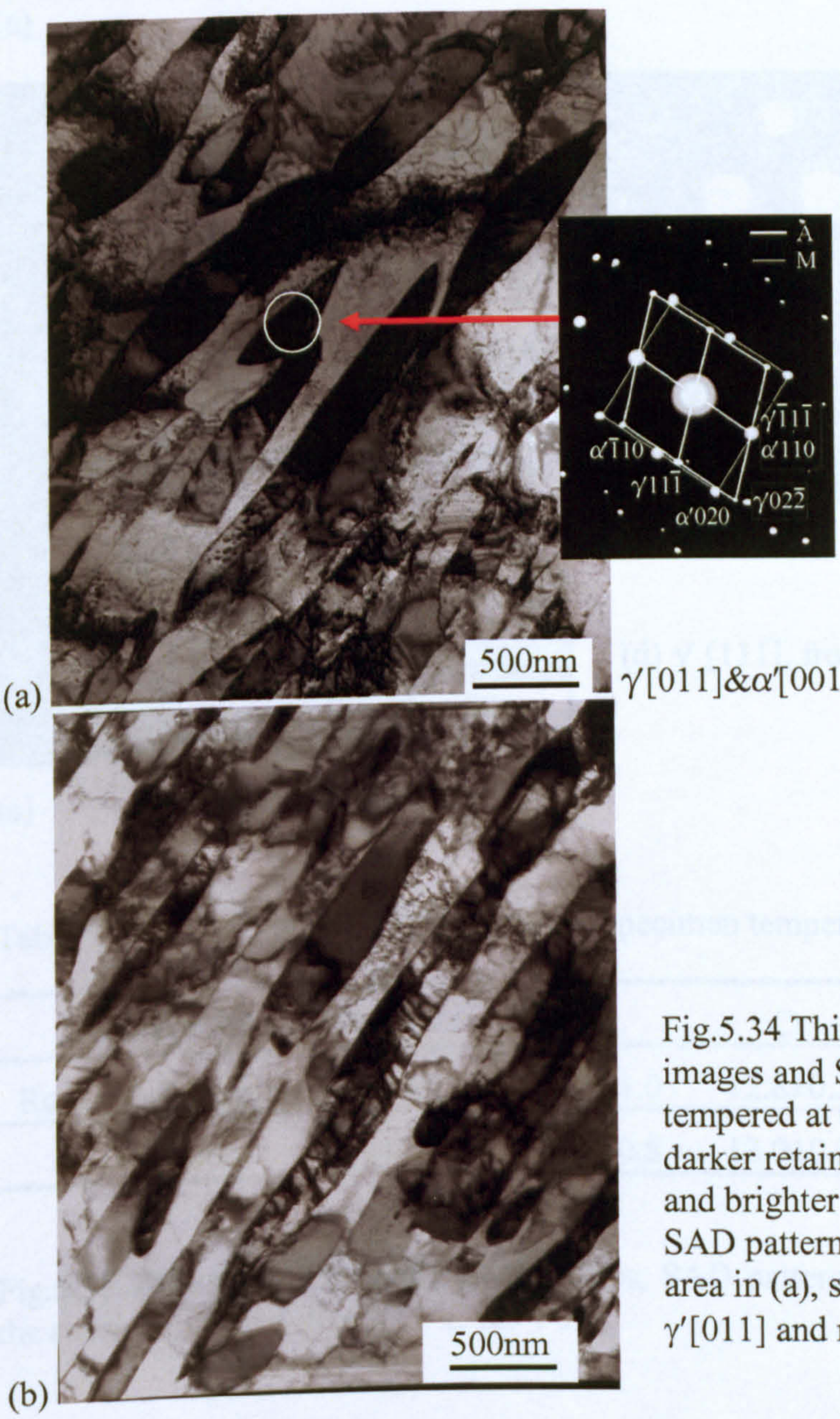

Fig.5.34 Thin foil TEM bright field images and SAD pattern of the specimen tempered at 630 °C for 4 h, showing darker retained austenite films/particles and brighter tempered martensite. The SAD pattern was taken from the marked area in (a), showing retained austenite γ′[011] and martensite α′[001].

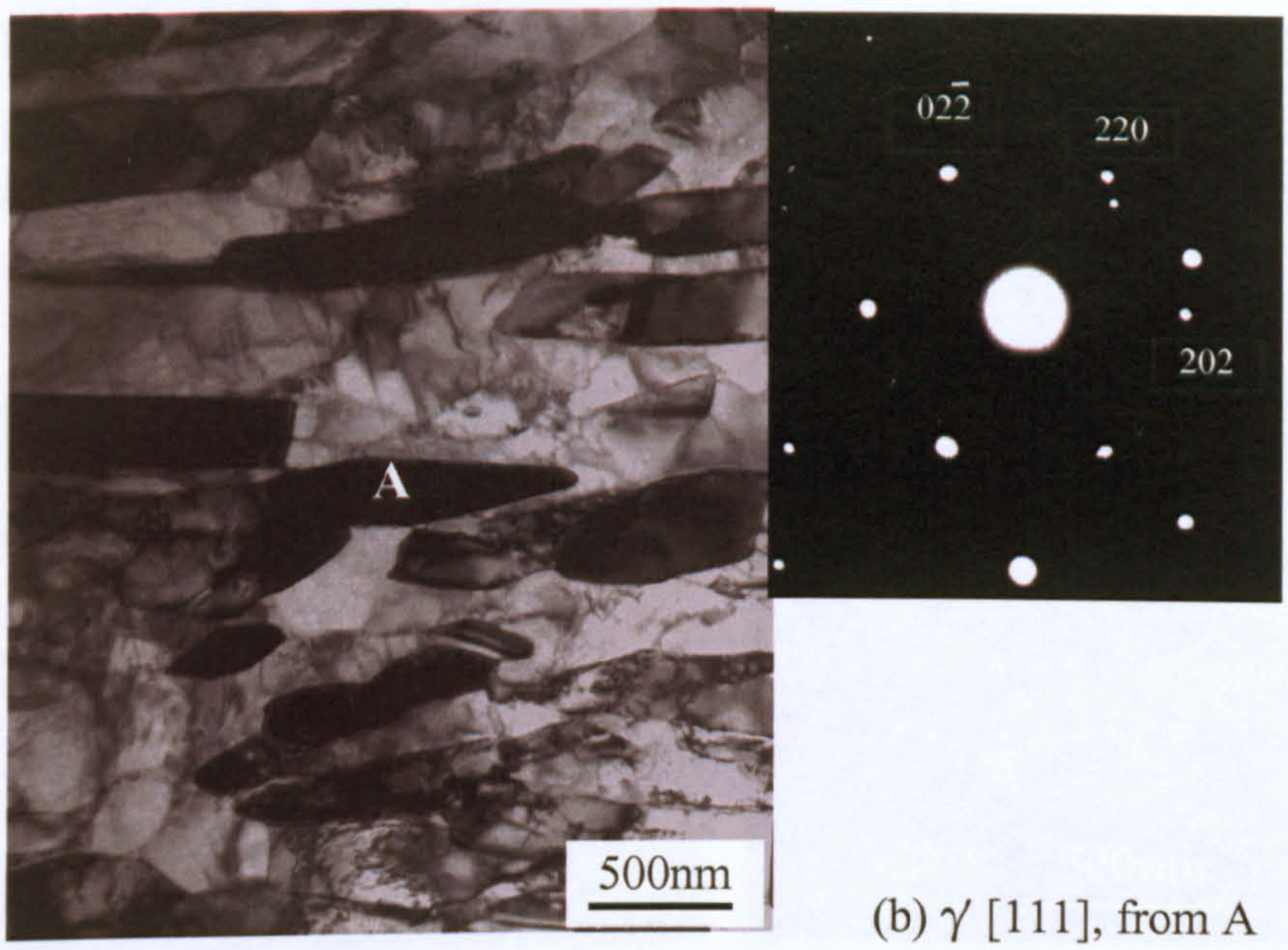

(a)

(b) γ [111], from A

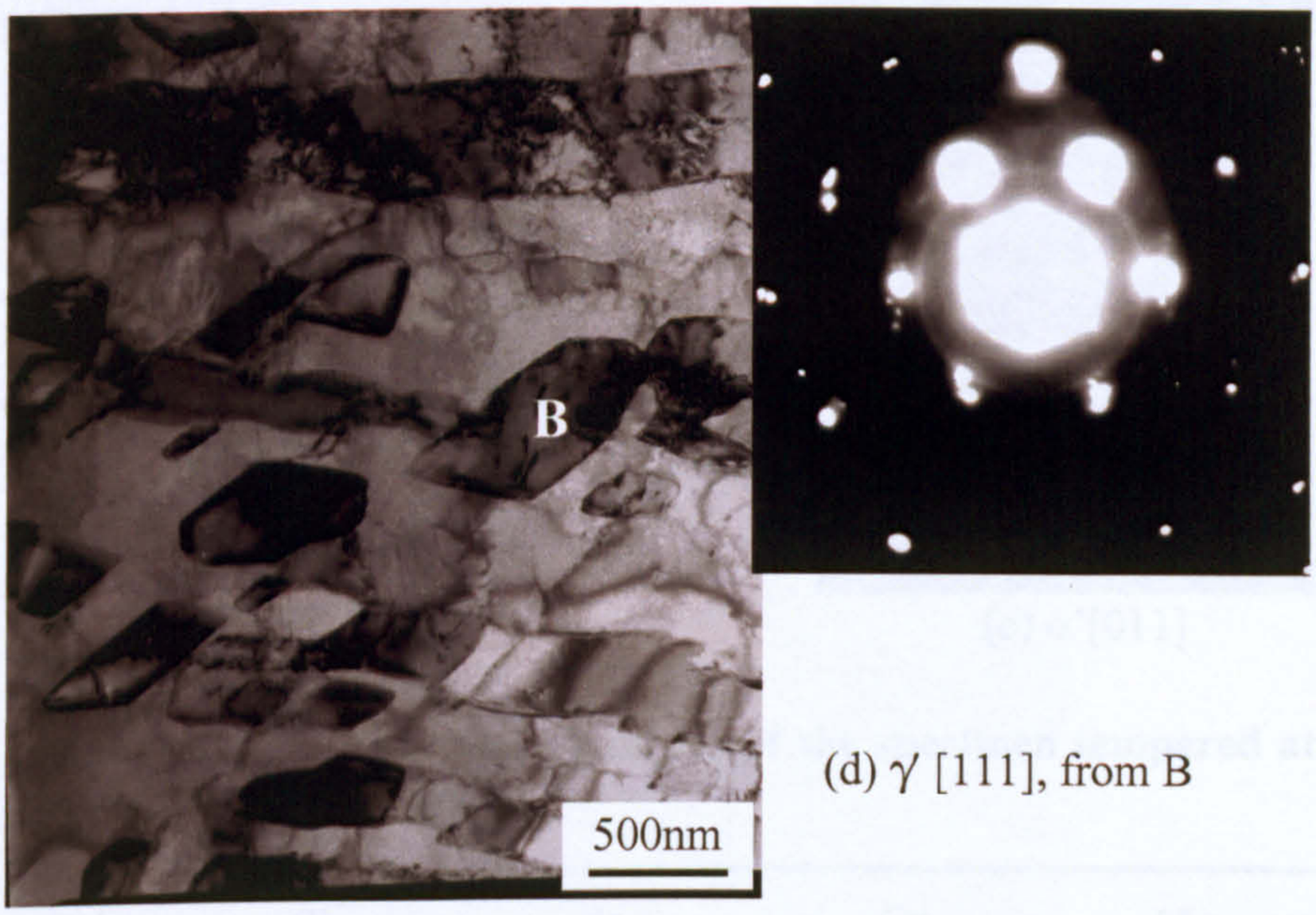

(c)

(d) γ [111], from B

Table 5.6 TEM EDX point analysis of the specimen tempered at 635 °C for 4 h (wt%)

Phase	Si	Fe	Cr	Mo	Ni
Retained Austenite	0.1±0.1	74.5±1.0	12.8±0.3	1.9±0.1	10.0±1.4
Martensite	0.1±0.1	79.6±0.8	13.0±0.3	2.6±0.1	4.4±0.8

Fig.5.35 Thin foil TEM bright field images, SAD patterns and EDX microanalysis of the specimen tempered at 635 °C for 4 h.

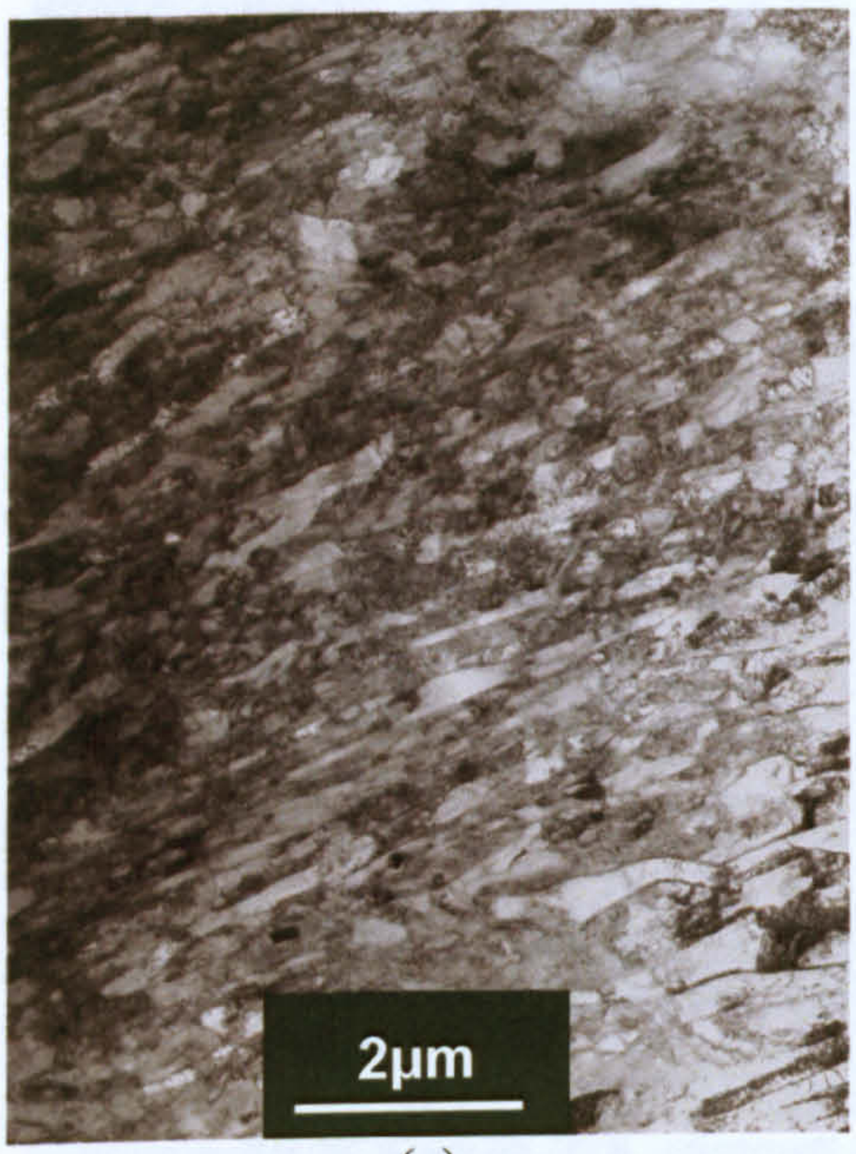

(a)

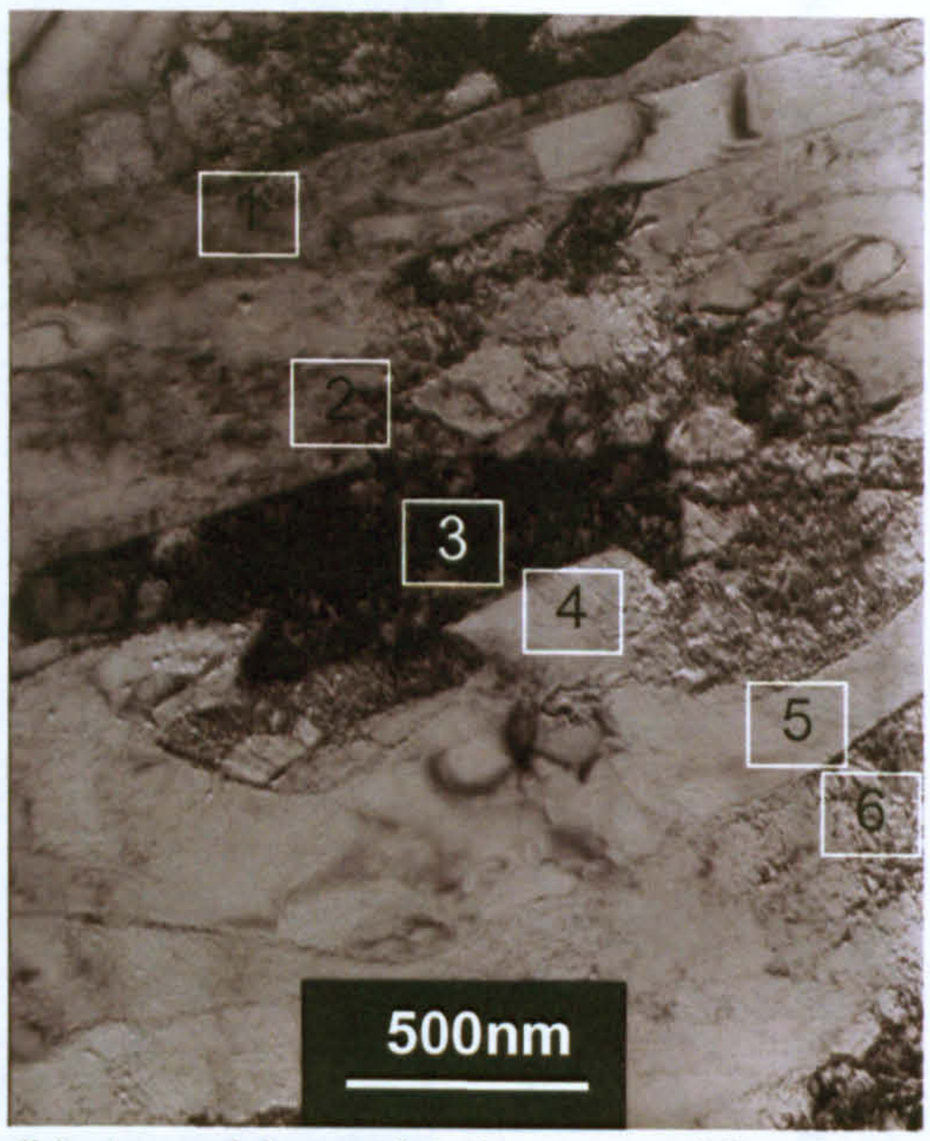

(b) Area (a) at a higher magnification.

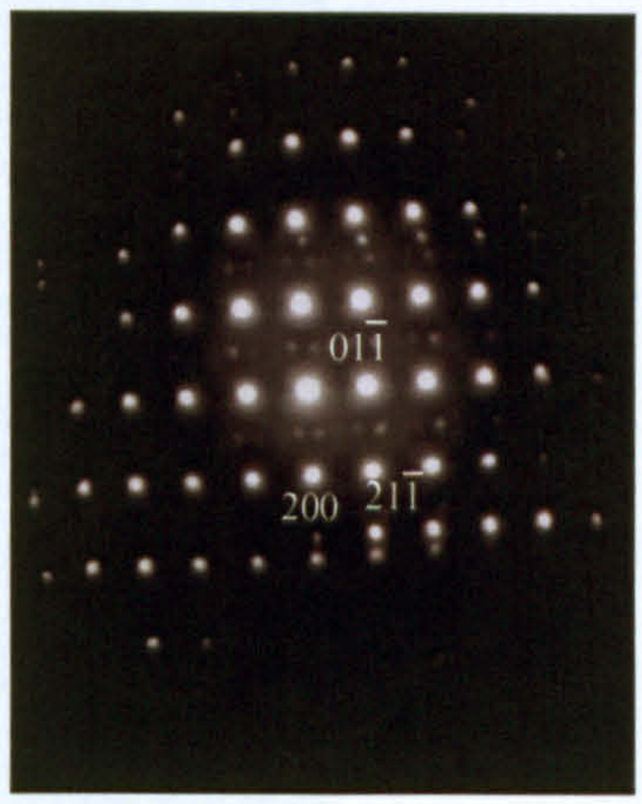

(c) α′[011]

Table 5.7 TEM EDX point analysis of the specimen tempered at 700 °C for 4 h (wt%)

Point	Si	Fe	Cr	Mo	Ni
1	0.2	81.0	11.7	1.9	5.2
2	0.3	79.9	11.5	2.2	6.2
3	0.8	78.7	11.4	2.5	6.6
4	0.5	81.3	12.3	3.5	2.4
5	0.6	82.0	12.1	3.6	1.7
6	0.4	78.4	11.5	2.3	7.5

Fig.5.36 Thin foil TEM bright field images, SAD pattern and EDX microanalysis of the specimen tempered at 700 °C for 4 h. The SAD pattern was taken from the marked area 3 in (b), showing fresh martensite α′[011].

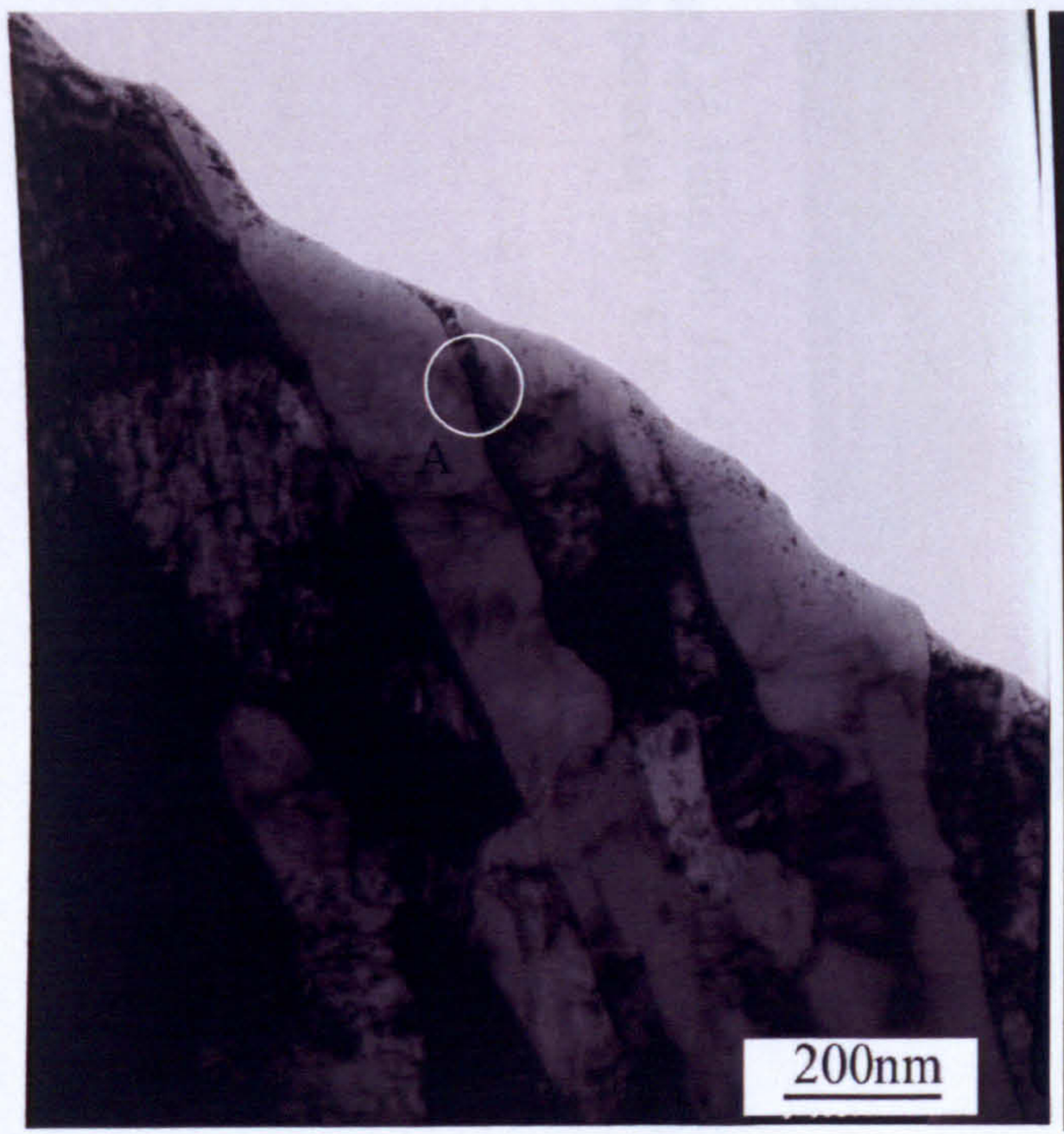

(a) Bright field image

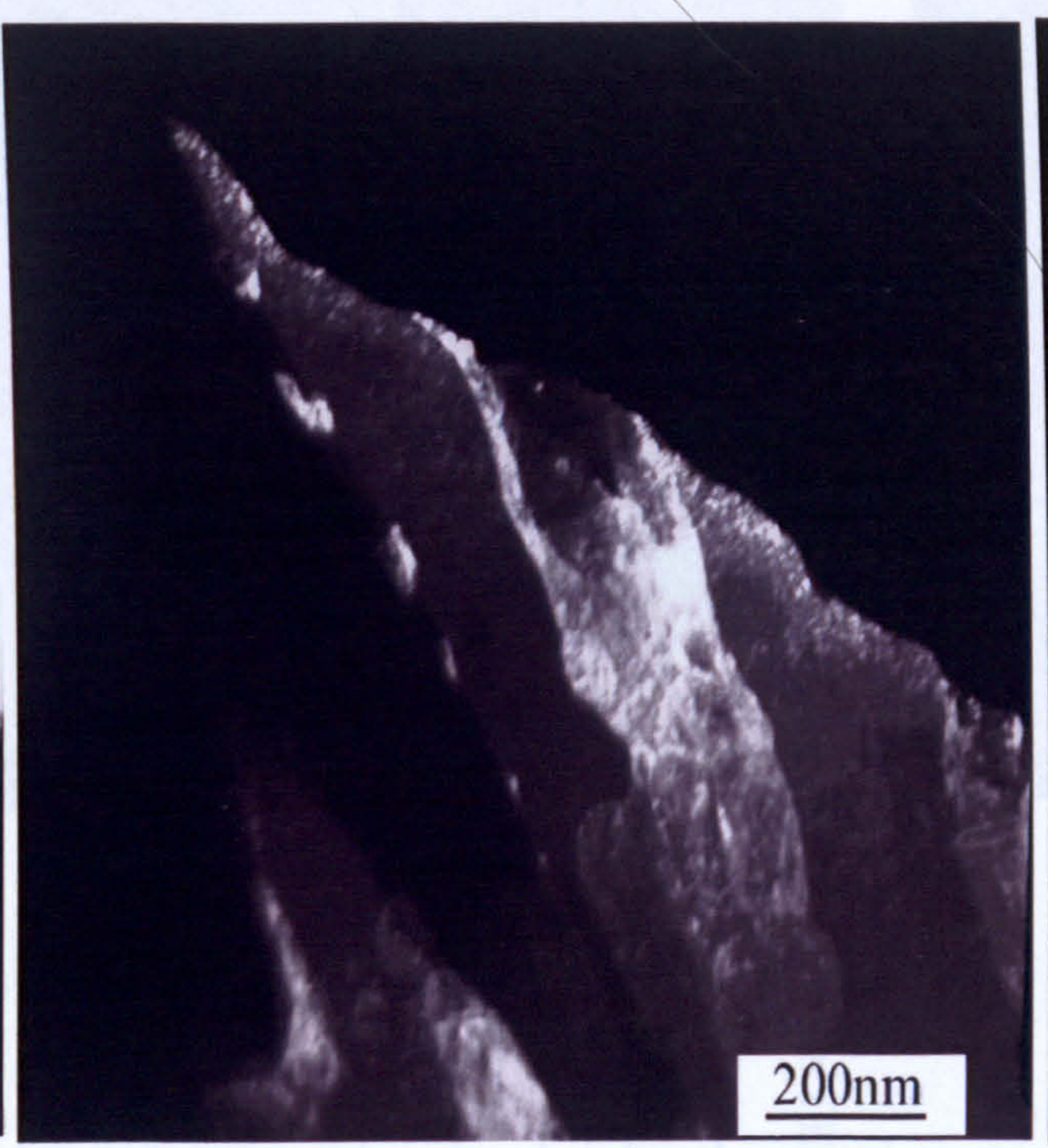

(b) Dark field image

(c) Selected area diffraction patterns from A in (a), showing $\gamma'[011]$ and $\alpha'[\bar{1}11]$

Fig.5.37 Thin foil TEM (a) Bright field image, (b) dark field image, and (c) SAD patterns of the specimen first tempered at 700 ºC for 4 h and then second tempered at 550 ºC for 2 h. The SAD patterns were taken from the marked area A in (a), showing retained austenite film.

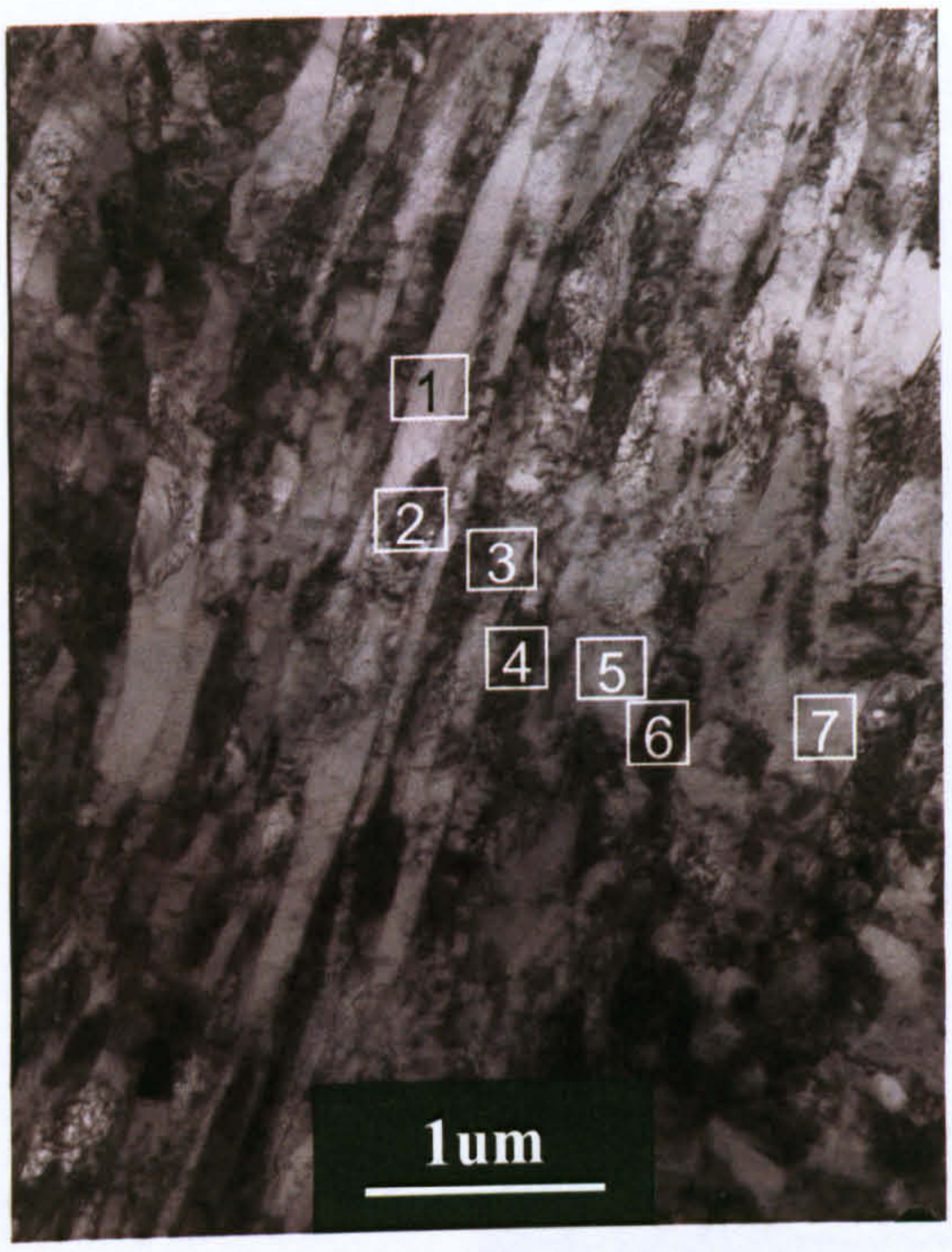

(a)

Table 5.8a TEM EDX point analysis (wt%)

Point	Si	Fe	Mo	Cr	Ni
1	0.2	81.9	2.7	12.4	2.9
2	0.2	76.4	2.0	11.8	9.5
3	0.1	82.1	1.9	12.1	3.7
4	0.2	75.5	1.7	12.2	10.4
5	-	81.8	1.8	12.4	4.8
6	-	76.5	2.0	12.3	9.2
7	0.1	81.5	1.8	11.8	4.8

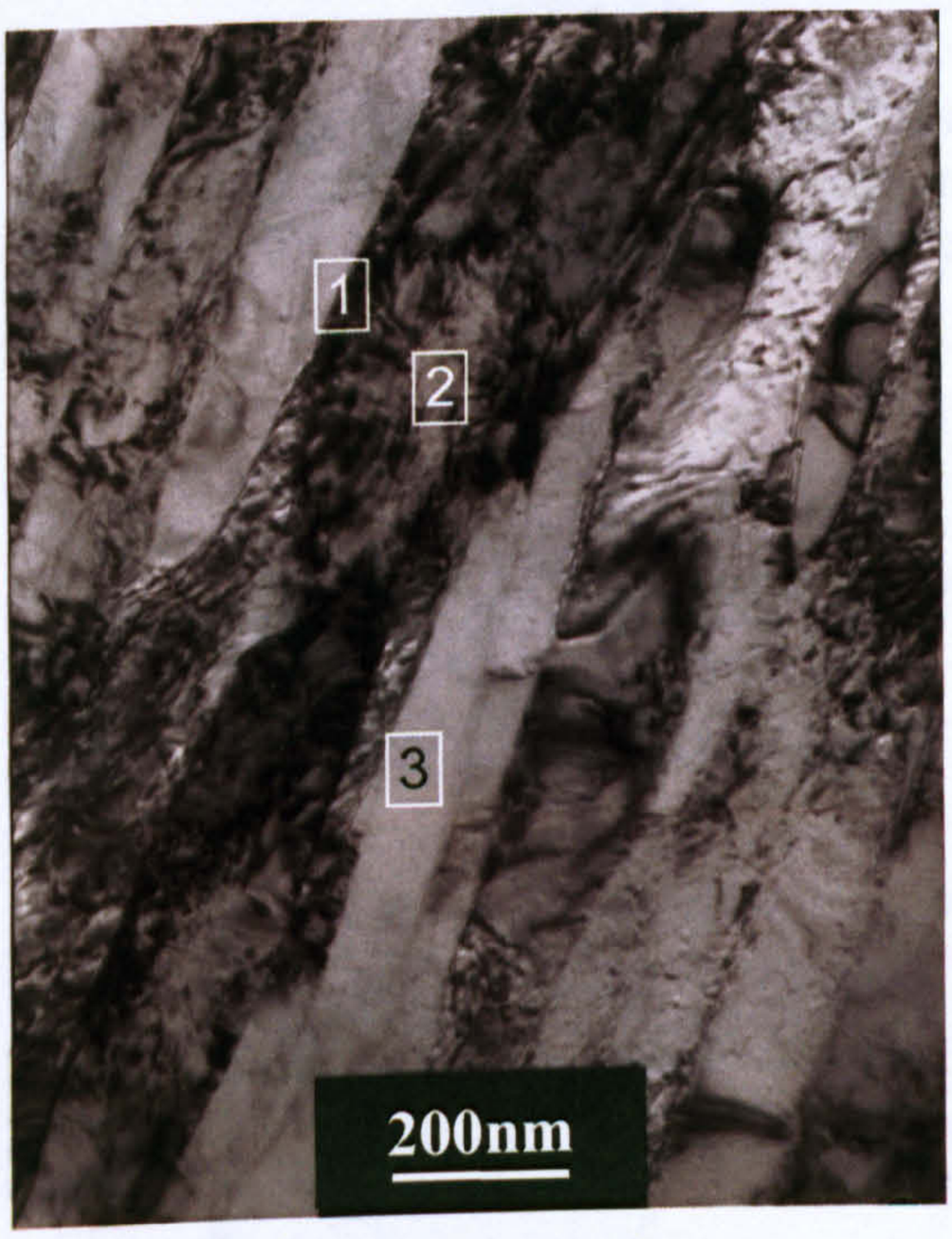

(b)

Table 5.8b TEM EDX point analysis (wt%)

Point	Si	Fe	Mo	Cr	Ni	V
1	0.2	79.3	1.5	12.0	7.1	-
2	0.2	76.4	2.0	13.2	8.1	0.1
3	-	83.1	2.4	12.7	1.8	-

Fig.5.38 Thin foil TEM bright field images and EDX microanalysis of the specimen first tempered at 700 °C for 4 h and then second tempered at 550 °C for 2 h.

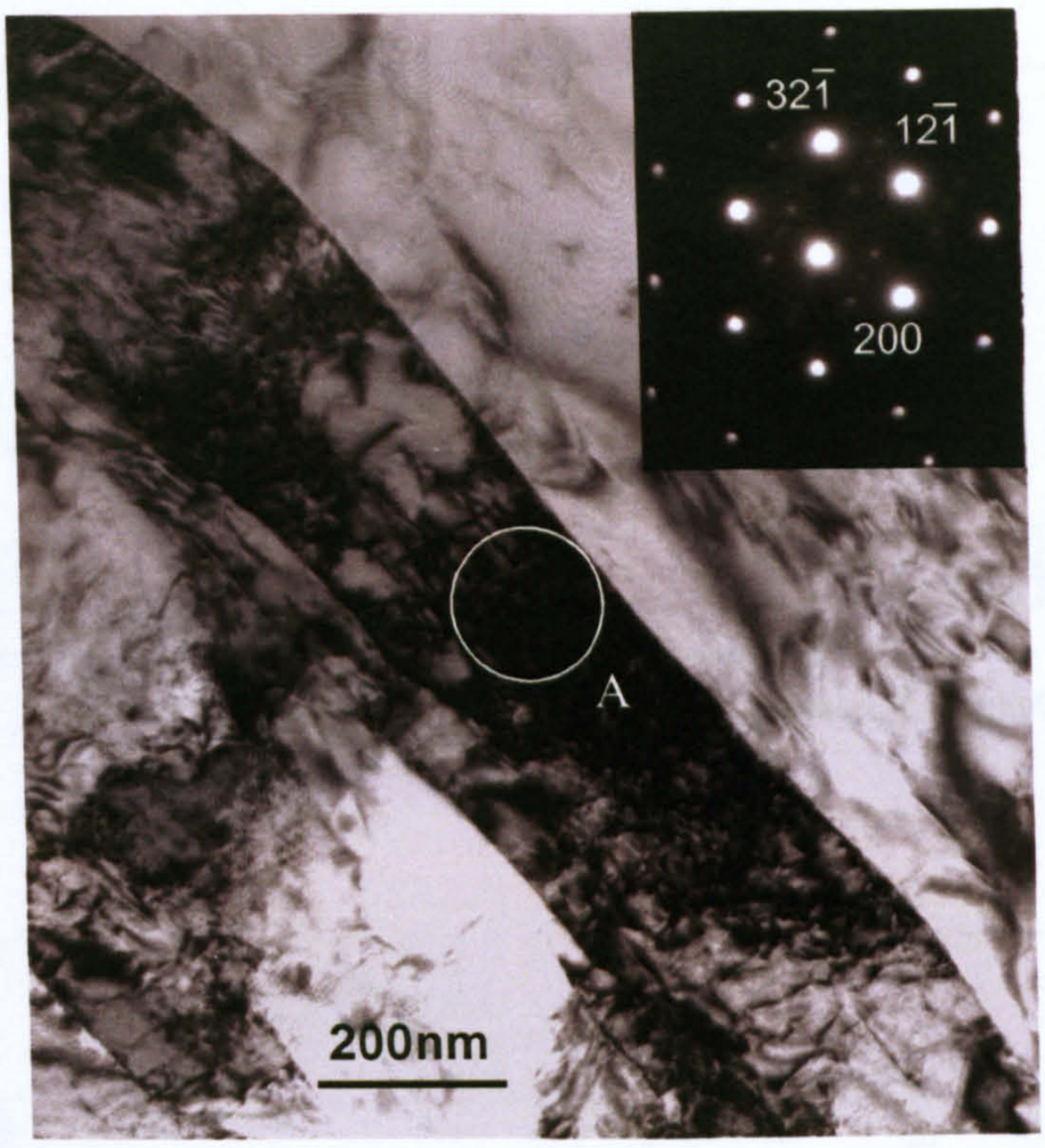

Fig.5.39 Thin foil TEM bright field image and SAD pattern of the specimen first tempered at 700 °C for 4 h and then second tempered at 550 °C for 2 h. The SAD pattern was taken from the marked area A, indicating the lath structure with a high dislocation density is martensite α′[012].

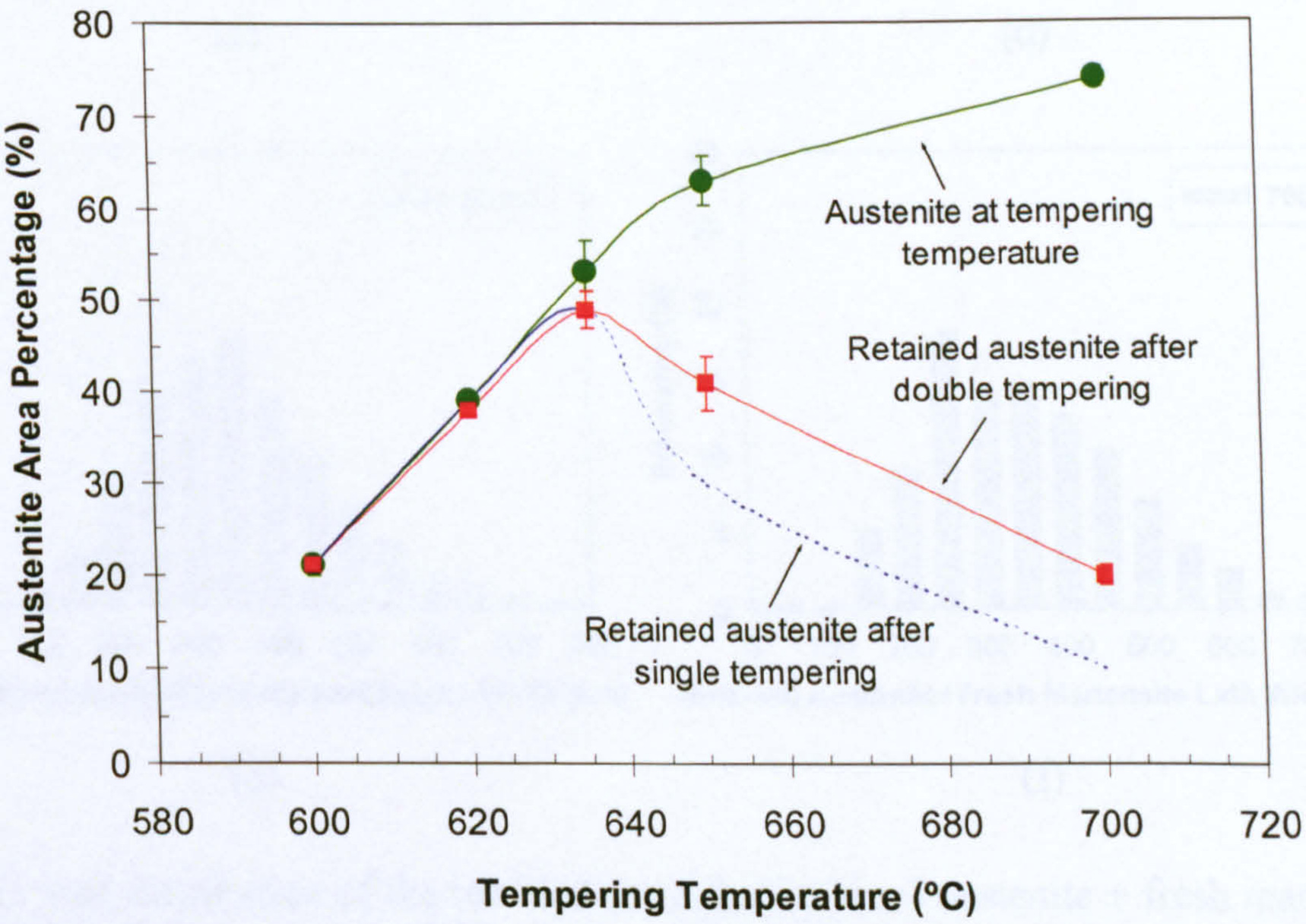

Fig.5.40 Image analysis showing area fraction of the austenite at tempering temperature and retained austenite after cooling to room temperature.

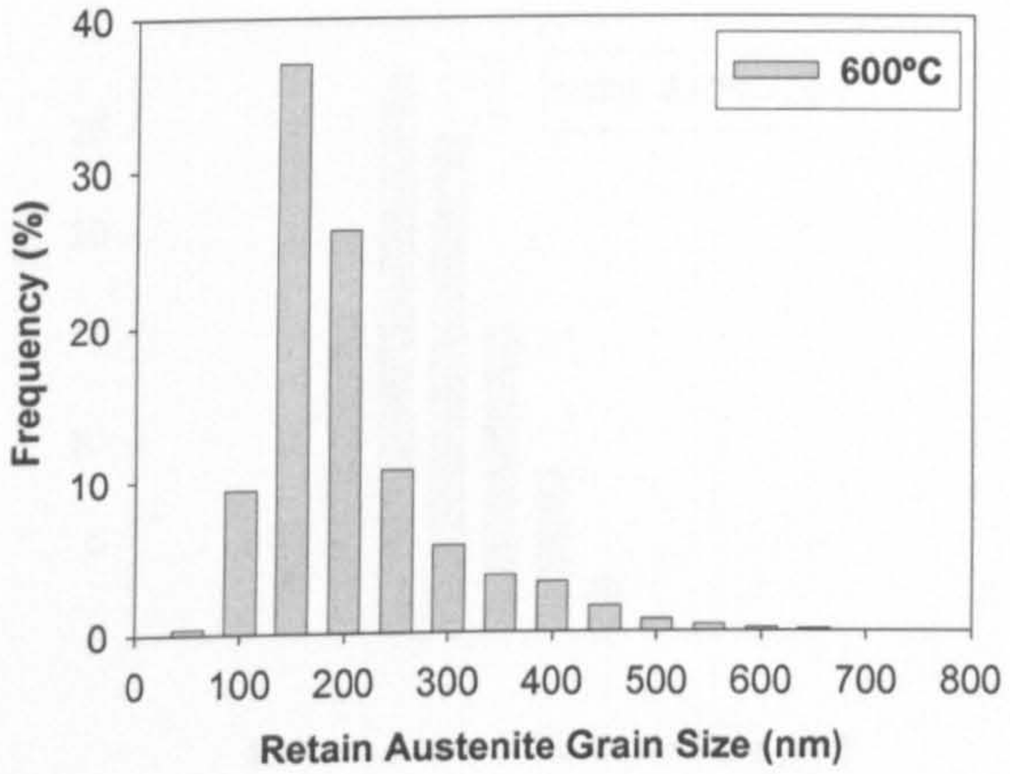

(a)

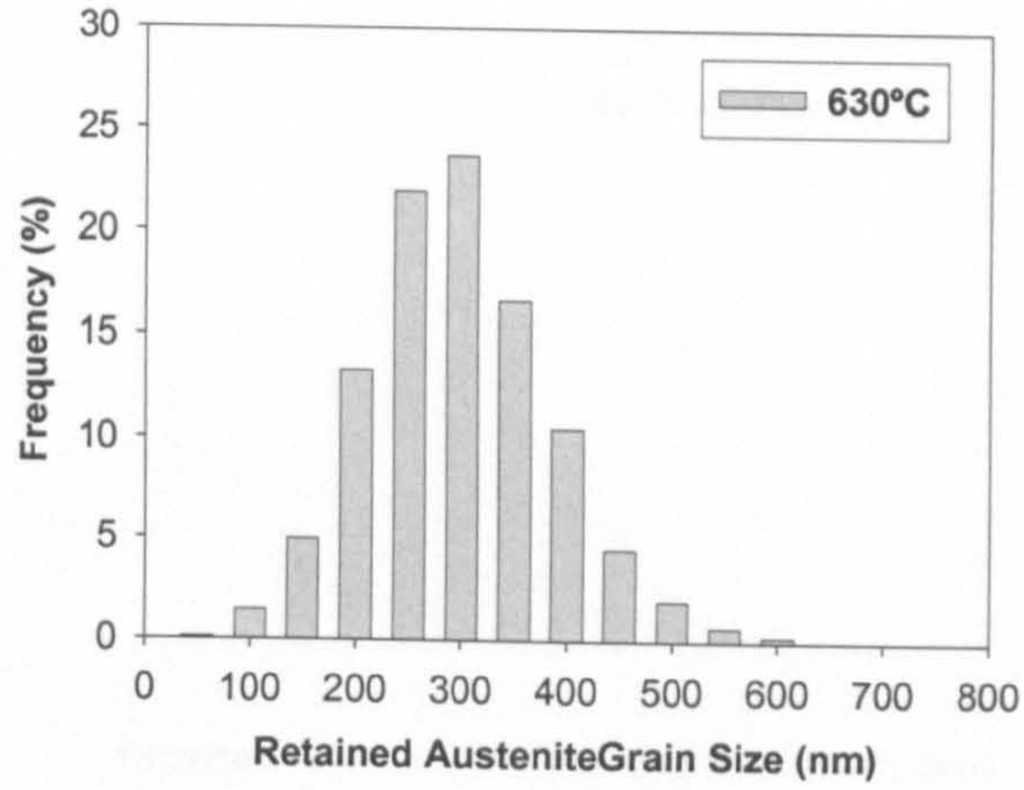

(b)

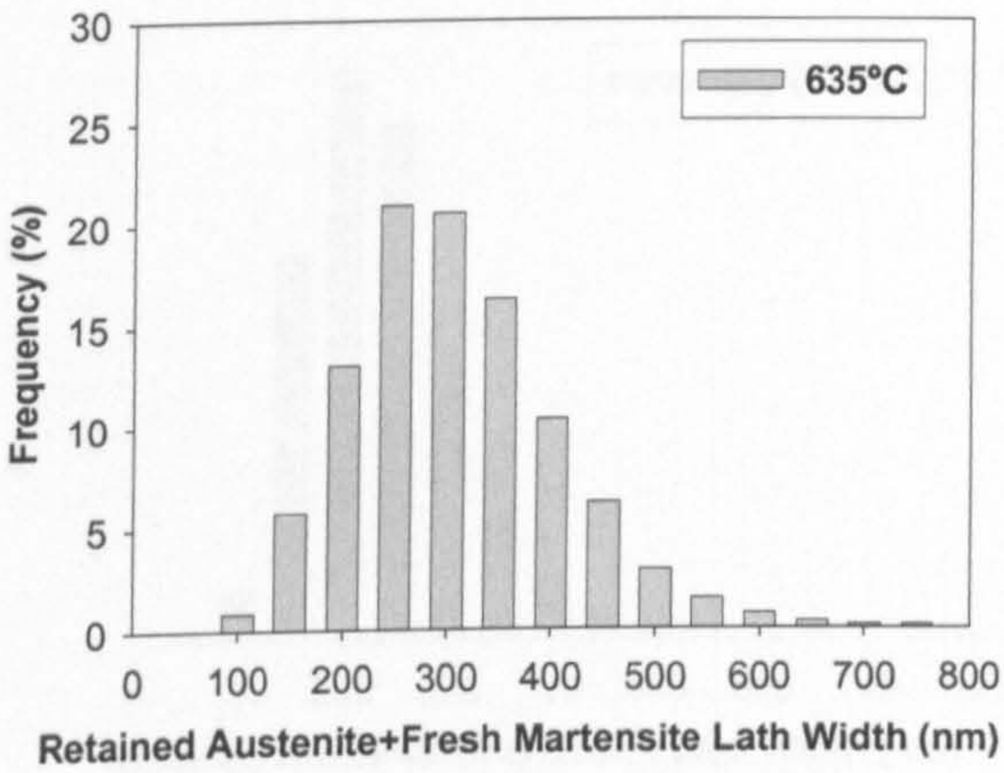

(c)

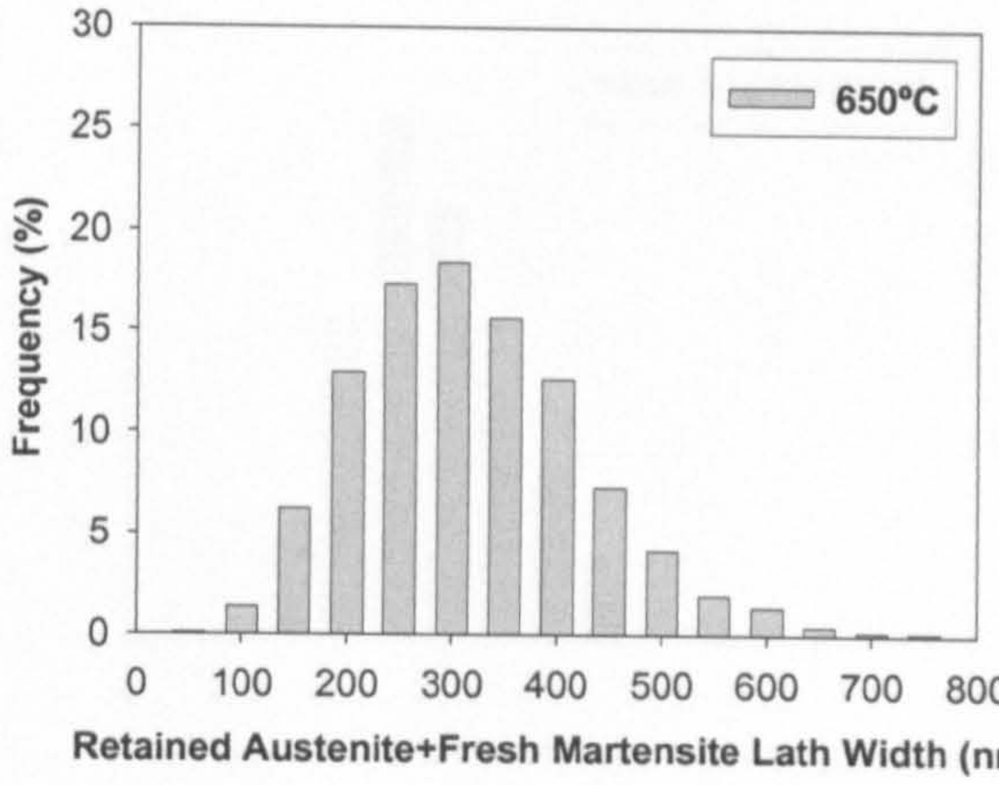

(d)

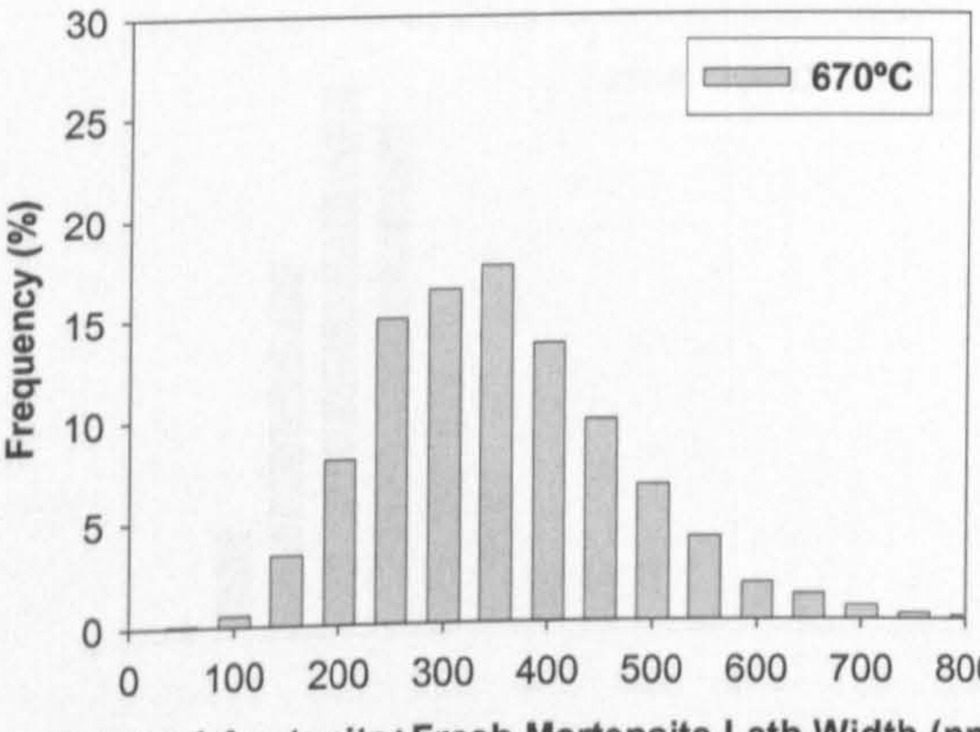

(e)

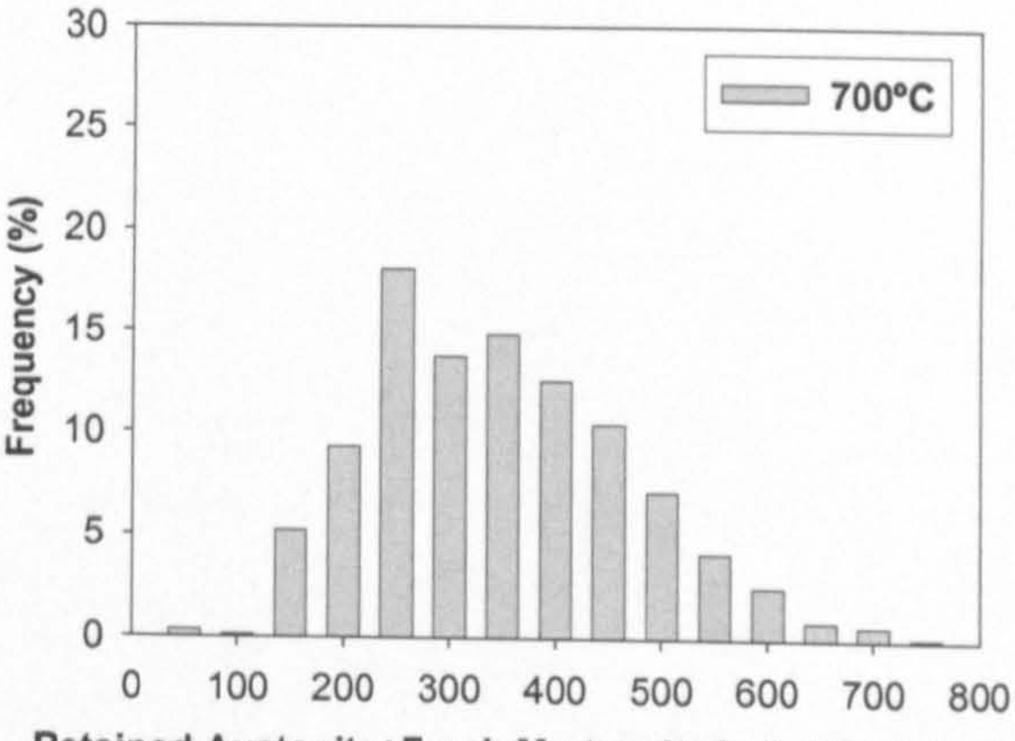

(f)

Fig.5.41 Size distribution of the retained austenite/"retained austenite + fresh martensite" (appeared brighter regions in SEI) measured from SEM micrographs of the specimens tempered at different temperatures for 4 h.

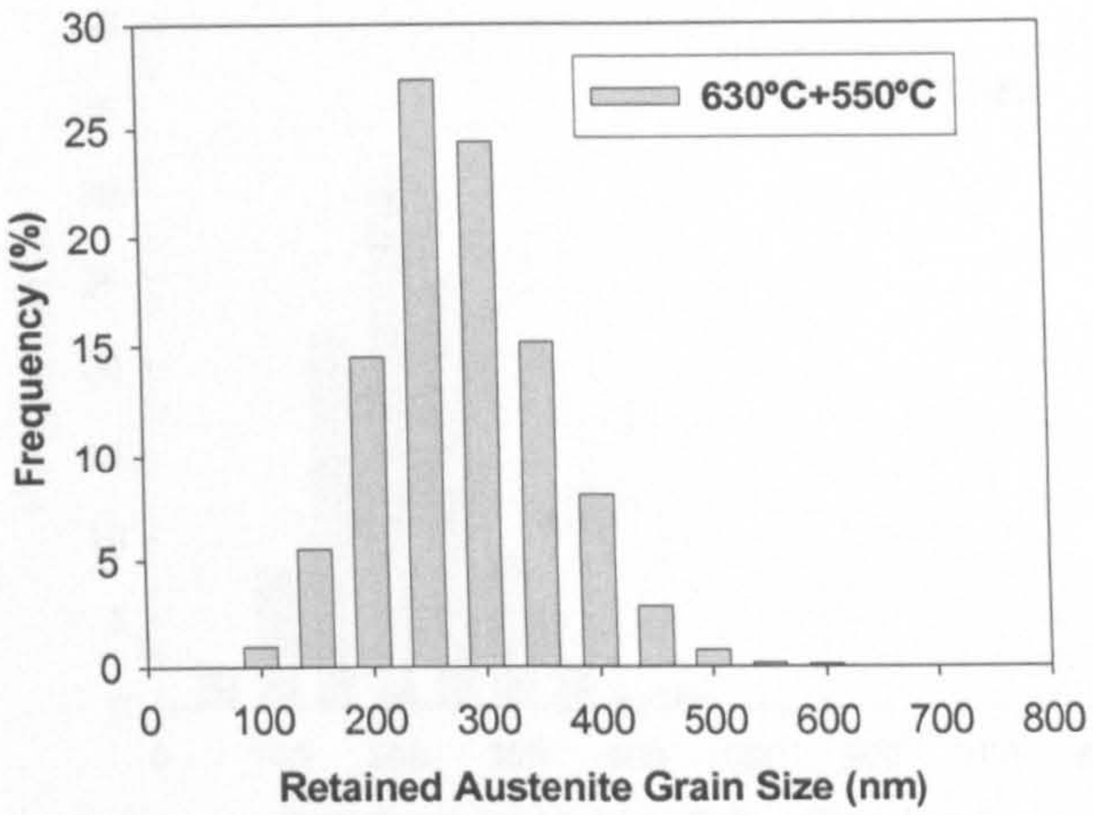

(a)

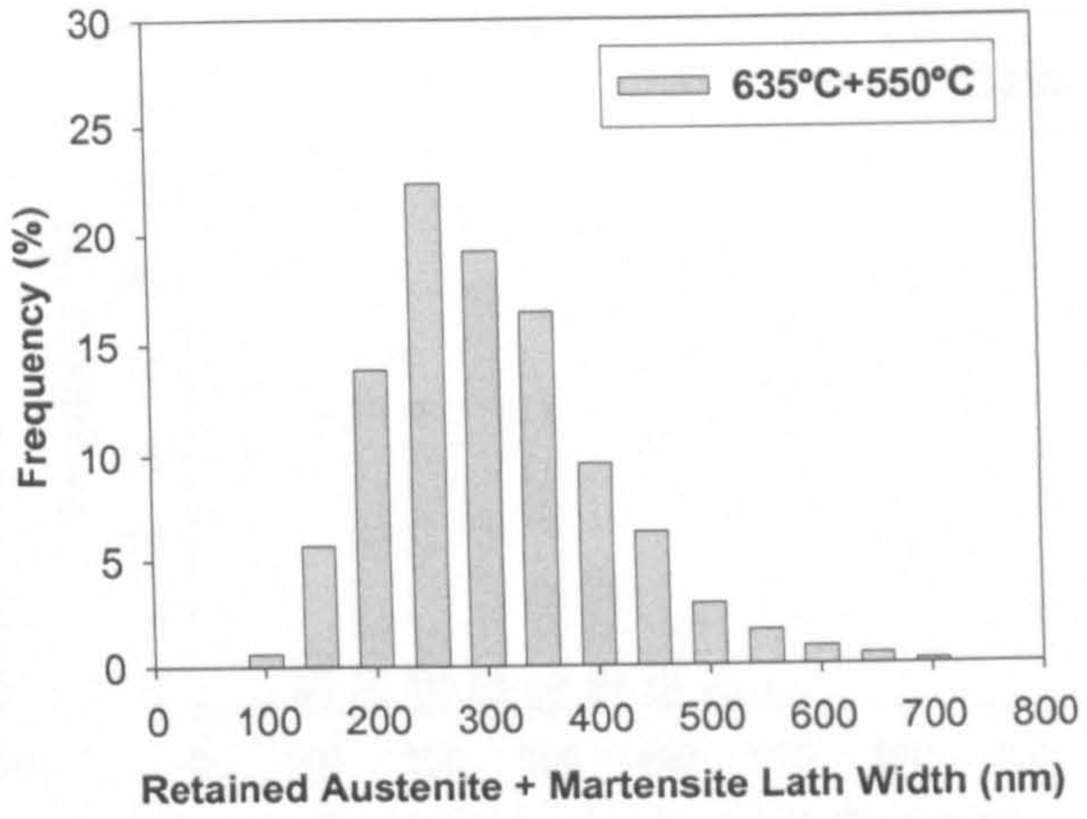

(b)

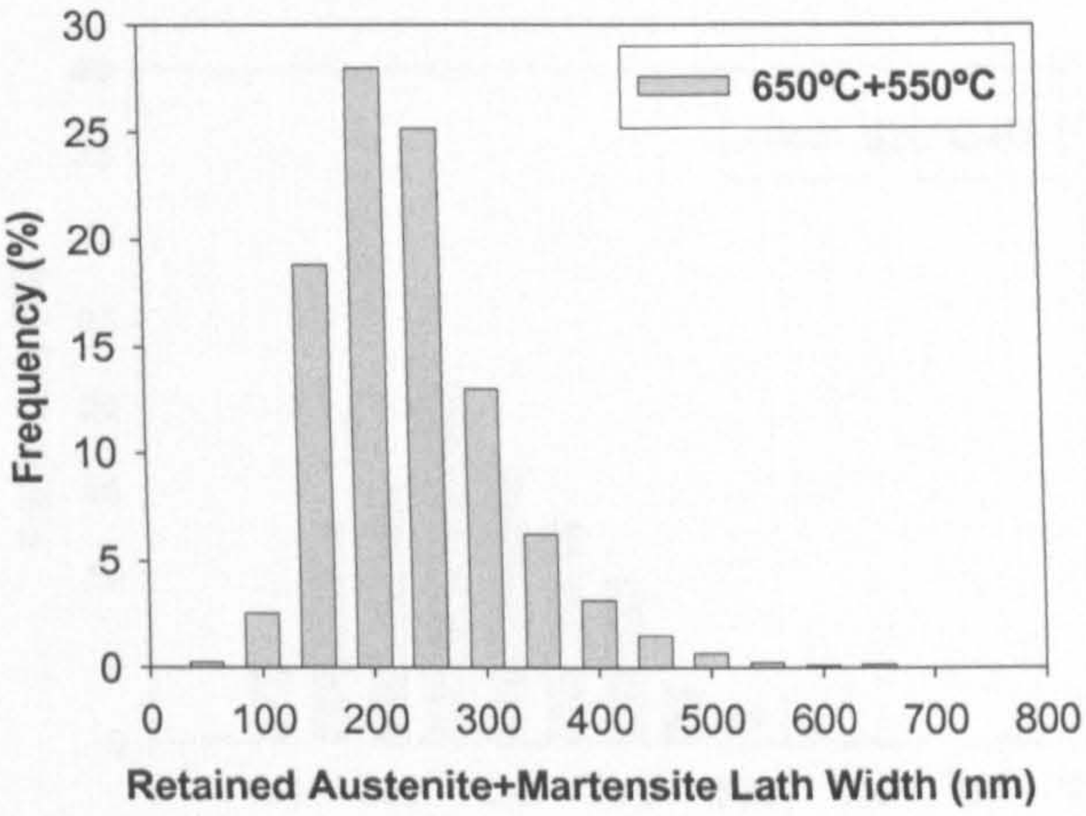

(c)

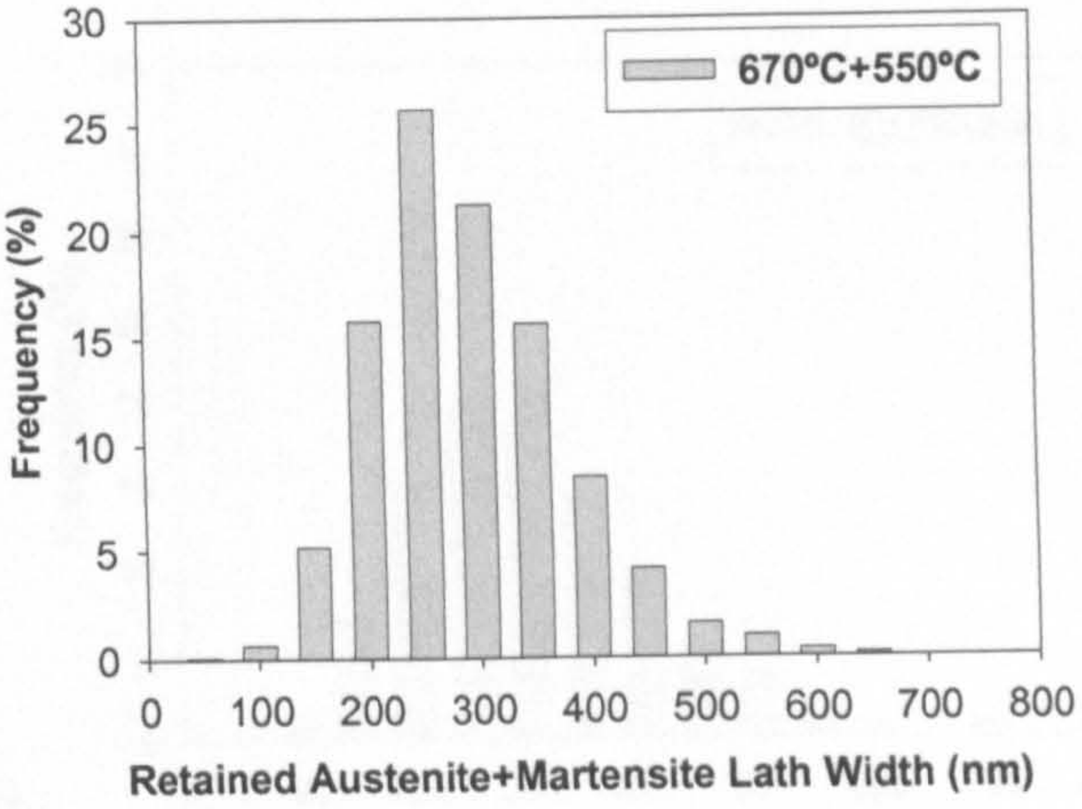

(d)

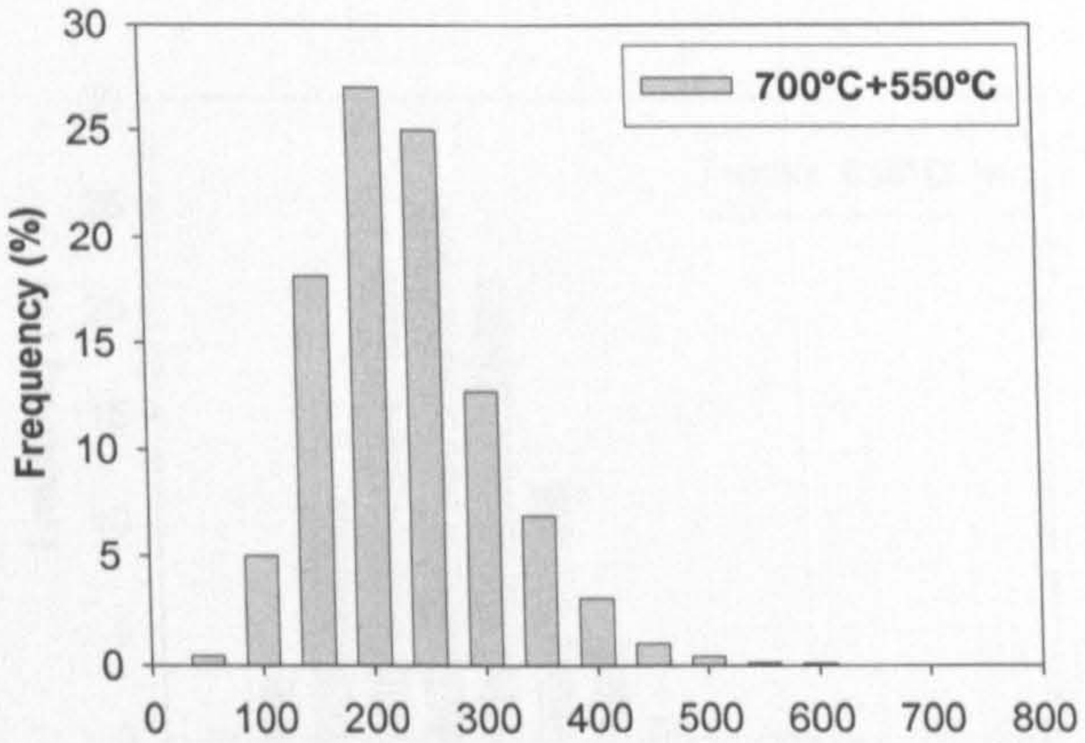

(e)

Fig.5.42 Size distribution of the retained austenite/(retained austenite + tempered martensite) (appeared brighter regions in SEI) measured from SEM micrographs of the specimens first tempered at different temperatures for 4 h and then second tempered at 550 °C for 2 h.

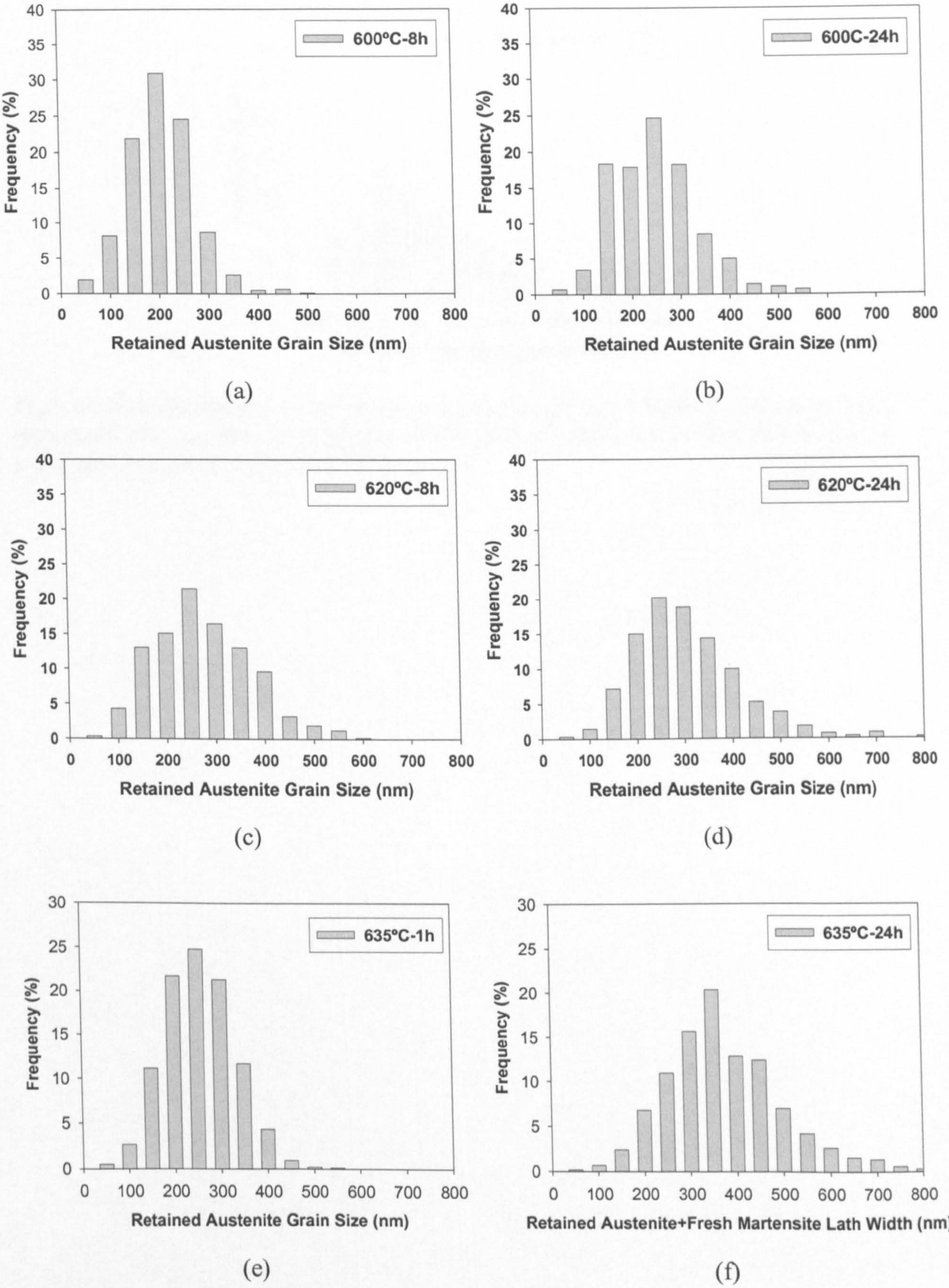

Fig.5.43 Size distribution of the retained austenite/"retained austenite + fresh martensite" (appeared brighter regions in SEI) measured from the SEM micrographs of the specimens tempered at 600 °C, 620 °C and 635 °C for different times.

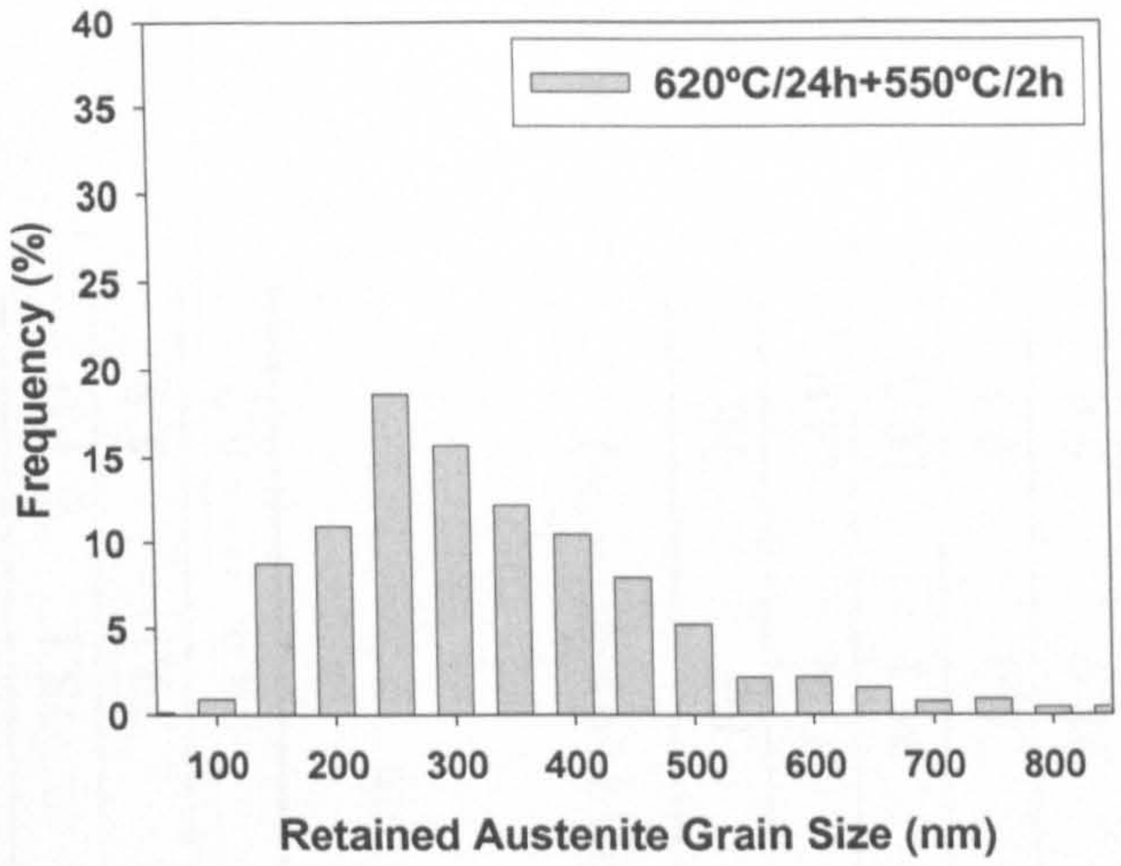

Fig.5.44 Size distribution of the retained austenite (appeared brighter regions in SEI) measured from the SEM micrographs of the specimen first tempered at 620 °C for 24 h and then second tempered at 550 °C for 2 h.

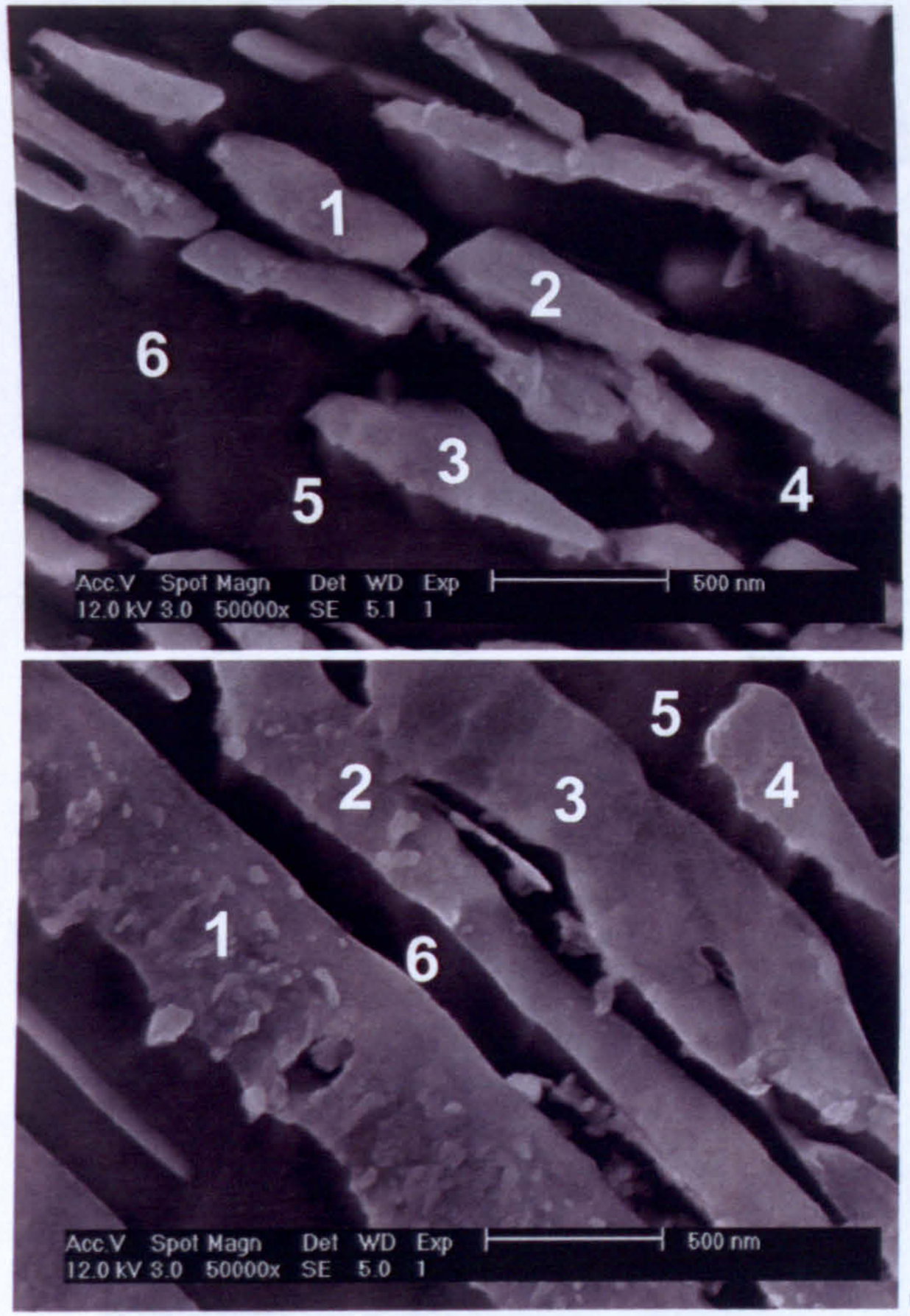

Table 5.4a SEM EDX composition point analysis (wt%)

Point	Si	Mo	Cr	Fe	Ni
1	0.3	1.8	12.3	74.1	11.5
2	0.4	1.7	12.4	73.5	12.0
3	0.4	1.9	12.3	72.9	12.6
4	0.4	1.9	12.7	78.1	7.0
5	0.6	2.0	12.8	79.1	5.5
6	0.5	2.0	12.4	78.9	6.2

(a) 600ºC/4h

Table 5.4b SEM EDX composition point analysis (wt%)

Point	Si	Mo	Cr	Fe	Ni
1	0.6	2.1	13.9	71.4	12.0
2	-	2.0	12.7	75.1	10.3
3	-	1.8	12.9	76.0	9.3
4	0.4	2.4	12.9	78.9	5.4
5	0.5	2.4	12.3	80.7	4.2
6	0.5	2.1	12.8	78.8	5.9

(b) 635ºC/4h + 550ºC/2h

Fig.5.45 SEI SEM images and EDX point analyses of the tempered specimens.

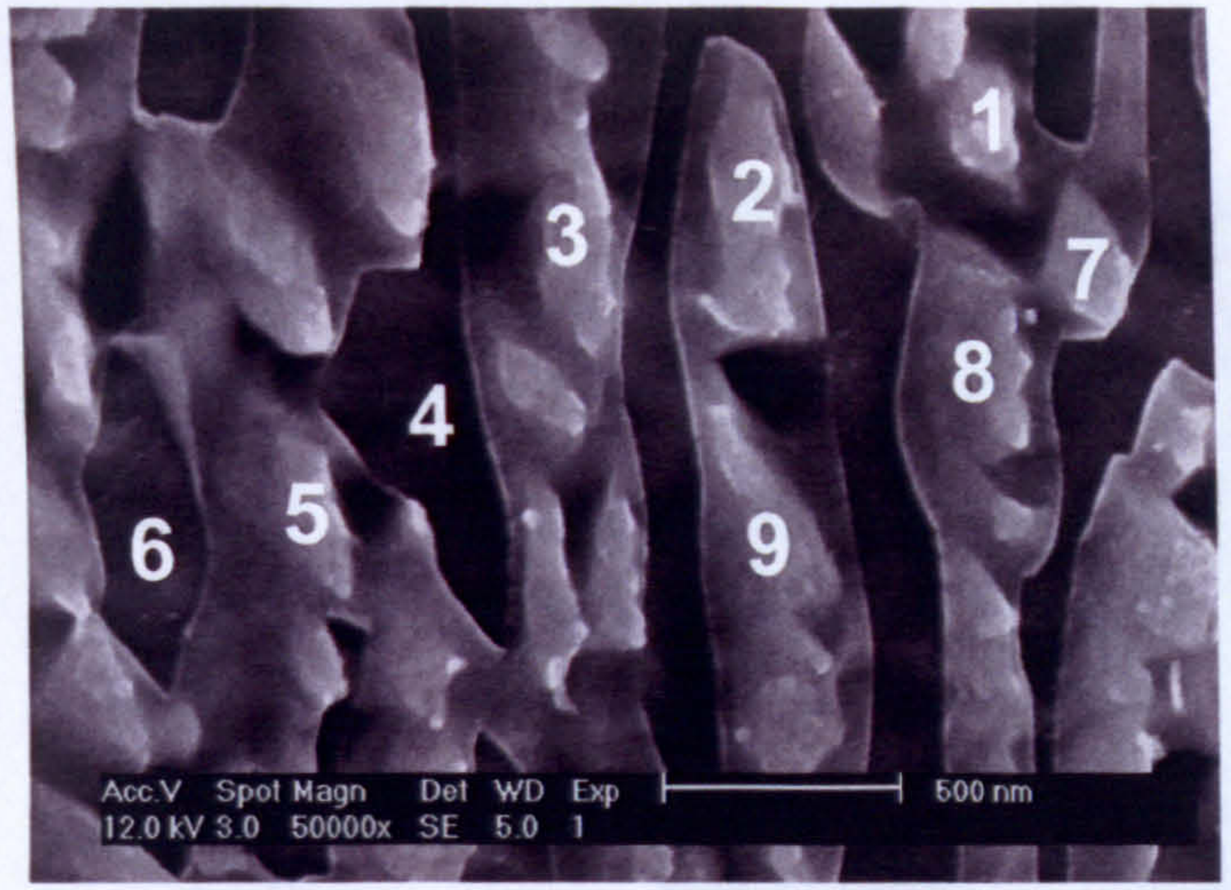

(c)

Table 5.4c SEM EDX composition point analysis (wt%)

Point	Si	Mo	Cr	Fe	Ni
1	0.5	2.6	12.4	79.9	4.6
2	0.5	1.8	12.1	77.0	8.6
3	0.4	1.4	12.1	76.0	10.1
4	0.5	2.0	12.7	80.4	4.4
5	0.6	2.0	11.6	78.0	7.8
6	0.8	2.0	12.6	79.2	5.5
7	0.6	2.4	12.3	79.9	4.8
8	0.5	1.7	12.1	77.9	7.8
9	0.5	2.1	11.7	78.2	7.6

(c) 700°C/4h

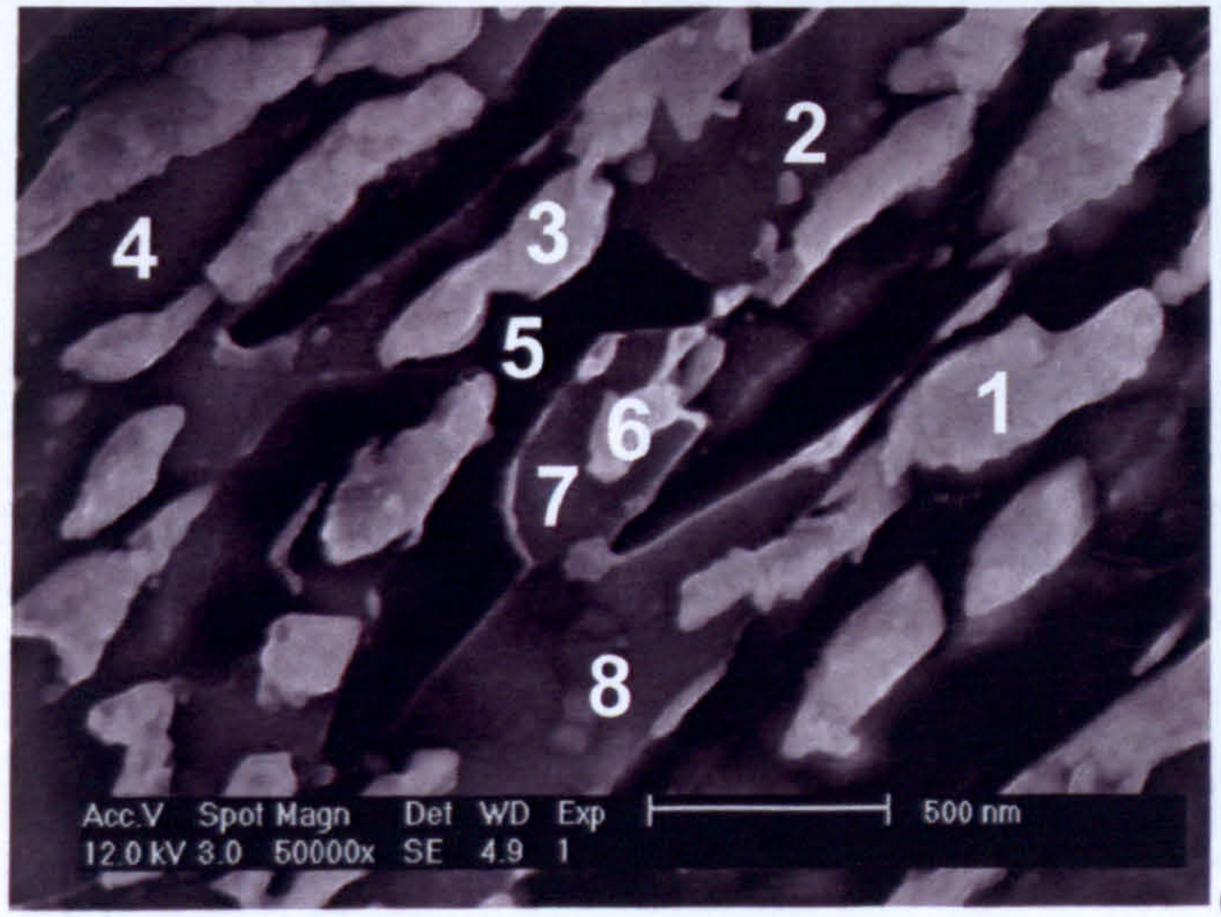

(d)

Table 5.4d SEM EDX composition point analysis (wt%)

Point	Si	Mo	Cr	Fe	Ni
1	0.5	2.1	12.8	73.5	11.1
2	0.5	1.9	12.5	78.6	6.6
3	0.4	1.8	12.4	75.0	9.9
4	0.7	2.4	11.7	81.6	3.7
5	0.6	2.1	13.2	79.4	4.7
6	0.5	1.9	11.7	75.5	10.4
7	0.4	2.0	11.9	78.7	7.1
8	0.5	2.1	12.7	76.0	8.7

(d) 700°C/4h + 550°C/2h

(Cont.) Fig.5.45 SEM micrographs and EDX point analyses of the tempered specimens.

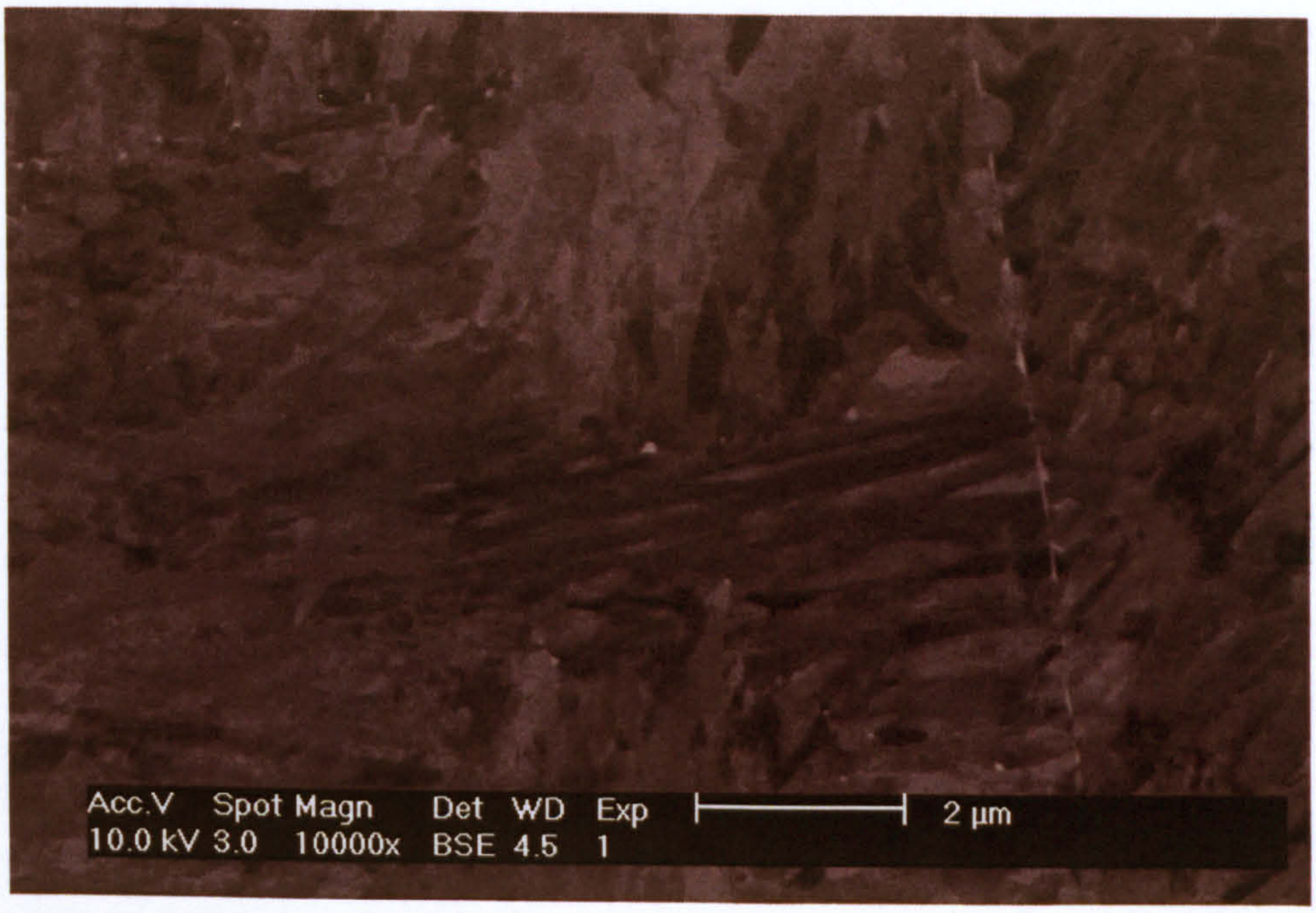

(a)

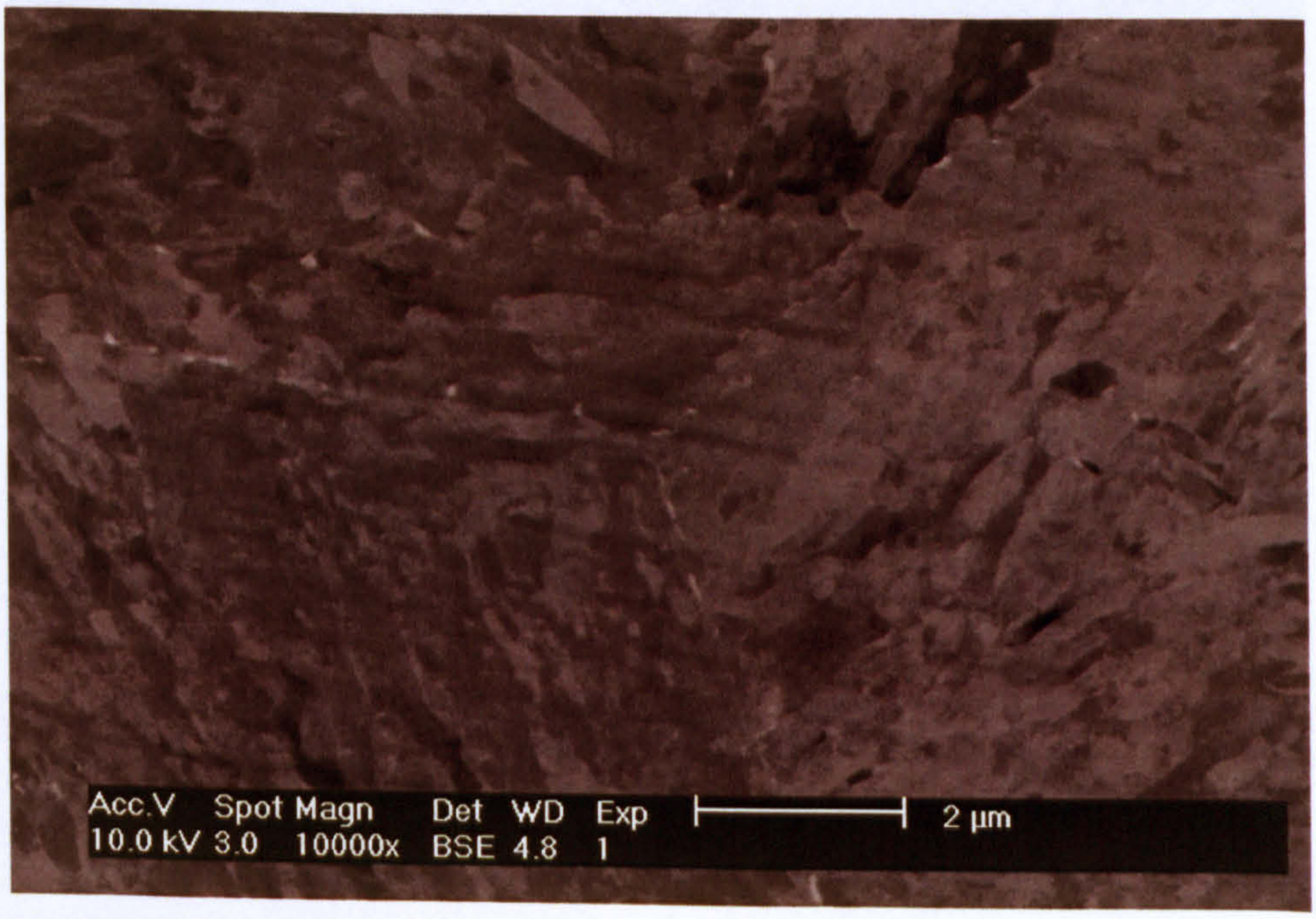

(b)

Fig.5.46 BEI SEM micrographs of the specimen tempered at 660 °C for 4 h, showing bright precipitate particles distributed along prior austenite grain boundaries.

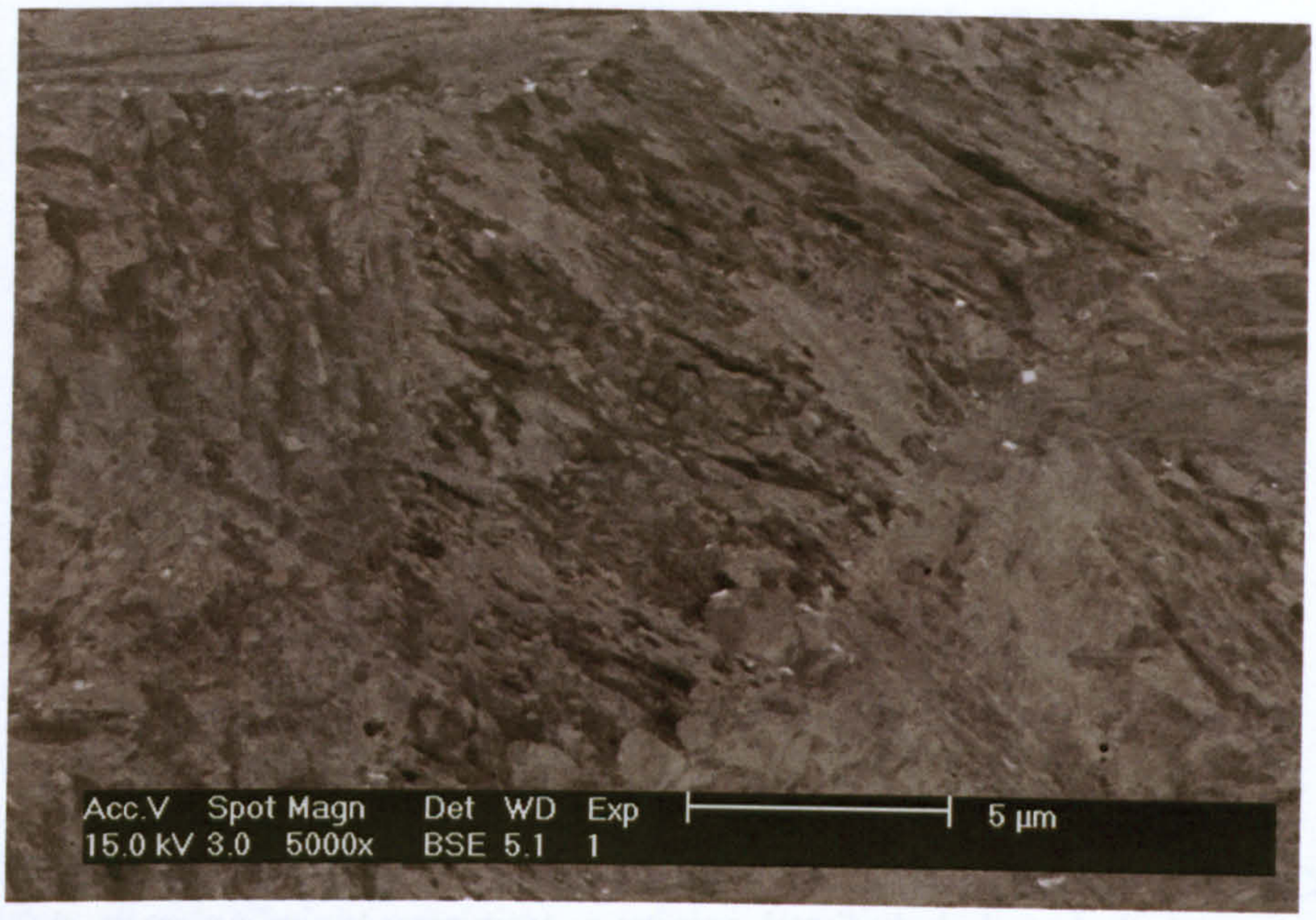

(a)

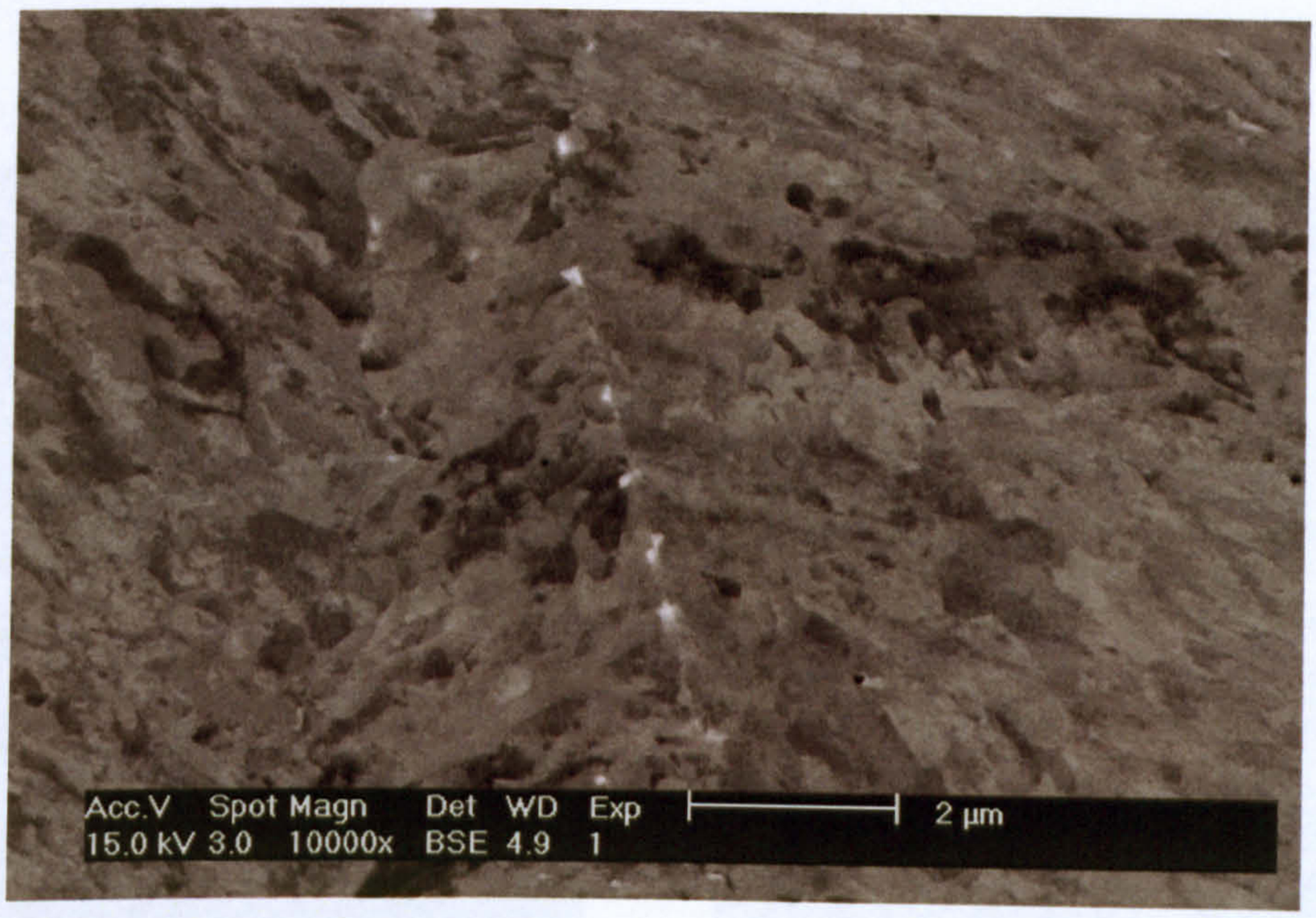

(a)

Fig.5.47 BEI SEM micrographs of the specimen tempered at 700 °C for 4 h, showing bright precipitate particles distributed along prior austenite grain boundaries.

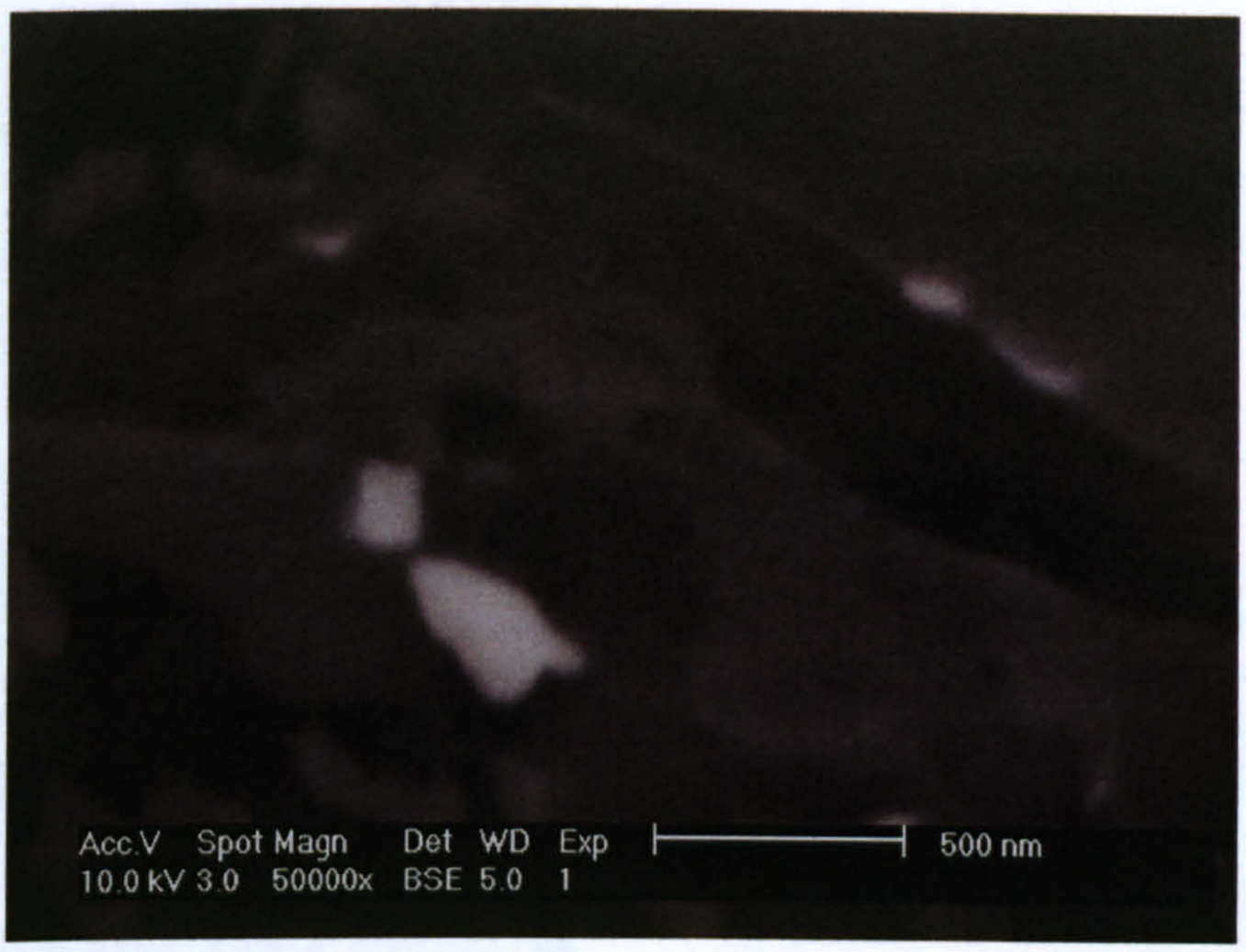

Fig.5.48 BEI SEM micrograph of the specimen double tempered at 700°C/4h + 550°C/2 h, showing bright precipitate particles distributed along laths boundaries.

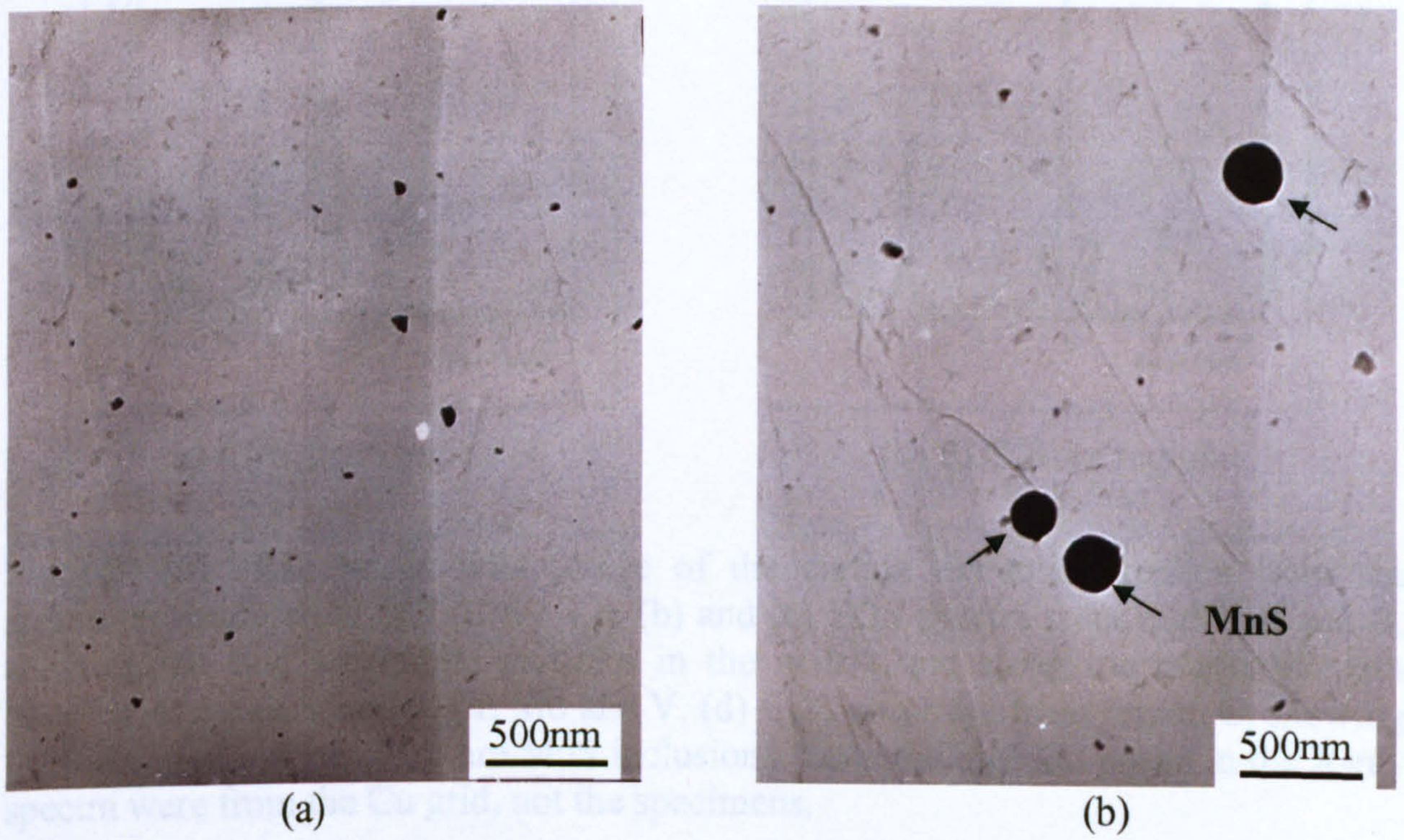

Fig.5.49 TEM images of the carbon extraction replica from the as-air cooled specimen (heated to 950 °C for 2 h, then air cooled). EDS microanalysis results indicate that the dark spherical particles in (b) were MnS inclusions.

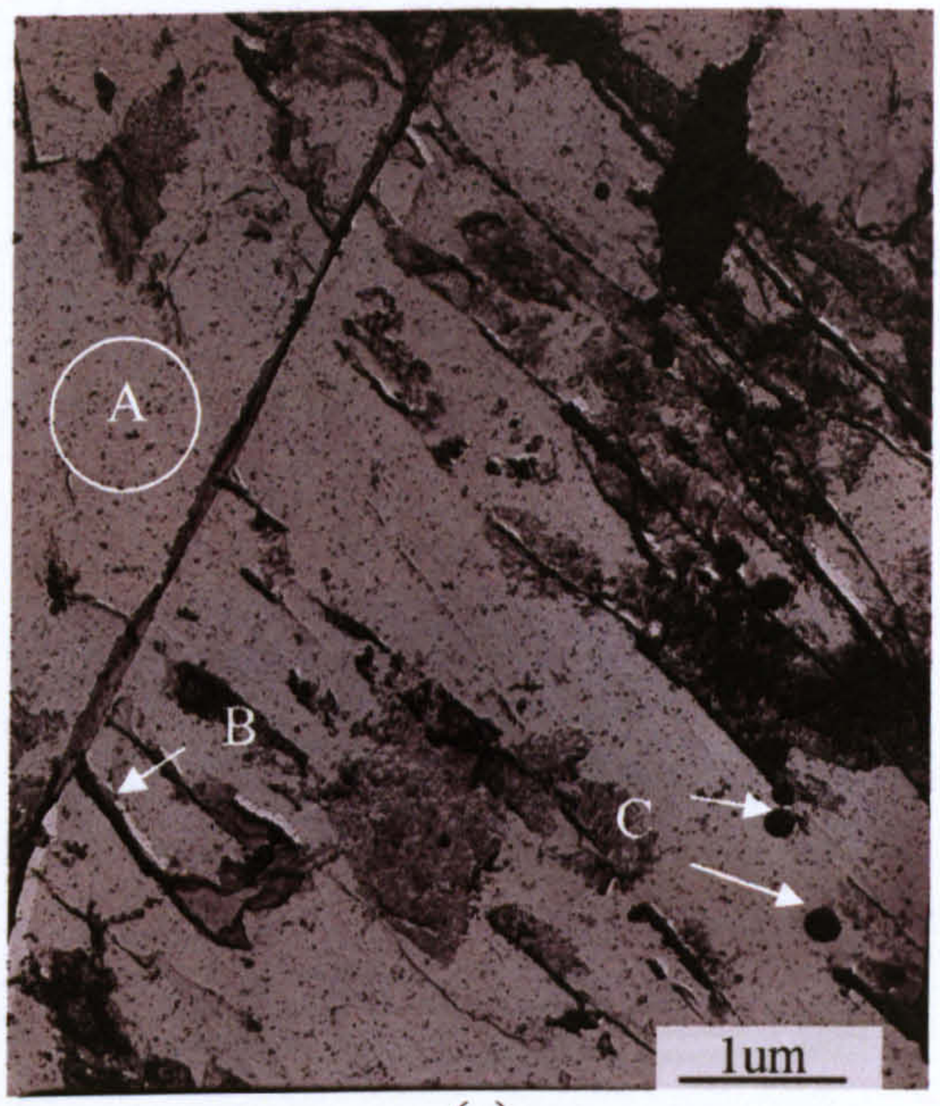

(a)

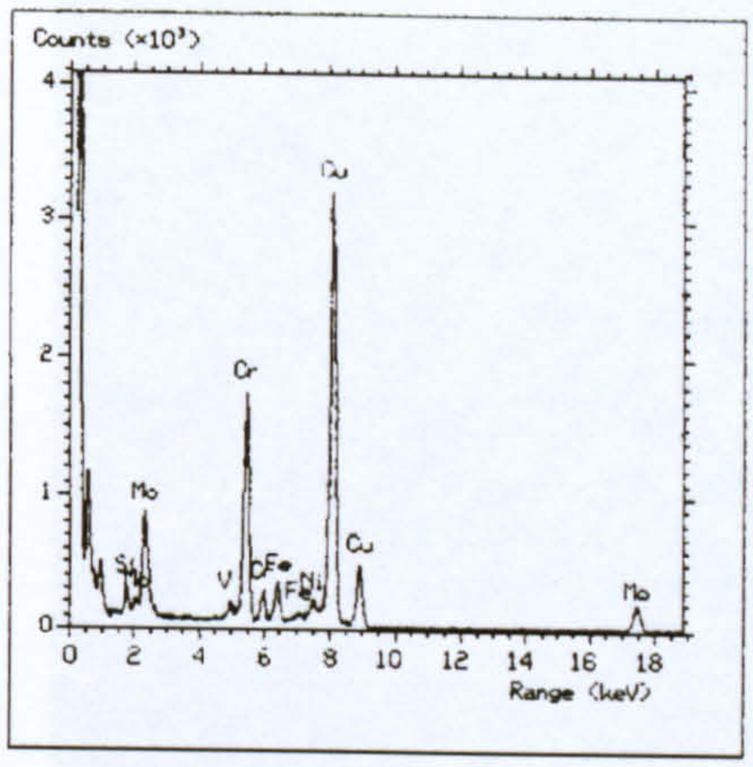

(b) EDS from region A

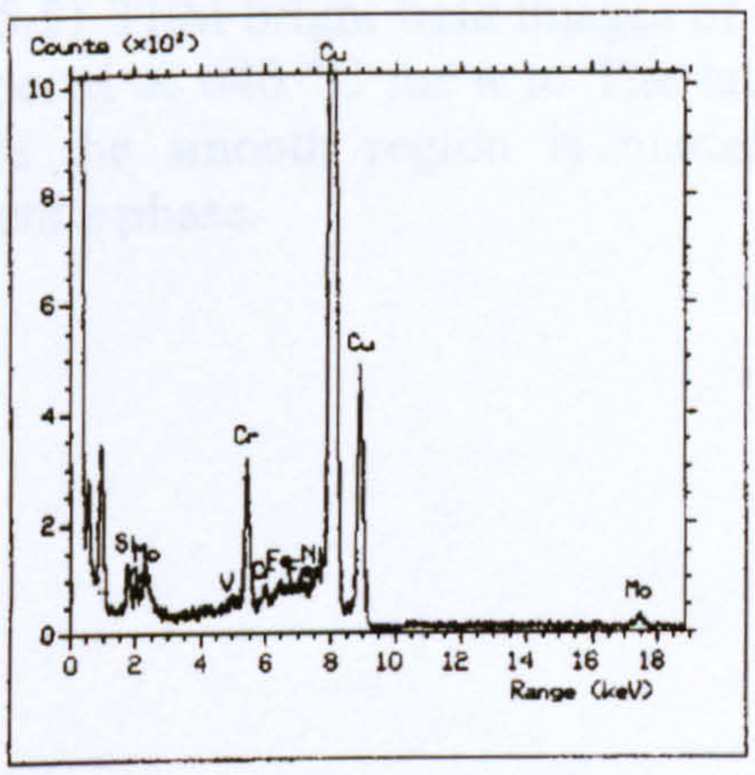

(c) EDS from region B

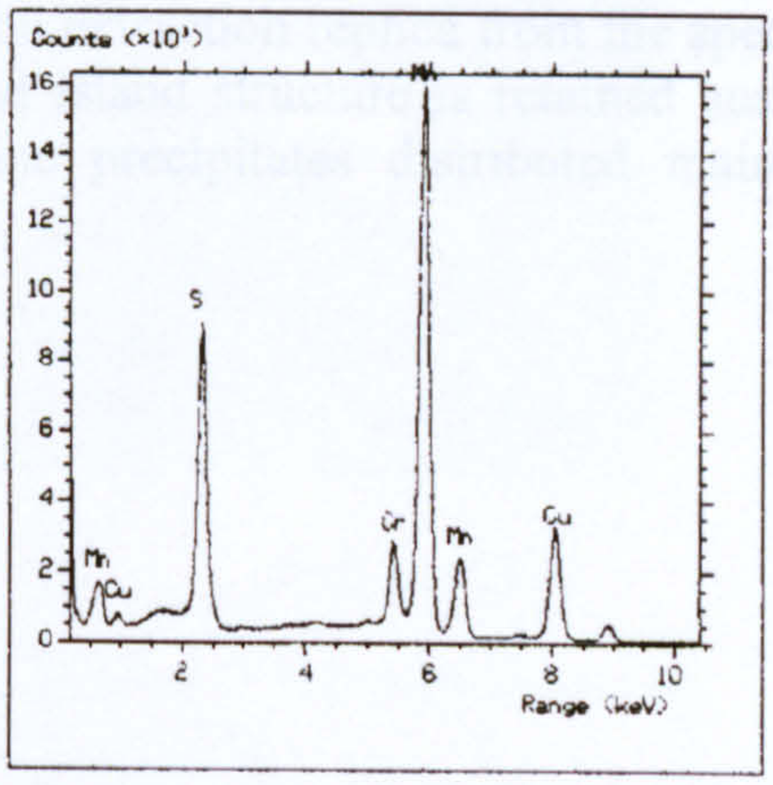

(d) EDS from region C

Fig.5.50 (a) TEM bright field image of the carbon extraction replica from the specimen tempered at 557 ºC for 4 h. (b) and (c) EDS spectra from region A and B, showing the fine precipitate particles in the matrix and along the martensite lath boundaries are enriched in Cr, Mo and V. (d) EDS spectrum from region C, showing the dark spherical particles are MnS inclusions. Note the high Cu peaks in the X-ray spectra were from the Cu grid, not the specimens.

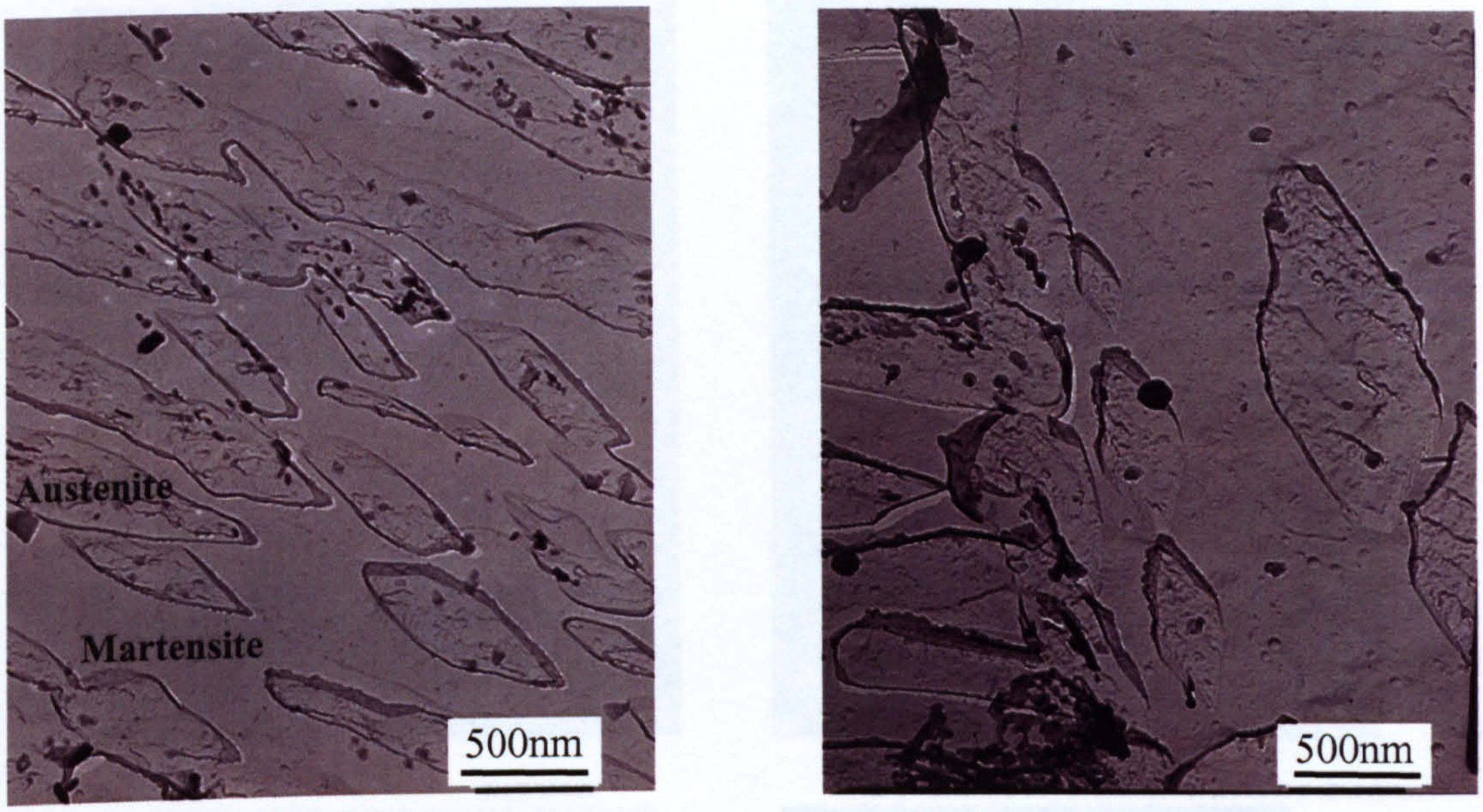

(a) (b)

Fig.5.51 TEM bright field images of the carbon extraction replica from the specimen tempered at 640 °C for 4 h. The lath/isolated island structure is retained austenite while the smooth region is martensite. Fine precipitates distributed mainly in austenite phase.

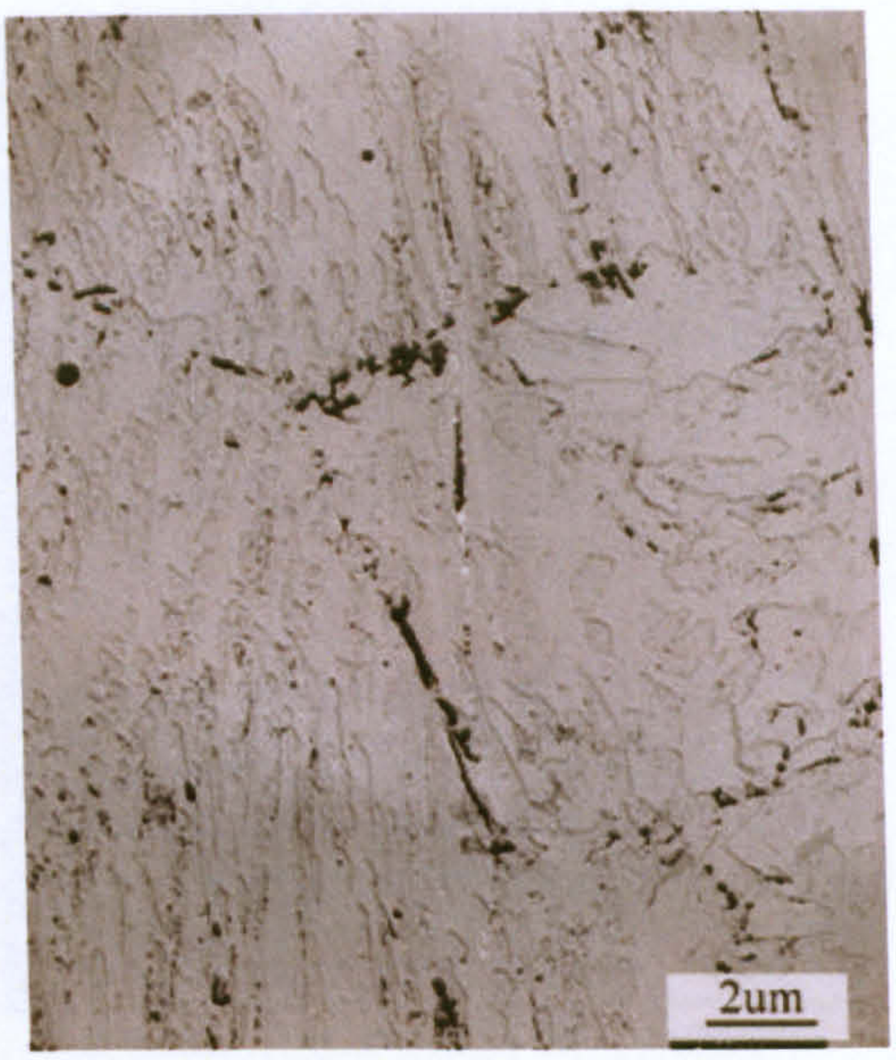

(a)

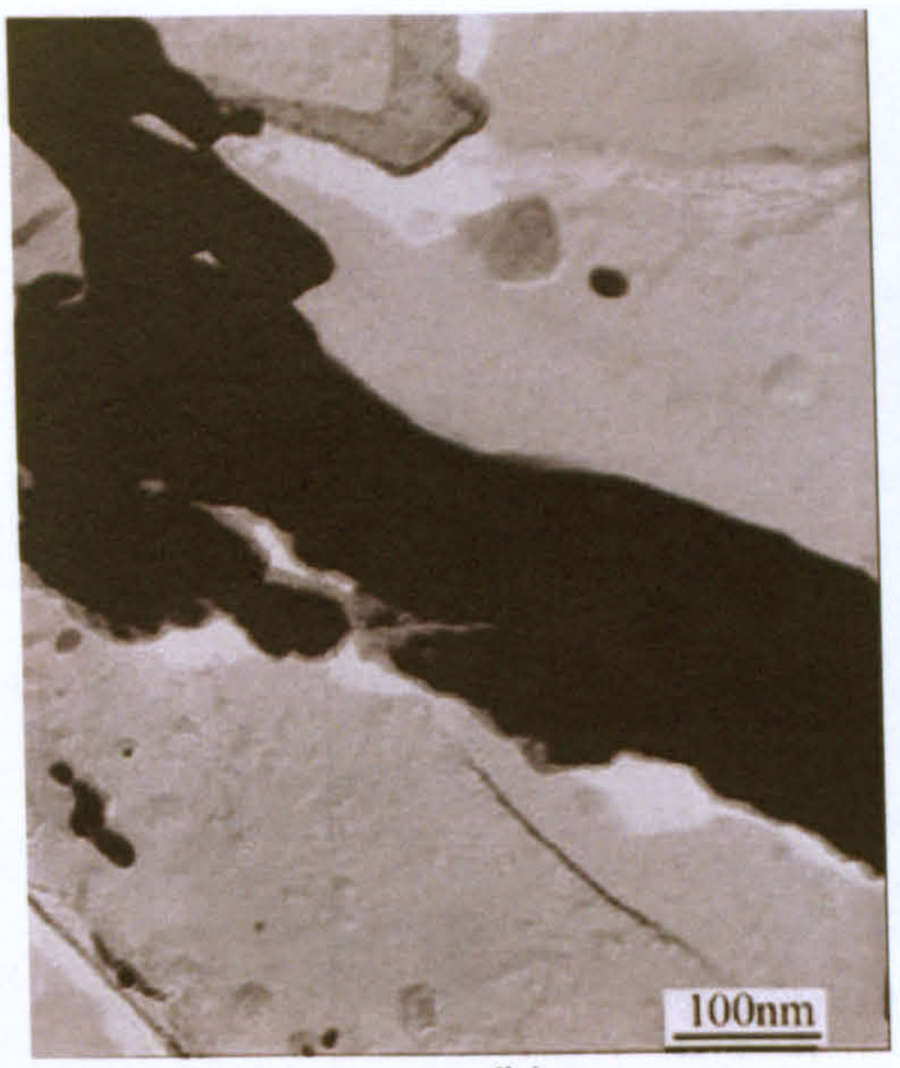

(b)

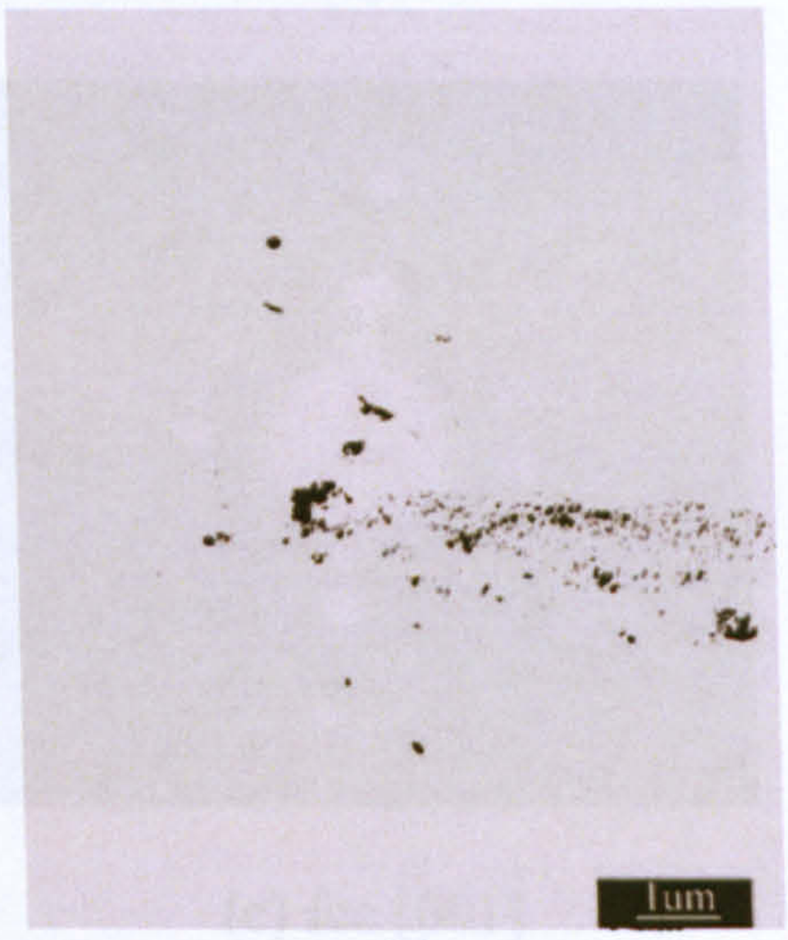

(c)

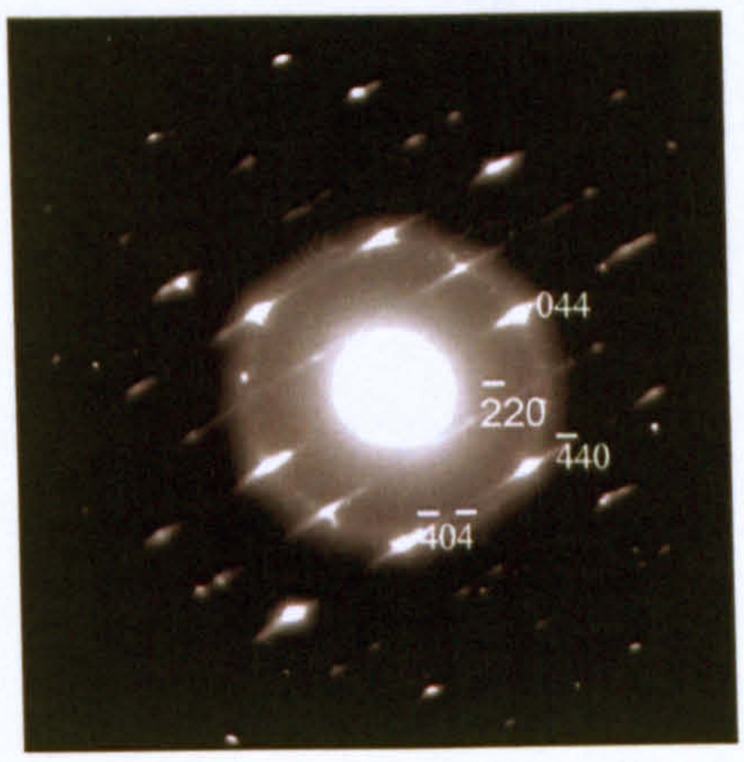

(d) fcc $\bar{1}11$

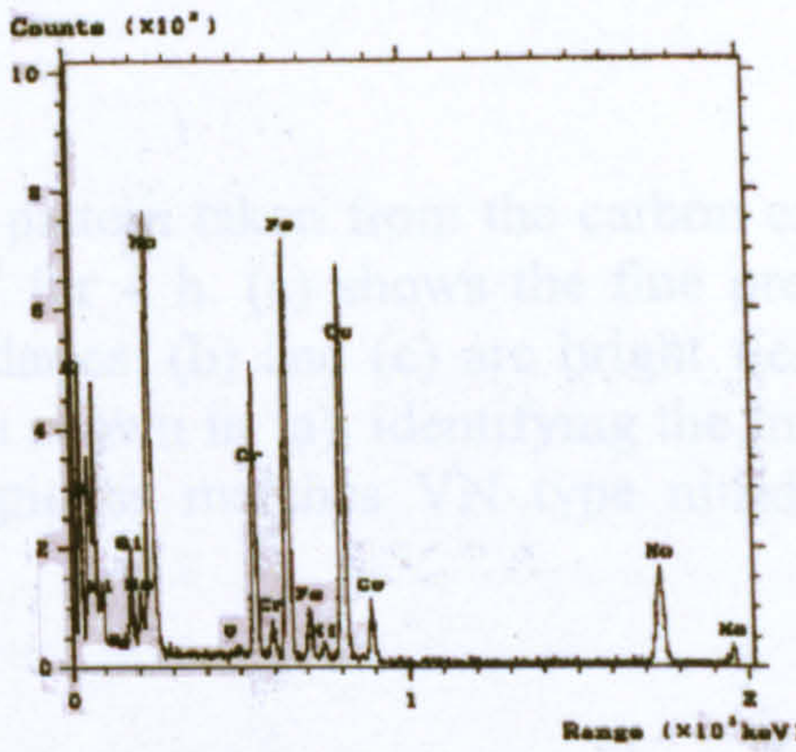

(e)

Fig.5.52 TEM images, SAD pattern and EDS spectrum taken from the carbon extraction replica of the specimen tempered at 640 °C for 4 h. (a) shows the fine precipitate particles distributed along the prior austenite grain boundaries. (b), (c) and (d) are bright field image, dark field image and SAD pattern taken from the particles shown in (a), identifying the interplanar spacing and lattice parameter of these intergranular particles matches M_6C type carbides (a_0 = 1.106nm). (e) is EDS spectrum taken from (b), identifying the presence of Mo-rich M_6C carbides.

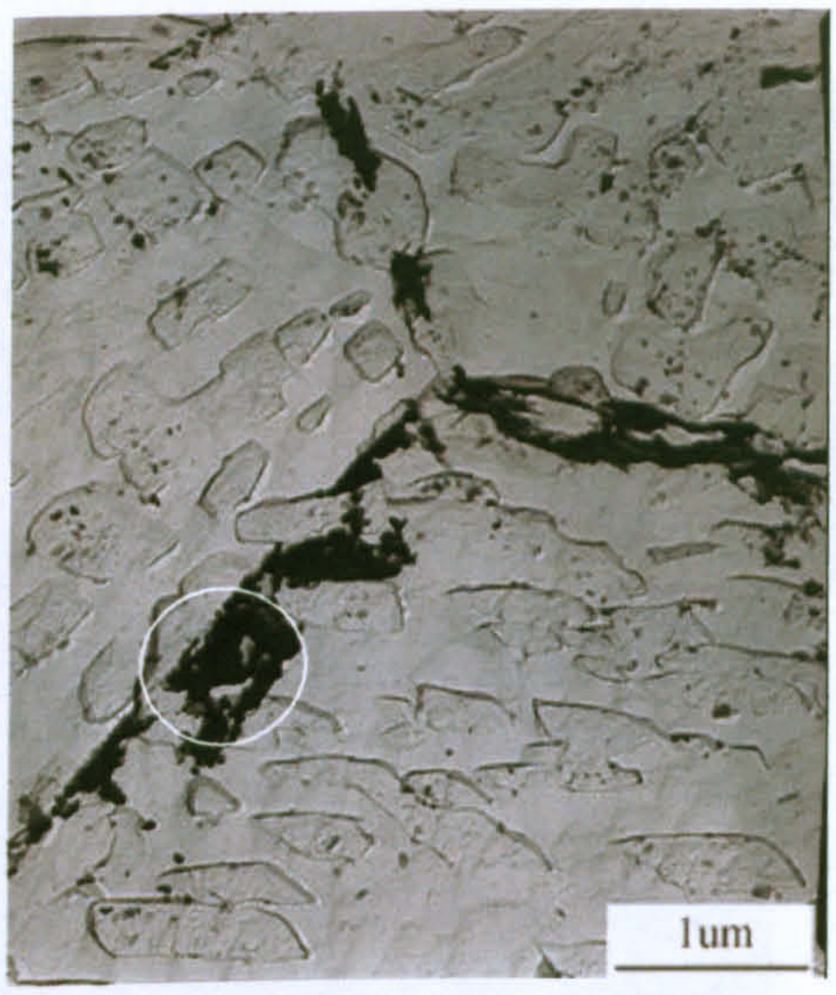

(a)

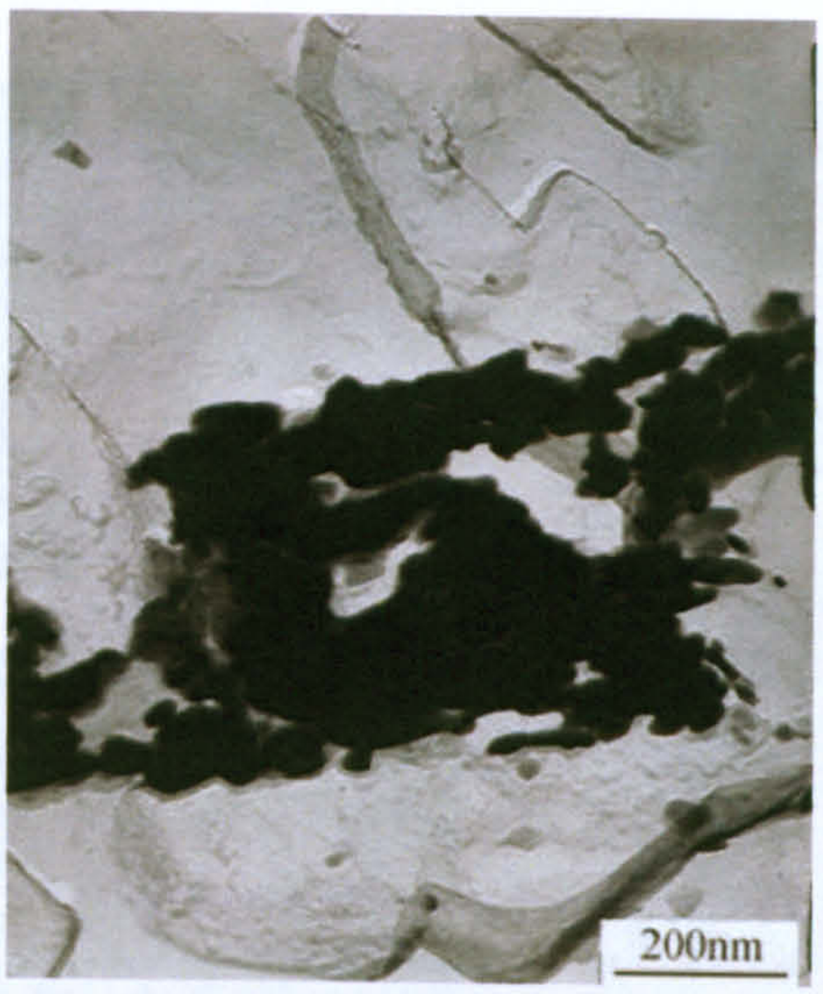

(b)

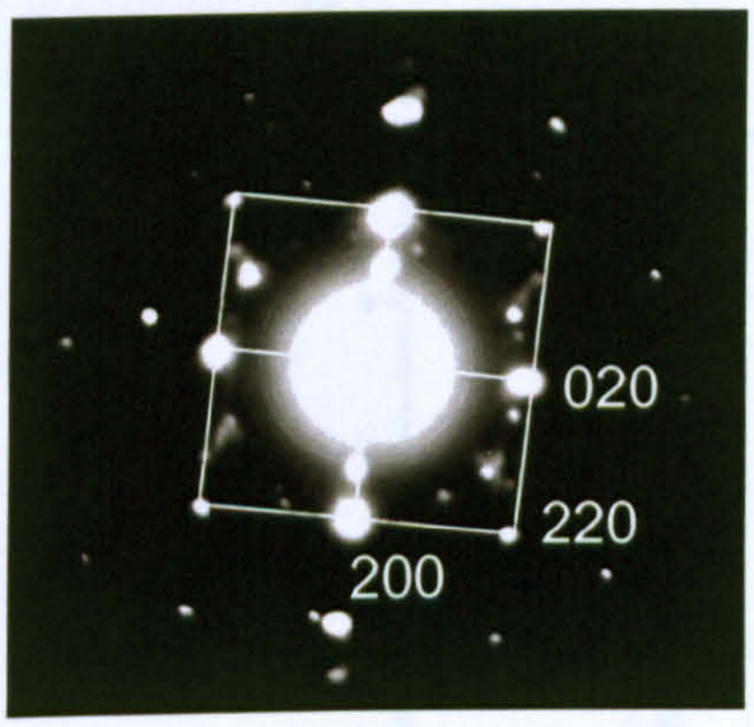

(c) fcc [001]

Fig.5.53 TEM bright field images and SAD pattern taken from the carbon extraction replica of the specimen tempered at 640 °C for 4 h. (a) shows the fine precipitates distributed along prior austenite grain boundaries. (b) and (c) are bright field image and SAD pattern taken from the marked area shown in (a), identifying the interplanar spacing and lattice parameter of the precipitates matches VN type nitrides (a_0 = 0.418nm).

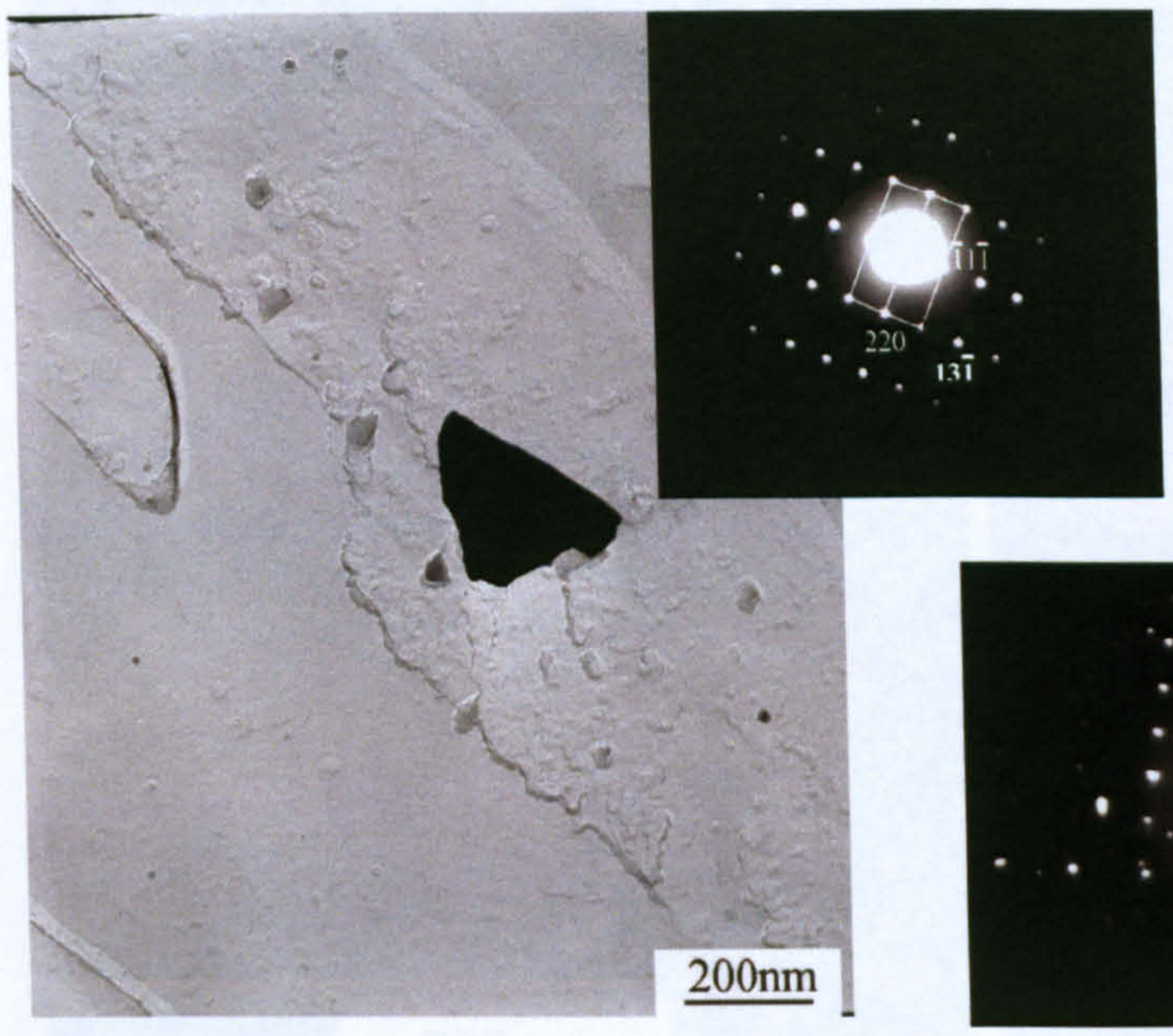

(a)

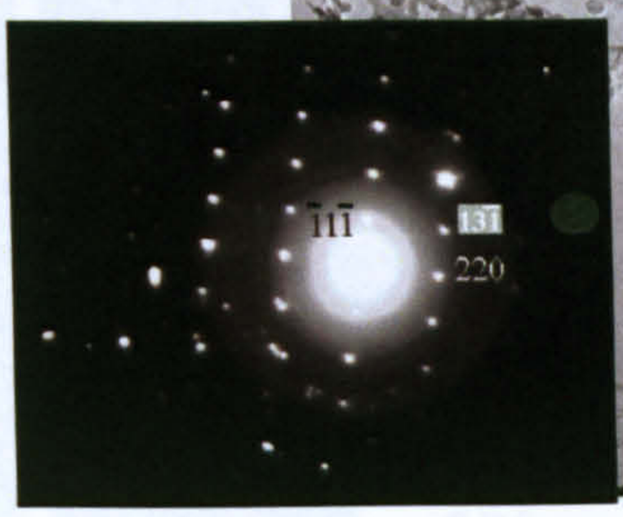

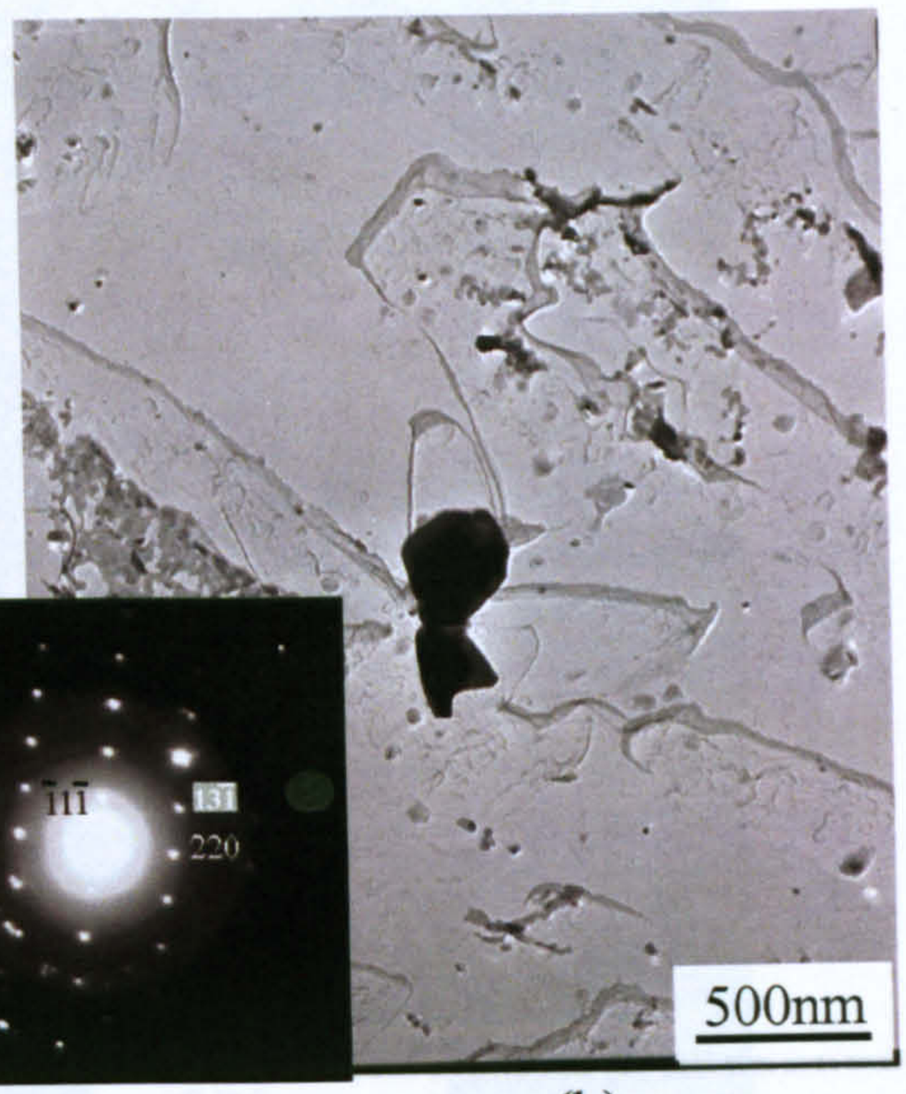

(b)

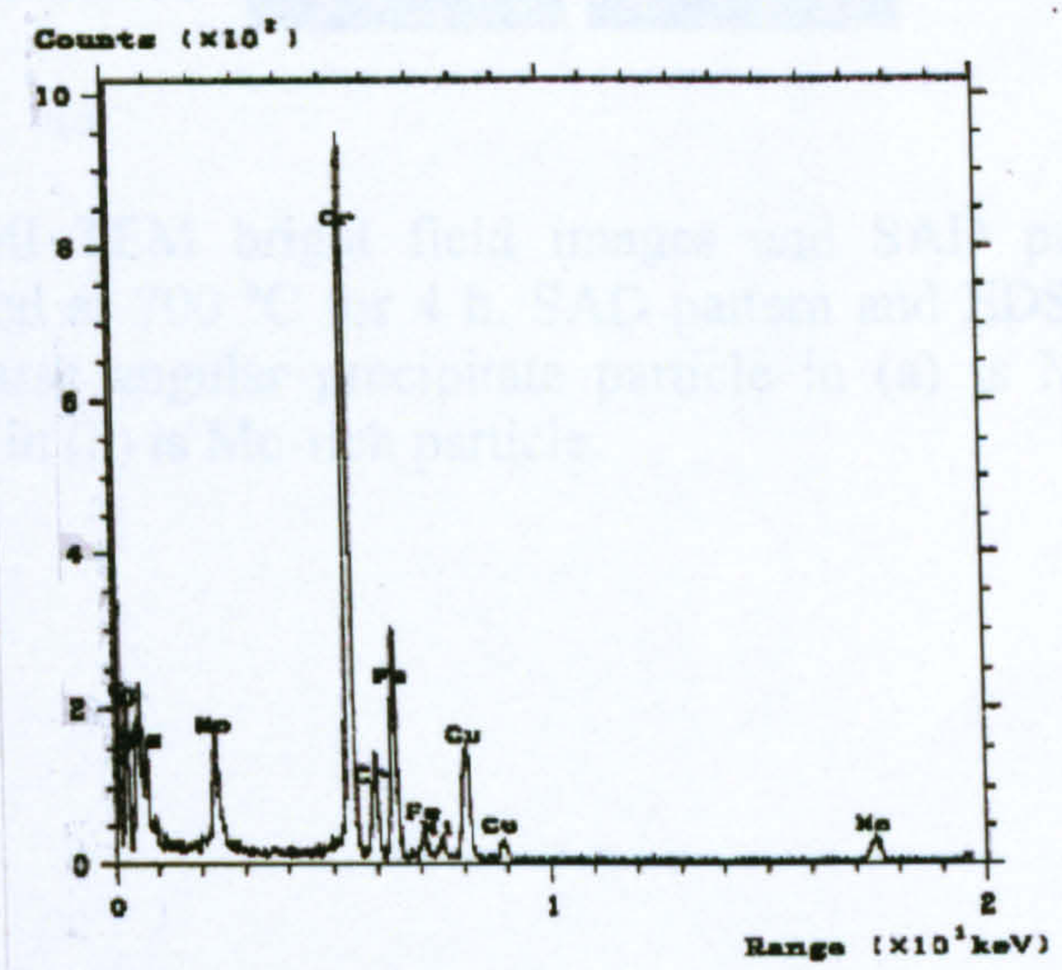

(c)

Fig.5.54 TEM bright field images, SAD pattern and EDS spectrum taken from the carbon extraction replica of the specimen tempered at 640 °C for 4 h. SAD pattern and EDS analysis indicated these coarse angular particles are Cr-rich $M_{23}C_6$ carbides (a_0 = 1.044nm).

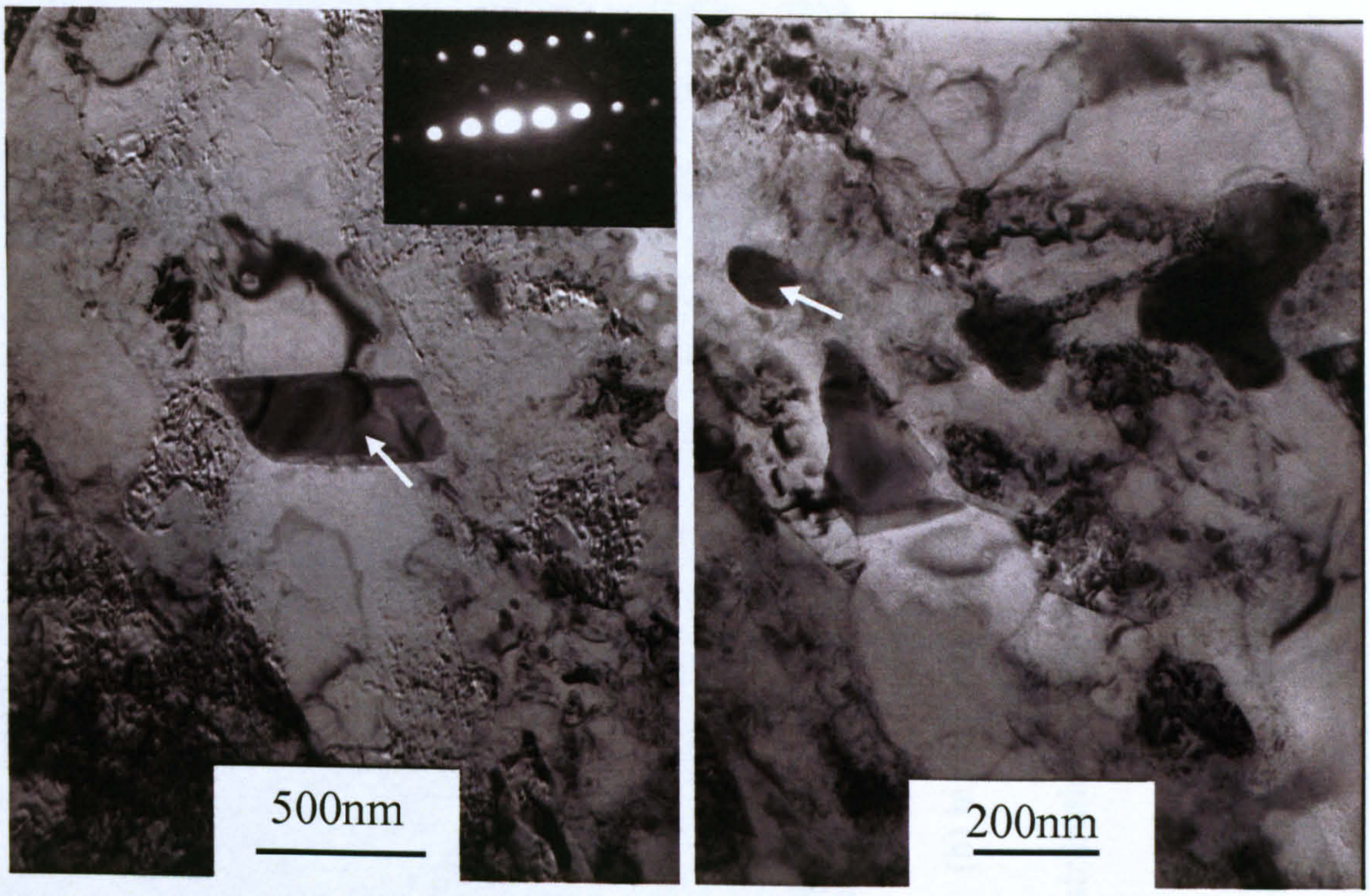

(a) (b)

Fig.5.55 Thin foil TEM bright field images and SAD pattern taken from the specimen tempered at 700 °C for 4 h. SAD pattern and EDS analysis (Table 5.11) indicated the coarse angular precipitate particle in (a) is $M_{23}C_6$ carbide and the spherical particle in (b) is Mo-rich particle.

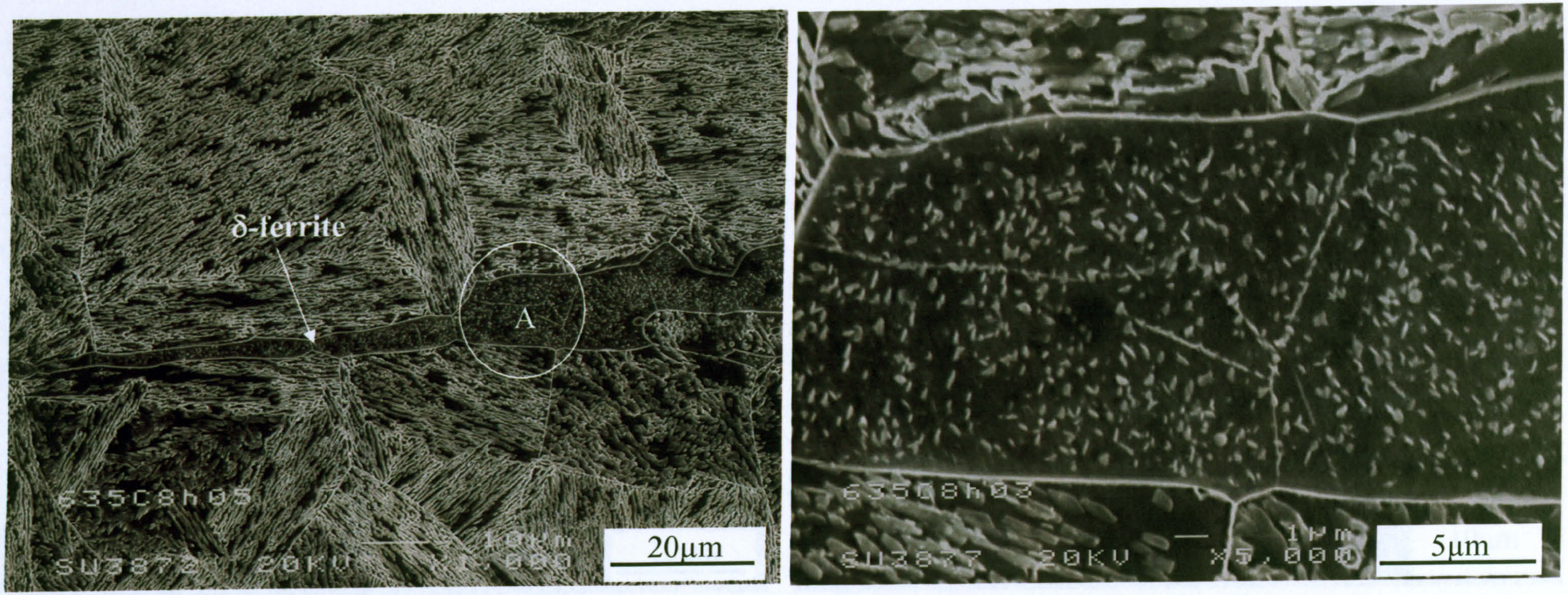

(a) (b) higher magnification of area A in (a)

Fig.5.56 SEI SEM images of the specimen tempered at 635 ºC for 8 h, showing the distribution of fine precipitate particles within δ-ferrite phase.

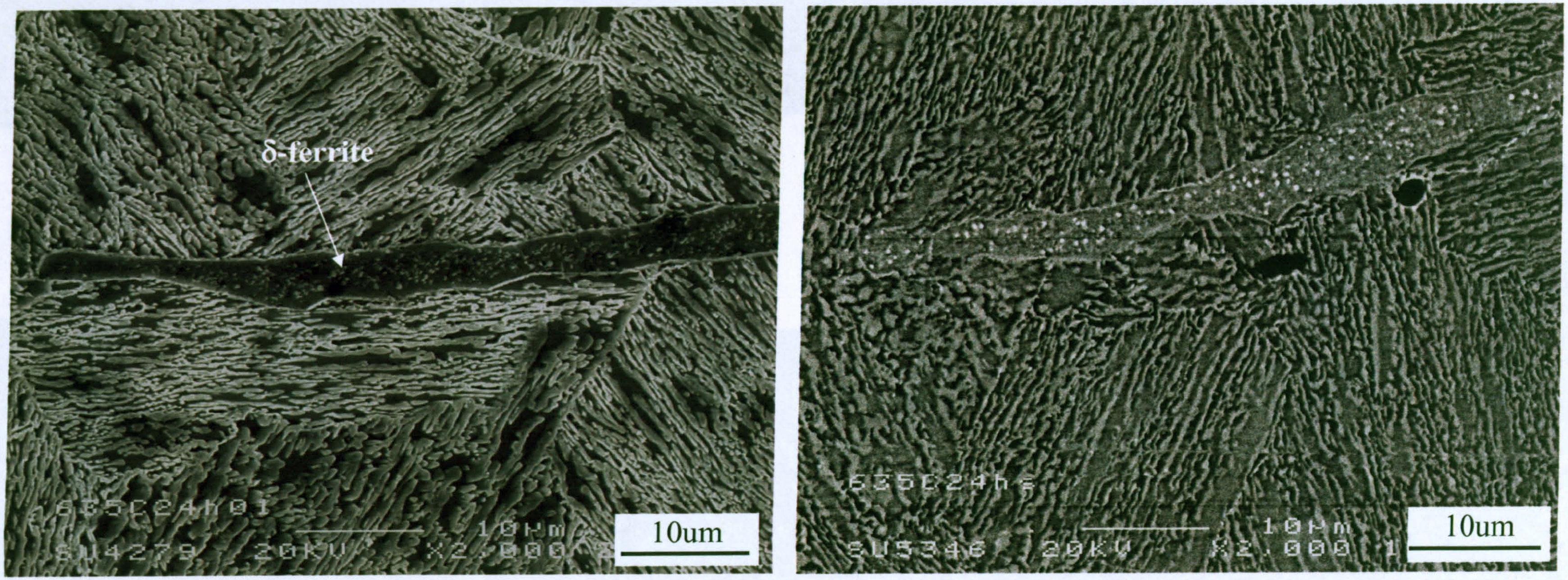

(a) SEI

(b) BEI

Fig.5.57 SEM images of the specimen temper at 635 ℃ for 24 h, showing the distribution of fine precipitate particles within δ-ferrite phase.

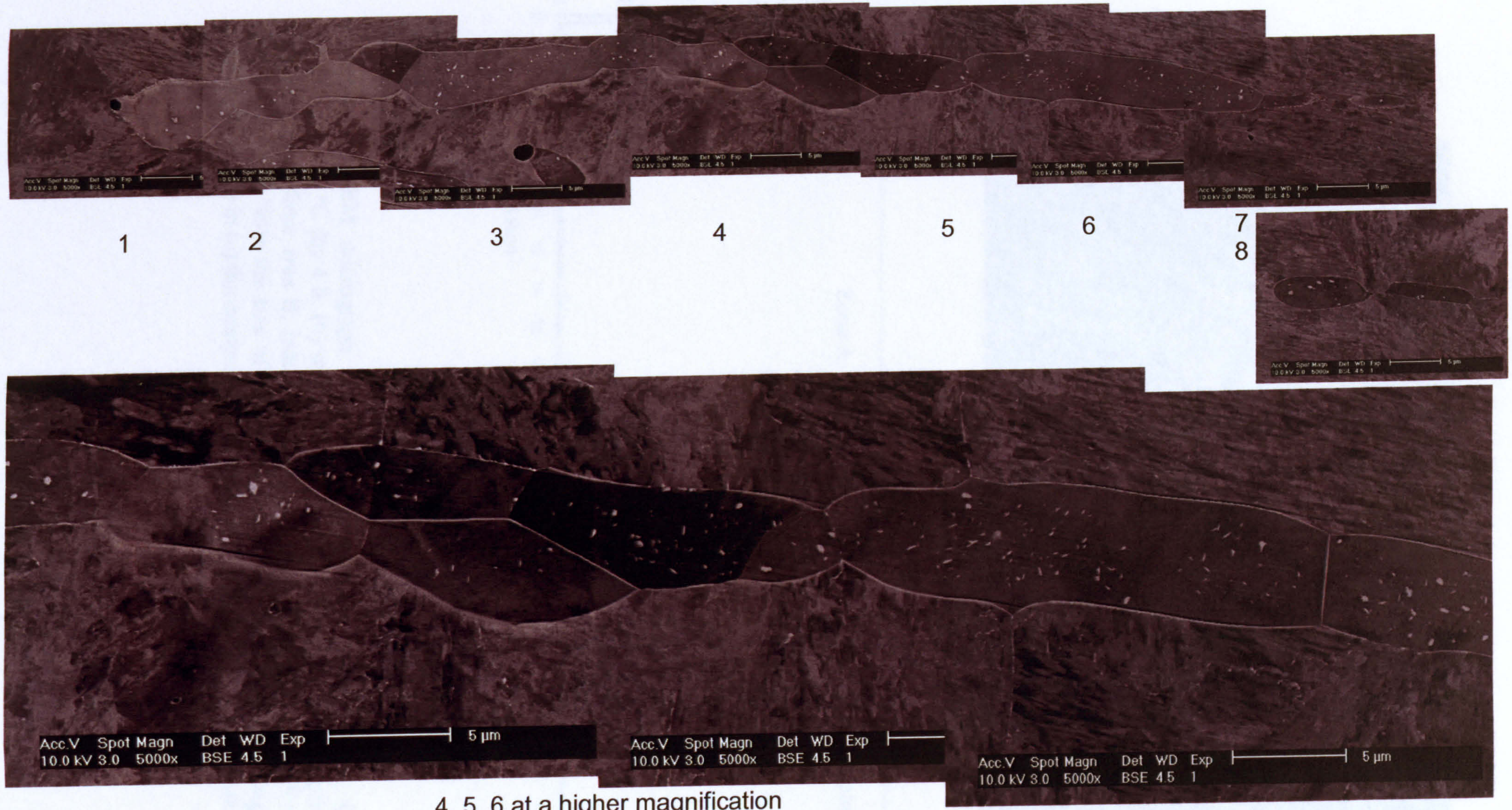

Fig.5.58 BEI SEM images of the specimen tempered at 660 ºC for 4 h, showing the distribution of fine precipitate particles within δ-ferrite phase.

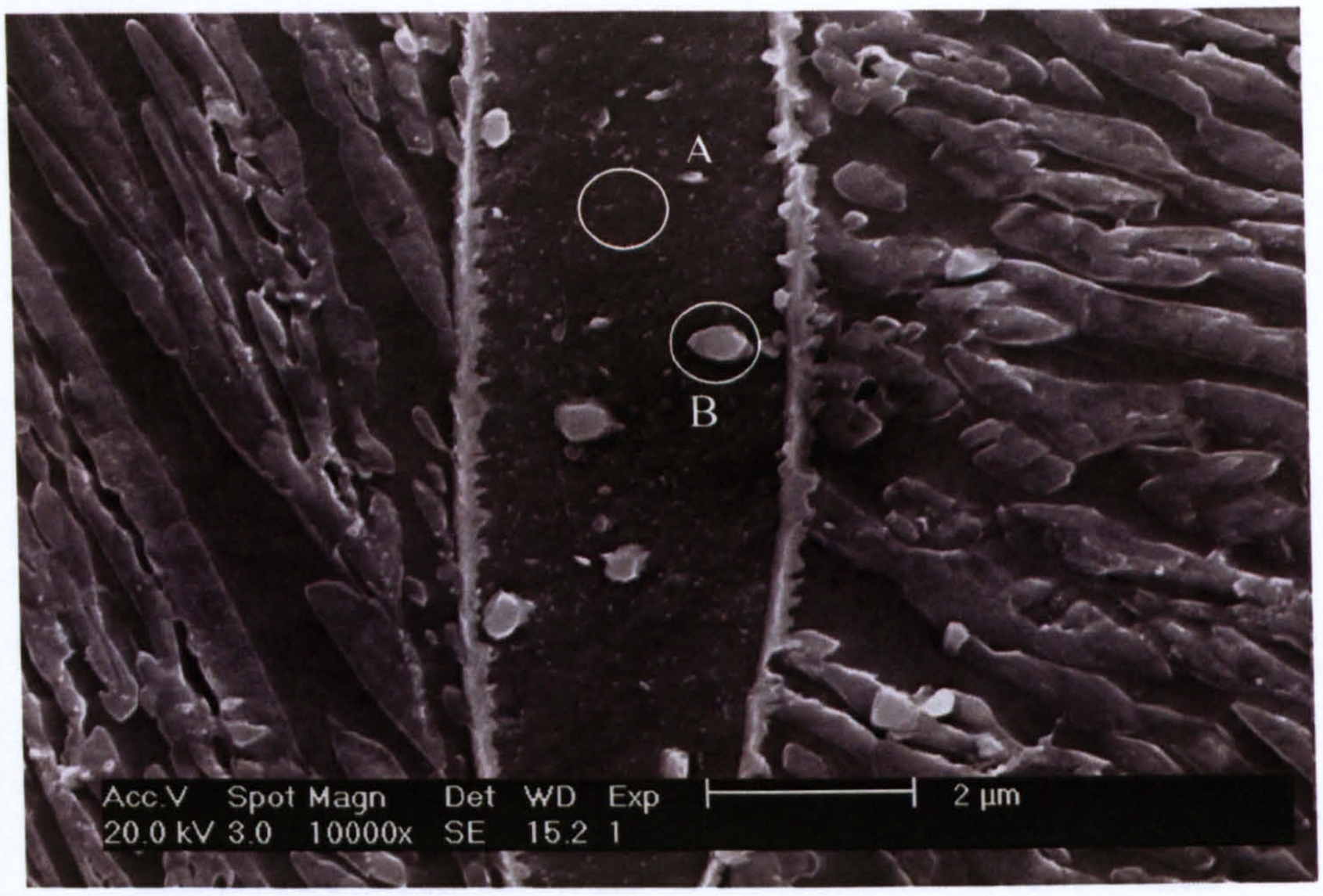

(a) SEI

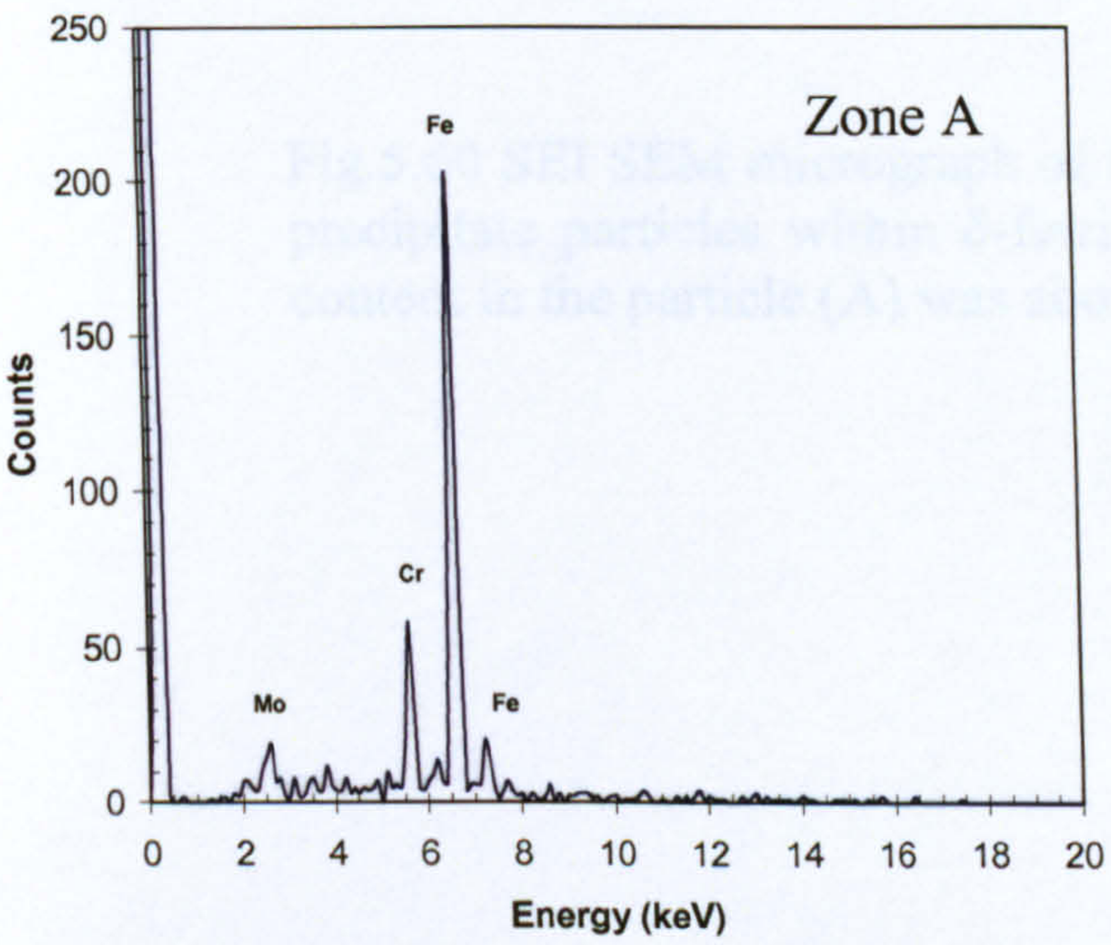

(b)

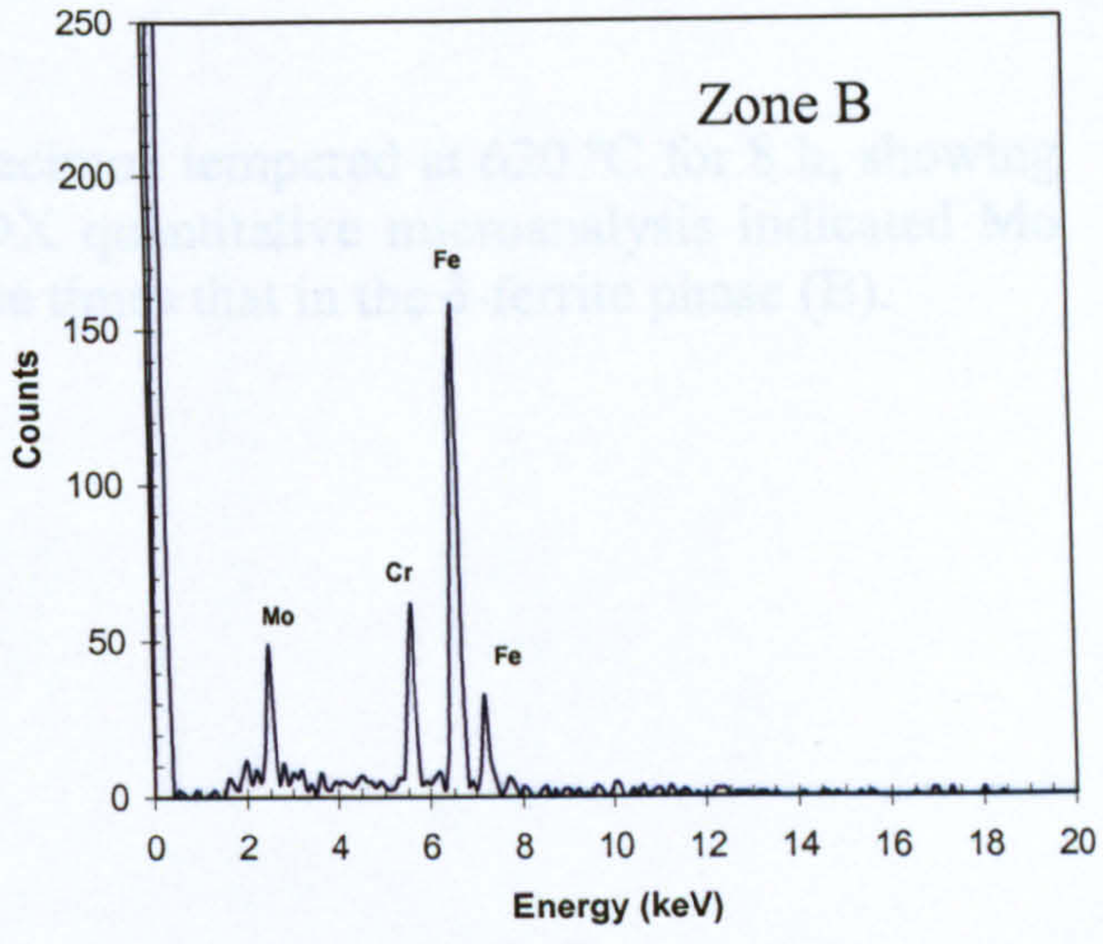

(c)

Fig.5.59 SEI SEM micrograph and EDX qualitative microanalysis of the specimen tempered at 670 °C for 4 h. (b) shows EDX spectrum taken from area A. (c) shows EDX spectrum taken from area B, indicating the particle precipitated within δ-ferrite phase is enriched in Mo. Note the size of the interaction value, zone B, is much bigger than the particle, therefore in (c) the composition included both the particle and δ-ferrite matrix.

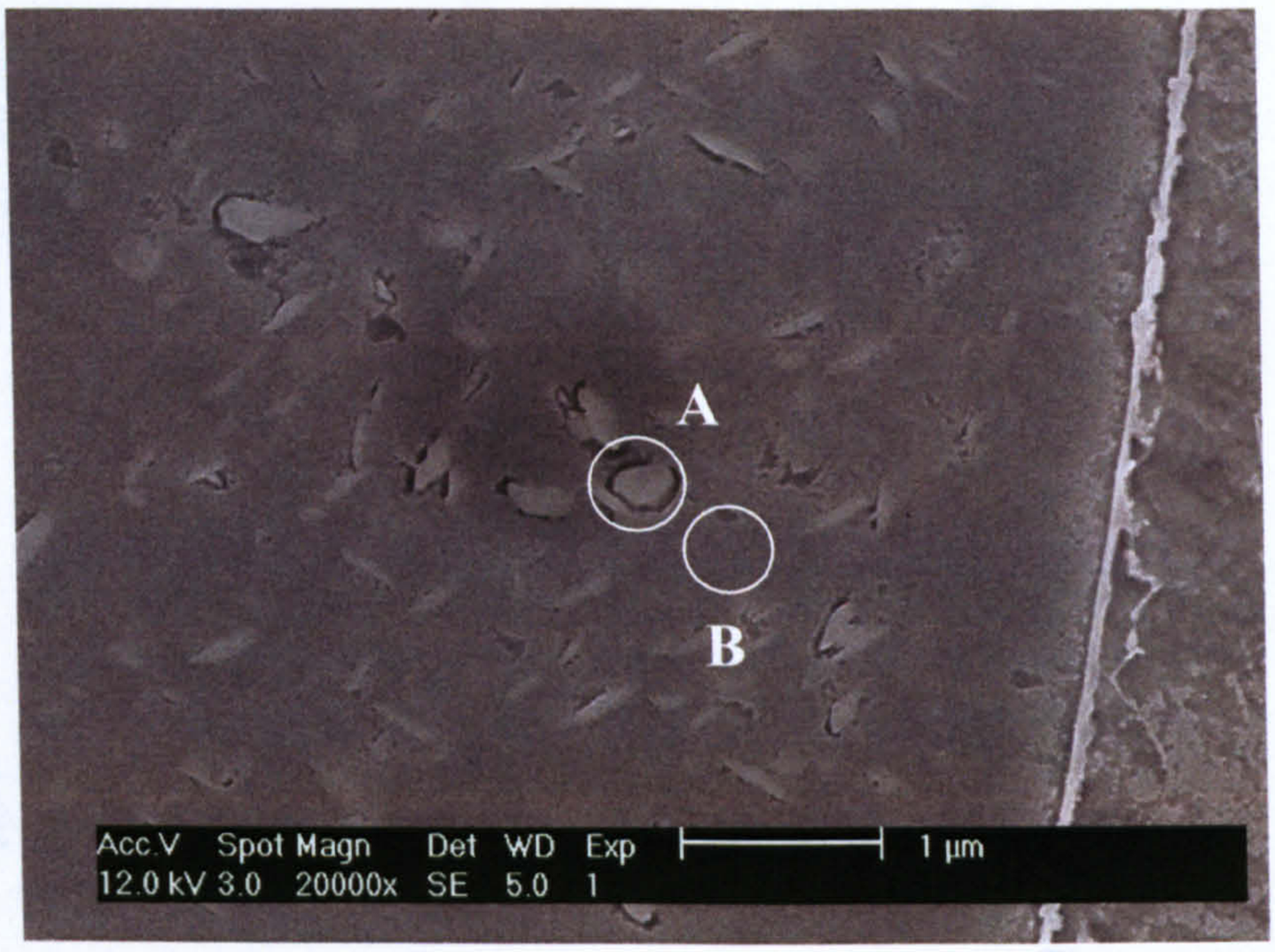

A: 11.3Mo-16.7Cr-3.2Ni-68.4Fe
B: 3.9Mo-16.6Cr-4.6Ni-75.4Fe

Fig.5.60 SEI SEM micrograph of the specimen tempered at 620 °C for 8 h, showing precipitate particles within δ-ferrite. EDX quantitative microanalysis indicated Mo content in the particle (A) was about three times that in the δ-ferrite phase (B).

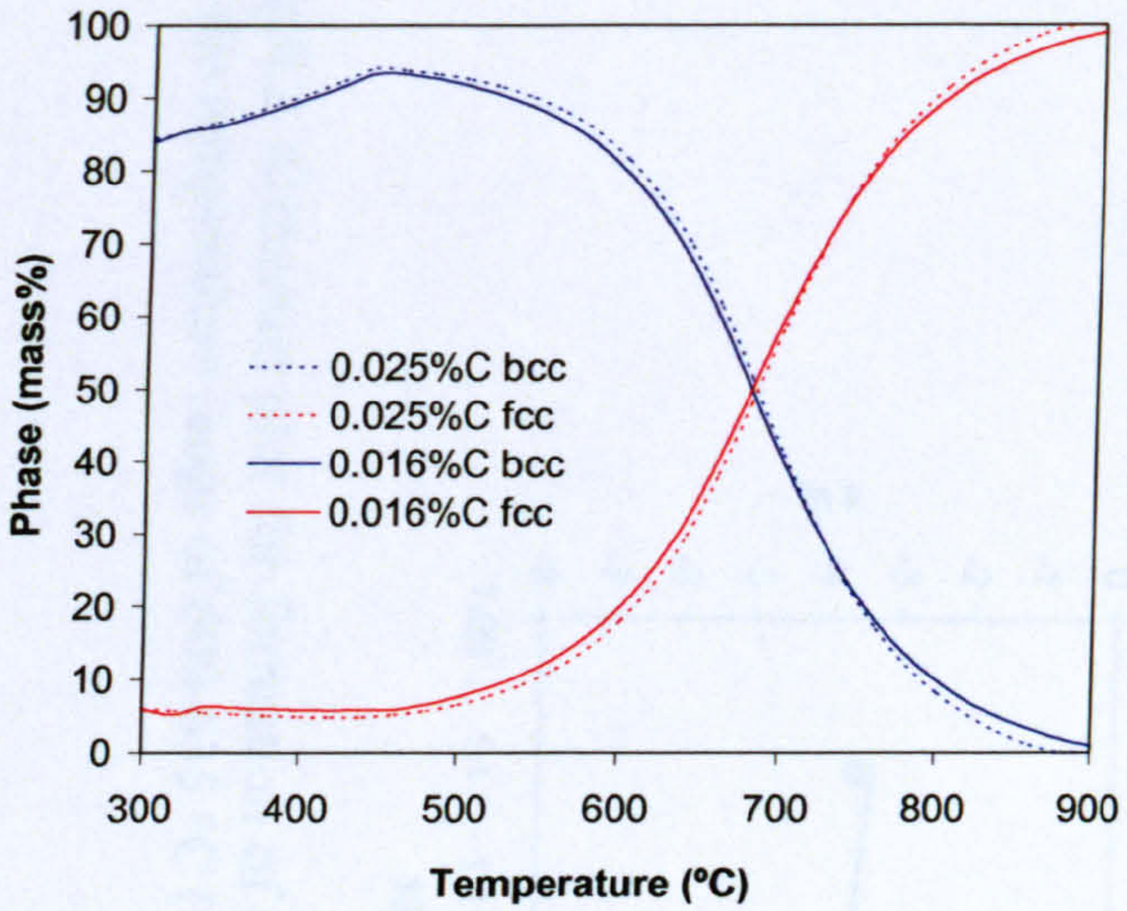

(a) Mass% of bcc martensite and fcc austenite in the temperature range 300-900 °C.

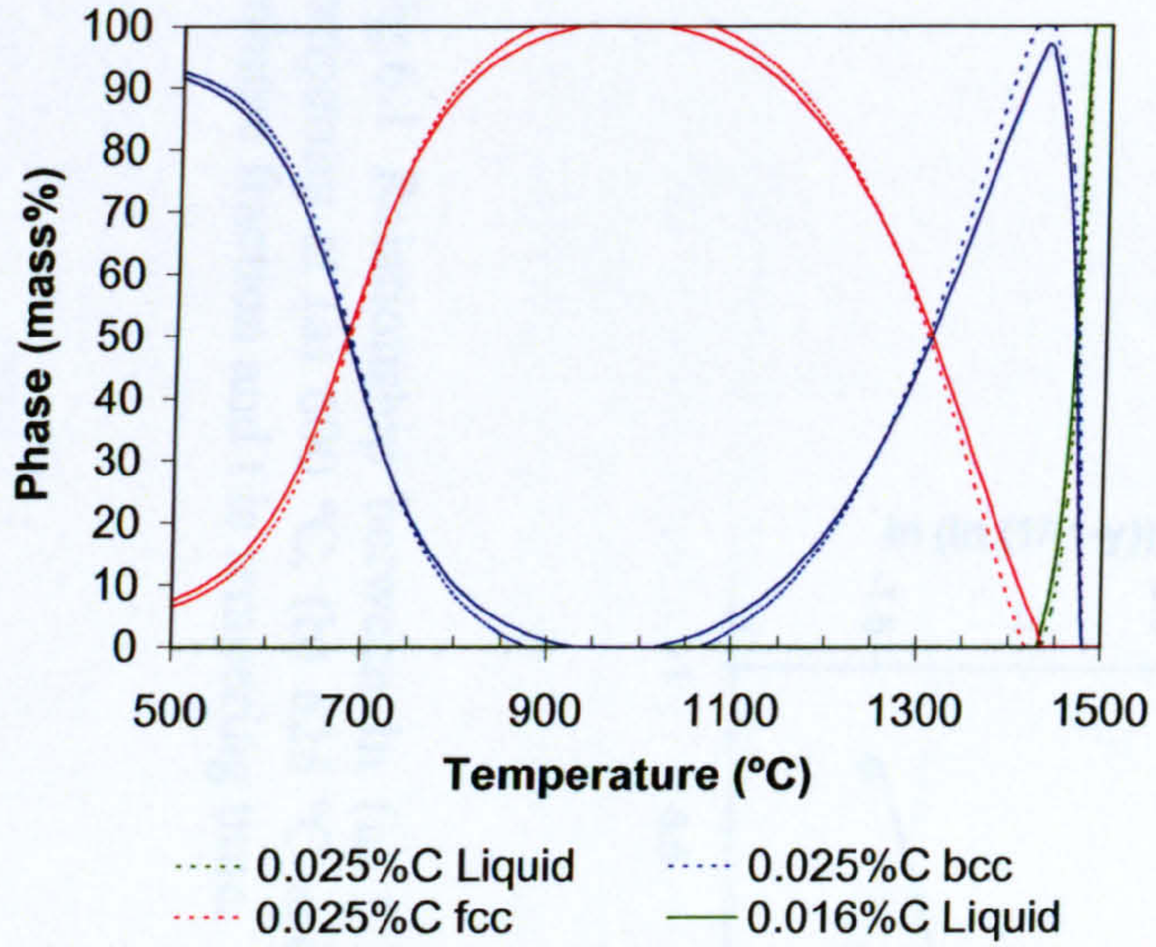

(b) Mass% of bcc martensite and fcc austenite in the temperature range 500–1500 °C.

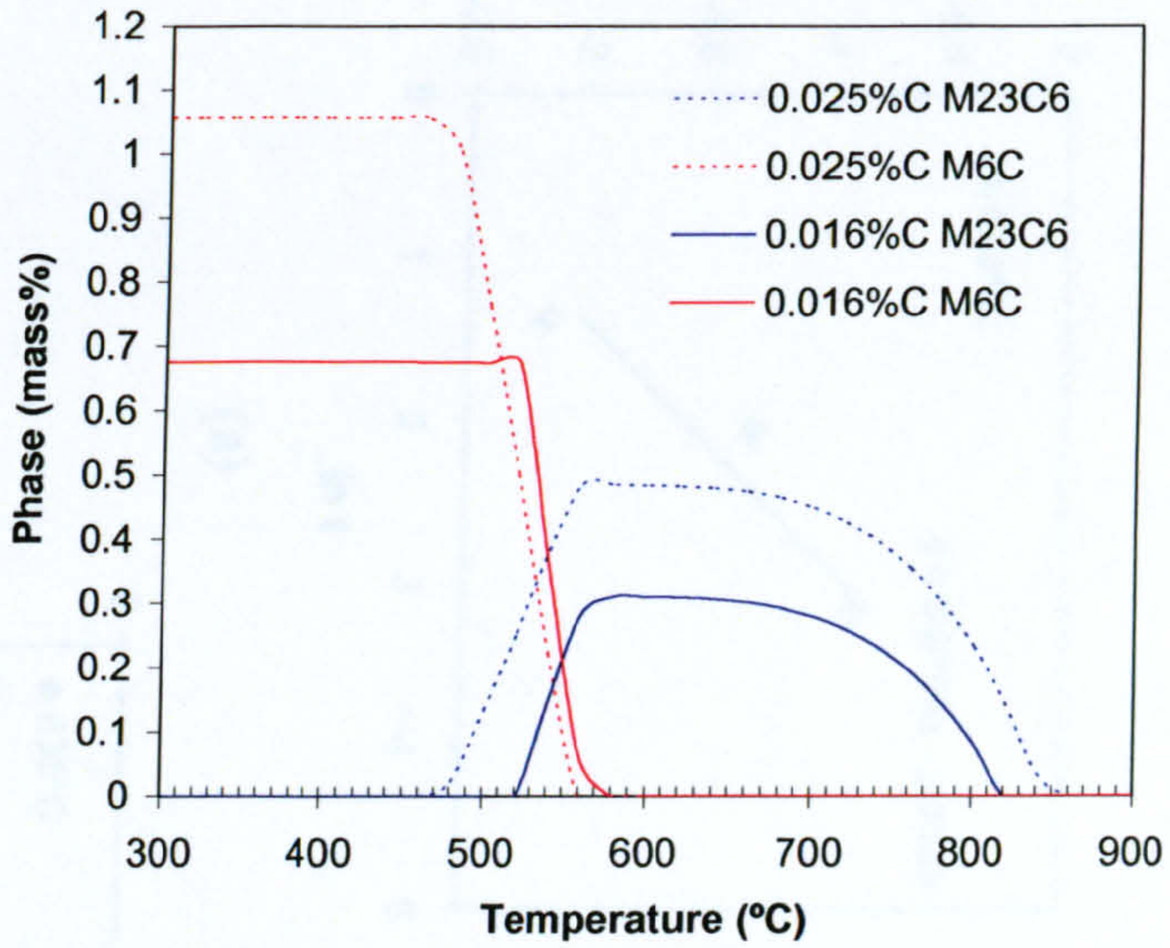

(c) $M_{23}C_6$ and M_6C carbides in the temperature range 300–900 °C.

Fig.5.61MT Data calculation results, showing (a) and (b) fcc austenite and bcc martensite phase transformation at different temperature range and (c) $M_{23}C_6$ and M_6C carbides formation with temperature in the two super 13% Cr stainless steels (Cast 1 and Cast 3, see Table 3.1).

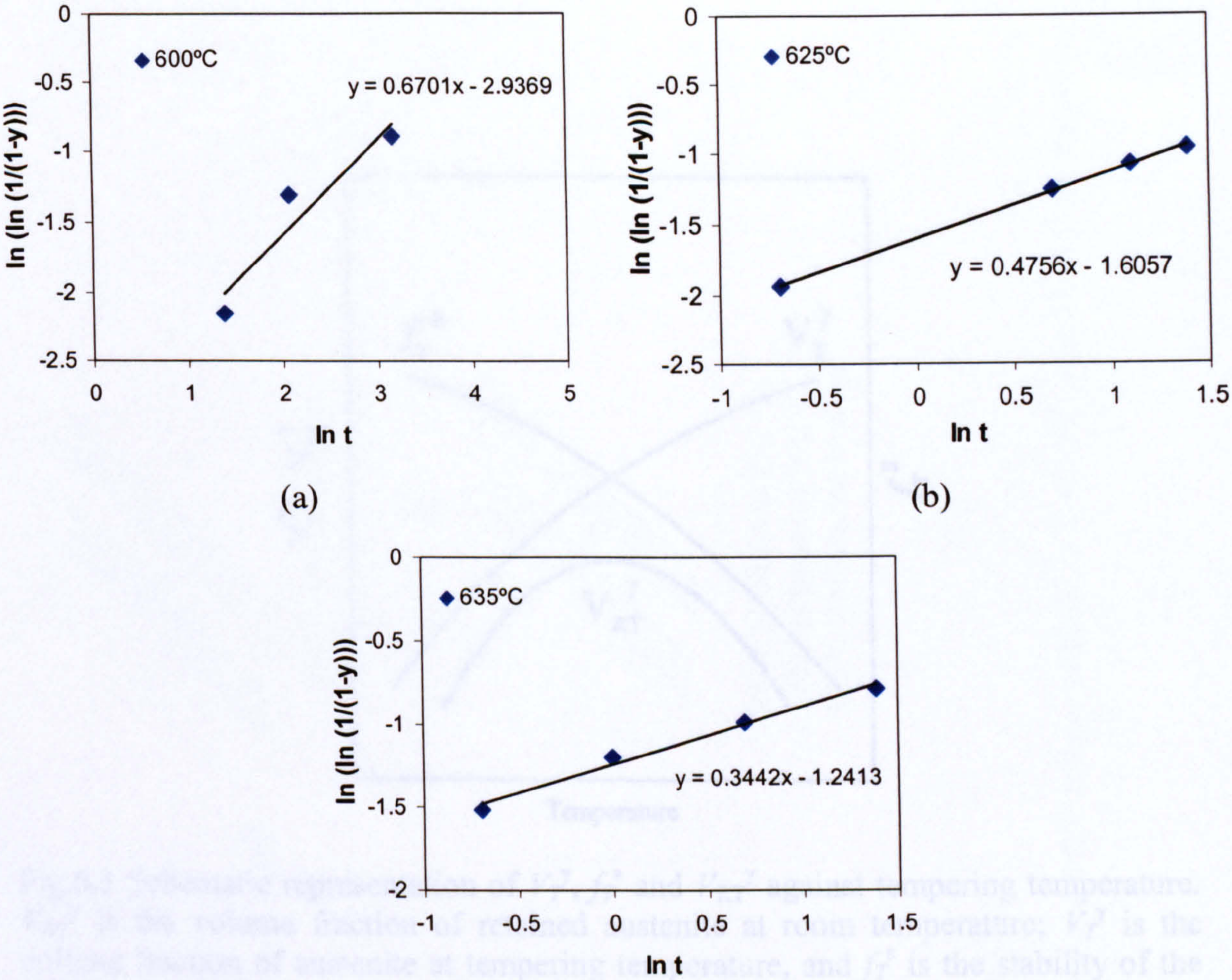

Fig.6.1 Relationship between ln (ln (1/(1-y))) and ln t for the super 13% Cr steel tempering at (a) 600 ºC, (b) 625 ºC and (c) 635 ºC for different times. y is austenite volume fraction and t is tempering time.

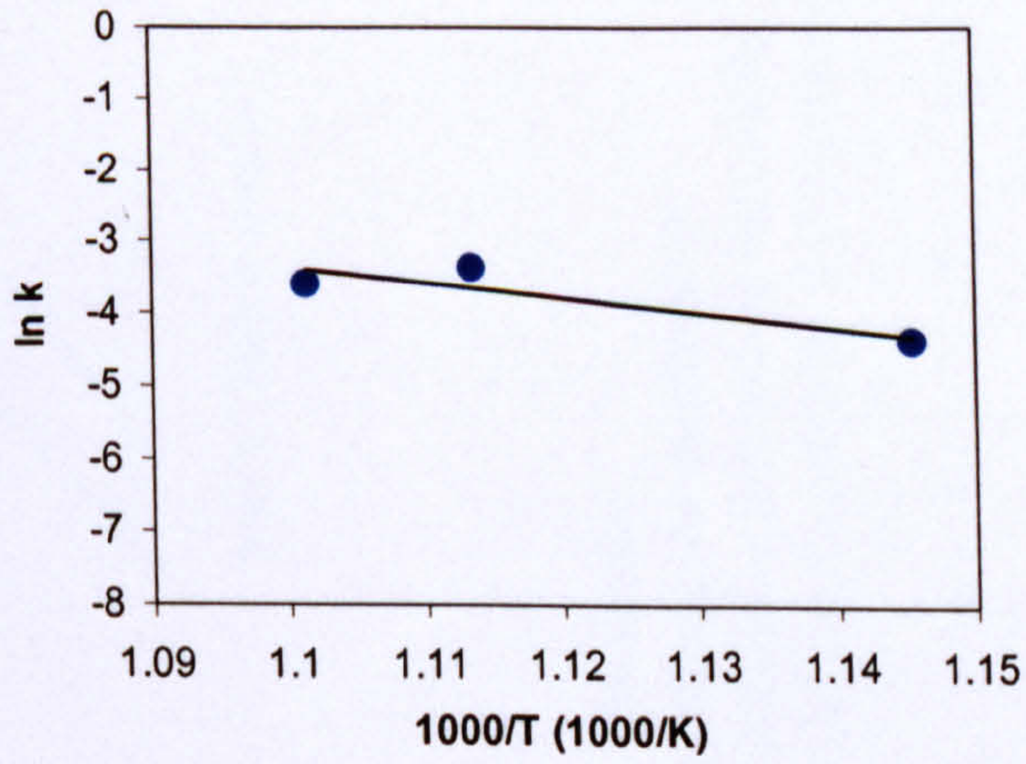

Fig.6.2 Arrhenius plot for formation of austenite in the super 13% Cr steel tempering at the temperature range of 600-635 °C (873-908 K).

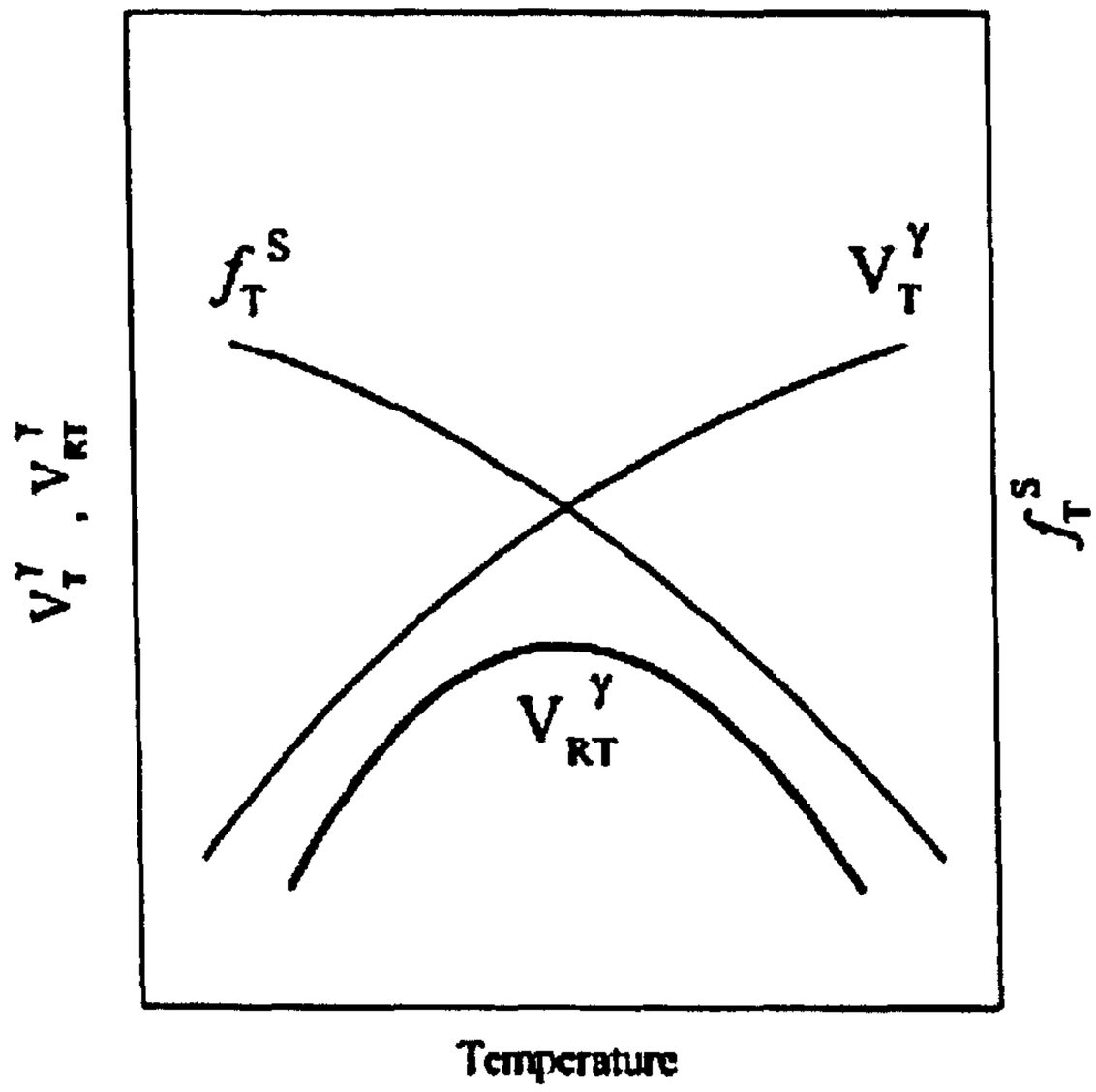

Fig.6.3 Schematic representation of V_T^γ, f_T^s and V_{RT}^γ against tempering temperature. V_{RT}^γ is the volume fraction of retained austenite at room temperature; V_T^γ is the volume fraction of austenite at tempering temperature, and f_T^s is the stability of the austenite at tempering temperature (Leem et al. 2001).

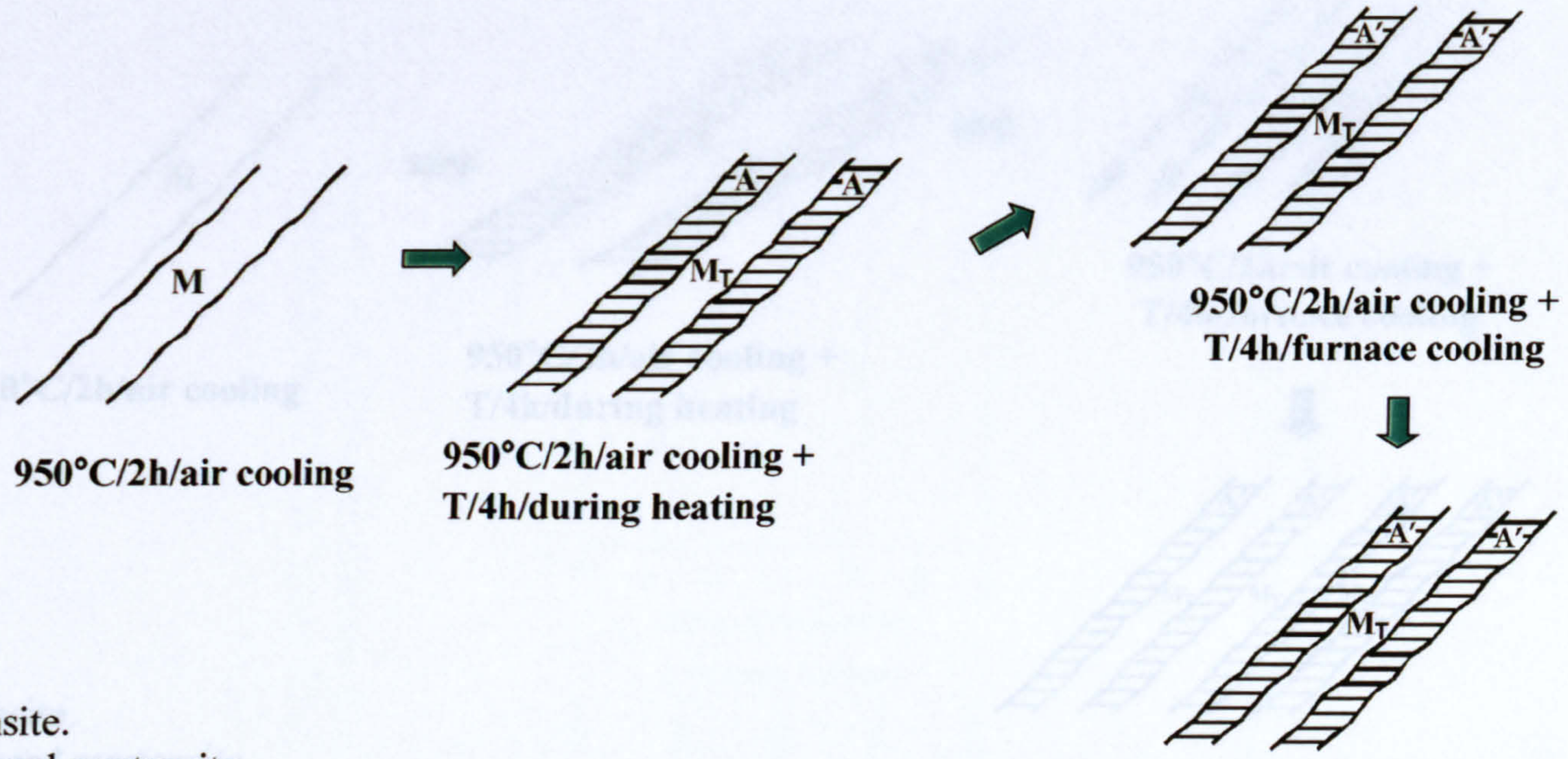

950°C/2h/air cooling

950°C/2h/air cooling + T/4h/during heating

950°C/2h/air cooling + T/4h/furnace cooling

950°C/2h/air cooling + T/4h/furnace cooling + 550°C/2h/furnace cooling

M: martensite.
M_T: tempered martensite.
A: austenite formed on tempering.
A′: retained austenite at room temperature.

$600°C \leq T < 635°C$

Fig.6.4 (a) Schematic of the structural evolution after two-stage tempering when the first temper at $600°C \leq T < 635°C$ (modified from reference: Bilmes et al. 2001).

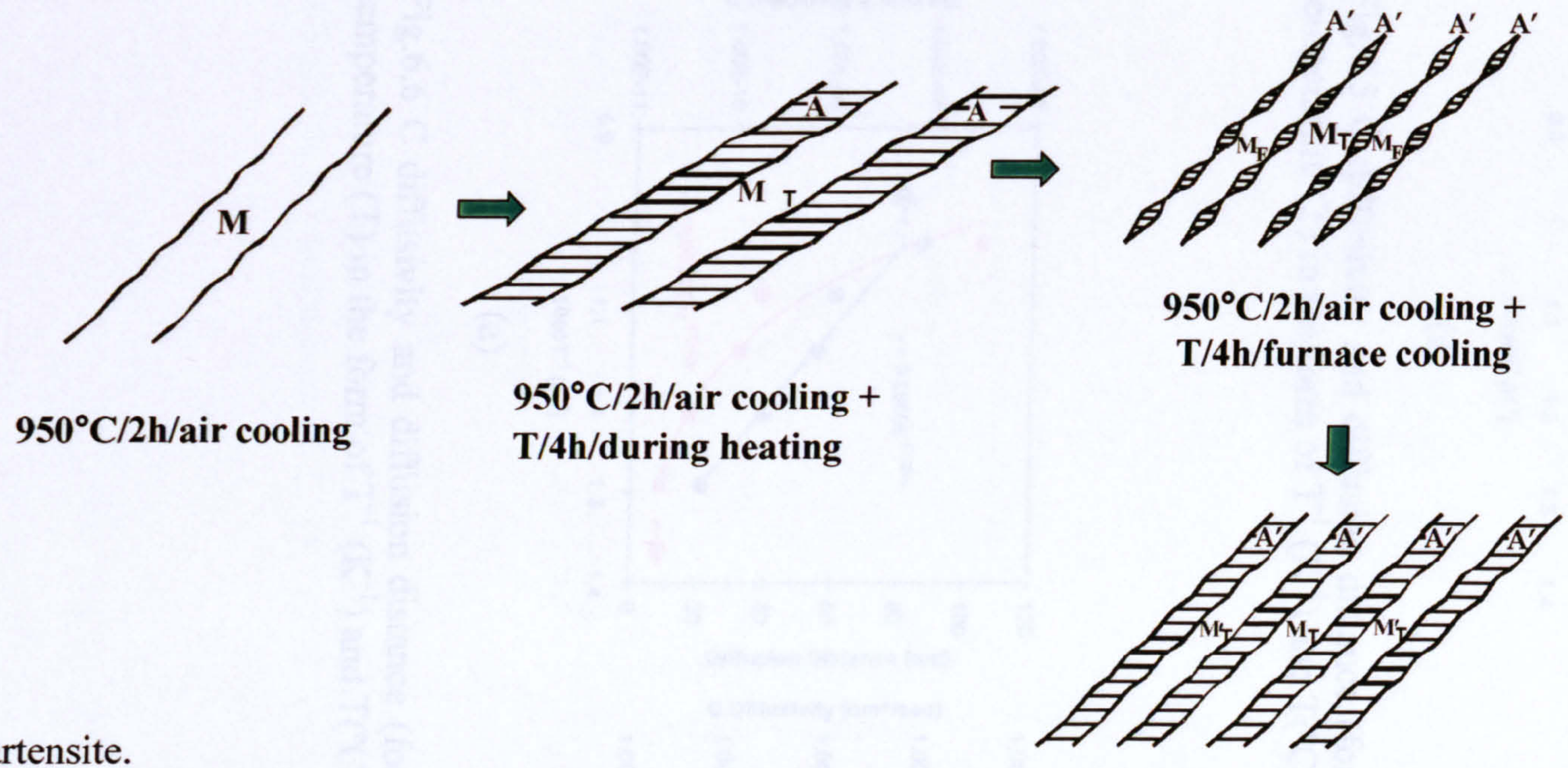

950°C/2h/air cooling

950°C/2h/air cooling +
T/4h/during heating

950°C/2h/air cooling +
T/4h/furnace cooling

950°C/2h/air cooling +
T/4h/furnace cooling +
550°C/2h/furnace cooling

M: martensite.
M_T: tempered martensite.
A: austenite formed on tempering.
A′: retained austenite at room temperature.
M_F: fresh martensite, originated from A.
M'_T: tempered martensite, originated from M_F.

$$635°C < T \leq 700°C$$

Fig.6.4 (b) Schematic of the structural evolution after two-stage tempering when the first temper at $635°C < T \leq 700°C$ (modified from reference: Bilmes et al. 2001).

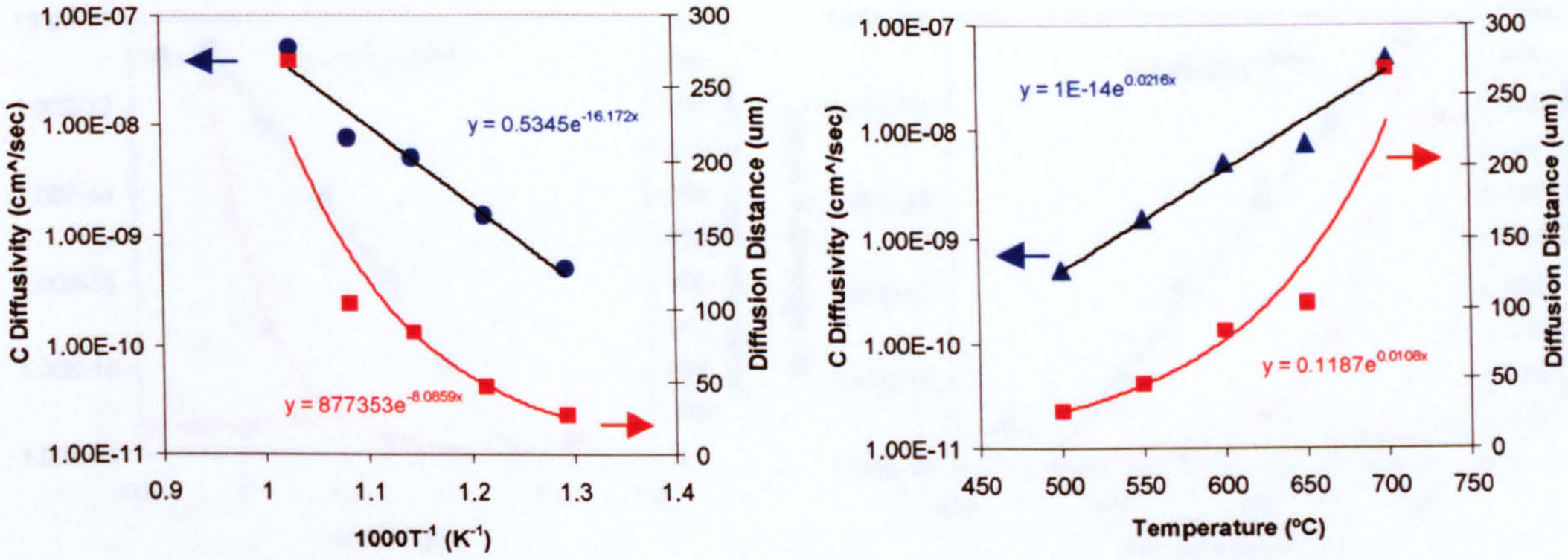

(a) (b)

Fig.6.5 C diffusivity and diffusion distance (for t = 4 h) in bcc iron as a function of temperature (T) in the form of T^{-1} (K^{-1}) and T(°C), respectively.

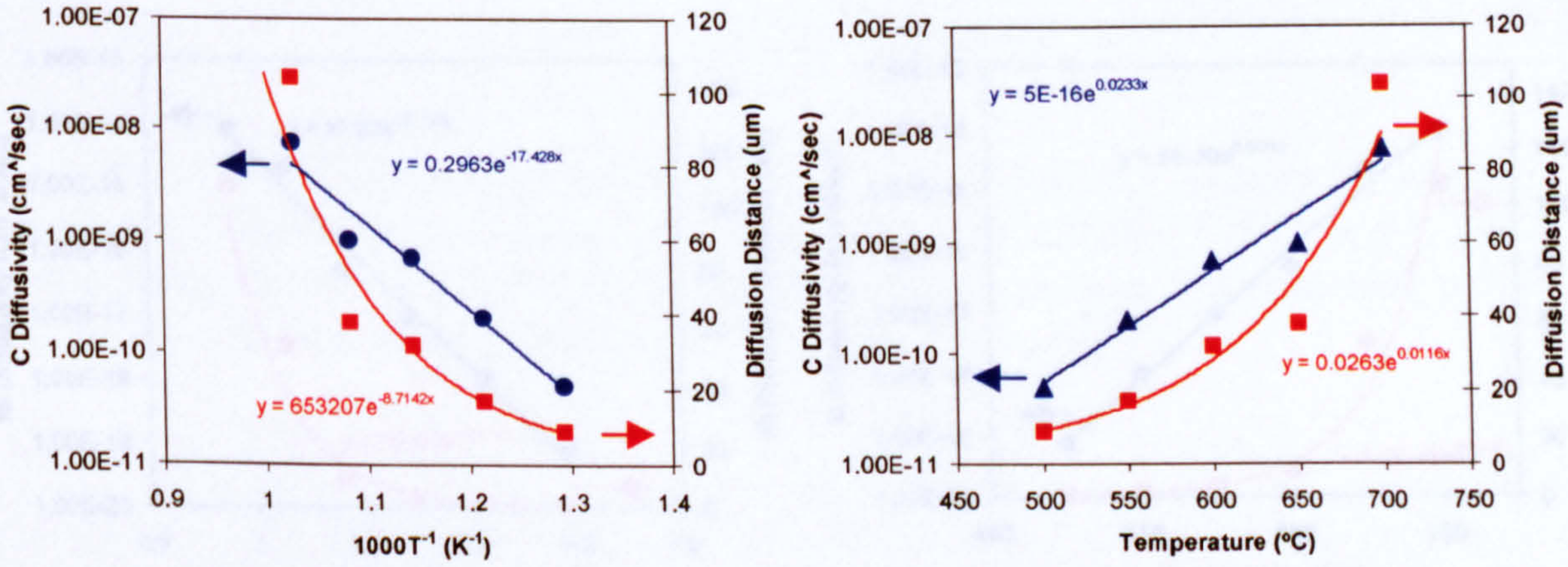

(a) (b)

Fig.6.6 C diffusivity and diffusion distance (for t = 4 h) in fcc iron as a function of temperature (T) in the form of T^{-1} (K^{-1}) and T(°C), respectively.

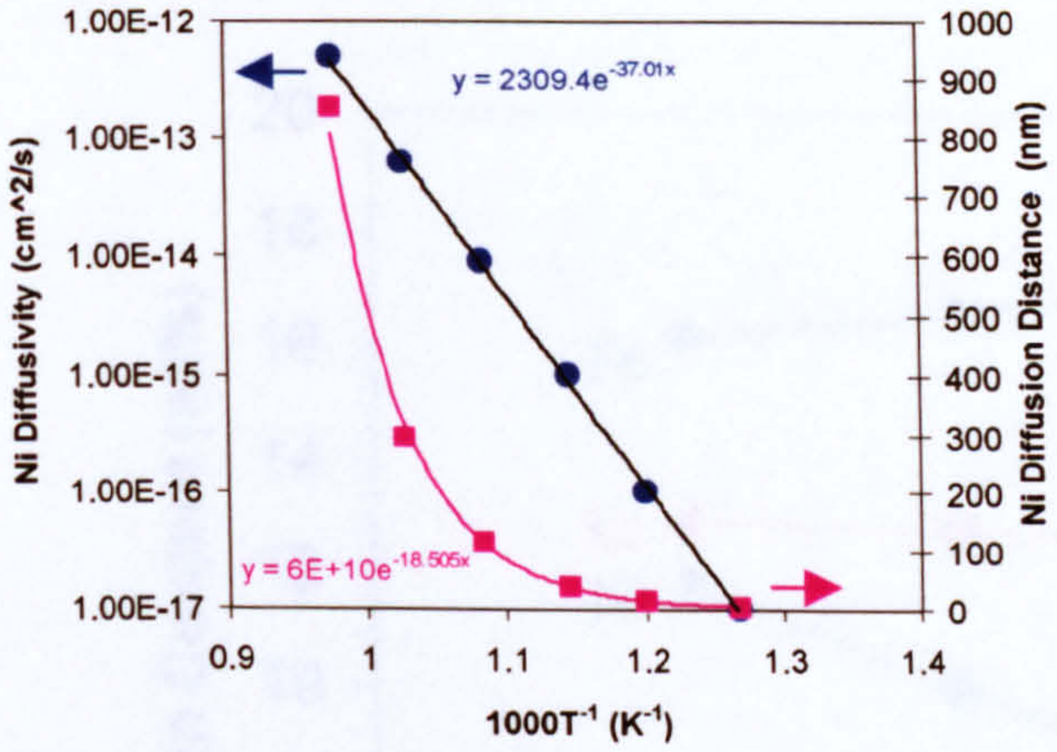

(a) (b)

Fig.6.7 Ni diffusivity and diffusion distance (for t = 4 h) in bcc iron as a function of temperature (T) in the form of T^{-1} (K^{-1}) and T(°C), respectively.

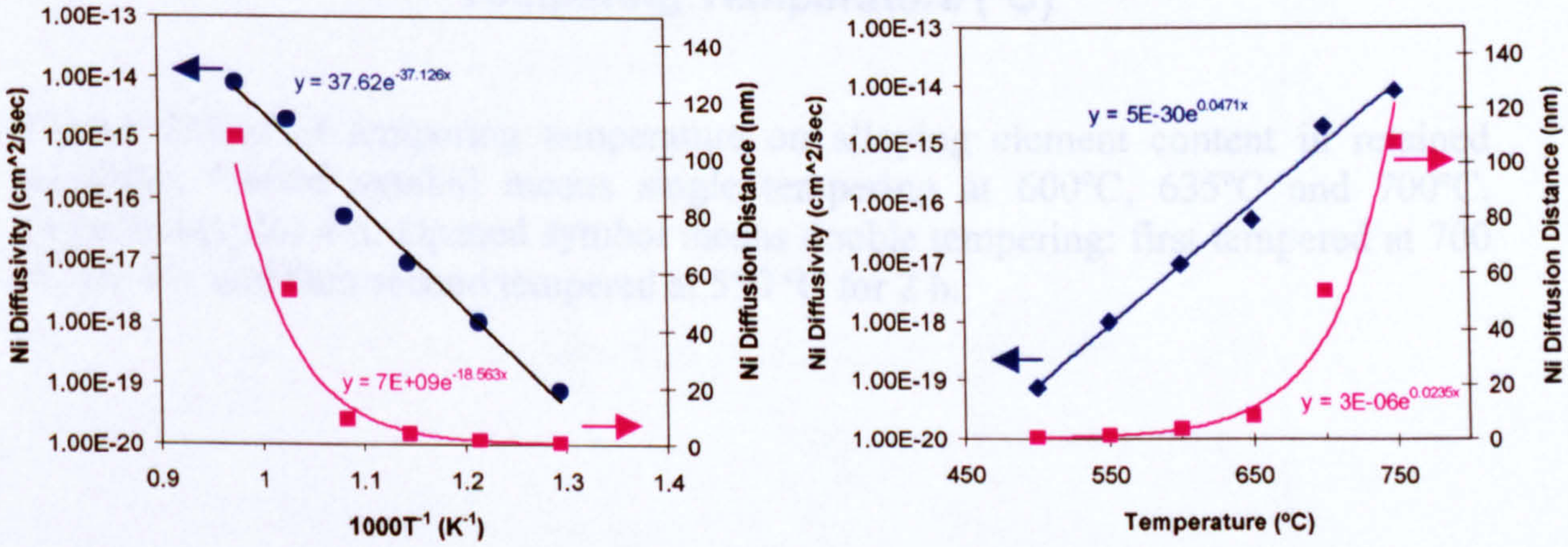

(a) (b)

Fig.6.8 Ni diffusivity and diffusion distance (for t = 4 h) in fcc iron as a function of temperature (T) in the form of T^{-1} (K^{-1}) and T(°C), respectively.

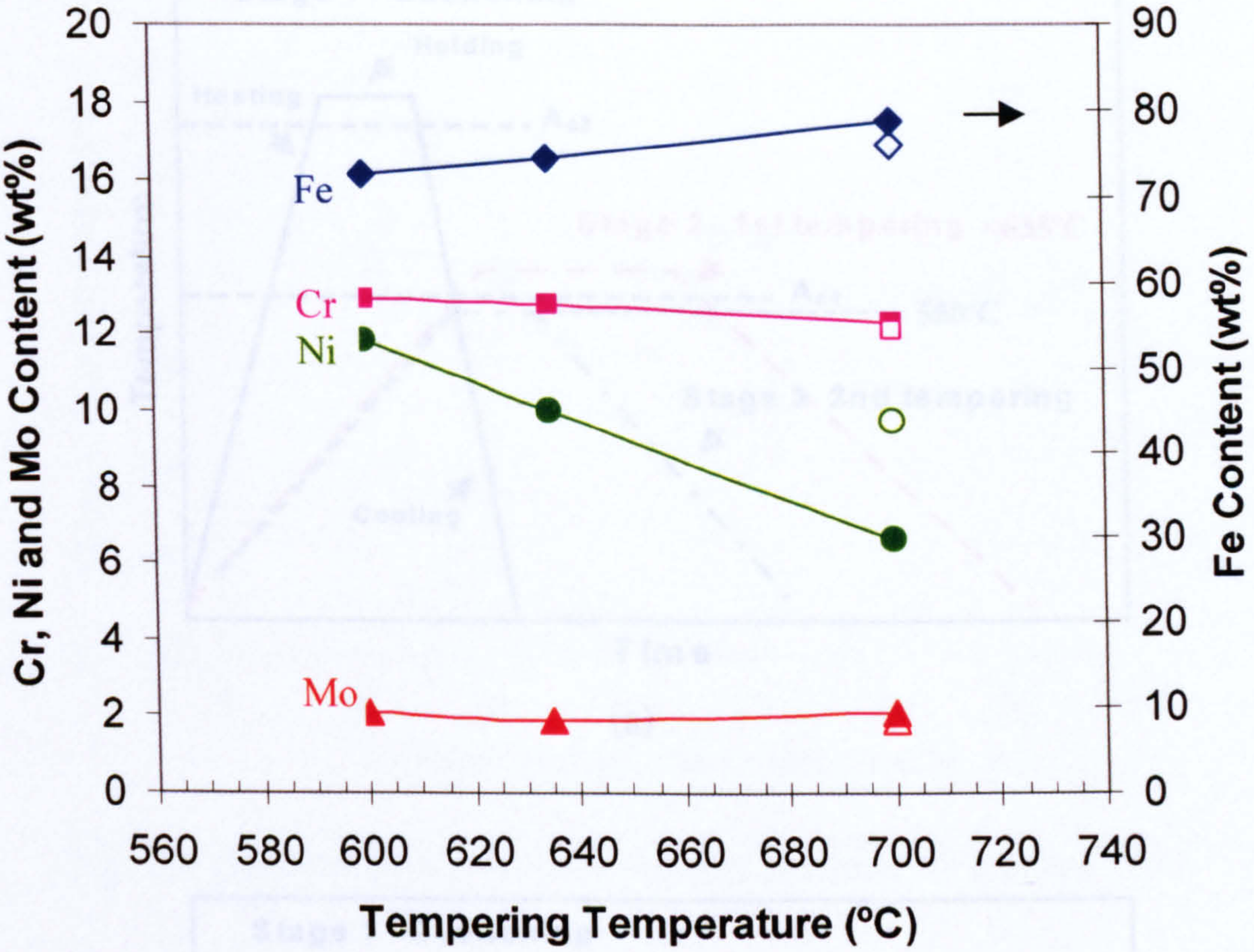

Fig.6.9 Effect of tempering temperature on alloying element content in retained austenite. Closed symbol means single tempering at 600°C, 635°C and 700°C, respectively, for 4 h. Opened symbol means double tempering: first tempered at 700 °C for 4 h, and then second tempered at 550 °C for 2 h.

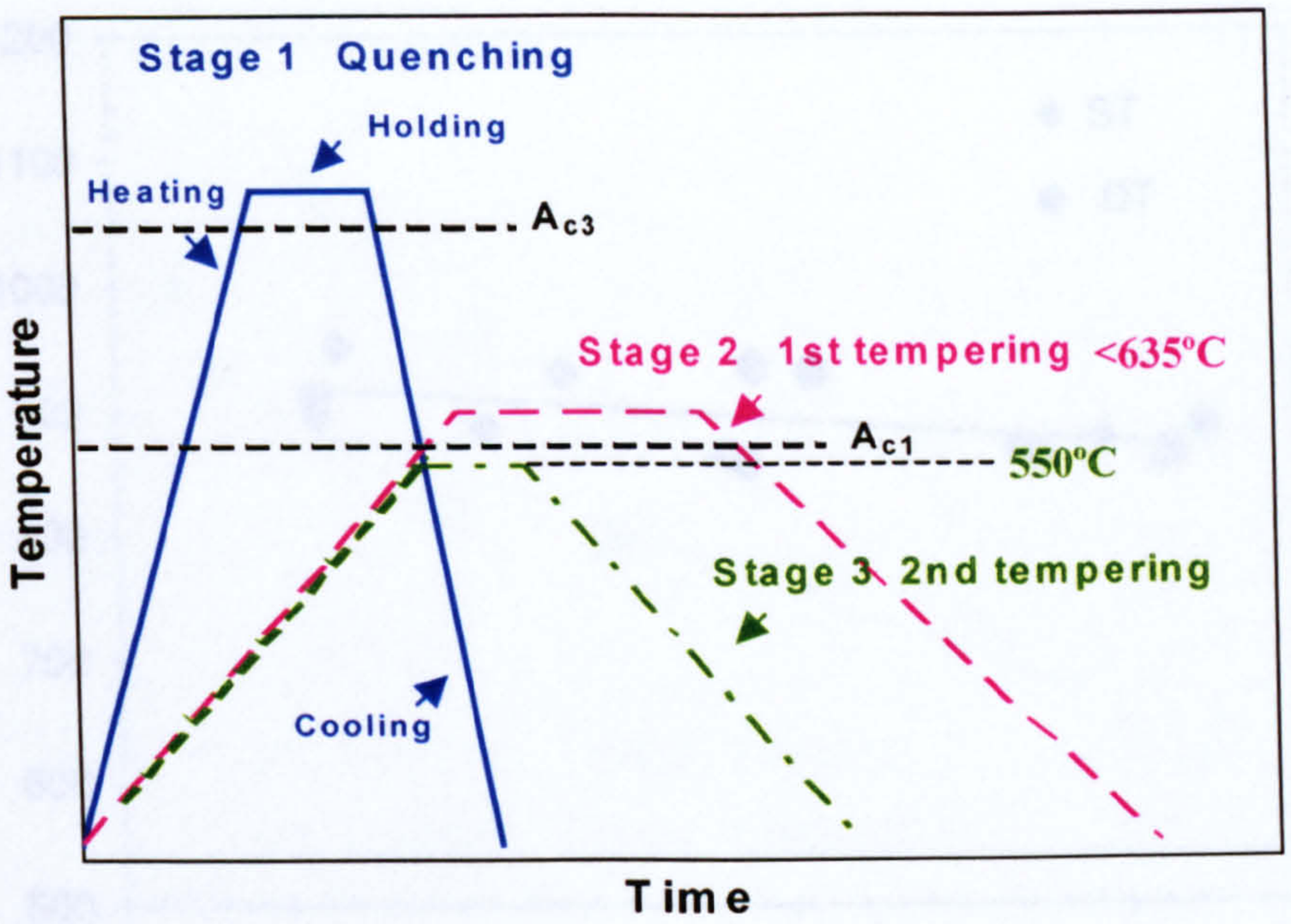

(a)

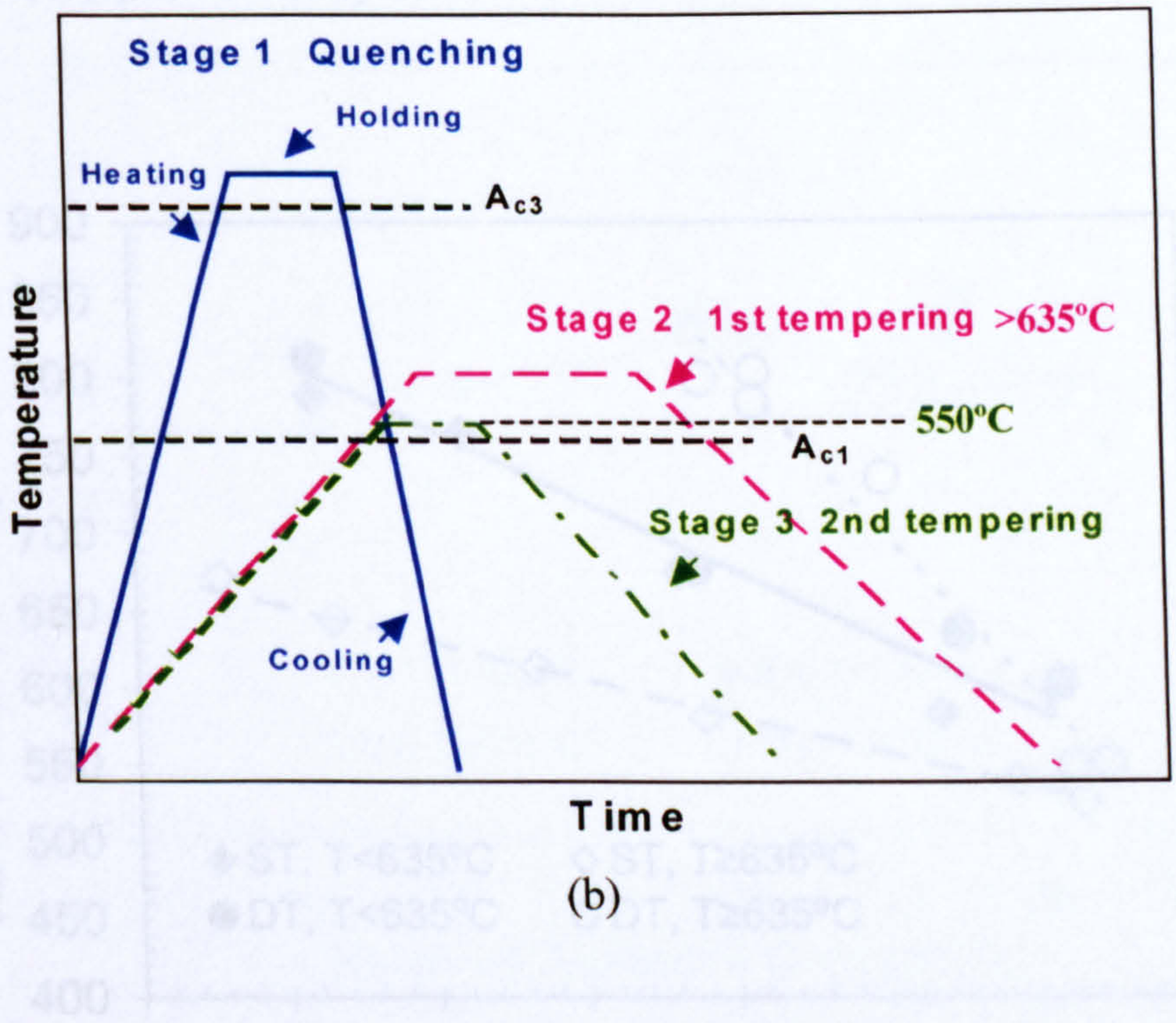

(b)

Fig.6.10 Schematic of the heat treatment process for the super 13% Cr steel investigated. (a) shows when the first stage tempering temperature <635 °C, the second tempering at 550 °C was below the A_{c1} temperature, therefore no new austenite formed during the second tempering. (b) shows when the first stage tempering temperature >635 °C, the second tempering at 550 °C was above the A_{c1} temperature, therefore new austenite formed during the second tempering, resulting in the total retained austenite content was increased.

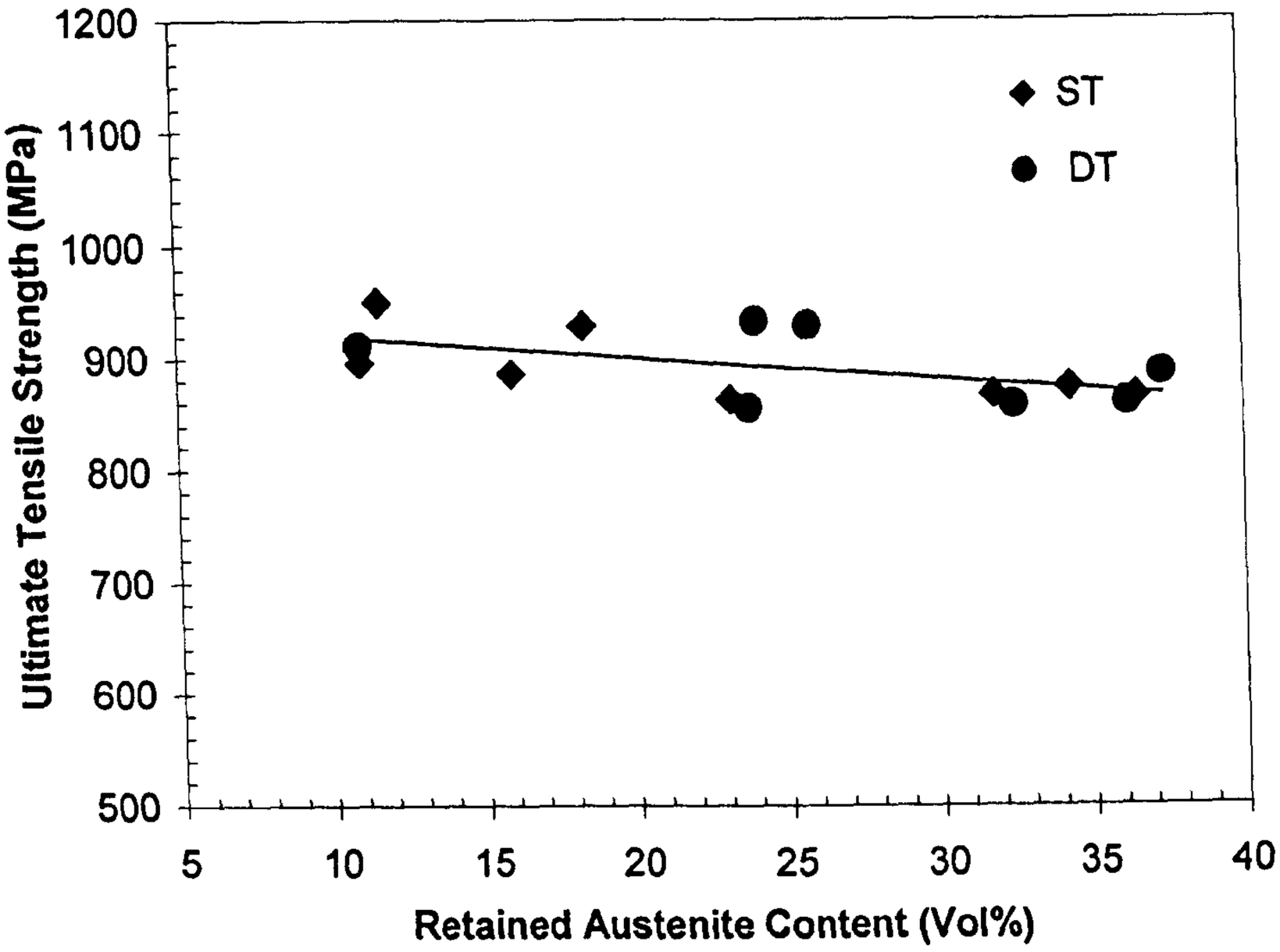

Fig.6.11 (a) Relationship between retained austenite content and UTS.

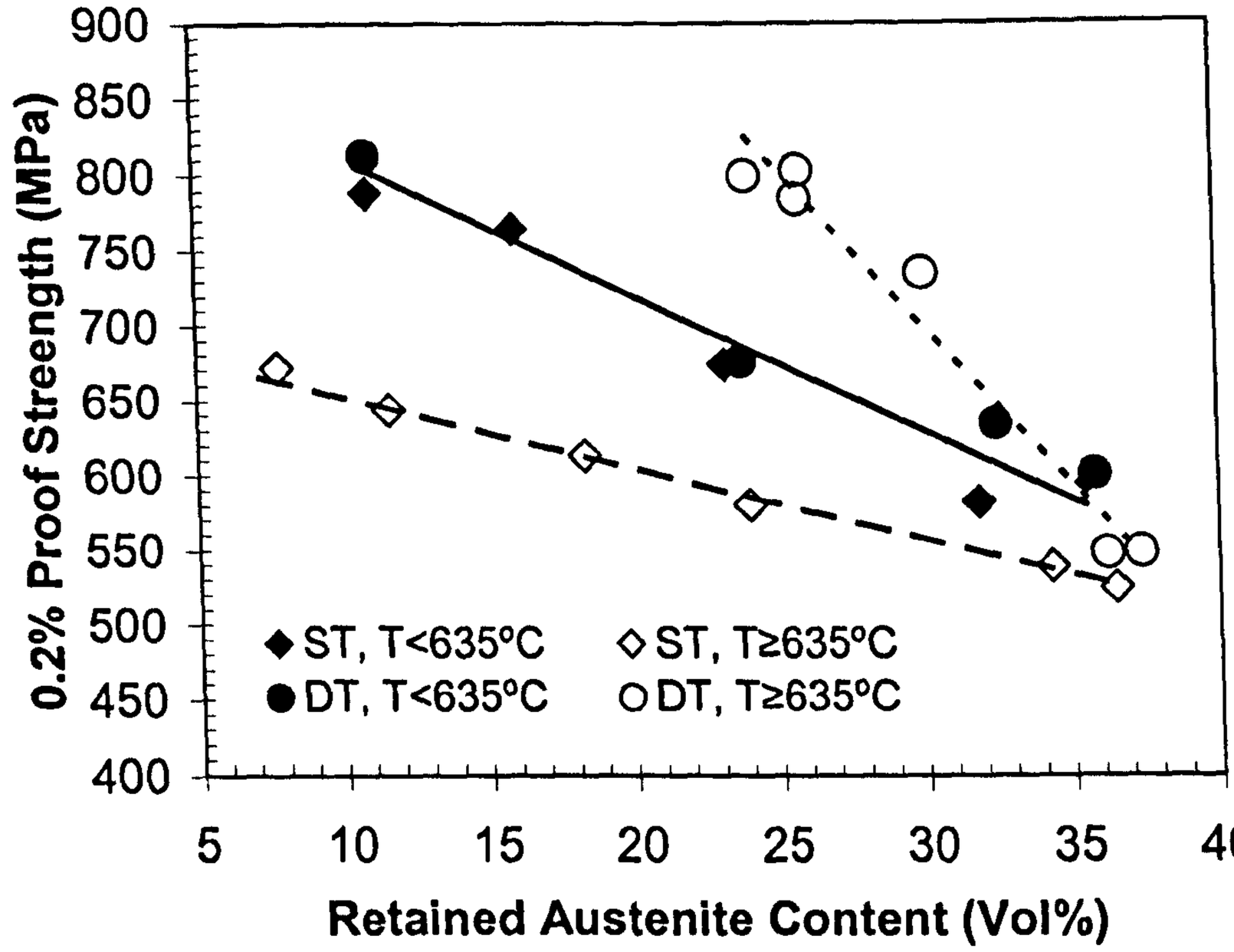

Fig.6.11 (b) Relationship between retained austenite content and 0.2% proof strength.

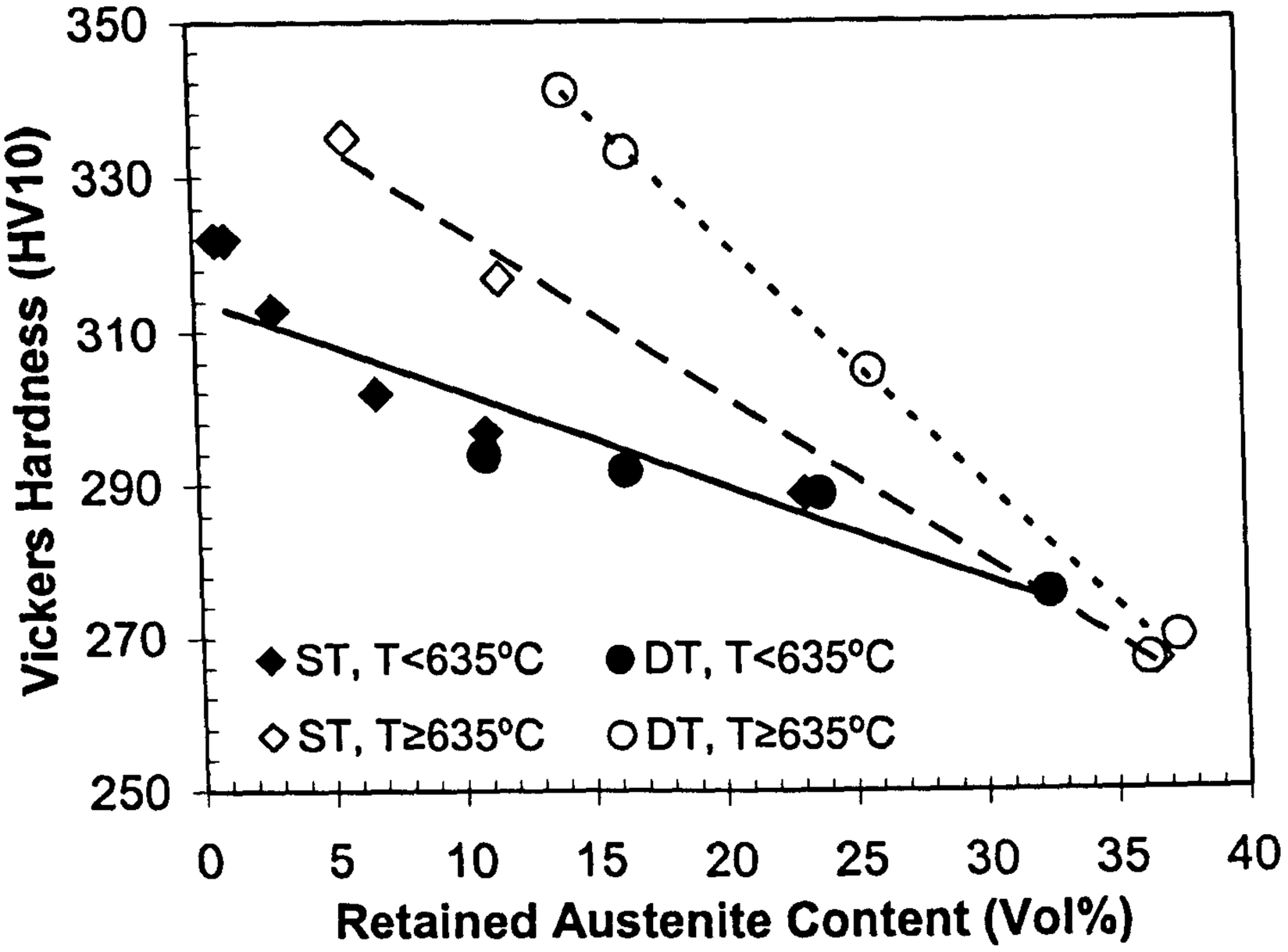

Fig.6.11 (c) Relationship between retained austenite content and hardness.

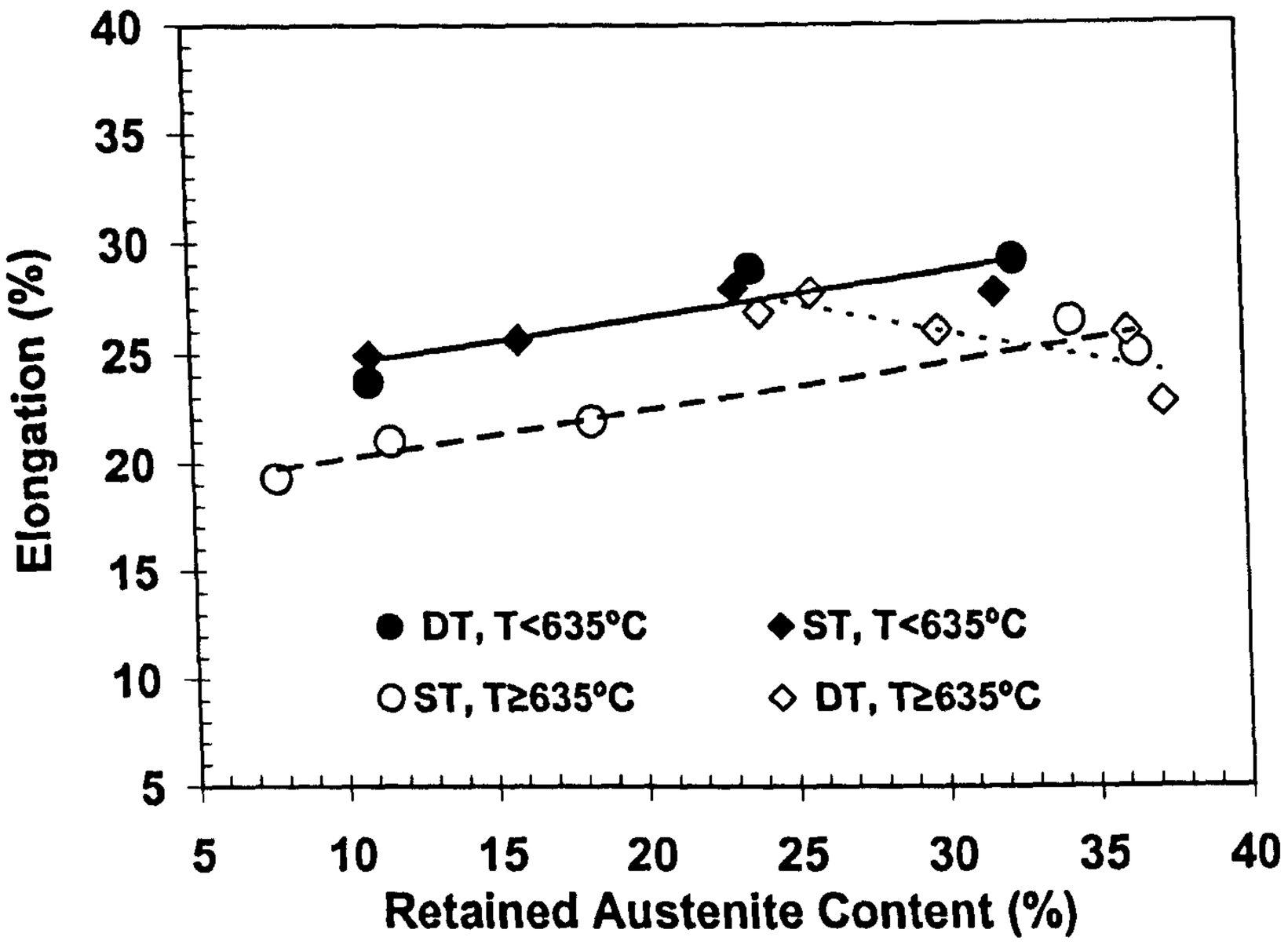

Fig.6.11 (d) Relationship between retained austenite content and percentage elongation.

Fig.6.11 Effect of retained austenite content on strength, hardness, and elongation of the specimens tempered at different temperature. ST means single tempering and DT means double tempering. Single tempering (and the first stage of double tempering) was in the range 600 ~ 670 °C, 4 h. The second stage of double tempering was at 550 °C for 2 h.

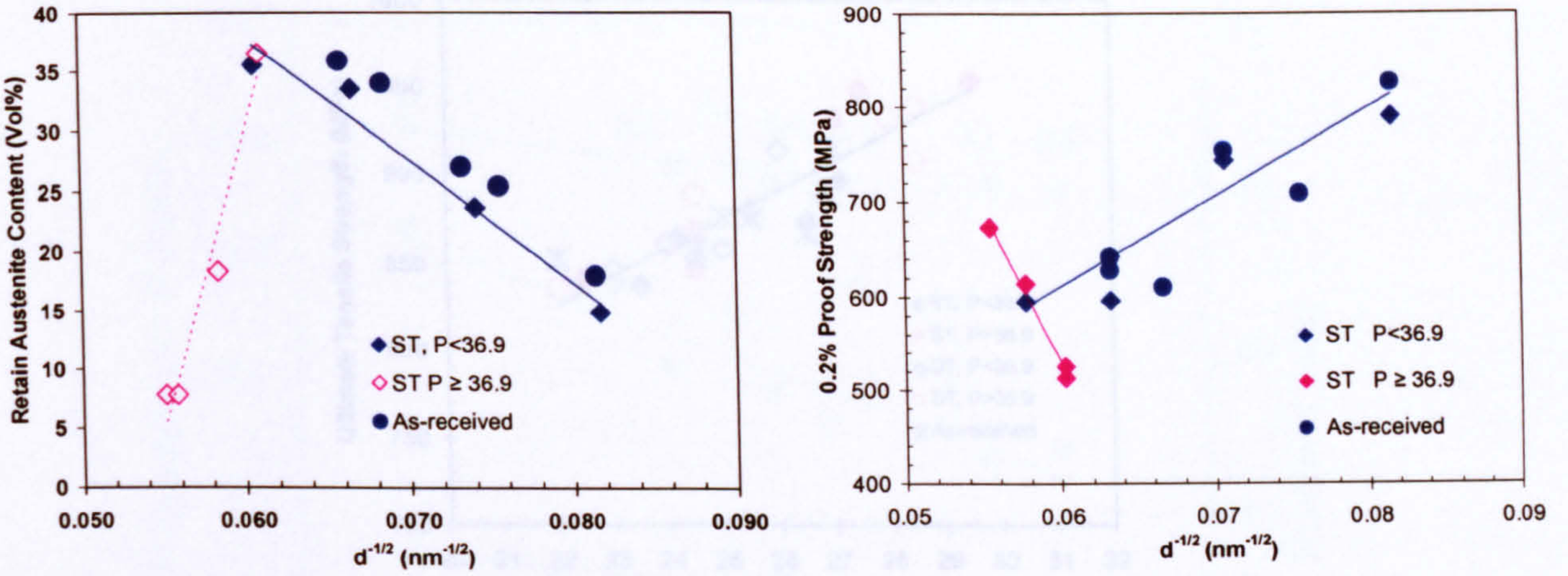

(a) (b)

Fig.6.12 (a) retained austenite content and (b) 0.2% proof strength as a function of $d^{-1/2}$ for the specimens after single tempering (ST). d is retained austenite grain size (for P<36.9), or 'retained austenite+fresh martensite' aggregate size (for P ≥ 36.9). P is the Holloman-Jaffe time-temperature parameter.

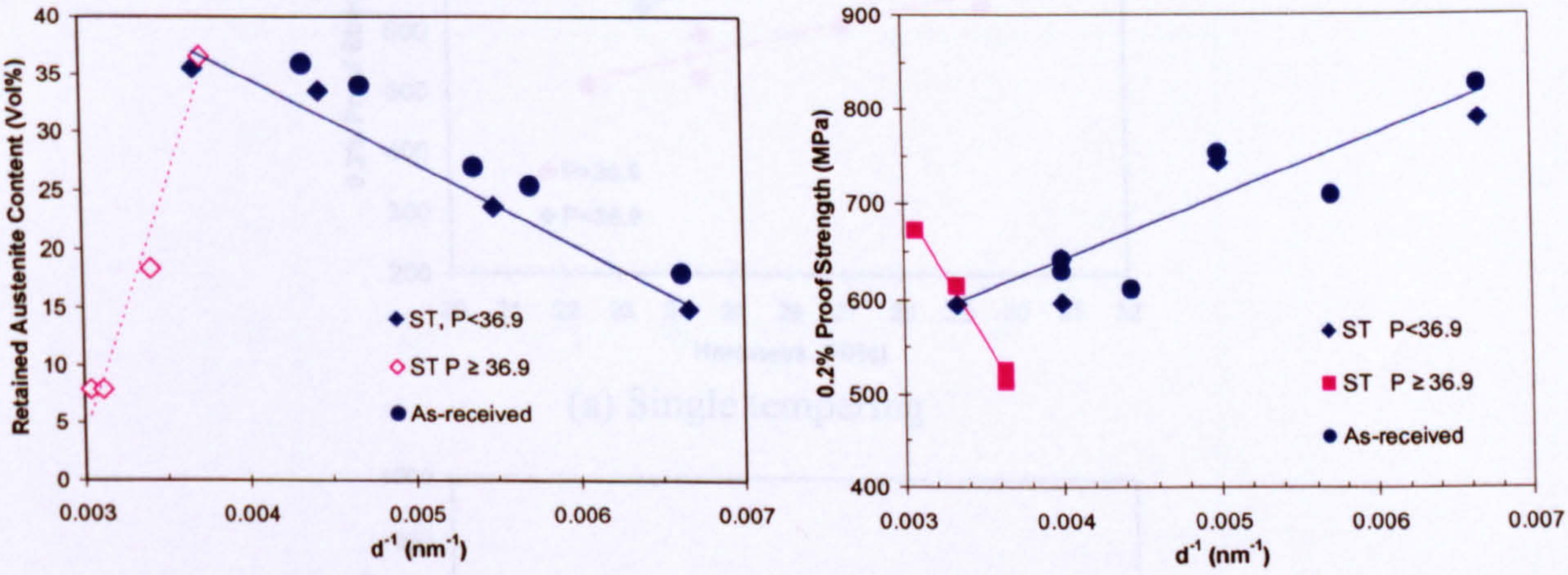

(a) (b)

Fig.6.13 (a) retained austenite content and (b) 0.2% proof strength as a function of d^{-1} for the specimens after single tempering (ST). d is retained austenite grain size (for P<36.9), or 'retained austenite+fresh martensite' aggregate size (for P ≥ 36.9). P is the Holloman-Jaffe time-temperature parameter.

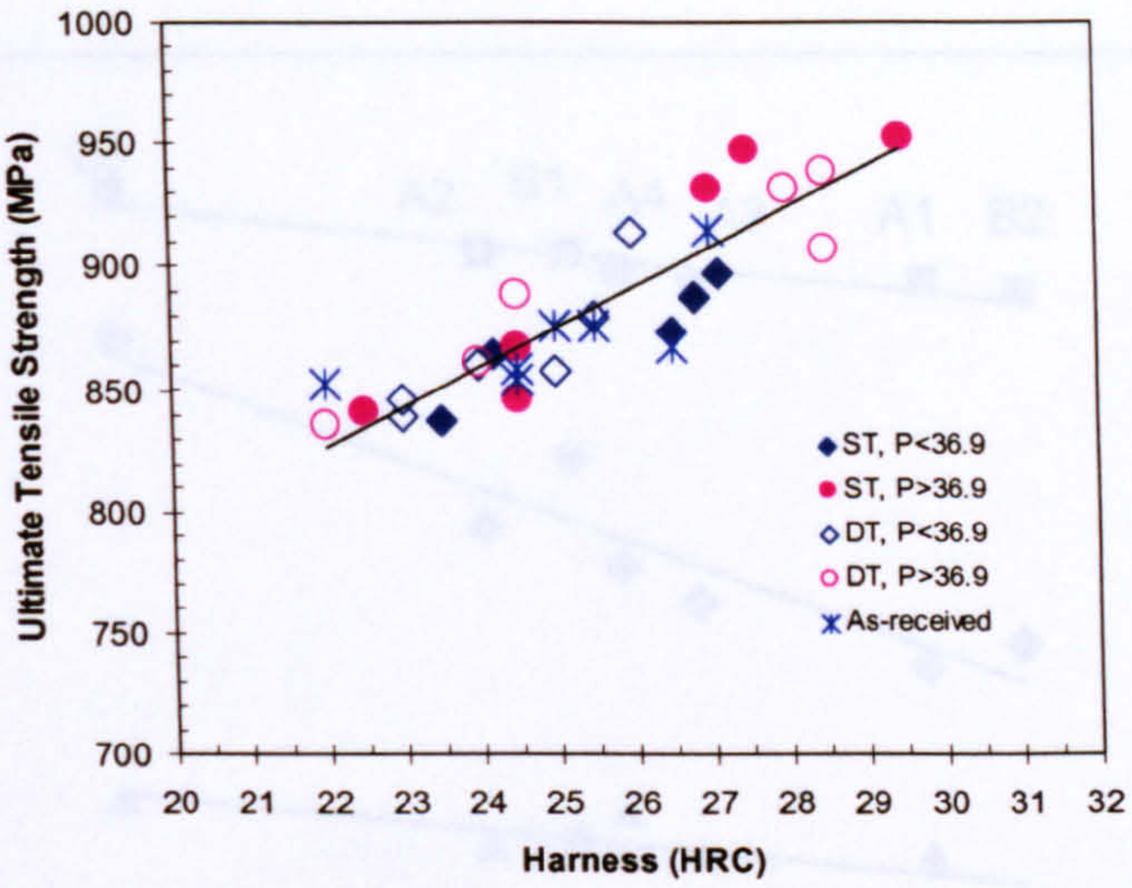

Fig.6.14 Relationship between hardness and UTS. ST: single tempering; DT: double tempering. P is the Hollomon-Jaffe tempering time-temperature parameter ($P = 273 + T(°C)) \times (40 + \log_{10} t(h)) \times 1000^{-1}$). The as-received data followed the trendline for laboratory re-heat treated data.

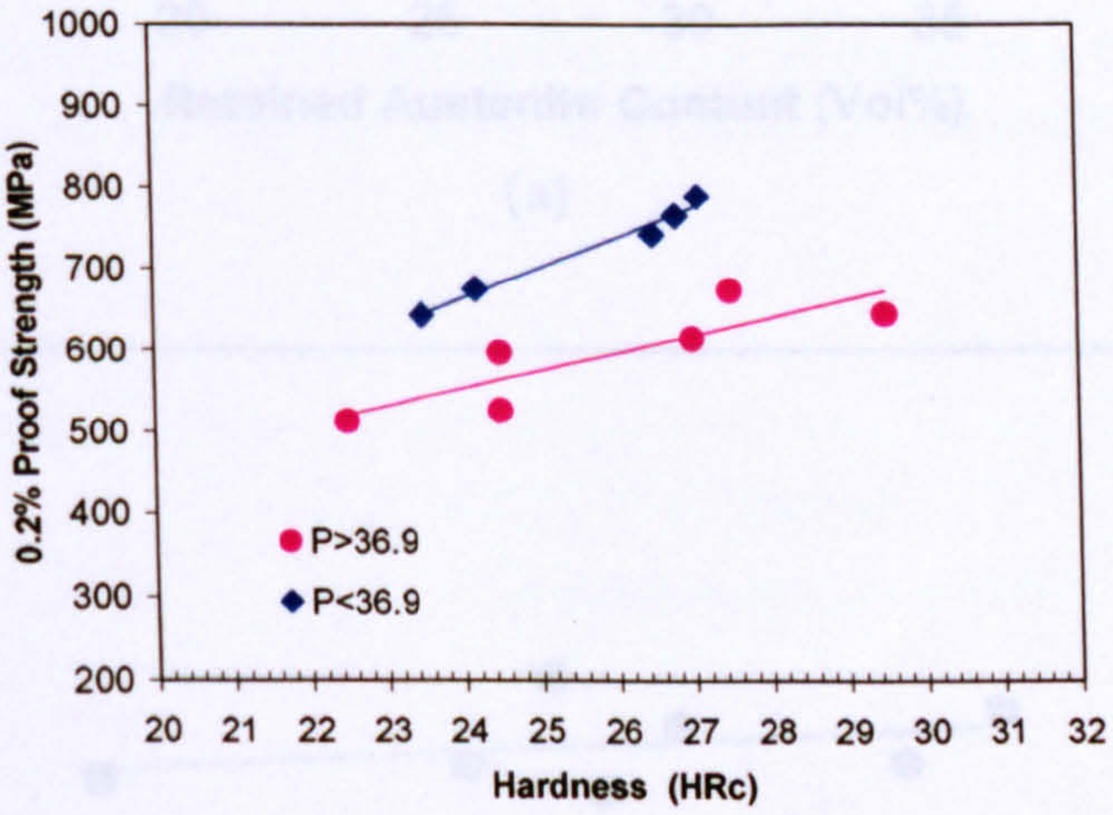

(a) Single tempering

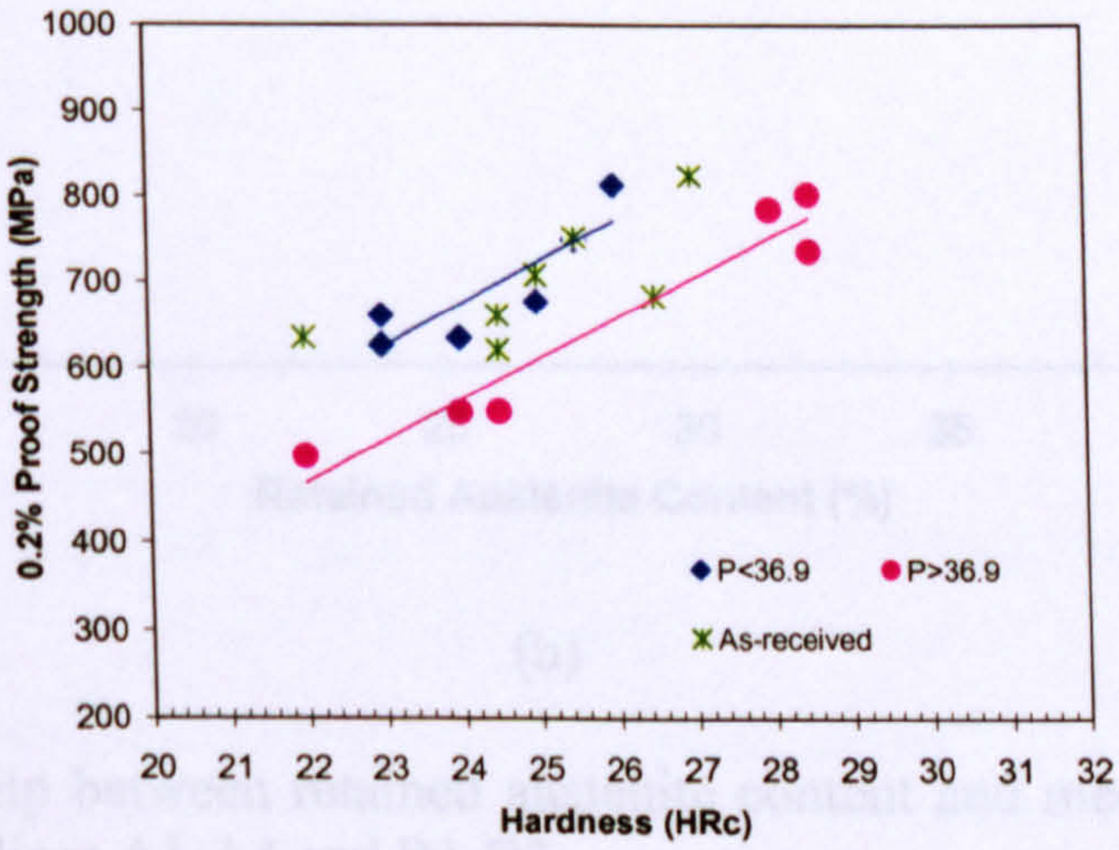

(b) Double tempering

Fig.6.15 Relationship between hardness and 0.2% proof strength for specimens after (a) single tempering (ST), and (b) double tempering (DT). P is the Hollomon-Jaffe tempering time-temperature parameter ($P = 273 + T(°C)) \times (40 + \log_{10} t(h)) \times 1000^{-1}$).

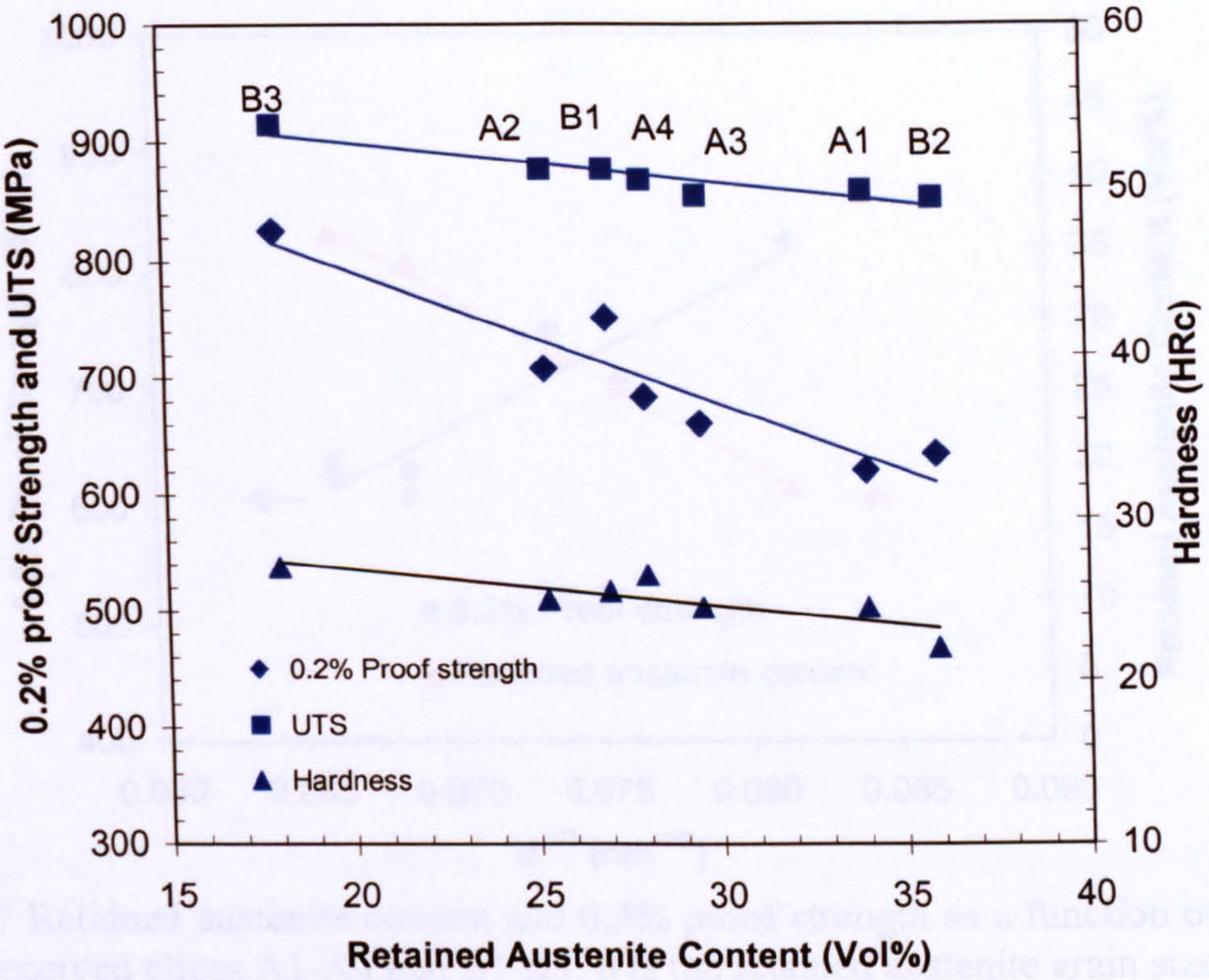

(a)

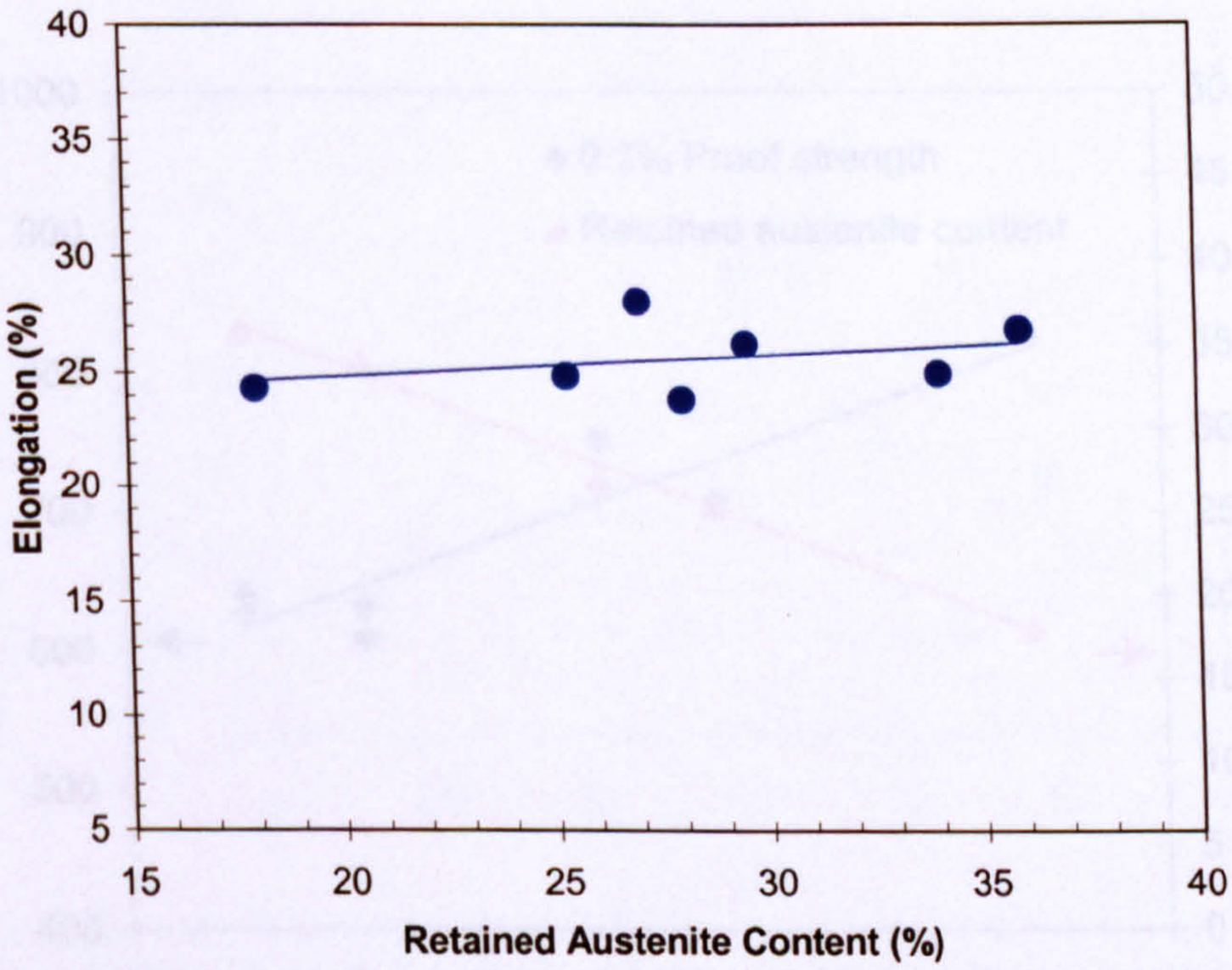

(b)

Fig.6.16 Relationship between retained austenite content and mechanical properties of the as-received slices A1-A4 and B1-B3.

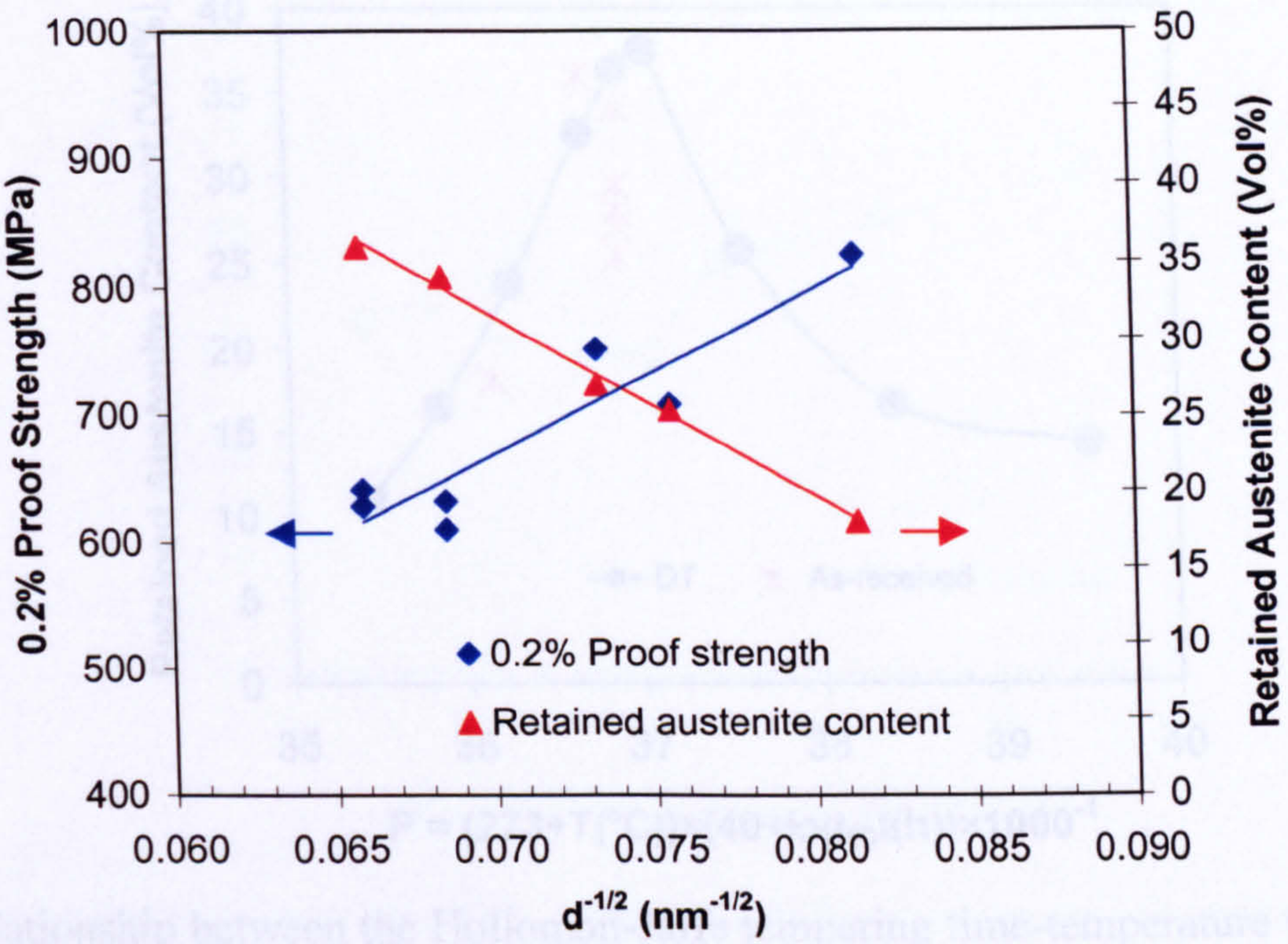

Fig.6.17 Retained austenite content and 0.2% proof strength as a function of $d^{-1/2}$ for the as-received clices A1-A4 and B1-B3. d is the retained austenite grain size.

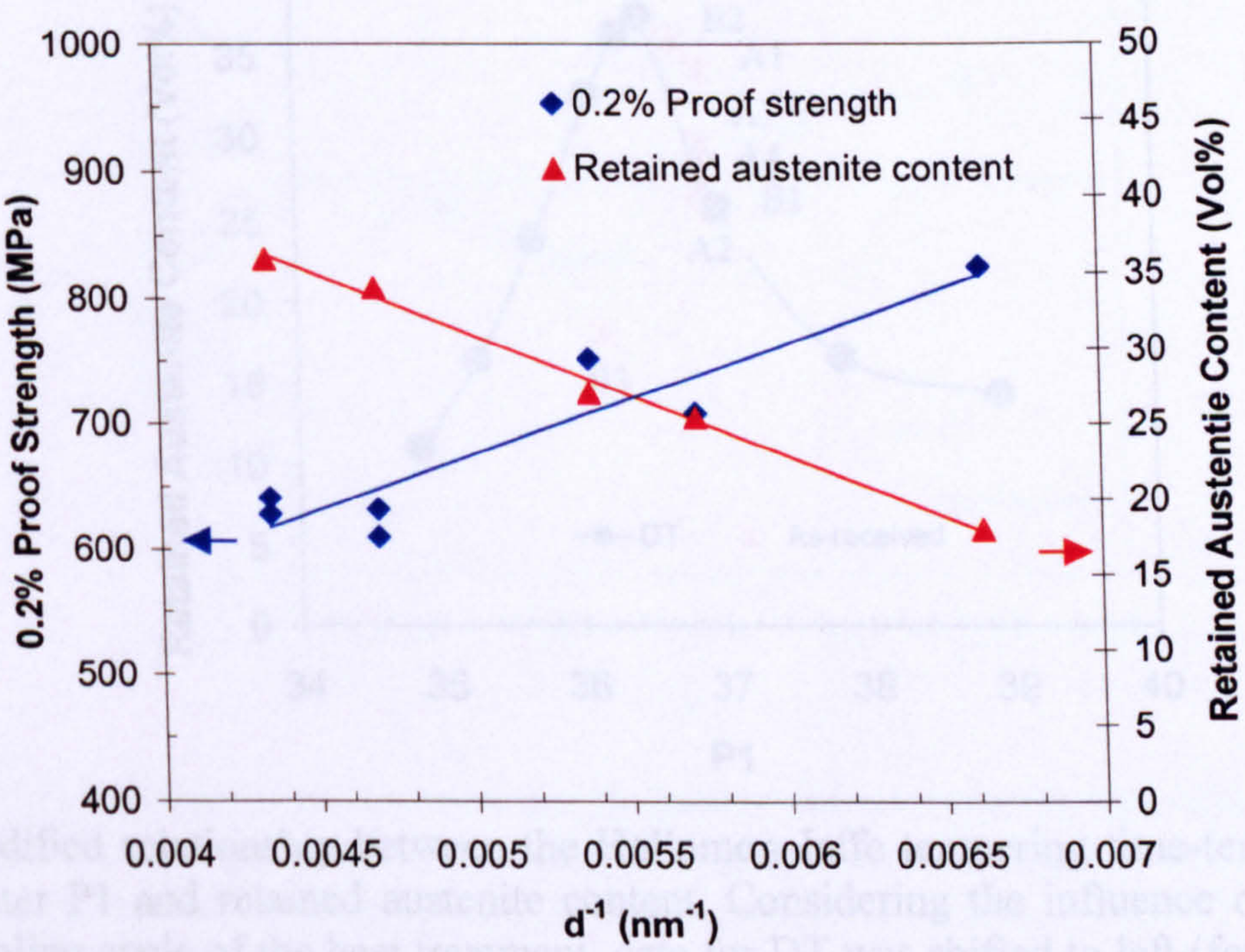

Fig.6.18 Retained austenite content and 0.2% proof strength as a function of d^{-1} for the as-received slices A1-A4 and B1-B3. d is the retained austenite grain size.

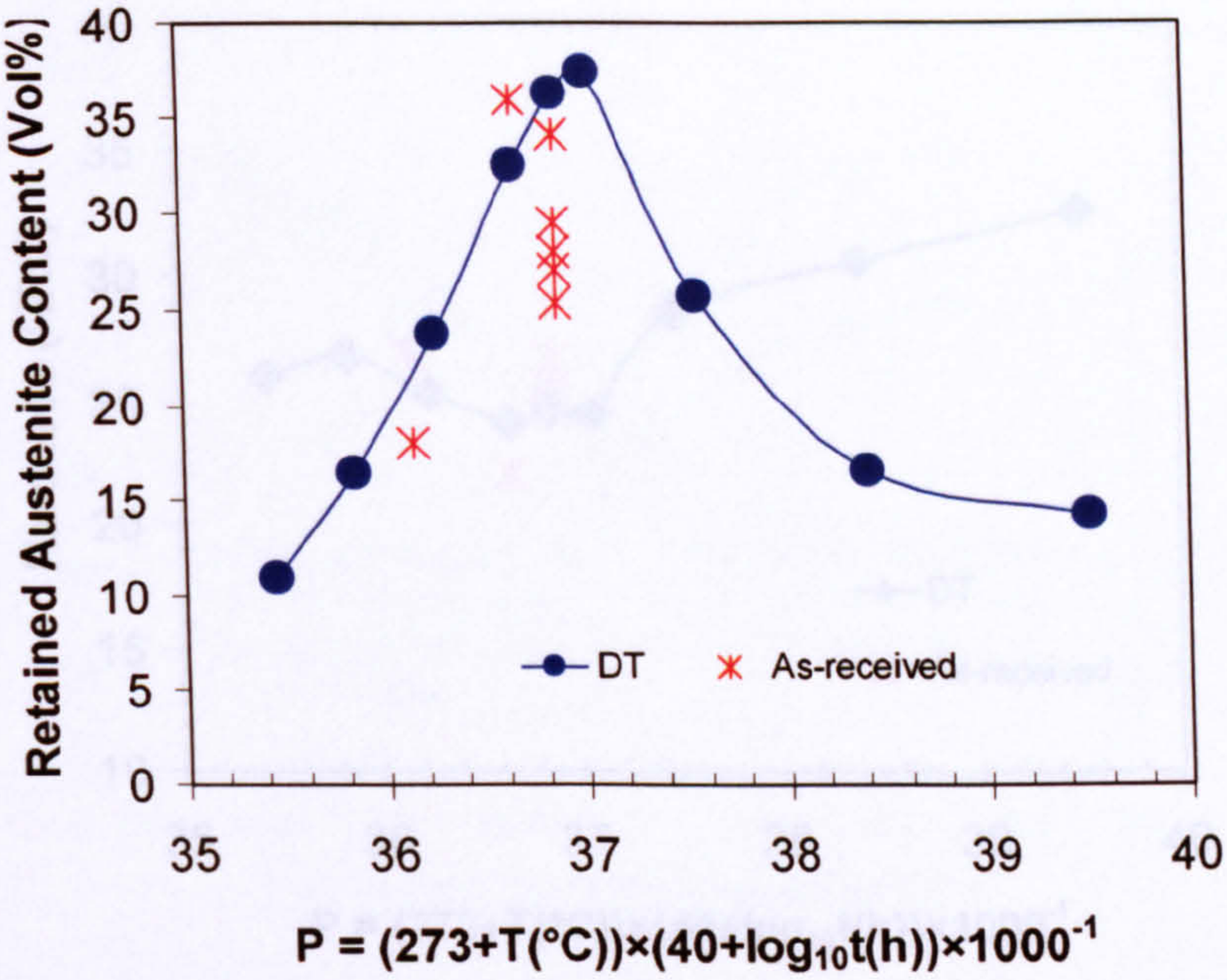

(a) Relationship between the Hollomon-Jaffe tempering time-temperature parameter P and retained austenite content. The parameter P given here did not consider the influence of heating and cooling cycle of the heat treatment.

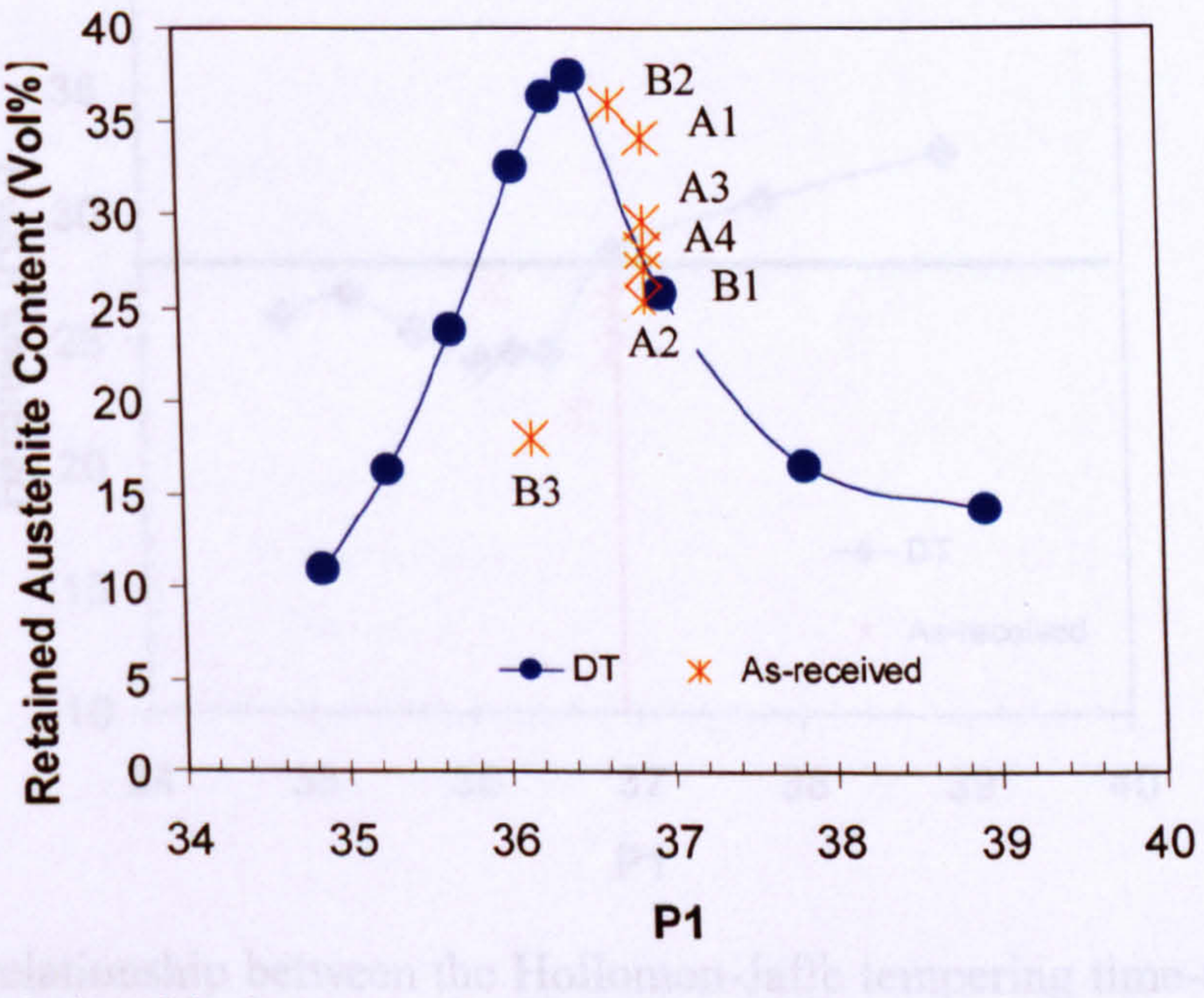

(b) Modified relationship between the Hollomon-Jaffe tempering time-temperature parameter P1 and retained austenite content. Considering the influence of heating and cooling cycle of the heat treatment, data for DT was shifted to left (for 14.5 °C) from the original position in (a).

Fig.6.19 Relating retained austenite content data for the laboratory re-heat treatment (DT) to retained austenite data for the industrial heat treatment. DT means laboratory double tempering.

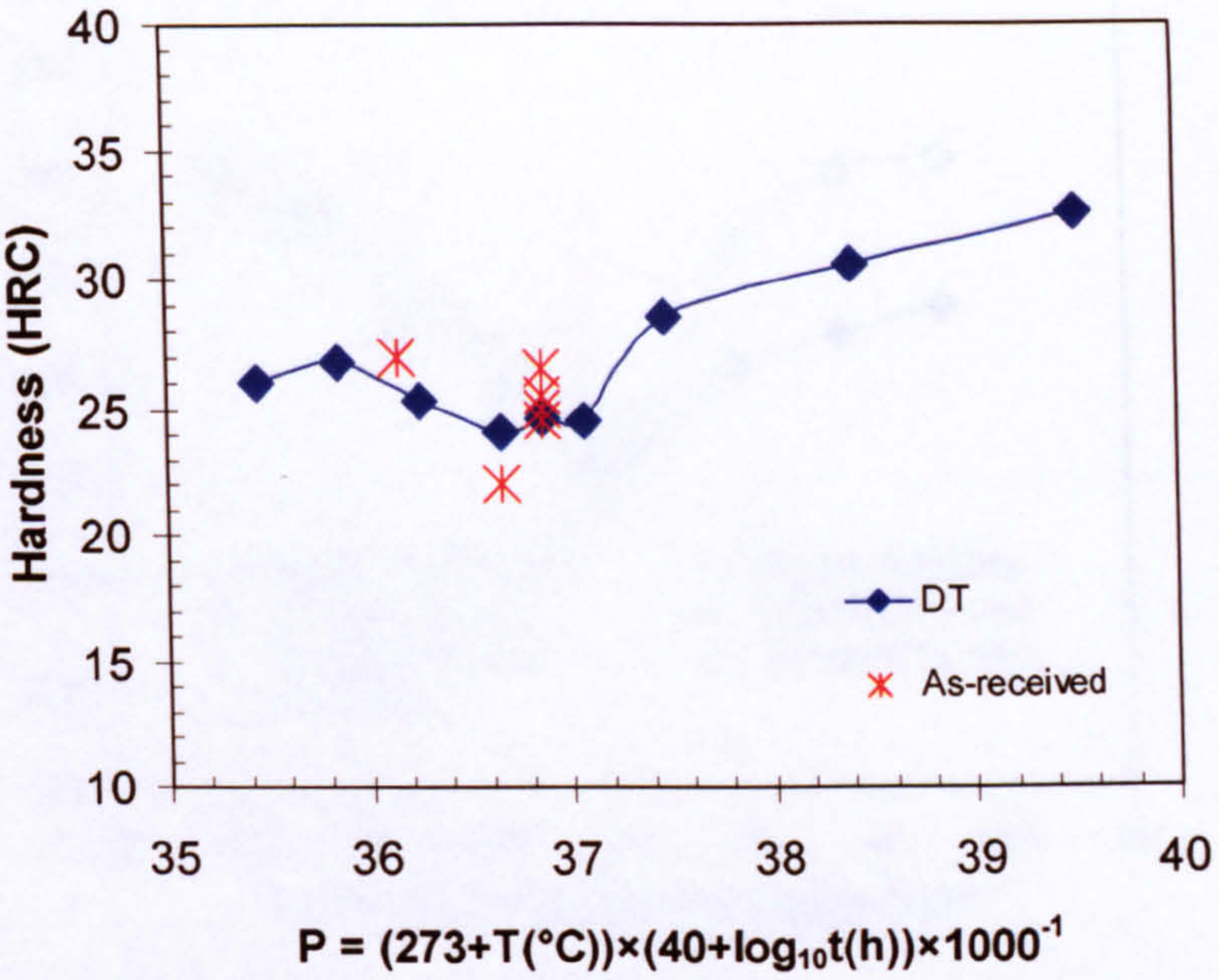

(a) Relationship between the Holloman-Jaffe tempering time-temperature parameter P and hardness. The parameter P given here did not consider the influence of heating and cooling cycle of the heat treatment.

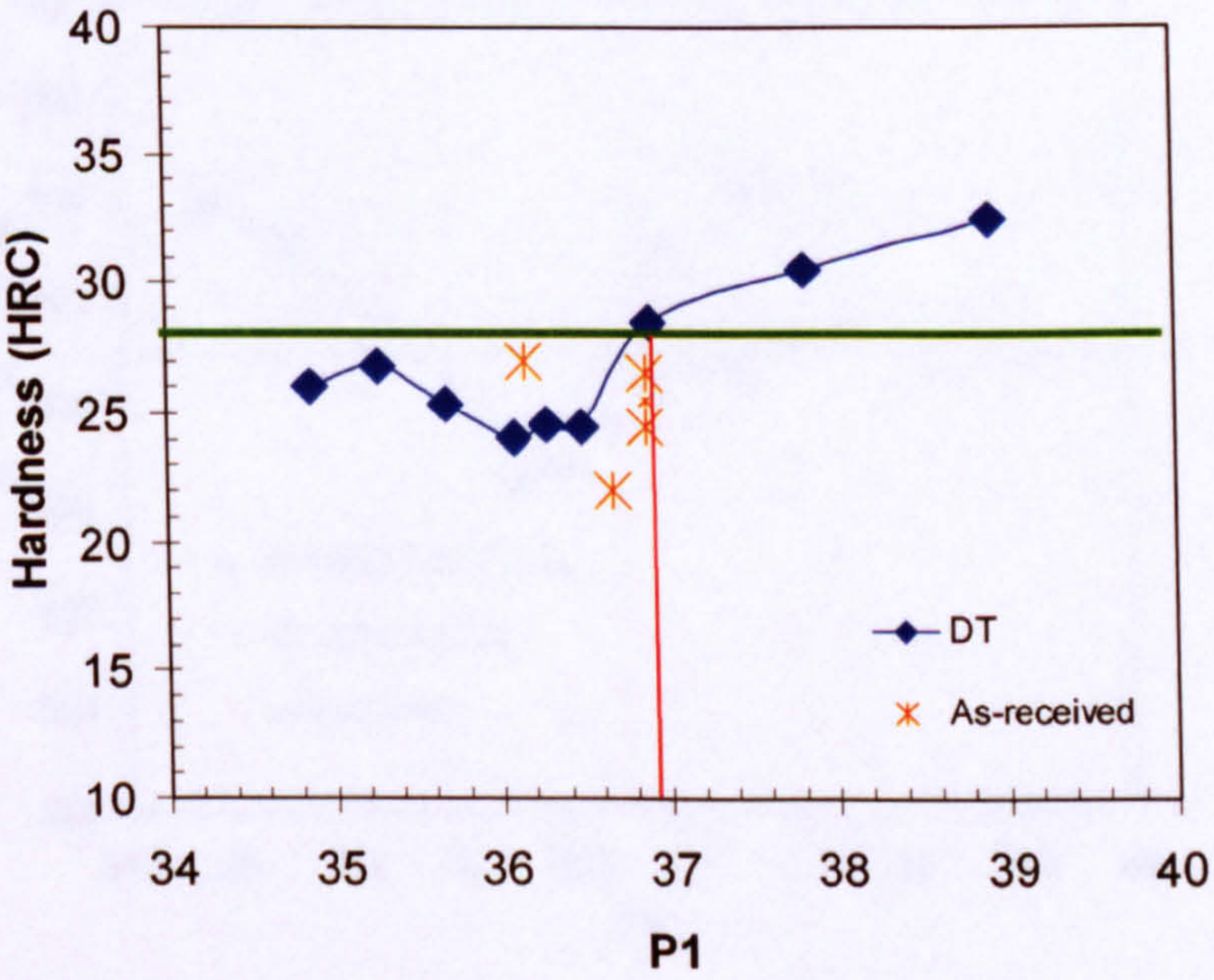

(b) Modified relationship between the Hollomon-Jaffe tempering time-temperature parameter P1 and hardness. Considering the influence of heating and cooling cycle of the heat treatment, data for the DT was shifted to left (for 14.5°C) from the original position in (a).

Fig.6.20 Relating hardness data for the laboratory re-heat treatment (DT) to hardness data for the industrial heat treatment. DT means laboratory double tempering. The green line represents the maximum hardness of 28 HRC. The red line indicated that to meet HRC$\leq$ 28, P1 should be on the left side of the red line, i.e. P1 $\leq$36.9.

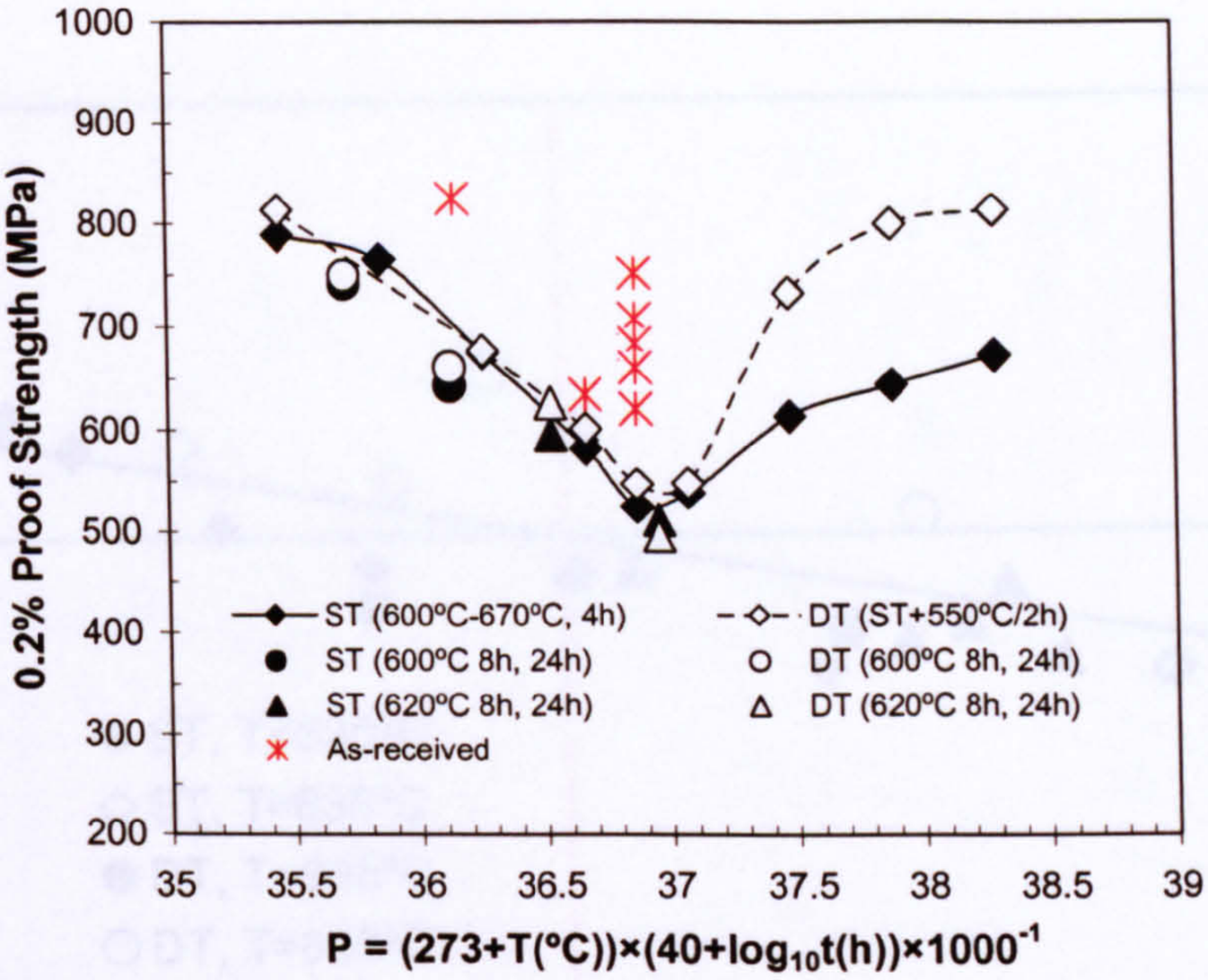

(a) Relationship between the Hollomon-Jaffe tempering time-temperature parameter P and 0.2% proof strength. The parameter P given here did not consider the influence of heating and cooling cycle of the heat treatment.

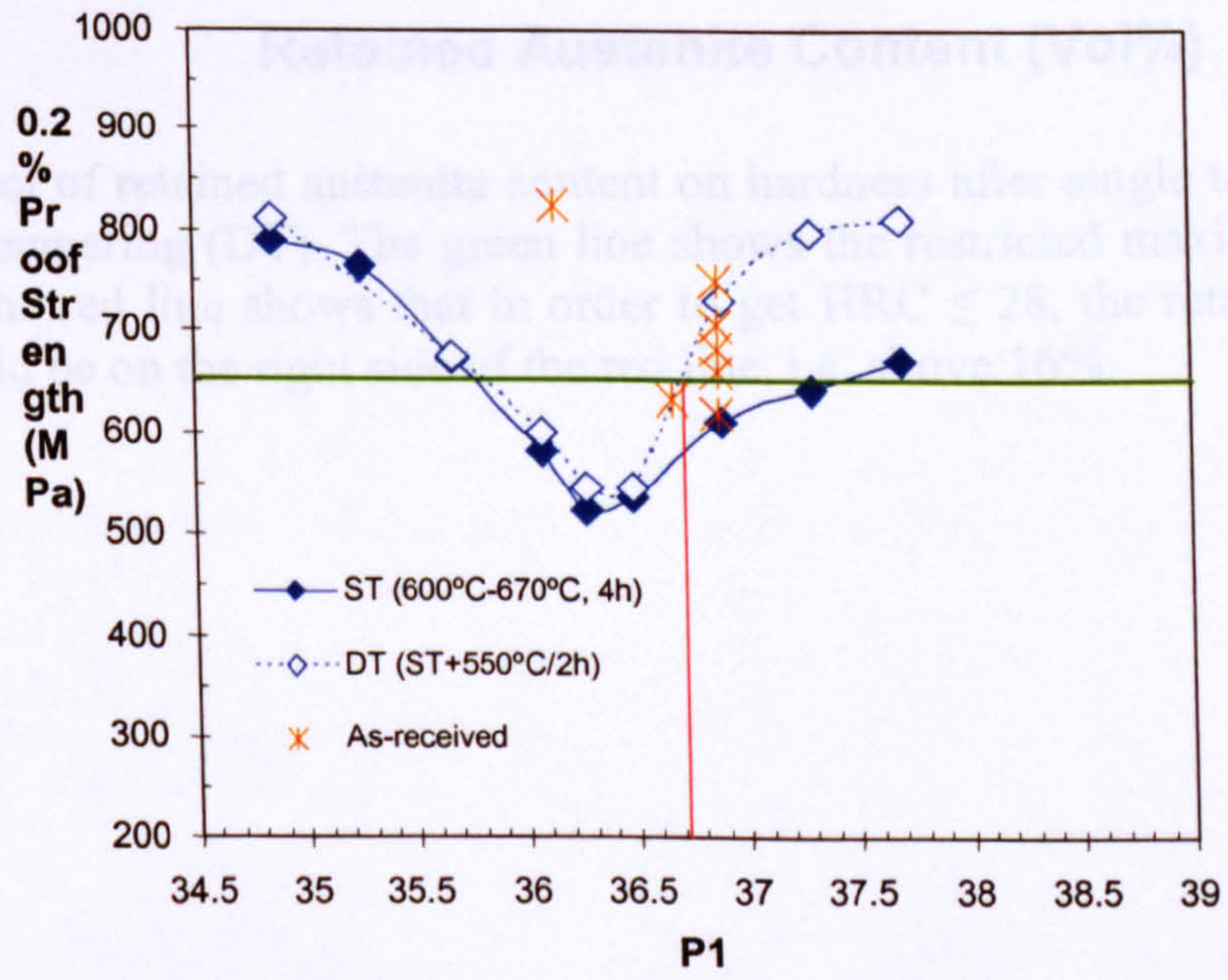

(b) Modified relationship between the Hollomon-Jaffe tempering time-temperature parameter P1 and 0.2% proof strength. Considering the influence of heating and cooling cycle of the heat treatment, data for the DT was shifted to left (for 14.5°C) from the original position in (a).

Fig.6.21 Relating 0.2% proof strength data for the laboratory re-heat treatment to 0.2% proof strength data for the industrial heat treatment. ST means single tempering and DT means double tempering. The green line represents the required minimum 0.2% proof strength of 655MPa. The red line indicated that to meet 0.2% proof strength $\geq$ 655MPa, P1 should be on the right side of the red line, i.e. P1 $\geq$ 36.7.

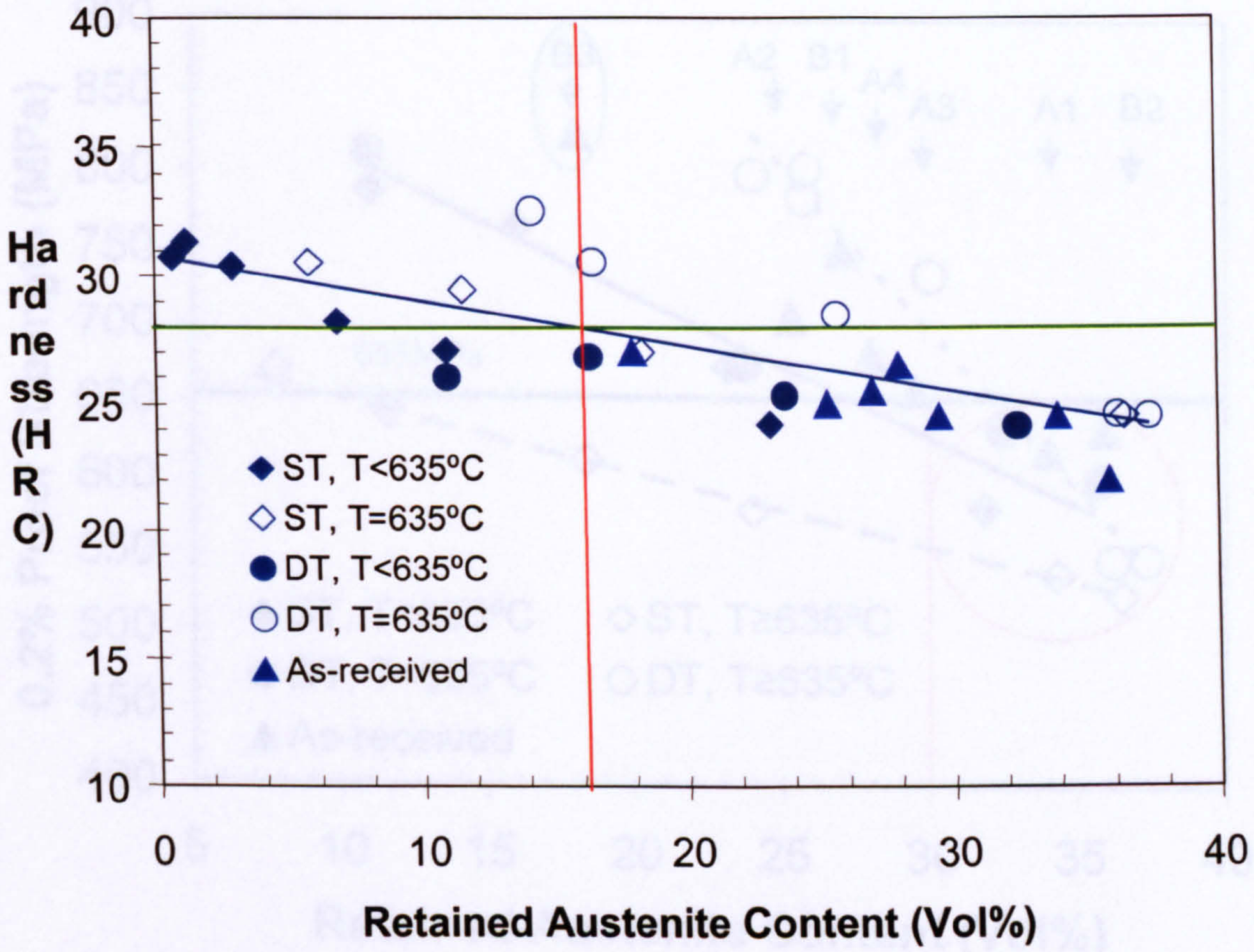

Fig.6.22 Effect of retained austenite content on hardness after single tempering (ST) and double tempering (DT). The green line shows the restricted maximum hardness of 28HRC; the red line shows that in order to get HRC $\leq$ 28, the retained austenite content should be on the right side of the red line, i.e. above 16%.

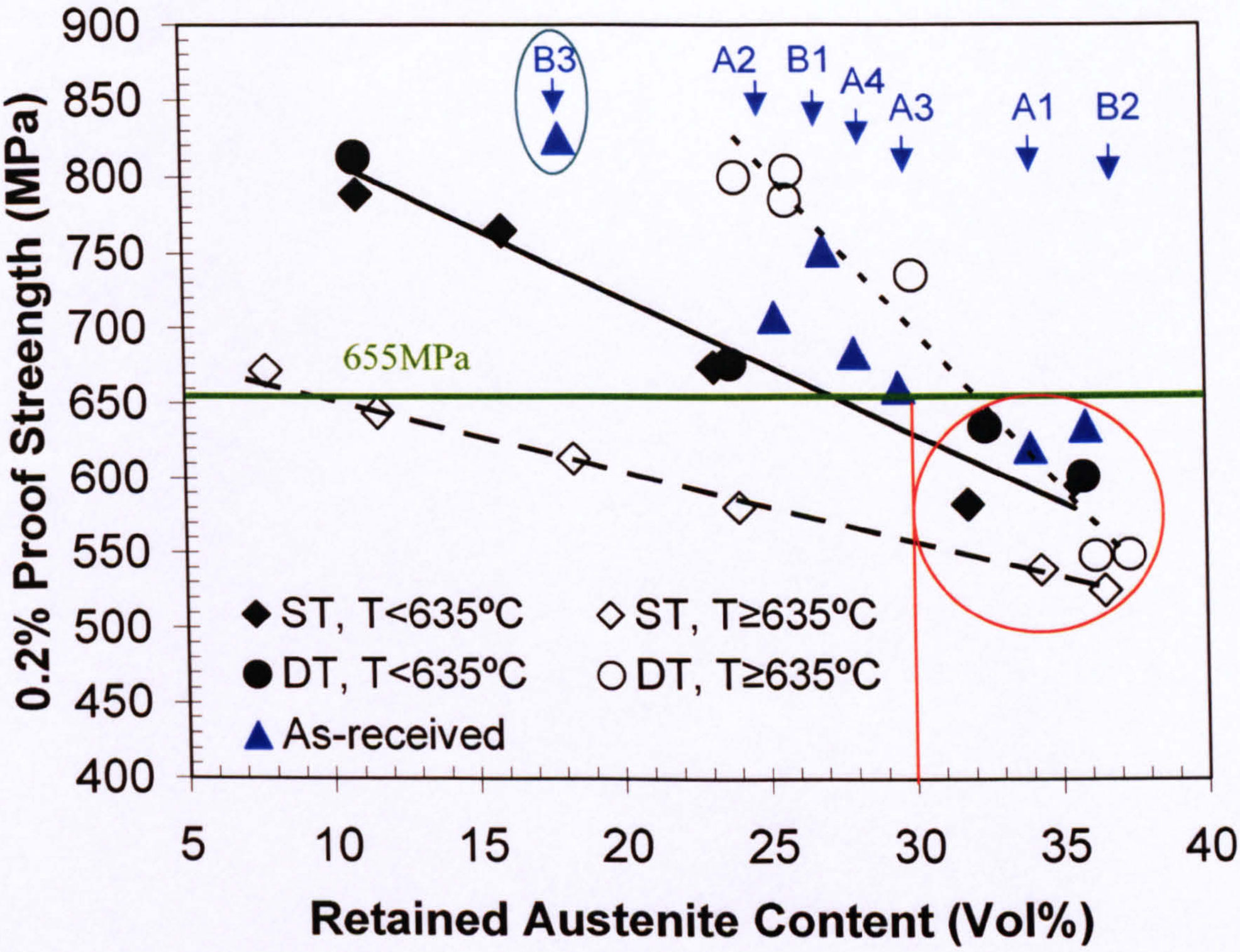

Fig.6.23 Effect of retained austenite content on 0.2% proof strength after single tempering (ST) and double tempering (DT). The green line shows the required minimum 655MPa 0.2% proof strength; the red line shows that in order to get 0.2% proof strength ≥ 655MP, after double tempering, the retained austenite content should on the left side of the red line, i.e. <30%. The red circle shows that in this austenite range, the steel failed to meet the required 655MPa 0.2% proof strength.